

ISSN 1521-3951  
Phys. Status Solidi B  
258 · No. 9 September  
(2021)

Check for updates

physica **p** status **s** solidi **s**<sup>b</sup>  
[www.pss-b.com](http://www.pss-b.com)

*basic solid state physics*

9  
2021



**SPECIAL ISSUE**

**Form and Function of Disorder**

Dedicated to David A. Drabold on the occasion of his 60th birthday

Edited by

Parthapratim Biswas  
Gang Chen  
Serge Nakhmanson  
Jianjun Dong

WILEY-VCH



**Editorial Advisory Board:**

Hiroshi Amano, *Nagoya University*  
 Ernst Bauer, *Arizona State University, Tempe, AZ*  
 Martin S. Brandt, *Technische Universität München*  
 Marília J. Caldas, *Universidade de São Paulo*  
 Zexian Cao, *Chinese Academy of Sciences, Beijing*  
 Andres Cuevas, *Australian National University, Canberra*  
 Peter Deák, *Universität Bremen*  
 David A. Drabold, *Ohio University, Athens, OH*  
 Wenhui Duan, *Tsinghua University, Beijing*  
 Alexander L. Efros, *Naval Research Laboratory, Washington, DC*  
 Claudia Felser, *Max-Planck-Institut für Chemische Physik fester Stoffe, Dresden*  
 Elvira Fortunato, *Universidade Nova de Lisboa*  
 Bernard Gil, *Université Montpellier-II*  
 Sebastian T. B. Gönnenwein, *Technische Universität Dresden*  
 Nicholas Grandjean, *École polytechnique fédérale de Lausanne*  
 J. Marty Gregg, *Queen's University Belfast*  
 Marius Grundmann, *Universität Leipzig*  
 Ken Haenen, *Universiteit Hasselt*  
 Axel Hoffmann, *Technische Universität Berlin*  
 Cheol Seong Hwang, *Seoul National University*  
 Chennupati Jagadish, *Australian National University, Canberra*  
 Michio Kondo, *National Institute of Advanced Industrial Science and Technology, Tsukuba*  
 Chun-Sing Lee, *City University of Hong Kong*  
 Shuit-Tong Lee, *Soochow University, Suzhou*  
 Günther Leising, *Technische Universität Graz*  
 Andrew R. Leitch, *The Nelson Mandela Metropolitan University, Port Elizabeth*  
 Zheng Liu, *Nanyang Technological University, Singapore*  
 Anita Lloyd-Spetz, *Linköping University*  
 Annick Loiseau, *Office National d'Etudes et de Recherches Aéropatiales, Châtillon*  
 Gerd O. Müller, *GOMMAconsult GmbH, Berlin*  
 Pablo Ordejón, *Centre d'Investigacions en Nanociència i Nanotecnologia, Barcelona*

S. N. Piramanayagam, *Nanyang Technological University, Singapore*  
 Pedro P. Prieto, *Universidad del Valle, Cali*  
 Uwe Rau, *Forschungszentrum Jülich*  
 John Robertson, *Cambridge University*  
 Ferdinand Scholz, *Universität Ulm*  
 Michael S. Shur, *Rensselaer Polytechnic Institute, Troy, NY*  
 G. Jeffrey Snyder, *Northwestern University, Evanston, IL*  
 James S. Speck, *University of California, Santa Barbara, CA*  
 Baoquan Sun, *Soochow University, Suzhou*  
 Tadeusz Suski, *Institute of High Pressure Physics of the Polish Academy of Sciences, Warsaw*  
 Maria C. Tamargo, *City College of New York, NY*  
 Christian Thomsen, *Technische Universität Berlin*  
 Hans-Rainer Trebin, *Universität Stuttgart*  
 Sergio E. Ulloa, *Ohio University, Athens, OH*  
 Xinqiang Wang, *Peking University, Beijing*  
 Rainer Waser, *Forschungszentrum Jülich*  
 John I. B. Wilson, *Heriot Watt University, Edinburgh*  
 Martin N. Wybourne, *Dartmouth College, Hanover, NH*  
 Deren Yang, *Zhejiang University, Hangzhou*  
 Włodzimierz Zawadzki, *Polish Academy of Sciences, Warsaw*  
 Di Zhang, *Shanghai Jiao Tong University*

<b>Editor-in-Chief:</b>	Stefan Hildebrandt
<b>Deputy Editor:</b>	Sabine Bahrs
<b>Editors:</b>	Dimitra Gkogkou Heike Höpcke Fangyuan Jiang Matt Lock Anke Osterland Nadezda Panarina Gaia Tomassello Huan Wang Marc Zastrow
<b>Administration:</b>	Julia Hübner Anja Habermann
<b>Production:</b>	Annkatrien Halbig
<b>Marketing:</b>	Karina Partisch
<b>Publishing Director:</b>	José Oliveira
<b>Editorial Office</b> <a href="mailto:pssb@wiley-vch.de">pssb@wiley-vch.de</a>	
<b>Manuscript Submission:</b> <a href="https://www.editorialmanager.com/pssb-journal">https://www.editorialmanager.com/pssb-journal</a>	

**Disclaimer:** The Publisher and Editors cannot be held responsible for errors or any consequences arising from the use of information contained in this journal; the views and opinions expressed do not necessarily reflect those of the Publisher and Editors, neither does the publication of advertisements constitute any endorsement by the Publisher and Editors of the products advertised.

For submission instructions, subscription, and all the latest information, visit <http://www.pss-b.com>

ISSN 1521-3951

© 2021 Wiley-VCH GmbH

# Form and Function of Disorder

Dedicated to Professor David A. Drabold on the occasion of his 60th birthday

Since Anderson's seminal paper "Absence of diffusion in certain random lattices" [*Phys. Rev.* 1958, 109, 1492] and its subsequent generalization by Mott to disordered electronic systems more than half a century ago, an extensive progress was made in the study of disordered condensed matter physics in the past decades. Mott's realization that electrons in disordered solids can be described by localized wave functions and the existence of mobility edges—the energy boundaries separating the extended and localized states—in the density of electronic states lead to the conclusion that a disordered solid can undergo a metal-insulator transition at zero temperature in the presence of sufficient disorder. The work of Mott and others opened up a new vista in condensed matter physics that resulted in remarkable achievements in the study of disorder and electronic correlations in solids in the decades to follow. The absence of translational symmetry in disordered solids implies that the cornerstone of the old solid state physics—the Bloch theorem—is no longer valid and so is the very concept of energy bands, on which the entire edifice of the  $k$ -space-based old theory is built upon. However, the vacuum was immediately filled by local approaches to electronic structure of solids in real space, where great emphasis was placed on bond order and density matrices. Of particular importance are the local approaches adopted by the French school under the leadership of Friedel, and Heine and others in the United Kingdom. These researchers have shown that the structure and electronic properties of noncrystalline solids can be effectively addressed from a chemist's bonding point of view by using advanced scattering theory and Green's functions. A description of electronic properties of disordered solids then naturally emerges from the local density of states and density matrices instead of energy bands. The importance of the density of states in studying disordered solids is perhaps most elegantly expressed by a theorem, due to Cyrot-Lackmann, that connects the moments of the local density of states to the topology of the local atomic environment of a network.

Viewing the subject in the light of its development over a period of the past five decades, it is evident that the field of disordered materials continues to present significant challenges and problems of outstanding interest to date. While the generic behavior of many disordered systems is now more or less understood, our knowledge and understanding of the properties of real disordered materials are still evolving and far from being complete. From a theoretical point of view, the main difficulty arises from the lack of knowledge of atomic positions in disordered solids. Diffraction experiments, while provide useful structural information through atomic pair-correlation functions, alone cannot determine the three-dimensional structure of



David A. Drabold

disordered solids via inversion of pair-correlation data. In view of this, the great majority of current theoretical methods for structural inference of disordered solids are limited to Monte Carlo and molecular-dynamics simulations, using a variety of total-energy functionals from classical and semi-classical to quantum-mechanical approaches. The last approach mostly relies on the density-functional theory (DFT), developed by Kohn and Sham in the sixties. While these approaches have been highly successful in determining structures and properties of many disordered solids, such as structural glasses, they are nonetheless limited to either small system sizes (via DFT calculations) or relatively simple amorphous/glassy solids for which accurate classical or semi-classical force-fields are available. The computational complexity associated with DFT calculations for large disordered systems continues to present a major obstacle in studying complex multi-component glasses of technological importance. Metallic glasses are classic examples in this category, the properties of which are often characterized by medium-range ordering on the nanometer length scale. Likewise, the interplay between magnetism and disorder remains largely an uncharted territory. While sophisticated theories of magnetism (for disordered materials) are already in place, a unified approach that simultaneously takes into account structural disorder and magnetic interactions between atoms is still missing.

In recent years, the emergence of a new breed of computational methods, which rely on experimental data and relevant structural information, brings fresh impetus to address the

DOI: 10.1002/pssb.202100366

problem of materials modeling from a data-centric point of view. These data-driven methods either construct a machine-learning (ML) potential, using a set of training data from a small number of high-quality DFT simulations and experiments, or generate realistic models of disordered solids by directly incorporating a set of experimental data and (approximate) total-energy functionals in an augmented solution space. Although it remains to be seen to what extent ML approaches can address some of the most difficult problems in materials modeling, involving multi-component glasses in a non-stoichiometric environment with associated length- and time-scale issues, there is a cautious optimism in the air that ML approaches can bring a paradigm shift in computational materials discovery. While we wait for the future to deliver a definitive answer, it is undoubtedly an exciting time for studying disordered materials when new data-driven methods and experimental results are reported regularly.

The current issue “Form and Function of Disorder” originates from our desire to honor and celebrate the sixtieth birthday of Professor David A. Drabold and his contributions in this field. Although we had to cancel the accompanying conference (May 30–31, 2020 in Athens, Ohio, USA), due to the outbreak of Covid19 pandemic in 2020, we are delighted that the special issue has finally come to fruition irrespective of the pandemic-related difficulties that we have experienced recently. The issue consists of twenty-two (22) articles of which fourteen (14) are directly related to the study of disordered systems/materials. The topics covered are diverse in nature and they range from applications of classical, quantum-mechanical, and ML approaches to glasses of technological interest, as well as generic understanding of disordered systems from geometric and topological points of view.

Following our discussion on emerging methods and their applications, and noting the limited availability of space, we briefly mention here a small number of articles that are thematically related to the title of the issue. The article by Konstantinou et al. ([pssb.202000416](#)) illustrates the use of machine-learning potentials with DFT accuracy in studying a phase-change material,  $\text{Sb}_2\text{Te}_3$ , whereas the application of a data-assisted FEAR approach is presented by Thapa et al. ([pssb.202000415](#)) to study an important metallic glassy system,  $\text{Cu}_{46}\text{-Zr}_{46}\text{-Al}_8$ .

The transition from glasses to crystalline structures is discussed by Sun et al. ([pssb.202000427](#)), where the authors examine the evolution of the interface between glassy and crystalline structures in lithium disilicate systems. The work by Dahal et al. ([pssb.202000447](#)) explores the origin of the fast sharp diffraction (FSDP) peak in amorphous silicon and provides some new insights on the relationship between the position of the FSDP in the wavevector space and a radial length scale in real space. Subedi et al. ([pssb.202000438](#)) discuss a fascinating approach to employ the Kubo-Greenwood formula for studying conductivity in amorphous solids that leads to identification of conductivity paths/regions in real space via construction of a conducting matrix. The article by Biswas ([pssb.202000610](#)) addresses the structure of energy landscapes of some highly degenerate model spin-glass systems. The author presents a new classification scheme by providing a two-dimensional description of high-dimensional potential-energy surfaces, showing the energy minima and barriers that separate them. The nature of atomic vibrations in models of vitreous silica has been studied by Shcheblanov et al. ([pssb.202000422](#)) with an emphasis on the low-frequency vibrational modes. The authors show that the modes are quasi-localized in nature and resulted from a mixing of non-localized and localized vibrational states. The latter have been found to exhibit both exponential and power-law decays. The article by Sadjadi et al. ([pssb.202000555](#)), on isostatic material frameworks, provides a brilliant discussion on how topological and geometric constraints in random networks can play a decisive role in understanding some generic properties of real disordered materials. The remaining articles are equally fascinating and enjoyable to read.

We thank the authors for delivering a high standard of scientific content in their articles for this special issue. Finally, we are grateful to the editorial team of *physica status solidi (b)*, and in particular Dr. Sabine Bahrs, who worked alongside us for the past year to make this issue finally appear in print.

Parthapratim Biswas  
Gang Chen  
Serge Nakhmanson  
Jianjun Dong

July 27, 2021





**Parthapratim Biswas** is Professor of Physics in the University of Southern Mississippi (Hattiesburg, MS, USA). He obtained his Ph.D. from S. N. Bose National Center for Basic Sciences in Kolkata (India) and did his postdoctoral research in the Netherlands, UK, USA, and Germany. The primary area of his research interest is electronic-structure theory of disordered solids. His current research involves development of information-based inverse and hybrid approaches to material structure determination, using geometric, topological, and experimental information.



**Gang Chen** received his Ph.D. in Materials Science and Engineering at Lehigh University (Bethlehem, PA, USA) in 2004. He is currently an Associate Professor in the Department of Physics and Astronomy at Ohio University (USA). His research is focused on fundamental understanding of the structure–property relations in amorphous electronic materials.



**Serge Nakhmanson's** research interests involve modeling of functional materials properties using quantum-mechanical and finite-element based computational tools. He is one of the original creators and a developer of the 'Ferret' code for simulating ferroic functionalities at mesoscale. Specific areas of interest include novel multifunctional materials and predicting their behavior; influence of shape, size and orientation on the material properties, as well as occasional excursions into "soft" ferroelectrics, such as polymers, oligomers and molecular crystals.



**Jianjun (JJ) Dong** is a Professor of Physics at Auburn University (Auburn, AL, USA). He received his Ph.D. degree from Ohio University in 1998, under the supervision of Prof. David Drabold. His research focuses on theories and simulations of real materials. A current research thrust is to develop new theories and computational methodologies to understand heat transfer properties of materials, such as materials at extreme low or high temperatures, very anharmonic crystals, disordered/glassy solids, and material interfaces.

## David Drabold Festschrift tribute by Ronald L. Cappelletti

It is with gratitude and affection and a sense of privilege that I pen these few words to celebrate my friend and colleague David Drabold on the occasion of his sixtieth birthday. I was on the team that interviewed David in 1993 to hire him as an Assistant Professor at Ohio University. Doing experimental work on amorphous materials, the prospect of having a faculty colleague doing state-of-the art complementary computational work was certainly intriguing. But little did I know that that interview would blossom into a deep and warm friendship of nearly thirty years with this kind, generous person over shared interests in Late Antiquity (Theodoric, Belisarius), Roman coinage, other historical areas, and family. (A shameless collector, David ever manages to impart enthusiasm about his latest acquisitions, projects and travels.) David, of course, proved himself to be a stellar addition to Ohio's faculty, rapidly rising through the ranks to

become a Distinguished Professor and mentoring a host of successful graduate students and post-docs through his well-funded research who continue to hold him in affection and esteem. It is no secret to all here that David's stature as an international leader in the field of computational amorphous materials is driven by a curious and original mind with keen insights penetrating brilliantly into the meaning and methods in this ever difficult area of physics. This very collection of articles on *Form and Function of Disorder* attests to his sustained accomplishments. I hope you will all join me in wishing David many more years of productive work in science (and, yes, avid collecting!)

Ronald L. Cappelletti  
Physicist,  
National Institute of Standards and Technology, USA

---

DOI: 10.1002/pssb.202100372



## David Drabold Festschrift tribute by Stephen Elliott

David is that ultimate ‘*rara avis*’ – a world-class scientist, but also a numismatist having a museum-quality collection of ancient coins and with a detailed knowledge of Anglo-Saxon England. He must be completely unique. He is also a great Anglophile, in love with not just its (ancient) history but also its quirky customs. I have much enjoyed hosting him in Cambridge on the numerous visits that he has made to the UK over the years to collaborate, often in association with my College there, Trinity, at which he has been a Visiting Fellow, as well as at Clare Hall. I think that, in a previous life, David must have been an Oxbridge don, for he always fits in so seamlessly with the arcane world of College life, with its strange rituals (Latin graces before and after High Table Dinner, the wearing of bat-like black gowns for such Formal Hall occasions *etc.*). Perhaps a sign of his love of Cambridge is that the image heading his publication list on his website is a photograph of Trinity Avenue leading down to the College, with a distant view of King’s College Chapel on the right.

David is well-known, of course, for his world-leading computational studies of the atomic and electronic structure of disordered materials, notably amorphous silicon, but also chalcogenide glasses, as well as oxide and metallic glasses.

He has pioneered a number of theoretical approaches in this field, often given wonderfully striking acronyms as names, e.g. FEAR (‘force-enhanced atomic refinement’), and its progeny, AIFEAR (‘*ab initio* force-enhanced atomic refinement’). His papers are always models of clarity, physical insight and timeliness. I have had the pleasure and honour of collaborating with David on a number of topics over the years, and we have published 16 papers together, the first appearing nearly 20 years ago, in 2001. This collaboration has continued, I am glad to say, to the present day. As I write, a joint paper (again on amorphous silicon!) is under consideration for publication.

It is a very great shame that, due to the Covid pandemic, it was not possible for a group of his many friends, co-workers and collaborators to gather together in May 2020, as planned, to mark his 60th birthday, and to honour his very many scientific achievements at a Festschrift meeting in Athens, Ohio. However, I am very pleased to be able to contribute this brief encomium, as well as a scientific paper, to his Festschrift Special Issue to be published by *physica status solidi*.

Happy birthday, Dave!  
Stephen Elliott

# CO<sub>2</sub> Conversion on Ligand-Protected Au<sub>25</sub> Nanoparticle: The Role of Structural Inhomogeneity in the Promotion of the Electrocatalytic Process

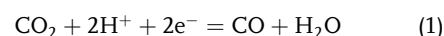
Dominic R. Alfonso

Dedicated to Professor David A. Drabold on the occasion of his 60th birthday

The possibility of direct integration with renewable electric sources adds more potential to the electrochemical method as a promising route for CO<sub>2</sub> conversion. Previous experimental breakthrough reveals that Au<sub>25</sub>(SR)<sub>18</sub><sup>−</sup> nanoclusters having 25 gold atoms and 18 protecting thiolate ligands can be utilized as catalysts for CO<sub>2</sub> electroreduction to CO. The reason for its observed activity toward CO<sub>2</sub> conversion is of fundamental importance that needs to be explained. Herein, the progress made in the first-principles mechanistic studies of the reduction process is described. Contrary to long-standing assumptions, the fully ligand protected version is not the active catalyst because of the weak adsorption of the relevant intermediates. Instead, the calculations based on computational hydrogen electrode method reveal that the reduction process is facilitated by a thermodynamically stable yet structurally inhomogeneous active site. This reaction center binds the intermediates in such a way that the process can occur at low overpotentials. The results point to the role of inhomogeneity in the surface region for this class of materials as a critical factor promoting the CO<sub>2</sub> conversion process under electrochemical environment.

The reduction of the CO<sub>2</sub> supplied in the cathode is facilitated by the transfer of proton and electron pairs from the electrolyte. If the cell is coupled with electricity generated from renewable sources such as wind, geothermal, solar, or hydroelectric, the electrochemical reactions can be realized in a carbon-neutral manner.<sup>[10–12]</sup>

The efficiency of this technology, however, is challenged at the key stages of the device operation. In particular, a catalytic material is required to enhance the selectivity in the cathode where CO<sub>2</sub> is reduced, for example, to high value product CO



Though the two-electron pathway has a relatively low redox potential of about −0.10 V versus the standard hydrogen electron (SHE) potential, the kinetics of the CO<sub>2</sub> reduction reaction (CO<sub>2</sub>RR) is contaminated by the simultaneous hydrogen evolution reaction (HER) occurring in the aqueous electrolytes

occurring in the aqueous electrolytes




To further nudge this conversion technology into practice, it is desirable to identify a catalytic cathode material that would yield significant improvements in terms of product selectivity, catalytic stability, and current density without compromising energetic efficiencies.<sup>[13]</sup> The utilization of gold for CO<sub>2</sub>RR began from the early experiments by Hori and co-workers where bulk gold metal electrodes were systematically investigated.<sup>[2,14]</sup> It was found that Au electrodes have high selectivity for CO production and can successfully reduce CO<sub>2</sub> with varying ratio of CO and H<sub>2</sub> product mixtures depending on the applied voltage. By tailoring physical structures to maximize surface area and undercoordinated binding sites, subsequent studies show that the performance can be improved achieving overpotentials below −0.30 V (for brevity, all applied potential indicated from hereon are relative to SHE) at a current density above 0.2 mA cm<sup>−2</sup>.<sup>[15–18]</sup>

Synthesis of gold clusters protected by thiolate ligands is a strategy that has been used to identify electrocatalysts effective for CO<sub>2</sub>RR. These atomically precise systems which contain

## 1. Introduction

Decreasing atmospheric CO<sub>2</sub> concentration via electrochemical reduction of the greenhouse gas under ambient temperature and pressure has gained considerable attention. Compared to geological sequestration, this artificial photosynthesis which mimics the process in green plants can also potentially convert CO<sub>2</sub> gas into CO, formic acid, methane, ethylene, or methanol providing sustainable source of feedstocks for the chemical and fuel sectors.<sup>[1–9]</sup> The typical device consists of three fundamental components (**Figure 1**), namely, the cathode and anode electrodes plus the electrolytes. Water is supplied into the anode compartment where the molecules are oxidized into individual ions that are subsequently incorporated into the electrolyte.

Dr. D. R. Alfonso  
 National Energy Technology Laboratory  
 US Department of Energy  
 Pittsburgh, Pennsylvania 15236, USA  
 E-mail: alfonso@netl.doe.gov

 The ORCID identification number(s) for the author(s) of this article can be found under <https://doi.org/10.1002/pssb.202000387>.

DOI: 10.1002/pssb.202000387



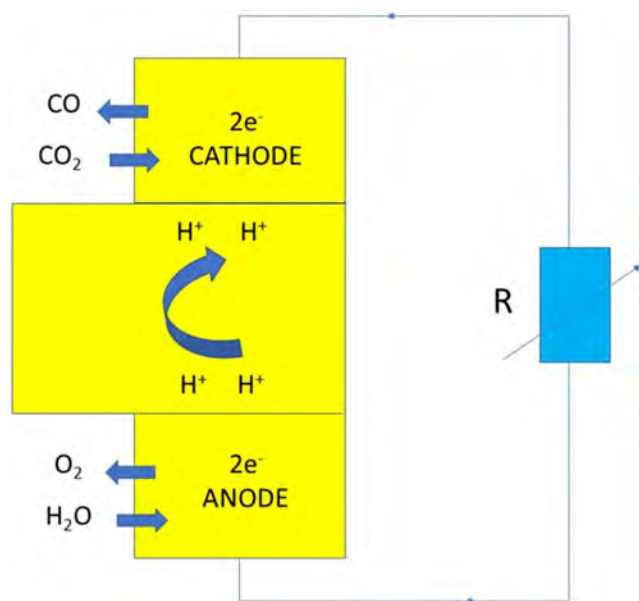


**Figure 1.** Operating stages of CO<sub>2</sub> reduction cell: 1) H<sub>2</sub>O splitting at the anode resulting into the incorporation of proton into the electrolyte accompanied by the transfer of charge from the anode to the cathode; 2) proton migration into the electrolyte; and 3) CO<sub>2</sub> reduction at the cathode.

10–100 metal atoms in the underlying inorganic core are often called nanoclusters to differentiate them from conventional Au nanoparticles.<sup>[19–23]</sup> The selective bonds formed by the ligand stabilizers with the surface atoms impart structural robustness and advances in synthetic methods have made it possible to achieve materials with molecular purity.<sup>[24,25]</sup> Since their size spans the ultrasmall regime (<3 nm in diameter), intrinsically unique and size-specific behavior were observed that are different from either atomically dispersed gold species or their traditional nanoparticle counterparts. For example, they exhibit molecular-like electronic structures since the energy levels become quantized.<sup>[26,27]</sup> This allows the studies of quantum confinement effects in the regime that spans the molecule-bulk transition region.

Moreover, these nanoclusters are more chemically active unlike their bulk gold counterpart. For example, they are found to be active in the oxidation of styrene, CO, and sulfur-containing compounds.<sup>[28–31]</sup> In particular, they have emerged as a promising catalyst for CO<sub>2</sub> mitigation under mild conditions. In 2012, Kauffman and co-workers reported selective CO<sub>2</sub> reduction to CO at an onset potential of  $-0.193\text{ V}^{[17]}$  which makes the conversion process energetically efficient. The reduction involves the use of negatively charged ligand protected Au<sub>25</sub>(SC<sub>2</sub>H<sub>4</sub>Ph)<sub>18</sub><sup>−</sup> nanocluster which catalyzed the two-electron conversion of CO<sub>2</sub> to CO in aqueous solution. The process on this nanocluster consisting of an icosahedral Au<sub>13</sub> core surrounded by six [−S−Au−S−Au−S] oligomers was observed to be at near 100% Faradaic efficiency at  $-1.0\text{ V}^{[32–34]}$ , a rate significantly higher than bulk Au.<sup>[17]</sup> Proof of concept studies using commercially available renewable energy resources yields stable operation and turn over reaction numbers during multiday experiments.<sup>[35]</sup> Nanocluster stability was established as a majority of the materials retain size and morphology after long-term electrocatalysis

experiments. A follow-up study in 2014 by Kauffman et al. revealed that the charged state and the electrochemical catalytic activity are strongly correlated<sup>[36,37]</sup> in that the neutral and cationic versions led to the reduction of the reactivity.

Cu-based materials have been widely investigated for CO<sub>2</sub> reduction but the main product at low overpotentials is either hydrocarbon or alcohol and not CO. Unlike the ligand protected Au<sub>25</sub> nanocluster, a higher voltage is required for CO production with a reported value of  $\approx -1\text{ V}$  for the bulk version.<sup>[38]</sup> Even a Cu nanostructured counterpart retains this feature, an example of which is the ligand protected Cu<sub>32</sub>H<sub>20</sub>L<sub>2</sub> (L = dithiophosphate).<sup>[39]</sup> The reported dominant product in this case is HCOOH at  $-0.3$  to  $-0.4\text{ V}$  with a Faradaic efficiency of 83–89%, whereas H<sub>2</sub> evolution is the dominant process for  $> -0.5\text{ V}$ . This trend is also confirmed by their complementary density functional theory (DFT) calculations.

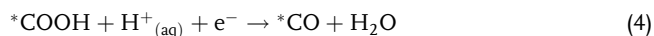
Theoretical studies of catalytically relevant phenomena under electrochemical environment have advanced enormously in the last decade due to 1) the use of a periodic representation of the electrode surface, 2) advances in algorithms that describe the electrode potential effects on the elementary reaction free energies and activation barriers, and 3) the development of solvation models to realistically account for the influence of the electrolytes.<sup>[40–46]</sup> The overall computational framework is to a large extent exploits the thermochemical relationships to correlate the chemical potential of electrons, ions, or electron-ion pairs in terms of neutral species which can be quantified readily through the first-principles calculations. The direct use of standard DFT for nonelectrochemical catalytic reactions imparts predictive quality to the simulation. With well-defined and practical models for the nanoclusters, hard to measure reaction mechanisms under realistic conditions and relevant observables such as the limiting potential, structures, and bonding of intermediate species can be obtained.

The establishment of the relationship between atomic level physical and chemical properties of the catalyst with observed chemical behavior is arguably the primary driver for heterogeneous catalytic research. Toward this goal, we describe in this account our theoretical efforts to achieve a fundamental understanding of CO<sub>2</sub>RR in ligand protected Au<sub>25</sub> nanocluster, to put the subject in context, to indicate what is known and what remains to be done. An essential element of computational catalysis is the identification of the nature of the active sites. In this article, we show how the atomic disorder at the surface boundaries can be correlated to the observed electrochemical catalytic activity. We also show here how the predicted atomic level insights can aid in the understanding of the observed activity Au<sub>25</sub> nanocluster with different charge states.

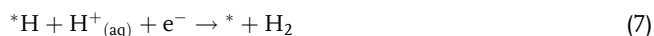
## 2. Aspects of Theoretical Modeling

### 2.1. Mechanism Overview

We adopted the following reaction mechanism scheme to identify the fundamental aspects of CO<sub>2</sub> conversion and the competing H<sub>2</sub> production. For CO<sub>2</sub> reduction, the 2e<sup>−</sup> CO<sub>2</sub>RR mechanism was assumed, i.e., the following three-step mechanism represented by<sup>[41,47]</sup>



It is essential to consider the competing HER reaction against CO<sub>2</sub>RR to properly evaluate catalyst, because the HER reaction can significantly impede the CO<sub>2</sub>RR activity of the desired reaction. The 2e<sup>−</sup> pathway producing H<sub>2</sub> is represented by<sup>[15,48]</sup>



The lone “\*” represents the active site in the nanoclusters. The symbols \*COOH, \*CO, and \*H refer to the nanocluster with adsorbed intermediates. For CO<sub>2</sub>RR, the mechanism involves two reduction states (Equation 3 and 4) each of which results to the addition of proton and electron pair. COOH first forms on the active site and it then undergoes a reduction reaction to form \*CO and H<sub>2</sub>O. In the last step (Equation 5), CO is released from the cluster. For HER, \*H first forms on the active site (Equation 6) followed by subsequent reduction reaction to yield the release of H<sub>2(g)</sub> (Equation 7).

HCOOH formation is not considered since the Au<sub>25</sub> nanocluster considered here is selective for CO. HCOOH formation is further ruled out due to the absence of methanol product. It should be noted that HCOOH is one of the precursor species for the alcohol formation.<sup>[49]</sup>

## 2.2. Density Functional Theory

Electronic structure calculations were performed within the framework of DFT as implemented in the Vienna ab initio simulation package (VASP), a plane wave pseudopotential code.<sup>[50]</sup> Within the generalized gradient approximation (GGA), the formulation of Perdew, Burke, and Enzerhof (PBE) was used to calculate the exchange-correlation energy.<sup>[51]</sup> The projector-augmented wave (PAW) method was used for core–valence treatment.<sup>[52]</sup> The Kohn–Sham one-electron valence eigenstates were expanded in terms of plane-wave basis sets with a cutoff energy of 600 eV. The ionic and electronic convergence limit was set to 0.03 eV Å<sup>−1</sup> and 1 × 10<sup>−5</sup> eV, respectively, whereas the Methfessel–Paxton scheme<sup>[53]</sup> was utilized having a smearing width of 0.1 eV. A 3D periodic cubic box with dimensions of 30 Å was inserted in the simulation models of the nanocluster to exclude periodic interaction between them. The sampling of the Brillouin zone was conducted with a *Γ*-point *k*-point mesh.

## 2.3. Computational Hydrogen Electrode Scheme

Solvent corrections were taken into account using the Poisson–Boltzmann implicit solvent model implemented in VASP by Matthew and Hennig.<sup>[54]</sup> The background dielectric constant of water is ε<sub>b</sub> = 80 with a cutoff charge density of 0.0025 Å<sup>−3</sup>. The cavitation energies were evaluated using a surface tension parameter of 0.525 meV Å<sup>−2</sup>. Free energy corrections for adsorbed species were applied assuming harmonic degrees of

freedom and those for gaseous species were quantified in the ideal gas limit. The free energy for liquid species was evaluated by applying free energy corrections to their room temperature solvated state. The voltage-dependent electrochemical free energy pathways were constructed from the computational hydrogen electrode (CHE) approach.<sup>[40]</sup> This framework takes advantage of the equivalence of the free energies of the proton–electron pair (G<sub>H<sup>+</sup>+e<sup>−</sup></sub>) and hydrogen gas ( $\frac{1}{2}$  G<sub>H<sub>2(g)</sub></sub>) at 0 V to rigorously evaluate the chemical potential of the electrode/electrolyte species. The relationship allows equating their free energies and applying a linear shift in potential by −e*U* where *U* is on the SHE scale. Based on this framework, the relative free energy of a general elementary reduction reaction, A\* + H<sup>+</sup><sub>(aq)</sub> + e<sup>−</sup> → AH\*, is Δ*G*(*U*) = G<sub>AH\*</sub> − G<sub>A\*</sub> −  $\frac{1}{2}$  G<sub>H<sub>2(g)</sub></sub> + e*U* where G<sub>AH\*</sub>, G<sub>A\*</sub>, G<sub>H<sub>2(g)</sub></sub> and e are the free energy of the product, free energy of the reactant, free energy of gas phase H<sub>2</sub>, and the elementary positive charge.

The limiting potentials for H<sub>2</sub> evolution *U*<sub>L</sub>(H<sub>2</sub>) and CO<sub>2</sub> reduction *U*<sub>L</sub>(CO<sub>2</sub>) are defined as the values that make all individual voltage-dependent or electrochemical steps (Equation 3, 4 and 6, 7 for CO<sub>2</sub>RR and HER, respectively) become exothermic, Δ*G* ≤ 0 eV.<sup>[55,56]</sup> Thus, *U*<sub>L</sub>(CO<sub>2</sub>) and *U*<sub>L</sub>(H<sub>2</sub>) are numerically equal to  $-\left\{\frac{\max(\Delta G(3), \Delta G(4))}{e}\right\}$  and  $-\left\{\frac{\max(\Delta G(6), \Delta G(7))}{e}\right\}$ , respectively. To not to be affected by the HER, the limiting potential of this process should be as negative as possible compared to CO<sub>2</sub>RR. The descriptor which represents the difference in the limiting potentials, *U*<sub>L</sub>(CO<sub>2</sub>) − *U*<sub>L</sub>(H<sub>2</sub>), can then be used to ascertain the trend in selectivity. That is, a positive value corresponds to preference for CO<sub>2</sub> reduction and the more positive the magnitude becomes, the higher the selectivity for CO<sub>2</sub> reduction of over H<sub>2</sub> evolution.

## 3. Carbon Dioxide Reduction on Au<sub>25</sub>(SR)<sub>18</sub>

### 3.1. Earlier DFT Modeling Efforts

Beginning in 2011, Kauffman et al. have studied the catalytic potential of (Au)<sub>*n*</sub>(SR)<sub>*m*</sub> nanoclusters to reduce CO<sub>2</sub> under electrochemical environment. A key focus of the early efforts was on Au<sub>25</sub>(SR)<sub>18</sub><sup>*q*</sup> (*q* = −1, 0, −1)<sup>[17,57]</sup> due to the availability of mature methods which permit efficient synthesis of these nanoclusters with molecular purity.<sup>[33,58]</sup> The negatively charged cluster was labeled as the captain of the great nanocluster ship due to its reputation of being a well structurally characterized system. This was made possible by the pioneering work of Tsukuda et al. who reported the formula of the anionic species using electrospray ionization mass spectrometry and subsequent investigations by Jin and Murray groups that ascertained among other things the corresponding crystal structure.<sup>[59,60]</sup> A key structural finding is that the nanocluster has three types of Au environment: central, shell site, and ligand sites (Figure 2). The central and shell sites consist of icosahedral inner Au<sub>13</sub> cluster plus exterior shell of Au<sub>12</sub>. This Au<sub>25</sub> structure is then protected by 18 thiolate ligands stabilizer. Alternatively, one can view the inner Au<sub>13</sub> as enveloped by six Au<sub>2</sub>(SR)<sub>3</sub> staple motifs where R represents a typical phenylethyl group (CH<sub>2</sub>CH<sub>2</sub>C<sub>6</sub>H<sub>5</sub>).



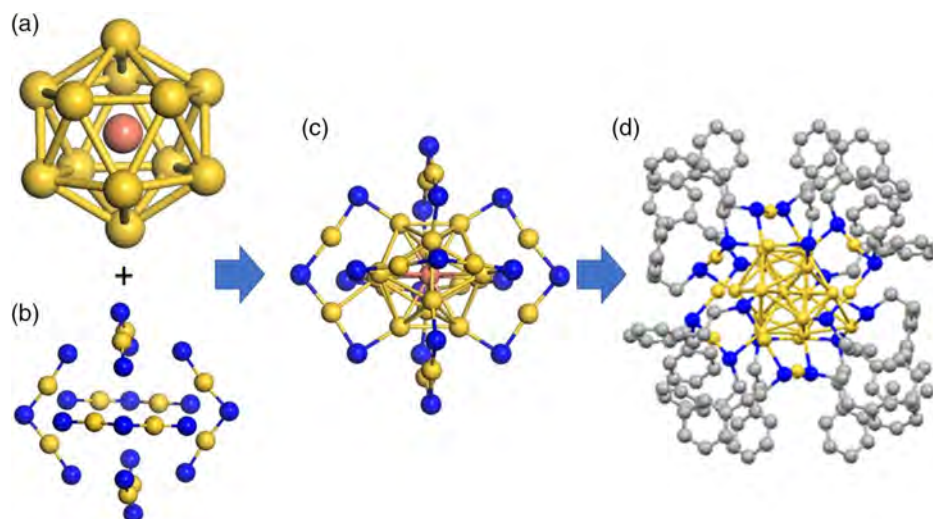


**Figure 2.** Building blocks of  $\text{Au}_{25}(\text{SR})_{18}^q$  where  $R = \text{CH}_2\text{CH}_2\text{C}_6\text{H}_5$ . a) Icosahedral  $\text{Au}_{13}$  core; b) the six  $\text{Au}_2(\text{SR})_3$  staple motifs. c)  $\text{Au}_{13}$  core enveloped by the the six  $\text{Au}_2(\text{SR})_3$  structures. d)  $\text{Au}_{25}(\text{SR})_{18}^q$  structure. Atom colors: Au core: light red; other Au: yellow; S: blue; and C portion of the ligand: gray. H atoms are not shown for clarity.

From the experimental work of Kauffman et al., it was demonstrated that  $\text{Au}_{25}(\text{SR})_{18}^-$  can successfully reduce  $\text{CO}_2$  to CO with product yield that is 7–700 times faster than that of conventional Au nanoparticles and bulk Au electrodes. Under aqueous condition, catalytic activity was observed to be as small as  $-0.193\text{ V}$  achieving a nearly 100% Faraday efficiency at  $\approx -1\text{ V}$ . A follow-up proof-of-concept studies provided a supporting argument in favor of the viability of this process at a practical level.<sup>[35]</sup> Using commercially available renewable energy resource such as solar cell and battery, stable operation and turn over numbers were both achieved during several days of experiments. Moreover, the stability of the material was not compromised as evidenced by the retention of cluster size and morphology after long-term operation. Charge state plays a role in that  $\text{CO}_2$  reduction to CO is also mediated by the positively charged and neutral species,  $\text{Au}_{25}(\text{SR})_{18}^+$  and  $\text{Au}_{25}(\text{SR})_{18}$ , albeit on a lesser degree, i.e., the observed formation rate is lower than the anionic species between  $-0.7$  and  $-1.3\text{ V}$ . A particular challenge from the modeling standpoint is the identification of a faithful representation of the nanocluster which at the same time is practical for the first-principles modeling. An  $\text{Au}_{25}(\text{SR})_{18}^q$  model based on a typical experimentally utilized 18 atom phenyl ethyl thiolate ( $-\text{SCH}_2\text{CH}_2\text{C}_6\text{H}_5$ ) ligand stabilizer consists of 349 atoms. This plus the use of a periodic box sufficiently large to blot out any unphysical effect due to image interaction would make the calculations computationally prohibitive within a DFT plane-wave basis set framework requiring an energy cutoff of about 600 eV to realistically model the electronic distribution. To remedy this, we utilized a methyl thiolate ( $-\text{SCH}_3$ ) where the phenyl-ethyl group is replaced by  $\text{CH}_3$ , thereby reducing the model to a relatively manageable 115 atoms size representation.<sup>[17]</sup> The resulting geometry optimization of  $\text{Au}_{25}(\text{SCH}_3)_{18}^-$  yielded structural parameters that compare very well with experiments (Figure 3a). For studies that would involve adsorption of intermediates, this approach is an upgrade compared to the previously used ( $-\text{SH}$ ) ligand representation<sup>[61]</sup> as such model can

potentially overestimate the electronegativity of the hydrocarbon portion of the real ligand.

Having attained a viable and more realistic atomic representation, we initially looked at the interaction of  $\text{CO}_2$  with the intact nanocluster to explain the observed catalytic activity. Since adsorption is a precursor to catalysis, we posited that the reduction can take place if the nanocluster is able to bind the molecule. After extensive search of stable  $\text{CO}_2$  adsorption was undertaken, our calculations identified several adsorbate configurations with binding energies up to about  $-0.2\text{ eV}$ . The most energetically favorable one features the oxygen end of  $\text{CO}_2$  having threefold interaction with adjacent sulfur atoms of the methyl thiolate ligands (Figure 3b). The picture of a weak  $\text{CO}_2$  binding is consistent with predicted density of states calculations which show no significant change in the electronic properties of  $\text{Au}_{25}(\text{SCH}_3)_{18}^-$  with the adsorbate withdrawing about 0.1 electrons from the cluster. A noted takeaway is that the reactant  $\text{CO}_2$  can bind on the nanocluster albeit weakly and this baseline data can be used as a platform for further investigations.

As a spot check, the van der Waals interaction was included for this particular configuration as previous DFT work yielded noticeable change in geometry coupled with an increase in the energetic stability of ligand protected  $\text{Au}_{18}(\text{SR})_{14}$ ,  $\text{Au}_{20}(\text{SR})_{16}$ , and  $\text{Au}_{24}(\text{SR})_{20}$  ( $R = \text{CH}_3$ ) clusters when this effect was considered.<sup>[62]</sup> With the use of DFT-D2 scheme<sup>[63]</sup> which incorporates long-range dispersion interaction to the PBE functional, the resulting geometry of the adsorbed  $\text{CO}_2$  is predicted to be unchanged though we found slight  $0.05\text{--}0.13\text{ \AA}$  bond contraction of its O end with the first-neighbor S. A  $0.11\text{ eV atom}^{-1}$  increase in the stability of the whole  $\text{CO}_2$ -nanocluster structure is also observed. The  $\text{CO}_2$  binding energy, however, is not significantly impacted,—i.e., the predicted enhancement is only  $\approx 0.02\text{ eV}$  when the van der Waals contribution is accounted for.

Reactant binding energy was also used to explain the observed charge state-dependent electrocatalytic  $\text{CO}_2\text{RR}$  activity

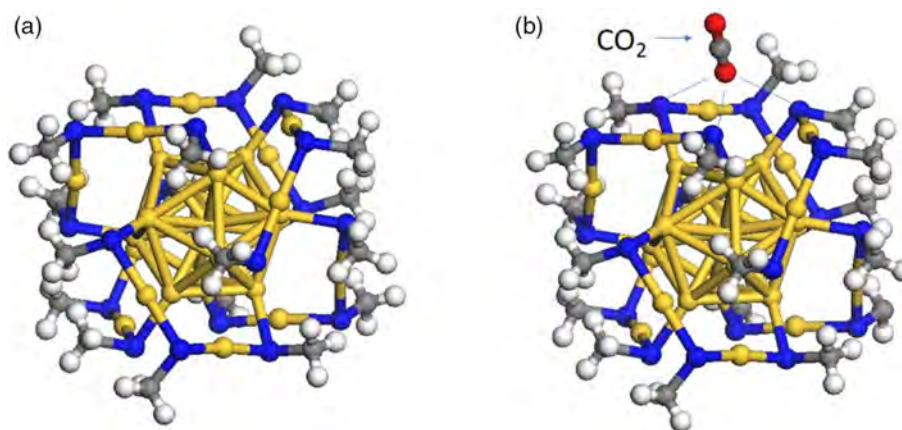


**Figure 3.** a) Bare  $\text{Au}_{25}(\text{SCH}_3)_{18}$ . b)  $\text{CO}_2$  adsorbed on  $\text{Au}_{25}(\text{SCH}_3)_{18}$ . Atom colors: Au: yellow; S: blue; H: white; C: gray; and O: red.

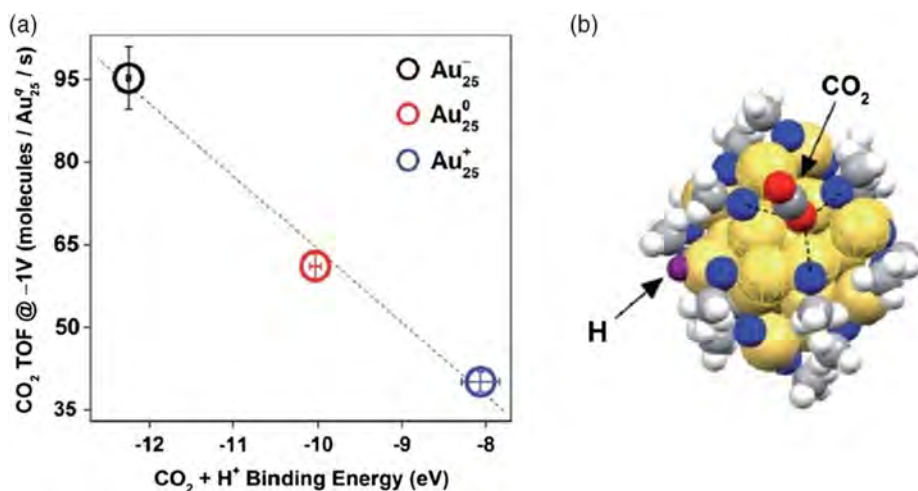


**Figure 4.** a) Correlation between reactant binding energy and reaction turnover frequency (TOF) for  $\text{CO}_2$  reduction to CO at  $-1\text{V}$ .  $\text{Au}_{25}^-$ ,  $\text{Au}_{25}^0$ , and  $\text{Au}_{25}^+$  refer to the anionic, neutral, and cationic version of  $\text{Au}_{25}(\text{SCH}_3)_{18}$ . b) Stable  $\text{CO}_2 + \text{H}^+$  geometry on  $\text{Au}_{25}(\text{SCH}_3)_{18}^-$ . Atom colors: Au: yellow; S: blue; H ligand: white; C: gray; O: red; and H adsorbate: purple. Adapted with permission.<sup>[57]</sup> Copyright 2014, The Royal Society of Chemistry.

of the nanocluster. Experiments show a reaction rate trend of  $\text{Au}_{25}(\text{SR})_{18}^- > \text{Au}_{25}(\text{SR})_{18} > \text{Au}_{25}(\text{SR})_{18}^+$  in acidic media.<sup>[36]</sup> An extensive search of stable  $\text{CO}_2$  and  $\text{H}^+$  adsorption was undertaken on the three nanoclusters. Inspection of the various ground state structures shows that the geometry of the clusters remains intact in the presence of the reactant (**Figure 4b**). The measured turnover number at the optimum operating voltage of  $-1\text{V}$  is shown in **Figure 4a** and a marked trend is seen between these values and the DFT calculated energetics of coadsorbed  $\text{CO}_2$  and  $\text{H}^+$ . Our results indicate that the magnitude of the binding energy has a positive correlation with the activity. That is,  $\text{CO}_2\text{RR}$  is the most pronounced in  $\text{Au}_{25}(\text{SR})_{18}^-$  because it performs better in terms of the stabilization of the  $\text{CO}_2$  and  $\text{H}^+$  reactants. From this conventional DFT calculations emerges a simple picture to explain the observed activity in  $\text{Au}_{25}(\text{SR})_{18}^q$ —adsorption of the reactant is a critical step and  $\text{CO}_2\text{RR}$  is promoted by stabilization of the reactant.

### 3.2. Computational Hydrogen Electrode Modeling: The Role of Surface Heterogeneity

The aforementioned studies establish realistic atomic models for the nanoclusters which are sufficiently practical at the DFT level of calculations. Relevant calculational details such as the magnitude of basis sets required for converged representation of the charge distribution was identified. It predicts that  $\text{Au}_{25}(\text{SR})_{18}^q$  is not completely inert with the binding of  $\text{CO}_2$  plus associated coreactant quantified and then correlated to reactivity. Although reactant binding is a precursor to catalysis, merely looking at such initial event offers a limited picture of the process. Other aspects such as the subsequent chemical transformation including its energetics have to be addressed. To further our understanding, it is then useful to look at the reaction profile, specifically under electrochemical conditions imposed in experiments.



The widely used CHE method described in Section 2.3 provides a predictive and a practical way to ascertain reaction energies. It takes advantage of the thermochemical relationship between the proton–electron pair and gaseous  $\text{H}_2$  coupled with the incorporation of electrode potential effects via a linear free energy relationship. In conjunction with periodic DFT framework, high-fidelity representations of extended solid nature of electrode surface can be generated allowing accurate consideration of the electronic structure. We initially deployed this approach on an electrocatalytic system involving  $\text{Ni}_6\text{S}_6$ -based nanoclusters, successfully predicting its observed activity towards  $\text{H}_2\text{O}$  splitting.<sup>[64]</sup> Buoyed by this effort, we then utilized it for  $\text{CO}_2\text{RR}$  on  $\text{Au}_{25}(\text{SR})_{18}^-$  to derive the energetics of the conversion process.<sup>[65]</sup>

The free energy profile for the reaction pathway based on  $\text{CO}_2\text{RR}$  steps outlined in Section 2.1 as well as the optimized intermediate structures on the intact cluster is shown in **Figure 5**. For an external potential of  $U = 0\text{ V}$ , the protonation of  $\text{CO}_2$  to form  $\text{COOH}^*$  was predicted to be thermodynamically uphill by  $\approx 2\text{ eV}$ , whereas the second one which involves the protonation and dissociation of  $\text{COOH}^*$  is exothermic. After surface  $\text{CO}$  was formed, it can detach with a small barrier to form the gas phase molecule. The most endothermic electrochemical step is the  $\text{COOH}^*$  formation and the lower limit of the overpotential is then approximated as  $2.04\text{ V}$ —namely, the applied voltage that causes the  $\Delta G$  values of all electrochemical reactions (Equation 3,4) to be  $\leq 0\text{ eV}$ . This predicted magnitude of the overpotential suggests that the reduction process is highly energy activated on the intact nanocluster. Initiation of  $\text{CO}$  production was experimentally observed at  $\approx -0.1\text{ V}$  with the Faraday

efficiency reaching nearly 100% at  $-1\text{ V}$ .<sup>[17]</sup> The calculations, on the other hand, indicate that it would require at least  $\approx -2\text{ V}$  to drive the reaction forward which is about an order of magnitude larger than the experimental values. A key take-away is that the intact form of the nanocluster is inactive for  $\text{CO}_2\text{RR}$  unless very high overpotentials are applied.

This result may not be surprising at all in the light of previous efforts showing similar inactivity of the intact nanocluster in the context of thermal  $\text{CO}$  oxidation.<sup>[28]</sup>  $\text{CO}$  adsorption, the critical precursor step for the process, was not detected by in situ infra-red spectroscopy. Their complementary DFT calculations confirm this picture as it predicts a weakly bound  $\text{CO}$  which can desorb to the gas phase at the reaction temperatures. A significant finding is that pronounced binding was only observed when defect on the surface region had been introduced through the partial removal of ligands. The presence of these undercoordinated atoms was also invoked as responsible for the catalytic activity for aldehyde hydrogenation and other oxidation reactions.<sup>[66,67]</sup> The ligands appear to function as a double-edged sword in that while they serve as a structural stabilizer, their presence can also negatively impact the reactivity due to site-blocking effects. This would explain why intact nanocluster is inert since this effect is maximal for this system. These results point to the presence of dethiolated sites as reaction centers on which the catalytic process can proceed.

The  $\text{CO}_2\text{RR}$  on an open metal site generated from a single dethiolation of the nanocluster was then reexamined. As shown in **Figure 6**, the presence of the exposed metal site has a dramatic impact on the free energy profile. In particular, the key intermediate  $\text{COOH}^*$  was significantly stabilized thereby reducing the

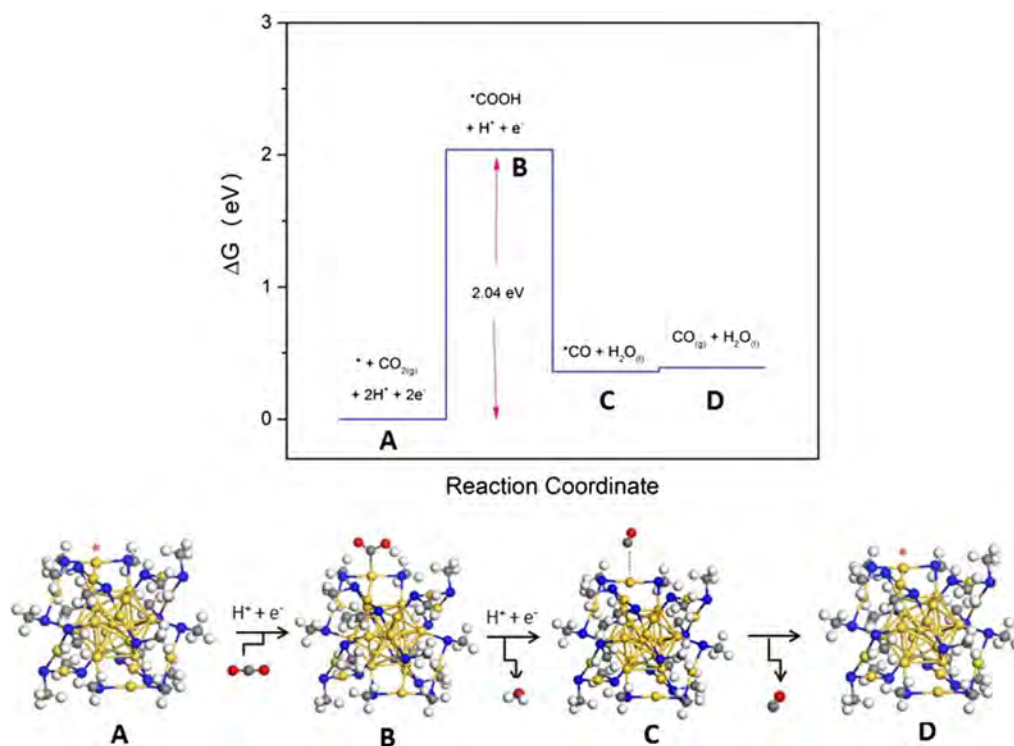


**Figure 5.** Adapted with permission.<sup>[65]</sup> Copyright 2016, The American Institute of Physics.

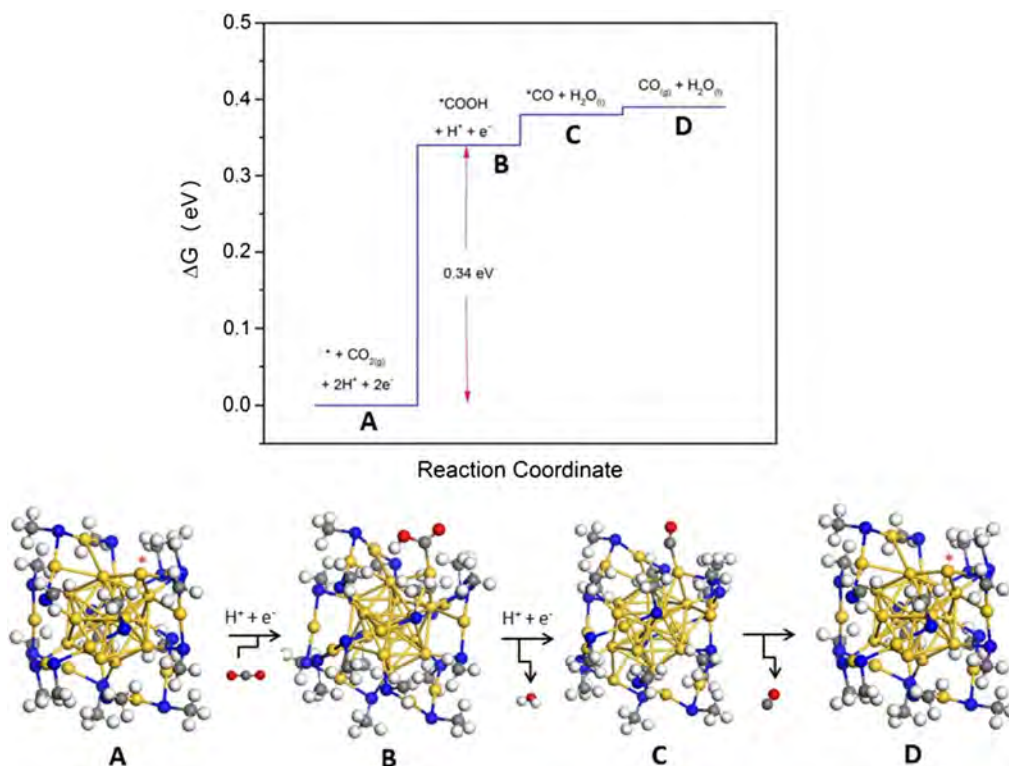


**Figure 6.** Adapted with permission.<sup>[65]</sup> Copyright 2016, The American Institute of Physics.

endothermicity of the first electrochemical step. Though the second one becomes thermodynamically uphill, it is not overly energy activated with predicted reaction energy less than 0.1 eV. The lower limit of the overpotential is predicted to be  $-0.34$  V which is in much better agreement with the measured value compared to the intact nanocluster. Reaction on a nonmetal site was considered in a subsequent study by Austin et al.<sup>[68]</sup> In this case, the hydrocarbon segment of a single ligand was removed producing a defect consisting of an undercoordinated S atom instead. This scenario was previously explored albeit on a different model catalysts such as Ni-Fe-S cubanes<sup>[69]</sup> and MoS<sub>2</sub>.<sup>[56]</sup> Reduction of overpotential was predicted resulting from the stabilization of the intermediates. To gain further insight into the trend in selectivity, Austin et al. used the descriptor described in Section 2.3 which represents the difference in the limiting potentials,  $U_L(\text{CO}_2) - U_L(\text{H}_2)$ , where the first and second term refer to limiting potentials for CO<sub>2</sub> reduction and H<sub>2</sub> evolution, respectively.

We simulated here the CO<sub>2</sub>RR and HER on the aforementioned S active site using our calculational methodology. This permits direct comparison with the corresponding process on the metal site using a consistent approach. Following previous work,<sup>[68]</sup> CH<sub>3</sub> from the dimeric stable motif of the ground state intact nanocluster was removed to expose S and the resulting Au<sub>25</sub>S(SCH<sub>3</sub>)<sub>17</sub><sup>-</sup> structure was optimized. We begin our analysis by looking at the free energy diagram shown in **Figure 7** consisting of both electrochemical SCH<sub>3</sub> and CH<sub>3</sub> events where each pathway involves a one-electron reduction resulting into the detachment of the ligand fragment and formation of a

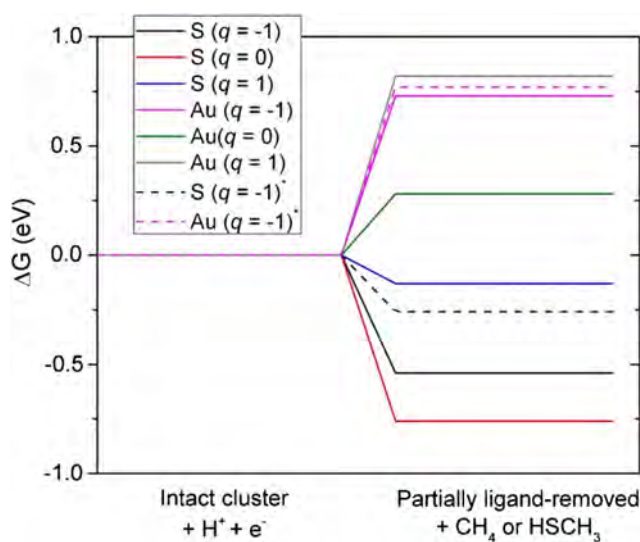


**Figure 7.** Free energy diagrams for Au and S sites generation on the Au<sub>25</sub>(SCH<sub>3</sub>)<sub>18</sub><sup>q</sup> ( $q = -1, 0, 1$ ). The dashed lines correspond to the previous DFT work by Austin et al.<sup>[68]</sup>

hydrogenated version. We predicted an endothermic and exothermic  $\Delta G$  for electrochemical formation of Au and S sites, respectively. In agreement with previous work, the stripping away of CH<sub>3</sub> is more thermodynamically favorable and that the stability of COOH, CO, and H intermediates is enhanced on the S site. The formation of COOH intermediate still requires

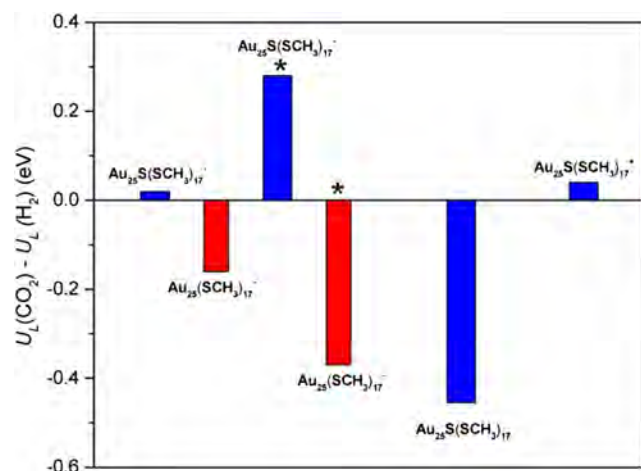


**Figure 8.** Difference in the limiting potentials of  $\text{CO}_2\text{RR}$  and  $\text{HER}$  on  $\text{Au}_{25}\text{S}(\text{SCH}_3)_{17}^q$  ( $q = -1, 0, 1$ ). The ones denoted by asterisk represent the values from the previous DFT calculations by Austin et al.<sup>[68]</sup>

an increase in  $\Delta G$ , whereas the endothermic electrochemical  $\text{CO}$  production becomes the potential limiting step for the  $\text{CO}_2\text{RR}$  process. In agreement with previous work,<sup>[68]</sup> selective  $\text{CO}_2\text{RR}$  is more favored on the S site as evidenced by the positive  $U_L(\text{CO}_2) - U_L(\text{H}_2)$  predicted value compared to the negative value found on the metal site (Figure 8). Although the predicted trends in  $U_L(\text{CO}_2) - U_L(\text{H}_2)$  for  $\text{Au}_{25}\text{S}(\text{SCH}_3)_{17}^-$  and  $\text{Au}_{25}(\text{SCH}_3)_{17}^-$  are consistent with the previous DFT work of Austin et al., it should be noted that the absolute values are noticeably different. This could have been due to some variations between the calculational details underlying these studies. Our DFT calculations were conducted using plane-wave basis set in combination with the PAW method for core–valence treatment, whereas the previous one used mixed Gaussian and plane-wave approaches plus the Goedecker, Teter, and Hutter (GTH) pseudopotentials<sup>[70]</sup> as implemented in the CP2K code.<sup>[71]</sup> Additionally, solvent corrections were considered in our work using a Poisson–Boltzmann implicit solvent model as mentioned in Section 2.3.

As a final note, these calculations were extended here to the  $q = 0$  and  $q = 1$  species using the CHE approach. In the previous section, the observed performance of the different charge state nanoclusters was simply explained on the basis of the trend in the intermediate binding energies using a conventional DFT method. The calculated  $\Delta G$  for the electrochemical  $\text{SCH}_3$  and  $\text{CH}_3$  removal from the intact nanocluster is shown in Figure 7 and as in the  $q = -1$  case, S site generation is the more energetically favorable in both  $q = 0$  and  $q = 1$  species. The  $\text{CO}_2\text{RR}$  and  $\text{HER}$  were then assessed on this S site as it is the more thermodynamically favored to form. In Figure 8, the calculated  $U_L(\text{CO}_2) - U_L(\text{H}_2)$  is negative indicating that the  $q = 0$  species is less selective towards  $\text{CO}_2\text{RR}$  in agreement with experimental data. For the  $q = 1$  case, our results show a more positive  $U_L(\text{CO}_2) - U_L(\text{H}_2)$  value compared to the  $q = -1$  species. Relying on this descriptor alone, our predictions indicate that the  $q = 1$  species is more selective for  $\text{CO}_2\text{RR}$  which is inconsistent with experiments. To explain the experiments,

complementary inspection of  $\Delta G$  for the S generation shown in Figure 8 was conducted. Comparison of  $\Delta G$  values indicates that the generation of S active site in  $q = 1$  case is the least energetically favorable. This might have been the reason why it is experimentally observed to be the least active among the charge state species. These results suggest that the energetics of the active site formation may have to be considered in the analysis of performance trends as both the nature of the active sites and their availability play a complementary role in tuning the selectivity.

## 4. Conclusion

The activity of atomically precise ligand protected anionic  $\text{Au}_{25}$  nanocluster towards  $\text{CO}_2\text{RR}$  was shown to be sensitive to the geometry of the surface region. Understanding how the structural features affect specific electrochemical reactivity is a grand challenge particularly from the fundamental standpoint. The generation of a realistic and a computationally practical simulation models is also indispensable in unraveling the detailed mechanism of the nanocluster. We showed that the presence of atomic heterogeneity in the form of defect resulting in either exposed S or metal site is critical to its observed reactivity as it enhanced the binding of the intermediates. DFT in combination with the SHE method suggests that an exposed outermost Au stabilizes both  $\text{COOH}$  and  $\text{CO}$ . Unless high overpotentials are applied, the intact counterpart is relatively inert due to the pronounced decrease in the free binding energies. We provided further theoretical confirmation that another mildly defective version which consists of an exposed S site exhibits better selectivity for  $\text{CO}_2\text{RR}$ . In contrast to the Au site, it stabilizes  $\text{COOH}$  while destabilizing H yielding a non-negative  $U_L(\text{CO}_2) - U_L(\text{H}_2)$ . These results provide insights into the structure–property relationship in that the thermodynamics of the electrochemistry is influenced by the type of surface heterogeneity.

It should be noted that the ultimate comparison of our work with experiments awaits the evaluation of kinetic barriers. Although the SHE method is a useful tool for generation of trends and semiquantitative interpretation of experimental observations, the predicted limiting potential has no direct correspondence to the experimental Tafel plot—a key observable that yields product current density versus electrode potential. When our work was undertaken, development of framework for evaluating electrochemical transition states from the first-principles had been in its infancy. Tremendous progress over the years has enabled the development of robust kinetic schemes that incorporates potential dependent reaction barriers permitting the prediction of simulated Tafel plots.<sup>[44,45,72]</sup> Their applications to  $\text{CO}_2\text{RR}$  on the surface of Cu-based bulks have been reported. In-house software implementation of microkinetic models for  $\text{CO}_2\text{RR}$  and  $\text{HER}$  over a general catalytic surface is underway in our group. This computational machinery incorporates specific reported algorithms to quantify barriers under electrochemical conditions. This is anticipated to provide further mechanistic insights of the electrochemical properties of  $\text{Au}_{25}$  nanoclusters, to generate kinetic information, and to validate conclusions that have arisen from the purely thermodynamic limiting potential model.



## Acknowledgements

The author is indebted to his doctoral adviser Professor David Drabold for his inspirational mentorship. Professor Drabold is the one who introduced the author to the field of first-principles based simulation of materials. The author would like to thank Dr. Douglas Kauffman for the fruitful collaboration. This report was prepared as an account of work sponsored by an agency of the United States Government. Neither the United States Government nor any agency thereof, nor any of their employees, makes any warranty, express or implied, or assumes any legal liability or responsibility for the accuracy, completeness, or usefulness of any information, apparatus, product, or process disclosed, or represents that its use would not infringe privately owned rights. Reference herein to any specific commercial product, process, or service by trade name, trademark, manufacturer, or otherwise does not necessarily constitute or imply its endorsement, recommendation, or favoring by the United States Government or any agency thereof. The views and opinions of author(s) expressed herein do not necessarily state or reflect those of the United States Government or any agency thereof.

## Conflict of Interest

The author declares no conflict of interest.

## Keywords

CO<sub>2</sub> conversion, computational electrocatalysis, nanostructured functional materials, structural disorder

Received: July 14, 2020

Revised: September 4, 2020

Published online: September 30, 2020

- [1] T. Sakakura, J.-C. Choi, H. Yasuda, *Chem. Rev.* **2007**, *107*, 2365.
- [2] Y. Hori, in *Modern Aspects of Electrochemistry* (Eds: C. G. Vayenas, R. E. White, M. E. Gamboa-Aldeco), Springer, New York **2008**, p. 89.
- [3] M. Mikkelsen, M. Jørgensen, F. C. Krebs, *Energy Environ. Sci.* **2010**, *3*, 43.
- [4] W. Wang, S. Wang, X. Ma, J. Gong, *Chem. Soc. Rev.* **2011**, *40*, 3703.
- [5] J. Qiao, Y. Liu, F. Hong, J. Zhang, *Chem. Soc. Rev.* **2014**, *43*, 631.
- [6] E. E. Benson, C. P. Kubiak, A. J. Sathrum, J. M. Smieja, *Chem. Soc. Rev.* **2009**, *38*, 89.
- [7] W. Zhang, Y. Hu, L. Ma, G. Zhu, Y. Wang, X. Xue, R. Chen, S. Yang, Z. Jin, *Adv. Sci.* **2018**, *5*, 1700275.
- [8] M. E. Dry, *Catal. Today* **2002**, *71*, 227.
- [9] H. Schulz, *Appl. Catal. A* **1999**, *186*, 3.
- [10] S. Chu, A. Majumdar, *Nature* **2012**, *488*, 294.
- [11] C. Graves, S. D. Ebbesen, M. Mogensen, K. S. Lackner, *Renew. Sustain. Energy Rev.* **2011**, *15*, 1.
- [12] M. R. Singh, E. L. Clark, A. T. Bell, *Proc. Natl. Acad. Sci. USA* **2015**, *112*, E6111.
- [13] D. T. Whipple, P. J. Kenis, *J. Phys. Chem. Lett.* **2010**, *1*, 3451.
- [14] Y. Hori, K. Kikuchi, S. Suzuki, *Chem. Lett.* **1985**, *14*, 1695.
- [15] H. Mistry, R. Reske, Z. Zeng, Z.-J. Zhao, J. Greeley, P. Strasser, B. Roldan Cuenya, *J. Am. Chem. Soc.* **2014**, *136*, 16473.
- [16] W. Zhu, R. Michalski, O. Metin, H. Lv, S. Guo, C. J. Wright, X. Sun, A. A. Peterson, S. Sun, *J. Am. Chem. Soc.* **2013**, *135*, 16833.
- [17] D. Kauffman, D. Alfonso, C. Matranga, H. Qian, R. Jin, *J. Am. Chem. Soc.* **2012**, *134*, 10237.
- [18] B. Hvolbæk, T. V. Janssens, B. S. Clausen, H. Falsig, C. H. Christensen, J. K. Nørskov, *Nano Today* **2007**, *2*, 14.
- [19] B. C. Gates, *Chem. Commun.* **2013**, *49*, 7876.
- [20] A. A. Herzing, C. J. Kiely, A. F. Carley, P. Landon, G. J. Hutchings, *Science* **2008**, *321*, 1331.
- [21] A. Corma, P. Concepción, M. Boronat, M. J. Sabater, J. Navas, M. J. Yacaman, E. Larios, A. Posadas, M. A. López-Quintela, D. Buceta, *Nat. Chem.* **2013**, *5*, 775.
- [22] J. Oliver-Meseguer, J. R. Cabrero-Antonino, I. Domínguez, A. Leyva-Pérez, A. Corma, *Science* **2012**, *338*, 1452.
- [23] M. Cowan, G. Mpourmpakis, *Dalton Trans.* **2020**, *49*, 9191.
- [24] N. L. Rosi, C. A. Mirkin, *Chem. Rev.* **2005**, *105*, 1547.
- [25] R. Jin, G. Wu, Z. Li, C. A. Mirkin, G. C. Schatz, *J. Am. Chem. Soc.* **2003**, *125*, 1643.
- [26] M. M. Alvarez, J. T. Khoury, T. G. Schaaff, M. N. Shafgullin, I. Vezmar, R. L. Whetten, *J. Phys. Chem. B* **1997**, *101*, 3706.
- [27] R. Jin, *Nanoscale* **2010**, *2*, 343.
- [28] Z. Wu, D.-e. Jiang, A. K. Mann, D. R. Mullins, Z.-A. Qiao, L. F. Allard, C. Zeng, R. Jin, S. H. Overbury, *J. Am. Chem. Soc.* **2014**, *136*, 6111.
- [29] S. Gaur, H. Wu, G. G. Stanley, K. More, C. S. Kumar, J. J. Spivey, *Catal. Today* **2013**, *208*, 72.
- [30] Y. Zhu, H. Qian, M. Zhu, R. Jin, *Adv. Mater.* **2010**, *22*, 1915.
- [31] X. Nie, H. Qian, Q. Ge, H. Xu, R. Jin, *ACS Nano* **2012**, *6*, 6014.
- [32] M. W. Heaven, A. Dass, P. S. White, H. K. M., R. W. Murray, *J. Am. Chem. Soc.* **2008**, *130*, 3754.
- [33] M. Zhu, C. M. Aikens, F. J. Hollander, G. C. Schatz, R. Jin, *J. Am. Chem. Soc.* **2008**, *130*, 5883.
- [34] J. Akola, M. Walter, R. L. Whetten, H. Hakkinen, H. Gronbeck, *J. Am. Chem. Soc.* **2008**, *130*, 3756.
- [35] D. R. Kauffman, J. Thakkar, R. Siva, C. Matranga, P. R. Ohodnicki, C. Zeng, R. Jin, *ACS Appl. Mater. Int.* **2015**, *7*, 15626.
- [36] D. R. Kauffman, D. Alfonso, C. Matranga, P. Ohodnicki, X. Deng, R. C. Siva, C. Zeng, R. Jin, *Chem. Sci.* **2014**, *5*, 3151.
- [37] J. W. Vickers, D. Alfonso, D. R. Kauffman, *Energy Technol.* **2017**, *5*, 775.
- [38] S. Nitopi, E. Bertheussen, S. B. Scott, X. Liu, A. K. Engstfeld, S. Horch, B. Seger, I. E. Stephens, K. Chan, C. Hahn, *Chem. Rev.* **2019**, *119*, 7610.
- [39] Q. Tang, Y. Lee, D.-Y. Li, W. Choi, C. Liu, D. Lee, D.-e. Jiang, *J. Am. Chem. Soc.* **2017**, *139*, 9278.
- [40] J. K. Nørskov, J. Rossmeisl, A. Logadottir, L. Linqvist, J. R. Kitchin, T. Bligaard, H. Jonsson, *J. Phys. Chem. B* **2004**, *108*, 17886.
- [41] A. A. Peterson, F. Abild-Pedersen, F. Studt, J. Rossmeisl, J. K. Nørskov, *Energy Environ. Sci.* **2010**, *3*, 1311.
- [42] J. S. Filhol, M. Neurock, *Angew. Chem. Int. Ed.* **2006**, *45*, 402.
- [43] R. Sundararaman, W. A. Goddard, A. T. Arias, *J. Chem. Phys.* **2017**, *146*, 114104.
- [44] J. D. Goodpaster, A. T. Bell, M. Head-Gordon, *J. Phys. Chem. Lett.* **2016**, *7*, 1471.
- [45] X. Liu, J. Xiao, H. Peng, X. Hong, K. Chan, J. K. Nørskov, *Nat. Commun.* **2017**, *8*, 1.
- [46] D. R. Alfonso, D. N. Tafen, D. R. Kauffmann, *Catalysts* **2018**, *8*, 424.
- [47] H. A. Hansen, J. B. Varley, A. A. Peterson, J. K. Nørskov, *J. Phys. Chem. Lett.* **2013**, *4*, 388.
- [48] W. Zhu, Y.-J. Zhang, H. Zhang, H. Lv, Q. Li, R. Michalsky, A. A. Peterson, S. Sun, *J. Am. Chem. Soc.* **2014**, *136*, 16132.
- [49] N. Kumar, N. Seriani, R. Gebauer, *Phys. Chem. Chem. Phys.* **2020**, *22*.
- [50] G. Kresse, J. Furthmüller, *Comput. Mater. Sci.* **1996**, *6*, 15.
- [51] J. P. Perdew, K. Burke, M. Ernzerhof, *Phys. Rev. Lett.* **1996**, *77*, 3865.
- [52] G. Kresse, D. Joubert, *Phys. Rev. B* **1999**, *59*, 1758.
- [53] M. Methfessel, A. T. Paxton, *Phys. Rev. B* **1989**, *40*.
- [54] K. Matthew, R. Sundararaman, K. Lechtworth-Weaver, T. A. Arias, R. Hennig, *J. Chem. Phys.* **2014**, *140*.
- [55] C. Shi, H. A. Hansen, A. C. Lausche, J. K. Nørskov, *Phys. Chem. Chem. Phys.* **2014**, *16*, 4720.

- [56] K. Chan, C. Tsai, H. A. Hansen, J. Norskov, *ChemCatChem* **2014**, 6, 1899.
- [57] D. Kauffman, D. Alfonso, P. Ohodnicki, X. Deng, R. Siva, C. Zeng, R. Jin, *Chem. Sci.* **2014**, 5, 3151.
- [58] M. Zhu, E. Lanni, N. Garg, M. E. Bier, R. Jin, *J. Am. Chem. Soc.* **2008**, 130, 1138.
- [59] S. Yamazoe, K. Koyasu, T. Tsukuda, *Acc. Chem. Res.* **2014**, 47, 816.
- [60] R. Jin, *Nanoscale* **2015**, 7, 1549.
- [61] O. Lopez-Acevedo, K. A. Kacprzak, J. Akola, H. Hakkinen, *Nat. Chem.* **2010**, 2.
- [62] Y. Bu, M. Zhao, Y. He, W. Gao, Q. Jiang, *ChemPhysChem* **2016**, 17, 2998.
- [63] S. Grimme, *J. Comput. Chem.* **2006**, 27, 1787.
- [64] D. Kauffman, D. Alfonso, D. Tafen, J. Lekse, C. Wang, X. Deng, J. Lee, H. Jang, J.-S. Lee, S. Kumar, C. Matranga, *ACS Catal.* **2016**, 6, 1225.
- [65] D. Alfonso, D. Kauffman, C. Matranga, *J. Chem. Phys.* **2016**, 144, 184705.
- [66] G. Li, H. Abroshan, Y. Chen, R. Jin, H. J. Kim, *J. Am. Chem. Soc.* **2015**, 137, 14295.
- [67] B. Zhang, S. Kaziz, H. Li, M. G. Hevia, D. Wodka, C. Mazet, T. Burgi, N. Barrabés, *J. Phys. Chem. C* **2015**, 119, 11193.
- [68] N. Austin, S. Zhao, J. McKone, R. Jin, G. Mpourmpakis, *Catal. Sci. Technol.* **2018**, 8, 3795.
- [69] J. Varley, H. Hansen, N. L. Ammitzbøll, L. Grabow, A. Peterson, J. Rossmeisl, J. Nørskov, *ACS Catal.* **2013**, 3, 2640.
- [70] S. Goedecker, M. Teter, J. Hutter, *Phys. Rev B* **1996**, 54, 1703.
- [71] J. VandeVondele, M. Krack, F. Mohamed, M. Parrinello, T. Chassaing, J. Hutter, *Comput. Phys. Commun.* **2005**, 167, 103.
- [72] A. Asthagiri, M. J. Janik, in *Computational Catalysis*, The Royal Society of Chemistry, Cambridge, UK **2014**, p. 151.



**Dominic Alfonso** is a GS-15 Physical Scientist at the US Department of Energy, National Energy Technology Laboratory (NETL). He received a B.S. degree in chemistry from the University of the Philippines and a Ph.D. degree in chemistry from Ohio University. Following postdoctoral works at the International Center for Theoretical Physics, University of Louisville, Pacific Northwest National Laboratory, and University of Pittsburgh, he joined NETL in 2002. His research involves the implementation of computational techniques based on classical thermodynamic and kinetic theories using ab initio calculated training sets to predict catalytic and materials properties.

# Prospect and Status of Polyanionic Lithium Cobalt Silicates as High Energy-Density and Safe Cathode Materials for Lithium-Ion Batteries

Wenqiang Du, Zhifeng Zhang, Zhenlian Chen, and Jun Li\*

Dedicated to Professor David A. Drabold on the occasion of his 60th birthday

Lithium cobalt silicate  $\text{Li}_2\text{CoSiO}_4$  (LCSO) is a promising but challenging high energy-density cathode for lithium-ion battery. Herein, recent studies of synthesis–structure–performance of LCSO are reported, in which carbon coating, element doping, and nanostructure designs are incorporated in a two-step synthesis starting with hydrothermal reaction. The initial performance is significantly improved with respect to previous reports in literature with the charge and discharge capacities now reaching 330 and 220  $\text{mAh g}^{-1}$ , respectively. The discharge voltage platform is compatible with the 4 V window of the nonaqueous organic electrolytes and presents no structural-change-induced voltage drops. The striking finding from the study of LCSO is the oxygen redox activity amid the second lithium deintercalation process, in which peroxo formation dominates the charge compensation to the high-voltage lithium capacity. First-principles modeling reveals an intrinsic and general relation between oxygen redox and cationic disorder in bulk compounds. Thus, LCSO is a new prototype of polyanionic materials with oxygen redox, which is the foundation of high-capacity Li-rich cathodes. This review is also aimed to narrate the progresses of LCSO within a broad domain of  $\text{Li}_3\text{PO}_4$ -based polyanionic structures that support the development of solid-state electrolytes for all solid-state batteries.

signal processing. Mainstream microelectronic devices use a 5 V for external power connection and a 3.3 V for internal circuits and communication. This architecture not only reduces the power consumption but achieves the high-speed performance in digital circuits. The state-of-the-art 4 V nonaqueous organic electrolytes with the same 4 V redox potential of the first-generation cathode oxide  $\text{LiCoO}_2$  provide the desired electrochemical functionality for electronic devices in both charging and discharging, far out-performance the other well-developed battery technologies with low voltages, such as 2.0 V lead–acid battery and 1.55 V nickel–hydrogen battery.

The voltage is also the primary functional factor of the battery for applications to clean energy technologies. While the new architecture for battery-driving vehicles is still at the early stage of development from the vision that may finally integrate electric vehicles (EVs) and green power stations with cellular networks, the


## 1. Introduction

Lithium-ion batteries (LIBs) play a pivotal role in the evolution of mobile technology and are now the solely power source of smart-phones that substantiate a proliferation of mobile e-commerce via cellular networks. In mobile electronics, the voltage is the more often used electrical quantity to carry the data, i.e., analog or digital signals, in nowadays computation, data transfer, and

4 V electrochemistry is far more attractive to massive applications as the assembling unit than is the 3 or 2 V candidate. Because the high operating voltage, like a typical 350 V used in electric cars, requires a massive battery packing to start and drive electrical motors, a smaller amount of 4 V batteries is not only more cost-efficient in manufacture, but also more reliable in assembling for series/parallel packing and thermal management, whose quality is critical to the electrical durability. Furthermore, on the massive scale, the safety of a single unit is as critical as its electrochemical function to store and release the electrical charge for EV. Cathode is the dominant component of a battery to decide the upper voltage range and to ignite the thermal runaway at high voltage and high-power application. The theoretical capacity of  $\text{LiCoO}_2$  is 278  $\text{mAh g}^{-1}$  but only 60% is used in the commercialized batteries due to the charging cut-off at 4.3 V. The cathode materials may release gaseous oxygen at the voltage above 4.3 V. The organic electrolytes will be oxidized by the oxygen then easily catch fire in overcharging. This is the major risk of first-generation LIBs to massive installment in EVs. Energy density depends on the production of voltage and capacity. Thus, the focus in the research of high

W. Du, Dr. Z. Zhang, Dr. Z. Chen, Prof. J. Li  
 Ningbo Institute of Material Technology and Engineering  
 Chinese Academy of Sciences  
 Ningbo, China  
 E-mail: lijun@nimte.ac.cn

Dr. Z. Chen  
 School of Chemical and Environmental Engineering  
 Jiangnan University  
 Sanjiaohu Road, Caidian District, Wuhan, Hubei, China

 The ORCID identification number(s) for the author(s) of this article can be found under <https://doi.org/10.1002/pssb.202000420>.

DOI: 10.1002/pssb.202000420



capacity cathode is to solve the intrinsic conflict between high voltage and safety in high energy-density electrochemistry.

The frontier of cathode research in the past decade has focused on the boost of lithium capacity by anionic oxygen redox discovered in Li-rich oxides.<sup>[1]</sup> Li-rich oxides and Li-excess rock salt materials shown in **Table 1** are often charged to above 4.2–4.4 V to active the oxygen redox for high capacity.<sup>[2–5]</sup> These systems in general confront the same oxygen release problem as in LiCoO<sub>2</sub>. While presenting high initial discharge capacity, Li-rich oxides suffer significant capacity and voltage plateau decay during the charge–discharge cycle. Li<sub>6</sub>CoO<sub>4</sub> and Li<sub>6</sub>MnO<sub>4</sub> materials with antifluorite structure showed high theoretical capacity.<sup>[6–8]</sup> Their first charging capacity can reach more than 700 mAh g<sup>−1</sup>, but they have very low conductivity, low voltage platform, low reversible capacity, and unstable structure.

Polyoxoanion compounds are a big family of oxygen-based compounds that contain a distinct polyanionic species such as CO<sub>3</sub><sup>2−</sup>, SO<sub>4</sub><sup>2−</sup>, PO<sub>4</sub><sup>3−</sup>, SiO<sub>4</sub><sup>4−</sup>, etc. The polyoxoanion compounds are emerging as a new generation of electrochemical materials for all solid-state batteries (SSBs), which are made of high voltage cathode and high conductive solid-state electrolytes. Among them, the olivine phosphate LiFePO<sub>4</sub> (LFP) has been the most successful polyanionic cathode for the application to EVs.<sup>[9]</sup> Orthosilicates Li<sub>2</sub>MSiO<sub>4</sub> (M = Fe, Mn, Co), cf. Table 1, are an attractive alternative to the olivine LFP as a new prototype of high capacity and high safety polyoxoanionic cathode candidate.<sup>[10–12]</sup> First, two lithium ions per silicate formula theoretically point to twice capacity of LFP. Second, silicates are made of polyanionic building units of SiO<sub>4</sub>, which has strong Si–O covalent bond as P–O covalent bond in LFP. To our knowledge, no oxygen release has been reported for silicates so far. Experimental progresses showed nearly 300 mAh g<sup>−1</sup> in nanostructured Li<sub>2</sub>FeSiO<sub>4</sub> (LFSO) and Li<sub>2</sub>MnSiO<sub>4</sub> (LMSO) samples.<sup>[13]</sup> However, both LFSO and LMSO presented structural changes in the process of charging and discharging, which lead to the decline of voltage platform and seriously impair the reusable energy-density.<sup>[14]</sup> It has been showed that below 4 V, the reversible capacity of LFSO was only about 120 mAh g<sup>−1</sup>, far less than the theoretical one Li capacity, ≈160 mAh g<sup>−1</sup> of silicates.<sup>[15]</sup> The electrochemical performance of Li<sub>2</sub>CoSiO<sub>4</sub> (LCSO) is much worse than those of LFSO and

LMSO. Previous works reported nearly zero cycling capacity and realized only about ≈110 mAh g<sup>−1</sup> reversible capacity in the first discharging, as shown in **Table 2**.<sup>[16–23]</sup> However, one electrochemical character catches our attention. Its discharge voltage plateaus seem be around 4 V, which ideally matches the 4 V window of the commercial organic electrolytes and is also higher than the 3.3 V of LFP. If that plateaus are the true redox character of its theoretical capacity, then, LCSO will have an edge on most of the reported high-capacity Li-rich oxides that can only discharge around 3 V, not preferred by the mainstream electronic or EV applications. Comparing with the well-developed phosphate systems, the extreme difficulty to realize a high initial charging and discharging capacity, cf. Table 2, is the main technical bottlenecks in the study of LCSO and the whole silicate systems. Thus, our primary interest in LCSO is to understand or verify what electrochemistry LCSO may offer, i.e., is it a true 4 V, 300 mAh g<sup>−1</sup> and safe cathode candidate?

Because of the bad performance, LCSO has become an unfavorable candidate in the cathode research. There were very limited studies in literature. That significantly limits the scope we can cover in this review. Our principal objectives here are to provide a concise understanding of the basic relation among synthesis, structure, and electrochemistry we have learned from the study of LCSO at NIMTE, CAS in recent years. This may benefit the study of the broad family of polyoxoanion compounds beyond LIBs. For example, phosphates and fluorophosphates have been proposed as cathode candidates in sodium-ion batteries in recent progresses.<sup>[24]</sup> Isostructural and multivalent anion substitution combined with carbon coating show effectivity to improve rate and cyclic stability for polyoxoanion compounds in general. Therefore, as a parallel objective, we aim to inspire fundamental thoughts on lithium-containing compounds (LCC) with polyanionic structures in a broad domain of electrochemical functionality. The knowledge we developed from silicates may find inviting applications to other LLC systems, especially for multi-ithiated compounds. Will there be a principle to discern whether the Li<sup>+</sup> is mobile in an LCC? Will it be functioned as an intercalating ion for the cathode or a conductive ion for solid-state electrolytes?

**Table 1.** High capacity cathode candidates for high energy-density cathode materials.

Cathode	Structure	Theoretical capacity [mAh g <sup>−1</sup> ]
Li-rich layered oxides	Li[Li <sub>x</sub> M <sub>1−x</sub> ]O <sub>2</sub> (M is a transition metal)	α-NaFeO <sub>2</sub> structure >300 <sup>[2]</sup>
Li-excess rock salt	Li <sub>1.2</sub> Mn <sub>0.4</sub> Ti <sub>0.4</sub> O <sub>2</sub>	394 <sup>[3]</sup>
	Li <sub>1.2</sub> Mn <sub>0.4</sub> Zr <sub>0.4</sub> O <sub>2</sub>	325 <sup>[4]</sup>
	Li <sub>1.3</sub> Nb <sub>0.3</sub> Mn <sub>0.4</sub> O <sub>2</sub>	383 <sup>[5]</sup>
High lithium TM oxides	Li <sub>5</sub> FeO <sub>4</sub>	Antifluorite structure >700 <sup>[6]</sup>
	Li <sub>6</sub> MnO <sub>4</sub>	1000 <sup>[7]</sup>
	Li <sub>6</sub> CoO <sub>4</sub>	1100 <sup>[8]</sup>
Polyanion cathode	LFSO	Li <sub>3</sub> PO <sub>4</sub> 332 <sup>[10]</sup>
	LMSO	tetrahedral structure 333 <sup>[11]</sup>
	LCSO	325 <sup>[12]</sup>

**Table 2.** The first charge and discharge capacities and retained capacity at the tenth cycle reported in literatures.<sup>[16–23]</sup>

Polymorphs <sup>a)</sup>	Voltage range	Capacity [mAh g <sup>−1</sup> ]			References
		First Charge	First Discharge	The 10th	
DP	3.0–4.6 V	1.4 Li	0.46 Li	No report	[16]
DP	2.0–4.6 V	180	30	Negligible	[17]
DP	2.0–4.6 V	162	33	< 30	[18]
TP	1.5–4.6 V	200	107	Very poor	[19]
TP	2.0–4.7 V	240	56	< 25	[20]
TP	2.0–4.65 V	167	112	101	[21]
P-LCSO	2.5–4.6 V	270	144	96.2	[12]
Al-LCSO	2.5–4.6 V	330.6	140	74.1	[22]
V-LCSO	1.5–4.6 V	299.0	220.1	126.8	[23]

<sup>a)</sup>DP – dual peak; TP – triple peak.

## 2. Characteristics of Polyanionic Structures

### 2.1. Preparation and Characterization of Polymorphs with Tetrahedral Structures

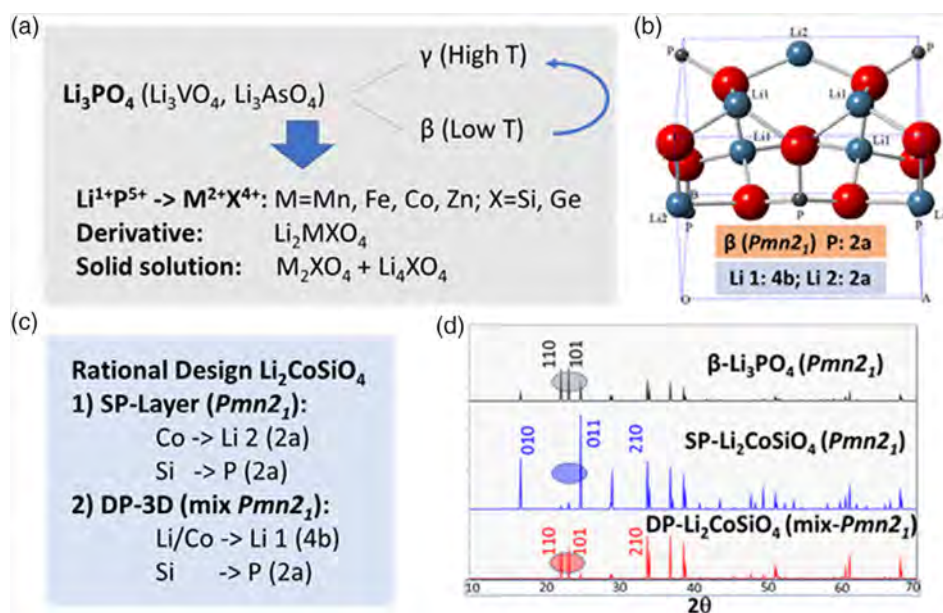
Recent rapid progresses in SSB have found on the horizon that 1) Ge-based ceramics, such as the base Lithium Super Ionic CONductor (LISICON) structure,<sup>[25]</sup>  $\text{Li}_2\text{ZnGeO}_4\text{--}3\text{Li}_4\text{GeO}_4$  and the second generation LISICON,<sup>[26]</sup>  $\text{Li}_4\text{GeO}_4\text{--Li}_3\text{VO}_4$ , showed promising ionic conduction in the range of  $10^{-6}$ – $10^{-5}$  S cm<sup>-1</sup>; 2) Silicates such as LFSO and LMSO showed doubled Li capacity from the commercial cathode materials,  $\text{LiCoO}_2$  and  $\text{LiFePO}_4$ . While these electrochemical systems look very different in their chemical structures, they all are LCC derivatives from the same base tetrahedral structure of polyanionic  $\text{Li}_3\text{PO}_4$  (LPO), and its sisters  $\text{Li}_3\text{VO}_4$  and  $\text{Li}_3\text{AsO}_4$ .<sup>[27]</sup> Thus, the study of LCSO will provide insights on polyanionic LCCs as electrochemical energy storage materials in general for SSB beyond conventional LIBs.

Figure 1 shows how LCSO systems, including pure LCSO and its modification, can be rationally designed from the parent structure, lithiophosphate  $\text{Li}_3\text{PO}_4$ . Not only the materials processing but also many fundamental properties of LCSO systems bear resemblances to its parent system LPO, which has been determined occurring in two main structures, low temperature  $\beta$  and high temperature  $\gamma$ . The  $\beta$  phase is naturally occurring lithiophosphate and can be prepared by heating mixtures of corresponding oxides or carbonates in air often under  $\approx 700^\circ\text{C}$ . The  $\gamma$  phase can often be obtained by quenching the  $\beta$  phase to ambient from a high temperature below its melting point. Figure 1a shows a rational replacement of the pair  $\text{Li}^+\text{P}^{5+}$  by a pair of charge equivalent  $\text{M}^{2+}\text{X}^{4+}$  to derive new tetrahedral structures, which fall in LISICON-type solid electrolytes and silicate cathodes. The complexities in the LPO tree come from two

phenomena. First, there are a variety of transitional phases between the two main structures ( $\beta$  and  $\gamma$ ), giving rise to many polymorphous phases. Second, all the materials in the family of  $\text{Li}_3\text{PO}_4$  including derivatives, such as  $\text{M}_2\text{XO}_4$  and  $\text{Li}_4\text{XO}_4$ , show extensive mutual solubility, resulting in more complicated solid-solution compositions. Polymorphism and solid solution make the accurate characterization of as-synthesized samples and a clear discerning of electrochemically active structural units extremely challenging. The sequence of phase transformation, polymorphism, and solid-solution is strongly depending on stoichiometry of chemical components, the preparation temperature, and the cooling rate adopted for individual compounds. On the positive side, these complexities provide an ample room to rational design and optimize the functionalities of LCCs if the materials principle can be worked out from the LPO tree.

Figure 1b shows an atomistic model of  $\beta\text{-Li}_3\text{PO}_4$  with space group  $\text{Pmn}2_1$ , pulled from Crystallography Open Database (COD, 9 012 500). In  $\beta\text{-Li}_3\text{PO}_4$ , three  $\text{Li}^+$  occupy on one 4b and one 2a Wyckoff positions, and the  $\text{P}^{5+}$  occupies at 2a. The 2a site is invariant under lattice a reflection:  $x \rightarrow -x$ , giving only two equivalent occupants per unit cell, whereas the 4b site is a general site, giving four equivalent occupants.  $\beta\text{-Li}_3\text{PO}_4$  consists of only corner-sharing tetrahedra, in which all the tetrahedra point toward the same orientation along the  $c$  axis, cf. Figure 1b.

Figure 1c illustrates two schemes to replace  $\text{Li}^+\text{P}^{5+}$  by a pair of  $\text{Co}^{2+}\text{Si}^{4+}$  while keeping the same space group  $\text{Pmn}2_1$ . The first replacement on two 2a sites results in a polymorph called SP phase, a term used to recall the X-ray powder diffraction (XRD) pattern, shown in Figure 1d, that presents only a single strong peak (011) in the  $2\theta$  range from  $20^\circ$  to  $25^\circ$ . The other two peaks, (110) and (101), of  $\beta\text{-Li}_3\text{PO}_4$  become ignorable weak after cationic replacements. The second one gives a dual peak (DP) phase, cf. the two eminent peaks at (110) and (101). The significance in DP scheme is to allow  $\text{Li}^+$  and  $\text{Co}^{2+}$  mix equally on the



**Figure 1.** Schemes of a) polyanionic  $\text{Li}_3\text{PO}_4$  and derivatives, b)  $\beta\text{-Li}_3\text{PO}_4$  model (COD), c) examples of LCSO rational design, d) simulated XRD using the same  $\beta\text{-Li}_3\text{PO}_4$  model (b) and with two cationic replacements shown in (c).

4b sites. In other words, the space group  $Pmn2_1$  is not a true crystalline symmetry of the polymorph. All simulated XRDs shown in Figure 1d use the same lattice parameters of  $\beta$ - $\text{Li}_3\text{PO}_4$ . Thus, the distinct XRD patterns illustrate the characteristics of cationic ordering in the derived polymorphs of LCSO.<sup>[28]</sup> The orthosilicate structures consist of slightly distorted close-packed oxygen layers, cations occupy 50% of the tetrahedral sites of the oxygen sub-lattice. Tetrahedral building blocks  $\text{TO}_4$ , ( $T = \text{Li, Fe, Mn, Co, and Si}$ ), distinguish themselves from the octahedral structures, e.g., the family of  $\text{LiCoO}_2$ . Tracking the XRD patterns provides a convenient discerning of the cationic ordering that responses to the synthesis and electrochemical reaction.

The SP pattern is the main XRD characteristics of synthesized  $\beta$ - and  $\gamma$ - $\text{Li}_2\text{MSiO}_4$  compounds ( $M = \text{Mn, Fe}$ ).<sup>[29]</sup> Different synthesis can lead to a small change in the peak distribution in  $\beta$ - and  $\gamma$ - $\text{Li}_2\text{MSiO}_4$  compounds. The two 2a replacement set up Li layers in the base structure for both  $\beta$  and  $\gamma$  polymorphs, which apparently open with high diffusive channels for lithium ion to move. Billaud et al. reported lithium-rich defect clusters in  $\text{Li}_{2.6}\text{Fe}_{0.7}\text{SiO}_4$  resulted in similar excellent lithium mobility as in  $\text{Li}_3\text{Zn}_{0.5}\text{GeO}_4$ , LISICON-type solid electrolyte, which has been attributed to “a mosaic of ordered substructures.”<sup>[15]</sup> However, the SP ordering seemed not electrochemical stable. The  $\text{Li}_2\text{MSiO}_4$  ( $M = \text{Mn, Fe}$ ) often undergo polymorph transition to DP pattern after first charging.

The DP pattern is the major XRD characteristics of low temperature  $\beta_{\text{II}}$ -LCSO polymorph. However, its mix- $Pmn2_1$  only validates in the context of cationic mixing disorder. The mix- $Pmn2_1$  polymorph is a 3D framework of  $\text{MO}_4$  ( $M = \text{Li, Co, Si}$ ): tetrahedral chains of  $\text{CoO}_4$ - $\text{LiO}_4$  (mixing on 4b sites) and  $\text{SiO}_4$ - $\text{LiO}_4$  (both on 2a sites) distribute parallel to the  $a$  axis. This type of 3D structure contains no 1D lithium-ion channels, a characteristic of 2D layered structures of SP pattern. The electrochemical stability of the 3D framework is superior to 2D layered structures. The high temperature  $\beta_1$  and  $\gamma$  phases present a triple peak (TP) pattern in the same  $2\theta$  range from  $20^\circ$  to  $25^\circ$ , similar to the original TP patterns of  $\beta$ - and  $\gamma$ - $\text{Li}_3\text{PO}_4$ , cf. Figure 1d. Saracibar et al. argued that it was pointless to use  $\beta$  and  $\gamma$  to identify electrochemical functionalities.<sup>[30]</sup> In our work, we use DP/TP with corresponding space groups to identify the structural characteristics of polymorphs.

The cationic replacement on 4b sites results in a 3D framework in LCSO.  $\gamma$ - $\text{Li}_3\text{PO}_4$  with space group  $Pmn\bar{b}$  (COD, 9012204 and 9012821) is built up by both corner and edge sharing tetrahedra and with half of the tetrahedra pointing to opposite orientations along the  $c$  axis against the other half. This leads to the twice length of axis  $b$  in  $\gamma$ - $\text{Li}_3\text{PO}_4$  with respect to  $\beta$ - $\text{Li}_3\text{PO}_4$ . All silicates inherit this basic difference between  $\beta$  and  $\gamma$  phases. In most  $\gamma$  structures, the tetrahedra are arranged in groups of three with the central tetrahedron pointing in the opposite direction to the outer two, with which it shares edges. In the  $\gamma_{\text{II}}$  structure, the group of three edge-sharing tetrahedra consists of a Li-M-Li sequence. This ordering is adopted by LISICON-type solid electrolyte  $\text{Li}_{2+2x}\text{Zn}_{1-x}\text{GeO}_4$ . The interstitial  $\text{Li}^+$  (in the octahedral sites and sharing two faces with the substituting  $\text{Li}^+$ ) gives rise to the higher conductivity of the solid solution compared with stoichiometric  $\text{Li}_2\text{ZnGeO}_4$ .

Both LISICON-type and high Li-concentrated silicates can be expressed by the same composite formula ( $n\text{Li}_2\text{O} + \text{MO} + \text{P}_2\text{O}_5/\text{GeO}_2/\text{SiO}_2$ ). Unfortunately, the complete phase diagram or

materials principle for the LPO family has not been developed, yet. While the polymorphism and solid solution indeed challenge the characterization of LPO and derivatives, they may also present a unique advantage in the design of the interfaces between electrolytes and cathodes. The high Li-ion transport impedance across the interface of cathodes and solid electrolytes is the major bottleneck in the practical application of all-SSBs. The high mutual solubility among LPO and derivatives may help reduce the huge Li mobile barriers if both cathode and solid electrolytes are from the same or similar LPO structures, because of no heterojunction in between.

## 2.2. Literature Review of LCSO Synthesis and Performance

While the newly developed and established synthesis routes in the LPO family may provide inspiring ideas for the synthesis of LCSO, there are tremendous difficulties in development of the high-quality LCSO. In the following, a brief review is given for LCSO with problems reported in literature.

Gong et al. were the first group to synthesize the pure LCSO and carried out the electrochemical testing.<sup>[16]</sup> They compared the ethanol solution route to hydrothermal synthesis using deionized water. The LCSO prepared by their solution route was mixed with 20 wt% carbon by the ball milling process. Alternatively, LCSO was prepared in situ with graphite in the hydrothermal reaction. The obtained LCSO comprised individual particles around  $2\text{ }\mu\text{m}$  with the best initial charge and discharge capacities of 234 and  $75\text{ mAh g}^{-1}$ , respectively.

Slightly later, Lyness et al. reported a comparative study of three polymorphs,  $\beta_{\text{II}}$ ,  $\beta_1$ , and  $\gamma_0$ .<sup>[17a]</sup> They started with the hydrothermal synthesis of  $\beta_{\text{II}}$  and heated to 700 and  $1100^\circ\text{C}$  and quench to obtain  $\beta_1$  and  $\gamma_0$ , respectively. They found that the pyrolysis of the carbon precursors above  $650^\circ\text{C}$  resulted in reduction of Co metal and  $\text{Li}_2\text{SiO}_3$ . Only the  $\beta_1$  polymorph could be coated with carbon without reduction, which presented a discharge capacity of  $60\text{ mAh g}^{-1}$  with no meaningful cycling. Later, their group combined Rietveld refinement of XRD, neutron power diffraction, and Li MAS NMR to find the polymorphs of LCSO were significantly impacted by the Li/Co cationic mixing. The  $\beta_{\text{II}}$  ( $Pmn2_1$ ) polymorph showed the highest cationic disorder.<sup>[17b]</sup>

He et al. reported the preparation of mesoporous LCSO using carbon/silica (MCS) as a template.<sup>[18]</sup> By controlling the molar ratio of  $\text{LiOH}:\text{Si}:\text{Co} = 8:1:1$ , they obtained very uniform LCSO/C spheres in the size range of 300–400 nm, which contained hollow or core-shell structures. Their samples were incorporated  $\approx 2\text{ wt\%}$  nanoscale carbon within LCSO aggregates. But its discharge capacity was only at  $33\text{ mAh g}^{-1}$ . The disappointed performance was attributed to the “internal reduction” of LCSO by the carbon coating.

Devaraju et al. prepared the LCSO with supercritical fluid process and observed the tetrahedral coordination by annular bright- and dark-field electron microscopy.<sup>[19]</sup> Their LCSO material showed a high capacity of  $107\text{ mAh g}^{-1}$ , but its discharging voltage platform crashed after two cycles, a structural change-induced voltage drop often observed in LFSO and LMSO. The “soft discharging” in the low voltage range between 2.0 and 2.5 V made up nearly one-third of their first discharge capacity.

Sol-gel technology has been often used in the preparation of mixed oxide ceramic materials. It allows better mixing of the

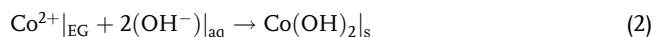
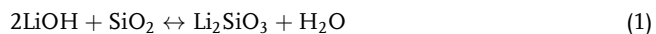


components at the molecular level, and hence yields more homogeneous ceramic composites. Thayumanasundaram et al. report the synthesis of LCSO by a sol–gel method and incorporated functionalized multiwalled carbon nanotubes as conductive additive in the fabrication of the electrode.<sup>[20]</sup> They estimated the diffusion coefficient of lithium after the addition of MWCNTs in the range from  $1 \times 10^{-14}$  to  $8 \times 10^{-14} \text{ cm}^2 \text{ s}^{-1}$  using Randles–Sevcik equation. Their first discharge capacity was only  $56 \text{ mAh g}^{-1}$ . Le et al. recently reported a sol–gel synthesis of  $\beta_1$  polymorph with *Pbn*2<sub>1</sub> space group using water-soluble silicon compounds.<sup>[21]</sup> Their homogeneous nanocrystalline LCSO/C composites delivered an initial discharge capacity of  $112 \text{ mAh g}^{-1}$ .

### 2.3. Two-Step Synthesis and Characterization of LCSO

From previous studies, the complex interplay between carbon coating and polymorph transition is the primary barrier to improve the electrochemical performance of LCSO. Our group develops a two-step scheme that provides consistent processing of the primary nanoparticles and secondary aggregates, surface mesoporous structures, and Co-impurity mitigation with carbon coating for LCSO and doped system.<sup>[12,31a]</sup> Figure 2 shows the synthesis procedure.

Figure 2a shows the synthesis of raw LCSO materials by a hydrothermal reaction in the following procedures.<sup>[31a]</sup>



In the typical route, nanosized  $\text{SiO}_2$ -Cabosil M5 (Cabot Co., USA) and  $\text{LiOH} \cdot \text{H}_2\text{O}$  (Aldrich, 98%) are mixed in the deionized water and processed in an ultrasonic bath to prepare clean  $\text{Li}_2\text{SiO}_3$  water solution. Second,  $\text{CoCl}_2 \cdot 6\text{H}_2\text{O}$  (Aldrich, 99%) is added to ethylene glycol (EG) with stirring to make the Co solution. Then, the  $\text{Li}_2\text{SiO}_3$  is mixed with the Co solution. The resulting suspension is transferred to a Teflon-lined autoclave. The remaining volume is topped off with deionized water. The sealed autoclaves are heated at  $150^\circ\text{C}$  for 72 h. The product is filtered and dried at  $120^\circ\text{C}$  for 12 h in the vacuum oven to obtain raw LCSO particles.

The second step is the pyrolysis of carbon sources on LCSO particles. The dried raw LCSO sample is mixed with carbon precursors like sucrose. Our experience shows the molar ratio of 7:1 between raw LCSO and carbon source is good to start with (the content of carbon is about 10 wt%). The powder is ball milled for 12 h and calcined at  $600^\circ\text{C}$  for 1 h under the Ar atmosphere to obtain final carbon-coated sample LCSO/C. While the carbon coating introduced here is an ex situ procedure, in situ carbon coating can be adopted in the hydrothermal step by mixing the LCSO precursor with carbon source. The in situ route may further prevent contact and inhibit particle aggregation to obtain a composite material with uniform carbon coating. Carbon sources can be selected from two categories. The first is organic carbon sources, such as citric acid, cellulose, sucrose, and poly-ethylene glycol (PEG). The other is inorganic carbon source, such as carbon black.

The solving of  $\text{SiO}_2$  in aqueous LiOH solution at procedure-1 of the hydrothermal step is a reversible reaction, depending on the  $[\text{OH}^-]$  concentration of the  $\text{Li}_2\text{SiO}_3$  solution, which can be

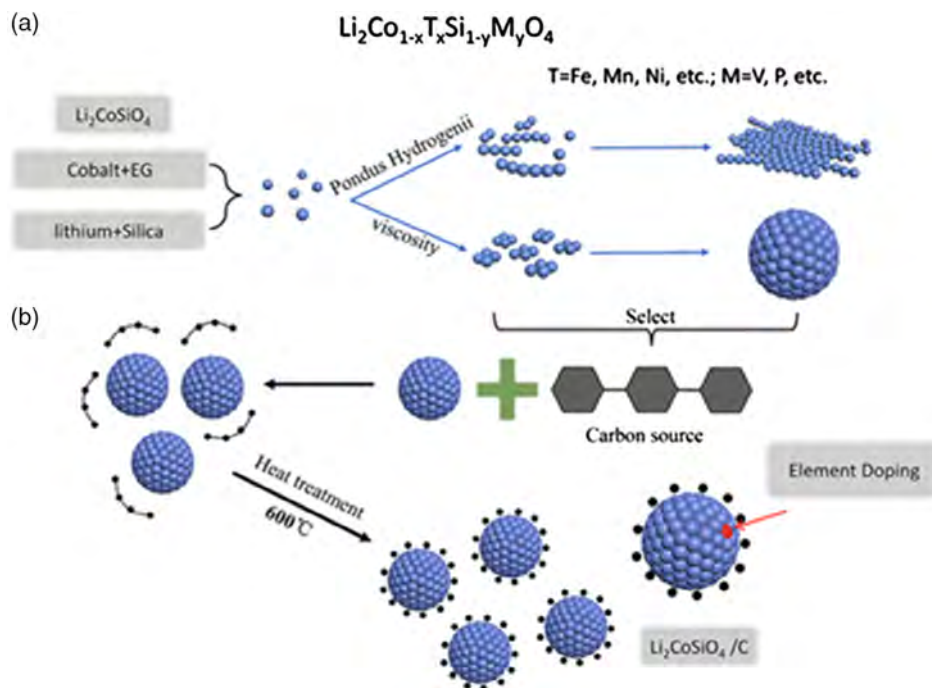


**Figure 2.** Two-step synthesis of LCSO system. a) Schematic paths of the hydrothermal synthesis of raw LCSO materials. b) Carbon coating LCSO/C. Dots and big balls are used to schematically indicate raw LCSO primary particles and secondary aggregates, respectively, and black dot for carbon coating.

easily monitored by the molar ratio  $\alpha$  between LiOH and SiO<sub>2</sub>. The volume ratio  $\beta$  between EG and H<sub>2</sub>O can be used to monitor the viscosity of the mixture suspension, which controls the coprecipitation rate of the Li<sub>2</sub>SiO<sub>3</sub> and Co(OH)<sub>2</sub> in the mixture. Because the OH<sup>−</sup> base precipitates Co ions from the EG solvent and the solid Li<sub>2</sub>SiO<sub>3</sub> is sedimented due to the reduced [OH<sup>−</sup>] concentration. The two ratios ( $\alpha$  and  $\beta$ ) can be used to regulate the morphology, particle size, and secondary aggregation of raw LCSO materials. This wet process provides atomistic-level mixing in the tiny uniform primary polymorphs that aggregate to form low-dimensional nanodot, nanosheet, and submicrometer spherical particles as well. Doping can be easily incorporated in the wet process. Such prepared raw materials contain rich porous structures on the grain boundary.<sup>[31a]</sup> All these structural characters are not changed in the carbon pyrolysis.

**Figure 3** shows an original transmission electron microscope (TEM) study of carbon-coated LCSO particles.<sup>[31b]</sup> Figure 3a shows the particles are loosely stacked aggregates of primary nanodots in the range of 20–50 nm. High-resolution TEM (Figure 3b) shows an amorphous carbon layer of less than

5 nm distributing on the surface of the particles. The nanodots in Figure 3d,e are combined into belt-like nanomaterials. 2D sheet-like LCSO/C material can be formed by uneven belt and dots. The dot-like LCSO/C material can also be directly aggregated into sphere-like LCSO/C materials, and the process of aggregation is isotropic.<sup>[31a]</sup> The energy dispersive X-ray spectroscopy (EDS) mapping of sphere-like LCSO/C material (Figure 3e) shows that the C, Si, Co, and O elements are evenly distributed, which indicates that the material morphology has no obvious effect on the element distribution. The typical percentage of carbon presenting in all the as-prepared coated samples is within 6 wt% by infrared spectroscopy,<sup>[22]</sup> which is consistent with the target pyrolysis. Raman spectroscopy of the coated samples displays two bands around 1352 and 1582 cm<sup>−1</sup> corresponding to the typical D (sp<sup>3</sup> type) and G (sp<sup>2</sup> type) bands of carbon. The intensity ratio between D and G bands ( $I_D/I_G$ ) falls in the range of 1.4–1.5,<sup>[22]</sup> which is often the optimized range for good electrical conductivity of polyanionic cathodes, LFP/C, LFSO/C, and LMSO/C nanocomposites. Brunauer–Emmett–Teller (BET) analysis of the isothermal adsorption of N<sub>2</sub> on the surface of particles reveals the mixed type-II/IV curves and H-3 hysteresis,<sup>[31a]</sup>

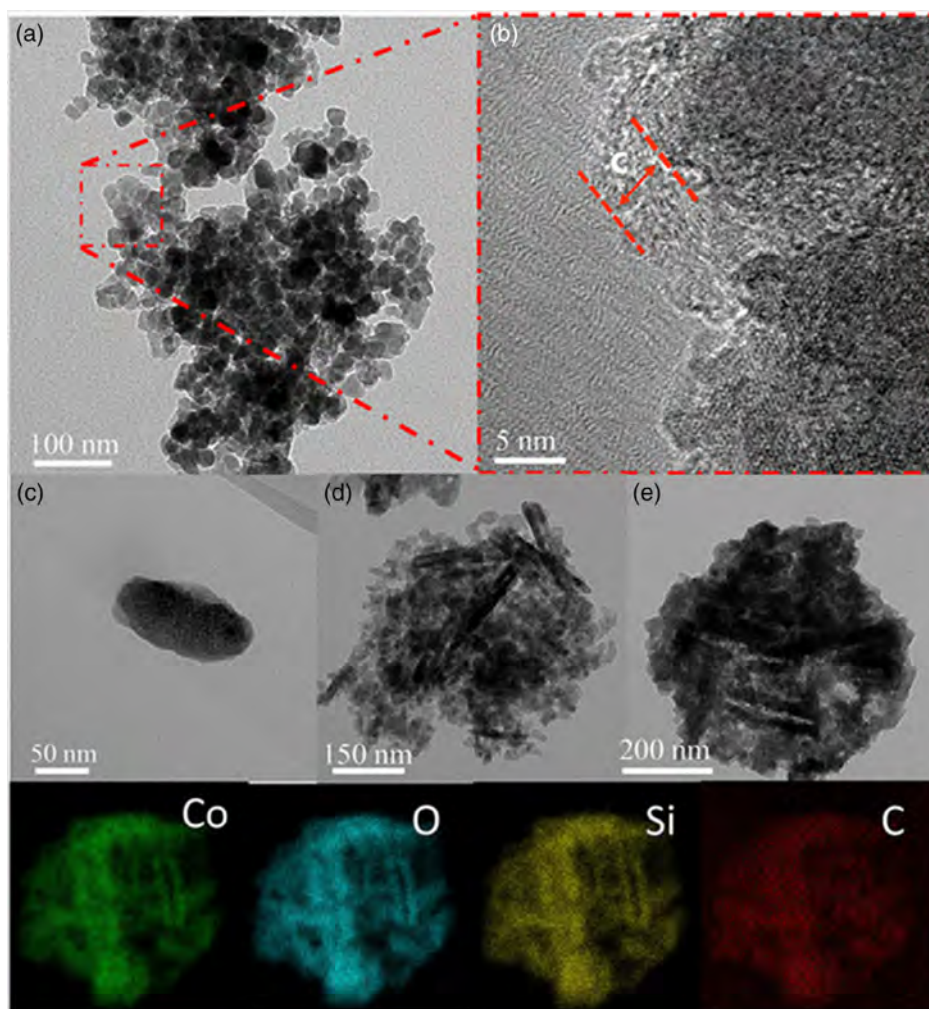


**Figure 3.** Transmission electron microscopic of a) LCSO/C particles, b) high-resolution TEM of carbon layers, c) nanorod, d) nanostructure with nanobelt, e) spherical secondary particles with EDS mapping of the Co, O, Si, and C elements. (Original<sup>[31b]</sup>).

similar to that reported for LFSO, which indicates the presence of mesopores in the ranges of 2–50 nm in our samples. The pore distribution diagram indicates the main pore is mesopores between 20 and 25 nm according to Barrett–Joyner–Halenda mode.<sup>[31a]</sup> Low-dimensional nanostructures contain much high portion of nanopores under 5 nm with the BET specific surface area at the level of  $\approx 90 \text{ m}^2 \text{ g}^{-1}$ . The presence of the mesopores is beneficial to increase the electrical conduction between the electrolyte and the active material.<sup>[31a]</sup> All these are essential to the electrochemical performance.

There are two significant changes in the carbon pyrolysis. One is the heating induced polymorph transition, the other is the carbon-induced Co reduction. **Figure 4a** shows the comparison of the XRD of raw LCSO from hydrothermal process to that of carbon coated spherical samples. The raw LCSO presents the DP patterns of the mix-*Pmn*2<sub>1</sub> agreeing with Figure 1d. In other words, there is a significant cation occupation disorder in the as-synthesized pure LCSO sample. The calcination process in the carbon-coating results in a portion of  $\beta_{II}$  polymorph transiting to TP  $\beta_I$ -polymorph with the space group *Pbn*2<sub>1</sub>. To verify if the new polymorph is a TP  $\beta_I$ -polymorph, instead of a SP pure *Pmn*2<sub>1</sub>, as shown in Figure 1d. We heated the raw LCSO at 800 °C for 12 h. Figure 4b shows the original Rietveld refinement of such heated sample (this sample contains a small Mn doping, but no difference in TP pattern from nondoped heat-treated LCSO). First, it shows clear crystalline characters of TP patterns. Second, the ratio between the highest peak (011) and the lower two, (110) and (101), is about 2:1. Furthermore, the pseudo-orthorhombic group of (002) reflections is the second highest peak group. This confirms the lattice framework of Co-based silicates is a 3D frame structure (either DP or TP in XRD), different from the 2D layered structure of LFSO and LMSO (SP dominating in XRD).

Our first-principles calculations showed the total energy difference between the mix-*Pmn*2<sub>1</sub> DP polymorph and the *Pbn*2<sub>1</sub> TP polymorph is very small, only 2 meV, which explains why the  $\beta_{II}$  phase is converted to the  $\beta_I$  phase around 700–800 °C.<sup>[28]</sup> Under higher temperature, the CoO<sub>4</sub> and LiO<sub>4</sub> of  $\beta_{II}$  polymorph can easily slid to the more stable cationic ordering of  $\beta_I$  polymorph, which presents the symbolic

TP characteristic in the XRD shown in Figure 4b. Nakayama et al. synthesized LCSO with a  $\beta_I$  polymorph with *Pbn*2<sub>1</sub> by a high-temperature solid reaction at 900 °C.<sup>[32]</sup> The reversible second-order phase transition from *Pbn*2<sub>1</sub> to mix-*Pmn*2<sub>1</sub> was confirmed by in situ XRD at high temperature, interpreted as the order–disorder transition of Co and Li cationic occupations. In addition to thermal-induced polymorph transition, Truong et al. observed that the volume expansion may create the cation-exchange disorder that leads to formation of different polymorphs in the supercritical synthesized  $\beta_{II}$  polymorph.<sup>[33]</sup>

Very interesting, through the systematic change of Al-doping contents, we showed the Si-site doping can effectively inhibit the formation of TP phase in the process of carbon coating and obtain a high-purity DP phase.<sup>[22]</sup> Our doping on Si sites with P, Al, and V presents the same phenomena.<sup>[12,22,23]</sup> But doping on Co site, for example, by Mn, does not have this effect, cf. the TP in the small Mn-doped sample in Figure 4b.<sup>[34]</sup>

There is a trade-off between stabilizing the polymorph at mix-*Pmn*2<sub>1</sub> and Co reduction in the carbon coating. As shown in Figure 4a, there is a visible Co impurity signal at 45° (2 $\theta$ ), agreeing with early reports. We found the TP phase can mitigate the Co reduction in the carbon coating. Our recent study also found some low-dimensional nanostructure can effectively inhibit the formation of Co impurities in the process of carbon coating as well.<sup>[31a]</sup> Another interesting finding is to use high valence transition metal dopant like V to substitute the Co reduction by carbon coating.<sup>[23]</sup>

In summary, we observed that three factors may play important roles in the carbon coating: nanostructure, polymorphs, and element doping. The doping process brings confusing effects. Compared with pure phase materials, the composites formed after doping are more likely to generate Co or Co-related impurities during the carbon coating process. That may be strongly due to the vulnerability of Co<sup>2+</sup> in the DP phase. Because the Si-site doping is more prone to Co reduction in the carbon-coating process. It is speculated that the structural stability of TP phase is better than that of DP phase from the point of mitigating the Co reduction. Thus, there is a room for further rational design to optimize the synthesis.

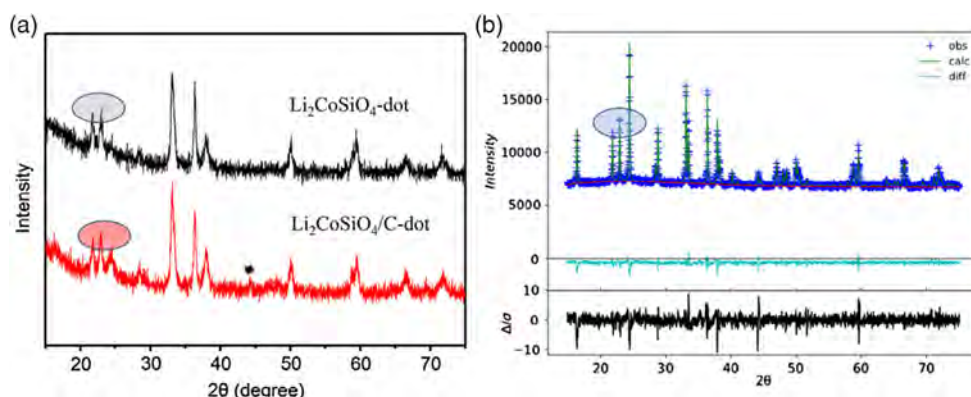


**Figure 4.** a) The XRD of raw LCSO-dot and carbon-coated LCSO-dot, \* Co reduction, b) GSAS Rietveld refinement of crystalline  $\beta_I$ -polymorph with the space group *Pbn*2<sub>1</sub> (goodness of fit  $\approx 1.59$ , wR  $\approx 1.85\%$ , no cationic mixing allowed). a) Reproduced with permission.<sup>[31a]</sup> Copyright 2020, IOP Publishing and b) original data.



### 3. Electrochemistry of LCSO

#### 3.1. Electrochemical Characters of LCSO

The modified LCSO materials by our two-step synthesis have greatly improved the electrochemical performance. The initial charge and discharge capacities increase to over 300 and 220 mAh g<sup>-1</sup>, respectively, competitive to other reported high capacity Li-rich oxides and the commercial LiCoO<sub>2</sub> and its ternary derivatives. The discharging voltage has been confirmed around the 4 V, matching to current electrolytes. No obvious change or “soft discharging” in voltage platform was found in the continuous cycles, proving its stable structural redox character distinct from those in LFSO and LMSO. However, the LCSO system suffers from large irreversible capacity loss and rapid decay of capacity in the cycling. Our study indicates that its electrochemical abnormalities root on the successive cationic and

anionic redox amid the two delithiation processes. This section will focus on the electrochemical characters and mechanisms occurring in the initial electrochemical cycling of LCSO. Fully identification and understanding of the electrochemical process and underlying chemistry are critical to the further electrochemical improvement of multithiated polyanionic structures in general and may inspire new rational designs of oxygen redox-based high energy-density cathodes.

**Figure 5** compiles the initial charging and discharging profiles of LCSO systems reported in our recent publications.<sup>[12,22,23,31a,35]</sup> Spherical (with the secondary particle size ≈900 nm) and low-dimensional sheet-like LCSO/C material can deliver charge and discharge capacities at 212/116 and 281/147 mAh g<sup>-1</sup>, respectively, between 2 and 4.6 V.<sup>[31a]</sup> The improved reversibility is largely attributed to the optimal ion transport channel between the electrolyte and nanostructures of the pure LCSO/C materials. The discharge capacity of

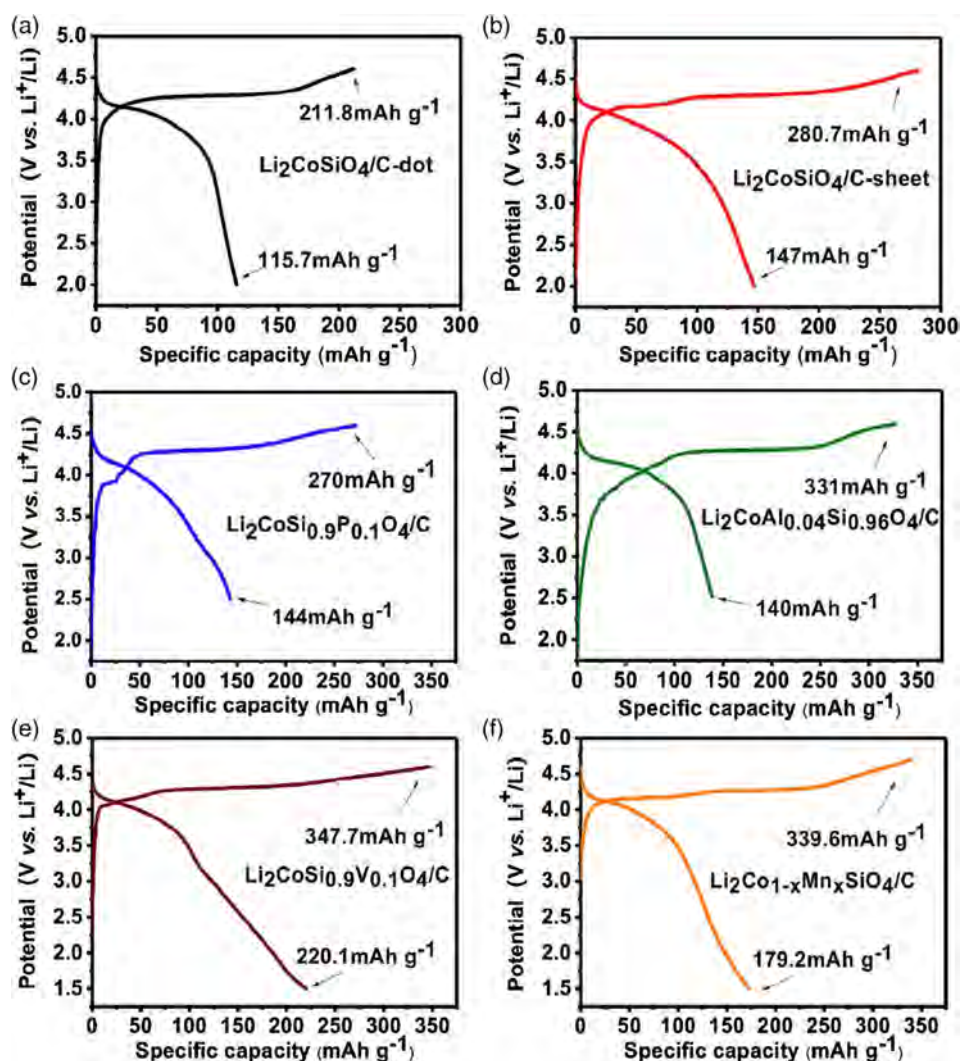


**Figure 5.** First cycle profile of a) LCSO/C-dot and b) LCSO/C-sheet between 2 and 4.6 V, c) Li<sub>2</sub>CoSi<sub>0.9</sub>P<sub>0.1</sub>O<sub>4</sub>/C, d) Li<sub>2</sub>CoSi<sub>0.96</sub>Al<sub>0.04</sub>O<sub>4</sub> between 2.5 and 4.6 V, e) Li<sub>2</sub>CoSi<sub>0.9</sub>V<sub>0.1</sub>O<sub>4</sub>/C, f) Li<sub>2</sub>Co<sub>1-x</sub>Mn<sub>x</sub>SiO<sub>4</sub>/C between 1.5 and 4.6 V. a,b) Reproduced with permission.<sup>[31a]</sup> Copyright 2020, IOP Publishing. c,e) Reproduced with permission.<sup>[12,23]</sup> Copyright 2020, Elsevier. d) Reproduced with permission.<sup>[22]</sup> Copyright 2020, the Royal Society of Chemistry. f) Original.<sup>[35]</sup>

147 mAh g<sup>-1</sup> is the highest reversible capacity reported for pure LCSO in the same electrochemical window. Figure 5a,b shows the clear evidence on the 4 V discharge voltage plateaus of LCSO, a majority of reusable discharge capacity is realized at above 2.5 V that is often the discharge voltage cut-off installed in commercial LiCoO<sub>2</sub> and its derived ternary cathodes. But the irreversible capacity loss is big with the Coulomb efficient only at 52–55%.

In our recent work, we pointed out that the polyhedral connection is the main structural character that impacts the bulk electrical conductivity.<sup>[8]</sup> Silicates, like SiO<sub>2</sub>, are typical insulators. Conductive carbon coating is an effective and simple strategy to improve the electrical conductivity of LCSO. But coating can only improve the conductivity of silicate materials with the outside, whereas ionic doping is aimed to improve the bulk's electronic conduction and ionic diffusion in the internal structure. The ion doping can be an effective way to improve the electrochemical performance regarding the structural stability, rate performance, and cycle stability. Therefore, our first attempt is to dope on the Si sites to inhibit the strong insulation of SiO<sub>4</sub><sup>4-</sup> network. Our first doping used phosphoric acid as a phosphorus source to successfully synthesize the Li<sub>2</sub>CoSi<sub>0.9</sub>P<sub>0.1</sub>O<sub>4</sub>/C sample, which showed performance better than LCSO/C with the charge and discharge capacities at 270 and 144 mAh g<sup>-1</sup> between 2.5 and 4.6 V, respectively.<sup>[12]</sup> The electrochemical improvement was attributed to the electric field modification of PO<sub>4</sub><sup>5-</sup> to the SiO<sub>4</sub><sup>4-</sup> network. In addition, we found that using only a small amount of Al doping can achieve similar higher electrochemical reversibility at Li<sub>2</sub>CoSi<sub>0.96</sub>Al<sub>0.04</sub>O<sub>4</sub> at 331 and 140 mAh g<sup>-1</sup> for the charge and discharge capacity, respectively.<sup>[22]</sup> The underlying mechanism is attributed to the mixture polymorphs of  $\beta_{II}$  and  $\beta_I$  phases.

Doping with transition metals will be different from nonmetal P and Al, because they may also make the charge compensation to Li capacity and activate at different redox potentials. From this hypothesis, Li<sub>2</sub>CoSi<sub>0.9</sub>V<sub>0.1</sub>O<sub>4</sub>/C was designed and successfully synthesized.<sup>[23]</sup> It delivers a much higher discharge capacity at 220.1 mAh g<sup>-1</sup> in the extended voltage range between 1.5 and 4.6 V. However, as shown in Figure 5e, the discharge slope changes from 3 to 1.5 V, contributing nearly half the reversible capacity. This indicates the redox potentials can be rationally designed by other active redox agents, especially being useful for Co-site doping, which may not only increase the usable capacity discharging above 3 V but also reduce the expensive Co for the massive applications. Figure 5f shows an original result with Li<sub>2</sub>Co<sub>1-x</sub>Mn<sub>x</sub>SiO<sub>4</sub>/C, in which a small amount (mole ratio  $x < 10\%$ ) of Mn was successfully doped on the Co sites.<sup>[35]</sup> Its discharge profile essentially reproduces that of pure LCSO but with a higher discharge capacity at 179 mAh g<sup>-1</sup>. The reusable capacity above 3.0 V is higher than that of Li<sub>2</sub>CoSi<sub>0.9</sub>V<sub>0.1</sub>O<sub>4</sub>/C.

The large irreversible capacity loss is a drawback of the LCSO systems. The intrinsically low electrical conductivity is the physical roots to the bad rate performance. We refer the interesting readers to our reports on the cycling and rate performance of pure LCSO and V-doped LCSO.<sup>[31a,23]</sup> Here, we use the dependence of charge and discharge capacities on the cathode loadings to illustrate the effects of the electrical conductivity on the reversible capacity. Figure 6 (original) shows the discharge capacity can

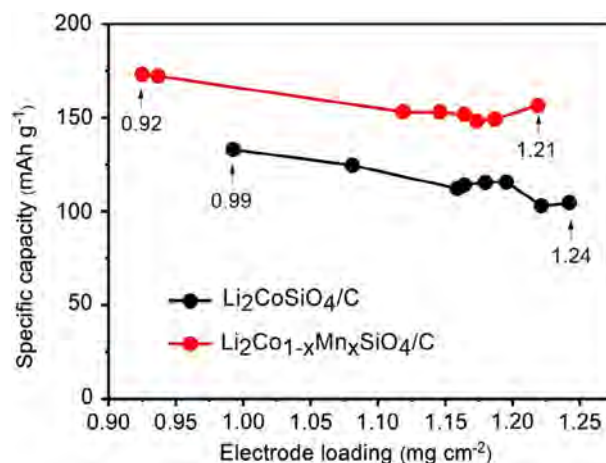


**Figure 6.** Reversible capacity versus active materials mass of electrodes for LCSO and Li<sub>2</sub>Co<sub>1-x</sub>Mn<sub>x</sub>SiO<sub>4</sub>.

vary about 30 mAh g<sup>-1</sup> between low and high electrode loadings, which is almost twice of the range, 16 mAh g<sup>-1</sup> in layered ternary oxide Li(NiCoMn)<sub>1/3</sub>O<sub>2</sub>.<sup>[36]</sup>

### 3.2. Redox Mechanism

Anionic redox due to the oxidization of lattice oxygen ions is a promising chemistry to boost capacity of cathode materials beyond conventional cationic redox-based LIBs, which has only been reported for Li-rich oxide compounds before.<sup>[37]</sup> These materials can deliver reversible capacities higher than 220 mAh g<sup>-1</sup>, largely from the cumulative cationic and anionic redox contributions to multilithium reactivity. In the pioneer 2013 work, Sathiyaraj et al. attributed the extra Li capacity of Li<sub>2</sub>Ru<sub>3/4</sub>Sn<sub>1/4</sub>O<sub>3</sub> to be compensated by an intermediate peroxo-like O<sub>2</sub><sup>6-</sup> dimer with unrealistic O–O bond length at  $\approx 2.4$  Å amid anionic redox.<sup>[1]</sup> However, since then, the study of oxygen redox in the oxide cathodes remains struggling in understanding what oxidized oxygen species determine the charge compensation and oxygen redox potentials.

Polyanionic structures like LCSO have not been expected as a candidate with oxygen redox. Because they do not comply in general with the octahedral d<sup>0</sup> configurations and the directional ligand bonding conformations, the essence of the widely accepted theory for the anionic redox in Li-rich oxides.<sup>[38]</sup> It has been widely accepted that oxygen oxidation arises from electron depletion of the nonbonding O-p states, which have often called as “electron hole” and “oxygen hole” in literature. Note, to avoid misunderstanding the term “hole” with either a more perceived concept for electronic states in semiconductors, or oxygen ionic vacancy in the structures, here we use “electron depletion” to describe the character of the electronic contribution from the lattice oxygen ions to the charge compensation to Li capacity. The further oxidation of lattice oxygen ions will destabilize the local coordination of oxygen ions, especially invokes TM ion migration, which is believed the origin of voltage hysteresis and capacity fading. The electron-depleted oxygen ions, analogue to free radicals if unconfined, are highly chemically reactive to

spontaneously dimerize to form peroxo and superoxo moieties. Then, the over-oxidized oxygen ions lead to oxygen release.<sup>[39,40]</sup> Because almost all high capacity Li-rich oxides have reported oxygen release in the deeply charged states, it has been wrongly assumed the equivalence between peroxo formation and oxygen release in literature.<sup>[39]</sup>

There is a significant difference in oxygen dimerization between on surface and in bulk. The latter is confined within the bulk lattice. **Figure 7a** presents a concise argument in terms of the diatomic molecular orbital diagram on the oxygen oxidation states from the lattice oxygen ions  $O^{2-}$  to molecular dioxygen  $O_2$ . The peroxo formation will consume a full electron per lattice oxygen ion. When the peroxo is oxidized to superoxo, no bonds need to break but the O—O bond shrinks. When the superoxo is further oxidized to molecule oxygen, the cleavage of the bond between the dimer and the binding cations should invoke additional charge transfer and bonding orbital energy for the occurring of degassing, cf. the binding mode of delithiated LCSO model shown in **Figure 7b**. It is also obvious from the orbital diagram in **Figure 7a** that the pure electron depletion is unlikely to offer a meaningful charge compensation to Li capacity. In bulk materials, however, one should expect the important competition in the oxygen coordination amid the dimerization. For instance, the highest occupied  $O_2^{2-}-\pi^*$  molecular orbitals may be competing with open TM-d orbitals for the oxidation and local coordination to charge compensation in the process of delithiation.<sup>[41]</sup> Thus, one should identify consistent spectroscopies showing both electronic and vibrational characteristics if the O—O dimers truly confined in the bulk, not just one of them. That should be the determining factor to not only

the dimer formation but also its lifetime to oxygen release. Unfortunately, extensive Raman spectroscopy, synchrotron X-ray absorption spectroscopy (XAS), resonant inelastic X-ray scattering (RIXS), X-ray photoelectron spectroscopy (XPS), and electron paramagnetic resonance (EPR) have so far only identified electronic characteristics associated with either electron-depleted lattice oxygen or gaseous dioxygen, i.e., the two extreme states of oxidized oxygen species in oxygen chemistry. The key transition from electron-depleted lattice ions to dioxygen, i.e., the intermedium peroxo/superoxo O—O dimer confined in charged cathode, has not yet identified in previous spectroscopic study of oxygen redox.

In our recent work, we combine analytic characterizations and first-principles simulations to demonstrate the complete evolution of charge compensation amid cumulative cationic and anionic redox in solid-solution polyoxyanionic  $Li_2Co_{0.9375}Mn_{0.0625}SiO_4$  (Mn-LCSO).<sup>[39]</sup> In this work, Mn-LCSO composite presents clearly two stages of charge compensations: the first one is mainly cationic oxidation with a small portion of electron-depletion at oxygen ions, and the successive one is mainly anionic oxidation. **Figure 8** shows unambiguously concurrent electronic (XAS) and vibrational (Raman) spectroscopies of peroxo formation amid the second  $Li^+$  extraction around  $LiCo_{0.9375}Mn_{0.0625}SiO_4$ .<sup>[39]</sup> During the charging, the intensity of the  $\nu$ -sym and  $\nu$ -asym vibrational bands increases significantly along with the peroxo dimer (dimer oxygen, DO) signature; in the discharging, the intensity of  $\nu$ -sym and  $\nu$ -asym decreases in the same trend as the DO peak evolution. The first-principles simulated X-ray absorption near edge structure (XANES) confirms the signature pre-edge peak of peroxo species, agreeing well with the ex situ synchrotron XAS.

The new finding of anionic redox mechanism in LCSO is completely different from the popular assumption of two-electron redox only of the transition-metal redox couples of  $Fe^{2+/4+}$  and  $Mn^{2+/4+}$  in LFSO, LMSO, and LCSO as well.<sup>[41,42]</sup> In previous density functional theory investigations, the poor electrochemical performance of  $Li_2MSiO_4$  materials has been associated in general to the instability of most  $M^{3+}$  and  $M^{4+}$  ions in the tetrahedral environment,  $MO_4$  structures are prompt to transform into other forms consisting in octahedral  $MO_6$  units. However, the evidence of peroxo in delithiated LCSO shows the basic difference between cationic redox and anionic redox in the polyanionic structures. Here, we provide a complementary comparison between cationic redox and anionic redox in LCSO.

The lattice evolution of Mn-LCSO during the first charging and discharging cycle reveals two distinct orthorhombic phases: called as Orth-1 and Orth-2.<sup>[39]</sup> Both phases present the characteristic solid-solution reaction in their respective delithiation ranges. The Orth-1 runs from 0 to 1.1  $Li^+$  extraction, whereas the Orth-2 covers from 0.8 to 1.7  $Li$  extraction, cf. **Table 3**. Between 0.8 and 1.3 delithiation is a coexist two phases. The lattice change from Orth-1 to Orth-2 is a stepwise jump in  $a$  and  $b$  axes, but almost no change for  $c$  axis. The expansion of  $a$ ,  $\approx 3.2\%$ , is almost compensated by the contraction of  $b$ ,  $\approx 3.0\%$ , thus the net volume change is almost unchanged from Orth-1 to Orth-2. **Table 2** shows that the conventional cationic redox models would predict 16.89% and 36.07% volume expansions for DP and TP models, respectively, whereas our testing TP models containing the peroxo will reduce only 5.21%, much smaller with respect to

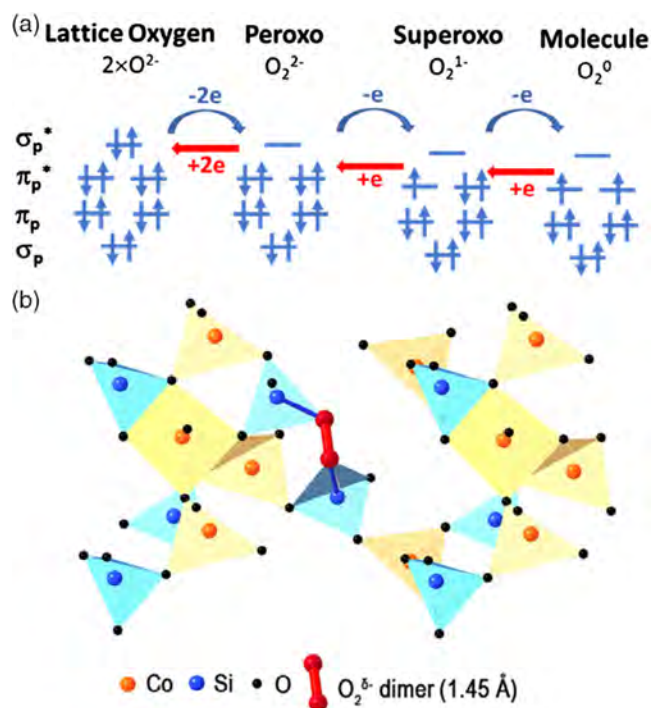


**Figure 7.** a) Diatomic molecular orbital diagrams for lattice oxygen ions, peroxo group, superoxo group, and molecular dioxygen; b) a first-principles  $CoSiO_4$  model containing a peroxo group with the bond length 1.45 Å.



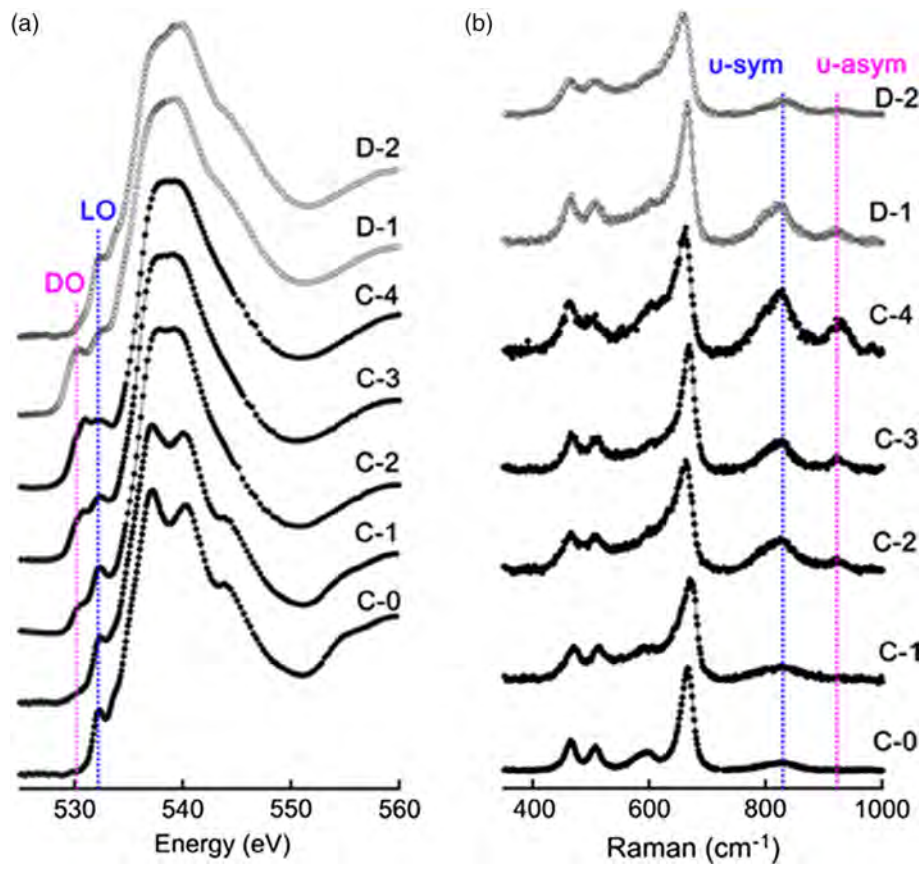


**Figure 8.** Ex situ spectroscopic signatures of oxygen redox in Mn-LCSO. a) Evolution of synchrotron O K-edge XANES in charging (C-0 to C-4 for charge capacity of 0, 80, 160, 240, and end of charge 273 mAh g<sup>-1</sup>), and discharging (D-1 and D-2 for discharge capacity of 10 and 160 mAh g<sup>-1</sup>, respectively); b) Evolution of Raman spectra at the same charging and discharging states. LO and DO indicate the lattice oxygen and the peroxo dimer signals. u-sym and u-asym vibrational bands are assigned to the O—O dimer stretching modes. Reproduced under the terms of a Creative Commons Attribution 4.0 (CC-BY) License.<sup>[39]</sup> Copyright 2021, The Authors, published by Wiley-VCH.

**Table 3.** Calculated crystal structure parameters, including lattice volume and changes. The model of Li<sub>0.5</sub>CoSiO<sub>4</sub> containing the O<sub>2</sub><sup>6-</sup>-dimer is labeled as TP-O<sub>2</sub>, all others no dimer.

	LCSO		LiCoSiO <sub>4</sub>		CoSiO <sub>4</sub>		Li <sub>0.5</sub> CoSiO <sub>4</sub>	Orth-1 (ex) <sup>[39]</sup>	Orth-2 (ex) <sup>[39]</sup>
	DP <sup>[43]</sup>	TP <sup>[23]</sup>	DP <sup>[43]</sup>	TP <sup>[23]</sup>	DP <sup>[23]</sup>	TP <sup>[23]</sup>	TP-O <sub>2</sub> <sup>[39]</sup>	0–1.1 Li <sup>+</sup>	0.8–1.7 Li <sup>+</sup>
<i>a</i> [Å]	6.312	6.31	6.757	6.37	7.155	8.43	6.31	6.289	6.49
<i>b</i> [Å]	5.393	10.78	5.133	10.76	5.278	10.18	10.72	10.787	10.463
<i>c</i> [Å]	4.999	5.00	5.035	5.03	5.268	5.40	5.09	4.956	5.01
Ω [Å <sup>3</sup> f.u. <sup>-1</sup> ]	85.095	85.03	87.302	86.19	99.464	115.7	89.46	83.999	85.051
ΔΩ [%]			2.59%	1.36%	16.89%	36.07%	5.21%		1.3%

1.3% experimental change. The large deviation of cationic redox model is due to the assumed Co<sup>3+/4+</sup> redox pair, which has been overtaken by the peroxo formation. Within the conventional cationic redox mechanism, the biggest lattice expansion is 13.36% along the *a* axis, which is perpendicular to a reflection mirror linking two Wyckoff 4b sites in the DP polymorph. Cationic tetrahedra are uniformly arranged along the same direction and share corners. The tetrahedral volume of CoO<sub>4</sub> contracts by about 18.90% from LCSO to LiCoSiO<sub>4</sub> and by a total of 28.17% from

LCSO to CoSiO<sub>4</sub>. Thus, lattice changes largely depend on the relaxation of the tetrahedral connections and reorganized by peroxo formation. The significant improvement of initial performance is attributed to the inherent cationic disorder that promotes the peroxo formation validated by the first-principles models.<sup>[39]</sup>

The first-principles calculations found both DP and TP polymorphs are Mott insulators within the first Li<sup>+</sup> extraction. The nature of insulating gaps strongly depends on the oxidation



states of Co ions. At  $\text{LiCoSiO}_4$ , there is a swapping of the interaction between  $3d(\text{Co})-2p(\text{O})$  orbitals, which changes the insulating gap from Mott–Hubbard-type to charge-transfer-type, a similar phenomenon has been observed in other polyanionic structure.<sup>[43]</sup> This swapping is an evident proof of the band structure change by lithium intercalation/extraction, which is different from simple energy-level shift in rigid-band model or redox couple pinning. The swapping of near-gap states correlates with the contraction of the oxidized  $\text{CoO}_4$  units, resulting in the cationic electrostatic field polarization. The coexistence of both lattice distortion and bandgap opening/increases indicates the occurring of Peierls distortions in  $\text{LiCoSiO}_4$ , whose major edge states are nonbonding states of oxygen ions, pointing to the electron depletion in anionic oxidation of oxygen. Similar band edge states have been identified in the model of  $\text{Li}_2\text{CoV}_{1/8}\text{Si}_{7/8}\text{O}_4$  with V doping at Si sites.<sup>[23]</sup> An oxygen dimer structure has been constructed for the V-doping models. The orbital order in the edge states near the Fermi level were examined. By comparing the local density of states of  $\text{Li}_{2-x}\text{CoV}_{1/8}\text{Si}_{7/8}\text{O}_4$  ( $x = 0, 1/8, 1, 1.5, 2$ ), it is found that V doping may change the activity of O dimer and inhibit the oxidation–reduction of Co and O in the early stage of delithiation.<sup>[23]</sup> This may account for the critical difference in the discharging slope shown in Figure 5e,f.

### 3.3. Modeling Lithium-Ion Transport

As shown in Figure 6, the major challenge of LCSO is to improve the low electrical conductivity, which includes electronic conduction and Li-ion diffusion. However, electronic conduction and ionic diffusion are difficult to separate from each other in terms of the electrochemical functionality for either cathode or solid electrolytes. There is no established theory to address the interplay between electronic transport and ionic mobility in general. Both cathode and solid electrolytes are ionic conductors. They differ mainly in the electronic conduction. Cathode must have good electronic conduction while electrolytes should be electronic insulators. The electrochemical impedance spectroscopy (EIS) study found that the radius of semicircles in the Nyquist plot, corresponding to interface resistance, of the charged  $\text{Li}_2\text{CoSi}_{0.96}\text{Al}_{0.04}\text{O}_4$  sample increases ten times of that before charging.<sup>[22]</sup> That indicates the charged structure has very poor electrical conductivity. This phenomenon is completely different from in layered oxide cathodes, which often become more conductive after the initial charging.<sup>[36]</sup> While this helps interpret the large irreversible capacity loss, its physical origin is very puzzling.

One possibility may be due to the fall-off of the carbon layer after the lithium-ion deintercalation, and the decrease in the crystallinity of the charged phase causes the disorder of the lithium-ion diffusion channel. However, the observed 1.3% volume change (Table 3) does not support this fall-off hypothesis, because the typical volume expansion in LFP is at the same level, while it has very stable carbon layers for high rate performance.

Bandgap generally impacts on the electronic conduction. All our calculations predict doping generally gives a smaller gap, which agrees with the improved performance. But it is a general trend that delithiated structures have reduced gap as well. Expanding lattices with shrinking tetrahedral units like  $\text{CoO}_4$  would indicate a large space for lithium ion moving, which

should favor a better rate capability and easy reintercalation. But both are against the EIS results. Considering the similarity between LCSO with its sister structures like LISICON electrolytes, they may have similar Li-ion diffusive mechanisms, in which interstitial Li ions may lower the energy required to move from site to site. However, the peroxo formation in the delithiated phase may make the interstitial positions become difficult to be accessible by mobile  $\text{Li}^+$ . The charge transfer between mobile  $\text{Li}^+$  and oxidized oxygen may alternate both electronic hopping and  $\text{Li}^+$  motion.

To alleviate the grand challenging in modeling lithium-ion transporting in LCSO systems, especially for the oxidized structures with peroxo, we tested a strategy to evaluate the electric field of polyanionic building blocks and use the lattice electrostatic energy to approximate the energy landscape along the ionic diffusion paths.

Here, we first use the P-doping models to illustrate the feature of electric field change in delithiation. We constructed an atomic model of P-substituted Si in LCSO using superstructure. Because P has one electron less than Si, the first-principles calculation of P-doped system with negative electric state is carried out.<sup>[12,41]</sup> This is equivalent to model a solid solution  $\text{Li}_{(4-x)}\text{Si}_{(1-x)}\text{P}_x\text{O}_4$ , i.e.,  $(1-x)\text{Li}_4\text{SiO}_4 + x\text{Li}_3\text{PO}_4$ . When the substitution of some  $\text{Si}^{4+}$  by  $\text{P}^{5+}$  in the lattice, the neutral charge results in the addition of interstitial Li ions, which may diffuse much more easily. As a good approximation, this effect can be viewed as a micro-electrical field on the lattice.

By comparing the models of  $\text{Li}_{1/2}\text{CoSiO}_4$  and  $\text{Li}_{1/2}\text{CoSi}_{7/8}\text{P}_{1/8}\text{O}_4$  in the 75% delithiated phase which is the pivoting phase to high capacity. We found that in the undoped model,  $\text{Li}^+$  has a symmetrical stepwise distribution, and the tetrahedron forms an orderly layer of space charge, indicating the high-stress network with Peierls distortion. That is not conducive channels to ion diffusion and electron conduction.<sup>[12]</sup> The P-doped model presents a significant redistribution of  $\text{Li}^+$  and  $\text{CoO}_4$  groups around the P site, which behaviors as repulsive positive charge centers, suppressing the asymmetric stress from Peierls distortion. However, this model utilized the conventional Co redox at 75% delithiated phase, which is not the oxidized structure of the polymorph. Oxygen dimerization is essentially a kind of electron-ion coupled relaxation as does the Peierls distortion. Thus, they are competitive during the delithiation process, which may be the key microfactor restricting the reversibility of both cationic and anionic redox. This modeling shows the importance of the electric field to modify the cationic distribution that may be a controlling factor to Li mobility.

We introduced an approximate scheme to evaluate the Li-ion diffusive path and compared the electric field model with first-principles total energy calculation.<sup>[23]</sup> Li migration behavior around Si and V were compared in V-doping model. The path along two corner-sharing tetrahedral sites through an octahedral interstitial site is shown in Figure 9a. The first-principles migration energy barriers are 0.48 and 0.28 eV for LCSO and V-LCSO, respectively, shown in Figure 9b. According to the standard Arrhenius relation, V doping increases the ionic transport by three orders of magnitude.<sup>[23]</sup> The migration energy barrier of V-LCSO is also lower than that of 0.39 eV in the edge-sharing hexagonal close-packed/face-centered cubic (hcp/fcc) tetrahedral solid electrolyte reported by Wang et al.<sup>[44]</sup>

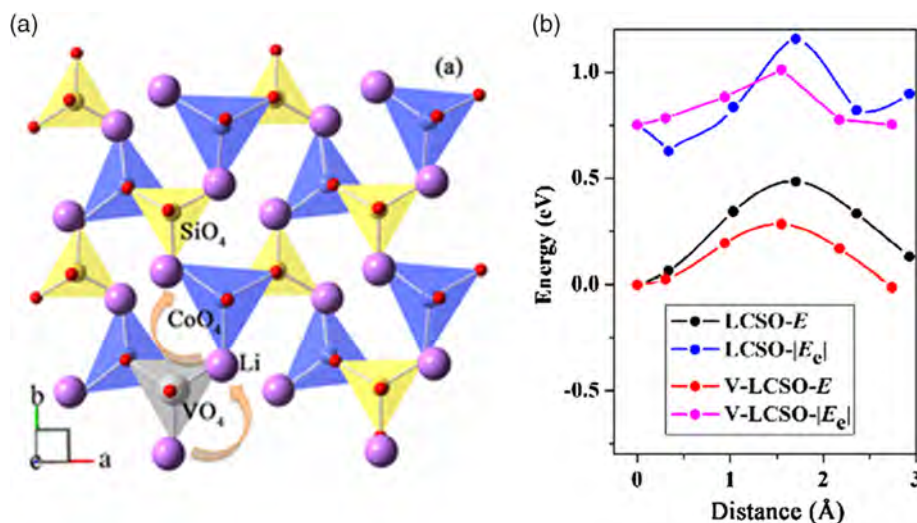


**Figure 9.** a) The Li-ion migration path along  $y$  direction in crystal model of  $\text{Li}_2\text{CoV}_{1/16}\text{Si}_{15/16}\text{O}_4$ ; b) first-principles (LCSO- $E$ , V-LCSO- $E$ ) and Madelung energy (LCSO- $|E_e|$ , V-LCSO- $|E_e|$ ) calculations of migration energy along the diffusive path for undoped and V-doped models. Reproduced with permission.<sup>[23]</sup> Copyright 2020, Elsevier.

We use Madelung matrix method to calculate the lattice electrostatic energy to approximate the migration energy and compare with first-principles results. Madelung matrix method uses the point charge approximation to calculate electrostatic interaction between neutral polyhedron units (NPU).<sup>[45]</sup> Each matrix element  $M_{ij}$  is solely determined by the geometric combination of NPUs, i.e., the  $\text{TO}_4$  groups ( $T = \text{Co}, \text{Si}$ ). The results of  $M_{ij}$  of  $\text{CoO}_4$  and  $\text{SiO}_4$  tetrahedra are shown in Table 4.  $M_{\text{Si-Si}}$  of  $\text{SiO}_4$  changes less than 1% while that of  $\text{CoO}_4$  increases by nearly 11%. This means that the onsite electrostatic interaction at  $\text{CoO}_4$  increases with Co oxidation, in accordance with the reduced Co—O bond length.  $\text{SiO}_4$  remains almost unchanged, pointing to strong covalent bonding between Si and O over all delithiation states. The effective electrostatic attractions between corner sharing  $\text{CoO}_4$  and  $\text{SiO}_4$  become stronger with increased delithiation, whereas for the other nonsharing  $\text{CoO}_4$  and  $\text{SiO}_4$ , the electrostatic interactions are close to zero over the course of the whole cycle. This indicates that electrostatic interactions between  $\text{CoO}_4$  and  $\text{SiO}_4$  groups are the main factor accounting for lattice changes in delithiation. This confirms what we have showed in the P-doping models. The microelectric field plays the important role on the lattice distortion. The Madelung energies, along

**Table 4.**  $\text{CoO}_4$  and  $\text{SiO}_4$  tetrahedral units and the Madelung matrix elements. Madelung matrix element  $M_{ij}$  are in units of  $\text{\AA}^{-1}$ . Positive  $M_{ij}$  means repulsion while negative attraction.<sup>[23]</sup>

mix- $\text{Pmn}2_1$	LCSO	$\text{LiCoSiO}_4$	$\text{CoSiO}_4$
Intra- $\text{CoO}_4$	−0.780	−0.828	−0.864
Intra- $\text{SiO}_4$	−0.933	−0.938	−0.940
$M_{\text{CoSi}}$	−0.173	−0.183	−0.199
$M_{\text{CoSi}}$	−0.168	−0.177	−0.194
$M_{\text{CoCo}}$	−0.001	−0.004	0.004
$M_{\text{Si-Si}}$	−0.001	0.001	0.002

the same Li migration path, are shown in Figure 8b. It is very clear that the approximate energy curve along the migration path substantially agrees with that by density-functional theory. The Madelung energy barrier of V-LCSO is much lower than that of LCSO, indicating that electrostatic interaction plays the main role in Li ionic migration and may offer a fast and high throughput alternative to otherwise accurate but time-consuming first-principles calculations.

## 4. Conclusion

Safety and energy-density are two key properties of cathode materials that need to be improved significantly for success of next-generation LIB to EVs and smart grid power systems. The high safe  $\text{LiFePO}_4$  motivates the early study of silicates,  $\text{Li}_2\text{MSiO}_4$ ,<sup>[46]</sup> ( $M = \text{Fe}, \text{Mn}, \text{Co}$ ), but now they confront extreme functional difficulties to move forward. Lithium cobalt silicate LCSO is a unique 3D framework cathode material with a high theoretical capacity above  $300 \text{ mAh g}^{-1}$  and a high voltage plateau around 4.0 V, which make it among the few candidates having theoretical energy density above  $1200 \text{ Wh kg}^{-1}$ . Thus, LCSO presents high potential as a high safe, energy-density cathode material compatible with the full working voltage window of the 4 V organic electrolytes.

This review summarizes the modification strategy to improve the electrochemical performance of LCSO, mainly by two disciplines: surface coating and element doping. Carbon coating shows effects to reduce the agglomeration of particles, shorten the lithium-ion diffusion path, suppress side reactions on the electrode surface, and thereby reduce the charge transfer resistance. Element doping can be implemented in LCSO on Li, Co, Si, and O sites. We show doping on different sites can have different effects. For example, heterovalent ion doping can lead to the formation of lattice vacancies or lithium-ion vacancies, which exerts on modification of the microelectric field of the polymorphs.

The most important perspective with LCSO is its two lithium ions in the process of charging and discharging, which is the first confirmed cationic and anionic redox systems among polyanionic structures. This provides a prototype to explore fundamental issues in the oxygen redox. The stable anionic redox mechanism may account for electrochemical abnormalities in performance. The poor conductivity of LCSO may originally roots on the strong insulation of polyanion  $\text{SiO}_4^{4-}$ . Si-site doping can weaken the O–Si–O bridge bonds thereby effectively improving conductivity. The oxidation states of oxidized oxygen species participating in the oxygen redox reaction may alter the electronic conductivity and Li mobility, which have not been able to study earlier.

To take advantage of SSBs, only a part of oxygen chemistry,  $\text{O}_2^{2-}|_s \leftrightarrow \text{O}_2|_g$ , in fuel cells/metal-air batteries is needed to incorporate in the intercalation host for metal-ion batteries such as LIBs or sodium-ion batteries. Peroxo confined in the bulk of LCSO brings in a new strategy to realize high capacity without oxygen release. The deep understanding of the redox mechanism in LCSO may inspire new designs of high-Li silicates as a new prototype of multilithiated compound cathodes. For example, in a loose context, LCSO can be expressed as a special case of composites ( $n\text{Li}_2\text{O} + \text{CoO} + \text{SiO}_2$ ) at  $n = 1$ . The high  $n$ ,  $>1$ , of the ratio of  $\text{Li}_2\text{O}$  versus  $\text{SiO}_2$ , indicates a high Li concentration, or a high theoretical Li capacity per silicate formula.<sup>[8]</sup> Both  $\text{Li}_8\text{SiO}_6$  ( $4\text{Li}_2\text{O} + \text{SiO}_2$ ) and  $\text{Li}_6\text{SiO}_5$  ( $3\text{Li}_2\text{O} + \text{SiO}_2$ ) have been reported as  $\text{CO}_2$  capture materials. Can the insights from improving LCSO help rationally convert  $\text{Li}_8\text{SiO}_6$  or  $\text{Li}_6\text{SiO}_5$  as a triple or even quadruple Li-capacity cathode? This perspective may accelerate the integration of oxygen chemistry with cationic redox in intercalation materials, offering an opportunity to significantly expand the scope of cumulative anionic and cationic redox for high energy-density cathodes in general.

## Acknowledgements

J.L. acknowledges programs supported by National Key R&D Program of China (nos. 2018YFB0704300 and 2018YFB0704302), and thanks Ailing Tian and Ying Zhang for participating in part of experimental works in their group.

## Conflict of Interest

The authors declare no conflict of interest.

## Keywords

anionic redox, cathodes, electrochemistry, lithium-ion batteries, polyanionic  $\text{Li}_3\text{PO}_4$ , polymorphs, silicates

Received: July 30, 2020

Revised: November 24, 2020

Published online: March 4, 2021

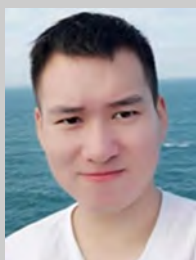
- [1] M. Sathiya, G. Rousse, K. Ramesha, C. P. Laisa, H. Vezin, M. T. Sougrati, M. L. Doublet, D. Foix, D. Gonbeau, W. Walker, A. S. Prakash, M. Ben Hassine, L. Dupont, J. M. Tarascon, *Nat. Mater.* **2013**, *12*, 827.

- [2] J. Li, R. Shunmugasundaram, R. Doig, J. R. Dahn, *Chem. Mater.* **2016**, *28*, 162.  
 [3] K. Zhou, S. Zheng, H. Liu, C. Zhang, H. Gao, M. Luo, N. Xu, Y. Xiang, X. Liu, G. Zhong, Y. Yang, *ACS Appl. Mater. Interfaces* **2019**, *11*, 45674.  
 [4] H. Ji, A. Urban, D. A. Kitchaev, D. Kwon, N. Artrith, C. Ophus, W. Huang, Z. Cai, T. Shi, J. Kim, H. Kim, G. Ceder, *Nat. Commun.* **2019**, *10*, 592.  
 [5] D. Chen, J. Wu, J. K Papp, B. D McCloskey, W. Yang, G. Chen, *Small* **2020**, *16*, e2000656.  
 [6] C. Zhan, Z. Yao, J. Lu, L. Ma, V. A. Maroni, L. Li, E. Lee, E. E. Alp, T. Wu, J. Wen, Y. Ren, C. Johnson, M. M. Thackeray, M. K. Y. Chan, C. Wolverton, K. Amine, *Nat. Energy* **2017**, *2*, 963.  
 [7] S. Kirklin, M. K. Y. Chan, L. Trahey, M. M. Thackeray, C. Wolverton, *Phys. Chem. Chem. Phys.* **2014**, *16*, 22073.  
 [8] Z. Chen, Z. Zhang, J. Li, *Phys. Chem. Chem. Phys.* **2018**, *20*, 20363.  
 [9] B. Goodenough, Y. Kim, *J. Power Sources* **2011**, *196*, 6688.  
 [10] T. Masese, Y. Orikasa, C. Tassel, J. Kim, T. Minato, H. Arai, T. Mori, K. Yamamoto, Y. Kobayashi, H. Kageyama, Z. Ogumi, Y. Uchimoto, *Chem. Mater.* **2014**, *26*, 1380.  
 [11] H. Duncan, A. Kondamreddy, P. H.J. Mercier, Y. Le Page, Y. Abu-Lebdeh, M. Couillard, P. S. Whitfield, I. J. Davidson, *Chem. Mater.* **2011**, *23*, 5446.  
 [12] Z. Zhang, Z. Chen, X. Zhang, D. Wu, J. Li, *Electrochim. Acta* **2018**, *264*, 166.  
 [13] D. Rangappa, K. D. Murukanahally, T. Tomai, A. Unemoto, I. Honma, *Nano Lett.* **2012**, *12*, 1146.  
 [14] M. S. Islam, R. Dominko, C. Masquelier, C. Sirisopanaporn, A. R. Armstrong, P. G. Bruce, *J. Mater. Chem.* **2011**, *21*, 9811.  
 [15] J. Billaud, C. Eames, N. Tapia-Ruiz, M. R. Roberts, A. J. Naylor, A. R. Armstrong, M. S. Islam, P. G. Bruce, *Adv. Energy Mater.* **2017**, *7*, 1601043.  
 [16] Z. L. Gong, Y. X. Li, Y. Yang, *J. Power Sources* **2007**, *174*, 524.  
 [17] a) C. Lyness, B. Delobel, A. R. Armstrong, P. G. Bruce, *Chem. Commun.* **2007**, *46*, 4890; b) A. R. Armstrong, C. Lyness, M. Ménétrier, P. G. Bruce, *Chem. Mater.* **2013**, *22*, 1892.  
 [18] G. He, G. Popov, L. F. Nazar, *Chem. Mater.* **2013**, *25*, 1024.  
 [19] M. K. Devaraju, Q. D. Truong, I. Honma, *RSC Adv.* **2013**, *3*, 20633.  
 [20] S. Thayumanasundaram, V. S. Rangasamy, J. W. Seo, J.-P. Locquet, *Ionics* **2018**, *24*, 1339.  
 [21] T. S. Le, T. H. Hoa, D. Q. Truong, *J. Electroanal. Chem.* **2019**, *842*, 133.  
 [22] H. Du, X. Zhang, Z. Chen, D. Wu, Z. Zhang, J. Li, *RSC Adv.* **2018**, *8*, 22813.  
 [23] L. Huai, W. Du, Z. Zhang, X. Zhang, Z. Zhang, Z. Chen, J. Wu, D. Wang, J. Li, *Electrochim. Acta* **2020**, *353*, 136564.  
 [24] a) Z. Gu, J. Guo, Z. Sun, X. Zhao, W. Li, X. Yang, H. Liang, C. Zhao, X. Wu, *Sci. Bull.* **2020**, *65*, 702; b) M. Wang, J. Guo, Z. Wang, Z. Gu, X. Nie, X. Yang, X. Wu, *Small* **2020**, *16*, 1907645; c) C. Zhao, J. Guo, Z. Gu, X. Zhao, W. Li, X. Yang, H. Liang, X. Wu, *J. Mater. Chem. A* **2020**, *8*, 17454.  
 [25] F. Zheng, M. Kotobuki, S. Song, M. Lai, L. Lu, *J. Power Sources* **2018**, *389*, 198.  
 [26] J. Kuwano, A. R. West, *Mater. Res. Bull.* **1980**, *15*, 1661.  
 [27] A. R. West, F. P. Glasser, *J. Solid State Chem.* **1972**, *4*, 20.  
 [28] C. Zhang, Z. Chen, J. Li, *Chem. Phys. Lett.* **2013**, *580*, 115.  
 [29] a) S. Nishimura, S. Hayase, R. Kanno, M. Yashima, N. Nakayama, A. Yamada, *J. Am. Chem. Soc.* **2008**, *130*, 13212; b) Q. Cheng, W. He, X. Zhang, M. Li, L. Wang, *J. Mater. Chem. A* **2017**, *5*, 10772.  
 [30] A. Saracibar, A. Van der Ven, M. E. Arroyo-de Dompablo, *Chem. Mater.* **2012**, *24*, 495.

- [31] a) W. Du, A. Tian, Y. Zhang, Z. Chen, Z. Zhang, D. Wang, J. Li, *Nanotechnology* **2020**, 31, 425602; b) W. Du, Master Degree Thesis, University of Chinese Academy of Sciences, Ningbo, China, **2020**.
- [32] N. Nakayama, T. Itoyama, K. Suemoto, K. Fujiwara, A. Nakatsuka, M. Isobe, Y. Ueda, *Trans. Mater. Res. Soc. Jpn.* **2011**, 36, 437.
- [33] Q. D. Truong, M. K. Devaraju, Y. Sasaki, H. Hyodo, I. Honma, *Chemistry* **2014**, 20, 16210.
- [34] Z. Zhang, Ph. D. Thesis, University of Chinese Academy of Sciences, Ningbo, China, **2017**.
- [35] X. Zhang, Z. Chen, L. Huai, D. Wang, J. Li, presented at *Materials Research Society (MRS) Conf.*, **2018**.
- [36] X. Zhang, Z. Chen, B. Schwarz, F. Sigel, H. Ehrenberg, K. An, Z. Zhang, Q. Zhang, Y. Li, J. Li, *Electrochim. Acta* **2017**, 227, 152.
- [37] G. Assat, J. Tarascon, *Nat. Energy* **2018**, 3, 373.
- [38] D. H. Seo, J. Lee, A. Urban, R. Malik, S. Kang, G. Ceder, *Nat. Chem.* **2016**, 8, 692.
- [39] Z. Chen, B. Schwarz, X. Zhang, W. Du, L. Zheng, A. Tian, Y. Zhang, Z. Zhang, X. C. Zeng, Z. Zhang, L. Huai, J. Wu, H. Ehrenberg, D. Wang, J. Li, *Angew. Chem. Int. Ed.* **2021**, <https://doi.org/10.1002/anie.202100730>.
- [40] Z. Chen, J. Li, X. C. Zeng, *J. Am. Chem. Soc.* **2019**, 141, 10751.
- [41] Z. Chen, J. Li, Z. Zhang, *J. Mater. Chem.* **2012**, 22, 18968.
- [42] G. Zhong, P. Yan, Z. Liu, M. Xie, H. Lin, *J. Phys. Chem. C* **2010**, 114, 3693.
- [43] C. Zhang, Z. Chen, Y. Zeng, Z. Zhang, J. Li, *J. Phys. Chem. C* **2014**, 118, 7351.
- [44] Y. Wang, W. D. Richards, S. P. Ong, L. J. Miara, J. C. Kim, Y. Mo, G. Ceder, *Nat. Mater.* **2015**, 14, 1026.
- [45] Z. Chen, J. Li, *J. Comput. Chem.* **37**, **2016**, 1476.
- [46] A. Nýtén, A. Abouimrane, M. Armand, T. Gustafsson, J. O. Thomas, *Electrochem. Commun.* **2005**, 7, 156.



**Wenqiang Du** is currently a RD engineer at Sinosteel Nanjing Research Institute. He received his master's degree in engineering from University of Chinese Academy of Sciences, in 2020. He is mainly engaged in research on new energy materials including LIB conductive paste, conductive ink material technology innovation, and commercialization.



**Zhifeng Zhang** is currently a RD director at AiTek Holding. He received his Ph.D. degree in Ningbo Institute of Material Technology and Engineering from Chinese Academy of Sciences, in 2017. His research focuses on materials for high energy storage LIBs and the electrochemical processes in cathode material. His current research is on ceramic powder additive for the performance and safety improvement of LIBs.



**Zhenlian Chen** is currently an associate professor in School of Chemical and Environmental Engineering at Jiangnan University. She received her Ph.D. degree from Department of Physics at Wuhan University, in 2011. Her current research interests focus on first-principles studies on crystal/electronic structures and X-ray spectroscopies to address issues related with oxygen redox in LIB and lithium-air battery.



**Jun Li** was a professor from 2010 to 2020 at Ningbo Institute of Material Technology and Engineering from Chinese Academy of Sciences. He received his Ph.D. degree from Institute of Physics at Chinese Academy of Sciences, in 1997. He specialized in computational modeling of materials and batteries with emphasis on electronic structures and new cathode prototype development. His research interests are on oxygen-based energy generation and storage systems.



# Oxide-Based Optoelectronics

Alexander A. Demkov,\* J. Elliott Ortmann, Marc Reynaud, Ali K. Hamze, Patrick Ponath, and Wente Li

Dedicated to Professor David A. Drabold on the occasion of his 60th birthday

Integrated Si photonics has the potential to revolutionize the processing of information between different integrated chips, as well as within a single chip itself. By performing at least a part of the task with photons rather than electrons, new opportunities for broad-band low-power communication and computing are created. Herein, the theoretical description of the linear electro-optic (EO), or Pockels, effect and a newly elucidated design rule for materials evaluation is summarized. Possible applications of Si-integrated optical elements based on perovskite oxides and their heterostructures are also discussed. In particular, the Pockels effect in BaTiO<sub>3</sub> films grown on Si and intersubband transitions in Si-integrated perovskite quantum wells (QWs) is described.

confinement can be produced artificially in TMO QWs via appropriate materials selection and band engineering. More importantly, these materials systems can now have a real technological impact due to a recently developed process that allows them to be integrated easily on Si and other semiconductors.<sup>[12]</sup>

In this article, we will briefly review the epitaxial integration of oxides on semiconductors, as well as the basics of the Pockels effect, as the reader may not be familiar with the subject. We will then review our recent work on exploiting the Pockels effect in semiconductor-integrated BaTiO<sub>3</sub> and

## 1. Introduction

Transition metal oxide (TMO) thin films and their heterostructures are astoundingly rich physical systems. The striking variety of emergent phenomena arising from the correlated physics of *d*-electrons in these materials has long piqued the interest of scientists and engineers working to develop integrated devices with advanced functionalities.<sup>[1,2]</sup> While many researchers have endeavored to integrate complex TMO films into oxide electronics,<sup>[3–6]</sup> photonics has emerged as another area in which the properties of TMO thin films can be exploited for a variety of technological applications, ranging from high-speed transceivers and sensors to quantum computing.<sup>[7–11]</sup> In this article, we focus primarily on two distinct phenomena being exploited in TMO thin films for utilization in advanced photonic technologies: the linear electro-optic (EO), or Pockels, effect and extreme electronic confinement in TMO quantum wells (QWs). The Pockels effect is the change in refractive index of a material induced by the application of a low-frequency or static electric field. This effect is found natively in many TMO materials, including lead zirconate titanate (PZT, PbZr<sub>x</sub>Ti<sub>1-x</sub>O<sub>3</sub>), lithium niobate (LN, LiNbO<sub>3</sub>), and most strongly barium titanate (BTO, BaTiO<sub>3</sub>). Extreme electronic


on room-temperature intersubband transitions in LaAlO<sub>3</sub>/SrTiO<sub>3</sub> QWs.

## 2. Epitaxial Integration of Oxides on Semiconductors

The modern era of integration of complex oxides, particularly perovskites, began with a stunning discovery by McKee and co-workers that SrTiO<sub>3</sub> (STO) can be epitaxially grown on Si by molecular beam epitaxy (MBE) using a very thin SrO buffer.<sup>[13]</sup> This was soon followed by integration of BaTiO<sub>3</sub> on Ge.<sup>[14]</sup> Initial interest in the epitaxial integration of oxides on Si was in using the high dielectric constant (high-*k*) of some perovskites to circumvent the gate leakage current problem in highly scaled silicon field-effect transistors (FETs) caused by the extremely low thickness of SiO<sub>2</sub> in the gate capacitor as dictated by scaling laws.<sup>[15]</sup> It was soon realized that STO-buffered Si is also a very convenient platform for further integration of other oxides on Si (001).<sup>[16]</sup> Subsequently, many other oxides were successfully integrated on almost all common semiconductors.<sup>[12]</sup>

Further work using MBE has shown that it is possible to directly integrate BTO on Si using a previously deposited STO template,<sup>[17–19]</sup> and to be able to do so while maintaining strong EO response.<sup>[8]</sup> As we have mentioned, BTO has a very large Pockels response in its bulk form, and thus is very appealing for integration with Si for photonics applications. It is therefore important to understand how BTO grows on Si because the strength of the Pockels effect has to do with both crystalline quality and how the polarization domains in the crystal orient themselves. The work of Dubourdieu et al. and Vaithyanathan et al. showed that when grown on Si via MBE, BTO tends to initially grow in the tetragonal *P4mm* phase with its long axis in the out-of-plane

Prof. A. A. Demkov, Dr. J. E. Ortmann, M. Reynaud, Dr. A. K. Hamze, Dr. P. Ponath, W. Li  
Department of Physics  
The University of Texas  
Austin, TX 78712, USA  
E-mail: demkov@physics.utexas.edu

 The ORCID identification number(s) for the author(s) of this article can be found under <https://doi.org/10.1002/pssb.202000497>.

DOI: 10.1002/pssb.202000497

direction and with out-of-plane polarization (perpendicular to the substrate surface) due to compressive strain.<sup>[17,18]</sup> However, as film thickness increases, the polarization of BTO tends to fall in-plane (parallel to the substrate surface) due to electrical boundary conditions. The tetragonal long axis falls in-plane, as well. Hsu et al. showed that by modifying the thickness of the STO buffer layer, it is possible to control the crystalline orientation of BTO films.<sup>[19]</sup> It was also seen that for thin films down to 25 nm, a small portion of BTO films will be in plane near the surface of the film even though the films are still experiencing considerable compressive strain, indicating a complex domain distribution.<sup>[20]</sup> Such a domain distribution can be modeled computationally for a thin BTO film using phase field modeling, as shown in **Figure 1**.<sup>[21]</sup> The bottom of the film is assumed to be grounded while for the top surface an open-circuit boundary condition is used. The bulk of the film is composed of *c*-axis oriented domains of opposite polarization, while the surface region is a single *a*-axis domain. The Pockels effect measured for such MBE-grown BTO on Si has been shown to produce the largest thin film Pockels response measured, at  $\approx 923 \text{ pm V}^{-1}$ .<sup>[8]</sup>

Pulsed laser deposition (PLD) is another widely used technique to deposit BTO on various substrates including Si. Optical properties of PLD thin films have been explored by Kim and Kwok.<sup>[22]</sup> Appleby and co-workers investigated the grain size control of the phase transition in PLD-grown BTO.<sup>[23]</sup> They have shown that for a thin film BTO grown in a columnar structure, the tetragonal phase is stabilized, which results in an increase in the remnant polarization. Aibud et al. focused on the link between the structural and electrical properties of BTO thin films grown on SrRuO<sub>3</sub>-buffered (001) STO substrates.<sup>[24]</sup> They used PLD in the 1–200 mTorr range. With the help of ab initio calculations, they explored the effects of Ba and Ti vacancies on the BTO lattice parameters. They also reported an increase in the dielectric constant in the high-pressure region. They interpreted the effect using the vicinity of the phase boundary between the out-of-plane and in-plane

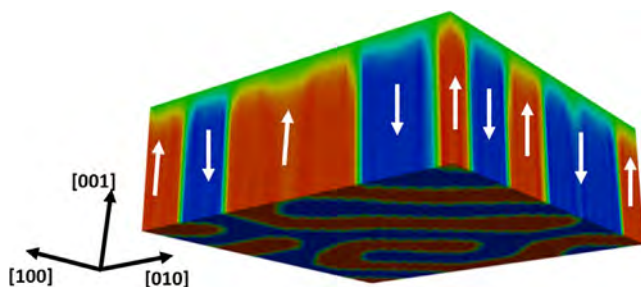


**Figure 1.** Results of the phase field simulation for a thin BTO film. Periodic boundary conditions are used along the [100] and [010] directions. Along the [001] directions, the electrically open-circuit boundary condition is used for the top surface and the bottom surface is grounded. A  $-0.76\%$  compressive in-plane strain is applied across the whole simulation cell. The red and blue areas represent the *c*-domains, where red is  $(0,0,P)$  and blue  $(0,0,-P)$  polarization, respectively, as indicated by the white arrows. The green areas represent the non-*c*-domain regions that are  $180^\circ$  domain walls separating the red and blue domains, while at the top surface they are *a*-domains, with  $(P,0,0)$ ,  $(-P,0,0)$ ,  $(0,P,0)$ , and  $(0,-P,0)$  polarization.

orientations of the tetragonal BTO films. Niu and co-workers also recently reported the epitaxial growth of BTO films on Si (001) that was buffered by a 5 nm-thick SrTiO<sub>3</sub> layer using PLD.<sup>[25]</sup> A ferroelectric BTO layer was demonstrated and *C*–*V* measurements indicated a memory window of 0.75 V, which opens the possibility of using Si-integrated BTO in nonvolatile memory applications. Generally, the memory window is the difference of threshold voltage values between the programmed and erased states, and the threshold voltage is the gate voltage corresponding to some set value of the drain current, say  $10^{-7} \text{ A/W/L}$ , where the *W* and *L* are the width and length of the channel, respectively.

Atomic layer deposition (ALD) is another promising technique to grow epitaxial oxides. The more complicated ALD super-cycle in ternary oxides requires additional considerations over the growth of binary oxides.<sup>[26]</sup> Generally, the deposition of a ternary oxide involves the intermixing of binary oxide cycles. Epitaxial BTO thin films have been grown by ALD on STO-buffered Si (001) at  $225^\circ\text{C}$  followed by a postdeposition annealing. X-ray diffraction confirmed compressive strain in BTO films after the low-temperature growth for films as thick as 66 nm, with the BTO *c*-axis oriented in the out-of-plane direction. Following the postdeposition annealing above  $650^\circ\text{C}$ , piezoresponse force microscopy (PFM) was used to verify the ferroelectric switching behavior of the ALD-grown films. Electrical and EO measurements confirm the BTO film ferroelectric behavior in out-of-plane and in-plane directions, respectively.<sup>[26]</sup>

Recently, Edmondson et al. explored the chemical solution deposition (CSD; commonly referred to as sol–gel deposition) of BTO on Si (001).<sup>[27]</sup> Commonly used in the production of BTO capacitors, this process offers a method for rapid, large-scale deposition without the need for specialized equipment on an appropriate substrate. The epitaxial BTO thin films were deposited on thin STO template layers on Si (001) from an alkoxide-based chemical solution under atmospheric conditions. These films yielded an effective Pockels coefficient of  $27 \pm 4 \text{ pm V}^{-1}$  for an  $\approx 85 \text{ nm}$  film. This technique possibly offers a very inexpensive route to produce EO-active BTO films.

In applications where high-quality, thick films are necessary, high growth rates are needed for enhanced throughput. Many chemical vapor deposition (CVD) processes allow growing thin films at high rates, but epitaxial BTO film formation typically requires high substrate temperatures. Reinke et al. have demonstrated that high vacuum CVD is capable of growing epitaxial BTO films on MgO, STO, and STO-buffered silicon substrates at process temperatures of  $400^\circ\text{C}$  and growth rates of up to 100 nm per hour without the need of an additional annealing step; this is the lowest substrate temperature reported for a CVD process.<sup>[28]</sup> The process needs optimization, but the initial report is very encouraging. Transmission electron microscopy (TEM) images of their films are shown in **Figure 2**. Figure 2a shows the interface between silicon and BTO; the usual amorphous silicon oxide interlayer layer is clearly seen between the crystalline STO buffer and BTO. The sample was oriented along the silicon [110] zone axis and the epitaxial relationship between the perovskite layers is visible. Aberration-corrected (AC) images show multiple defects both in the STO buffer layer and in the BTO film. For example, in Figure 2d, a low-angle grain boundary in BTO can be seen.

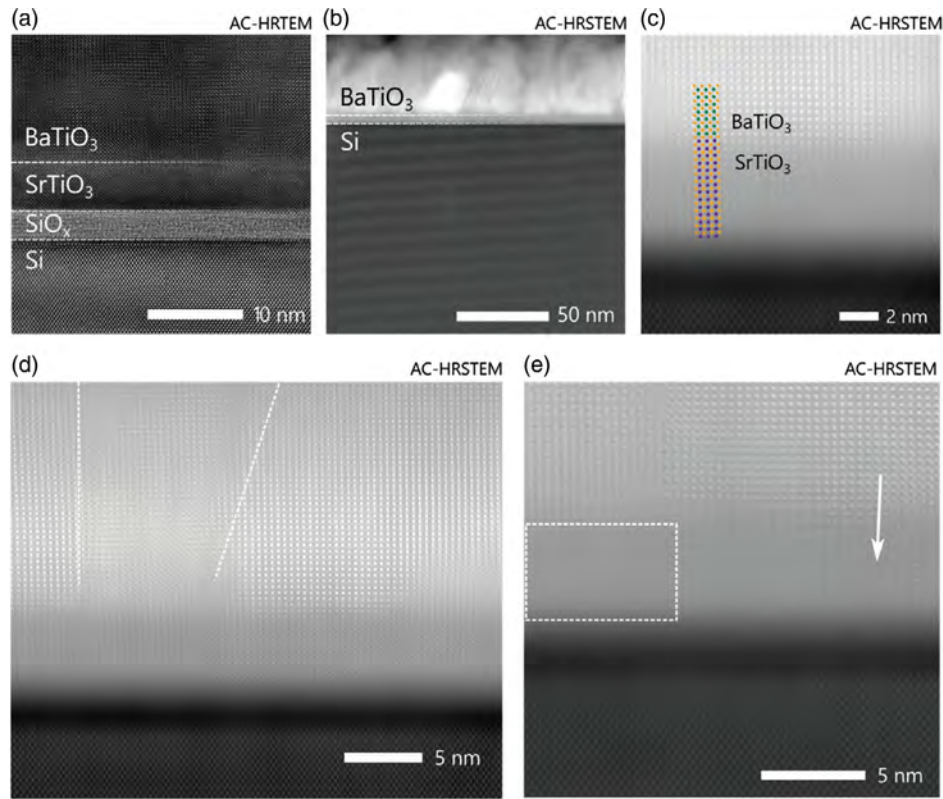


**Figure 2.** a) Aberration-corrected, high-resolution TEM and b–e) aberration-corrected, high-resolution scanning TEM (STEM) analysis of the deposited BTO films. Reproduced with permission.<sup>[28]</sup> Copyright 2017, Wiley-VCH.

### 3. EO Effect

The linear EO, or Pockels, effect describes how the refractive index of a crystal changes under the influence of an applied electric field. It is traditional to introduce it in the context of a change in the coefficients that define the optical indicatrix (the indices of refraction) as follows<sup>[29]</sup>

$$\Delta\left(\frac{1}{n_{ij}^2}\right) = \Delta(\epsilon_{ij}^{-1}) = \sum_{\gamma} r_{ij\gamma} E_{\gamma} \quad (1)$$

Here,  $n_{ij}$  and  $\epsilon_{ij}$  are components of the refractive index and dielectric tensor, respectively;  $r_{ij\gamma}$  is the Pockels tensor component, and  $E_{\gamma}$  is the component of the applied field. The name is somewhat unfortunate because it is actually the first nonlinear optical effect. Note that because this effect is linear in the applied field, it is only nonzero in noncentrosymmetric crystals. It can also be written as the first-order change to the dielectric tensor induced by an applied electric field  $E_{\gamma}$ <sup>[30]</sup>

$$d\epsilon_{ij} = - \sum_k r_{ij\gamma} \epsilon_{ik} \epsilon_{kj} dE_{\gamma}(\omega) \quad (2)$$

In piezoelectric crystals such as BTO, the lattice response to the electric field can, in turn, affect the index of refraction. Therefore, we expand the full differential of the dielectric tensor into purely electronic, ionic, and piezoelectric contributions

$$\begin{aligned} \left[ \frac{d\epsilon_{ij}(R, \eta_0, E)}{dE_{\gamma}} \right]_{R_0, \eta_0, E=0} &= \left[ \frac{\partial \epsilon_{ij}(R_0, \eta_0, E)}{\partial E_{\gamma}} \right]_{E=0} \\ &+ 4\pi \sum_{k, \alpha} \left[ \frac{\partial \chi_{ij}^{(1)}(R, \eta_0)}{\partial \tau_{k\alpha}} \right]_{R_0} \tau_{k\alpha}^{E_{\gamma}} \\ &+ 4\pi \sum_{\mu, \nu=1}^3 \left[ \frac{\partial \chi_{ij}^{(1)}(R_0, \eta)}{\partial \eta_{\mu\nu}} \right]_{\eta_0} \eta_{\mu\nu}^{E_{\gamma}} \end{aligned} \quad (3)$$

Here,  $E_{\gamma}$  is the electric field component in direction  $\gamma$ ,  $R$  represents the ionic coordinates,  $\eta_{\mu\nu}$  is the  $(\mu, \nu)$  element of the strain tensor describing the distortion due to the electric field, the naught refers to values at equilibrium,  $\chi_{ij}^{(1)}$  is the electronic susceptibility, and  $\tau_{k\alpha}$  is the displacement of atom  $k$  in the  $\alpha$  direction. The superscript  $E_{\gamma}$  denotes a derivative being taken with respect to that variable.

The first term on the right-hand side (RHS) of Equation (3) represents the purely electronic contribution, which comes from the interaction of the electric field with the valence electrons, assuming the ions to be clamped at their equilibrium positions. It is related to the second-harmonic generation (SHG) effect. The electronic contribution can be written in terms of  $\chi^{(2)}$ , which is a third derivative of the electric enthalpy with respect to the electric field.<sup>[31]</sup> In perovskites, this term tends to be relatively small.<sup>[32,33]</sup>

The second term on the RHS of Equation (3) is the ionic response of the crystal and describes the effect of the movement

of the ions, assuming the lattice is held fixed. The derivative of the electronic susceptibility (in the brackets) with respect to the ionic displacement can be expanded in terms of the phonon eigendisplacements and then written in terms of the Raman susceptibility.<sup>[31]</sup> It is useful to express the derivative of the ionic displacement with respect to the electric field in terms of the mode polarity, a product of the Born effective charge, and the phonon eigendisplacements.<sup>[31]</sup> Then, the ionic contribution becomes a sum over the mode-dependent product of the mode polarity, the Raman susceptibility, the inverse square of the phonon frequencies, and constants of the crystal. The ionic term typically dominates the Pockels response in perovskites, including unstrained and strained BTO,<sup>[34,35]</sup> strained STO,<sup>[32]</sup> and strained PbTiO<sub>3</sub> (PTO).<sup>[36]</sup>

The last term on the right represents the converse piezoelectric effect. If the frequency of the applied electric field is too high, the crystal will be “clamped,” and the lattice vectors will not change. When the frequency of the applied field is low enough (below 10<sup>4</sup> Hz) to trigger the converse piezoelectric effect, the full (“unclamped”) response needs to be computed. The piezoelectric response can be written in terms of the piezoelectric strain coefficients  $d_{\gamma\mu\nu}$  and elasto-optic coefficients  $p_{ij\mu\nu}$ .<sup>[31]</sup> In some situations, this term can be the dominant contribution to the Pockels tensor,<sup>[36]</sup> but typically its magnitude is  $\approx 10\%$  the ionic contribution.<sup>[32,33,36,37]</sup>

Altogether, the unclamped Pockels tensor (for a low-frequency external field), in the principal axes of the crystal, is given by

$$r_{ij\gamma}^{\sigma} = -\frac{8\pi}{n_i^2 n_j^2} \chi_{ijl}^{(2)} \Big|_{l=\gamma} + -\frac{4\pi}{\sqrt{\Omega_0} n_i^2 n_j^2} \sum_m \frac{\alpha_{ij}^m p_{m,\gamma}}{\omega_m^2} + \sum_{\mu,\nu=1}^3 p_{ij\mu\nu} d_{\gamma\mu\nu} \quad (4)$$

where  $n$  is the index of refraction,  $\chi^{(2)}$  is the nonlinear susceptibility,  $\Omega_0$  is the volume of the unit cell (u.c.),  $\alpha_{ij}^m = \sqrt{\Omega_0} \sum_{\kappa,\beta} u_m(\kappa\beta) \times \partial \chi_{ij}^{(1)} / \partial \tau_{\kappa\beta}$  is the Raman susceptibility,  $p_{m,\gamma} = \sum_{\kappa,\beta} Z_{\kappa,\gamma\beta}^* u_m(\kappa\beta)$  is the mode polarity,  $u_m$  is the eigendisplacement of mode  $m$ , and  $\omega_m$  is the frequency of phonon mode  $m$ . The first two terms of Equation (4) are the clamped Pockels tensor, commonly denoted  $r_{ij\gamma}^{\eta}$ .

From the aforementioned expressions, it is clear that distortions in the ionic positions can heavily impact the response. Thus, strain can have a profound effect on the crystal lattice and is known to modify properties of epitaxial films. Fredrickson et al. showed that in strained epitaxial BTO films, for both out-of-plane and in-plane polarization, the Pockels effect is enhanced under strain due to the divergence of the dielectric susceptibility.<sup>[34]</sup> The divergence is caused by strain-induced soft modes and manifests by an extinguishing of polarization in certain directions under strain. The first-principles calculations suggest very large EO effects can be obtained via controlling the lattice mismatch to the substrate, a previously unexplored route of tuning the EO effect in active elements of Si nanophotonics. This was further explored by Hamze and Demkov, who used density functional theory to study the Pockels effect in epitaxially strained STO.<sup>[32]</sup> They calculated the electro-optical response of STO under biaxial strain ranging from  $-2.0\%$  to  $2.0\%$  relative to the theoretically optimized lattice constant. Under  $1.0\%$  tensile strain, the Pockels tensor components increase dramatically,

with the largest components reaching maximum values of  $r_{111} = r_{222} = 505.64 \text{ pm V}^{-1}$ . Under  $1.2\%$  compressive strain, the Pockels tensor exhibited a similarly large peak with a maximum value of  $r_{333} = 236.55 \text{ pm V}^{-1}$ . These peaks in the electro-optical response originate from the softening of the phonon modes associated with ferroelectric phase transitions that result in the loss of inversion symmetry. This suggests that under the right circumstances, STO can yield a very large electro-optical response, comparable with that of BTO, which has one of the largest known responses. Similar strain-induced increases in the Pockels response have also been discussed for PTO.<sup>[36]</sup>

The enhancements in the Pockels responses exhibited by BTO, STO, and PTO all occur at strains at which the phonons go soft. As soft phonons are often present in materials with large thermal expansions, the thermal expansion coefficient could potentially be a proxy for having a large Pockels response. Hamze et al. investigated this line of thinking by studying LiB<sub>3</sub>O<sub>5</sub> (LBO), a noncentrosymmetric crystal with a thermal expansion coefficient an order of magnitude larger than that of BTO, and the related crystal CsB<sub>3</sub>O<sub>5</sub> (CBO).<sup>[33]</sup> The predicted Pockels response in LBO, however, was extremely small ( $< 5 \text{ pm V}^{-1}$  for all components). By investigating the terms in the ionic response (see the second term in Equation (4)), they showed the high phonon frequencies diminished the response in LBO. To circumvent this problem, they replaced Li with heavier Cs, knowing the larger mass would soften the phonon frequencies. This improvement, however, was counteracted by CBO's small Raman susceptibilities, leading again to a suppressed EO response. This suggested that the Raman susceptibility had an underestimated importance in strong Pockels materials. To verify this, Hamze et al. compared their results with those computed for biaxially strained STO at two different strains,  $-1.0\%$  strain and the critical  $-1.2\%$  strain at which the Pockels tensor exhibited its greatest enhancement.<sup>[32,33]</sup> The frequency of the softest phonon mode in STO drops from  $47$  to  $18.3 \text{ cm}^{-1}$  from  $-1.0\%$  strain to  $-1.2\%$  strain. In **Figure 3**, we plot the Raman susceptibilities and the mode polarities of the optical phonon modes of STO at these two strains. We see that the mode polarities are essentially strain independent, while the Raman susceptibility of the softest mode (and several others) increases by an order of magnitude. The increase in the Pockels response of strained STO is thus not solely due to the softening ferroelectric phonon mode—it also required the order-of-magnitude increase in the Raman susceptibility. This highlights the importance of the Raman susceptibility in strong Pockels materials: even if soft phonons are present, if the Raman susceptibility is small, the Pockels response will be small. This is precisely what was seen in CBO. In LBO, on the contrary, the Raman susceptibility was decently large, but the phonon frequencies were too high. Thus, it is the combination of a large Raman susceptibility and soft phonons that leads to strong Pockels materials. The mode polarities are bounded by the magnitude of the Born effective charges, so they cannot induce the large responses observed in BTO and other perovskites.

Finally, to better understand what is needed to have a large Raman susceptibility, Hamze et al. studied a tight-binding model of a two-atom, 1D crystal and computed the derivative of the electronic susceptibility with respect to atomic displacements—the key component of the Raman susceptibility, as the mode



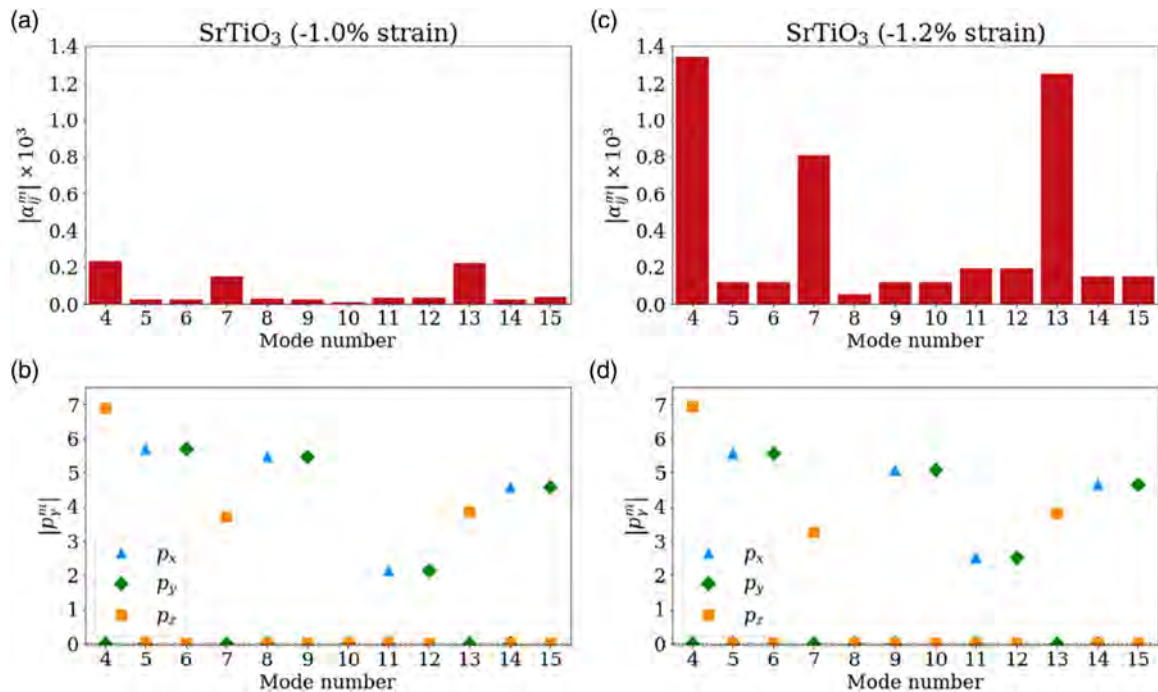


**Figure 3.** Raman susceptibilities of strained STO at a)  $-1.0\%$  strain and c)  $-1.2\%$  strain, and the mode polarities at b)  $-1.0\%$  strain and d)  $-1.2\%$  strain. The mode polarities are essentially strain independent, while the Raman susceptibilities increase by an order of magnitude from  $-1.0\%$  strain to  $-1.2\%$  strain. Reproduced with permission.<sup>[33]</sup> Copyright 2020, Springer Nature.

eigendisplacements are normalized.<sup>[33]</sup> In this model, they found a 2% change in bond length led to an  $\approx 20\%$  change in the electronic susceptibility. The electronic susceptibility in tight-binding is dominated by the inverse cube of the bandgap. Therefore, the change in the gap with respect to atomic displacements will dominate the Raman susceptibility. This is precisely the deformation potential, a commonly used proxy for the strength of the electron–phonon coupling. Hamze et al. computed the deformation potentials for LBO, CBO, and STO and found that LBO and STO had large deformation potentials,<sup>[32,33]</sup> while CBO had a negligible deformation potential, exactly in line with the predicted Raman susceptibilities. This suggests that materials with soft phonons and large electron–phonon couplings (and therefore, large Raman susceptibilities) will be strong Pockels materials.

One can imagine a device in which electrically controlled strain can modify the optical properties of a BTO film via the Pockels effect. Indeed, Cho et al. studied the nonlinear optical response in a strained BTO film using piezoelectric  $\text{Pb}(\text{Mg}_{1/3}\text{Nb}_{2/3})\text{O}_3\text{-PbTiO}_3$  (PMN-PT) (001) as a variable strain substrate and La-doped STO as a conductive buffer layer.<sup>[38]</sup> The rotation-anisotropic second-harmonic intensity profile shows hysteretic modulation corresponding to strain variation from the inverse piezoelectric response of the substrate. As shown in Figure 4, an enhancement of 15% is observed at  $1.2 \text{ kV cm}^{-1}$ , while a control sample shows negligible change as a function of piezovoltage. Reflection high-energy electron diffraction, X-ray photoelectron spectroscopy, and high-resolution scanning transmission electron microscopy reveal the epitaxial interface. X-ray diffraction and PFM confirm tetragonal distortion and ferroelectricity of the BTO overlayer. Their results suggested a

promising route to enhance the performance of nonlinear optical oxides for the development of novel nanooptomechanical devices.

Retention is another important characteristic of a working EO device. Ponath et al. investigated polarization retention in 10–19 nm-thick ferroelectric BTO grown on Ge (001) by MBE.<sup>[39,40]</sup> The out-of-plane direction and reversibility of the electric polarization were confirmed using PFM. After reverse-poling selected regions of the BTO films to a value  $P$  with a biased atomic force microscope (AFM) tip, relaxation of their net polarization was monitored for as long as several weeks using optical SHG microscopy. As shown in Figure 5, all films retained reversed polarization throughout the observation period. Thick BTO films (10 nm) relaxed monotonically to a saturation value  $0.9P$  after 27 days, while 19 nm films relaxed to  $0.75P$  after 24 h.

While BTO films have shown great promise in a variety of novel device concepts, perhaps nowhere is this promise closer to technological relevance than in BTO-based waveguide devices. Recent work has demonstrated bulk-like Pockels coefficients in BTO thin films heterogeneously integrated onto thermally oxidized silicon substrates and patterned with Si and SiN strip waveguides.<sup>[8,11]</sup> Such BTO-based hybrid waveguide devices have been utilized for a variety of technological demonstrations, including high-speed EO modulation at room temperature and cryogenic temperatures,<sup>[8,11]</sup> electro-optical memory applications for use in neuromorphic computing hardware,<sup>[41]</sup> and ultra-low power EO tuning.<sup>[10]</sup> The strong Pockels effect in BTO thin films can be used to finely and precisely tune the effective index of such waveguide devices while consuming only picowatts of static power, suggesting near-term uses for such devices in thermal compensation and tunable filtering in photonic integrated

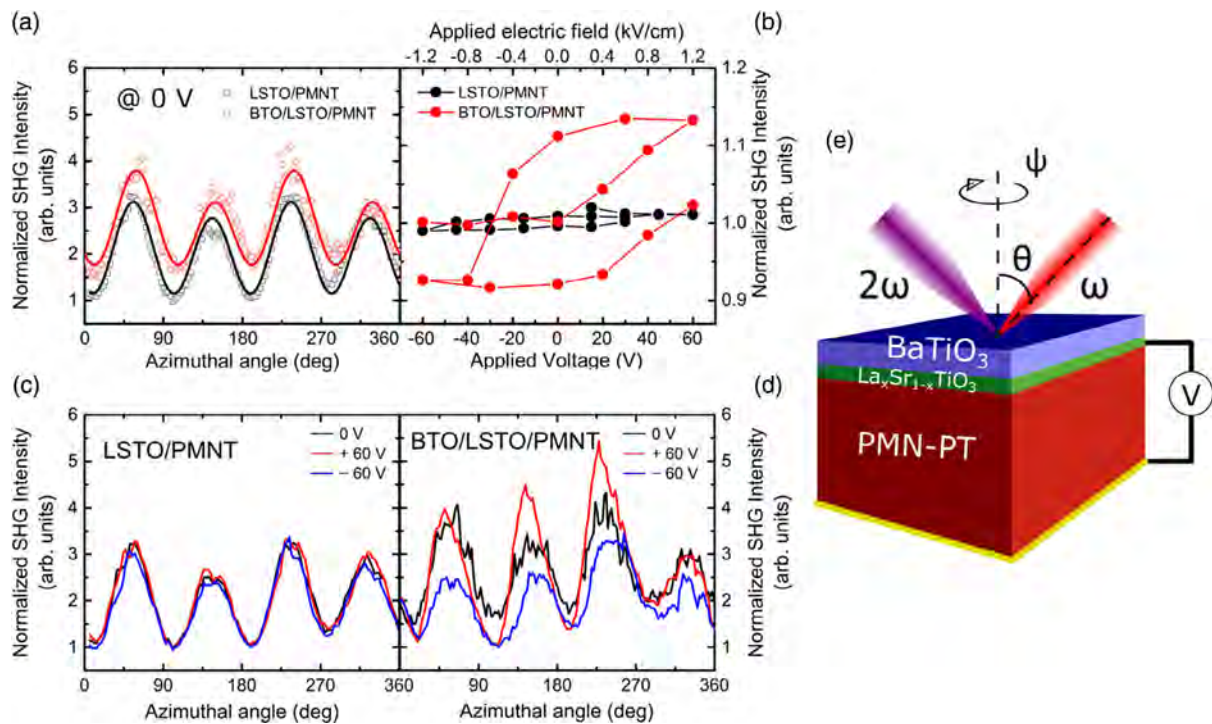


**Figure 4.** a) Rotational anisotropy SHG (RASHG) pattern on the control sample and the heterostructure without external voltage applied on the PMN-PT substrate. Open circles are experimental data and solid lines are fits from Equation (1); b) SHG intensity change at different voltages. Black (red) circles indicate SHG intensities on the control (heterostructure) sample. c,d) RASHG at 0 and  $\pm 60$  V on the control sample and the heterostructure sample, respectively. e) Schematic of RASHG measurement with in situ voltage control. Reproduced with permission.<sup>[38]</sup> Copyright 2018, American Institute of Physics.

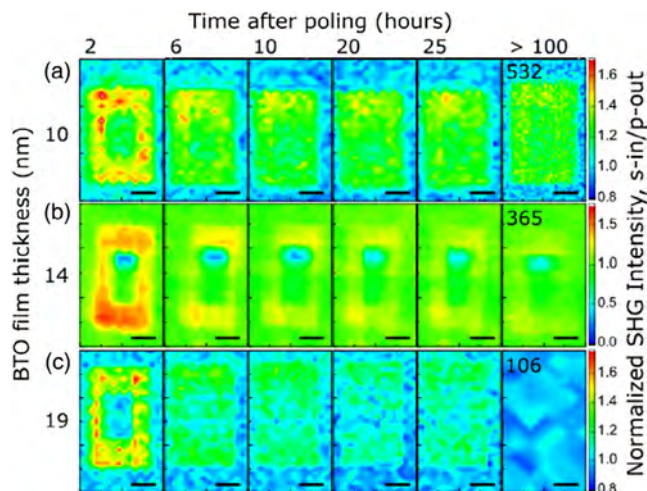


**Figure 5.** Time evolution of SHG micrographs on a) 10, b) 14, and c) 19 nm BTO samples. Numbers on the top and inside the micrographs indicate time elapsed after poling. The scale bar is 10 nm. Reproduced with permission.<sup>[40]</sup> Copyright 2018, American Institute of Physics.

circuits (Figure 6).<sup>[10]</sup> Given the extraordinary Pockels response of BTO and the progress that has already been made developing BTO-based photonic integrated circuits, many additional breakthroughs in BTO-based photonics technologies should be expected over the coming decade.

## 4. Quantum Confinement

While advanced thin film deposition techniques such as PLD and MBE have enabled the fabrication of many types of high-quality TMO thin films, these techniques' power perhaps resides in their ability to facilitate the engineering of artificial material systems via the layering of multiple distinct materials. Such engineered materials often display emergent phenomena not shared by their parent compounds, such as 2D superconductivity at the interface of band insulators,<sup>[42–44]</sup> magnetism at the interface between two nonmagnetic compounds,<sup>[42,43,45–47]</sup> and many other types of electronic reconstruction.<sup>[1,2,48–51]</sup> Such emergence is fascinating in its own right, but the compatibility of TMO thin films with the ubiquitous industrial semiconductors Si and Ge also suggests the utilization of such heterostructures in technologies such as integrated electronics and photonics.<sup>[5,52–57]</sup>

Although it is challenging to purposefully engineer thin film heterostructures to display such emergent interfacial properties, TMO thin films also allow for highly predictable band engineering and can be utilized to enable quantum confinement via QWs.<sup>[58,59]</sup> A QW is an engineered thin film structure consisting of two (or more) distinct materials layered periodically. The conduction band (CB) offset between these materials provides quantum confinement of electrons along one direction  $z$ , while the valence band offset confines holes. By combining extremely large and highly controllable band offsets with the plethora of correlated phenomena found in TMO QW heterostructures, one could

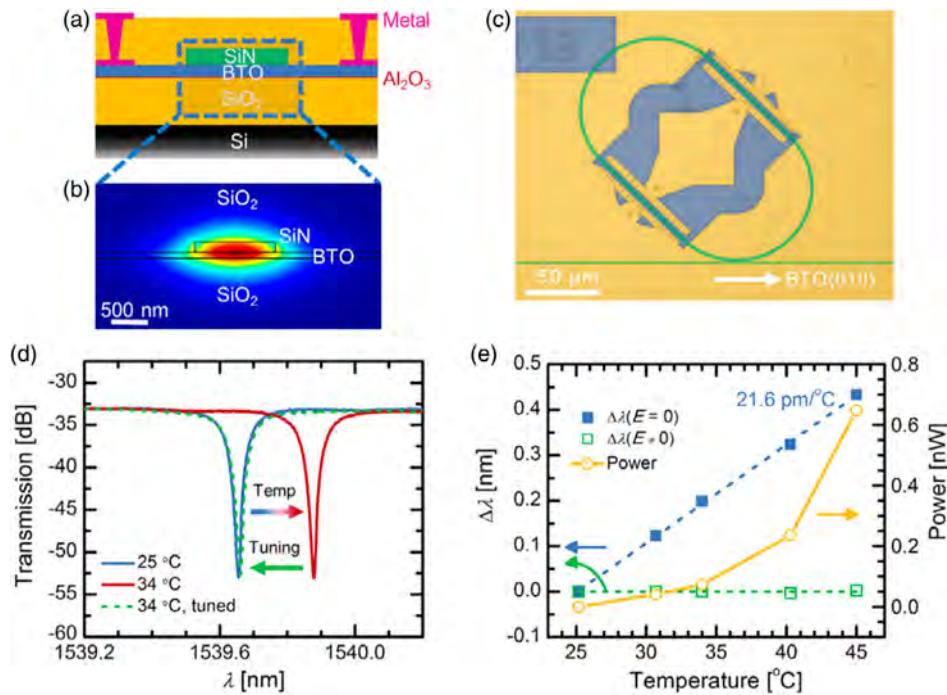


**Figure 6.** a) Schematic cross section and b) simulated fundamental TE mode in hybrid BTO-SiN waveguide devices. The overlap of the optical mode with the Pockels-active BTO film allows electric field tuning of the waveguide effective index, as required for many active photonics devices including switches and modulators. c) False color optical micrograph of active racetrack resonator fabricated from SiN-loaded BTO. The green lines represent the SiN waveguides, blue areas indicate exposed SiO<sub>2</sub> cladding, and gold areas show metal electrodes. d) Demonstration of thermal compensation in active BTO racetrack resonator device. The room-temperature resonance position (blue, solid line) is thermally red-shifted (red, solid line) and subsequently returned to its room-temperature position via electrostatic tuning (green, dashed line). e) Resonance shift and tuning power as a function of temperature. Over 20 °C of thermal drift can be compensated with less than 1 nW of static power consumption. Reproduced with permission. Reproduced with permission.<sup>[10]</sup> Copyright 2019, American Chemical Society.

imagine the design and fabrication of Si-compatible QW devices with advanced functionalities.

In the effective mass approximation, if the size of the quantum confinement is much larger than the atomic size of the QW crystal, the QW eigenvalue problem can be simplified as

$$\left(-\frac{\hbar^2}{2m^*}\nabla^2 + U(z)\right)F_n(\mathbf{r}) = \epsilon F_n(\mathbf{r}) \quad (5)$$

where  $F_n(\mathbf{r})$  is the so-called envelope function. The eigenenergy can be written as

$$E = E_z + \frac{\hbar^2}{2m^*}k_{//}^2 \quad (6)$$

indicating that the energy is quantized along the direction of confinement ( $z$ ) and can be approximated as a free electron with effective mass  $m^*$  in the orthogonal in-plane direction.

If we dope the QW to be n-type, the doped electrons can begin to populate the quantized levels in the CB. With an external pump photon source, these electrons can then absorb photons and be excited to higher quantized levels or emit photons and fall back to lower states, which are the so-called intersubband transitions. By engineering the quantum confinement via controlling the width of the QW, the depth of the CB offset, and other material properties, we can tune the quantized energy

levels and control the intersubband transitions to optimize the QW optical properties. The aforementioned Schrödinger equation plus the electrostatic Poisson equation describing these doped electrons form the Schrödinger–Poisson system,<sup>[60]</sup> where the electrostatic potential can influence  $U(z)$  in the Schrödinger equation, thus altering the wave functions used to build the charge density. **Figure 7** shows an example of a self-consistent

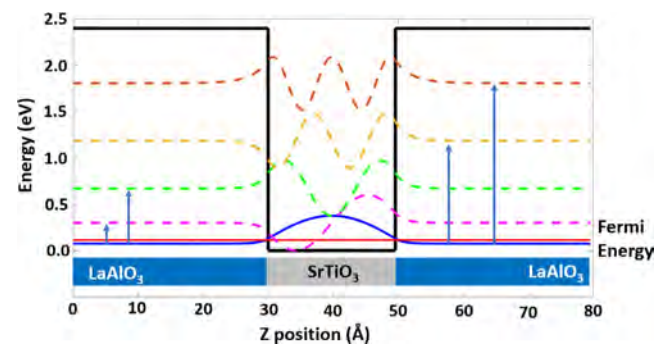


**Figure 7.** Sample LAO/STO QW solution of the Schrödinger–Poisson equation. This QW holds five bound states. The doping density is  $8.33 \times 10^{19} \text{ cm}^{-3}$ , resulting in the position of the Fermi energy indicated by the solid red line. The blue solid line represents occupied ground level and other dashed colored lines represent unoccupied excited levels. Blue arrows represent different intersubband transitions from the ground level.



solution of the Schrödinger–Poisson system for a LAO/STO QW, with the intersubband transitions indicated by blue arrows.

In addition to the Pockels effect, QWs offer another avenue to design and fabricate integrated photonic and EO devices. Optical modulation of quantum-confined electrons in LAO/STO QWs has been demonstrated at wavelengths around the critical telecom C-band (1530–1565 nm).<sup>[61]</sup> The relatively high energy of these intersubband transitions, as compared with those in conventional GaAs-based QWs,<sup>[62]</sup> is due to the extreme CB offset in the LAO/STO system, a feature that is expected to be reproducible in a wide array of oxide-based thin film heterostructures with

appropriate band engineering.<sup>[58]</sup> In addition to such free-space demonstrations, simulation and modeling work has suggested the potential for oxide-based QWs to find use in integrated devices utilizing the quantum-confined Stark effect for modulation and switching.<sup>[9]</sup> This potential is strongly bolstered by recent work demonstrating the fabrication of high-quality LAO/STO QWs of arbitrary thickness, including their monolithic integration on Si (001) substrates.<sup>[63,64]</sup> The scanning tunneling microscopy (STEM) image of such a structure grown by MBE on an LAO substrate is shown in **Figure 8**. Heterostructures with three-, four-, and five-u.c. thick wells, with up to 80 well/barrier periods, were

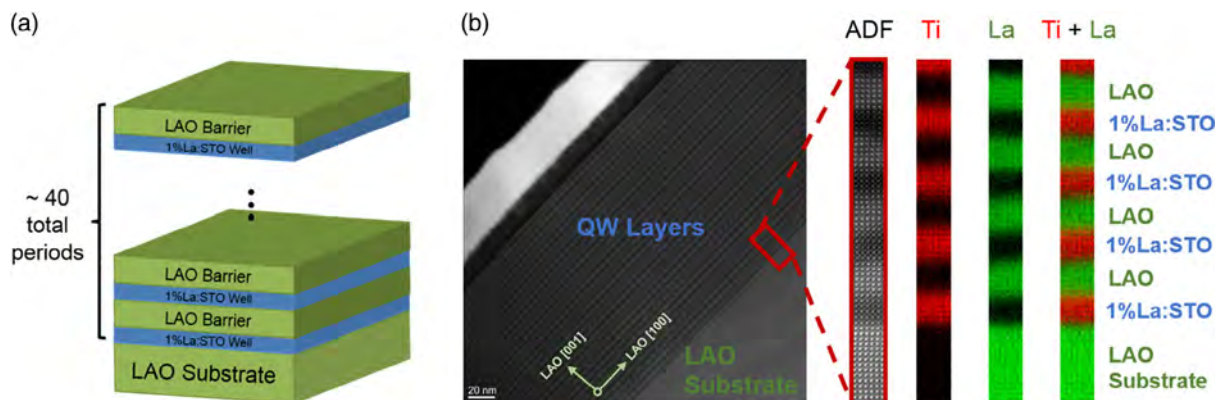


**Figure 8.** a) Schematic of the general design of our QW heterostructures. b) Large-field STEM image over the entire thickness of a six-u.c. well heterostructure, demonstrating clearly separated STO well and LAO barrier layers. A magnified view of a small region of the heterostructure is also presented, showing an annular dark-field (ADF) image as well as corresponding La and Ti EELS spectra. Reproduced with permission.<sup>[61]</sup> Copyright 2018, American Chemical Society.

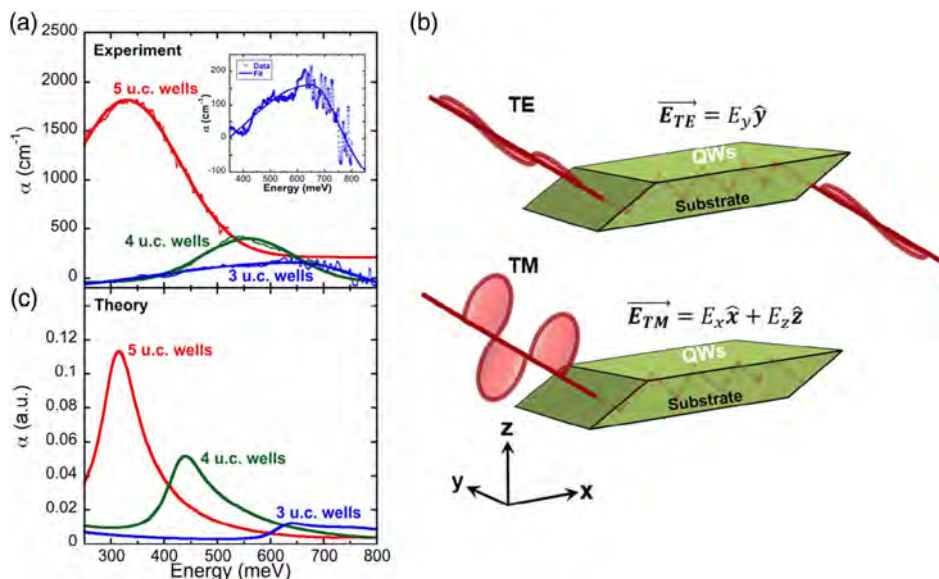


**Figure 9.** a) Absorption spectra for three-, four-, and five-u.c. well samples. The circles are experimental data, while the solid lines are Gaussian fits to the data. The calculation of the absorption coefficient in units of  $\text{cm}^{-1}$  from the raw spectra is discussed in the Supporting Information of ref. [61]. Inset: a zoom-in of the absorption peak in the three-u.c. well sample and a bi-Gaussian fit giving the peak energy at  $\approx 650$  meV (see Supporting Information of ref. [61]). b) Experimental geometry, indicating the two polarization states used for consecutive measurements. This approach is used to remove the ambiguity as to the origin of any observed absorptions, as intersubband absorption is only stimulated when the optical electric field is perpendicular to the plane of the wells (here, TM). c) Tight-binding calculations of the imaginary part of the dielectric function of STO QWs of three-, four-, and five-u.c. widths. Reproduced with permission.<sup>[61]</sup> Copyright 2018, American Chemical Society.

grown on LAO substrates. La serves as an electron donor in STO when substituting for Sr. The authors demonstrated room-temperature intersubband absorption on the order of hundreds of meV, including absorption at energies near the critically important telecommunications wavelength of 1.55  $\mu\text{m}$ . In **Figure 9**, we show the intersubband transitions measured by Ortmann et al.<sup>[61]</sup> Experimental results are in excellent agreement with theoretical predictions.<sup>[65]</sup> Further fabrication advancements, including integration of such epitaxial QWs onto thermally oxidized silicon via direct deposition and the 3D integration of crystalline silicon and epitaxial oxides, promise to bring a variety of oxide-based QW technologies, including infrared photodetectors, quantum cascade lasers, and EO modulators, closer to reality.<sup>[66,67]</sup>

## 5. Conclusions

Integration of  $\text{ABO}_3$  perovskite oxides on Si (001) ushered in a new era of oxide-based optoelectronics. Unlike most semiconductors, the complex structure of these oxides as well as the presence of the *d*-shell in some of the B-cations, e.g., Ti, give these materials internal degrees of freedom that enable a wide range of physical phenomena. Light can couple to these internal degrees of freedom, which, in turn, can be controlled by external electric and magnetic fields, strain, and temperature. Perovskite heterostructures also offer ample opportunities for band engineering that is helped by a close lattice match among many materials in this class, as well as their remarkable ability to sustain relatively high levels of strain. This points to multiple opportunities to build optical devices and sensors integrated on a conventional Si platform with possible applications in nanophotonics, neuromorphic computing, and quantum computing. EO modulators based on Si-integrated BTO have also been demonstrated. The competing technology based on  $\text{LiNbO}_3$  is still relatively new, and as a Pockels material, BTO has significant advantages over  $\text{LiNbO}_3$ . Therefore, this technology will likely find applications in the next 5 years. The QW structures have a longer way to go, as there is a much more established competition based on conventional semiconductors.

## Acknowledgements

The authors thank Agham Posadas and Therese Paoletta for insightful discussions and critical readings of the article. The work was supported by the Air Force Office of Scientific Research under grant FA9550-18-1-0053.

## Conflict of Interest

The authors declare no conflict of interest.

## Keywords

electro-optic effect, molecular beam epitaxy, optoelectronics, epitaxial oxides, perovskites, quantum wells, silicon photonics

Received: September 14, 2020

Revised: March 22, 2021

Published online: May 2, 2021

- [1] H. Y. Hwang, Y. Iwasa, M. Kawasaki, B. Keimer, N. Nagaosa, Y. Tokura, *Nat. Mater.* **2012**, *11*, 103.
- [2] J. Chakhalian, J. W. Freeland, A. J. Millis, C. Panagopoulos, J. M. Rondinelli, *Rev. Mod. Phys.* **2014**, *86*, 1189.
- [3] C. H. Ahn, K. M. Rabe, J. M. Triscone, *Science* **2004**, *303*, 5657.
- [4] R. Ramesh, D. G. Schlom, *MRS Bull.* **2008**, *33*, 11.
- [5] J. Mannhart, D. G. Schlom, *Science* **2010**, *327*, 5973.
- [6] M. Lorenz, M. S. Ramachandra Rao, T. Venkatesan, E. Fortunato, P. Barquinha, R. Branquinho, D. Salgueiro, R. Martins, E. Carlos, A. Liu, F. K. Shan, M. Grundmann, H. Boschker, J. Mukherjee, M. Priyadarshini, N. DasGupta, D. J. Rogers, F. H. Teherani, E. V. Sandana, P. Bove, K. Rietwyk, A. Zaban, A. Veziridis, A. Weidenkaff, M. Muralidhar, M. Murakami, S. Abel, J. Fompeyrine, J. Zuniga-Perez, R. Ramesh, et al., *J. Phys. D: Appl. Phys.* **2016**, *49*, 43.
- [7] K. Alexander, J. P. George, J. Verbist, K. Neyts, B. Kuyken, D. Van Thourhout, J. Beeckman, *Nat. Commun.* **2018**, *9*, 3444.
- [8] S. Abel, F. Eltes, J. E. Ortmann, A. Messner, P. Castera, T. Wagner, D. Urbonas, A. Rosa, A. M. Gutierrez, D. Tulli, P. Ma, B. Baeuerle, A. Josten, W. Heni, D. Caimi, L. Czornomaz, A. A. Demkov, J. Leuthold, P. Sanchis, J. Fompeyrine, *Nat. Mater.* **2019**, *18*, 42.
- [9] J. E. Ortmann, M. A. Duncan, A. A. Demkov, *Opt. Mater. Express* **2019**, *9*, 7.
- [10] J. E. Ortmann, F. Eltes, D. Caimi, N. Meier, A. A. Demkov, L. Czornomaz, J. Fompeyrine, S. Abel, *ACS Photonics* **2019**, *6*, 11.
- [11] F. Eltes, G. E. Villarreal-Garcia, D. Caimi, H. Siegwart, A. A. Gentile, A. Hart, P. Stark, G. D. Marshall, M. G. Thompson, J. Barreto, J. Fompeyrine, S. Abel, *Nat. Mater.* **2020**, *19*, 1164.
- [12] A. A. Demkov, A. B. Posadas, *Integration of Functional Oxides with Semiconductors*, Springer, New York **2014**.
- [13] R. A. McKee, F. J. Walker, M. F. Chisholm, *Phys. Rev. Lett.* **1998**, *81*, 3014.
- [14] R. A. McKee, F. J. Walker, M. F. Chisholm, *Science* **2001**, *293*, 468.
- [15] G. D. Wilk, R. M. Wallace, J. M. Anthony, *J. Appl. Phys.* **2001**, *89*, 5243.
- [16] K. J. Kormondy, Y. Popoff, M. Sousa, F. Eltes, D. Caimi, M. D. Rossell, M. Fiebig, P. Hoffmann, C. Marchiori, M. Reinke, M. Trassin, A. A. Demkov, J. Fompeyrine, S. Abel, *Nanotechnology* **2017**, *28*, 075706.
- [17] C. Dubourdieu, J. Bruley, T. M. Arruda, A. Posadas, J. Jordan-Sweet, M. M. Frank, E. Cartier, D. J. Frank, S. V. Kalinin, A. A. Demkov, V. Narayanan, *Nat. Nanotechnol.* **2013**, *8*, 748.
- [18] V. Vaithyanathan, J. Lettieri, W. Tian, A. Sharan, A. Vasudevarao, Y. L. Li, A. Kochhar, H. Ma, J. Levy, P. Zschack, J. C. Woicik, L. Q. Chen, V. Gopalan, D. G. Schlom, *J. Appl. Phys.* **2006**, *100*, 024108.
- [19] M.-H. M. Hsu, D. Van Thourhout, M. Pantouvaki, J. Meerschaert, T. Conard, O. Richard, H. Bender, P. Favia, M. Vila, R. Cid, J. Rubio-Zuazo, G. R. Castro, J. Van Campenhout, P. Absil, C. Merckling, *Appl. Phys. Express* **2017**, *10*, 065501.
- [20] J. Nordlander, F. Eltes, M. Reynaud, J. Nürnberg, G. De Luca, D. Caimi, A. A. Demkov, S. Abel, M. Fiebig, J. Fompeyrine, M. Trassin, *Phys. Rev. Mater.* **2020**, *4*, 034406.
- [21] A. Y. Woldman, C. M. Landis, *Int. J. Solids Struct.* **2019**, *178–179*, 19.
- [22] D. H. Kim, H. S. Kwok, *Appl. Phys. Lett.* **1995**, *67*, 1803.
- [23] D. J. R. Appleby, N. K. Ponon, K. S. K. Kwa, S. Ganti, U. Hannemann, P. K. Petrov, N. M. Alford, A. O'Neill, *J. Appl. Phys.* **2014**, *116*, 124105.

- [24] A. Aidoud, T. Maroutian, S. Matzen, G. Agnus, B. Amrani, K. Driss-Khodja, P. Aubert, P. Lecoeur, *Eur. Phys. J. Appl. Phys.* **2017**, *80*, 30303.
- [25] G. Niu, S. Yin, G. Saint-Girons, B. Gautier, P. Lecoeur, V. Pillard, G. Hollinger, B. Vilquin, *Microelectron. Eng.* **2011**, *88*, 1232.
- [26] M. D. McDaniel, T. Q. Ngo, S. Hu, A. Posadas, A. A. Demkov, J. G. Ekerdt, *Appl. Phys. Rev.* **2015**, *2*, 041301.
- [27] B. I. Edmondson, S. Kwon, C. H. Lam, J. E. Ortmann, A. A. Demkov, M. J. Kim, J. G. Ekerdt, *J. Am. Ceram. Soc.* **2019**, *103*, 1209.
- [28] M. Reinke, Y. Kuzminykh, F. Eltes, S. Abel, T. LaGrange, A. Neels, J. Fompeyrine, P. Hoffmann, *Adv. Mater. Interfaces* **2017**, *4*, 18.
- [29] I. P. Kaminow, E. H. Turner, *Appl. Optics* **1966**, *5*, 10.
- [30] S. H. Wemple, M. Didomenico Jr., *Appl. Solid Sci.* **1972**, *3*, 263.
- [31] M. Veithen, X. Gonze, P. Ghosez, *Phys. Rev. B* **2005**, *71*, 125107.
- [32] A. K. Hamze, A. A. Demkov, *Phys. Rev. Mater.* **2018**, *2*, 005200.
- [33] A. K. Hamze, M. Reynaud, J. Geler-Kremer, A. A. Demkov, *npj Comput. Mater.* **2020**, *6*, 130.
- [34] K. D. Fredrickson, V. V. Vogler-Neuling, K. J. Kormondy, D. Caimi, F. Eltes, M. Sousa, J. Fompeyrine, S. Abel, A. A. Demkov, *Phys. Rev. B* **2018**, *98*, 075136.
- [35] T. Paoletta, A. A. Demkov, *Phys. Rev. B* **2021**, *103*, 014303.
- [36] C. Paillard, S. Prokhorenko, L. Bellaiche, *npj Comput. Mater.* **2019**, *5*, 6.
- [37] J. F. Nye, *Physical Properties of Crystals*, Oxford University Press, Oxford **1985**.
- [38] K. J. Kormondy, Y. Cho, A. B. Posadas, L. Zheng, K. Lai, Q. Wang, M. J. Kim, Q. He, A. Y. Borisevich, M. C. Downer, A. A. Demkov, *Appl. Phys. Lett.* **2018**, *113*, 132902.
- [39] P. Ponath, A. B. Posadas, M. Schmidt, A.-M. Kelleher, M. White, D. O'Connell, P. Hurley, R. Duffy, A. A. Demkov, *J. Vac. Sci. Technol. B* **2018**, *36*, 031206.
- [40] Y. Cho, P. Ponath, L. Zheng, B. Hatanpaa, K. Lai, A. A. Demkov, M. C. Downer, *Appl. Phys. Lett.* **2018**, *112*, 162901.
- [41] S. Abel, D. J. Stark, F. Eltes, J. E. Ortmann, D. Caimi, J. Fompeyrine, in *2017 IEEE Int. Conf. on Rebooting Computing (ICRC)*, IEEE, Piscataway, NJ **2017**, pp. 1–3.
- [42] L. Li, C. Richter, J. Mannhart, R. C. Ashoori, *Nat. Phys.* **2011**, *7*, 762.
- [43] J. A. Bert, B. Kalisky, C. Bell, M. Kim, Y. Hikita, H. Y. Hwang, K. A. Moler, *Nat. Phys.* **2011**, *7*, 767.
- [44] N. Reyren, S. Thiel, A. D. Caviglia, L. Fitting Kourkoutis, G. Hammerl, C. Richter, C. W. Schneider, T. Kopp, A.-S. Rüetschi, D. Jaccard, M. Gabay, D. A. Muller, J.-M. Triscone, J. Mannhart, *Science* **2007**, *317*, 5842.
- [45] J.-S. Lee, Y. W. Xie, H. K. Sato, C. Bell, Y. Hikita, H. Y. Hwang, C.-C. Kao, *Nat. Mater.* **2013**, *12*, 703.
- [46] B. Kalisky, J. A. Bert, B. B. Klopfer, C. Bell, H. K. Sato, M. Hosoda, Y. Hikita, H. Y. Hwang, K. A. Moler, *Nat. Commun.* **2012**, *3*, 922.
- [47] A. Brinkman, M. Huijben, M. van Zalk, J. Huijben, U. Zeitler, J. C. Maan, W. G. van der Wiel, G. Rijnders, D. H. A. Blank, H. Hilgenkamp, *Nat. Mater.* **2007**, *6*, 493.
- [48] J. Biscaras, N. Bergeal, A. Kushwaha, T. Wolf, A. Rastogi, R.C. Budhani, J. Lesueur, *Nat. Commun.* **2010**, *1*, 1.
- [49] S. Okamoto, A. J. Millis, *Nature* **2004**, *428*, 630.
- [50] D. Doennig, R. Pentcheva, *Sci. Rep.* **2015**, *5*, 7909.
- [51] M. Huijben, G. Rijnders, D. H. A. Blank, S. Bals, S. V. Aert, J. Verbeeck, G. V. Tendeloo, A. Brinkman, H. Hilgenkamp, *Nat. Mater.* **2006**, *5*, 556.
- [52] R. A. McKee, F. J. Walker, J. R. Conner, E. D. Specht, D. E. Zelmon, *Appl. Phys. Lett.* **1991**, *59*, 782.
- [53] J. W. Park, D. F. Bogorin, C. Cen, D. A. Felker, Y. Zhang, C. T. Nelson, C. W. Bark, C. M. Folkman, X. Q. Pan, M. S. Rzechowski, J. Levy, C. B. Eom, *Nat. Commun.* **2010**, *1*, 94.
- [54] P. Ponath, K. Fredrickson, A. B. Posadas, Y. Ren, X. Wu, R. K. Vasudevan, M. Baris Okatan, S. Jesse, T. Aoki, M. R. McCartney, D. J. Smith, S. V. Kalinin, K. Lai, A. A. Demkov, *Nat. Commun.* **2015**, *6*, 6067.
- [55] D. F. Bogorin, P. Irvin, C. Cen, J. Levy, *Multifunctional Oxide Heterostructures*, Oxford University Press, Oxford **2012**.
- [56] L. Bjaalie, B. Himmetoglu, L. Weston, A. Janotti, C. G. Van de Walle, *New J. Phys.* **2014**, *16*, 025005.
- [57] S. Abel, T. Stöferle, C. Marchiori, C. Rossel, M. D. Rossell, R. Erni, D. Caimi, M. Sousa, A. Chelnokov, B. J. Offrein, J. Fompeyrine, *Nat. Commun.* **2013**, *4*, 1671.
- [58] J. Robertson, *J. Vac. Sci. Technol. B* **2000**, *18*, 1785.
- [59] T. A. S. Pereira, M. G. Bezerra, J. A. K. Freire, V. N. Freire, G. A. Farias, *Braz. J. Phys.* **2006**, *36*, 347.
- [60] P. Harrison, A. Valavanis, *Quantum Wells, Wires and Dots: Theoretical and Computational Physics of Semiconductor Nanostructures*, 4th ed., John Wiley and Sons, New York **2016**.
- [61] J. E. Ortmann, N. Nookala, Q. He, L. Gao, C. Lin, A. B. Posadas, A. Y. Borisevich, M. A. Belkin, A. A. Demkov, *ACS Nano* **2018**, *12*, 7682.
- [62] J. Batey, S. L. Wright, *J. Appl. Phys.* **1986**, *59*, 200.
- [63] J. E. Ortmann, A. B. Posadas, A. A. Demkov, *J. Appl. Phys.* **2018**, *124*, 015301.
- [64] J. E. Ortmann, S. Kwon, A. B. Posadas, M. J. Kim, A. A. Demkov, *J. Appl. Phys.* **2019**, *125*, 155302.
- [65] C. Lin, A. Posadas, M. Choi, A. A. Demkov, *J. Appl. Phys.* **2015**, *117*, 034304.
- [66] J. E. Ortmann, M. R. McCartney, A. Posadas, D. J. Smith, A. A. Demkov, *ACS Appl. Nano Mater.* **2019**, *2*, 12.
- [67] J. E. Ortmann, A. Y. Borisevich, S. Kwon, A. B. Posadas, M. J. Kim, A. A. Demkov, *ACS Appl. Nano Mater.* **2021**, *4*, 2153.



**Alex Demkov** is a professor of physics at the University of Texas at Austin. He earned his Diploma in Materials Science from the Moscow Institute of Steel and Alloys in 1986 and Ph.D. in Theoretical Condensed Matter Physics from Arizona State University in 1995. He joined the University of Texas in 2005, after working in Motorola's R&D organization, where he investigated materials-related problems of electronic devices making significant contributions to the understanding of high dielectric constant materials. His current research is focused on transitional metal oxides integrated with semiconductors. He does both theory and oxide molecular beam epitaxy (MBE).





**J. Elliott Ortmann** graduated summa cum laude from Tulane University in 2013 with the B.S. degree in Physics and Mathematics. He received his Ph.D. degree in Condensed Matter Physics in spring 2019 from the University of Texas at Austin, where he was a National Science Foundation GRFP Fellow. His graduate research focused on the fabrication and characterization of novel TMO thin film heterostructures with a focus on utilizing their many unique properties for the development of electronic and photonic technologies. He currently works in the photonics industry as an R&D engineer.



**Marc Reynaud** is a graduate student in the Materials Physics Lab of Professor Demkov. He works on the MBE growth, crystalline characterization, and nonlinear optical characterization of oxide thin films, particularly BaTiO<sub>3</sub>. The research is applied toward furthering research in silicon-integrated photonics systems.



**Ali Hamze** received his Ph.D. in Physics from the University of Texas at Austin in 2019. During his Ph.D., he studied the electro-optic effect in perovskite oxides, with a focus on discovering a design rule for materials searches. He is now a materials scientist at Samsung Semiconductor, Inc. with the Advanced Materials Lab, a part of the Samsung Advanced Institute of Technology. His current research interests include perovskite oxides, dielectric materials, anharmonic phonons, 2D semiconductors, high-throughput computational methods, and applications of machine learning to materials science.



**Patrick Ponath** received his undergraduate degree in Physics in 2010 from the University of Würzburg, Germany. During an academic exchange year with the University of Texas at Austin, he received his MA in Physics in 2011. Intrigued by academic research, Patrick decided to join the group of Professor Demkov at the University of Texas at Austin where he finished with a Ph.D. in Physics in 2017. After graduation, Patrick then started working as a process engineer at Lam Research for about 2 years and has been working as a research scientist at KLA since 2019.



**Wente Li** earned his B.S. in Physics from Zhejiang University, China, in 2016. The same year, he started his graduate studies in the Department of Physics at the University of Texas at Austin. He joined Professor Demkov's group in 2017. He conducts theoretical/computational research in condensed matter physics. His research is mainly focused on functional materials, transition metal oxides, and related heterostructures. He uses various computational tools, such as density functional theory and phase field simulations.

# Photons, Orbital Angular Momentum, and Neutrons

Ronald L. Cappelletti\* and John Vinson

Dedicated to Professor David A. Drabold on the occasion of his 60th birthday

A traveling wave or wave packet may possess orbital angular momentum (OAM) in the form of a phase vortex about its propagation axis. These OAM states are a general wave property and exist in single-particle wave packets, in a beam of unstructured wave packets of particles or in a mixture. OAM states of photons were first created almost 30 years ago. Recently work has been done to create these states with massive particles: electrons and neutrons. OAM waves can be generated by passing an unstructured wave through a vortex phase plate. This technique is reliant on each particle adequately sampling the area of the vortex plate. While laser sources provide sufficient transverse coherence, beams of massive particles are more challenging. If incident wave packets do not interrogate the discontinuity at the center of the vortex phase plate, the probability of detecting a single particle having a unit of OAM about the packet center decreases substantially and the expectation value of the OAM about that center vanishes. Herein, using laser light, we restrict the transverse size of a beam to either illuminate the discontinuity or not and consider the implications for producing OAM in individual neutrons.

or propagation. Typically, an OAM state is considered to carry angular momentum associated with the azimuthal angle  $\varphi$  about the axis of propagation in the form of  $e^{il\varphi}$  where for integer values of  $l$  the beam has  $l\hbar$  units of OAM in the direction of propagation. Aided by the ease of generating coherent, monochromatic light, optical studies constitute the bulk of experimental realizations of OAM states. However, because the OAM is, by construction, a property of the wave function, there has been great interest in also creating such states with matter. This has led to demonstration of OAM behavior in electrons<sup>[6–8]</sup> and OAM-like behavior in neutron beams,<sup>[9]</sup> but the interpretation of such measurements in neutrons can be ambiguous as to the existence of single-particle OAM states.<sup>[10]</sup>

Depending on the type of measurement, the nature of the single-particle

wave function may or may not be probed. A double slit, illuminated by waves with sufficient spatial coherence, will form an interference pattern that requires each particle individually to behave as a wave. In the absence of sufficient coherence, the interference pattern fades. In much the same way, an OAM beam can be made either of single particles with little transverse coherence and an unremarkable structure forming a beam that collectively has the properties of an OAM state<sup>[9]</sup> or individual particles each described by a wave function with definite OAM character. The distinction determines what properties such a beam possesses and what measurements can be made on or using it, and it is these properties which promise to open up new avenues for probing interactions.<sup>[11–13]</sup>


In this paper we consider intentional restrictions on the creation of OAM states. Passing a laser beam through an interferometer, we generate an OAM state in one arm and observe the expected dislocation pattern from an  $l = 1$  OAM state interfering with an off-axis plane wave. Using an iris on a translation stage, adjustable perpendicular to the beam, we create a beam with restricted transverse coherence and show that the presence of an OAM state is dependent on the transverse coherence. The creation of fractional OAM states by such a technique is well known in the photon optical community,<sup>[14]</sup> but here we are interested in integer OAM states. After reviewing specifics of coherence and OAM states, we present our setup and main results. We then discuss the implications that these light experiments have for generating OAM states of neutrons.

## 1. Introduction

Thermal and cold neutrons have been demonstrated to be uniquely valuable probes of the properties of condensed matter systems because their wavelengths and energies are suitably matched to study both structure and dynamics of materials.<sup>[1]</sup> The addition of a new quantum degree of freedom, orbital angular momentum (OAM), promises to extend the usefulness of this probe to new areas of materials studies. The generation and manipulation of OAM states of both light and matter have garnered significant attention in recent years.<sup>[2–5]</sup> An OAM state is a subset of what are more generally referred to as structured waves, a class that includes any system where the shape or phase structure of the wave itself is important to its properties, interactions,

Dr. R. L. Cappelletti  
 NIST Center for Neutron Research  
 National Institute of Standards and Technology  
 100 Bureau Drive, Gaithersburg, MD 20899, USA  
 E-mail: ronald.cappelletti@nist.gov

Dr. J. Vinson  
 Material Measurement Laboratory  
 National Institute of Standards and Technology  
 100 Bureau Drive, Gaithersburg, MD 20899, USA

 The ORCID identification number(s) for the author(s) of this article can be found under <https://doi.org/10.1002/pssb.202000257>.

DOI: 10.1002/pssb.202000257

### 1.1. Transverse Restriction and Transverse Coherence

The laser light emanating from the beam expander used in the experiments described here has a longitudinal coherence much larger than any dimension in the geometry of the apparatus used and a transverse coherence considerably larger than the irises or other optical objects restricting the beam. Moreover, each photon in the laser beam has approximately the same character as photons are bosons. Using an adjustable iris to control the transverse size of the incident beam and displacing its center, we can explore the effects of restriction on producing vortex states.

In free space, neutrons are fermions moving in dispersive wave packets as distinguished from photons which are bosons moving in nondispersive wave packets. But with respect to the production of OAM states and transverse coherence which are strictly wave phenomena, the behavior of photons is an analog of that of neutrons. Hence, we can confidently model the behavior of a neutron with a small transverse coherence length compared with the size of a vortex wave plate (VPP) using a laser in conjunction with an adjustable iris to restrict the position and diameter of the beam, making it smaller than the VPP. We describe two experiments examining this effect. The first uses interference between plane and restricted vortex beams. A second examines the effect of restriction on the image produced by such a beam using a lens.

### 1.2. OAM States and Their Representation

When discussing optical OAM states, it is convenient to use the Laguerre–Gaussian functions,  $B_{nl}$ , as the basis. See a previous study<sup>[3]</sup> for more details. Any paraxial beam may be described by the Laguerre–Gaussian functions by virtue of their completeness,  $\psi = \sum_{n=0}^{\infty} \sum_{l=-\infty}^{\infty} C_{nl} B_{nl}$ , where  $C$  is some complex coefficient subject to normalization. This motivates us to make a distinction between the expectation value of the orbital momentum state  $\langle L_z \rangle \equiv \langle \psi | \hat{L}_z | \psi \rangle$  and the probability of the state having a specific integer OAM  $P(L_z = l\hbar) \equiv \sum_{n=0}^{\infty} |\langle B_{nl} | \psi \rangle|^2$ . As an example, consider the wave function  $\psi = 1/\sqrt{2} B_{10} + 1/\sqrt{2} B_{12}$  where the expectation is  $\langle L_z \rangle = \hbar$  whereas  $P(L_z = \hbar) = 0$ .

We consider a parallel focused laser beam which is coherent across its front. When this beam is incident upon a transmission vortex phase plate a spatially dependent phase is imparted to the beam which is linearly proportional to the azimuthal angle around the center of the VPP device. By design, the VPP's proportionality constant is set to be an integer, e.g.,  $l = 1$  for the wavelength of laser light being used. If the center of the laser beam is aligned to pass through the center of the VPP, then we may describe the beam as being predominately in an  $l = 1$  OAM state. The expectation value will approach  $\hbar$  and  $P(\hbar) \approx 1$ . Furthermore, as a laser produces a coherent beam of bosons, we may regard each photon as having a wave function that is structured similarly to the beam itself. For a beam not passing through the center of the VPP, the value of the OAM about the beam axis may be fractional. The case of neutron beams is more complicated, but we can mimic some of the difficulties by restricting the transverse size of the laser beam.

## 2. Experimental Techniques

### 2.1. Spatial Light Modulator in a Twyman–Green Interferometer

The arrangement for using the spatial light modulator (SLM) to produce a vortex wave in a Twyman–Green interferometer is shown in **Figure 1**. Using the beam splitter, a portion of the collimated beam selected by a translatable iris was directed in one arm toward a mirror and in the other toward the SLM. The reflected beams were collected by the beam splitter and directed to the detecting charge-coupled device (CCD) camera where they combined to produce a phase-contrast image. The SLM can be programmed to provide a variety of structured wave fronts.<sup>[17]</sup> In particular, it can act like a VPP introducing a unit of twist to the wavefront reflected from its surface.

### 2.2. Transmission Vortex Phase Plate in a Mach–Zehnder Interferometer

A second method for introducing a twist to an incident wave is through the use of a transmission VPP. The particular device used in this experiment was a model VPP-1c from RPC Photonics.<sup>[18]</sup> It was placed into one leg of a Mach–Zehnder interferometer, as shown in **Figure 2**. The VPP was mounted on an  $(x, y)$  translation stage perpendicular to the incident beam and it was positioned such that the laser beam illuminated the region of the VPP-1C designed to produce a  $2\pi$  twist with 980 nm light. The laser source was coupled by a fiber cable to the beam expander and collimated using a shear plate. This arrangement allowed the observation of an interference pattern by inclining the second arm of the interferometer slightly. The detector was the PixeLINK CCD camera used in the Twyman–Green arrangement. In addition, a lens could be placed to focus the beam from either arm onto the detector plane to study the images produced.

## 3. Experimental Results and Simulation

### 3.1. 635 nm Results for a $2\pi$ Twist

In this section we show the results using both methods of producing vortex beams on the restriction of the transverse size of

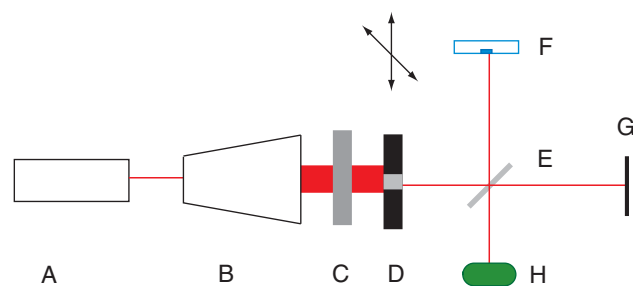


**Figure 1.** Twyman–Green interferometer setup with SLM: (A) 635 nm diode laser source;<sup>[15]</sup> (B) beam expander; (C) rotatable polarizer; (D) adjustable and translatable iris selects and steers a portion of the beam; (E) beam splitter: one arm goes to (F), the SLM, and the other to (G), a mirror. The beams reflected from the mirror and SLM recombine at (E) and are detected by (H), the PixeLINK<sup>[16]</sup> CCD camera.



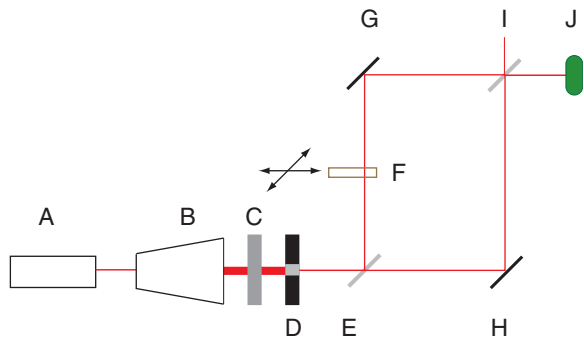


**Figure 2.** Mach-Zehnder interferometer. A Thorlabs 980 nm laser source (A), fiber-coupled to a beam expander (B), directs light through a rotatable linear polarizer (C) and adjustable iris (D) to a beam splitter (E). The beam in the lower horizontal arm proceeds to a corner mirror (H), which directs it to a second beam splitter (I) and on to the detector (J). The vertical arm is directed through a vortex phase plate, VPP, mounted on a horizontal/vertical translation stage (F) and on to a corner mirror (G), which steers it toward the second beam splitter where it combines with the beam coming from the lower arm and is collected by the detector. The iris is used to restrict the transverse size of the beam incident on the VPP. The VPP can be moved to accept the beam anywhere in its working area.

the beam incident on the vortex-producing device. Referring to Figure 1, **Figure 3** shows the result of using an iris to restrict the transverse size of the beam incident on the SLM. The beam has been translated so that its center is not coincident with the center of the vortex-producing SLM. The characteristic dislocation interference pattern has been circled in red for convenience. As the iris is closed down in successive images a) through f), the dislocation eventually disappears from the observed interference pattern. In e) and f), it is no longer visible, which corresponds to the beam no longer containing a unit of twist about the VPP axis. By this it is meant that, while the beam can always be described as a

superposition of a complete set of orthogonal Laguerre–Gauss<sup>[3]</sup> modes having positive and negative integer OAM values, the *expectation value* of the OAM is less than one unit and the *probability* of any photon possessing one unit approaches zero. In **Figure 4** the iris is first restricted and then translated to occlude the center of the SLM from the beam. Then it is reopened to reveal the center again. The figure shows how restriction of the transverse size and displacement of the beam can produce a wavefront no longer characterized by an integer value of OAM.

The result shown in Figure 4 can be modeled by the interference patterns to be expected from combining a plane wave slightly offset along  $x$  from the  $z$  axis of propagation and a wave with one twist, both having a transverse planar Gaussian envelope of width parameter  $W$ , as described by Equation (1):

$$\left| e^{-\left(\frac{x^2+(y-Y)^2}{W}\right)} \{ e^{i3x} + e^{-i(\arctan(y/x))} \} \right|^2 \quad (1)$$

The factor  $3x$  in the phase of the plane wave is chosen to conveniently display several fringes in the plotting region. The Gaussian is offset along the  $y$  direction by  $Y$  in successive images to mimic the behavior of the iris in Figure 4. The simulation is shown in **Figure 5** and will be discussed later.

### 3.2. 980 nm Results for a $2\pi$ Twist

Although similar results to those shown in Figure 3 and 4 were obtained at this wavelength in the Mach-Zehnder arrangement, we do not show them here. Instead, we concentrate on the Fraunhofer diffraction pattern images of the restricted beams obtained through a 15 mm lens with its image focal plane coincident with the detector plane of the CCD camera. At the top of each image in **Figure 6** we show the result of the plane-wave-illuminated circular opening of the iris. Below that we show the result of such a restricted beam passing through a VPP.

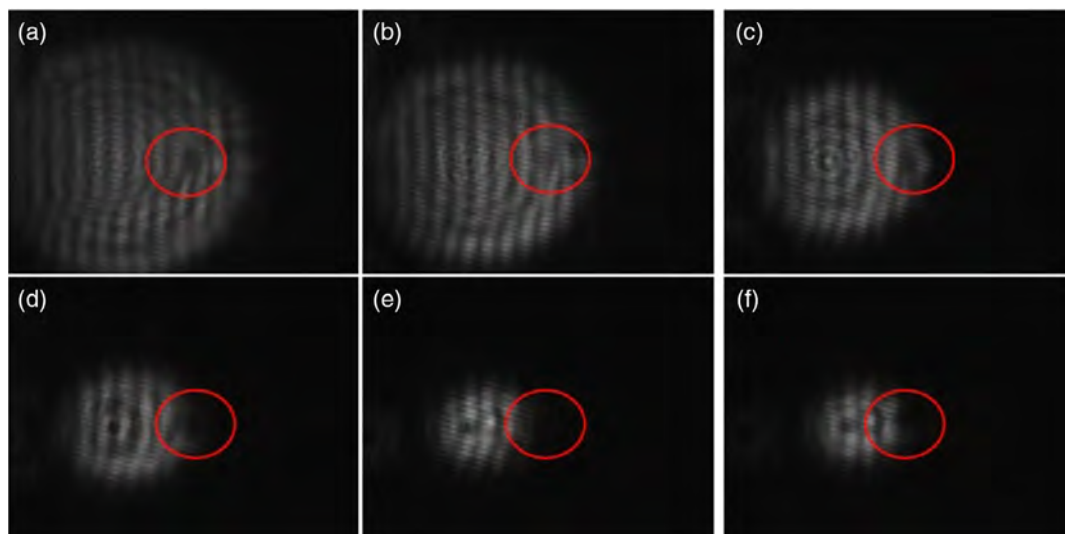


**Figure 3.** Dislocation interference pattern/hologram arising from overlapping of a  $2\pi$  twisted wave with an inclined plane wave. The dislocation area is encircled. The twisted wave is produced by an SLM using 635 nm laser light. Successive images (a–f) occur as the iris is closed down, eventually occluding the center of the SLM.

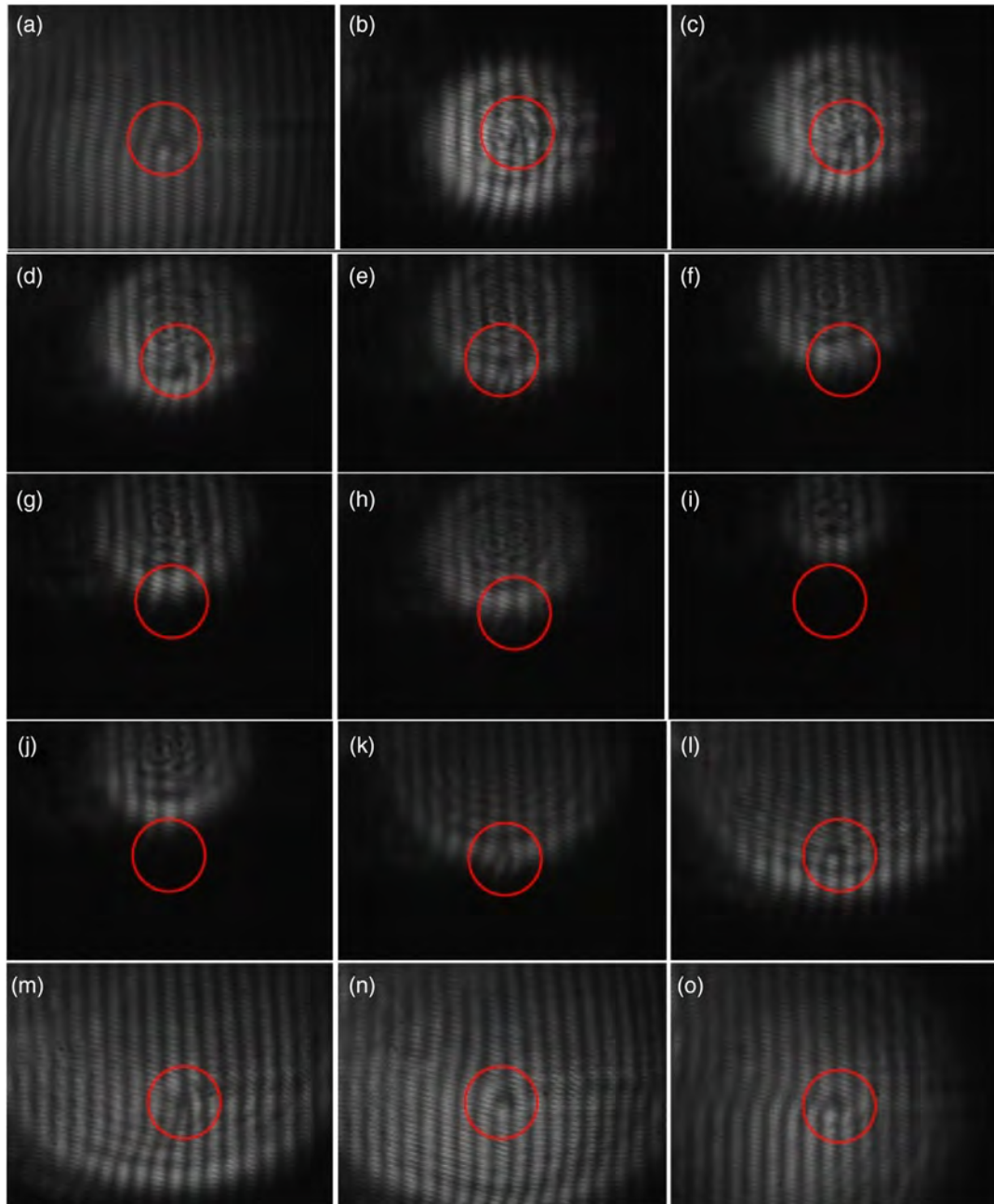


**Figure 4.** Dislocation interference pattern/hologram arising from overlapping of a  $2\pi$  twisted wave with an inclined plane wave. The center of the pattern is circled in red for convenience. In images (a–c) the iris is closed down, still admitting the center of the pattern. In images (d–i) the iris is moved upward so that eventually the center of the SLM is no longer illuminated and the center of the pattern is no longer visible. In images (j–o) the translated iris is successively opened to again allow illumination of the SLM center and the dislocation pattern again comes into view.

For the VPP whose center is illuminated, the wave will have a unit of OAM and the pattern observed is the expected “donut” shape shown at the bottom of the leftmost image in Figure 6.<sup>[2]</sup> (The center of this image does not have exactly zero intensity as it would if an unrestricted plane wave was incident upon the VPP.<sup>[19]</sup>) As the center of the restricted beam incident on the VPP is displaced upward, the recorded image is distorted, finally coming to resemble the image of the restricted plane wave arm (top image in each frame) when the center of the VPP is no longer

in view. Beyond this point the resulting light from this arm no longer contains a unit of OAM and hence the probability of observing a photon containing exactly one unit of OAM approaches zero.

#### 4. Discussion

The adjustable iris in this experiment was used as a stand-in to demonstrate the effects of limited transverse coherence on

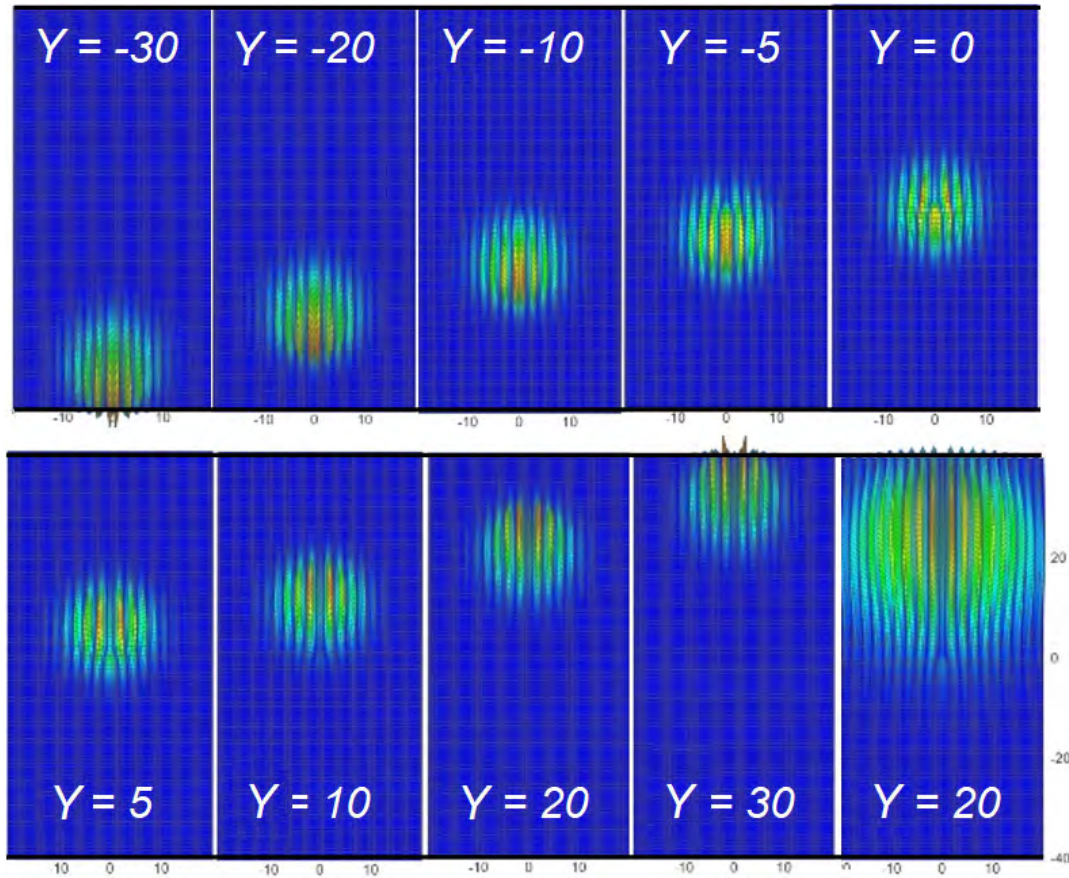


**Figure 5.** Simulation of dislocation interference pattern/hologram arising from overlapping of a  $2\pi$  twisted wave with an inclined plane wave as calculated from Equation (1). The Gaussian width parameter is taken as 100 for all but the rightmost image where it is increased to 500 to show the reappearance of the fork pattern.

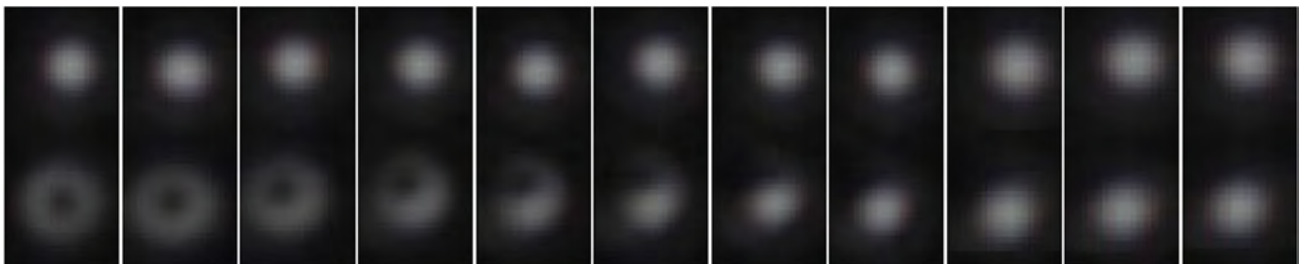


**Figure 6.** 980 nm light passing through an iris diameter of  $\approx 3.0$  mm focused by a 15 mm lens onto the detector plane of a CCD camera. Each image shows the light collected from the displaced blank arm of a Mach-Zehnder interferometer at the top and the light collected from the interferometer arm containing the VPP at the bottom. In the first image on the left the light is focused on the center of the VPP adding a  $2\pi$  twist to 980 nm light, and a characteristic “donut” shape is manifest. From left to right the position of the VPP is raised by 0.25 mm. By the seventh image in the sequence (1.5 mm displacement), the center of the VPP square is on the periphery of the beam permitted by the setting of the iris. Further displacement moves the center of the VPP beyond the range of the iris opening, and the image approaches that of the light from the blank arm. Beyond this point the expectation value OAM vanishes and the probability of observing a photon containing exactly one unit of OAM falls off substantially.

producing OAM states. If the light source had a small transverse coherence (compared with the size of the beam or VPP) then each photon would only interrogate a small section of the VPP, an effect replicated using the iris. When the restricted beam striking the VPP did not cover the discontinuity at the plate center no dislocation pattern was created.

It is clear from the diffraction patterns in Figure 4 that as the edge of the restricted beam excludes the center of the VPP, the expectation value of creating an OAM state becomes less than one unit. The same result is seen clearly in the simulation shown in Figure 5 which qualitatively agrees with Figure 4.



We can model the beam cross-section as a uniform disk of radius  $a$  whose centroid hits the VPP at a distance  $b$  from the VPP center. The acquired phase leaving the VPP is given by  $\exp(i l \phi')$  where  $\phi'$  is the azimuthal angle around the VPP designed to create an OAM of integer  $l$ . The  $\phi$  dependence of the beam leaving the VPP is given by  $\psi \propto e^{i\{l \arctan[\rho \sin \phi / (\rho \cos \phi - b)]\}}$  where we are using cylindrical coordinates  $(\rho, \phi)$  centered on the beam. The expectation value of the OAM can be evaluated using  $\langle L_z \rangle = -i\hbar \langle \psi | \partial / \partial \phi | \psi \rangle$ , giving  $\hbar l(1 - b^2/a^2)$  when  $a > b$  and 0 when  $a \leq b$ . While the expectation value is strictly zero if the beam does not illuminate the center of the VPP, the probability of  $l \neq 0$  OAM states is only approximately so. For small, off-center beams,  $a \ll b$ , the probability of detecting a particle in the  $l = 1$  OAM state using an  $l = 1$  VPP is  $\approx a^2/8b^2$ . This is approximately the same as the probability of an  $l = -1$  state, whereas  $P(l = 0) \approx 1 - a^2/4b^2$ .

An important point is that even though a source with small transverse coherence will produce a vanishingly small number of photons in an  $l = 1$  state, a *beam* of such photons wide enough to cover the SLM (or VPP) will produce phase-contrast images that will look the same as if it consisted of photons with large transverse coherence. This can be seen by noticing that the effect of iris translation and reopening in Figure 4 are not to change the underlying interference pattern, but to illuminate different sections of it. Thus, by accumulating a composite image consisting of individual images produced by a randomly placed small iris,

one can reproduce the image displayed when the iris is wide open. From this it is clear that phase-contrast images *alone* can not demonstrate the creation of single-particle OAM states in general, whether the beam consists of photons or neutrons.

We support this assertion by a model calculation in which the interference pattern intensities of 81 beams striking the VPP in a grid pattern are added together. Each beam is described as in Equation (1), with the Gaussian width parameter  $W$  but now with offsets from the origin by  $X$  and  $Y$ , respectively. The results are shown in Figure 7. We can safely extrapolate from this result that if the VPP were peppered by a large random array of narrow  $W = 1$  beams, the resulting phase-contrast image would be experimentally indistinguishable from one in which a single wide  $W = 500$  beam of equivalent intensity was incident.

It should be pointed out, however, that any method of producing twisted waves that fails to allow every narrow incident “ray” to sufficiently overlap its unstructured partner in an interferometer setting, such as with a pair of cylindrical lenses configured as a  $\pi/2$  conversion plate,<sup>[20]</sup> may allow distinguishing between the phase-contrast patterns produced by one broadly transverse-coherent and many very narrowly transverse-coherent beams.

In contrast, several effects or measurements are explicitly reliant on single-particle OAM states. These include interference experiments such as single-particle OAM sorting<sup>[21]</sup> but also spectroscopy where the interactions are dependent on the OAM character of the light.<sup>[22,23]</sup> For this latter category, structured waves provide an opportunity to explore new phenomena.

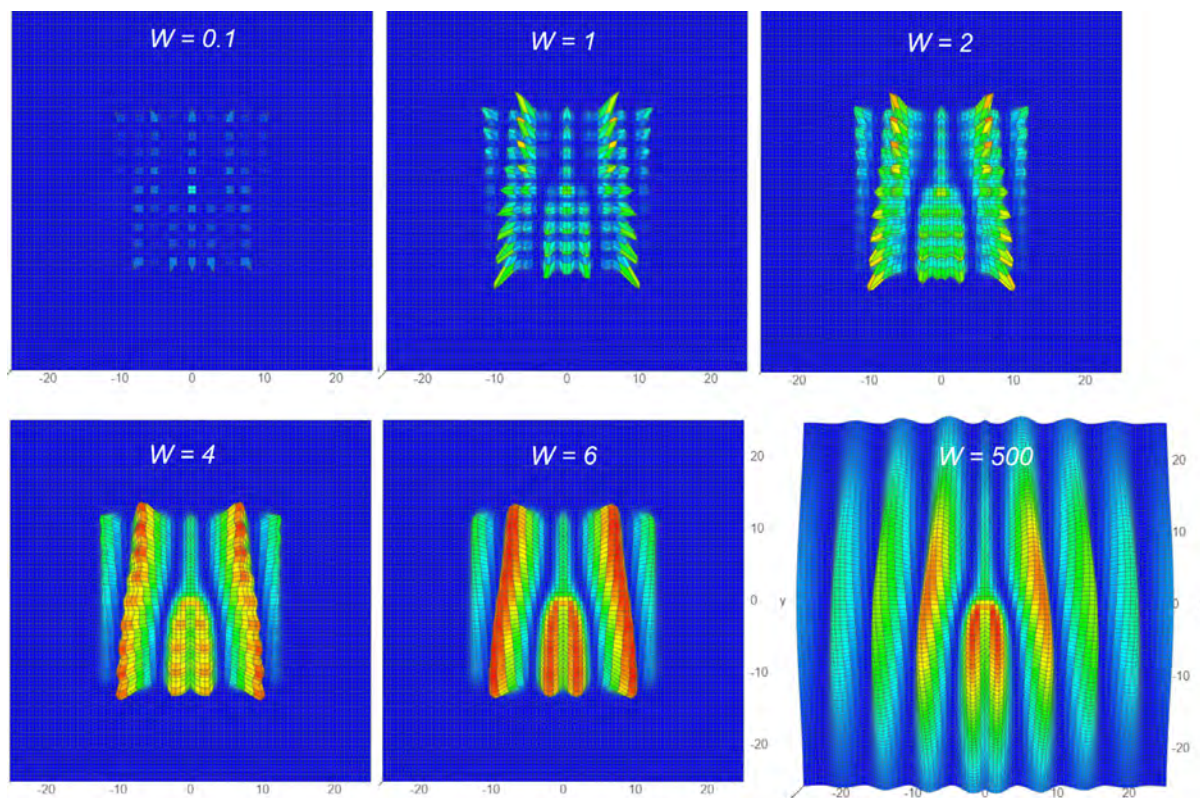


**Figure 7.** Sum of intensities of a grid of 81 interference patterns, calculated as described in the Discussion section, showing the emergence of the underlying fork in the phase-contrast image. The Gaussian width parameter  $W$  increases from left to right. The emergence of the fork is already apparent at  $W = 1$ .

transverse coherence, each part of a split-neutron wave packet can combine with its partner to produce interference because of the near-perfect alignment of the lattice planes.<sup>[24]</sup>

## 4.2. Future Work

With a dimensional mismatch of up to three orders of magnitude, the fraction of neutrons passing near enough to the center of such a device is vanishingly small.<sup>[10]</sup> Further work to produce individual neutrons possessing a unit of OAM will require bridging this gap in some way. One can envisage a transmission VPP consisting of an appropriate array of spiral-producing regions each on a scale consistent with the measured transverse coherence of the neutrons. Using such a device, a significant fraction of the neutrons in currently available beams would have a reasonably high probability of emerging with a unit of OAM. Experiments unambiguously testing the presence of OAM in individual neutrons, in analogy with light experiments, could then be conducted by choosing target nuclei exhibiting single-quantum interactions with a selection rule causing them to respond differently to neutrons either having or not having units of OAM.

The authors wish to give special thanks to Dr. Stephan Stranick for the use of his laboratory and equipment in the performance of the optical experiments described here. The RPC VPP-1c plate was kindly provided for our use in this experiment by Drs. Jay Knutson and Alessio Andreoni of the Optical Spectroscopy Division of the National Heart Lung and Blood Institute at the National Institutes of Health, Bethesda, MD. Useful discussions with Drs. Terrence Jach and Chuck Majkrzak are also acknowledged.

The authors declare no conflict of interest.

## neutrons, orbital angular momenta, photons, transverse coherence

Received: May 5, 2020  
Revised: August 12, 2020  
Published online: September 20, 2020

- [1] R. L. Cappelletti, C. J. Glinka, S. Krueger, R. A. Lindstrom, J. W. Lynn, H. J. Prask, E. Prince, J. J. Rush, J. M. Rowe, S. K. Satija, B. H. Toby, A. Tsai, T. J. Udovic, *J. Res. Natl. Inst. Stand. Technol.* **2001**, 106 187.
- [2] A. M. Yao, M. J. Padgett, *Adv. Opt. Photon.* **2011**, 3, 161.
- [3] K. Bliokh, I. Ivanov, G. Guzzinati, L. Clark, R. V. Boxem, A. Béché, R. Juchtmans, M. Alonso, P. Schattschneider, F. Nori, J. Verbeeck, *Phys. Rep.* **2017**, 690, 1.
- [4] J. C. T. Lee, S. J. Alexander, S. D. Kevan, S. Roy, B. J. McMorran, *Nat. Photon.* **2019**, 13, 205.
- [5] A. T. O’Neil, I. MacVicar, L. Allen, M. J. Padgett, *Phys. Rev. Lett.* **2002**, 88, 053601.
- [6] M. Uchida, A. Tonomura, *Nature* **2010**, 464, 737.

- [7] J. Verbeeck, H. Tian, P. Schattschneider, *Nature* **2010**, 467, 301.
- [8] S. M. Lloyd, M. Babiker, G. Thirunavukkarasu, J. Yuan, *Rev. Mod. Phys.* **2017**, 89, 035004.
- [9] C. W. Clark, R. Barankov, M. Huber, M. Arif, D. Cory, D. Pushin, *Nature* **2015**, 525, 504.
- [10] R. L. Cappelletti, T. Jach, J. Vinson, *Phys. Rev. Lett.* **2018**, 120, 090402.
- [11] H. He, M. E. J. Friese, N. R. Heckenberg, H. Rubinsztein-Dunlop, *Phys. Rev. Lett.* **1995**, 75, 826.
- [12] N. B. Simpson, K. Dholakia, L. Allen, M. J. Padgett, *Opt. Lett.* **1997**, 22, 52.
- [13] M. F. Andersen, C. Ryu, P. Cladé, V. Natarajan, A. Vaziri, K. Helmerson, W. D. Phillips, *Phys. Rev. Lett.* **2006**, 97, 170406.
- [14] Y. Pan, X.-Z. Gao, Z.-C. Ren, X.-L. Wang, C. Tu, Y. Li, H.-T. Wang, *Sci. Rep.* **2016**, 6, 29212.
- [15] Model TLD001-635, Issue 1 Mod A, T-Cube fiber-coupled Diode Laser Source, Thorlabs, Newton, NJ, USA. Certain pieces of equipment are identified in this paper to foster understanding. Such identification does not imply recommendation or endorsement by the National Institute of Standards and Technology, nor does it imply that these are necessarily the best available for the purpose.
- [16] PixeLINK PL-E424C Camera, PixeLINK, Ottawa, Canada.
- [17] LCOS-SLM, 10468 Series, Hamamatsu Photonics K.K., Hamamatsu City, Japan.
- [18] Model VPP-1c, RPC Photonics, Inc., Rochester, NY, USA.
- [19] G. A. Swartzlander, R. I. Hernandez-Aranda, *Phys. Rev. Lett.* **2007**, 99, 163901.
- [20] M. J. Padgett, L. Allen, *Opt. Quantum Electron.* **1999**, 31, 1.
- [21] J. Leach, M. J. Padgett, S. M. Barnett, S. Franke-Arnold, J. Courtial, *Phys. Rev. Lett.* **2002**, 88, 257901.
- [22] C. T. Schmiegelow, J. Schulz, H. Kaufmann, T. Ruster, U. G. Poschinger, F. Schmidt-Kaler, *Nat. Commun.* **2016**, 7, 12998.
- [23] A. A. Sirenko, P. Marsik, C. Bernhard, T. N. Stanislavchuk, V. Kiryukhin, S.-W. Cheong, *Phys. Rev. Lett.* **2019**, 122, 237401.
- [24] H. Rauch, S. A. Werner, *Neutron Interferometry: Lessons in Experimental Quantum Mechanics, Wave-Particle Duality, and Entanglement*, 2nd ed, Oxford University Press, Oxford **2015**, Ch. 4.
- [25] H. Rauch, H. Wolwitsch, H. Kaiser, R. Clothier, S. A. Werner, *Phys. Rev. A* **1996**, 53, 902.
- [26] H. Kaiser, S. A. Werner, E. A. George, *Phys. Rev. Lett.* **1983**, 50, 560.
- [27] M. Kitaguchi, H. Funahashi, T. Nakura, K. Taketani, M. Hino, Y. Otake, H. M. Shimizu, *J. Phys. Soc. Jpn.* **2003**, 72, 3079.
- [28] C. Pruner, M. Fally, R. Rupp, R. P. May, J. Vollbrant, *Nucl. Instrum. Methods A* **2006**, 560, 598.
- [29] D. A. Pushin, M. Arif, M. G. Huber, D. G. Cory, *Phys. Rev. Lett.* **2008**, 100, 250404.
- [30] Y. Seki, H. Funahashi, M. Kitaguchi, M. Hino, Y. Otake, K. Taketani, H. M. Shimizu, *J. Phys. Soc. Jpn.* **2010**, 79, 124201.
- [31] A. Wagh, S. Abbas, W. Treimer, *J. Phys.: Conf. Ser.* **2010**, 251, 012074.
- [32] C. F. Majkrzak, N. F. Berk, B. B. Maranville, J. A. Dura, T. Jach, arXiv:1911.07974, **2019**.
- [33] Y. Deng, D. Chu, *Sci. Rep.* **2017**, 7, 5893.



# Forced Enhanced Atomic Refinement Modeling of the Metallic Glass $\text{Cu}_{46}\text{Zr}_{46}\text{Al}_8$

Rajendra Thapa,\* Kashi Nath Subedi, Bishal Bhattacharai, and David A. Drabold

Herein, the structure of  $\text{Cu}_{46}\text{Zr}_{46}\text{Al}_8$  is inverted from X-ray structure factor data and energy minimizations as implemented with forced enhanced atomic refinement (FEAR). The models generated are in good agreement with structural data obtained from diffraction experiment. Voronoi tessellation analysis shows reasonable agreement with previous results, and the models include structural units believed to have slow dynamics near glass transition and be responsible for the excellent glass forming ability of this metallic glass. It is shown, with constant temperature molecular dynamics (MD), that there is a significant increase in the fraction of these particular clusters near the glass transition. Space-projected conductivity (SPC) calculations show that conduction through Zr dominates over Cu. Vibrational modes are strongly localized on a few Al atoms at high frequencies and distributed almost uniformly on Cu and Zr atoms at low frequencies.

Al atoms. The Zr–Al bonding is also demonstrated by nuclear magnetic resonance (NMR) studies by Xi et al.<sup>[13]</sup> Both extended X-ray absorption spectra (EXAFS)<sup>[10]</sup> and X-ray diffraction studies<sup>[11,12]</sup> have shown that the addition of Al to Cu–Zr BMG increases the fraction of icosahedron such as clusters and makes the distribution of Al homogeneous, which enhances the GFA by increasing the structural incompatibility with the crystalline phases. X-ray diffraction pattern from samples with varying Al concentration has showed that even at 4% Al concentration, a fully amorphous rod up to 5 mm in size can be produced.<sup>[17]</sup> Yu et al.<sup>[17]</sup> also found that the critical cooling rate for Cu–Zr BMG drops from 250 to 40 K s<sup>−1</sup> with just 4% Al doping.

## 1. Introduction

Bulk metallic glasses (BMGs) form a family of one of the most researched amorphous materials. The ever growing scientific attention can be attributed to their unique properties, such as ultrahigh strength, resistance to wear and corrosion,<sup>[1]</sup> etc. Such properties enable its diverse applicability, ranging from sporting goods to nanotechnology and biomedical applications.<sup>[2]</sup> Despite having numerous models for structure,<sup>[3–6]</sup> glass forming ability (GFA),<sup>[7]</sup> and its relation to the structure, a plethora of basic questions still remains unanswered. Cu–Zr BMG gained particular interest after its discovery challenged the pre-existing understanding of GFA.<sup>[8]</sup> For these reasons, Cu–Zr–Al forms one of the most highly researched materials in the BMG family with both experimental<sup>[9–13]</sup> and theoretical work<sup>[14–16]</sup> being reported. Georgarakis et al.,<sup>[9]</sup> with his X-ray pair distribution function (PDF) experiments, showed that the addition of Al to Cu–Zr BMG induces changes in the atomic structure in the short and medium range order, attributed to the strong bonding preference between Zr and

Molecular dynamics (MD) simulations by Zhang et al.<sup>[16]</sup> have also revealed superior GFA in  $\text{Cu}_{46}\text{Zr}_{46}\text{Al}_8$  relative to other compositions, in agreement with experiment.<sup>[11,12]</sup> Structure inversion with reverse Monte Carlo (RMC) of Cu–Zr–Al BMGs from experimental information has already been carried out with large number of atoms.<sup>[11,12,18]</sup> However, traditional RMC alone may produce non-physical solutions even for elemental systems.<sup>[19]</sup> In this work, we report on models designed to closely agree with experiment and, at the same time, be a suitable minimum of a standard density functional theory (DFT) code.

The rest of this article is organized as follows: Section 2 has discussions about computational methodology and model generation using forced enhanced atomic refinement (FEAR) and melt quench (MQ). Section 3 deals with results obtained from structural, electronic, and vibrational calculations, and Section 4 summarizes our conclusions.


## 2. Methodology and Models

In this study, we perform an ab initio simulation of  $\text{Cu}_{46}\text{Zr}_{46}\text{Al}_8$  to determine the structural and electronic properties using the FEAR<sup>[20–23]</sup> technique and a traditional MQ method. FEAR has shown promise in modeling a wide range of amorphous systems, ranging from a-Si,<sup>[24]</sup> a-SiO<sub>2</sub>, silver-doped GeSe<sub>3</sub>, sodium silicate glass,<sup>[25]</sup> and a-C<sup>[23,26]</sup> to complex BMGs.<sup>[27]</sup>

FEAR aims to use experimental information to aid and accelerate ab initio simulation of disordered materials. Of course, diffraction data by itself are grossly inadequate to determine the structure of a complex system with rich local chemical and topological order. However, when chemical information is included (from an accurate quantum mechanical code), we have

R. Thapa, K. N. Subedi, Prof. D. A. Drabold  
Department of Physics and Astronomy  
Ohio University  
Athens, OH 45701, USA  
E-mail: rt887917@ohio.edu

Dr. B. Bhattacharai  
Department of Physics  
Missouri University of Science and Technology  
Rolla, MO 65409, USA

 The ORCID identification number(s) for the author(s) of this article can be found under <https://doi.org/10.1002/pssb.202000415>.

DOI: 10.1002/pssb.202000415

repeatedly shown that FEAR produces models equal or superior to MQ, even in total energy, and requires a fraction of the (expensive) force calls needed by MQ methods.

To provide some more detail, we start with some definitions. If  $V$  is an energy functional and  $\chi^2$  gauges the discrepancy between a diffraction experiment and a computer model, we seek to find a set of atomic coordinates that renders  $V$  a minimum, and  $\chi^2$  within experimental error. FEAR is a simple iterative process consisting of 1) producing a structural model with random coordinates and 2) invoking  $N$  accepted moves within conventional RMC followed by  $M$  conjugate-gradient (CG) steps using ab initio interactions. We then iterate 2) until convergence. The final results do not depend heavily on the numerical values of  $N$  and  $M$ , which were chosen to be 150 and 5, respectively, for the present work. FEAR avoids the problem of the relative weighting of  $V$  and  $\chi^2$  in a penalty or target energy functional as in hybrid approaches. If the density of the material is unknown, it is possible to run the simulation at zero pressure (with variable cell geometries) in the CG loop and simply pass the modified supercell vectors back to the RMC loop.

## 2.1. FEAR-I

A FEAR model of  $\text{Cu}_{46}\text{Zr}_{46}\text{Al}_8$  was made with 300 atoms in a box of size 17.0805 Å corresponding to an experimental density of  $7.38 \text{ g cc}^{-1}$ .<sup>[12]</sup> A sequence of partial RMC fitting using RMCProfile<sup>[28]</sup> and partial energy minimizations, using Vienna ab initio simulation package (VASP),<sup>[29–31]</sup> complemented each other and were iterated until convergence (when the structure factor of the model was close to experiment and the forces were near zero at a suitable potential energy minimum). We used the experimental data of the previous study<sup>[12]</sup> and the code RMCProfile. Our total energy/force code is the ab initio plane-wave DFT package VASP. After convergence, the converged structure is then fully relaxed with VASP until the forces on each atom drop to below  $0.005 \text{ eV Å}^{-1}$ . The maximum move for each atomic species during the RMC refinement was kept at 0.085 Å. Energy minimization steps in VASP with a plane wave basis set and a projector-augmented wave (PAW) method<sup>[32,33]</sup> with Perdew–Burke–Ernzerhof (PBE) functional.<sup>[34]</sup> The final relaxation step used VASP for  $\Gamma(k=0)$ , a plane-wave cutoff of 280 eV and an energy convergence tolerance of  $10^{-5} \text{ eV}$ . A total of 400 FEAR steps were used to reach the desired convergence.

The computational cost for this model was  $\approx 1866$  core hours at BRIDGES at Pittsburgh Supercomputer Center.

## 2.2. FEAR-II

This model was made with exactly the same implementation as FEAR-I but starts from a different initial configuration: the atomic positions of a well-equilibrated liquid melt at 1500 K were taken as the starting model.

## 2.3. Melt Quench

For the purpose of comparison and cross validation of the models created, we also prepared an MQ model, starting with the same

random coordinates used in FEAR-I, using VASP. The model was heated to 1500 K, equilibrated at 1500 K, cooled to 1000 K, equilibrated at 1000 K, cooled to 300 K, and finally equilibrated at 300 K. This equilibrated model is finally relaxed using the CG method until the forces on each atom drop to below  $0.005 \text{ eV Å}^{-1}$ . Throughout the simulation, a time step of 2.0 fs was adopted, and the total simulation time was 45 ps for a computational time of 11 000 core hours on the same machine as model FEAR-I.

To keep it simple and consistent, we follow the same “color nomenclature” for the atomic species: red for Zr, green for Cu, and blue for Al in the figures.

## 3. Results and Discussion

### 3.1. Structural Properties

In **Figure 1**, we show the final relaxed atomic structure of the FEAR-I. Atoms are packed in continuous random arrangement, the dense composition being responsible for a high coordination number. The distribution of Al seems reasonably homogeneous, with no clustering, and is believed to be responsible for suppressing crystallization and thereby increasing the GFA.<sup>[10–12]</sup>

The structure factor and pair distribution function of the models are shown in **Figure 2**. The left panel displays a comparison of  $S(q)$  between the experiment<sup>[12]</sup> and the models, showing good agreement. On the right panel, PDF  $G(r)$  is similarly compared. Broad peaks in the PDF of the models suggest the amorphous nature of the material. The first minimum of the PDF obtained from the models matches with the experiment suggesting a good agreement in short-range order. The first peak arises from joint contributions from all six partial PDFs (**Figure 3**).

To study the bonding preferences of the atomic species involved, we calculated the number of nearest neighbors around each atom using a cutoff radius of 3.5 Å, and the details of are given in **Table 1**. The table suggests that Al bonds preferentially

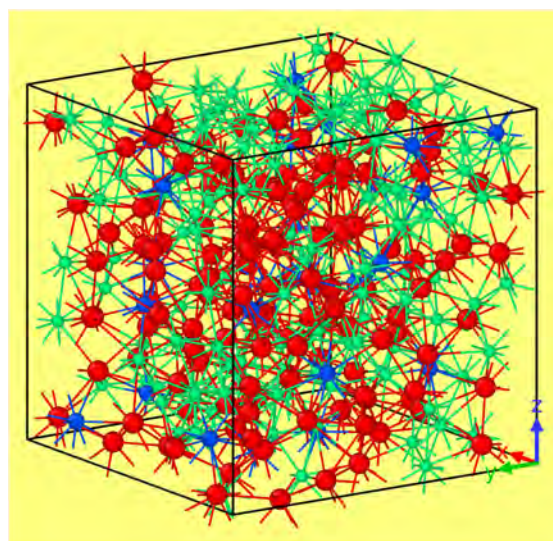


**Figure 1.** Simulated atomic structure obtained for FEAR-I. Zr, Cu, and Al atoms are shown in red, green, and blue, respectively, and the same “color nomenclature” will be used in all figures.

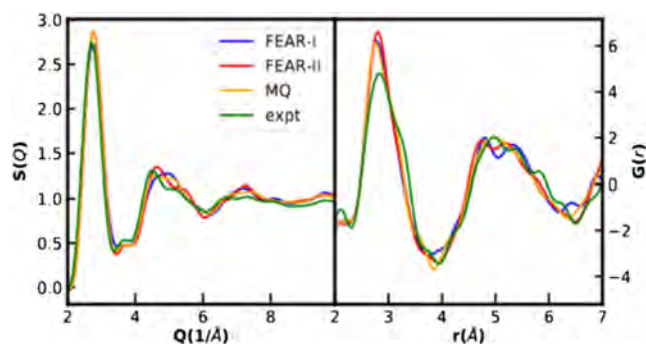


**Figure 2.** Comparison of structure factor and pair distribution function obtained from models with experiment.

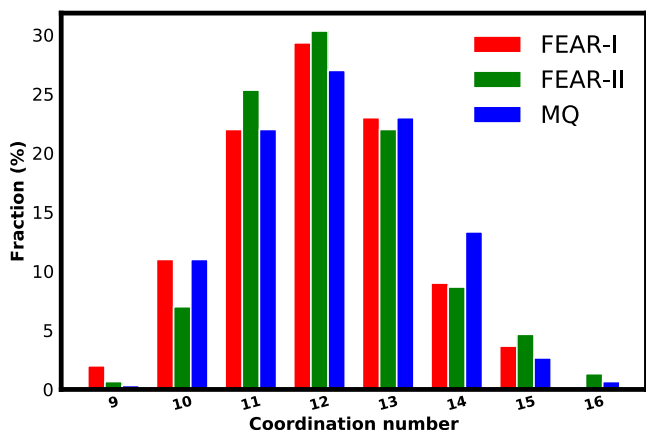


**Figure 3.** Fraction of different coordination numbers present in the samples. The coordination number is peaked around 12, suggesting dominance of icosahedron structures.

**Table 1.** Coordination statistics: average coordination number and its distribution of constituent atoms.

	Atom	$n$	$n(\text{Zr})$	$n(\text{Cu})$	$n(\text{Al})$
FEAR-I	Zr	12.86	5.91	5.80	1.15
	Al	11.79	6.63	5.08	0.08
	Cu	11.22	5.80	4.54	0.88
FEAR-II	Zr	13.10	5.81	6.12	1.17
	Al	11.83	6.70	4.96	0.17
	Cu	11.30	6.12	4.32	0.86
MQ	Zr	13.07	5.78	6.08	1.21
	Al	12.12	6.96	4.92	0.25
	Cu	11.24	6.08	4.30	0.86

with Zr over Cu in agreement with previously reported strong interaction between Zr and Al atoms.<sup>[9]</sup>

### 3.2. Voronoi Analysis

The nearest neighbor environment of the atoms was studied using the poly-disperse Voronoi tessellation, as implemented

in the OVITO software,<sup>[35]</sup> with the Goldschmidt radius (1.60 Å for Zr, 1.43 Å for Al, and 1.28 Å for Cu). The Voronoi cell of an atom is the region of real space closer to that particle than any other.<sup>[36]</sup> Details about the Voronoi polyhedra can be found elsewhere.<sup>[36]</sup> In general, a Voronoi polyhedron (VP) for an atom can be manually constructed by connecting perpendicular bisector planes between that atom and all its nearest neighbors. The 3D geometry thus obtained is characterized with indexes written in the form  $\langle n_3 n_4 n_5 n_6 \rangle$ , where  $n_i$  denotes the number of faces with  $i$  edges present in the VP. The distribution of prominent Voronoi polyhedra is shown in **Figure 4**. A polyhedron is called prominent if it makes up more than 3% of the total number of polyhedra. For Zr atoms, most of the dominant polyhedra are not perfect icosahedra (ICO) ( $\langle 00120 \rangle$ ) but ICO-like with Voronoi indices  $\langle 0285 \rangle$ ,  $\langle 0286 \rangle$ ,  $\langle 01104 \rangle$ , etc. However, there are ideal ICO clusters in the network centered at Cu and Al atoms. These cluster statistics are in good agreement with results from the previous study.<sup>[16]</sup>

The Cu-centered  $\langle 00120 \rangle$ ,  $\langle 0282 \rangle$  and Zr-centered  $\langle 01104 \rangle$  are believed to have the slowest dynamics in Cu–Zr liquids<sup>[37,38]</sup> and are associated with the excellent GFA. These polyhedra also make up a significant fraction of the Voronoi polyhedra in our models. To study the fluctuations of the fraction of these clusters with temperature, together with other dominant VPs, we perform a constant temperature MD simulation of the MQ model at several different temperatures. The results, averaged over 500 configurations (the last ps of the MD simulation), are shown in **Figure 5**. In the vicinity of the glass transition temperature for  $\text{Cu}_{46}\text{Zr}_{46}\text{Al}_8$  ( $\approx 700$  K), our models show a significant increase in the fraction of clusters that are believed to have slow dynamics,<sup>[37,38]</sup> which explains the high GFA associated with this stoichiometry. There is a gradual increase in the fraction of  $\langle 0281 \rangle$  VP, making it the most common VP in the MQ model, in agreement with Wang et al.<sup>[12]</sup>

In addition to the ideal ICO, the Cu atoms have ICO-like ( $\langle 0282 \rangle$ ,  $\langle 0364 \rangle$ ,  $\langle 0281 \rangle$ ) clusters in large numbers. If we look at the system as a whole, it is obvious that ideal ICO are not the most dominant structure, again in agreement with Wang et al.<sup>[12]</sup>

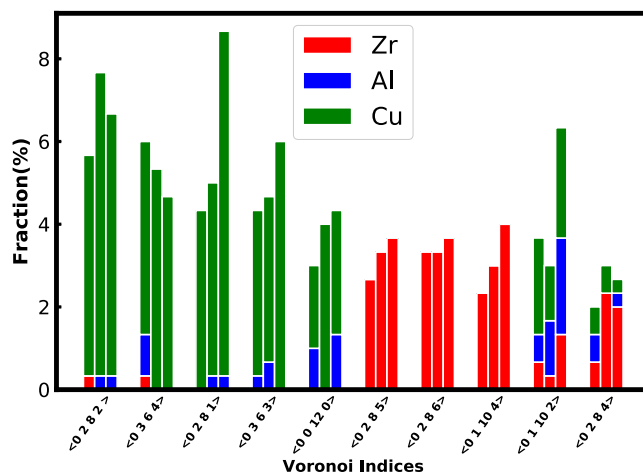


**Figure 4.** Concentration (in %) of the dominant polyhedra. The left bars on each Voronoi index correspond to FEAR-I, middle bar to FEAR-II, and the right to MQ models.



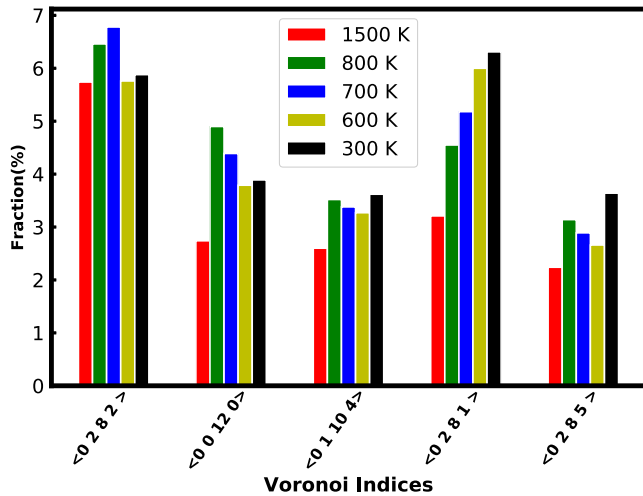


**Figure 5.** Temperature dependence of the fraction of slow dynamics clusters. A gradual increase in the concentration of  $\langle 0281 \rangle$  Voronoi polyhedra with the decrease in temperature is seen.

### 3.3. Electronic Properties

The electronic structure of the models was studied using total density of states (DoS), partial DoS, and inverse participation ratio (IPR). The DoS for FEAR-I is very similar to other models and is shown in **Figure 6**. The Fermi level corresponds to the zero of the energy scale marked by vertical drop lines. Significant contributions to the total DoS arise from the hybridization of

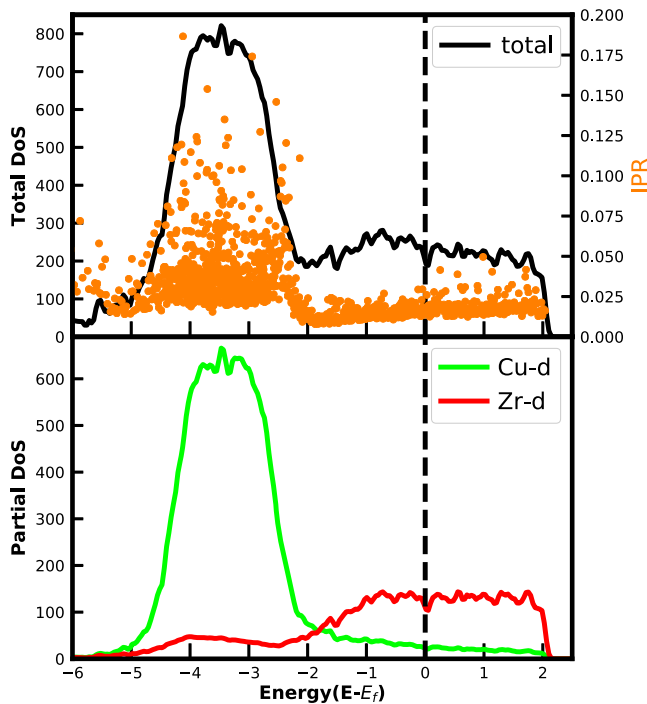


**Figure 6.** Electronic DoS of the FEAR-I model. The localization of the states is shown with IPR. Partial DoS that contributes most significantly to the DoS near the Fermi level is shown in the bottom panel.

the d-orbitals of Cu and Zr, whereas the contribution of Al remains nominal. Existence of states in the vicinity of the Fermi level suggests conducting behavior of the samples. The contribution from Zr atoms, however, is much higher than that of Cu near the Fermi level, and a result is also seen in Hall coefficient measurements of the Cu–Zr–Al system.<sup>[39]</sup> Similar electronic analysis on Cu<sub>50</sub>Zr<sub>50</sub><sup>[40]</sup> showed qualitatively the same results, which suggest that 8% Al doping does not significantly impact electronic properties. Details of the more active conduction parts of the network will be discussed in the next section.

The localization of Kohn–Sham states is given by IPR defined as

$$\mathcal{I}(\psi_n) = \frac{\sum_i |a_n^i|^4}{(\sum_i |a_n^i|^2)^2} \quad (1)$$

where  $a_n^i$  is the contribution to the eigenvector  $\psi_n$  from the  $i$ th atomic orbital (s, p, and d) as calculated with VASP. In simple terms, localized states have high IPR value (ideally equal to  $\mathcal{I} = 1$ ), whereas a completely extended state produces a value of  $(1/N)$ , i.e., evenly distributed over  $N$  atoms. Close to the Fermi level, we observe low IPR indicating delocalized states and conducting behavior of the models.

#### 3.3.1. Space-Projected Conductivity

The information given by DoS about the species decomposed contribution near the Fermi level is not a full treatment of conduction activity within the network, because the conduction also depends on the localization of the electronic states and momentum matrix elements between Kohn–Sham states near the Fermi level. Recently, we have developed a technique to visualize conductivity in real space by undertaking a spatial decomposition of the Kubo–Greenwood<sup>[41,42]</sup> formula. We start by defining a discrete grid in real space and show that the quantity

$$\zeta(\mathbf{x}) = \left| \sum_{\mathbf{x}'} \Gamma(\mathbf{x}, \mathbf{x}') \right| \quad (2)$$

may be interpreted as a space-projected conductivity (SPC), providing information about what parts of the network are contributing to electronic conduction. Here,  $\mathbf{x}$  is a grid point, and we introduce

$$\Gamma(\mathbf{x}, \mathbf{x}') = \sum_{ij\alpha} g_{ij} \zeta_{ij}^{\alpha}(\mathbf{x}) (\zeta_{ij}^{\alpha}(\mathbf{x}'))^* \quad (3)$$

The quantity  $\Gamma$  is a Hermitian, positive-semidefinite matrix whose eigenvectors are rank ordered conduction paths according to their conjugate eigenvalue.<sup>[43]</sup> The quantity  $g_{ij}$  is defined as<sup>[43]</sup>

$$g_{ij}(\mathbf{k}, \omega) = \frac{2\pi e^2}{3m^2 \omega \Omega} [f_i(\mathbf{k}) - f_j(\mathbf{k})] \delta(\varepsilon_j(\mathbf{k}) - \varepsilon_i(\mathbf{k}) - \hbar\omega) \quad (4)$$

where  $\Omega$  is the cell volume, and  $f$  is the Fermi–Dirac distribution.  $\zeta_{ij}^{\alpha}(\mathbf{x}) \equiv \psi_i^*(\mathbf{x}) p^{\alpha} \psi_j(\mathbf{x})$  is a complex-valued function,  $\psi_i(\mathbf{x})$  is the  $i$ th Kohn–Sham eigenfunction, and  $p^{\alpha} = \frac{\hbar}{i} \frac{\partial}{\partial x_{\alpha}}$ , ( $\alpha = x, y, z$ ). We have used this approach to successfully describe transport in a solid electrolyte material,<sup>[43]</sup> Cu-doped  $\alpha$ -alumina,<sup>[44]</sup> and Cu-doped tantalum.<sup>[45]</sup>

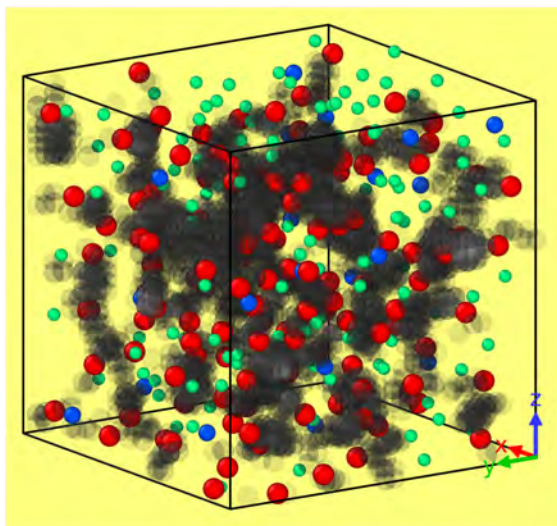


**Figure 7.** SPC for FEAR-I shown in grayscale. The Zr sites have higher SPC values than the Cu sites, and Al seems almost irrelevant to conduction.

The SPC for FEAR-I model is visualized as a grayscale plot in **Figure 7**. The SPC is distributed on both Cu and Zr, but a close analysis reveals that the Zr atoms have higher SPC values than the Cu atoms in the network.

### 3.4. Vibrational Properties

FEAR-II was well relaxed with the lattice vectors being allowed to change to attain zero pressure. This produces a slightly non-orthogonal supercell and an overall volume change of 45%. Each atom was displaced in six directions ( $\pm x$ ,  $\pm y$ ,  $\pm z$ ) by ( $\approx 0.015$  Å), and after each of these small displacements, forces were computed on all atoms, to obtain the force constant matrix and dynamical matrix. Normal modes were computed from the dynamical matrix by direct diagonalization. The vibrational density of states (VDoS) is defined as

$$g(\omega) = \frac{1}{3N} \sum_{i=1}^{3N} \delta(\omega - \omega_i) \quad (5)$$

with  $N$  and  $\omega_i$  representing the number of atoms and the eigenfrequencies of normal modes, respectively. The elemental contribution to the VDoS was computed with species projected VDoS defined as<sup>[46]</sup>

$$g_\alpha(\omega) = \frac{1}{3N} \sum_{i=1}^{N_\alpha} \sum_n |e_i^n|^2 \delta(\omega - \omega_n) \quad (6)$$

$|e_i^n|^2$  are the eigenvectors of the normal modes, and  $N_\alpha$  is the total number of atoms of  $\alpha$  species.

As shown in **Figure 8**, the VDoS is peaked at  $\approx 125$   $\text{cm}^{-1}$  arising from a joint contribution of vibrations of heavier atoms (Cu, Zr), whereas Al only contributes to vibrations at higher end of the vibrational spectrum. The partial VDoS plot supports these findings.

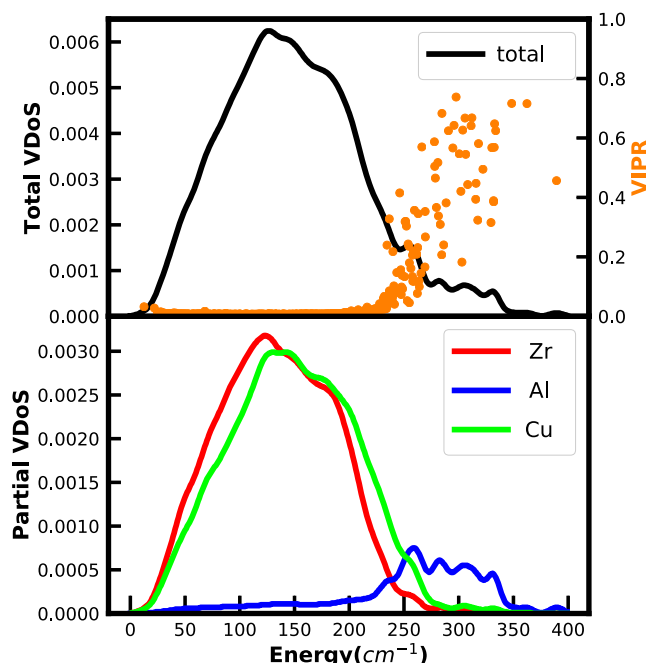


**Figure 8.** Total vibrational DoS for the FEAR-II model (top panel). The total vibrational localization (VIPR), shown by orange dots, shows that low-frequency modes are extended, whereas those at high frequencies are localized. Species projected VDoS (bottom panel) shows high-frequency modes dominated by the lightest atom and low frequency by heavier atoms, as expected.

#### 3.4.1. Localization of Vibrational Modes

The localization of vibrational modes is not easily observable from experiments. To study the localization of vibrational modes, we calculate the vibrational IPR (VIPR), the vibrational analogue of the electronic IPR, from the eigenvectors as follows

$$\mathcal{V}(\omega_n) = \frac{\sum_{i=1}^N |\mathbf{u}_n^i|^4}{(\sum_{i=1}^N |\mathbf{u}_n^i|^2)^2} \quad (7)$$

where  $(\mathbf{u}_n^i)$  is the displacement vector of  $i$ th atom at normal mode frequency  $\omega_n$ .

A small value of VIPR for a particular eigenfrequency indicates evenly distributed vibration among the atoms, whereas a higher value implies vibration localized on few atoms. We have plotted the total VIPR in **Figure 8**. Low values of VIPR below  $\approx 250$   $\text{cm}^{-1}$  suggest extended/localized vibrational modes at low frequencies. However, above  $250$   $\text{cm}^{-1}$ , we observe higher VIPR and localized vibrations.

To gain a visual insight into the localization/delocalization of vibrations, suitable animations were made. The higher frequency animation shows that Al atoms exhibit local motion (both bond stretching and bending) like that of a rattler inside a cage of Cu, Zr atoms. Similar, rattler motion of light atoms inside a cage of metal atoms has been seen previously in a Pd–Ni–P BMG.<sup>[27]</sup>

## 4. Conclusion

We have generated realistic models of a complex BMG with FEAR that agrees reasonably well with the experiment. Both FEAR models have the same level of agreement with the experiment and topologically similar to the MQ model (all ab initio roads lead to  $\text{Cu}_{46}\text{Zr}_{46}\text{Al}_8$ ). However, the computational efficiency of the FEAR model was almost six times that of the MQ model. A similar efficiency increase was reported earlier for Pd–Ni–P BMG.<sup>[27]</sup> The Voronoi statistics agree well with previous results, and our models may well be suited to catch the local dynamics of the clusters in the material. The addition of Al introduces structural clusters that are believed to have slow dynamics, thereby enhancing the GFA. We have also shown the temperature dependence of the distribution of some important Voronoi clusters and achieved reasonable agreement with published results. The electronic DoS of our models is very close to that of  $\text{Cu}_{50}\text{Zr}_{50}$ ,<sup>[40]</sup> suggesting that 8% Al concentration is not enough to significantly change the electronic properties.

## Acknowledgements

The authors thank the National Science Foundation (NSF) for support under DMR award 1507670. They also thank Extreme Science and Engineering Discovery Environment (XSEDE), supported by NSF grant number ACI-1548562, for providing computation resources under the allocations DMR-190008P.

## Conflict of Interest

The authors declare no conflict of interest.

## Keywords

forced enhanced atomic refinement, glass forming ability, space-projected conductivity

Received: July 27, 2020

Revised: November 20, 2020

Published online: January 6, 2021

- [1] V. Kumar, T. Fujita, K. Konno, M. Matsuura, M. W. Chen, A. Inoue, Y. Kawazoe, *Phys. Rev. B* **2011**, 84, 134204.
- [2] H. Li, Y. Zheng, *Acta Biomater.* **2016**, 36, 1.
- [3] J. D. Bernal, *Nature* **1960**, 185, 68.
- [4] P. H. Gaskell, *Nature* **1978**, 276, 484.
- [5] D. Miracle, *Nat. Mater.* **2004**, 3, 697.
- [6] P. Guan, T. Fujita, A. Hirata, Y. Liu, M. W. Chen, *Phys. Rev. Lett.* **2012**, 108, 175501.
- [7] A. Takeuchi, A. Inoue, *Mater. Trans.* **2005**, 46, 2817.
- [8] T. R. Anantharaman, C. Suryanarayana, *J. Mater. Sci.* **1971**, 6, 1111.
- [9] K. Georgarakis, A. R. Yavari, D. V. Louzguine-Luzgin, J. Antonowicz, M. Stoica, Y. Li, M. Satta, A. LeMoulec, G. Vaughan, A. Inoue, *Appl. Phys. Lett.* **2009**, 94, 191912.
- [10] J. Antonowicz, A. Pietnoczka, W. Zalewski, R. Bacewicz, M. Stoica, K. Georgarakis, A. Yavari, *J. Alloys Compd.* **2011**, 509, S34.
- [11] L. Yang, G.-Q. Guo, L.-Y. Chen, S.-H. Wei, J.-Z. Jiang, X.-D. Wang, *Scr. Mater.* **2010**, 63, 879.
- [12] X. Wang, Q. Jiang, Q. Cao, J. Bednarcik, H. Franz, J. Jiang, *J. Appl. Phys.* **2008**, 104, 093519.
- [13] X. K. Xi, M. T. Sandor, H. J. Wang, J. Q. Wang, W. H. Wang, Y. Wu, *J. Phys.: Condens. Matter* **2011**, 23, 115501.
- [14] Y. Q. Cheng, E. Ma, H. W. Sheng, *Phys. Rev. Lett.* **2009**, 102, 245501.
- [15] V. Kokotin, H. Hermann, J. Eckert, *J. Phys.: Condens. Matter* **2011**, 23, 425403.
- [16] Y. Zhang, N. Mattern, J. Eckert, *J. Alloys Compd.* **2012**, 514, 141.
- [17] P. Yu, H. Bai, M. Tang, W. Wang, *J. Non-Cryst. Solids* **2005**, 351, 1328.
- [18] I. Kaban, P. Jovari, B. Escher, D. Tran, G. Svensson, M. Webb, T. Regier, V. Kokotin, B. Beuneu, T. Gemming, J. Eckert, *Acta Mater.* **2015**, 100, 369.
- [19] D. A. Drabold, *Eur. Phys. J. B* **2009**, 68, 1.
- [20] A. Pandey, P. Biswas, D. A. Drabold, *Sci. Rep.* **2016**, 6, 33731.
- [21] A. Pandey, P. Biswas, D. A. Drabold, *Phys. Rev. B* **2015**, 92, 155205.
- [22] A. Pandey, P. Biswas, B. Bhattacharai, D. A. Drabold, *Phys. Rev. B* **2016**, 94, 235208.
- [23] B. Bhattacharai, A. Pandey, D. Drabold, *Carbon* **2018**, 131, 168.
- [24] I. Igram, B. Bhattacharai, P. Biswas, D. Drabold, *J. Non-Cryst. Solids* **2018**, 492, 27.
- [25] Q. Zhou, T. Du, L. Guo, M. Smedskjaer, M. Bauchy, *J. Non-Cryst. Solids* **2020**, 536, 120006.
- [26] B. Bhattacharai, P. Biswas, R. Atta-Fynn, D. A. Drabold, *Phys. Chem. Chem. Phys.* **2018**, 20, 29.
- [27] B. Bhattacharai, R. Thapa, D. A. Drabold, *Modell. Simul. Mater. Sci. Eng.* **2019**, 27, 075002.
- [28] M. G. Tucker, D. A. Keen, M. T. Dove, A. L. Goodwin, Q. Hui, *J. Phys.: Condens. Matter* **2007**, 19, 335218.
- [29] G. Kresse, J. Furthmüller, *Phys. Rev. B* **1996**, 54, 11169.
- [30] M. Hacene, A. Anciaux-Sedrakian, X. Rozanska, D. Klahr, T. Guignon, P. Fleurat-Lessard, *J. Comput. Chem.* **2012**, 33, 2581.
- [31] M. Hutchinson, M. Widom, *Comput. Phys. Commun.* **2012**, 183, 1422.
- [32] P. E. Blochl, *Phys. Rev. B* **1994**, 50, 17953.
- [33] G. Kresse, D. Joubert, *Phys. Rev. B* **1999**, 59, 1758.
- [34] J. P. Perdew, K. Burke, M. Ernzerhof, *Phys. Rev. Lett.* **1996**, 77, 3865.
- [35] A. Stukowski, *Simul. Modelling, Mater. Sci. Eng.* **2010**, 18, 015012.
- [36] E. A. Lazar, J. Han, D. J. Srolovitz, *Proc. Natl. Acad. Sci. USA* **2015**, 112, E5769.
- [37] S. Q. Wu, C. Z. Wang, S. G. Hao, Z. Z. Zhu, K. M. Ho, *Appl. Phys. Lett.* **2010**, 97, 021901.
- [38] S. G. Hao, C. Z. Wang, M. J. Kramer, K. M. Ho, *J. Appl. Phys.* **2010**, 107, 053511.
- [39] U. Mizutani, Y. Yamada, C. Mishima, T. Matsuda, *Solid State Commun.* **1987**, 62, 641.
- [40] J. Antonowicz, A. Pietnoczka, K. Pkaa, J. Latuch, G. A. Evangelakis, *J. Appl. Phys.* **2014**, 115, 203714.
- [41] R. Kubo, *J. Phys. Soc. Jpn.* **1957**, 12, 570.
- [42] D. A. Greenwood, *Proc. Phys. Soc.* **1958**, 71, 585.
- [43] K. Prasai, K. N. Subedi, K. Ferris, P. Biswas, D. A. Drabold, *Phys. Status Solidi RRL* **2018**, 12, 1800238.
- [44] K. N. Subedi, K. Prasai, M. N. Kozicki, D. A. Drabold, *Phys. Rev. Mater.* **2019**, 3, 065605.
- [45] R. Thapa, B. Bhattacharai, M. N. Kozicki, K. N. Subedi, D. A. Drabold, *Phys. Rev. Mater.* **2020**, 4, 064603.
- [46] A. Pasquarello, J. Sarnthein, R. Car, *Phys. Rev. B* **1998**, 57, 22.



# Simulation of Phase-Change-Memory and Thermoelectric Materials using Machine-Learned Interatomic Potentials: $\text{Sb}_2\text{Te}_3$

Konstantinos Konstantinou, Juraj Mavračić, Felix C. Mocanu, and Stephen R. Elliott\*

Dedicated to Professor David A. Drabold on the occasion of his 60th birthday

Density-functional-theory (DFT)-based, ab initio molecular dynamics (AIMD) simulations of amorphous materials generally suffer from three computer-resource-related limitations due to their  $O(N^3)$  cubic scaling with model system size,  $N$ . They are limited to a maximum model size of  $N \approx 500$  atoms; they are limited to time scales  $< 1$  ns; and, usually, only a single model can be simulated in any one investigation. This article discusses a machine-learned, linear-scaling ( $O(N)$ ), DFT-accurate interatomic potential (a Gaussian approximation potential, GAP), originally developed by Mocanu et al. [*J. Phys. Chem. B* 2018, 122, 8998] using a Gaussian process regression method for the ternary phase-change-memory material  $\text{Ge}_2\text{Sb}_2\text{Te}_5$  (GST). The chemical transferability of this GAP potential is explored in an application to the case of simulating amorphous models of the phase-change-memory and thermoelectric material  $\text{Sb}_2\text{Te}_3$ , an end-member of the GST compositional tie-line  $\text{GeTe-Sb}_2\text{Te}_3$ . The GAP-model results are compared with those obtained from conventional DFT-based AIMD simulations.

devices.<sup>[1,2]</sup> Such phase-change, random-access memory (PCRAM) devices function by the application of Joule-heating voltage pulses, which switch the memory material, ultra-rapidly ( $\approx \text{ns}$ ) and reversibly, between metastable structural states (the “phase change”), consisting of a crystalline (c-), electrically conducting (degenerate semiconductor) phase (“1”) and a glassy (g-), electrically resistive (intrinsic semiconductor) phase (“0”). The canonical PCM material is  $\text{Ge}_2\text{Sb}_2\text{Te}_5$  (GST-225), a composition on the  $\text{GeTe-Sb}_2\text{Te}_3$  compositional tie-line, whose metastable crystalline form has a simple rock salt ( $\text{NaCl}$ ), cation-vacancy-containing atomic structure.

Although there has been a lot of experimental work performed on GST-225 and other PCM materials, most often, it is computer simulation that can provide the most detailed knowledge of their physical behavior


and its origin at the *atomistic* level. Not least, this is because in situ experimental studies of PCM materials in actual PCRAM devices are so challenging. This is due to the ultra-short times involved in the phase transformations ( $\approx 10$  ns), the very small size of the active memory element ( $\approx 10$ – $100$  nm), and the fact that the actual memory material is buried deep in a real device, surrounded by electrodes, heater, insulating dielectric, etc.

The most accurate computer simulations and electronic-structure calculations of solids are carried out on the basis of density-functional theory (DFT). However, such ab initio molecular dynamics (AIMD) simulations, for example, are extremely computer-intensive, because they generally scale cubically ( $O(N^3)$ ) with the number of atoms,  $N$ , in the simulation box. As a result, such AIMD simulations of amorphous systems generally suffer from three severe, computer-resource-related limitations: 1) the maximum number of atoms in models that can be simulated in this way is very small, typically  $N \approx 500$ ; 2) the simulation time is limited to  $\approx 1$  ns; and 3) the number of models that can be generated in the course of an AIMD study is generally limited to a single example, thereby precluding a statistical investigation of the properties of an ensemble of amorphous models, all prepared in the same manner. Although these limitations essentially preclude the use of AIMD simulations to study most glass-forming systems, nevertheless, they

## 1. Introduction

Phase-change-memory (PCM) materials are a contender for next-generation, non-volatile electronic-memory technology (a replacement for silicon complementary metal-oxide-semiconductor flash memory) and for new storage-class memory

Dr. K. Konstantinou,<sup>[†]</sup> J. Mavračić,<sup>[††]</sup> Dr. F. C. Mocanu,<sup>[†††]</sup>  
 Prof. S. R. Elliott<sup>[††††]</sup>  
 Department of Chemistry  
 University of Cambridge  
 Cambridge CB2 1EW, UK  
 E-mail: sre1@cam.ac.uk

 The ORCID identification number(s) for the author(s) of this article can be found under <https://doi.org/10.1002/pssb.202000416>.

<sup>[†]</sup>Present address: Computational Physics Laboratory, Tampere University, Tampere FI-33720, Finland.

<sup>[††]</sup>Present address: Cavendish Laboratory, University of Cambridge, Cambridge CB3 0HE, UK.

<sup>[†††]</sup>Present address: Laboratoire de Physique de l'École Normale Supérieure, ENS, Université PSL, CNRS, Sorbonne Universités, Université de Paris, F-75005 Paris, France.

<sup>[††††]</sup>Present address: Trinity College, University of Cambridge, Cambridge CB2 1TQ, UK.

DOI: 10.1002/pssb.202000416

are appropriate for the simulation of (e.g., phase transformations between) PCM materials, because their crystallization (“SET”) and vitrification (“RESET”) processes are so extremely rapid ( $\approx 1$  ns, comparable to the maximum simulation time achievable with AIMD). PCM materials are extremely *bad* glass formers, in which they crystallize so readily and rapidly on annealing. Moreover, the size of the active region of actual PCM cells is also comparable to the maximum system size achievable by AIMD (reversible PC transformations in real memory cells scale down to  $\approx 2$  nm).

However, it is also very desirable to be able to simulate PCM materials on much larger length scales, and for longer times, to access microscopic, rather than nanoscopic, behavior, as well as to create ensembles of amorphous models for a statistical study of their properties, e.g., the electronic behavior. To be able to do this, one needs *linear-scaling* ( $O(N)$ ) interatomic potentials, with DFT accuracy in energies and forces. The first machine-learned (ML)  $O(N)$  potential for a PCM material was developed by Sosso et al.<sup>[3]</sup> for the binary material, GeTe, one end-member of the GST compositional tie-line, using a neural-network (NN) approach to fit the electronic-energy surfaces of various training-set atomic configurations, calculated using DFT methods. The first DFT-accurate ML potential for the ternary PCM system, GST, was developed by Mocanu et al.<sup>[4]</sup> This used the Gaussian process regression method<sup>[5]</sup> to fit the potential (a “Gaussian Approximation Potential” [GAP]) to the DFT-calculated electronic-energy surfaces of more than 3300 training-set atomic configurations of (partially) crystalline, glassy, and liquid states of elemental (Ge, Sb, Te), binary (GeTe, Sb<sub>2</sub>Te<sub>3</sub>), and ternary (GST) systems, at various temperatures. This GAP potential for GST was subsequently used to create an ensemble of 30 models of *g*-GST, from which a statistical understanding of the gap-state electronic structure of this material was obtained.<sup>[6]</sup> It has also been used to simulate very large models of *g*-GST (up to 24 300 atoms), and glassy models of GST quenched from the liquid at rates as slow as 1 K ps<sup>−1</sup>.<sup>[7]</sup>

We should note that, overall, GAP force fields are a highly (quantum) accurate family of ML interatomic potentials that have been successfully used to model a number of elemental (B, C, P, Si, W)<sup>[8–12]</sup> and binary (H<sub>2</sub>O, HfO<sub>2</sub>, Ga<sub>2</sub>O<sub>3</sub>) materials.<sup>[13–15]</sup> In the GAP method, a representation of local atomic environments, such as the “smooth overlap of atomic positions” (SOAP) descriptor,<sup>[16]</sup> is mapped onto the energies, atomic forces, and virial stresses that have been calculated from model systems generated with a reference computational method. Following a careful training and appropriate benchmarking, the GAP model can show excellent agreement with the reference *ab initio* data.<sup>[17]</sup> We note that the reference method is typically DFT-based; however, in principle, any method can be used to generate data for the training set. The computational efficiency of the GAP-generated potentials is typically in-between that of traditional pairwise potentials and that of *ab initio* calculations. GAP-based molecular-dynamics (MD) simulations scale linearly with system size, and they have allowed for the simulations of very large systems and for long time scales.<sup>[7]</sup>

Although considerable attention has been paid previously to the PCM material, GeTe, a binary end-member of the GST compositional tie-line,<sup>[3,18]</sup> there has been relatively little study made up of the other PCM (and thermoelectric) binary end-member of

the GST GeTe–Sb<sub>2</sub>Te<sub>3</sub> tie-line, viz., Sb<sub>2</sub>Te<sub>3</sub>. In fact, there is also another composition in the binary Sb–Te system, which forms the basis of yet another PCM family, namely, Sb<sub>2</sub>Te. This is commonly doped, e.g., with Ag and In, to increase the crystallization temperature, e.g., as in the representative composition Ag<sub>5</sub>In<sub>5</sub>Sb<sub>60</sub>Te<sub>30</sub> (“AIST”).<sup>[19]</sup> AIST exhibits very fast, growth-limited crystallization, in contrast to the nucleation-limited crystallization shown by GST materials.<sup>[19]</sup>

Sb<sub>2</sub>Te<sub>3</sub> also has a very high crystallization speed and, therefore, is a potential candidate material to surpass the data-rate limit imposed by the rate-limiting crystallization process of other PCM materials.<sup>[20]</sup> However, it also has a low crystallization temperature and, hence, poor thermal stability of the amorphous phase, which is, therefore, detrimental to data retention in the glassy state (“0”) at high operating temperatures.<sup>[21]</sup> In addition, the relatively low electrical resistivity of Sb<sub>2</sub>Te<sub>3</sub>, compared with that of GST, leads to large RESET currents and, hence, high switching power.<sup>[21,22]</sup> Doping with various elements has, therefore, also been used to try to improve the performance of Sb<sub>2</sub>Te<sub>3</sub>, including dopants, such as C,<sup>[23]</sup> N,<sup>[20]</sup> O,<sup>[24]</sup> Al,<sup>[25]</sup> Si,<sup>[26]</sup> Ti,<sup>[27]</sup> Cr,<sup>[28]</sup> Zn,<sup>[29]</sup> Ge,<sup>[30]</sup> Ag,<sup>[31]</sup> Y,<sup>[32]</sup> and Sc.<sup>[33]</sup> Very recently, a nano-engineered hetero-structure, consisting of alternating layers of a few nanometers (3–5 nm) of Sb<sub>2</sub>Te<sub>3</sub> and TiTe<sub>2</sub>, has been shown to exhibit much-improved PCM behavior, particularly relating to a reduction in time-dependent resistance “drift” and in electrical noise in the glassy state of the PCM material, Sb<sub>2</sub>Te<sub>3</sub>.<sup>[34]</sup>

It should also be mentioned that Sb<sub>2</sub>Te<sub>3</sub> is of interest, and has been under intense investigation, for a very different application, viz., as a thermoelectric-generation (TEG) material, particularly in conjunction with the related material, Bi<sub>2</sub>Te<sub>3</sub>.<sup>[35]</sup> Crystalline Sb<sub>2</sub>Te<sub>3</sub> has a very high value of the TEG figure-of-merit, *ZT*, where *Z* is inversely proportional to the thermal conductivity,<sup>[35]</sup> which is very low in this material. An even higher *ZT* factor is achievable for very thin films, even monolayers, of Sb<sub>2</sub>Te<sub>3</sub>.<sup>[36]</sup> A DFT-based simulation study of undoped and Y-doped crystalline Sb<sub>2</sub>Te<sub>3</sub> has shown that both the electronic and lattice thermal conductivities can be reduced on doping.<sup>[37]</sup>

No ML  $O(N)$  potential has previously been developed specifically for Sb<sub>2</sub>Te<sub>3</sub>, as far as we are aware. However, there have been two recent reports on the development of simple two-body classical potentials for (crystalline) Sb<sub>2</sub>Te<sub>3</sub>, consisting of a Morse-potential term for short-range (covalent-like) interactions and a coulombic term for longer range interactions. The interatomic-potential parameters were optimized using elastic constants calculated from the first principles and experimental lattice parameters,<sup>[38]</sup> or fitted to DFT-calculated potential-energy surfaces for a range of distorted unit cells of crystalline Sb<sub>2</sub>Te<sub>3</sub>.<sup>[39]</sup> The former potential was used in an MD study of a 22 680-atom model of crystalline Sb<sub>2</sub>Te<sub>3</sub> to calculate the lattice thermal conductivity for TEG assessment.<sup>[38]</sup> ML interatomic potentials, such as the GAP used in this study, have some advantages over their classical, traditionally fitted counterparts. The flexibility of the local atomic descriptors used in the GAP-training method can be exploited to interpolate with excellent accuracy the *ab initio* potential-energy surface, including many-body contributions, which usually cannot be captured by classical (two-body) force fields. In addition, ML-GAP potentials can be re-trained in an iterative manner, providing the opportunity to improve the accuracy and transferability of the generated potential model with

additional data.<sup>[11]</sup> However, we should note that ML-GAP potentials are computationally more expensive, compared with classical pair potentials, due to the use of the high-dimensional descriptors and the long cutoffs that are needed to satisfy the underlying assumptions of locality. Moreover, the representation of multi-species environments usually requires large amounts of computer resources for both training and evaluation. In general, ML interatomic potentials do not typically include long-range interactions beyond their specified cutoff; the inclusion of such long-range corrections to the local energy remains an active topic of research to date.<sup>[40,41]</sup>

There have been relatively few simulation studies of glassy  $\text{Sb}_2\text{Te}_3$ , particularly compared with those for GeTe and especially compared with the number of AIMD studies of glassy GST (e.g., GST). Caravati et al.<sup>[42]</sup> first carried out an AIMD study of glassy (and liquid)  $\text{Sb}_2\text{Te}_3$ , followed by Zhang et al.<sup>[43]</sup> who also simulated  $g\text{-Sb}_2\text{Te}_3$  in an AIMD study, otherwise, mainly focused on  $g\text{-Sb}_2\text{Te}$ , and then, more recently, Guo et al.<sup>[44]</sup> also performed an AIMD study of liquid and glassy  $\text{Sb}_2\text{Te}_3$ . There have also been a few AIMD simulations of doped  $\text{Sb}_2\text{Te}_3$ , notably containing Sc<sup>[33]</sup> and Y<sup>[37,45]</sup> dopants. An AIMD-based, high-throughput materials-discovery investigation of electrical dopants in  $\text{Sb}_2\text{Te}_3$  also found that Sc, Y, and Hg were the most suitable dopants for this material.<sup>[46]</sup>

In this article, we report the results of computer simulations of models of  $g\text{-Sb}_2\text{Te}_3$ , quenched from the liquid, using the  $O(N)$  GST GAP potential<sup>[4]</sup> for this purpose, to ascertain, thereby, its degree of chemical transferability; these results are compared with those of conventional (DFT-based) AIMD simulations of  $g\text{-Sb}_2\text{Te}_3$  that we have also performed on this system.

## 2. Results and Discussion

### 2.1. Short-Range Order

The total neutron-scattering function (structure factor),  $S(q)$ , was computed for the 1000-atom GAP-MD and 250-atom DFT-MD generated liquid structures from the inverse Fourier transforms of the respective radial distribution functions (RDFs) of the liquid models at  $T = 1200$  K, and compared with previously reported experimental data at the same temperature.<sup>[47]</sup> The calculated  $S(q)$  functions of the equilibrated liquid structures of the simulated models are shown in **Figure 1**, and comparison with the neutron-diffraction data for liquid  $\text{Sb}_2\text{Te}_3$  from the previous study<sup>[47]</sup> reveals overall very good agreement, which is indicative of the quality of the liquid  $\text{Sb}_2\text{Te}_3$  models generated in this work. Comparison of the structure factors of the GAP-MD liquid model and the DFT-MD liquid model in **Figure 1** shows that the GST GAP potential is able to reproduce a liquid structure in close agreement with the DFT model, highlighting the effective chemical transferability of the GST GAP interatomic potential. This is the case, even though it was not trained explicitly for the  $\text{Sb}_2\text{Te}_3$  composition and, significantly, although the  $\text{Sb}_2\text{Te}_3$  DFT configurations used as a training set in the generation of the GST GAP potential<sup>[4]</sup> were *not* the same as those generated in the AIMD simulations reported in this article. The small second peak at  $\approx 3.1 \text{ \AA}^{-1}$  is somewhat smaller for the GAP model than for

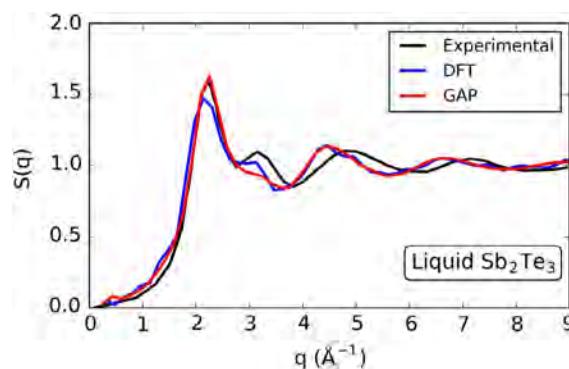


**Figure 1.** Neutron-weighted structure factors calculated for models of liquid  $\text{Sb}_2\text{Te}_3$  at 1200 K, simulated using the GAP potential (1000-atom model structure) and by DFT-MD (250-atom model structure), compared with experimental data.<sup>[47]</sup>

the DFT-MD model (but both are less pronounced than the experimental peak); otherwise, the curves are very similar.

**Figure 2** shows the plots of the reduced RDFs for liquid  $\text{Sb}_2\text{Te}_3$  at 1200 K (**Figure 2a**) and glassy  $\text{Sb}_2\text{Te}_3$  at 300 K (**Figure 2b**), both simulated by DFT-MD, whereas **Figure 3** shows the total RDF for the GAP-MD glassy  $\text{Sb}_2\text{Te}_3$  model at 300 K, together with a view of the 1000-atom amorphous GAP model. Comparison of **Figure 2a,b** shows that the RDFs of liquid and glassy  $\text{Sb}_2\text{Te}_3$  simulated by DFT-MD are qualitatively similar,

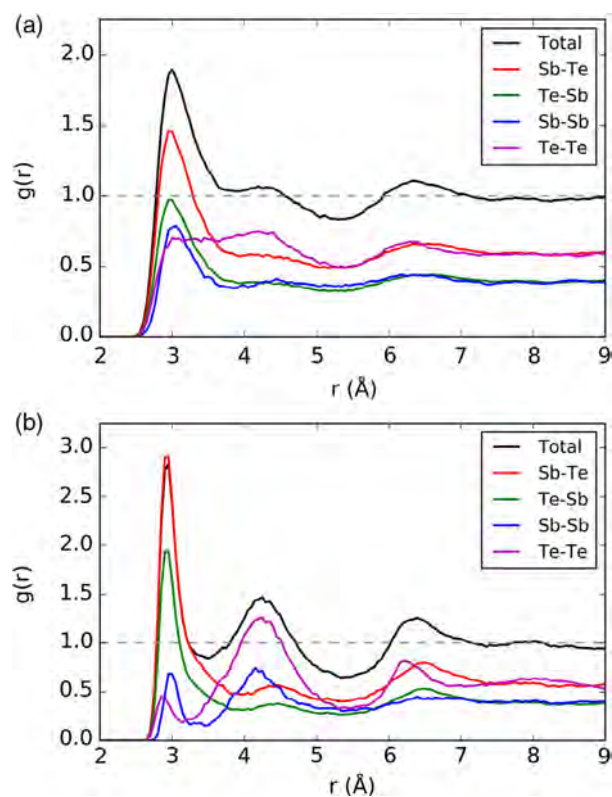


**Figure 2.** Total and partial atom-atom reduced RDFs,  $g(r)$ , simulated by DFT-MD for the 250-atom model of: a) liquid  $\text{Sb}_2\text{Te}_3$  at 1200 K and b) glassy  $\text{Sb}_2\text{Te}_3$  at 300 K.



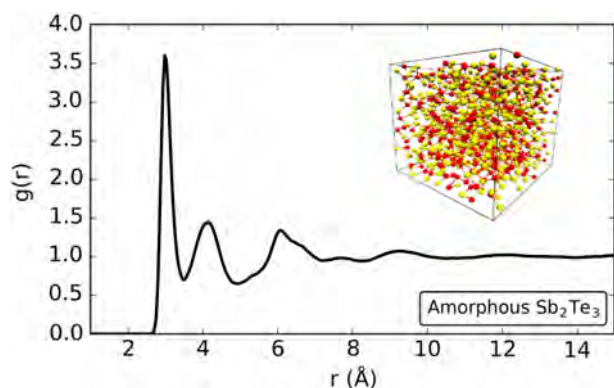


**Figure 3.** Total RDF,  $g(r)$ , calculated from the GAP-MD-generated glassy  $\text{Sb}_2\text{Te}_3$  model of 1000 atoms at 300 K. The inset shows a view of the 1000-atom GAP model of glassy  $\text{Sb}_2\text{Te}_3$ . Sb atoms are red, and Te atoms are yellow.

but that the peaks are very considerably broadened in the liquid case as a result of the increased thermal and topological structural disorder in the high-temperature liquid state. The total RDFs of the models of glassy  $\text{Sb}_2\text{Te}_3$  simulated by DFT-MD and GAP-MD are very similar, except that the maximum of the first peak for the GAP glass model is appreciably greater (and the width smaller) than for the DFT model, indicating that the degree of bond-length disorder is less for the GAP model (because the nearest-neighbor coordination numbers (CNs) are nearly identical for the two models—see Table 1). In addition, the third peak for the GAP model is at a slightly larger  $r$ -value and is narrower and more structured, indicative of a greater degree of medium-range order (MRO), than for the DFT model.

The values of nearest-neighbor partial CNs calculated from the RDFs of the DFT-MD and GAP-MD models of liquid and glassy  $\text{Sb}_2\text{Te}_3$  are given in Table 1. It is shown that the CNs for the DFT and GAP models of a given phase are almost identical, except that there appear to be significantly fewer like-atom bonds (Sb–Sb, Te–Te) in the GAP model of the glass than in the corresponding DFT model. However, there is a much higher prevalence of homopolar (Sb–Sb, Te–Te) bonds in the liquid models than in

**Table 1.** Coordination numbers for the first coordination shell and different bonding arrangements in liquid and glassy  $\text{Sb}_2\text{Te}_3$ , computed from the respective RDFs for the DFT-MD (250-atom structures) and GAP-MD (1000-atom structures) models using the bond cutoff distances (in Å): (liquid) Sb–Te, 3.9; Sb–Sb, 3.8; Te–Te, 3.6; (glass) Sb–Te, 3.9; Sb–Sb, 3.3; Te–Te, 3.2.

	Liquid (1200 K)		Glass (300 K)	
	DFT-MD	GAP-MD	DFT-MD	GAP-MD
Sb–X	6.1	6.2	5.2	5.4
Te–X	4.7	5.1	3.5	3.6
Sb–Te	4.1	4.5	4.6	5.0
Te–Sb	2.7	3.0	3.1	3.4
Sb–Sb	2.0	1.7	0.6	0.3
Te–Te	2.0	2.1	0.4	0.3

the corresponding glassy models. The Sb-centered CN value in the liquid state for the DFT model (respectively, GAP model) [CN = 6.1 (6.2)] is consistent with octahedral local coordination; the corresponding value for the glassy state is somewhat smaller [CN = 5.2 (5.4)], indicative of defective, near-octahedral coordination for Sb atoms in that case. Guo et al.<sup>[44]</sup> quote a value of CN = 5.4, but Zhang et al.<sup>[43]</sup> give a value of CN = 4.1, for their glassy DFT-MD models at 300 K. The Te-centered CN value for the liquid model was found to be smaller [CN = 4.7 (5.1)] than the Sb-centered value, and smaller again for the glass model at 300 K, viz., CN = 3.5 (3.6). Guo et al.<sup>[44]</sup> quote CN = 3.4, but Zhang et al.<sup>[43]</sup> quote CN = 2.8. These CN values depend on the precise values of bond cutoff distances used, and whether a uniform value is used or different ones are used (as here), depending on the bond type.

The total bond-angle distribution (BAD) functions for the DFT-MD models of liquid  $\text{Sb}_2\text{Te}_3$  at 1200 K and glassy  $\text{Sb}_2\text{Te}_3$  at 300 K are shown in Figure 4. The BAD curve for the high-temperature liquid model is very considerably broader than that for the low-temperature glassy model, as expected due to the increased structural disorder, but both curves exhibit a maximum at a bond angle of  $\approx 90^\circ$ , supporting the identification of predominantly octahedral-like local bonding configurations in both phases. It is noticeable that the peak corresponding to  $60^\circ$  bond angles is very significantly greater in the liquid state, perhaps indicative of a greater proportion of triangular configurations. In contrast, the well-defined peak at  $\approx 160^\circ$  in the glass BAD curve is smeared out in the liquid state, indicating that the well-defined, near-linear configurations of triads of atoms (corresponding to axial configurations in octahedral-like environments) that exist in the glassy phase are much less prevalent in the more disordered liquid state.

The corresponding partial BAD curves for different triads of atoms, from which the total BAD curves in Figure 4 are generated, are shown in Figure 5 for the liquid state (Figure 5a) and the glassy state (Figure 5b) for the DFT-MD models. It is noteworthy from examination of Figure 5b that the peak in the total BAD curve at a bond angle of  $\approx 160^\circ$ , evident in Figure 4, is due solely to near-linear (axial) arrangements of chemically ordered Te–Sb–Te triads. The Te–Sb–Te BAD function for the 1000-atom GAP-MD glassy model of  $\text{Sb}_2\text{Te}_3$ , shown in Figure 6, reveals a

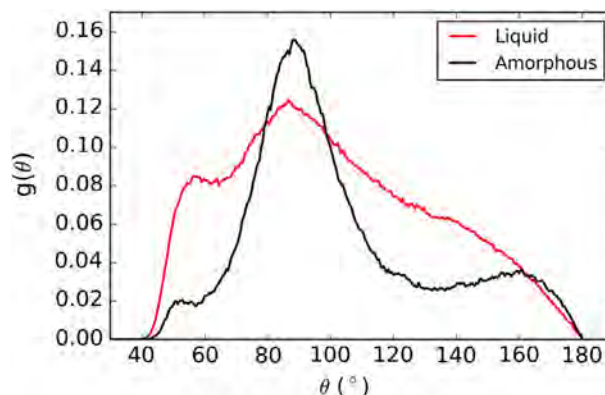


**Figure 4.** Total BAD function for liquid (1200 K) and glassy (300 K)  $\text{Sb}_2\text{Te}_3$  models simulated by DFT-MD.

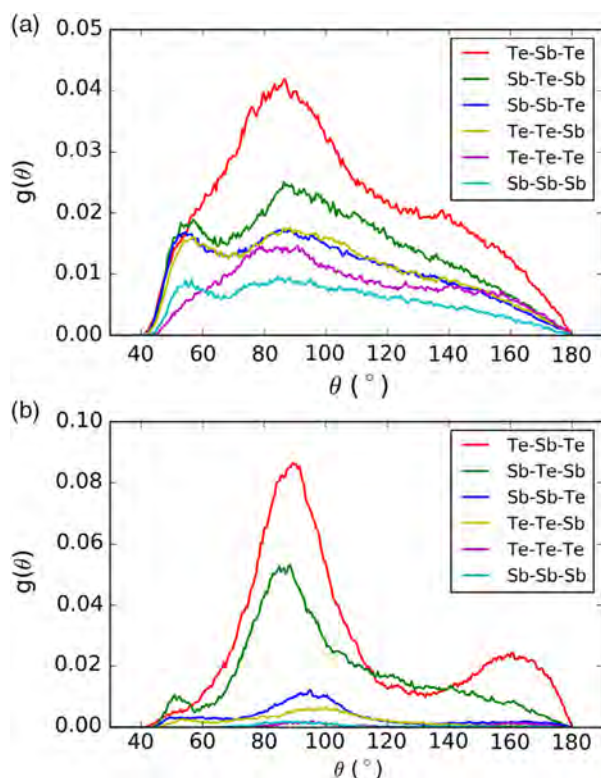


**Figure 5.** Partial BAD functions for different types of triads of atoms for the 250-atom DFT-MD models of: a) liquid  $\text{Sb}_2\text{Te}_3$  (1200 K) and b) glassy  $\text{Sb}_2\text{Te}_3$  (300 K).

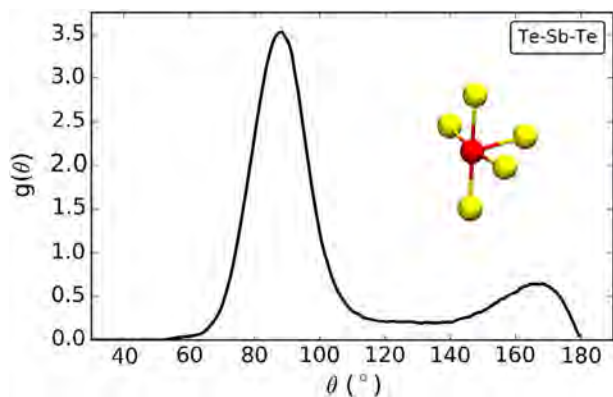


**Figure 6.** Te-Sb-Te BAD function calculated for the 1000-atom GAP-MD model of amorphous  $\text{Sb}_2\text{Te}_3$  at 300 K. The peak at a bond angle of  $168.5^\circ$  is indicative of the near-linear (axial) arrangements of chemically ordered Te-Sb-Te triads found in the modeled systems. The inset shows the five-coordinated (defective octahedral) local environment of an Sb atom in the 1000-atom GAP model of glassy  $\text{Sb}_2\text{Te}_3$ , indicating the occurrence of such near-linear configurations, as well as the predominant  $90^\circ$  bond angles. The Sb atom is red, and Te atoms are yellow.

similar peak at a bond angle of  $\approx 169^\circ$ , highlighting the presence of these almost-linear Te-Sb-Te configurations within the amorphous network of the GAP model as well. It is noted that similar behavior was also found by Guo et al.<sup>[44]</sup>

## 2.2. Medium-Range Order

The MRO of the liquid and amorphous GAP and DFT  $\text{Sb}_2\text{Te}_3$  models was characterized by calculating the statistics of the sizes of shortest-path rings using the Franzblau algorithm,<sup>[48]</sup> as implemented in the QUIP code.<sup>[5]</sup> The ring-size distributions for the 250-atom DFT-MD structures of the model liquid, at 1200 K, and the model glass, at 300 K, are shown in Figure 7a. The resulting ring-size distributions of shortest-path rings in the 1000-atom GAP-MD  $\text{Sb}_2\text{Te}_3$  model are shown for the liquid phase (1200 K) and the amorphous phase (300 K) in Figure 7b, for comparison. It is shown that the distributions for the DFT and GAP liquid models are very similar: the dominant ring sizes are 3 and 4 in both cases, and there is a more-or-less constant distribution of rings of sizes from 7 to 15 (DFT model) and 7 to 19 (GAP model). This difference is probably a size effect, because the GAP model is larger than the DFT model and so can contain a greater number of larger rings. It can be assumed that this size effect is also responsible for the decrease from a constant distribution of ring sizes in the liquid state, evident for both models for the largest ring sizes.<sup>[7]</sup>

For the case of the DFT and GAP glass models, however, there appears to be a substantial difference in the ring-size

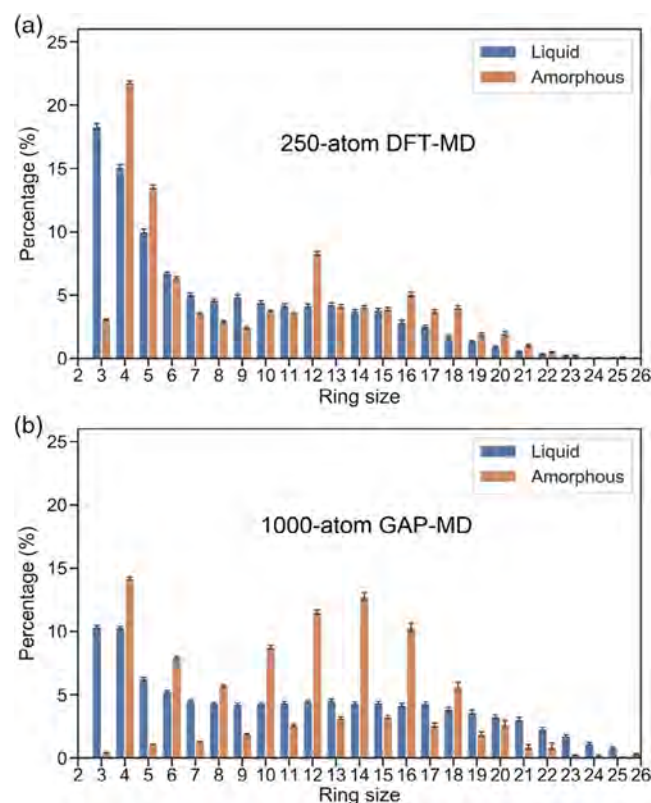


**Figure 7.** MRO in  $\text{Sb}_2\text{Te}_3$  as analyzed through ring-size statistics. Shortest-path ring distributions in models of liquid (1200 K) and glassy (300 K)  $\text{Sb}_2\text{Te}_3$  for: a) 250-atom model structures simulated by DFT-MD and b) 1000-atom model structures generated by GAP-MD. Error bars, in each plot, depict the variation over multiple configurations sampled at 1200 and 300 K for the liquid and glassy models, respectively.

distributions. Although fourfold rings (e.g., Sb–Te–Sb–Te) are the dominant structural motif in both cases, as found for GST-225,<sup>[7]</sup> only the GAP model (Figure 7b) exhibits clear evidence for an even-odd-even-odd alternation of ring sizes, as seen in GST-225,<sup>[7]</sup> whereas the DFT model is much more disordered (Figure 7a). This difference in the extent of MRO, evident in the ring-size distribution, is mirrored in the shape of the third peak in the RDF (Figure 2b and 3), which is more structured in the case of the GAP-MD model, indicative of a more pronounced MRO. Moreover, we note that the reduced number of fivefold and sevenfold rings in the GAP model relative to the DFT model for the glass is a result of the fewer number of homopolar Sb–Sb bonds in the GAP amorphous model, as evidenced from the reduced intensity of the first peak in the Sb–Sb partial RDF (see Figure S1, Supporting Information).

### 2.3. Electronic Structure

The electronic structure of the final equilibrated, DFT-MD-generated 250-atom model of glassy Sb<sub>2</sub>Te<sub>3</sub> was calculated by performing a geometry optimization with a hybrid functional (PBE0). The electronic-structure calculation produces a highest-occupied molecular-orbital–lowest-unoccupied molecular-orbital (HOMO–LUMO) Kohn–Sham bandgap,  $E_g$ , of 0.75 eV for the relaxed ground state, which agrees well with the value ( $E_g = 0.69$  eV) that was previously reported by a different DFT-MD modeling study of *g*-Sb<sub>2</sub>Te<sub>3</sub>,<sup>[42]</sup> whereas it also agrees reasonably well with the experimentally reported value ( $E_g = 0.52$  eV).<sup>[49]</sup> A very similar value of  $E_g = 0.70$  eV was calculated for the relaxed ground state of the 250-atom GAP-MD model of *g*-Sb<sub>2</sub>Te<sub>3</sub>, from a hybrid-DFT geometry optimization performed using the same non-local functional (PBE0). It should be noted that the 1000-atom GAP model is too large on which to carry out similar calculations.

In addition, the total electronic densities of states (DOSs) of the 250-atom DFT-MD and GAP-MD models of *g*-Sb<sub>2</sub>Te<sub>3</sub> are shown in Figure 8a,b, respectively. It is shown that, in both cases, these models produce a “clean” bandgap, devoid of defect-related gap states. However, examination of an ensemble of, ideally larger, models (e.g., produced by GAP-MD) would be necessary to gain a statistical understanding of the prevalence of possible gap states, as demonstrated for the case of GST-225.<sup>[6]</sup> No significant overall differences can be observed between the electronic structures of the two *g*-Sb<sub>2</sub>Te<sub>3</sub> models, except that the pseudogap at approximately –12 eV in the lower part of the valence band for the DFT-MD model becomes a full gap for the GAP-MD model. This high degree of similarity in the overall DOS implies that the differences in the MRO between the two glassy models, evident in the ring-size distributions (Figure 7), are of little account in determining the electronic structure in this case. Instead, it is the close similarity in the short-range order of the two models which is the main factor controlling the shape of the DOS profiles.

We note that the close similarity of the DOS profiles, together with the very similar calculated values of the energy bandgaps, highlights the good agreement in the electronic structure between the GAP and DFT models of *g*-Sb<sub>2</sub>Te<sub>3</sub> generated in this work. This is also indicative of the overall good transferability of

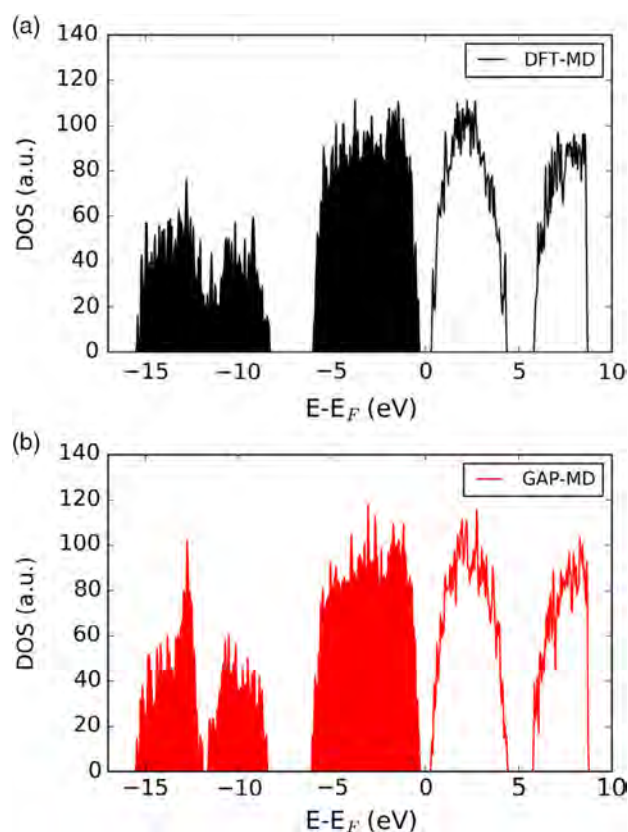


**Figure 8.** Total electronic DOS for 250-atom glassy Sb<sub>2</sub>Te<sub>3</sub> models generated by: a) DFT-MD simulations and b) GAP-MD simulations. The obtained HOMO–LUMO bandgaps, from the hybrid-functional electronic-structure calculations, are 0.75 and 0.70 eV for the DFT and GAP models, respectively. The Fermi level lies approximately at the middle of the energy bandgap in both modeled systems.

the ML potential, originally developed for ternary Ge–Sb–Te materials, to the case of binary Sb<sub>2</sub>Te<sub>3</sub>.

### 3. Conclusion

We report on the results of MD simulations of liquid and glass models of the PCM (and thermoelectric) material, Sb<sub>2</sub>Te<sub>3</sub>, one end-member of the GeTe–Sb<sub>2</sub>Te<sub>3</sub> tie-line containing the composition of the canonical PCM material, GST. Two types of MD simulations have been performed: one involved classical MD simulations using an ML, DFT-accurate, linear-scaling interatomic potential (GAP) recently developed by our group for the ternary GST system, and the other involving conventional DFT-based ab initio simulations. A comparison of the atomic and electronic structures of the GAP- and DFT-MD models of glassy Sb<sub>2</sub>Te<sub>3</sub> revealed very good agreement overall, indicating a good degree of chemical transferability of the GAP potential, originally developed for GST, to the case of Sb<sub>2</sub>Te<sub>3</sub>.

As we have shown the good transferability of the GST GAP potential for the case of glassy Sb<sub>2</sub>Te<sub>3</sub>, and demonstrated its appreciable computational speedup relative to DFT-MD simulations, the prospect arises, therefore, of using this GAP potential



(perhaps suitably modified with additional training and fitting) to simulate, for the first time, very large quantum-accurate models of *crystalline*  $\text{Sb}_2\text{Te}_3$  containing extended defects for investigating their possible thermoelectric characteristics.<sup>[50–52]</sup>

#### 4. Computational Methods

A glassy model of  $\text{Sb}_2\text{Te}_3$  containing 1000 atoms was generated using classical MD simulations and using the ML GAP potential, recently developed by our group for Ge–Sb–Te materials, specifically GST,<sup>[4]</sup> to model the interactions between the atoms. Note that this model size is approximately twice the maximum size that can normally be simulated using conventional AIMD simulations. The GAP-MD simulations were performed using the LAMMPS package,<sup>[53]</sup> and the glass structure was generated from the liquid state following a conventional “melt-and-quench” approach. The canonical (NVT) ensemble, with a Nosé–Hoover thermostat, was applied during the MD simulations to control the temperature fluctuations, whereas a time-step of 1 fs was used to integrate the equations of motion. The initial configuration was heated up at 3000 K with a 20 ps MD run to ensure that the system melted. The molten structure was subsequently cooled down to 1200 K and equilibrated, using first the NVT and then the NVE (microcanonical) ensembles with 20 and 10 ps MD runs, respectively, to obtain an equilibrated liquid structure at this temperature and to collect data for structural analysis, respectively. The system was then cooled down to 300 K with a linear quenching rate of  $-15 \text{ K ps}^{-1}$ . At 300 K, the glass structure was equilibrated for 20 ps, followed by a 10 ps MD run with the NVE ensemble, to gather structural data. In addition, a 250-atom  $\text{Sb}_2\text{Te}_3$  amorphous model was also generated by GAP-MD simulation, following the same protocol as mentioned earlier, to calculate its electronic structure using hybrid-functional DFT calculations.

A glassy model of  $\text{Sb}_2\text{Te}_3$  containing 250 atoms was generated by AIMD simulation using the VASP code,<sup>[54]</sup> with the Perdew–Burke–Ernzerhof (PBE) exchange–correlation functional.<sup>[55]</sup> Outer s and p electrons were treated as valence electrons, and the plane-wave energy cutoff was set to 250 eV. Cubic supercells were used in all calculations, and only the supercell  $\Gamma$ -point was used for Brillouin-zone integration. To create the initial structure of the liquid system, a simple cubic unit cell was defined, which was then extended sevenfold in all three dimensions to enable appropriate placement of atoms and vacancies on the 343 lattice positions; 100 Sb atoms, 150 Te atoms, and 93 vacancies were placed randomly at the lattice sites within the cubic supercell, keeping the  $\text{Sb}_2\text{Te}_3$  stoichiometry. As the density of liquid  $\text{Sb}_2\text{Te}_3$  was not known at the time of the simulations, it was estimated to be  $5.60 \text{ g cm}^{-3}$  from a previous study, where the molar volumes of various liquid Sb–Te systems are reported.<sup>[56]</sup> The lattice parameter of the cubic supercell was then rescaled to match the target liquid density by moving the atoms accordingly. An advantage of this approach is that one can generate an initial structure avoiding non-physically small interatomic distances between the atoms. This initial structure is energetically unfavorable at the selected density; hence, in the following mixing step at high temperature, we expect any resemblance to the initial configuration to be erased. Therefore, in that way, we can ensure that

the generated liquid  $\text{Sb}_2\text{Te}_3$  structure does not carry any memory effect of the initial, randomly generated, structure. An MD simulation in the NVT ensemble was performed at 3000 K using a Langevin thermostat, for an overall time of 15 ps, with a time-step of 4 fs, to mix and randomize the initial configuration. Simulation of the liquid phase, equilibrated at 1200 K, was carried out using the Langevin thermostat for 10 ps, followed by a linear quench at a rate of  $-15 \text{ K ps}^{-1}$  to 300 K, also using the Langevin thermostat. The resulting glass structure was then equilibrated at 300 K for 10 ps in the NVE ensemble, followed by an  $NpH$  simulation for 15 ps to estimate the equilibrium density of the glassy phase. The computed value ( $5.46 \text{ g cm}^{-3}$ ) of the glass density is slightly lower than the value ( $5.64 \text{ g cm}^{-3}$ ) calculated by Caravati et al.<sup>[42]</sup>

The atomic configurations of the two 250-atom  $\text{Sb}_2\text{Te}_3$  amorphous models, generated by the melt-and-quench DFT-MD and GAP-MD simulations, respectively, were then optimized, using DFT implemented in the CP2K code,<sup>[57]</sup> to calculate the electronic structure of the glass models. The non-local PBE0 functional was used for this calculation, with a cutoff radius of 2 Å for the truncated Coulomb operator,<sup>[58]</sup> because the inclusion of the Hartree–Fock exchange can provide a good description of the bandgap and identification of any possible localized (gap) states in the glassy model, as was demonstrated in our recent work for amorphous GST.<sup>[6]</sup> The CP2K code uses a Gaussian basis set with an auxiliary plane-wave basis set.<sup>[59]</sup> All atomic species were represented using a double- $\zeta$  valence-polarized (DZVP) Gaussian basis set<sup>[60]</sup> in conjunction with the Goedecker–Teter–Hutter (GTH) pseudopotential,<sup>[61]</sup> while the plane-wave energy cutoff was set to 400 Ry. The Broyden–Fletcher–Goldfarb–Shanno (BFGS) algorithm was applied in the geometry optimizations, and the forces on atoms were minimized to within  $0.023 \text{ eV Å}^{-1}$ . It is noted that the computational cost of the hybrid-functional calculation can be reduced using the auxiliary density-matrix method (ADMM), an approach in which the electron density is mapped onto a much sparser Gaussian basis set containing less diffuse and fewer primitive Gaussian functions than the one used in the rest of the calculation.<sup>[62]</sup>

We would like to highlight that an indication of the computational speedup arising from the use of GAP-MD instead of DFT-MD to simulate the models of  $\text{Sb}_2\text{Te}_3$  is the following. To perform the same number of MD steps (2000) using the same number of cores (192),  $\approx 5 \text{ h}$  are needed for the 250-atom DFT model, whereas only  $\approx 1 \text{ h}$  is needed for the 1000-atom GAP model.

#### Supporting Information

Supporting Information is available from the Wiley Online Library or from the author.

#### Acknowledgements

This paper is dedicated to Professor David Drabold on the occasion of his 60<sup>th</sup> birthday. David is a great Anglophile, and S.R.E. recalls with much pleasure the many visits that he has made to Cambridge over the years to discuss matters amorphous. Via our membership of the UK’s HEC Materials Chemistry Consortium, which was funded by EPSRC (EP/L000202, EP/R029431), this work used the ARCHER UK National Supercomputing Service (<http://www.archer.ac.uk>).

## Conflict of Interest

The authors declare no conflict of interest.

## Keywords

ab initio molecular dynamics, amorphous  $\text{Sb}_2\text{Te}_3$ , density functional theory, Gaussian approximation potential, machine-learned potentials, phase-change-memory materials, thermoelectric materials

Received: July 28, 2020

Revised: November 5, 2020

Published online: November 30, 2020

- [1] P. Noé, C. Vallée, F. Hippert, F. Fillot, J.-Y. Raty, *Semicond. Sci. Technol.* **2018**, 33, 013002.
- [2] M. Le Gallo, A. Sebastian, *J. Phys. D: Appl. Phys.* **2020**, 53, 213002.
- [3] G. C. Sossio, G. Miceli, S. Caravati, J. Behler, M. Bernasconi, *Phys. Rev. B* **2012**, 85, 174103.
- [4] F. C. Mocanu, K. Konstantinou, T. H. Lee, N. Bernstein, V. L. Deringer, G. Csányi, S. R. Elliott, *J. Phys. Chem. B* **2018**, 122, 8998.
- [5] A. P. Bartók, G. Csányi, *Int. J. Quantum Chem.* **2015**, 115, 1051.
- [6] K. Konstantinou, F. C. Mocanu, T. H. Lee, S. R. Elliott, *Nat. Commun.* **2019**, 10, 3065.
- [7] F. C. Mocanu, K. Konstantinou, S. R. Elliott, *J. Phys. D: Appl. Phys.* **2020**, 53, 244002.
- [8] W. J. Szlachta, A. P. Bartók, G. Csányi, *Phys. Rev. B* **2014**, 90, 104108.
- [9] A. P. Bartók, J. Kermode, N. Bernstein, G. Csányi, *Phys. Rev. X* **2018**, 8, 041048.
- [10] P. Rowe, G. Csányi, D. Alfè, A. Michaelides, *Phys. Rev. B* **2018**, 97, 054303.
- [11] N. Bernstein, G. Csányi, V. L. Deringer, *npj Comput. Mater.* **2019**, 5, 99.
- [12] V. L. Deringer, M. A. Caro, G. Csányi, *Nat. Commun.* **2020**, 11, 5461.
- [13] T. T. Nguyen, E. Székely, G. Imbalzano, J. Behler, G. Csányi, M. Ceriotti, A. W. Götz, F. Paesani, *J. Chem. Phys.* **2018**, 148, 241725.
- [14] G. Sivaraman, A. N. Krishnamoorthy, M. Baur, C. Holm, M. Stan, G. Csányi, C. Benmore, Á. Vázquez-Mayagoitia, *npj Comput. Mater.* **2020**, 6, 104.
- [15] Y.-B. Liu, J.-Y. Yang, G.-M. Xin, L.-H. Liu, G. Csányi, B.-Y. Cao, *J. Chem. Phys.* **2020**, 153, 144501.
- [16] A. P. Bartók, R. Kondor, G. Csányi, *Phys. Rev. B* **2013**, 87, 184115.
- [17] N. Bernstein, B. Bhattacharai, G. Csányi, D. A. Drabold, S. R. Elliott, V. L. Deringer, *Angew. Chem. Int. Ed.* **2019**, 58, 7057.
- [18] J.-Y. Raty, M. Wuttig, *J. Phys. D: Appl. Phys.* **2020**, 53, 234002.
- [19] M. Wuttig, N. Yamada, *Nat. Mater.* **2007**, 6, 824.
- [20] X. Li, F. Rao, Z. Song, M. Zhu, W. Liu, Z. Sun, *J. Appl. Phys.* **2011**, 110, 094318.
- [21] X. Li, Z. Sun, Z. Song, F. Rao, L. Wu, W. Liu, *Solid State Sci.* **2011**, 13, 131.
- [22] L. Zhang, N. Miao, J. Zhou, J. Mi, Z. Sun, *J. Alloys Compd.* **2018**, 738, 270.
- [23] G. Wang, J. Zhou, S. R. Elliott, Z. Sun, *J. Alloys Compd.* **2019**, 782, 852.
- [24] Y. Yin, S. Morioka, S. Kozaki, R. Satoh, S. Hosaka, *Appl. Surf. Sci.* **2015**, 349, 230.
- [25] C. Peng, L. Wu, Z. Song, F. Rao, M. Zhu, X. Li, B. Liu, L. Cheng, S. Feng, P. Yang, *Appl. Surf. Sci.* **2011**, 257, 10667.
- [26] X. Li, F. Rao, Z. Song, K. Ren, W. Liu, Z. Sun, *Appl. Surf. Sci.* **2011**, 257, 4566.
- [27] M. Zhu, M. Xia, F. Rao, X. Li, L. Wu, X. Ji, S. Lv, Z. Song, S. Feng, H. Sun, *Nat. Commun.* **2014**, 5, 4086.
- [28] Q. Wang, B. Liu, Y. Xia, Y. Zheng, R. Huo, M. Zhu, S. Song, S. Lv, Y. Cheng, Z. Song, *Phys. Status Solidi RRL* **2015**, 9, 470.
- [29] G. Wang, Q. Nie, X. Shen, R. Wang, L. Wu, Y. Lv, J. Fu, T. Xu, S. Dai, *Mater. Lett.* **2012**, 87, 135.
- [30] J. Yu, B. Liu, T. Zhang, Z. Song, S. Feng, B. Chen, *Appl. Surf. Sci.* **2007**, 253, 6125.
- [31] J. Xu, B. Liu, Z. Song, S. Feng, B. Chen, *Mater. Sci. Eng. B* **2006**, 127, 228.
- [32] Z. Li, C. Si, J. Zhou, H. Xu, Z. Sun, *ACS Appl. Mater. Interfaces* **2016**, 8, 26126.
- [33] F. Rao, K. Ding, Y. Zhou, Y. Zheng, M. Xia, S. Lv, Z. Song, S. Feng, I. Ronneberger, R. Mazzarello, W. Zhang, E. Ma, *Science* **2017**, 358, 1423.
- [34] K. Ding, J. Wang, Y. Zhou, H. Tian, L. Lu, R. Mazzarello, C. Jia, W. Zhang, F. Rao, E. Ma, *Science* **2019**, 366, 210.
- [35] R. Venkatasubramanian, E. Siivola, T. Colpitts, B. O'Quinn, *Nature* **2001**, 493, 517.
- [36] B. Xu, J. Zhang, G. Yu, S. Ma, Y. Wang, and Y. Wang, *J. Appl. Phys.* **2018**, 124, 165104.
- [37] Z. Li, N. Miao, J. Zhou, H. Xu, Z. Sun, *J. Appl. Phys.* **2017**, 122, 195107.
- [38] I. Jeong, Y.-G. Yoon, *J. Korean Phys. Soc.* **2018**, 73, 1541.
- [39] P. R. Chowdhury, T. Feng, X. Ruan, *Phys. Rev. B* **2019**, 99, 155202.
- [40] M. J. Willatt, F. Musil, M. Ceriotti, *Phys. Chem. Chem. Phys.* **2018**, 20, 29661.
- [41] A. Grisafi, M. Ceriotti, *J. Chem. Phys.* **2019**, 151, 204105.
- [42] S. Caravati, M. Bernasconi, M. Parrinello, *Phys. Rev. B* **2010**, 81, 014201.
- [43] W. Zhang, I. Ronneberger, Y. Li, R. Mazzarello, *Monatsh. Chem.* **2014**, 145, 97.
- [44] Y. R. Guo, F. Dong, C. Qiao, J. J. Wang, S. Y. Wang, M. Xu, Y. X. Zheng, R. J. Zhang, L. Y. Chen, C. Z. Wang, K. M. Ho, *Phys. Chem. Chem. Phys.* **2018**, 20, 11768.
- [45] Y. Zhou, L. Sun, G. M. Zewdie, R. Mazzarello, V. L. Deringer, E. Ma, W. Zhang, *J. Mater. Chem. C* **2020**, 8, 3646.
- [46] S. Hu, B. Liu, Z. Li, J. Zhou, Z. Sun, *Comput. Mater. Sci.* **2019**, 165, 51.
- [47] T. Satow, O. Uemura, Y. Sagara, *Phys. Status Solidi A* **1982**, 71, 555.
- [48] D. S. Franzblau, *Phys. Rev. B* **1991**, 44, 4925.
- [49] J.-W. Park, S. H. Baek, T. D. Kang, H. Lee, Y.-S. Kang, T.-Y. Lee, D.-S. Suh, K. J. Kim, C. K. Kim, Y. H. Khang, J. L. F. Da Silva, S.-H. Wei, *Appl. Phys. Lett.* **2008**, 93, 021914.
- [50] X. Fu, Q. Ding, Z. Hu, T. Zhu, Q. Yu, Z. Zhang, *Scr. Mater.* **2017**, 135, 10.
- [51] J.-J. Wang, J. Wang, Y. Hu, T. Xin, Z. Song, M. Pohlmann, M. Kaminski, L. Lu, H. Du, C.-L. Jia, R. Mazzarello, M. Wuttig, W. Zhang, *Phys. Status Solidi RRL* **2019**, 13, 1900320.
- [52] J. Wang, C. Zhou, Y. Yu, Y. Zhou, L. Lu, B. Ge, Y. Cheng, C.-L. Jia, R. Mazzarello, Z. Shi, M. Wuttig, W. Zhang, *Nano Energy* **2021**, 79, 105484.
- [53] S. Plimpton, *Comput. Phys.* **1995**, 117, 1.
- [54] G. Kresse, J. Furthmüller, *Phys. Rev. B* **1996**, 54, 11169.
- [55] J. P. Perdew, K. Burke, M. Ernzerhof, *Phys. Rev. Lett.* **1996**, 77, 3865.
- [56] K. J. Singh, R. Satoh, Y. Tsuchiya, *J. Phys. Soc. Jap.* **2003**, 72, 2546.
- [57] J. VandeVondele, M. Krack, F. Mohamed, M. Parrinello, T. Chassaing, J. Hutter, *Comput. Phys. Commun.* **2005**, 167, 103.
- [58] M. Guidon, J. Hutter, J. VandeVondele, *J. Chem. Theory Comput.* **2009**, 5, 3010.
- [59] G. Lippert, J. Hutter, M. Parrinello, *Mol. Phys.* **1997**, 92, 477.
- [60] J. VandeVondele, J. Hutter, *J. Chem. Phys.* **2007**, 127, 114105.
- [61] S. Goedecker, M. Teter, J. Hutter, *Phys. Rev. B* **1996**, 54, 1703.
- [62] M. Guidon, J. Hutter, J. VandeVondele, *J. Chem. Theory Comput.* **2010**, 6, 2348.

# Investigation of Gamma-Radiation Shielding Properties of Cadmium Bismuth Borate Glass Experimentally and by Using XCOM Program and MCNP5 Code

Yasser Saleh Mustafa Alajerami, David A. Drabold, M. H. A. Mhareb, Katherine Leslee A. Cimat, Gang Chen, and K. M. Abushab

New glass systems of bismuth borate with various concentrations of cadmium oxide are prepared based on the melt-quenching method. The X-ray diffraction (XRD) reveals a fully amorphous structure of the prepared glasses (S1–S4), and the UV–vis results display good transparency (>50%) in the visible and near-UV region. In addition, the radiation shielding properties (mass attenuation coefficient, half-value layer, tenth value layer, mean free path, effective atomic number, and electron density) of the new glass system are determined at selected energies experimentally and by using MCNP5 simulation code and XCOM computer program. Based on the calculated relative difference, the obtained values from MCNP5 and XCOM are in good agreement with the experimental data. The mean free path of the current systems (particularly S4) shows optimistic results when compared with the barite and chalcocite concretes.

exhibits desirable properties such as low cost, simple preparation, high transparency, chemical durability, and high thermal stability. These features recommend borate glass for solid-state lasers, radiation dosimeters, telecommunication devices, and radiation shielding materials.<sup>[1–4]</sup> Although ionizing radiation has essential applications in medical and industrial fields, this radiation has an adverse effect on human biological tissue. Great efforts and financial investments have been made to protect patients, employees, and the public from radiation.

For several years, concrete and lead shielding materials have been used for medical facilities and nuclear plants. Many disadvantages have been reported

## 1. Introduction

Recently, borate glasses with different oxide modifiers have received extensive interest from researchers. This type of glass

with concrete such as bacterial corrosion, leaching, expansion and aggregation, unrecyclable, and opaque to visible light.<sup>[5–7]</sup> Metallic lead has been used most often as a radiation shielding material mainly because it provides an effective shielding against penetrative radiation. In addition, it has a high atomic number, high density, low cost, and easy processability. However, metallic lead (Pb) is known for its toxicity, leads to environmental pollution, and has an extremely low level of neutron absorption.<sup>[8–11]</sup> Most of these drawbacks can be exceeded by glassy materials, which are effective attenuators, recyclable, hard, brittle, and transparent to visible light.<sup>[3,12]</sup> The bismuth borate glasses have received attention from researchers due to its clear potential applications. In addition to the previously mentioned glass features, this type of glass has low thermal expansion and shows high resistance to thermal shock.<sup>[1,12,13]</sup> Previous studies showed that excellent features were achieved by adding cadmium oxide (CdO) to the borate glass system (improved mechanical strength and density and maintained the amorphous structure of the glass network).<sup>[14–16]</sup> Both bismuth oxide and CdO provide compatibility with the borate glass system by increasing stabilization, improving chemical durability, and of course, increasing glass density.<sup>[17–20]</sup>

This study continues our previous research in determining the gamma shielding properties of new glassy borate systems with a constant amount of bismuth oxide and different CdO concentrations.<sup>[21]</sup> The gamma-ray shielding parameters of these samples were determined and compared with the standard radiation shielding (concrete and lead glass). The essential radiation shielding parameters such as mass attenuation coefficient


Dr. Y. S. M. Alajerami, Dr. D. A. Drabold, Dr. G. Chen  
Department of Physics and Astronomy  
Ohio University  
Athens, OH 45701, USA

Dr. Y. S. M. Alajerami, Dr. K. M. Abushab  
Medical Imaging Department  
Applied Medical Sciences Faculty  
Al Azhar University-Gaza  
Jamal Abdl Naser St., Gaza Strip, P.O. BOX 1277, Gaza, Palestine

Dr. M. H. A. Mhareb  
Department of Physics  
College of Science  
Imam Abdulrahman Bin Faisal University  
P.O. Box 1982, Dammam 31441, Saudi Arabia

Dr. M. H. A. Mhareb  
Basic and Applied Scientific Research Center  
Imam Abdulrahman Bin Faisal University  
P.O. Box 1982, Dammam 31441, Saudi Arabia

Dr. K. L. A. Cimat  
Department of Chemistry and Biochemistry  
Ohio University  
Athens, OH 45701, USA

 The ORCID identification number(s) for the author(s) of this article can be found under <https://doi.org/10.1002/pssb.202000417>.

DOI: 10.1002/pssb.202000417



( $\mu/\rho$ ), half-value layer (HVL), tenth value layer (TVL), mean free path (MFP), effective atomic number ( $Z_{\text{eff}}$ ), and electron density ( $N_e$ ) were estimated and calculated by using the Monte-Carlo N-particle transport code MCNP5 and the XCOM computer program. In addition, to verify the simulated and calculated results, the obtained values were compared with experimental values by establishing a compatible irradiation setup to determine the shielding parameters.

## 2. Experimental Section

### 2.1. Glass Preparation

Four borate glass systems were prepared based on the conventional quenching method according to the following formula

$$(70 - x)\% \text{B}_2\text{O}_3 - 30\% \text{Bi}_2\text{O}_3 - x\text{CdO} \quad (1)$$

( $x$ : 0, 5, 10, and 15 mol%)

As usual, the required quantities of the proposed chemicals were taken as powders and mixed well mechanically, and then melted in alumina crucibles at 1100 °C for 60–70 min (depend on CdO concentration). The melt was mixed during the melting process and finally poured into preheated pouring plates (300 °C) with rectangular molds. Prepared samples were kept 3 h to remove internal stress then cooled down slowly ( $-10^\circ\text{C min}^{-1}$ ) to the room temperature.

### 2.2. Density and Molar Volume Measurements

The densities of the prepared samples were determined based on Archimedes principle (Equation (1)) by using toluene as the

immersion fluid ( $0.865 \text{ g cm}^{-3}$ ). All densities were measured at room temperature and the measurement was repeated 3 times for each sample. Based on the obtained densities and molecular weight of the proposed composition ( $M$ ), the molar volume ( $V_m$ ) was calculated for all prepared samples (Equation (3)).

$$\rho = \frac{0.865 W_{\text{air}}}{(W_{\text{air}} - W_{\text{liquid}})} \quad (2)$$

$$V_m = \frac{M}{\rho} \quad (3)$$

Here, the  $W_{\text{air}}$  represents the sample's weight in the air and  $W_{\text{liquid}}$  denotes the sample's weight in liquid.

### 2.3. UV-vis Spectroscopy and Bandgap

Shimadzu 3101 absorption spectrophotometer was utilized to obtain the absorption and transmittance spectra for current glass samples from 300 to 900 nm at room temperature. The bandgap ( $E_g$ ) was determined from the UV absorption edge by utilizing Mott and Davis relation as illustrated below<sup>[22]</sup>

$$h\nu\alpha = A(h\nu - E_g)^n \quad (4)$$

where  $\alpha$ ,  $A$ , and  $h\nu$  denote the absorption coefficient, constant, and photon energy, respectively.

### 2.4. Irradiation Setup

In the current study, the glasses were irradiated with different energy levels of gamma rays obtained from radiation sources located in the Edwards Nuclear Accelerator Laboratory at Ohio

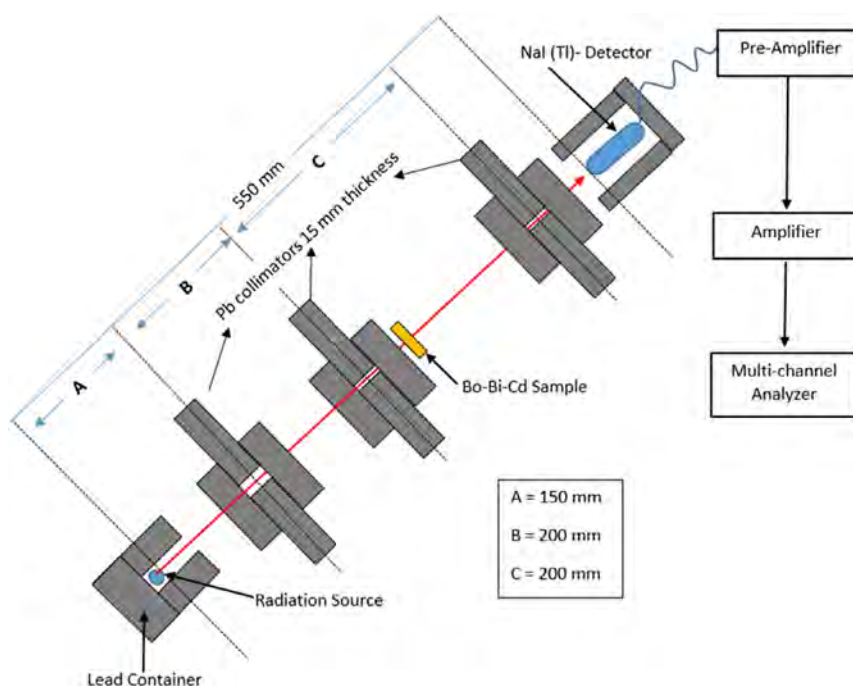


**Figure 1.** Schematic view for the setup of the irradiation process.

University, USA. The experimental setup of the irradiation and detection process is shown in **Figure 1**. Five different gamma-ray sources  $^{57}\text{Co}$  (122 keV),  $^{133}\text{Ba}$  (356 keV),  $^{137}\text{Cs}$  (662 keV),  $^{60}\text{Co}$  (1173 and 1332 keV), and  $^{22}\text{Na}$  (511 and 1275 keV) were used to irradiate the prepared glasses. These 12 samples (3 for each concentration) with a thickness range of 0.211–0.315 cm were prepared for irradiation and placed after the second lead collimator, as shown in Figure 1. A 3"  $\times$  3" NaI(Tl) scintillation detector connected with a preamplifier and an amplifier was used as the radiation detector to collect transmitted gamma ray from irradiated samples and convert the analog signal to electron counts. A gamma-ray spectrometer with a 16 K multichannel analyzer (CANBERRA Industries) and an energy resolution of 7.5% at

661.6 keV for a gamma ray from Cs-137 were used to collect incident and transmitted intensities  $I_0$  and  $I$ , respectively. The distance between the radiation source and NaI detector was 65 cm for all irradiation process (either with or without samples).

Three Pb collimator sets with whole different sizes were used to avoid the detection of background radiation. Both radiation source and detector were housed in a lead shield (C-shape). Finally, the spectrometer was frequently calibrated for each trial and any given energy.

All radiation shielding equations needed for evaluation and measurement of shielding properties are shown in **Table 1**.

## 2.5. XCOM Program

The theoretical mass attenuation coefficients ( $\mu/\rho$ ) for the prepared glasses were obtained from the known computer program XCOM.<sup>[23]</sup> This program can estimate the mass attenuation coefficient of an element, compound, and mixture at different energy

**Table 1.** Mathematical expressions for evaluating the radiation shielding properties.

Parameter	Formula	Symbols
Linear attenuation coefficient ( $\mu$ ) <sup>[38]</sup>	$\mu = \ln\left(\frac{I_0}{I}\right) \left(\frac{1}{t}\right)$	$I_0$ : intensity without sample $I$ : intensity with sample $t$ : the thickness of the sample
Total photon interaction cross section ( $\sigma_t$ ) <sup>[39]</sup>	$\sigma_t = \frac{M\mu_m}{N_A}$	$N_A$ : Avogadro's number $M$ : the molecular weight of glass
Mean free path (MFP) <sup>[40]</sup>	$\text{MFP} = 1/\mu$	$\mu$ : linear attenuation coefficient
Tenth value layer (TVL) <sup>[40]</sup>	$\text{TVL} = (\ln 10)/\mu$	
Half value layer (HVL) <sup>[40]</sup>	$\text{HVL} = \frac{0.693}{\mu}$	
Effective atomic number ( $Z_{\text{eff}}$ ) <sup>[41]</sup>	$Z_{\text{eff}} = \frac{\sum f_i A_i^{(Z_i)} / Z_i^{(Z_i)}}{\sum f_i Z_i^{(Z_i)}}$	$f_i$ is the fractional abundance of the element $i$ , $A_i$ is the atomic weight, and $Z_i$ is the atomic number.
Effective electron number ( $N_e$ ) <sup>[42]</sup>	$N_e = \left(\frac{Z_{\text{eff}}}{M}\right) N_A \sum n_i$	$M$ : molecular weight $n_i$ : number of formula units

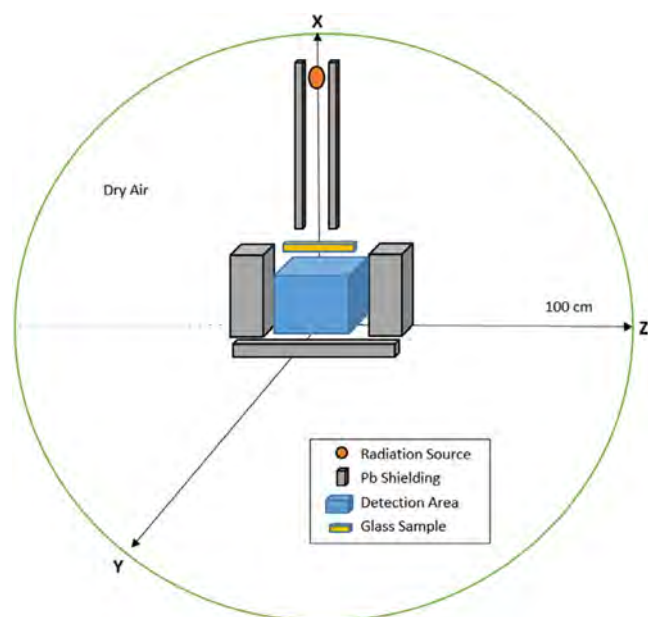


**Figure 2.** Total simulation geometry using MCNP5.

**Table 2.** Chemical composition, density, and molar volume of the prepared samples.

Sample code	Chemical composition [mol%]			Density [g cm <sup>-3</sup> ]	Molar volume [cm <sup>3</sup> mol <sup>-1</sup> ]	Bandgap ( $E_g$ ) [eV]
	Bi <sub>2</sub> O <sub>3</sub>	CdO	B <sub>2</sub> O <sub>3</sub>			
S1	30	0	70	4.315	46.689	2.907
S2	30	5	65	4.711	40.641	3.106
S3	30	10	60	5.068	38.358	3.259
S4	30	15	55	5.375	36.714	3.442

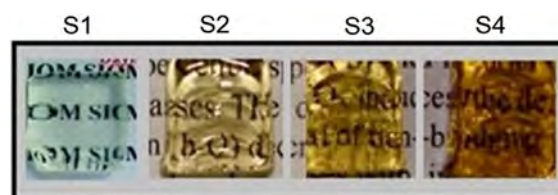


**Figure 3.** The new prepared glasses (S1–S4).

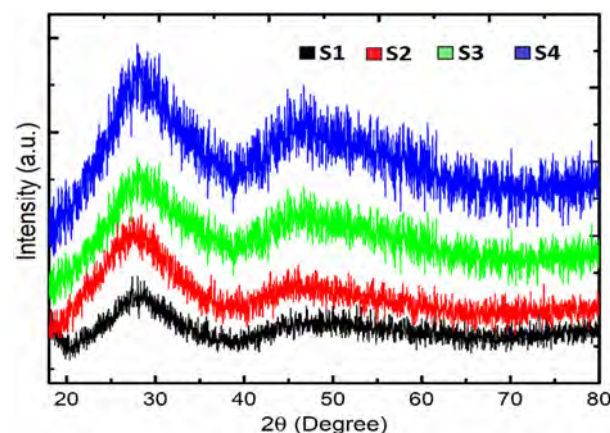


**Figure 4.** XRD of the new prepared glass systems.

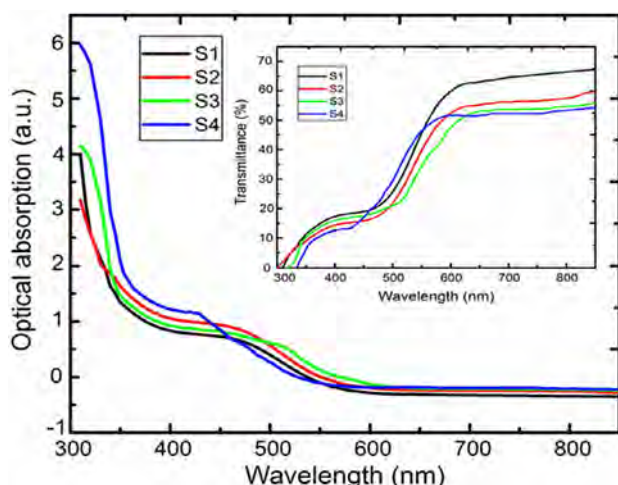


**Figure 5.** The optical absorption of all prepared glasses (inset, corresponding transmission spectra) in the wavelength range 300–800 nm.

levels (0.001 up to  $10^5$  MeV). Based on the estimated  $\mu/\rho$  and the calculated densities, the linear attenuation coefficient can be

easily determined. The other radiation shielding parameters were also determined by using the equations from Table 1 (except the first equation).

## 2.6. MCNP5 Simulation Code

The current experimental setup was simulated by MCNP5, which is used for modeling the interaction of electromagnetic radiation (X-ray), photon (gamma ray), and particles (electron and neutron). Previous related studies have validated and reported the high efficiency of MCNP5 to evaluate and estimate radiation shielding parameters.<sup>[24–27]</sup>

In the current study, MCNP5 was used to estimate the newly prepared glasses' radiation shielding parameters. The simulation was applied in a sphere of 100 cm radius filled with dry air ( $\rho = 1.205 \times 10^{-3} \text{ g cm}^{-3}$ ), as shown in Figure 2. The radiation source was assumed as a point source with a monoenergetic beam emission and positioned perpendicularly to the front surface of the glass sample (in the  $x$ -axis direction). The irradiation process was completely guided by Pb shielding collimators to eliminate the possibility of background radiation detection. The simulation was repeated based on the mol% of CdO and

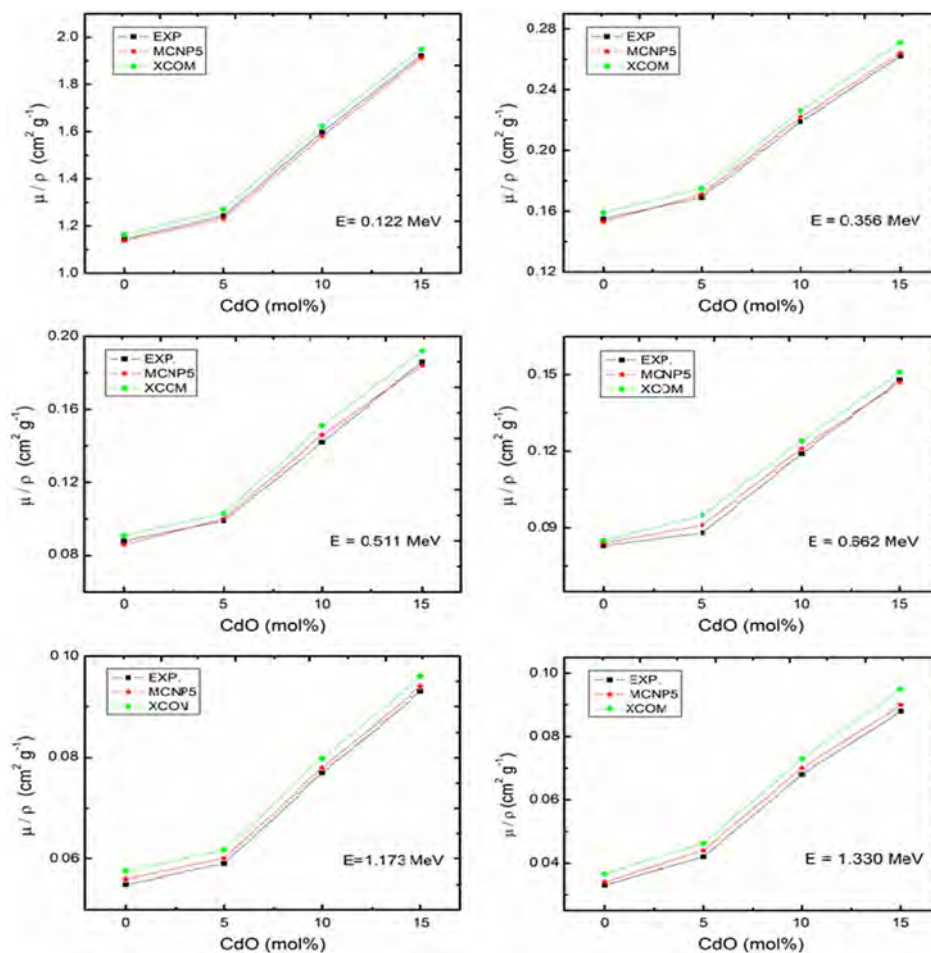


**Figure 6.** Dependency of  $\mu/\rho$  of the  $\text{Bi}_2\text{O}_3$ - $x$ - $\text{B}_2\text{O}_3$  glasses on  $x$ -CdO contents at different energy levels (comparison is made between experimental, MCNP5, and XCOM values).



**Table 3.** Mass attenuation coefficients at specific energies (experimental, MCNP, and XCOM) (Exp., Experiment).

Energy [MeV]		S1	S2	S3	S4
0.122	Exp.	1.144 ± 0.003	1.242 ± 0.005	1.598 ± 0.006	1.932 ± 0.003
	MCNP5	1.139 ± 0.004	1.231 ± 0.003	1.581 ± 0.005	1.921 ± 0.005
	XCOM	1.153	1.269	1.624	1.949
0.356	Exp.	0.149 ± 0.003	0.169 ± 0.005	0.219 ± 0.004	0.259 ± 0.006
	MCNP5	0.157 ± 0.004	0.172 ± 0.002	0.221 ± 0.003	0.268 ± 0.003
	XCOM	0.160	0.177	0.226	0.271
0.511	Exp.	0.094 ± 0.002	0.101 ± 0.003	0.142 ± 0.003	0.186 ± 0.003
	MCNP5	0.097 ± 0.003	0.103 ± 0.004	0.146 ± 0.005	0.184 ± 0.004
	XCOM	0.101	0.108	0.151	0.188
0.662	Exp.	0.083 ± 0.003	0.009 ± 0.003	0.119 ± 0.004	0.143 ± 0.004
	MCNP5	0.086 ± 0.003	0.091 ± 0.004	0.121 ± 0.003	0.146 ± 0.003
	XCOM	0.091	0.097	0.128	0.152
1.173	Exp.	0.056 ± 0.003	0.065 ± 0.003	0.078 ± 0.003	0.094 ± 0.003
	MCNP5	0.057 ± 0.004	0.068 ± 0.004	0.080 ± 0.004	0.096 ± 0.005
	XCOM	0.060	0.070	0.084	0.101
1.332	Exp.	0.044 ± 0.003	0.052 ± 0.003	0.067 ± 0.004	0.085 ± 0.004
	MCNP5	0.045 ± 0.004	0.054 ± 0.004	0.071 ± 0.003	0.087 ± 0.008
	XCOM	0.047	0.057	0.081	0.091

repeated 3 times for each sample (S1–S4). All required data cards and commands such as energy (ERG), type of particle (PAR), position (POS), and beam direction (DIR) were defined accordingly. Several termination steps were applied to reduce errors and variance, such as increasing the number of histories (NPS > 10<sup>8</sup>), simplifying the geometry, and utilizing the CUT-OFF option to eliminate low radiation (<1 keV). Regarding energy detection, mesh tally (type F4) was used to get the sum of all contributions in the proposed detecting area. All measurements (collimation thickness, distance from the source to detectors, and sample size) were set based on the experimental data.

### 3. Results and Discussion

Details about the prepared samples including sample code, mol% of chemical composition, measured densities, and molar volumes are shown in Table 2.

**Table 4.** Relative difference between the MCNP5/XCOM results and the experimental values.

Glass code	Incident photon energy [MeV]											
	0.122		0.365		0.511		0.662		1.173		1.332	
	MCNP	XCOM	MCNP	XCOM	MCNP	XCOM	MCNP	XCOM	MCNP	XCOM	MCNP	XCOM
S1	0.437	0.787	5.370	7.382	3.191	7.447	2.381	7.143	1.786	7.142	2.273	6.818
S2	0.886	2.174	1.775	4.734	1.980	6.930	1.111	7.778	4.615	7.692	3.846	7.694
S3	1.064	1.627	0.913	3.196	2.817	6.338	1.681	7.563	2.564	7.692	0	6.944
S4	0.570	0.880	3.474	4.633	1.075	1.075	2.098	6.294	2.128	7.447	2.353	7.059

The density of the prepared samples increased gradually with the variation of CdO content from 0 to 15 mol%. The calculated densities were in the range of 4.315–5.375 g cm<sup>-3</sup> with a probable error of 0.005. The density is composition-dependent and the observed increase in the value can be attributed to the high molecular weight of CdO (128.41 g mol<sup>-1</sup>) compared with that of B<sub>2</sub>O<sub>3</sub> (32.01 g mol<sup>-1</sup>). Reverse relation was reported with the molar volume; from Table 2, the values were reduced from 46.689 cm<sup>3</sup> mol<sup>-1</sup> for S1 to 36.714 cm<sup>3</sup> mol<sup>-1</sup> for S4.

The prepared glass was highly transparent, and gradually changed into brown with the increase in Bi<sub>2</sub>O<sub>3</sub>, as shown in Figure 3.

The structure of the current samples was examined with X-ray diffraction (XRD). The amorphous state was confirmed by the continuous diffraction pattern with no sharp peak and the broad peak centered on 2θ = 25° (Figure 4). The peak broadening can be attributed to its amorphous structure.

Figure 5 shows the optical absorption spectra for all prepared glasses in the range of 300–900 nm. The inset figure shows the calculated transmittance spectra obtained from the absorption values. All glass systems exhibit good transparencies (>50%) in the visible and near-UV region. This result is expected with a borate glass system. In all samples, the fraction of B<sub>2</sub>O<sub>3</sub> is more than 50%, a fixed amount of Bi<sub>2</sub>O<sub>3</sub> (30 mol%) and the amount of CdO does not exceed 15 mol%.

From Figure 5 and by using Mott and Davis equation, we can determine  $E_g$ . The  $E_g$  was computed from the intercept horizontal axis of  $h\nu$  and  $(ah\nu)^2$ . This intercept can be drawn as a tangent line along the absorption edge  $(ah\nu)^2$  to reach the  $h\nu$  ( $x$ -axis), this is called  $E_g$ . It can be noted from Table 2 that the bandgap results increase gradually with the addition of the CdO to the glass system that ascribed to the formation of bridging oxygen in the glass structure.<sup>[28,29]</sup>

#### 3.1. Mass Attenuation Coefficient

The simulated (by MCNP5) and estimated (by XCOM) values of  $\mu/\rho$  of the different glass systems are shown in Figure 6 for different photon energy. The experimental data of  $\mu/\rho$  of the same samples were compared with those obtained by MCNP5 and XCOM at specific energy levels (0.122, 0.356, 0.511, 0.662, 1.173, and 1.330 MeV), as listed in Table 3. The values of  $\mu/\rho$  that have been obtained experimentally and by simulation are the average of three repeating trials plus/minus the standard deviation of these trials, respectively.

The dependency of  $\mu/\rho$  of the new glass samples on the concentration of CdO at different energy levels, by using irradiation

setup, simulation, and XCOM program, is displayed in Figure 6. Good agreement was reported between the three estimation methods at a photon energy of 0.122, 0.356, 0.511, 0.662, 1.173, and 1.332 MeV (with insignificant variations). Also, the mass attenuation coefficient was increased by increasing CdO content (mol%) and decreased by increasing the energy level. This behavior indicates that the higher interactions of a photon with a glass system take place at high CdO and low photon energy. Based on the values obtained from Table 3 and Figure 6, as the energy changed from 0.122 to 0.511 MeV, the  $\mu/\rho$  decreased quickly (photoelectric effect abundance  $Z^{4.0-4.5}/E^3$ ), and no substantial variation at the energy range of 0.511 and 1.332 MeV due to the high possibility of Compton scattering ( $Z/E$ ).<sup>[26,30]</sup>

**Table 5.** HVL of the new glasses at specific energies (experimental, MCNP, and XCOM) (Exp., Experiment).

Energy [MeV]		S1	S2	S3	S4
0.122	Exp.	0.172	0.150	0.109	0.166
	MCNP5	0.173	0.152	0.110	0.151
	XCOM	0.171	0.147	0.107	0.083
0.356	Exp.	1.323	1.105	0.797	0.706
	MCNP5	1.256	1.086	0.790	0.675
	XCOM	1.232	1.055	0.773	0.598
0.511	Exp.	2.240	1.89	1.23	0.991
	MCNP5	2.032	1.867	1.196	0.941
	XCOM	1.842	1.667	1.156	0.862
0.662	Exp.	2.375	2.122	1.505	1.117
	MCNP5	2.292	2.052	1.443	1.119
	XCOM	2.142	1.849	1.353	1.046
1.173	Exp.	3.651	3.012	2.328	1.781
	MCNP5	3.459	2.746	2.183	1.719
	XCOM	3.286	2.434	2.055	1.605
1.332	Exp.	3.805	3.199	2.361	2.001
	MCNP5	3.741	3.131	2.279	1.933
	XCOM	3.651	3.012	2.156	1.781

The relative difference (RD) between the three estimation methods (experimental, MCNP5, and XCOM) of the calculated values was calculated according to the following equation<sup>[27]</sup>

$$RD = \frac{\text{Theoretical} - \text{Experimental}}{\text{Experimental}} \times 100 \quad (5)$$

**Table 4** shows the RD values for MCNP and XCOM results for all samples. The RD values show close agreement between mass attenuation coefficients obtained by experiment, MCNP5, and XCOM. This agreement between experiment and MCNP5 was quite encouraging, the RD was in the range of 0–5.37%, and for XCOM values were in the range of 0.787–7.778%. This RD is acceptable and supports the usage of MCNP5 to estimate glass shielding properties for other glass compositions.

**Table 5** shows the HVL of the new glasses at different concentrations of CdO and specific energy levels. The glass with the smallest HVL means the highest efficiency to attenuate the photon beam. The smaller HVL indicates that this composition is cost-effective, high transparent, and requires simple fabrication.<sup>[30]</sup> **Figure 7a** shows the dependency of HVL on the CdO concentration; gradual reduction in the HVL values is reported with increasing CdO concentration. We can also say that MCNP5 showed closer agreement with the experimental data compared with XCOM values. **Figure 7b** shows the glasses' HVL of S4 (the smallest HVL) at different energy levels using the three estimation methods (experimental, MCNP5, and XCOM). The HVL increased gradually with increasing energy of the incident photon (0.122–1.330 MeV). As discussed in the mass attenuation coefficients, the HVL values' variation with increasing energy of an incident photon is attributed to the variations of dominance photon interaction.<sup>[30–33]</sup>

The TVL of the prepared glasses was also calculated. The TVL can be defined as the attenuator thickness that can reduce the photon intensity to 10th of its initial intensity. **Figure 8** shows a simple comparison of the TVL (experimental values) of all prepared glasses as a function of photon energies. The TVL values have increased with increasing the incident photon (0.112–1.332 MeV) and decreased with increased CdO content, which is attributed to increasing sample density.<sup>[32]</sup>

The average distance between two successive interactions of a photon (or moving particle) inside a target material is known

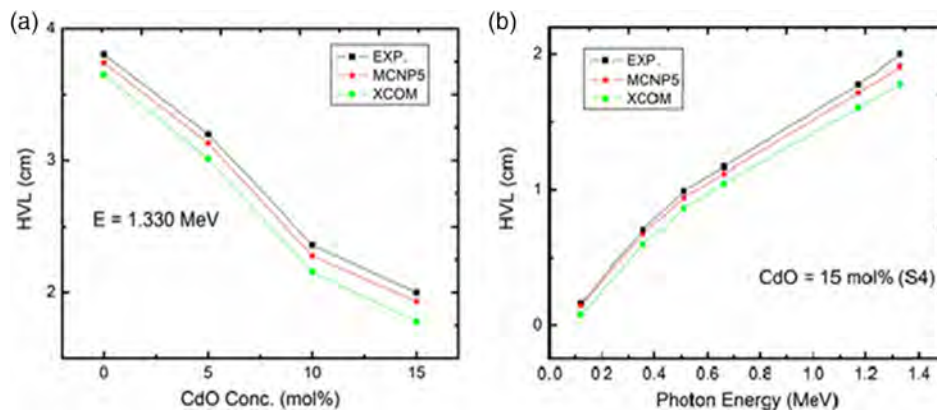


**Figure 7.** a) The HVL of the prepared glasses with x-concentrations of CdO at different energy levels. b) The HVL of S4 (the smallest HVL) at different energy levels using the three estimation methods (experimental, MCNP5, and XCOM).

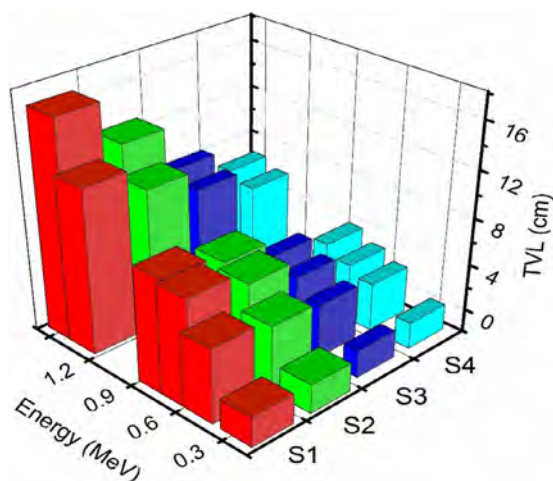


**Figure 8.** Comparison between TVL of different glass systems as a function of photon energies.

as the MFP.<sup>[34]</sup> This concept indicates the photon direction, energy, and other particle properties significant for shielding consideration. The MFP of the current samples was calculated by using the equation listed in Table 1 and Table 6. The values were calculated by conducting the three estimation methods (experimental, MCNP5, and XCOM) and compared with the MFP of barite and chalcocite concretes. The lowest MFP is reported in the S4 glass sample (the highest CdO content) and it is 2 times lower than the values obtained with barite and chalcocite concretes.

The  $Z_{\text{eff}}$  of all samples was obtained using the XCOM program for a high range of energy, starting from 0.01 up to 100 MeV, as shown in Figure 9. Generally, the values of  $Z_{\text{eff}}$  decreased by

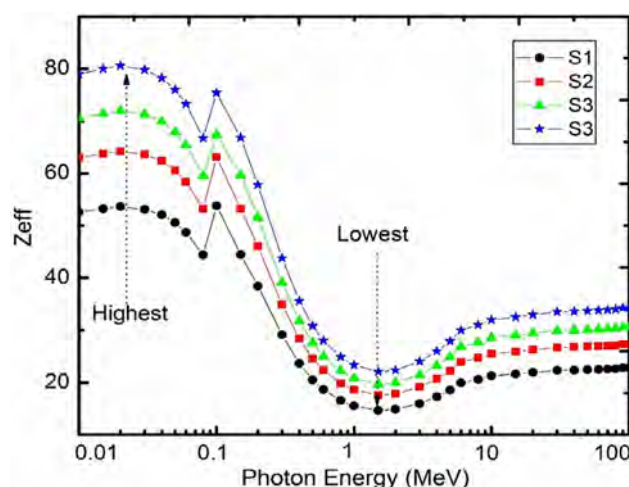


**Figure 9.** Variation of  $Z_{\text{eff}}$  of the prepared glasses with energy for the various concentrations of CdO.

increasing photon energy and increased by increasing CdO content. The highest  $Z_{\text{eff}}$  was reported at 0.02 MeV (53.611) and the lowest values at 0.15 MeV (14.670). The abrupt features observed at 0.08 MeV, which is attributed to the K-edge of Bi.<sup>[35]</sup> The slight increase reported after the 3 MeV region attributed to the dominance of pair production in the energy level.<sup>[36]</sup>

Based on Table 1, the  $Z_{\text{eff}}$  and effective electron density ( $N_{\text{eff}}$ ) of the prepared glasses are calculated via experiment, MCNP5, and XCOM program and listed in Table 7 and 8, respectively. Regarding the values listed in Table 7, the comparison was performed based on the available six radiation sources used for experiment calculations (0.122–1.332 MeV). The  $Z_{\text{eff}}$  at this energy range was increased with increasing photon energy

**Table 6.** Mean free path of the new prepared samples.

Shielding material	Density [ $\text{g cm}^{-3}$ ]	0.122 MeV			0.356 MeV			0.511 MeV		
		Exp.	MCNP	XCOM	Exp.	MCNP	XCOM	Exp.	MCNP	XCOM
S1	4.315	0.249	0.250	0.247	1.909	1.812	1.179	3.233	2.933	2.659
S2	4.711	0.217	2.199	0.212	1.594	1.567	1.522	2.722	2.695	2.406
S3	5.068	0.158	0.161	0.155	1.151	1.140	1.115	1.775	1.726	1.669
S4	5.375	0.121	0.122	0.120	0.903	0.873	0.863	1.258	1.271	1.244
Barite concrete	3.350	–	0.592	0.686	–	2.617	2.469	–	3.356	3.597
Chalcocite concrete	3.703	–	1.271	1.273	–	2.633	2.645	–	3.174	3.175
Shielding material	Density [ $\text{g cm}^{-3}$ ]	0.662 MeV			1.173 MeV			1.332 MeV		
		Exp.	MCNP	XCOM	Exp.	MCNP	XCOM	Exp.	MCNP	XCOM
S1	4.315	3.428	3.308	3.092	5.268	4.991	4.741	7.295	6.322	5.268
S2	4.711	3.061	2.961	2.668	4.346	3.963	3.513	5.614	4.990	4.346
S3	5.068	2.172	2.083	1.954	3.360	3.150	2.964	3.761	3.545	3.111
S4	5.375	1.659	1.602	1.509	2.570	2.437	2.316	2.888	2.689	2.570
Barite concrete <sup>a)</sup>	3.350	3.371	3.355	3.382	–	5.381	5.350	5.521	5.782	5.711
Chalcocite concrete	3.703	–	3.445	3.559	–	4.667	4.739	–	5.777	5.025

<sup>a)</sup>The MFP values of barite concrete and chalcocite concrete were obtained from previous studies.<sup>[26,43,44]</sup>



**Table 7.** Experimental, MCNP5, and XCOM values of  $Z_{\text{eff}}$  of the new glasses.

Shielding material	0.122 MeV			0.356 MeV			0.511 MeV		
	Exp.	MCNP	XCOM	Exp.	MCNP	XCOM	Exp.	MCNP	XCOM
S1	15.099	16.224	17.111	16.643	17.009	17.778	18.569	19.005	19.021
S2	18.092	19.156	19.565	19.942	20.554	21.211	22.249	23.335	23.813
S3	20.263	21.554	22.011	22.335	23.112	24.010	24.919	25.555	26.014
S4	22.695	23.112	24.771	25.015	26.276	26.832	27.910	28.282	29.087
Shielding material	0.662 MeV			1.173 MeV			1.332 MeV		
	Exp.	MCNP	XCOM	Exp.	MCNP	XCOM	Exp.	MCNP	XCOM
S1	19.718	20.221	21.005	21.179	22.022	22.898	21.456	22.221	23.833
S2	23.626	24.777	25.112	25.377	26.266	27.066	25.709	26.410	28.332
S3	26.461	27.890	28.044	28.423	29.029	29.789	28.795	29.033	30.774
S4	29.637	30.111	31.088	31.833	31.935	32.994	32.250	33.012	33.876

**Table 8.** Experimental, MCNP5, and XCOM values of  $N_e$  of the new glasses.

Shielding material	0.122 MeV			0.356 MeV			0.511 MeV		
	Exp.	MCNP	XCOM	Exp.	MCNP	XCOM	Exp.	MCNP	XCOM
S1	9.125	9.138	9.149	5.711	5.705	5.720	3.986	3.993	4.011
S2	9.255	9.267	9.288	5.426	5.433	5.452	4.111	4.108	4.116
S3	9.424	9.430	9.442	5.548	5.552	5.565	4.769	4.777	4.785
S4	9.118	9.927	9.934	5.582	5.487	5.499	4.878	4.883	4.892
Shielding material	0.662 MeV			1.173 MeV			1.332 MeV		
	Exp.	MCNP	XCOM	Exp.	MCNP	XCOM	Exp.	MCNP	XCOM
S1	3.708	3.714	3.722	3.137	3.133	3.143	3.075	3.073	3.065
S2	3.788	3.794	3.803	3.151	3.149	3.158	3.069	3.065	3.075
S3	3.939	3.944	3.953	3.159	3.163	3.168	3.078	3.075	3.084
S4	3.169	3.174	4.181	3.168	3.171	3.177	3.093	3.089	3.097

(dominant of pair production) and increased with increasing CdO content (S4 has the highest  $\mu/\rho$  and density).

Regarding  $N_e$  of the new glass systems, the  $N_e$  relies on the  $Z_{\text{eff}}$  of the material. Therefore,  $N_e$  has increased by increasing the CdO concentration (replacement of boron element ( $Z = 5$ ) by cadmium ( $Z = 48$ )). The  $N_e$  values vary with photon energy, attributed to the cross-section dependence, as discussed before.

The new glasses' performance in attenuation of gamma rays is determined in terms of radiation protection efficiency (RPE). This parameter was calculated from the values of  $I$  and  $I_0$  obtained from the experimental setup irradiation and based on the following equation<sup>[37]</sup>

$$\text{RPE} = \left(1 - \frac{I}{I_0}\right) \times 100 \quad (6)$$

**Figure 10** shows the calculation of RPEs for the new glasses for the selected six energies in the current study. The results show that the RPE values have decreased with the increasing

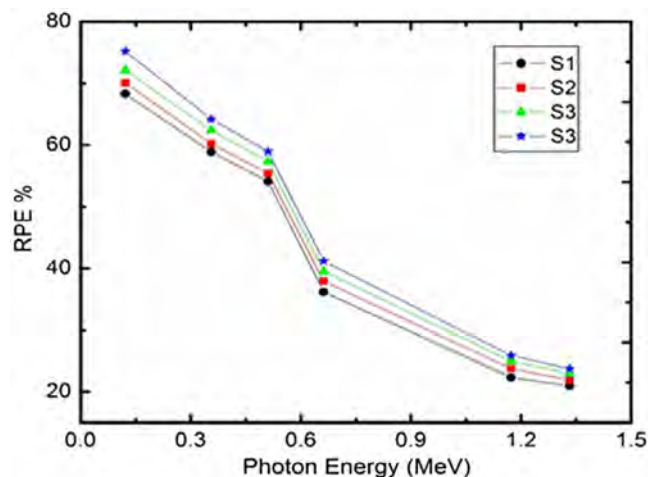


**Figure 10.** Experimental radiation protection efficiency of the prepared glasses at different photon energies.

energy of the incident photon. High performance was achieved at low energies (0.122, 0.356, and 0.511 MeV) and decreased with high energies (0.662, 1.173, and 1.332 MeV). The current values also show that the sample with a higher concentration of CdO (S4) has the highest attenuation efficiency than the other samples. This performance has wholly agreed with the results obtained in the effective atomic number. This reflects that replacing a lighter molecule ( $\text{B}_2\text{O}_3$ ) with a heavier molecule (CdO) leads to an increase in the glasses' attenuation efficiencies.

## 4. Conclusion

Bismuth borate glass systems ( $30\text{Bi}_2\text{O}_3 + 70-x\text{B}_2\text{O}_3$ ) with different concentrations of CdO ( $x = 0-15$  mol%) were prepared by the conventional melt-quenching technique. This study aims to increase glass density (replacing lighter atoms with heavier atoms) while maintaining borate glass transparency. Structural characterization for the newly prepared glasses was conducted by utilizing XRD and UV-vis spectroscopy. Synchronize increase in the prepared glasses' density was reported with the gradual rise of CdO with a reduction of molar volume and energy bandgap. The radiation properties were determined experimentally at specific energies (0.112, 0.356, 0.511, 0.662, 1.173, and 1.332 MeV) and compared with MCNP5 and XCOM simulated values. The new glasses show optimistic radiation shielding properties (high mass attenuation coefficients, accepted atomic number, and shorter MFP and TVL values). Compared with barite and chalcocite concretes, the proposed composition is highly recommended for radiation shielding applications.

## Acknowledgements

The authors would like to gratefully acknowledge the financial support obtained from International Institute of Education (IIE)—Fulbright Program—and from Nanoscale Quantum Phenomena Institute (NQPI)/Ohio University. In addition, G.C. and D.A.D. acknowledge the support from US National Science Foundation under Grant DMR-1507670.

## Conflict of Interest

The authors declare no conflict of interest.

## Keywords

bismuth borate glass, MCNP5, radiation shielding, XCOM

Received: July 29, 2020

Revised: November 4, 2020

Published online: December 4, 2020

- [1] M. G. Dong, M. I. Sayyed, G. Lakshminaravana, M. Çelikkilek Ersundu, A. E. Ersundud, P. Nayar, M. A. Mahdi, *J. Non-Cryst. Solids* **2017**, 468, 12.
- [2] Y. S. M. Alajerami, S. Hashim, W. M. S. Hassan, A. T. Ramli, *Physica B* **2012**, 407, 2390.
- [3] S. Sunil Kumar, J. Khatei, S. Kasthuriengan, K. S. R. Koteswara Rao, K. P. Ramesh, *J. Non-Cryst. Solids* **2011**, 357, 842.
- [4] M. H. A. Mhareb, S. Hashim, S. K. Ghoshal, Y. S. M. Alajerami, M. A. Saleh, S. A. B. Azizan, M. A. Karim, *J. Radioanal. Nucl. Chem.* **2015**, 2, 469.
- [5] C. M. Lee, Y. H. Lee, K. J. Lee, *Prog. Nucl. Energy* **2007**, 49, 303.
- [6] M. Kurudirek, Y. Ozdemir, O. Simsek, R. Durak, *J. Nucl. Mater.* **2010**, 407, 110.
- [7] R. Bagheri, A. K. Moghaddam, Hassan Yousefnia, *Nucl. Eng. Technol.* **2017**, 49, 216.
- [8] Agency for Toxic Substances and Disease Registry (ATSDR), *Toxicological Profile for Lead (Draft for Public Comment)*, U.S. Department of Health and Human Services, Public Health Service, Atlanta, GA **2019**.
- [9] O. Oyar, A. Kislalioglu, *Diagn. Interv. Radiol.* **2012**, 18, 147.
- [10] V. P. Singh, N. M. Badiger, S. Kothan, S. Kaewjaeng, T. Korkut, H. J. Kim, J. Kaewkhao, *Nucl. Sci. Tech.* **2016**, 27, 103.
- [11] J. P. McCaffrey, H. Shen, B. Downton, E. Mainegra-Hing, *Med. Phys.* **2007**, 34, 530.
- [12] S. R. Manohara, S. M. Hanagodimath, L. Gerward, *J. Nucl. Mater.* **2009**, 393, 465.
- [13] P. Kaur, K. J. Singh, M. Kurudirek, S. Thakur, *Spectrochim. Acta A: Mol. Biomol. Spectrosc.* **2019**, 223, 117309.
- [14] V. Sharma, S. Singh, G. Mudahar, K. Thind, *New J. Glass Ceram.* **2012**, 2, 128.
- [15] S. Bahammam, S. Abd El Al, F. M. Ezz-Eldin, *Results Phys.* **2017**, 7, 241.
- [16] R. Ezhil Pavai, P. Shalini Priya Dharsini, *Sci. Res.* **2017**, 8, 17242.
- [17] K. Kirdsiri, J. Kaewkhao, N. Chanthima, P. Limsuwan, *Ann. Nucl. Energy*, **2011**, 38, 1438.
- [18] K. Singh, H. Singh, V. Sharma, R. Nathuram, A. Khanna, R. Kumar, S. S. Bhatti, H. S. Sahota, *Nucl. Instrum. Methods B* **2002**, 194, 1.
- [19] N. Singh, K. J. Singh, K. Singh, H. Singh, *Nucl. Instrum. Methods B* **2004**, 225, 305.
- [20] W. M. Abd-Allah, A. M. Fayad, H. A. Saudi, *Opt. Quantum Electron.* **2019**, 51, 165.
- [21] Y. S. Alajerami, D. Drabold, M. Mhareb, K. A. Leslee Cimat, G. Chen, *Ceram. Int.* **2020**, 46, 12718.
- [22] N. F. Mott, E. A. Davis, *Materials*, Clarendon Press, Oxford, **1971**.
- [23] M. J. Berger, J. H. Hubbell, *XCOM: Photon Cross Sections on a Personal Computer*, NBSIR 87-3597, National Bureau of Standards, Gaithersburg, MD **1987**.
- [24] M. G. Dong, R. El-Mallawany, M. I. Sayyed, H. O. Tekin, *Radiat. Phys. Chem.* **2017**, 141, 172.
- [25] H. O. Tekin, U. Kara, *J. Commun. Comput.* **2016**, 13, 32.
- [26] K. A. Mahmoud, M. I. Sayyed, O. L. Tashlykov, *Radiat. Phys. Chem.* **2019**, 165, 108426.
- [27] M.Kh. Hamad, M. H. A. Mhareb, Y. S. Alajerami, M. I. Sayyed, G. Saleh, Y. Maswadeh, Kha. Ziq, *Radiat. Phys. Chem.* **2020**, 174, 108920.
- [28] M. H. A. Mhareb, M. Alqahtani, F. Alshahri, Y. S. M. Alajerami, N. Saleh, N. Alonizan, M. I. Sayyed, M. G. B. Ashiq, T. Ghrib, S. Ibrahim Al-Dhafar, T. Alayed, M. A. Morsy, *J. Non-Cryst. Solids* **2020**, 541, 120090.
- [29] M. H. A. Mhareb, Y. S. M. Alajerami, M. I. Sayyed, N. Dwaikat, M. Alqahtani, F. Alshahri, N. Saleh, N. Alonizan, T. Ghrib, S. Ibrahim Al-Dhafar, *J. Non-Cryst. Solids* **2020**, 550, 120360.
- [30] T. Kaur, J. Sharma, T. Singh, *Prog. Nuclear Energy* **2019**, 113, 95.
- [31] M. G. Dong, O. Agar, H. O. Tekin, O. Kilicoglu, K. M. Kaky, M. I. Sayyed, *Composites B: Eng.* **2019**, 165, 636.
- [32] Y. S. Alajerami, D. A. Drabold, M. H. A. Mhareb, K. N. Subedi, K. Leslee, A. Cimat, G. Chen, *J. Appl. Phys.* **2020**, 127, 175102.
- [33] A. Sharma, M. I. Sayyed, O. Agar, H. O. Tekin, *Results Phys.* **2019**, 13, 102199.
- [34] N. Tsoulfanidis, S. Landsberger, *Measurement and Detection of Radiation*, 4th ed., CRC Press, Boca Raton, FL **2015**.
- [35] M. G. Sayyed, M. I. Sayyed, M. Çelikkilek Ersundu, A. E. ErsundudPriyank Nayar, M. A. Mahdi, *J. Non-Cryst. Solids* **2017**, 468, 12.
- [36] K. Ashok, M. G. Dong, M. I. Sayyed, G. Lakshminarayana, X. X. Xue, M. A. Mahdi, *Glass Phys. Chem.* **2018**, 44, 292.
- [37] M. I. Sayyed, H. O. Tekin, O. Kilicoglu, O. Agar, M. H. M. Zaid, *Results Phys.* **2018**, 11, 40.
- [38] G. F. Knoll, *Radiation Detection and Measurement*. University of Michigan, Ann Arbor, MI **2002**.
- [39] O. S. Shamsan, M. I. Sayyed, D. K. Gaikwad, P. P. Pawar, *Radiat. Phys. Chem.* **2018**, 148, 86.
- [40] M. I. Sayyed, *J. Alloys Compd.* **2017**, 695, 3191.
- [41] F. Akman, R. Durak, M. F. Turhan, M. R. Kacal, *Appl. Radiat. Isot.* **2015**, 101, 107.
- [42] S. Singh, A. Kumar, D. Singh, K. S. Thind, G. S. Mudahar, *Nucl. Instrum. Methods Phys. Res. B* **2008**, 266, 140.
- [43] I. Akkurt, H. Akyildirim, B. Mavi, S. Kilincarslan, C. Basyigit, *Ann. Nucl. Energy* **2010**, 37, 910.
- [44] R. Bagheri, A. Khorrami Moghaddam, H. Yousefnia, *Nucl. Eng. Technol.* **2017** 49, 216.

# Quasilocalized Vibrations in Vitreous Silica

Nikita S. Shcheblanov, Mikhail E. Povarnitsyn, Jamie D. Wiles, Stephen R. Elliott, and Sergei N. Taraskin\*

Dedicated to Professor David A. Drabold on the occasion of his 60th birthday

The properties of quasilocalized atomic vibrations in numerical models of vitreous silica are studied by means of a demixing technique. The low-frequency vibrational modes are decomposed into bare non-localized (plane-wave-like) modes and bare localized modes (BLMs). The BLMs are shown to exhibit three distinct spatial regions, characterized by different decay behaviors of the displacement field amplitude: the core, tail, and crossover regions. In the core region near the center of localization, the displacement amplitude decays exponentially with a typical localization length being on the order of the interatomic spacing. In the tail region, the decay of the displacement amplitude follows approximately a power law characterized by a decay exponent  $\alpha$ , found to be in the range  $1 \lesssim \alpha \lesssim 2$ . The crossover between the core and tail regions takes place at about 10 Å. By means of a local symmetry-mode comparative projection technique, a distinct similarity in the local vibrational motion for quasilocalized modes in vitreous silica and optic phonons in  $\alpha$ -cristobalite is demonstrated.

sound waves, resulting in a parabolic dependence of the vibrational density of states (VDOS) on frequency,  $\nu$ , known as the Debye law. In computer models of disordered solids, such as glasses, in addition to plane-wave-like excitations, quasilocalized modes (QLMs) appear.<sup>[1–11]</sup> These vibrational modes are believed to play an apparently important role in heat conduction<sup>[12,13]</sup> and mechanical properties of glasses under load.<sup>[14]</sup> The QLMs, as seen in computer-generated structural models, have a distinct spatial structure,<sup>[15]</sup> i.e., a localized core in which a few atoms vibrate with significant amplitude, as compared with less pronounced vibrations of atoms for the rest (tail) of the mode displacements. Such a spatial structure can be imagined as a result of hybridization between acoustic plane-wave-like modes,

## 1. Introduction

The atomic vibrational spectra of disordered systems exhibit some peculiarities when compared with the phonon spectra of crystals. In particular, the only vibrational modes contributing to the low-frequency part of the spectrum in crystals are the


i.e., bare non-localized modes (BNLMs) and low-frequency localized modes,<sup>[4,10,16,17]</sup> i.e., low-frequency bare localized modes (BLMs).<sup>[18]</sup> Hybridization between the BLMs and the BNLMs occurs, because these modes overlap in space and their frequencies are in the same range, and these lead to their transformation into QLMs and NLMs, respectively.

Dr. N. S. Shcheblanov  
 Université Paris-Est, Laboratoire NAVIER (UMR 8205)  
 CNRS  
 ENPC  
 Université Gustave Eiffel  
 F-77420 Marne-la-Vallée, France

Dr. N. S. Shcheblanov  
 Laboratoire des Solides Irradiés CEA-CNRS  
 École polytechnique  
 F-91128 Palaiseau, France

Dr. N. S. Shcheblanov  
 Centre de Physique Théorique  
 CNRS  
 École polytechnique  
 F-91128 Palaiseau, France

Dr. M. E. Povarnitsyn  
 Joint Institute for High Temperatures, RAS  
 13 Building 2 Izhorokaya Street, Moscow 125412, Russia

 The ORCID identification number(s) for the author(s) of this article can be found under <https://doi.org/10.1002/pssb.202000422>.

DOI: 10.1002/pssb.202000422

J. D. Wiles  
 Cavendish Laboratory  
 University of Cambridge  
 Cambridge CB3 0HE, UK

Prof. S. R. Elliott  
 Department of Chemistry  
 University of Cambridge  
 Cambridge CB2 1EW, UK

Prof. S. R. Elliott  
 Trinity College  
 University of Cambridge  
 Cambridge CB2 1TQ, UK

Dr. S. N. Taraskin  
 Department of Chemistry  
 University of Cambridge  
 Cambridge CB2 1EW, UK  
 E-mail: [snt1000@cam.ac.uk](mailto:snt1000@cam.ac.uk)

Dr. S. N. Taraskin  
 St. Catharine's College  
 University of Cambridge  
 Cambridge CB2 1RL, UK



A significant amount of effort has been put in to establish the nature of the QLMs. One of the main difficulties there is related to the separation of contributions coming from the BNLM and BLM, and actually establishing a criterion according to which modes can be treated as QLMs. Two approaches were suggested for dealing with these hybridization effects: 1) a demixing technique<sup>[4]</sup> and 2) separating the frequency range of the QLMs from that for the NLMs, by, e.g., tuning the system size<sup>[9,19]</sup> or internal stress.<sup>[20]</sup> Within the latter approach, the QLMs are identified by their frequencies being smaller than the lowest frequency of NLMs (acoustic waves) allowed by the finite size of the simulation box for a structural model. The VDOS of the QLMs defined according to such a criterion was found to increase with frequency as  $g_{QLM}(\nu) \propto \nu^4$ .<sup>[9]</sup> A similar approach was used, even in the situation when the QLMs and NLMs coexist in the same frequency range, by introducing a threshold value for the participation ratio (PR),  $p_0$ , artificially separating NLMs (with  $p > p_0$ ) from the QLMs for which  $p < p_0$ .<sup>[10,11]</sup> The same quartic frequency law for the VDOS,  $\propto \nu^4$ , was found for such identified QLMs.

In this article, we use and develop an alternative mode-demixing procedure<sup>[4]</sup> to investigate the nature of the QLMs in simulated models of vitreous silica. In particular, we address the question about the properties of the BLMs, including their spatial shape and type of vibrational motion, and compare these properties with those for high-frequency, truly localized modes (TLMs).

## 2. Demixing Technique

In our study, we used computer-generated models of vitreous silica ( $\nu$ -SiO<sub>2</sub>) and of its crystalline counterpart,  $\alpha$ -cristobalite.<sup>[21–24]</sup> The glass model of  $\nu$ -SiO<sub>2</sub>, with a total number of atoms  $N = 24\,000$ , was produced by means of classical molecular-dynamics simulations (see Supporting Information and the study by Shcheglov et al.<sup>[18]</sup> for more detail). The dynamical matrices,  $\mathbf{D}$ , for the relaxed structural model were diagonalized, giving complete sets of orthonormal eigenvectors,  $\mathbf{e}^n = \{\mathbf{e}_i^n\}$  (the index  $i$  runs over all atoms in the model, whereas the index  $n$  enumerates all  $3N$  eigenmodes), normalized displacement vectors,  $\mathbf{u}^n = \{\mathbf{u}_i^n\}$  with  $\mathbf{u}_i^n = m_i^{-1/2} \mathbf{e}_i^n / \sum_i^N m_i^{-1} |\mathbf{e}_i^n|^2$  ( $m_i$  is the mass of atom  $i$ ), and eigenvalues (squared vibrational frequencies),  $\nu_n^2$ . The vibrational spectrum of  $\nu$ -SiO<sub>2</sub> and the frequency dependence of the PR

$$p(\nu_n) = N^{-1} \left( \sum_{i=1}^N |\mathbf{u}_i^n|^2 \right)^2 \left( \sum_{i=1}^N |\mathbf{u}_i^n|^4 \right)^{-1} \quad (1)$$

quantifying the degree of localization of mode  $n$  are shown in Figure 1a,b, respectively. The extended modes are characterized by  $p \sim 1$ , whereas the localized modes (in the high-frequency tails, e.g., at  $37 \lesssim \nu \lesssim 40$  THz) and some QLMs (in the low-frequency range,  $\nu \lesssim 1$  THz) are characterized by  $p \ll 1$ .

The inset in Figure 1b displays a typical picture for the PR of the low-frequency vibrational modes in numerical models of finite size. In this frequency range, there are two types of modes: 1) plane-wave-like modes (acoustic phonon-like NLMs), grouped near the frequencies corresponding to sound waves of wavelengths comparable with the simulation box size and characterized by increasing values of PR ( $p \gtrsim 0.4$ ) with decreasing frequency; and 2) QLMs characterized by relatively small values of PR decreasing with decreasing frequency. The modes of these two types, NLMs and QLMs, result from hybridization between the corresponding bare modes, i.e., BNLMs and BLMs.

The finite size of simulated structural models plays an important role in the appearance of QLMs characterized by relatively small values of PR and with a clearly detectable, spatially localized atomic vibrational core. Such a spatial structure of the QLMs is a consequence of the finite-size effects leading to the sparse spectrum of the BNLMs in the low-frequency range. An increase in the model size up to a macroscopic scale would lead to the appearance of a continuous spectrum of the BNLMs. This, in turn, should result in significant hybridization effects between the BLMs and BNLMs, so that the resulting QLMs would be effectively “dissolved” in a continuous spectrum of the BNLMs, thus being characterized by a PR on the order of unity and not exhibiting any clear localization core (see the previous study,<sup>[25]</sup> where this effect is demonstrated by solving a simple analytical model for a single localized state interacting with a continuum of extended states). In other words, the difference between QLMs and NLMs should disappear in macroscopically large structures. Therefore, the observation of the QLMs with a small PR and a detectable localization core seems to be a purely finite-size effect, although it gives an opportunity to investigate the nature and origin of extra vibrational states present in the low-frequency part of the spectrum of disordered systems.

To reveal the nature of the QLMs, mode demixing has been suggested in a previous study.<sup>[4]</sup> The aim of the demixing procedure (which conserves the number of modes in the system) is to separate the non-localized and localized contributions into NLMs

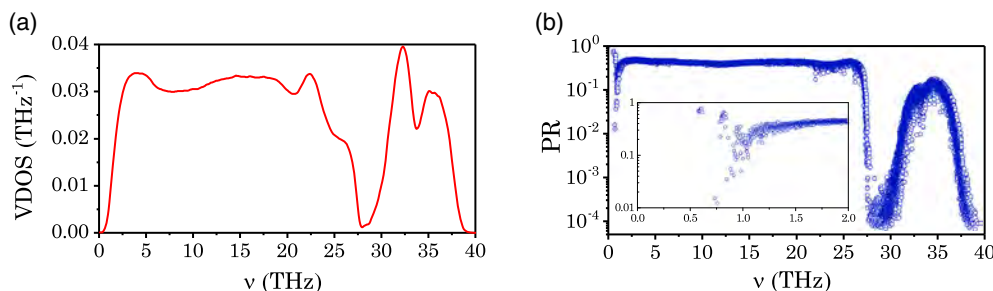


**Figure 1.** a) VDOS for the total range of frequencies for the  $\nu$ -SiO<sub>2</sub> model of  $N = 24\,000$  atoms. b) Frequency dependence of the PR in the whole and low-frequency (inset) ranges for the  $\nu$ -SiO<sub>2</sub> model of  $N = 24\,000$  atoms.

and QLMs (see Supporting Information). The true eigenmodes in the low-frequency range, ( $\mathbf{e}$ ), are assumed to be composed of BLMs and BNLMs, ( $\mathbf{e}'$ ), from a certain frequency range; i.e., true eigenmodes ( $\mathbf{e}$ ) can be represented as linear combinations of ( $\mathbf{e}'$ ). Equivalently, by inversion, the BLMs and BNLMs, which we aim to extract, can be searched for in the form of a linear combination of true modes, that is

$$(\mathbf{e}')^n = \sum_{m: \nu_m \in [\nu_n - \Delta\nu_n, \nu_n + \Delta\nu_n]} a_{nm} \mathbf{e}^m \quad (2)$$

where the parameter of the model,  $\Delta\nu_n$ , describes the width of the frequency mixing range, i.e., the frequency range of true modes to which the demixed mode ( $\mathbf{e}'$ )<sup>n</sup> can contribute. The mixing coefficients  $a_{nm}$  entering Equation (1) can be found by pairwise sequential rotations of the eigenvectors  $\mathbf{e}^n$  and  $\mathbf{e}^m$  for all eigenmodes for which the frequencies,  $\nu_m \in [\nu_n - \Delta\nu_n, \nu_n + \Delta\nu_n]$ .<sup>[4,18]</sup> The angles of pairwise rotations are determined by the condition that the PR of the partially demixed displacement mode ( $\mathbf{u}'$ )<sup>n</sup> reaches a minimal value after each pairwise rotation. The demixing procedure is performed for all eigenmodes in the low-frequency range characterized by PR values less than some threshold value,  $p_c$ , the second parameter of the model, with  $p_c = 0.25$  being found to be a reasonable estimate for vitreous silica models (see Supporting Information where the results of the demixing procedure are presented for other values of  $p_c$ ). The value of  $p_c$  gives a rough indication for an approximate split of true modes into QLMs (with

$p \lesssim p_c$ ) and NLMs (with  $p \gtrsim p_c$ ). We should emphasize that the mode assignment as being QLM is only qualitative and approximate and valid for relatively small finite-size models in which the low-frequency vibrational modes characterized by a small PR can be identified.

The resulting set of new demixed modes,  $\{(\mathbf{e}')^n\}$ , is orthonormal, but these modes are no longer the eigenmodes of  $\mathbf{D}$ , and their frequencies,  $\nu'_n$ , can be estimated as<sup>[4,18]</sup>  $\nu_n'^2 = \sum_m a_{nm}^2 \nu_m^2$ , where the summation is taken over the eigenmodes from the same range as in Equation (1). The width of the frequency mixing range  $\Delta\nu_n$  can be approximately evaluated from the frequency distributions of the mixing coefficients  $a_{nm}$ , which typically have a peak of a certain width. Both the position and width of the peak for a given  $n$  do not depend significantly on the value of  $\Delta\nu_n$  (see Figure 2b). Following the previous study,<sup>[4]</sup> we assumed that the frequency range of interactions scales linearly with the frequency; thus, using  $\Delta\nu_n/\nu_n$  as a parameter of the model, with the value  $\Delta\nu_n/\nu_n = 0.3$ , is used in a further analysis.

The results of the demixing procedure for the values of PR in the low-frequency range are shown in Figure 2a. It follows from this figure that the demixing allows the BLMs and BNLMs to be well separated. Indeed, the values of the PR for the BLMs are significantly smaller than those for QLMs, whereas the PR of BNLMs after demixing follows the same tendency (i.e., the PR increases toward unity with decreasing frequency), as in crystals. The frequencies of the BLMs are distributed near  $\nu^* \approx 1.1 \pm 0.1$  THz. Not surprisingly, the position of  $\nu^*$  approximately coincides with the frequency at which the depletion

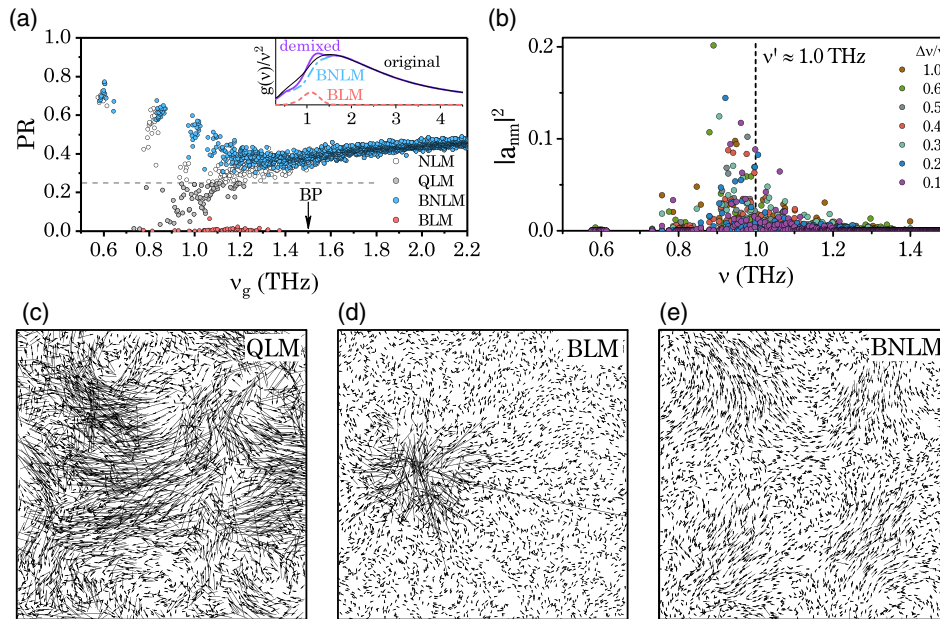


**Figure 2.** a) PR versus frequency,  $\nu_g$ , for NLMs (open black circles corresponding to  $p > p_c$ ), QLMs (gray circles corresponding to  $p < p_c$ ), demixed BNLMs (solid blue circles), and BLMs (red solid circles) for  $\Delta\nu/\nu = 0.3$  and  $p_c = 0.25$  and  $N = 24000$ . The dashed horizontal line shows the threshold PR value,  $p_c = 0.25$ . The arrow labeled by “BP” shows the location of the boson peak. The inset shows the relative contribution of BLMs (red dashed curve) and BNLMs (blue dashed-dotted curve) to the reduced VDOS (black curve). b) The distribution of the square of the mixing coefficients,  $a_{nm}^2$ , for several BLMs with frequencies  $\nu'_n \approx 1.0$  THz over the frequencies of true modes  $\nu_m$  for various widths of mixing ranges, as indicated in the legend. Displacement field for 2d slabs with  $31 \leq z \leq 41$  Å cut from the cubic structural glass model of linear size  $L \approx 72$  Å for several representative eigenmodes: c) QLM with frequency  $\nu \approx 1.0$  THz and  $p(\nu) \approx 0.20$ ; d) demixed BLM with frequency  $\nu' \approx 1.0$  THz and  $p(\nu') \approx 0.0028$ ; and e) demixed BNLM with frequency  $\nu' \approx 1.0$  THz and  $p(\nu') \approx 0.55$ .

of the QLMs from acoustic-like phonons occurs before demixing. The reason for such a depletion is due to the finite size,  $L$ , of the simulation box, leading to discretization of the sound-like modes characterized by discrete wavevectors,  $\mathbf{q}_{n_x, n_y, n_z} = 2\pi L^{-1}(n_x, n_y, n_z)$ , where  $n_{x,y,z} \in \mathbb{Z}$ . In disordered atomic structures, these modes are broadened by disorder, and around the depletion frequency, such broadening becomes comparable with the distance between frequencies corresponding to different wavevectors.<sup>[17]</sup>

### 3. Spatial Structure of Vibrational Eigenmodes

The QLMs before demixing exhibit inhomogeneity in the displacement field, with some regions showing significantly larger displacements than others (see Figure 2c). We call such regions “localization spots.” Some of the QLMs, such as that shown in panel (c) of Figure 2, have several such spots separated by sets of atoms with significantly smaller displacements. After demixing, typically a single localization spot (core region) survives (see Figure 2d) for BLMs, and none for BNLMs which exhibit wave-like displacement patterns (see Figure 2e). The presence of a single distinguishable localization spot, the localization core, for the majority of the BLMs gives us an opportunity to define the position vector,  $\mathbf{r}_{0,n}$ , for the center of localization of the  $n$ th BLM as follows

$$\mathbf{r}_{0,n} = \frac{\sum_{i \in N_n} |\mathbf{u}_i^{(n)}|^2 \mathbf{r}_i}{\sum_{i \in N_n} |\mathbf{u}_i^{(n)}|^2} \quad (3)$$

where  $\mathbf{r}_i$  is the position vector of atom  $i$ , and the summation is taken over the set  $N_n$  of  $N_{\text{core}}$  atoms, which are the nearest neighbors to the atom characterized by the maximal displacement amplitude. A similar definition was used in the previous studies.<sup>[4,26]</sup> In further analysis, we used  $N_{\text{core}} = 10$ , but the results do not significantly depend on this value, even if  $N_{\text{core}} = N$ .

For QLMs, the amplitudes,  $|\mathbf{u}_i^{(n)}|$ , of atomic displacements of atoms  $i$  decay with their distance from the center of localization,  $|\mathbf{r}_i - \mathbf{r}_{0,n}|$ . This decay is shown in **Figure 3** both for a representative QLM (panel (a)), two BLMs obtained by demixing from the QLM (panel (b) and (c)) and TLMs (panel (d)–(f)) from the high-frequency tails, for comparison. In this figure, the displacement amplitudes of all atoms within the half-simulation box distance from the center of localization are shown by solid circles (in panel (a)) and open gray circles (in panels (b)–(d)). To reveal the decay law of  $|\mathbf{u}|$  with  $|\mathbf{r} - \mathbf{r}_0|$ , we performed angular averaging by splitting the space into spherical shells of thickness  $\delta r$  (the value of  $\delta r = 1 \text{ \AA}$  was used for the data presented in the following) and finding the median values of  $|\mathbf{u}|$  for all atoms within the shells (the same method has been used in previous studies<sup>[9,26]</sup>). Such angular averaging significantly reduces the noise in the displacement field. The median values for  $|\mathbf{u}|$  are shown in panels (b)–(d) of Figure 3 by solid circles.

It follows from Figure 3 that the amplitude of atomic displacements decays differently for the low- and high-frequency modes. As expected, the high-frequency localized modes decay

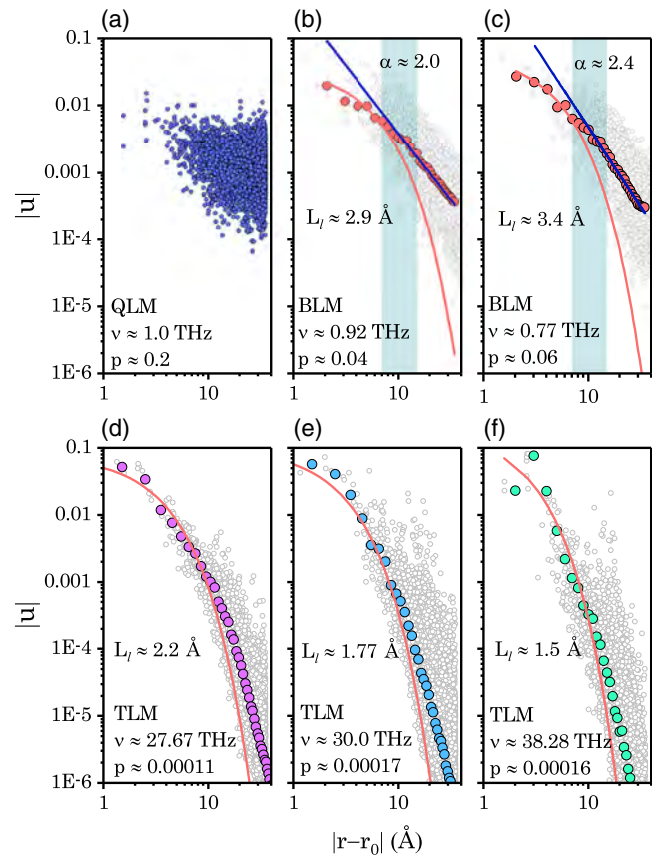


**Figure 3.** Spatial decay of the displacement amplitude  $|\mathbf{u}|$  versus distance from the center of localization,  $|\mathbf{r} - \mathbf{r}_0|$ , for: a) QLM; b,c) BLMs; and d–f) TLM, with frequencies,  $\nu$ , and PR,  $p$ , indicated in the panels. The solid circles in (a) and open circles in (b)–(f) show the data for individual atoms. The red solid (in (b,c)) and pink, blue, and green (in (d)–(f)) circles refer to median displacement amplitudes obtained by angular averaging, as described in the text. The red curves in (b)–(f) show the exponential fit according to Equation (3) with the values of  $L_{l,n}$  shown in the panels. The blue lines in (b,c) show the power-law fit according to Equation (4), with exponents  $\alpha$  quoted in the panels. The light-blue strips in (b,c) show crossover regions.

exponentially with the distance from the center of localization (see Figure 3d), i.e., as

$$|\mathbf{u}_i^{(n)}| \simeq u_{0n} e^{-|\mathbf{r}_i - \mathbf{r}_{0,n}|/L_{l,n}} \quad (4)$$

where  $u_{0n}$  is a pre-factor, and  $L_{l,n}$  is the localization length for the  $n$ th vibrational eigenmode. Strictly speaking, the assignment of the high-frequency tail modes as being truly localized requires finding the localization threshold (critical) frequency(ies) by means of, e.g., multifractal analysis.<sup>[27]</sup> Here, we use an exponential decay of the eigenmode as an indication for the mode to be truly localized.

For all BLMs (see **Figure 4**), we can distinguish three spatial regions: 1) the core region,  $|\mathbf{r} - \mathbf{r}_0| \lesssim r^*$ , with an approximately exponential decay of the displacement amplitude with distance from the localization center; 2) the tail region,  $|\mathbf{r} - \mathbf{r}_0| \gtrsim r^*$ , where the displacement amplitude approximately decays according to a power law, i.e., as



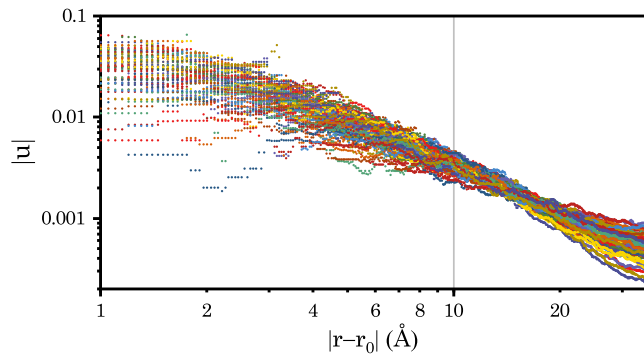


**Figure 4.** The displacement amplitude  $|u|$  versus  $|r - r_0|$  for all BLMs obtained by the demixing procedure with  $\Delta\nu/\nu = 0.3$  and  $p_c = 0.25$  in the model of  $\nu$ -SiO<sub>2</sub> containing 24 000 atoms.

$$|u_i^{(n)}| \propto |r_i - r_{0,n}|^{-\alpha_n}; \quad (5)$$

and 3) a crossover region,  $|r - r_0| \sim r^*$  (see the light-blue strips around  $|r - r_0| \sim r^* \sim 10$  Å in panels (b) and (c)).

The characteristics of the decay functions, the localization length  $L_\ell$  and exponent  $\alpha$  for exponential and power-law decays, respectively, can be estimated from the fits of the numerical data by the corresponding functions (see solid lines in Figure 3b–d). The corresponding extracted values of the localization lengths for BLMs and TLMs are displayed in Figure 5 as functions of the corresponding mode frequency. For both BLMs and TLMs, the values of the localization length are  $L_\ell \sim 1$  Å, i.e., are of inter-atomic scale, signaling a fast decay of the displacement field away from the center of localization.

An alternative way to characterize the spatial decay of the displacement field near the center of localization is by defining a correlation length<sup>[28]</sup>

$$L_{c,n}^2 = \frac{\sum_i^N |r_i - r_{0,n}|^2 |u_i^{(n)}|^2}{\sum_i^N |u_i^{(n)}|^2} \quad (6)$$

In the limit of continuum infinite media, for a purely exponential decay of the amplitude of the displacement field, the correlation length is simply related to the localization length, i.e.,  $L_c/L_\ell = \sqrt{3}$  (see Supporting Information). In the case of BLMs, the ratio is in the range,  $2 \lesssim L_c/L_\ell \lesssim 6$  (see Figure 5), which is consistent with the presence of a power-law tail in the displacement field.

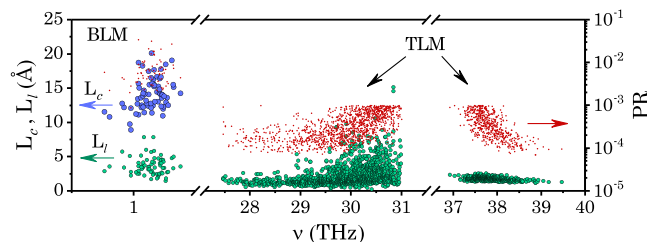


**Figure 5.** Localization length,  $L_\ell$  (green circles), correlation length,  $L_c$  (blue circles), and PR (red dots) versus frequency of BLMs ( $\nu \lesssim 1.4$  THz) and TLMs ( $27.7 \lesssim \nu \lesssim 31$  THz and  $\nu \gtrsim 37$  THz).

The power-law tail in the displacement field of BLMs is characterized by an exponent  $\alpha$  (see Equation (4)). This exponent varies both with frequency and PR, as shown in Figure 6a,b, respectively. For the majority of the BLMs,  $\alpha < 2$ , which is different from the value of  $\alpha \approx 2$  found for QLMs in structural glasses.<sup>[9]</sup> The reason for such values of  $\alpha$  for BLMs in  $\nu$ -SiO<sub>2</sub> is not completely clear and requires additional investigation.

#### 4. Comparative Symmetry-Mode Projection Technique

In Section 3, the spatial decay of the displacement field of localized eigenmodes was discussed. In this section, we analyze the type of vibrational motion characteristic of BLMs. This is done using the comparative symmetry-mode local projection technique introduced in the previous study.<sup>[18]</sup> The technique is based on comparing the displacement field for local structural units, such as SiO<sub>4</sub> tetrahedra in vitreous silica, in glassy vibrational eigenmodes with that exhibited by phonons in a crystalline counterpart material, e.g.,  $\alpha$ -cristobalite in the case of silica.

Quantitatively, this is done by evaluation of the projector,  $\mathcal{P}_{i_g, i_c}^{n_g, n_c}$  (see the previous study<sup>[18]</sup> for a precise definition), where the index  $i_g$  counts all structural units in a glass model,  $i_c$  counts all distinct structural units in a crystalline counterpart,  $n_g$  counts all glassy vibrational modes, and  $n_c$  counts all phonons characterized by wavevectors  $\mathbf{q}$  and branch numbers  $\beta$ . The aim of the comparative projection analysis is to find phonons with local atomic vibrations most similar to those in a glassy mode. To achieve this, we define a binary projector  $\hat{\mathcal{P}}_{i_g}(\nu_g, (\beta\mathbf{q})_{\max})$ , which is related to the maximum value (among all possible crystalline modes,  $n_c$ , and units,  $i_c$ ) of the projector  $\mathcal{P}_{i_g, i_c}^{n_g, n_c}$ , that is

$$\hat{\mathcal{P}}_{i_g}(\nu_g, (\beta\mathbf{q})) = \begin{cases} 1, & \text{if } \varepsilon < \max_{n_c, i_c} \{\mathcal{P}_{i_g, i_c}^{n_g, n_c}\} \leq 1 \\ 0, & \text{otherwise} \end{cases} \quad (7)$$

where  $\varepsilon$  is the close-to-unity tolerance parameter,  $\nu_g$  stands for the frequency of the glassy eigenmode  $n_g$ , and  $(\beta\mathbf{q})$  describes a phonon with a frequency  $\nu_c \equiv \nu_\beta(\mathbf{q})$  for which the maximum value of  $\mathcal{P}_{i_g, i_c}^{n_g, n_c}$  is achieved, i.e.,  $(\beta\mathbf{q}) \equiv (\beta\mathbf{q})_{\max}$ . The binary projector given by Equation (7) counts the pairs of structural units in the glass and crystal for which the vibrations are similar. Several glassy units can contribute to the same phonon, and thus, the quantity,  $\mathcal{P}(\nu_g, (\beta\mathbf{q}))$ , averaged over all glassy units

$$\mathcal{P}(\nu_g, (\beta\mathbf{q})) = \frac{1}{N_g} \sum_{i_g} \hat{\mathcal{P}}_{i_g}(\nu_g, (\beta\mathbf{q})) \quad (8)$$

represents the discrete distribution over the phonon spectrum of the similarity parameter, called “crystallinity.” For a given point  $\mathbf{q}$  in the Brillouin zone and branch number  $\beta$ ,  $\mathcal{P}(\nu_g, (\beta\mathbf{q}))$  represents the relative number of glassy units in a glassy mode  $\nu_g$ , which exhibit a local motion similar to that of one of the structural units for this phonon. Summation over all phonons with fixed phonon frequency defines the frequency distribution of crystallinity or the frequency-frequency “correlation” function

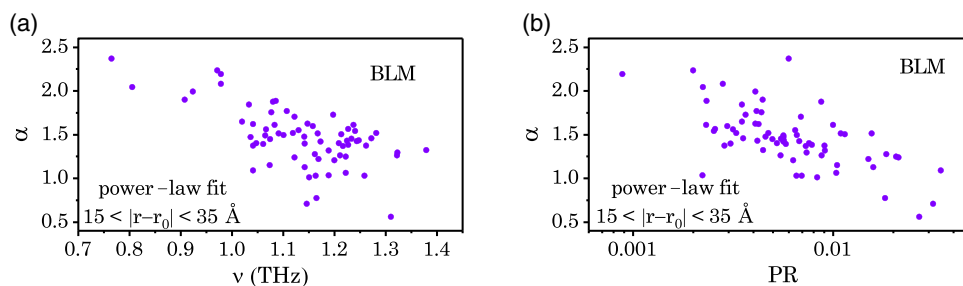


**Figure 6.** The decay exponent  $\alpha$  in the power-law decay of the displacement amplitude with distance from the center of localization, as defined by Equation (4), versus a) frequency and b) PR for BLMs. The range for the power-law fit in the tail region is indicated in the panels.

$$\mathcal{P}(\nu_g, \nu_c) = \sum_{\beta\mathbf{q}} \mathcal{P}(\nu_g, (\beta\mathbf{q})) \delta(\nu_c - \nu_{\beta}(\mathbf{q})) \quad (9)$$

being a similarity characteristic between a glassy mode  $\nu_g$  and phonons with frequency near  $\nu_c$ .

The frequency distribution of crystallinity for a representative QLM mode with frequency  $\nu_g \simeq 1.1$  THz is shown by the solid black line in **Figure 7**. The demixing procedure for QLMs does not affect significantly the frequency distribution of crystallinity, and the functions  $\mathcal{P}(\nu_g, \nu_c)$  for both BLMs and NLMs, with approximately the same glassy frequency, basically coincide with that for QLMs (see the red and blue curves with the black curve in **Figure 7**).

It is evident from the position of the peaks in **Figure 7** that the dominant contributions in local motion (which is of  $F_1$ -rotation type in this frequency range) for all QLMs, BLMs, and NLMs come from groups of transverse-optic phonons with the frequencies around 4–4.5 and 5.5 THz. The other QLMs and, moreover, the glassy eigenmodes in the boson-peak frequency region,  $\nu_g \simeq 1.5$  THz, show a very similar frequency behavior of  $\mathcal{P}(\nu_g, \nu_c)$  (see the previous study<sup>[18]</sup>). This means that the local tetrahedral vibrations for all glassy low-frequency modes, including the boson-peak region and even the lowest-frequency ( $\simeq 0.57$  THz for our finite-size model of 24 000 atoms) plane-wave-like glassy modes, are similar to those for optic phonons with the frequencies of 4–4.5 and 5.5 THz, in  $\alpha$ -cristobalite.

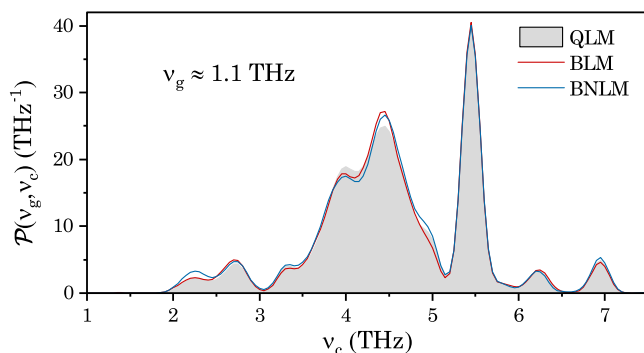


**Figure 7.** The frequency distribution of crystallinity,  $\mathcal{P}(\nu_g, \nu_c)$ , for QLM, BLM, and BNLM of frequency  $\nu_g \simeq 1.1$  THz in a model of  $\nu$ -SiO<sub>2</sub>, versus phonon frequencies  $\nu_c$  in a model of  $\alpha$ -cristobalite for projections onto the tetrahedral vibrational  $T_d$ -group symmetry modes.

## 5. Conclusions

In summary, a numerical analysis of quasilocalized vibrational modes in a computer-simulated model of vitreous silica containing 24 000 atoms is presented in this article. The analysis was undertaken in two directions related to: 1) a comparative investigation of the spatial structure and localization properties of the displacement field for low- and high-frequency modes; and 2) an analysis of local vibrational motion by means of the symmetry-mode projection technique developed in the previous study.<sup>[18]</sup> The emphasis was made for a detailed study of localization properties of the low-frequency QLMs. To achieve this aim, we used a demixing technique<sup>[4]</sup> for splitting quasilocalized and non-localized low-frequency modes into bare localized and non-localized contributions and conducted a further analysis for the BLMs. The BLMs exhibit more distinctive localization properties, because the plane-wave components are mainly removed from them by the demixing procedure.

The BLMs typically have a single center of localization, a point in space characterizing the mean position of atoms with maximal amplitude of atomic vibrations. The displacement field decays with the distance from the center of localization. This decay is not uniform, and three regions can be distinguished for the BLMs: the core, the tails, and the crossover between the first two. In the core region near the center of localization, the amplitude of the displacement field decays exponentially with a typical decay length, called the localization length,  $L_\ell$ , which is found to be of interatomic scale,  $2 \lesssim L_\ell \lesssim 6$  Å. In the tail region, the decay of the displacement amplitude follows approximately a power law characterized by the exponent  $\alpha$ . The value of the decay exponent shows a tendency to increase with decreasing frequency, and its values cover the range,  $1 \lesssim \alpha \lesssim 2$ . The crossover between the core and tail regions is located  $\sim 10$  Å away from the center of localization.

The comparative local symmetry-mode projection technique was used to investigate the type of local vibrational modes in QLMs. It is demonstrated that the low-frequency modes exhibit a significant and distinct similarity with the local motion for optic phonons in  $\alpha$ -cristobalite, with the frequencies about 4–5 THz. Both the optic-like character of local vibrations for the BLMs and the exponential decay of their displacement field in the core region are consistent with the following scenario for the origin of the low-frequency modes.<sup>[18]</sup> The BLMs in vitreous silica are the modes from the low-frequency tail of the optic band(s) formed by

disorder-induced band broadening in a crystalline counterpart. The predominant optic character supports their origin from the optic band. The exponential decay of their displacement field is very similar to that of truly localized high-frequency modes and akin to that occurring in disorder-induced Anderson localization.

## Supporting Information

Supporting Information is available from the Wiley Online Library or from the author.

## Acknowledgements

M.E.P. was supported by The Ministry of Science and Higher Education of the Russian Federation (Agreement with Joint Institute for High Temperatures RAS No 075-15-2020-785). The results were obtained using the equipment of Shared Resource Center "Far Eastern Computing Resource" IACP FEB RAS.

## Conflict of Interest

The authors declare no conflict of interest.

## Keywords

boson peak, cristobalite, glassy silica, quasilocalized states

Received: July 30, 2020

Revised: October 11, 2020

Published online: November 16, 2020

- 
- [1] B. B. Laird, H. R. Schober, *Phys. Rev. Lett.* **1991**, 66, 636.
  - [2] H. R. Schober, B. B. Laird, *Phys. Rev. B* **1991**, 44, 6746.
  - [3] V. Mazzacurati, G. Ruocco, M. Sampoli, *Europhys. Lett.* **1996**, 34, 681.
  - [4] H. R. Schober, C. Oligschleger, *Phys. Rev. B* **1996**, 53, 11469.
  - [5] H. R. Schober, G. Ruocco, *Philos. Mag.* **2004**, 84, 1361.

- [6] N. Xu, V. Vitelli, A. J. Liu, S. R. Nagel, *Europhys. Lett.* **2010**, 90, 56001.
- [7] P. Derlet, R. Maass, J. Löffler, *Eur. Phys. J. B* **2012**, 85, 148.
- [8] Y. M. Beltukov, C. Fusco, D. A. Parshin, A. Tanguy, *Phys. Rev. E* **2016**, 93, 023006.
- [9] E. Lerner, G. Düring, E. Bouchbinder, *Phys. Rev. Lett.* **2016**, 117, 035501.
- [10] H. Mizuno, H. Shiba, A. Ikeda, *Proc. Natl. Acad. Sci. USA* **2017**, 114, E9767.
- [11] L. Wang, A. Ninarello, P. Guan, L. Berthier, G. Szamel, E. Flenner, *Nat. Commun.* **2019**, 10, 26.
- [12] N. Xu, V. Vitelli, M. Wyart, A. J. Liu, S. R. Nagel, *Phys. Rev. Lett.* **2009**, 102, 038001.
- [13] V. Vitelli, N. Xu, M. Wyart, A. J. Liu, S. R. Nagel, *Phys. Rev. E* **2010**, 81, 021301.
- [14] M. L. Manning, A. J. Liu, *Phys. Rev. Lett.* **2011**, 107, 108302.
- [15] M. Shimada, H. Mizuno, M. Wyart, A. Ikeda, *Phys. Rev. E* **2018**, 98, 060901.
- [16] S. N. Taraskin, S. R. Elliott, *Phys. Rev. B* **1997**, 56, 8605.
- [17] E. Bouchbinder, E. Lerner, *New J. Phys.* **2018**, 20, 073022.
- [18] N. S. Shcheblanov, M. E. Povarnitsyn, J. D. Wiles, S. R. Elliott, S. N. Taraskin, *Phys. Rev. B* **2020**, 102, 024202.
- [19] E. Lerner, E. Bouchbinder, *J. Chem. Phys.* **2018**, 148, 214502.
- [20] E. Lerner, E. Bouchbinder, *Phys. Rev. E* **2018**, 97, 032140.
- [21] S. N. Taraskin, S. R. Elliott, *Europhys. Lett.* **1997**, 39, 37.
- [22] S. N. Taraskin, *J. Phys.: Condens. Matter* **2007**, 19, 455215.
- [23] A. I. Chumakov, G. Monaco, A. Monaco, W. A. Crichton, A. Bosak, R. Rüffer, A. Meyer, F. Kargl, L. Comez, D. Fioretto, H. Giefers, S. Roitsch, G. Wortmann, M. H. Manghnani, A. Hushur, Q. Williams, J. Balogh, K. Parliński, P. Jochym, P. Piekarczyk, *Phys. Rev. Lett.* **2011**, 106, 225501.
- [24] A. I. Chumakov, G. Monaco, A. Fontana, A. Bosak, R. P. Hermann, D. Bessas, B. Wehinger, W. A. Crichton, M. Krisch, R. Rüffer, G. Baldi, G. Carini, G. Carini, G. D'Angelo, E. Gilioli, G. Tripodo, M. Zanatta, B. Winkler, V. Milman, K. Refson, M. T. Dove, N. Dubrovinskaya, L. Dubrovinsky, R. Keding, Y. Z. Yue, *Phys. Rev. Lett.* **2014**, 112, 025502.
- [25] S. N. Taraskin, S. R. Elliott, *Phys. Rev. B* **1999**, 59, 8572.
- [26] L. Gartner, E. Lerner, *Phys. Rev. E* **2016**, 93, 011001.
- [27] J. J. Ludlam, S. N. Taraskin, S. R. Elliott, *Phys. Rev. B* **2003**, 67, 132203.
- [28] M. Marinov, N. Zotov, *Phys. Rev. B* **1997**, 55, 2938.



# Thermal Annealing Effects on Naturally Contacted Monolayer MoS<sub>2</sub>

Maryam Bizhani, Ruhi Thorat, William Poston, Thushan Wickramasinghe, Shrouq H. Aleithan, and Eric Stinaff\*

Dedicated to Professor David A. Drabold on the occasion of his 60th birthday

Transition metal dichalcogenides such as MoS<sub>2</sub>, which can be produced in monolayer form, have attracted attention because of their interesting and potentially useful electrical and optical properties. These properties often depend sensitively on material properties such as defect density and crystallinity. Herein, the effects of postgrowth annealing on monolayer MoS<sub>2</sub> grown using a novel chemical vapor deposition process are investigated. In this process bulk molybdenum patterns serve as the nucleation site and source material for high-quality MoS<sub>2</sub> material growth. After postgrowth thermal annealing, the photoluminescence is found to blueshift and become more uniform up to an annealing temperature of 300 °C. At higher temperatures, isolated monolayers begin to crack along the grain boundaries, which leads to variations in luminescence, whereas after annealing temperature of 200 °C, material anchored to the molybdenum patterns is found to easily ablate.

high carrier mobility of up to 200 cm<sup>2</sup> V<sup>-1</sup> s<sup>-1</sup>, photoluminescence (PL) enhancement up to  $4 \times 10^{-3}$ , and strong spin-orbit coupling.<sup>[2–8]</sup> Therefore, MoS<sub>2</sub> has a great potential for applications in the production of future electronic and optoelectronic devices.

As with most materials, defects such as grain boundaries play a critical, and often detrimental, role in their properties. Theoretical investigations, based on density functional theory,<sup>[9]</sup> reveal that grain boundaries can noticeably change the electronic structure of monolayer MoS<sub>2</sub> due to induced midgap states, while experiments have confirmed the optical and electrical properties of monolayer MoS<sub>2</sub> can be strongly affected by grain boundaries.<sup>[10]</sup>

Both the fabrication method of the 2D material as well as any postfabrication processing may contribute significantly to the quality and crystallinity of the material.

Traditional mechanical exfoliation has been shown to produce extremely high-quality and highly crystalline material; however, it is often in quantities useful only for laboratory research. Chemical vapor deposition (CVD) has emerged as one of the most common synthesis routes for thin-film TMD growth.<sup>[11–18]</sup> The process involves the direct chemical vapor phase reaction of an oxide precursor and chalcogen powder, which may result in the formation of many high-quality and large (tens to hundreds of square micrometer) single crystals, though the nucleation tends to be random and the coverage often incomplete or not of uniform thickness.<sup>[13,15,19,20]</sup> Large-area growth has been achieved through the reaction of thin transition metal films with a chalcogen precursor.<sup>[12,21–26]</sup> However, the growth may depend sensitively on the quality of the predeposited material, with the resulting TMD inheriting the amorphous nature of the deposited seed layer, resulting in small crystal domain sizes of the order of tens to hundreds of square nanometer.


It has been shown that the morphology, substrate–material bonding, defect density, and optical and electrical performance of monolayer MoS<sub>2</sub> can be modified and often improved through thermal annealing. Thermal annealing under vacuum has shown an enhancement in the PL intensity due to the introduction of anion vacancies in monolayer MoS<sub>2</sub>.<sup>[27]</sup> Also, improvement in electrical performance of MoS<sub>2</sub> field effect transistors has been observed after in situ thermal annealing under vacuum.<sup>[28]</sup>

## 1. Introduction

The field of 2D materials has been attracting significant attention since the successful isolation of monolayer graphene.<sup>[1]</sup> A growing collection of layered materials has since been investigated showing exceptional characteristics such as high mobilities, semiconducting and superconducting behavior, ferromagnetism, and excellent thermal properties. Among these are transition metal dichalcogenides (TMDs), a class of layered materials that demonstrate a progressive confinement-induced shift from an indirect- to a direct-gap semiconductor in the monolayer limit.<sup>[2]</sup> The most studied of these, monolayer MoS<sub>2</sub>, has shown

M. Bizhani, R. Thorat, W. Poston, Dr. T. Wickramasinghe, Prof. E. Stinaff  
 Department of Physics and Astronomy  
 Nanoscale and Quantum Phenomena Institute  
 Ohio University  
 Athens, OH 45701, USA  
 E-mail: stinaff@ohio.edu

Prof. S. H. Aleithan  
 Department of Physics  
 College of Science  
 King Faisal University  
 P.O. Box 400, Al-Ahsa 31982, Saudi Arabia

 The ORCID identification number(s) for the author(s) of this article can be found under <https://doi.org/10.1002/pssb.202000426>.

DOI: 10.1002/pssb.202000426

In situ two-cycle thermal annealing studies of monolayer MoS<sub>2</sub> film on Si/SiO<sub>2</sub>, up to 305 °C have shown that the film–substrate bonding was significantly improved and polymer residues were burned off, which altered and improved the optical and electrical performance of MoS<sub>2</sub>.<sup>[28]</sup> It has also been shown that thermal stress can be used to crystallize amorphous MoS<sub>2</sub>. R. H. Kim demonstrated that local heating of amorphous ultrathin MoS<sub>2</sub> films via a pulsed light source up to 390 °C resulted in crystallization of semiconductor 2D materials.<sup>[29]</sup>

This work presents optical investigations into the quality and crystallinity of as-grown and thermally annealed 2D MoS<sub>2</sub> produced using a novel CVD technique.<sup>[30]</sup> Here, monolayer MoS<sub>2</sub> is produced using a technique by which material is found to grow around lithographically defined patterns of bulk transition metals. Unlike the aforementioned sulfurization of thin metal films, the resulting material in this case migrates outward along the substrate, forming highly crystalline films with domain sizes of the order of tens of micrometers.<sup>[30,31]</sup> In addition, the material typically remains physically and electrically contacted to the residual bulk transition metal patterns, which results in as-grown, naturally contacted, and controllably located mono-to-few-layer TMD material.

## 2. Results and Discussion

Monolayer MoS<sub>2</sub> samples were grown on Si/SiO<sub>2</sub> substrates using a variation of the CVD technique described in a previous work.<sup>[30]</sup> This technique has been used to produce as-grown device structures and complex material geometries.<sup>[32,33]</sup> At typical growth temperatures, around 750 °C, the MoS<sub>2</sub> forms a continuously connected film around the bulk transition metal pattern and no random, unconnected, MoS<sub>2</sub> growth is observed. At higher growth temperatures, around 850 °C, the MoS<sub>2</sub> more easily migrates away from the patterns and may form isolated, free, regions of material, as shown in Figure 1d. This allows for the concurrent investigation of what we will term as “free” and “anchored” material.

PL was used as the primary tool for analysis (typical spectra acquired from the material are shown in Figure 2 and 3). There has been an enormous amount of work published related to the PL from thin-film MoS<sub>2</sub> following from the first reports of bright emission in the monolayer limit.<sup>[2,34]</sup> Multilayer MoS<sub>2</sub> has an indirect bandgap determined by the valence band maximum located at the  $\Gamma$ -point and the conduction band minimum, midway between the  $K$  and  $\Gamma$ -points and tends to show weak emission. As the number of layers reduces, peaks in the visible range, related to a direct-gap transition at the  $K(K')$  point, increase dramatically in intensity and the near-IR emission from the indirect transition severely blueshifts and effectively vanishes. This direct-gap region gives rise to the well-studied A and B exciton states derived from the spin–orbit split valence band and the degenerate conduction band. Throughout the literature, the energies of these excitonic peaks often display variability, although the lower energy A peak to be around 1.85 eV (670 nm) and the higher energy B peak around 2 eV (620 nm). This variability may arise from the sensitivity of the monolayer material to external factors such as substrate, dielectric environment, and strain.<sup>[35–37]</sup> It has been shown that

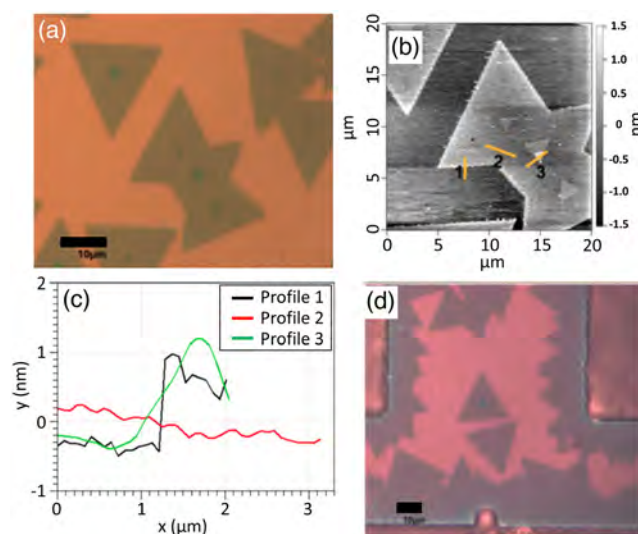


**Figure 1.** a) Optical image of “free” monolayer MoS<sub>2</sub> material. b) Atomic force microscopy image of the three merged triangles shown in (a). c) Extracted line scans from the AFM image indicating monolayer thickness (profile 1), continuous film over a region where the individual triangular single crystals merge (profile 2), and bilayer growth in the center (profile 3). d) Larger area optical image demonstrating the concurrent formation of isolated “free” monolayer MoS<sub>2</sub> material and “anchored” monolayer MoS<sub>2</sub> material around the bulk molybdenum patterns. The scale bars in (a) and (d) are both 10  $\mu$ m.

strain can induce a large redshift in the optical bandgap of 99 meV/%,<sup>[38]</sup> while the specific substrate for CVD-grown material may give rise to both strain and charge doping effects.<sup>[39]</sup> In addition to shifts of the main neutral exciton peaks, additional emission peaks may be observed, the most common being the negatively charged exciton, or negative trion ( $A^-$ ),<sup>[40]</sup> which is sensitive to carrier density and appears  $\approx 20$  meV lower in energy than the A peak. Finally, impurities and defects can result in the emergence of new peaks or relaxation channels such as impurity bound excitons and free-to-bound transitions.<sup>[41]</sup> It has been shown that the B/A intensity ratio is a measure of the defect density and the relative magnitude of nonradiative relaxation channels, where a low B/A ratio is indicative of low defect density.<sup>[42]</sup>

With the many possible relaxation pathways and effects, unambiguous identification of those most affected by thermal annealing is challenging at best. We are currently in the process of performing additional experiments including electrical gating to tune carrier density, excitation power dependence, and time-resolved measurements to gain insight into recombination mechanisms. For the current study we restrict our analysis to PL line shapes and intensity ratios. All the spectra, discussed in more detail subsequently, are best fitted by two Lorentzian peaks. Although this might suggest predominantly neutral A and B excitons and low carrier concentrations, it will be important to track the separation between the A and B peaks ( $\Delta_{AB}$ ). With strain-induced changes in the spectra, the A and B peaks have been reported to move in tandem,<sup>[43]</sup> while variations in the separation would suggest the emergence of new peaks.<sup>[41]</sup> As discussed earlier, such peaks may arise from the emergence or suppression of trions or impurity states. As reported elsewhere,<sup>[42]</sup>

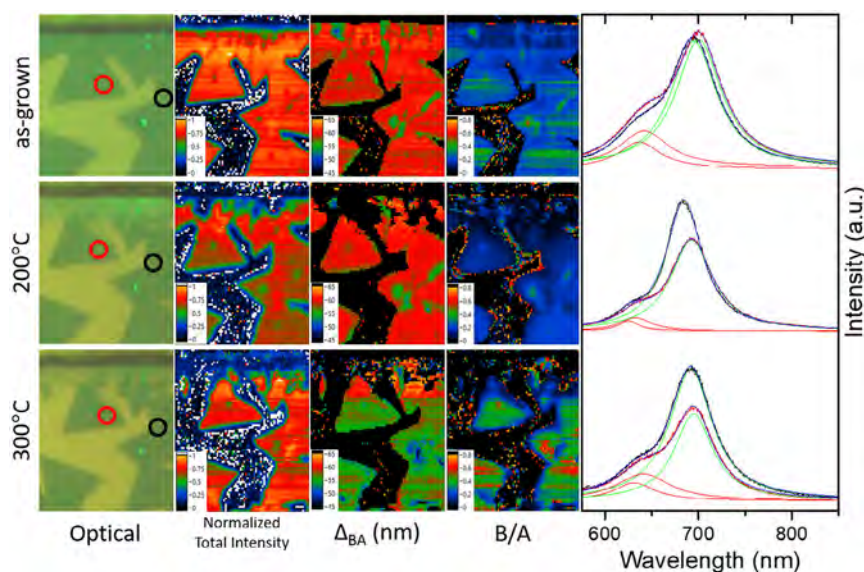


**Figure 2.** A sequence of results of “anchored” material from the sample shown in Figure 1a–c. Each row consists of an optical image, normalized total intensity, separation of the peaks labeled A and B, the ratio of the intensities of the B to A peak, and representative spectra from the circled regions in the optical images. The colored maps were derived from fits to the spectra at each of the positions to a sum of two Lorentzians. Examples of such fits are shown in the representative spectra. PL spectra were taken using a 532 nm laser with either a 50× (0.85 NA) or 100× (0.90 NA) objective lens. The laser power was maintained at  $\approx 1$  mW.

the ratio of the B to A intensities (B/A) can give insight into the defect density in the material. Therefore, we will also track the variation of B/A as we anneal the samples.

With these points in mind, we will first consider the “anchored” material, a region clearly connected to the bulk molybdenum pattern, which was identified and characterized as shown in **Figure 2**. All PL measurements were taken at room temperature using a 532 nm laser with either a 50× (0.85 NA) or 100× (0.90 NA) objective lens. The samples were annealed at temperatures of 200 and 300 °C. For the “free” material we also annealed at 400 °C. For the annealing process, the sample was placed on a graphite boat at the center of a 2 in. diameter quartz tube within the furnace, which was flushed with ultrahigh purity Ar gas at a rate of 0.5 LPM for 30 min. The furnace was then brought up to the desired annealing temperature while a constant flow of Ar was maintained. The sample stayed at the target temperature and was brought back to room temperature naturally after 30 min. The PL spectrum of the sample was taken at room temperature after annealing. Interestingly for the “anchored” material, upon completing the first anneal step at 200 °C, it was found that the material ablated at laser powers comparable to those used to characterize the “free” regions ( $\approx 1$  mW). The ablation of the material occurs in the region closest to the contact and may be due to a decrease in the crystallinity of the material near the contact or possibly a thermally induced separation of the material from the substrate. Although others have observed laser-induced thinning of few-layer MoS<sub>2</sub>,<sup>[44]</sup> the reported powers at which this occurs were an order of magnitude higher than used here and even with such high powers, it was reported that the monolayer would remain. Further investigations are currently underway to determine the mechanism leading to this laser ablation. In spite of the loss of material

adjacent to the contact, there was enough remaining material to analyze. **Figure 2** shows a series of data taken after annealing the sample at 200 and 300 °C along with the as-grown data. The ablation mentioned previously can be clearly seen in the sequence of optical images in the first column. The two circled regions in the optical images correspond to the highlighted spectra in the right-most column. Looking first at these representative spectra, there is a clear blueshift and an increase in intensity of the black region relative to the red region. Correlating this with the change in the peak separation,  $\Delta_{AB}$ , and B/A ratio suggests that the shifting of the peaks may be related to the emergence of other lines as opposed to strain. A narrowing of the linewidth for the lower energy peak is also observed with annealing. This could indicate a change in the homogeneity or lifetime of the associated recombination. We are currently working to acquire time-resolved measurements to further investigate these effects.

For comparison we have also investigated the PL properties of “free” material. **Figure 1a–c** shows the optical image and atomic force microscopy (AFM) image of a merged set of MoS<sub>2</sub> triangular single crystals (20  $\mu$ m in width) on which PL measurements were performed. Similar to **Figure 2**, **Figure 3** shows a series of data taken after annealing the sample at 200, 300, and 400 °C along with the as-grown data. Unlike the “anchored” material, no obvious physical change is observed in the optical images until the 400 °C anneal, at which point visible cracks begin to emerge along grain boundaries. Similar to the spectra for the “anchored” material, there is a clear blueshift for both regions. Although we were unable to obtain similar signal-to-noise ratios to those of the “anchored” regions, tentative correlation of the blueshift with the change in the peak separation,  $\Delta_{AB}$ , and B/A ratio again suggests that the shifting of the peaks may be related



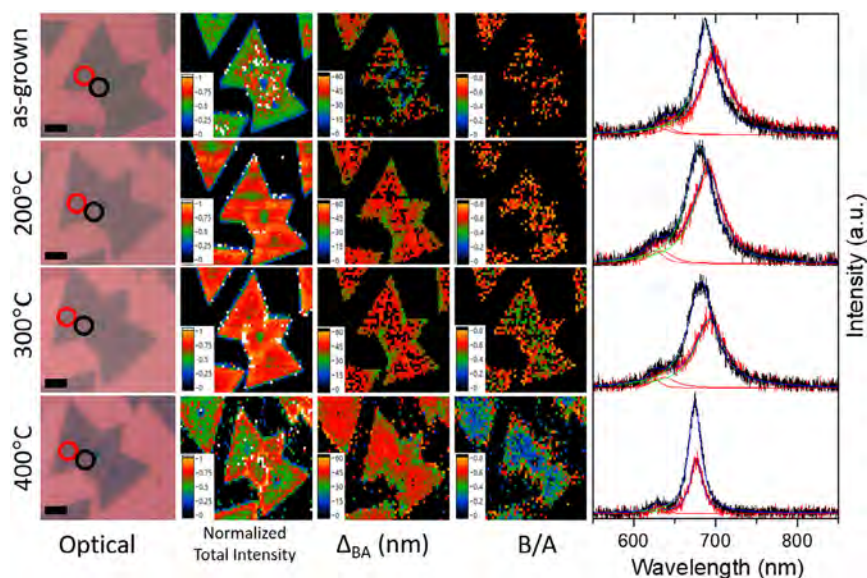


**Figure 3.** A sequence of results of “free” material from the sample shown in Figure 1a–c. Each row consists of an optical image, normalized total intensity, separation of the peaks labeled A and B, the ratio of the intensities of the B to A peak, and representative spectra from the circled regions in the optical images. The colored maps were derived from fits to the spectra at each of the positions to a sum of two Lorentzians. Examples of such fits are shown in the representative spectra. PL spectra were taken using a 532 nm laser with either a 50× (0.85 NA) or 100× (0.90 NA) objective lens. The laser power was maintained at  $\approx 1$  mW.

to the emergence of other lines as opposed to strain. Again, a narrowing of the linewidth for the lower energy peak is also observed with annealing. Looking at the “Normalized Total Intensity” column in Figure 3 for 200 and 300 °C respectively, a more uniform PL map is observed. For example, the PL intensity of the film in the regions highlighted by the red circle compared to the PL intensity of the grain boundary within the black circle became highly uniform after annealing the sample up to 300 °C. The sample was then further annealed at 400 °C, which resulted in enhanced PL around the grain boundary region, similar to the as-grown measurements. As mentioned, although the optical image of the sample after annealing at 400 °C showed no obvious changes in the size or orientation of the flakes, cracks

along the grain boundaries were observed. Again, correlating this change in intensity with the change in the peak separation,  $\Delta_{AB}$ , and B/A ratio suggests that these effects may be related to the emergence of other lines as opposed, or in addition, to strain. We note that previous studies have shown that the structure of the crystal at the grain boundaries can be molybdenum (Mo) or sulfur (S) rich, which would result in n- or p-doping in the grain boundary region, respectively.<sup>[10]</sup> A potential explanation for the nonuniform PL map after annealing the sample at 400 °C is that the structure of the MoS<sub>2</sub> crystal along the cracks contains dangling bonds that act as absorption centers and p-dope the region by absorbing impurities such as O<sub>2</sub> or H<sub>2</sub>O as has been reported previously.<sup>[45]</sup> Raman spectroscopy analysis

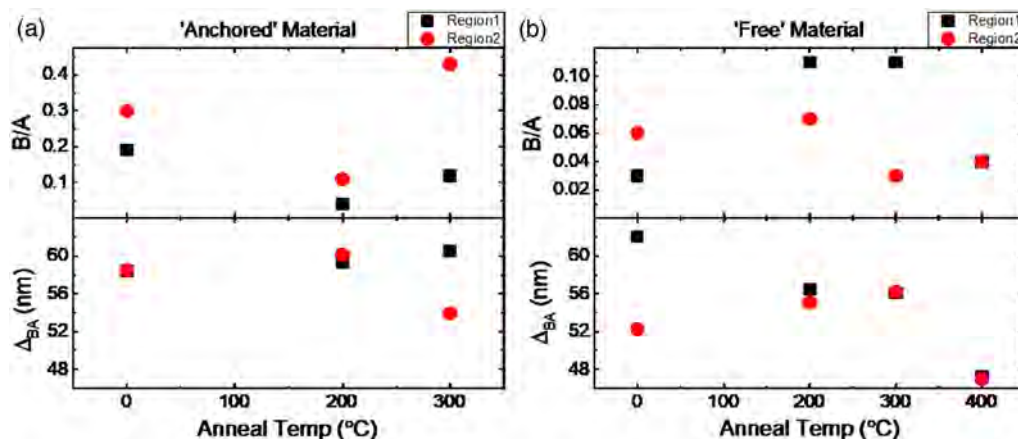


**Figure 4.** Plots of the separation of the peaks labeled A and B, and the ratio of the intensities of the B to A peak, extracted from the fits to the representative spectra from the circled regions in the optical images in Figure 2 and 3.



of the region, presented in the Supporting Information, indicates that while the  $E_{2g}^1$  mode remains the same, the  $A_{1g}$  mode blueshifts  $\approx 2\text{ cm}^{-1}$  at the cracks when compared to the monolayer region, which implies that the cracks may be p-doped.<sup>[46]</sup> This may also be an explanation for some of the inhomogeneities in intensity observed in the “anchored” material. **Figure 4** plots the values for the peak separation,  $\Delta_{AB}$ , and the B/A ratio extracted from the fits to the spectra in Figure 2 and 3. There appear to be opposite trends with regard to the B/A ratio for the “anchored” versus “free” material, whereas for both, the peak separation either slightly decreases or remains constant. These results suggest potential differences in the doping and/or defects for the two, laying the foundation for further studies into their specific origins.

### 3. Conclusion

The production of large areas of high-quality, crystalline, 2D material is necessary for industrial-scale applications. Although large-area film growth has been demonstrated, it is often amorphous and with variable thickness. In this work, the effect of postgrowth thermal annealing of 2D MoS<sub>2</sub> was investigated on material grown using a novel CVD technique that results in large areas of self-contacted material with large crystal domains. Under certain growth conditions random nucleation also occurred resulting in isolated triangular crystalline regions of “free” material. PL investigations revealed a blueshift in the emission along with the intensity becoming more uniform across the monolayer up to 300 °C, whereas, at 400 °C the monolayer began to crack along the grain boundaries. Interestingly, it was found that the contacted, or “anchored,” material became highly susceptible to laser ablation after the first annealing step at 200 °C. This may indicate a thermally induced separation of the material from the substrate or reduced crystallinity near the contacts. Further experiments are underway to determine the cause of this observation. PL investigations of the remaining “anchored” material revealed similar results to those for the “free” material, although differences were observed in the homogeneity of the PL intensity. These results lay a foundation for continued investigations of these naturally contacted CVD-grown materials where a deeper understanding would provide valuable insight into the nucleation, growth mechanism, and defect properties for the material.

### Supporting Information

Supporting Information is available from the Wiley Online Library or from the author.

### Acknowledgements

This work was supported by the Ohio University Innovation Strategy as well as the Ohio University Nanoscale & Quantum Phenomena Institute. The authors extend their appreciation to the Deputyship for Research and Innovation, Ministry of Education in Saudi Arabia for funding this research work through the project number (776).

### Conflict of Interest

The authors declare no conflict of interest.

### Keywords

2D materials, chemical vapor deposition, MoS<sub>2</sub>, photoluminescence, Raman, transition metal dichalcogenides

Received: July 31, 2020

Revised: November 22, 2020

Published online: January 15, 2021

- [1] K. S. Novoselov, A. K. Geim, S. V. Morozov, D. Jiang, Y. Zhang, S. V. Dubonos, I. V. Grigorieva, A. A. Firsov, *Science* **2004**, 306, 666.
- [2] K. F. Mak, C. Lee, J. Hone, J. Shan, T. F. Heinz, *Phys. Rev. Lett.* **2010**, 105, 136805.
- [3] X. Xu, W. Yao, D. Xiao, T. F. Heinz, *Nat. Phys.* **2014**, 10, 343.
- [4] Q. H. Wang, K. Kalantar-Zadeh, A. Kis, J. N. Coleman, M. S. Strano, *Nat. Nanotechnol.* **2012**, 7, 699.
- [5] H. Zeng, X. Cui, *Chem. Soc. Rev.* **2015**, 44, 2629.
- [6] K. J. Koski, Y. Cui, *ACS Nano* **2013**, 7, 3739.
- [7] A. Splendiani, L. Sun, Y. Zhang, T. Li, J. Kim, C.-Y. Chim, G. Galli, F. Wang, *Nano Lett.* **2010**, 10, 1271.
- [8] M. Chhowalla, H. S. Shin, G. Eda, L.-J. Li, K. P. Loh, H. Zhang, *Nat. Chem.* **2013**, 5, 263.
- [9] W. Zhou, X. Zou, S. Najmaei, Z. Liu, Y. Shi, J. Kong, J. Lou, P. M. Ajayan, B. I. Yakobson, J.-C. Idrobo, *Nano Lett.* **2013**, 13, 2615.
- [10] A. M. van der Zande, P. Y. Huang, D. A. Chenet, T. C. Berkelbach, Y. You, G.-H. Lee, T. F. Heinz, D. R. Reichman, D. A. Muller, J. C. Hone, *Nat. Mater.* **2013**, 12, 554.
- [11] Y. Shi, H. Li, L.-J. Li, *Chem. Soc. Rev.* **2015**, 44, 2744.
- [12] Y. Zhan, Z. Liu, S. Najmaei, P. M. Ajayan, J. Lou, *Small* **2012**, 8, 966.
- [13] Y.-H. Lee, X.-Q. Zhang, W. Zhang, M.-T. Chang, C.-T. Lin, K.-D. Chang, Y.-C. Yu, J. T.-W. Wang, C.-S. Chang, L.-J. Li, T. W. Lin, *Adv. Mater.* **2012**, 24, 2320.
- [14] Y. Shi, W. Zhou, A.-Y. Lu, W. Fang, Y.-H. Lee, A. L. Hsu, S. M. Kim, K. K. Kim, H. Y. Yang, L.-J. Li, J. C. Idrobo, *Nano Lett.* **2012**, 12, 2784.
- [15] C. Cong, J. Shang, X. Wu, B. Cao, N. Peimyoo, C. Qiu, L. Sun, T. Yu, *Adv. Opt. Mater.* **2014**, 2, 131.
- [16] M. Okada, T. Sawazaki, K. Watanabe, T. Taniguchi, H. Hibino, H. Shinohara, R. Kitaura, *ACS Nano* **2014**, 8, 8273.
- [17] Y. Zhang, Y. Zhang, Q. Ji, J. Ju, H. Yuan, J. Shi, T. Gao, D. Ma, M. Liu, Y. Chen, X. Song, *ACS Nano* **2013**, 7, 8963.
- [18] A. L. Elias, N. Perea-Lopez, A. Castro-Beltran, A. Berkdemir, R. Lv, S. Feng, A. D. Long, T. Hayashi, Y. A. Kim, M. Endo, H. R. Gutiérrez, *ACS Nano* **2013**, 7, 5235.
- [19] J. Xia, X. Huang, L.-Z. Liu, M. Wang, L. Wang, B. Huang, D.-D. Zhu, J.-J. Li, C.-Z. Gu, X.-M. Meng, *Nanoscale* **2014**, 6, 8949.
- [20] J.-K. Huang, J. Pu, C.-L. Hsu, M.-H. Chiu, Z.-Y. Juang, Y.-H. Chang, W.-H. Chang, Y. Iwasa, T. Takenobu, L.-J. Li, *ACS Nano* **2014**, 8, 923.
- [21] D. Kong, H. Wang, J. J. Cha, M. Pasta, K. J. Koski, J. Yao, Y. Cui, *Nano Lett.* **2013**, 13, 1341.
- [22] Y.-C. Lin, W. Zhang, J.-K. Huang, K.-K. Liu, Y.-H. Lee, C.-T. Liang, C.-W. Chu, L.-J. Li, *Nanoscale* **2012**, 4, 6637.
- [23] J.-G. Song, J. Park, W. Lee, T. Choi, H. Jung, C. W. Lee, S.-H. Hwang, J. M. Myoung, J.-H. Jung, S.-H. Kim, C. Lansalot-Matras, *ACS Nano* **2013**, 7, 11333.
- [24] X. Wang, H. Feng, Y. Wu, L. Jiao, *J. Am. Chem. Soc.* **2013**, 135, 5304.
- [25] P. T. K. Loan, W. Zhang, C.-T. Lin, K.-H. Wei, L.-J. Li, C.-H. Chen, *Adv. Mater.* **2014**, 26, 4838.

- [26] R. Gatensby, N. McEvoy, K. Lee, T. Hallam, N. C. Berner, E. Rezvani, S. Winters, M. O'Brien, G. S. Duesberg, *Appl. Surf. Sci.* **2014**, 297, 139.
- [27] S. Tongay, J. Suh, C. Ataca, W. Fan, A. Luce, J. S. Kang, J. Liu, C. Ko, R. Raghunathanan, J. Zhou, F. Ogletree, J. Li, J. C. Grossman, J. Wu, *Sci. Rep.* **2013**, 3, 2657.
- [28] L. Su, Y. Yu, L. Cao, Y. Zhang, *Phys. Rev. Appl.* **2017**, 7, 034009.
- [29] R. H. Kim, J. Leem, C. Muratore, S. Nam, R. Rao, A. Jawaideh, M. Durstock, M. McConney, L. Drummy, R. Rai, A. Voevodin, N. Glavin, *Nanoscale* **2019**, 11, 13260.
- [30] S. Khadka, M. Lindquist, S. H. Aleithan, A. N. Blumer, T. E. Wickramasinghe, M. E. Kordesch, E. Stinaff, *Adv. Mater. Interfaces* **2017**, 4, 1600599.
- [31] G. H. Han, N. J. Kybert, C. H. Naylor, B. S. Lee, J. Ping, J. H. Park, J. Kang, S. Y. Lee, Y. H. Lee, R. Agarwal, A. T. C. Johnson, *Nat. Commun.* **2015**, 6, 6128.
- [32] S. Khadka, T. E. Wickramasinghe, M. Lindquist, R. Thorat, S. H. Aleithan, M. E. Kordesch, E. Stinaff, *Appl. Phys. Lett.* **2017**, 110, 261109.
- [33] S. Aleithan, T. Wickramasinghe, M. Lindquist, S. Khadka, E. Stinaff, *ACS Omega* **2019**, 4, 9557.
- [34] A. Splendiani, L. Sun, Y. Zhang, T. Li, J. Kim, C.-Y. Chim, G. Galli, F. Wang, *Nano Lett.* **2010**, 10, 1271.
- [35] M. Buscema, G. A. Steele, H. S. J. van der Zant, A. Castellanos-Gomez, *Nano Res.* **2014**, 7, 561.
- [36] Y. Lin, X. Ling, L. Yu, S. Huang, A. L. Hsu, Y. H. Lee, J. Kong, M. S. Dresselhaus, T. Palacios, *Nano Lett.* **2014**, 14, 5569.
- [37] A. Castellanos-Gomez, R. Roldán, E. Cappelluti, M. Buscema, F. Guinea, H. S. J. Van Der Zant, G. A. Steele, *Nano Lett.* **2013**, 13, 5361.
- [38] D. Lloyd, X. Liu, J. W. Christopher, L. Cantley, A. Wadehra, B. L. Kim, B. B. Goldberg, A. K. Swan, J. S. Bunch, *Nano Lett.* **2016**, 16, 5836.
- [39] W. H. Chae, J. D. Cain, E. D. Hanson, A. A. Murthy, V. P. Dravid, *Appl. Phys. Lett.* **2017**, 111, 143106.
- [40] K. F. Mak, K. He, C. Lee, G. H. Lee, J. Hone, T. F. Heinz, J. Shan, *Nat. Mater.* **2013**, 12, 207.
- [41] D. Kaplan, K. Mills, J. Lee, S. Torrel, V. Swaminathan, *J. Appl. Phys.* **2016**, 119, 214301.
- [42] K. M. McCreary, A. T. Hanbicki, S. V. Sivaram, B. T. Jonker, *APL Mater.* **2018**, 6, 111106.
- [43] K. He, C. Poole, K. F. Mak, J. Shan, *Nano Lett.* **2013**, 13, 2931.
- [44] A. Castellanos-Gomez, M. Barkelid, A. M. Goossens, V. E. Calado, H. S. J. van der Zant, G. A. Steele, *Nano Lett.* **2012**, 12, 3187.
- [45] H. Nan, Z. Wang, W. Wang, Z. Liang, Y. Lu, Q. Chen, D. He, P. Tan, F. Miao, X. Wang, J. Wang, Z. Ni, *ACS Nano* **2014**, 8, 5738.
- [46] B. Chakraborty, A. Bera, D. V. S. Muthu, S. Bhowmick, U. V. Waghmare, A. K. Sood, *Phys. Rev. B* **2012**, 85, 161403.

# Effects of Surface Orientation and Termination Plane on Glass-to-Crystal Transformation of Lithium Disilicate by Molecular Dynamics Simulations

Wei Sun, Volkmar Dierolf, and Himanshu Jain\*

Dedicated to Professor David A. Drabold on the occasion of his 60th birthday

Glass-to-crystal transformation of lithium disilicate is studied using molecular dynamics simulations using an effective partial charge potential. The structural evolution of the interface between glassy and crystalline lithium disilicate is analyzed to simulate crystallization of glass on pre-existing crystal seeds. Besides previously used atomic number density, the distribution of  $Q_n$  species (Si tetrahedra with  $n$  bridging oxygen) is shown to be an effective parameter for following this transformation quantitatively. The early stages of crystal growth are significantly affected by the orientation and termination of the surface of adjacent crystal, as indicated by calculated atomic density, partial ordering, atomic segregation, and an increase in  $Q_3$  concentration. In particular, under-coordinated Si within the outer crystal layer is found to be most effective in transforming the amorphous structure toward crystallinity. The increase in  $Q_3$  in the glass close to interface region most clearly shows the initial stage of lithium disilicate crystal growth.

## 1. Introduction

Lithium silicate glasses have been studied extensively for years, owing to their applications in scintillators<sup>[1]</sup> and commercial glass-ceramics.<sup>[2,3]</sup> The crystallization behavior of lithium silicate glass systems has been investigated experimentally for decades and continues to be an active research area of glass science. In addition, lithium silicate glasses serve as model systems in nucleation and crystal growth studies due to their convenient glass formation and homogenous nucleation,<sup>[4]</sup> which has been observed and reported by a variety of experimental techniques.<sup>[5–11]</sup> In general, lithium disilicate glass (LS2-glass) with composition  $\text{Li}_2\text{O}-2\text{SiO}_2$  has a propensity to nucleate lithium disilicate (LS2-crystal) crystal phase.<sup>[12]</sup> Nevertheless, the lack of knowledge of structural evolution of crystallization of lithium silicate glass systems limits the ability to further understand, control, and to


predict the underlying processes and phenomena. For example, it has been a continuing challenge to reconcile many orders of magnitude discrepancy between the observed and predicted rates of crystallization of LS2-glass.<sup>[13–15]</sup>

Classical molecular dynamics (MD) simulations of crystal and glass systems<sup>[16–19]</sup> have been used to provide insights into short and medium-range structures. McKenzie et al. reported the hybrid MD and Monte Carlo simulations of crystal nucleation of lithium disilicate glasses<sup>[20]</sup> via an implicit glass model, where the growing cluster matches the experimental structure. The interface model that combines crystal and glass parts has been used to simulate the crystal growth of glass using different crystal seeds, yet the computational characterization of glassy

and crystalline structures in the interface region remains challenging and poorly understood. Garofalini and co-workers reported a series of MD simulations regarding silica and alumina, including the structures of silica/alumina interfaces,<sup>[21]</sup> calcium silicate/alumina interfaces,<sup>[22]</sup> and calcium-aluminosilicate glasses/alumina interfaces.<sup>[23,24]</sup> Jiang and Garofalini reported an MD study on  $\beta\text{-Si}_3\text{N}_4$ /rare-earth-doped silicon oxynitride glassy interfaces and found crystal growth on the prism surface in  $\beta\text{-Si}_3\text{N}_4$ .<sup>[25]</sup> Rushton et al.<sup>[26]</sup> showed distinct atomic density profiles of interfaces between sodium lithium borosilicate and different  $\text{MgO}/\text{CaO}$  crystal surfaces. Sun and Du<sup>[27]</sup> reported that in the MD simulated  $\text{MgAl}_2\text{O}_4$ /aluminoborosilicate glass<sup>[27]</sup> interface, a highly ordered  $[\text{SiO}_4]$  tetrahedron layer forms near Al-terminated  $\text{MgAl}_2\text{O}_4$  crystal.

The characterization of crystallization at an interface can be difficult to assess and may depend on the parameter used to distinguish crystallinity from amorphousness. In the early studies mentioned earlier, this distinction was based on the atomic density profiles along the interface normal. Recently, Sun and Du<sup>[27,28]</sup> reported the structures of interfacial region between aluminoborosilicate glass and  $\text{MgAl}_2\text{O}_4$  spinel crystals using the recently developed classic interatomic potentials.<sup>[29]</sup> The results show that the coordination number changes, and the bond distance between O and Al/B atoms can be a useful indicator of crystallization of glass owing to the distinct

Dr. W. Sun, Prof. V. Dierolf, Prof. H. Jain  
Institute for Functional Materials and Devices  
Lehigh University  
Bethlehem, PA 18015, USA  
E-mail: h.jain@lehigh.edu

 The ORCID identification number(s) for the author(s) of this article can be found under <https://doi.org/10.1002/pssb.202000427>.

DOI: 10.1002/pssb.202000427

coordination number of such species in the two states. However, these parameters are not useful for identifying the boundary between glassy and crystalline lithium disilicate, as the local structure around Si defined by  $\text{SiO}_4$  tetrahedral units is very similar for the two cases. On the other hand, the medium-range order, which depicts larger structures, indicates quite distinct glass former units in crystalline and glassy states.<sup>[30,31]</sup> An example of such distinctive characteristic is the distribution of bridging oxygen ( $n$ ) around silicon atoms, called  $Q_n$  species in silicate compositions, which has been compared experimentally in crystal versus glass by magic angle spinning nuclear magnetic resonance (MAS-NMR).<sup>[32]</sup>

Although much of the current knowledge has been acquired in terms of the structural behavior of crystal/glass interfaces from computational studies, a comprehensive understanding of interfacial behavior such as the role of crystal orientation and a rigorous characterization of crystalline and glassy phase in the lithium disilicate system is still lacking. Accordingly, the aim of this work is to investigate the crystal growth process by focusing on the congruent transformation of glass to an existing crystal within a model system that has been investigated most extensively experimentally: lithium disilicate glass (LS2-glass) to crystal (LS2-crystal) conversion by examining the crystal/glass interface region. In particular, we explore the effect of how the crystal's orientation and surface termination in contact with glass may affect the growth of perfect LS2-crystal from the random glassy matrix of the same average composition. This information about the interfacial region will help us understand the early stages of homogeneous single crystal growth without the complications of chemical effects encountered in heterogeneous crystal growth. Here, we also investigated the usefulness of the  $Q_n$  distribution analysis as a medium-range order parameter for characterizing glass  $\rightarrow$  crystal transformation.

## 2. Computational Methods and Models

DL\_POLY package was used to carry out the classic MD simulations of glass and glass/crystal interfaces. Integration of the equation of motion was carried out using the Velocity Verlet method with a time step of 1 fs. The ion-ion interactions included long-range coulombic and short-range Buckingham terms, where fractional charge potentials were used to describe the partial covalent and partial ionic nature of the chemical bonding. The Buckingham potential is given by

$$V_{ij}(r_{ij}) = A_{ij} \exp\left(-\frac{r_{ij}}{\rho_{ij}}\right) - \frac{C}{r_{ij}^6} \quad (1)$$

where  $r_{ij}$  represents the interatomic distance between atoms  $i$  and  $j$ ;  $A$ ,  $\rho$ , and  $C$  are the fitting parameters for this potential. Their values along with charges for short-range interactions are given in Table 1.<sup>[29,33]</sup> For the simulation of bulk lithium disilicate ( $\text{Li}_2\text{Si}_2\text{O}_5$ ) crystal, a classical atomistic method is adopted using General Utility Lattice Program (GULP)<sup>[34]</sup> with the potential parameters listed in Table 1. Good agreement between the calculated and experimental LS2-crystal lattice parameters along with calculated stable crystal cell at low temperatures with isothermal-isobaric NPT ensemble (note that N, P, T, V, and E in NPT, NVE, and NVT stand for total number of atoms,

**Table 1.** Atomic charges and Buckingham potential parameters.<sup>[29,33]</sup>

Pairs	$A_{ij}$ [eV]	$\rho_{ij}$ [Å]	$C_{ij}$ [eV Å <sup>6</sup> ]
$\text{O}^{-1.2}-\text{O}^{-1.2}$	2029.2204	0.343645	192.58
$\text{Si}^{2.4}-\text{O}^{-1.2}$	13702.905	0.193817	54.681
$\text{Li}^{0.6}-\text{O}^{-1.2}$	41051.9380	0.151160	0.000

pressure, temperature, volume, and total energy, respectively) validates the structure generated using these potential sets (please see Supporting Information).

A slab model with applied 3D periodic boundary condition is adopted to simulate the crystal/glass interface. The initial configuration contains the LS2-glass layer and as-cleaved crystal surface layer of LS2-crystal. For the crystal surface half, slab models for lithium disilicate (001), (010), (100), and (110) faces were generated based on as-cleaved, optimized LS2-crystal without allowing any relaxation of the established lattice. It is shown in Figure 1 that each LS2-crystal surface model has unique surface termination that characterizes the exposed outer layer. The surface slab consists of repeated layers stacking along surface normal direction (identified as  $z$ -direction), with terminated full or half repetitive layer on the two sides. For example, the LS2(110) surface model has  $\text{SiO}$  termination on the right-hand side and  $\text{SiO}_2$  termination on the left-hand side, which are both part of the  $\text{Si}_2\text{O}_3$  layer within the layer sequence. In addition, two LS2(001) surfaces, LS2(001)-a and LS2(001)-b, with different terminations were simulated to investigate the effect of crystal surface termination on an interface structure. LS2(001)-a has  $\text{Si}_2\text{O}_3$  termination on one side and  $\text{O}_2$  on the other side, whereas LS2(001)-b contains  $\text{Si}_2\text{O}_5$  termination on both sides. Figure 1 shows the schematic structures of all the  $\text{Li}_2\text{Si}_2\text{O}_5$  crystal planes investigated in this study. The cleaved LS2-crystal (100), (010), (110), (001)-a, and (001)-b surface slabs for interface building contain 864, 2160, 864, 720, and 720 atoms, respectively.

To build the crystal/glass interface, the  $x$  and  $y$  dimensions of simulated glass cell were designed the same as the adjacent LS2-crystal surface cell, as shown in Figure 2. The four chosen crystal surface cells in this study were cleaved with different  $x$ ,  $y$ , and  $z$  dimensions; therefore, four glass cells with corresponding  $x$  and  $y$  dimensions were generated. As all the glass cells have the same density and numbers of atoms, the  $z$  dimensions of glass cells were determined accordingly. The initial glass model was generated with 2160 atoms by randomly placing all the atoms into the corresponding cell. This step was followed by heating the cell to 6000 K using constant volume NVT and microcanonical NVE ensembles, and then quenching down to 300 K with a cooling rate of 5 K ps<sup>-1</sup>. The final glass structure was then used to construct the interface with cleaved crystal surface cell.

The interface was constructed by assembling LS2-crystal and -glass parts along surface normal direction, with applied 3D periodic condition and a 5 Å vacuum gap in between. The initial interface was then melted in 6000 K followed by an iterative quench to 300 K with the same cooling rate of 5 K ps<sup>-1</sup> with constant volume NVT ensemble and microcanonical NVE ensemble. The dimensions of final constructed interfaces of LS2(100)/LS2-glass, LS2(010)/LS2-glass, LS2(110)/



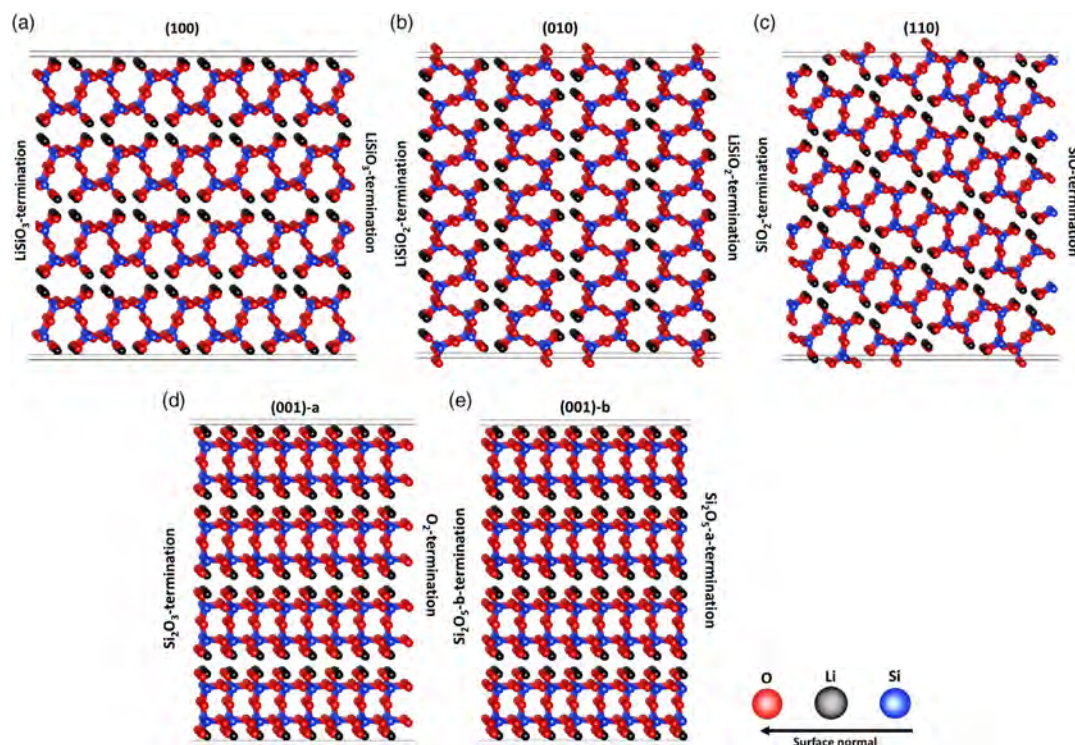


**Figure 1.** Schematic structure of  $\text{Li}_2\text{Si}_2\text{O}_5$  crystal surfaces: a) (100), b) (010), c) (110), d)  $\text{SiO}_3$ -terminated (001), and e)  $\text{SiO}_5$ -terminated (001).

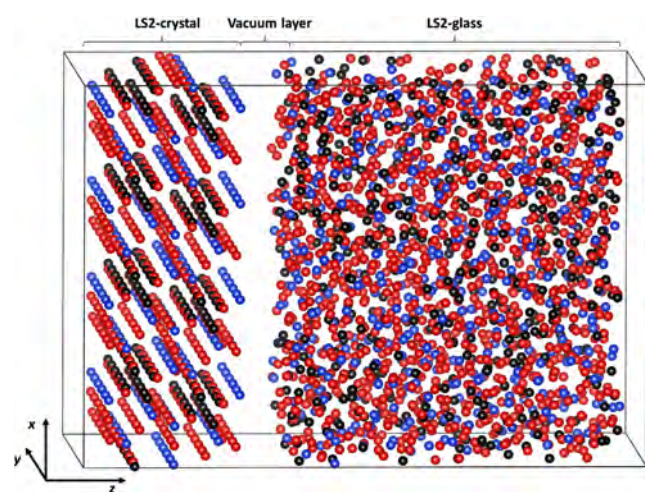


**Figure 2.** Schematic structure of initial generated LS2-crystal/LS2-glass interface model.

LS2-glass, LS2(001)-a/LS2-glass, and LS2(001)-b/LS2-glass were  $29.0 \times 28.5 \times 47.2$ ,  $28.1 \times 28.5 \times 63.2$ ,  $27.9 \times 30.6 \times 44.9$ ,  $28.6 \times 28.8 \times 44.7$ , and  $28.6 \times 28.8 \times 43.9$  Å, respectively.

The atomic position in the crystalline component was fixed during this process because of the small density difference between LS2-crystal and LS2-glass. Pair distribution function (PDF) and bond angle distribution (BAD) were determined to study the short-range structures of LS2-crystals, glasses, and interfaces. The medium-range structure feature was studied by analyzing the distribution of  $Q_n$  species, which represent network forming,

silicon tetrahedral units with  $n$  bridging oxygens. They describe the connectivity of the covalent silicate network.

### 3. Results

#### 3.1. Structure of Bulk LS2-Crystal and LS2-Glass

The short-range structure is often described by PDF and BAD. To compare the short-range structures of the crystal and glass, the simulated total PDF of Si–O, Li–O, Li–Si, and O–O pairs in LS2-crystal and LS2-glass was obtained, as shown in **Figure 3**. For both forms of lithium disilicate, Si shows very similar Si–O (Figure 3a) bond length of 1.60 Å and 100% coordination number of four, indicating the stable local structure around Si regardless of long-range order/disorder. This result agrees well with prior reports on silicate glasses, such as lithium disilicate,<sup>[35]</sup> borosilicate,<sup>[36]</sup> and aluminosilicate<sup>[37]</sup> obtained from MD simulations as well as experimental X-ray absorption spectra analysis.<sup>[38]</sup> The Li species in LS2-glass, a glass modifier, has a main peak of Li–O locating at around 1.88 Å (shown in Figure 3b), in good agreement with previous MD and experimental X-ray diffraction (XRD) and extended X-ray absorption fine structure (EXAFS) results.<sup>[35,39]</sup> In addition, the PDF of Li–O indicates that the average Li–O bond length in LS2-glass is smaller than that in LS2-crystal. Distributions of Si and Li coordination species for the two structures are summarized in **Table 2**. The Li ion in LS2-glass is 62.1% three coordinated to oxygen and 29.4% four coordinated to oxygen. By comparison, the Li in LS2-crystal is 100% fourfold coordinated, thus serving as a potentially useful indicator of the crystallinity at a local level.

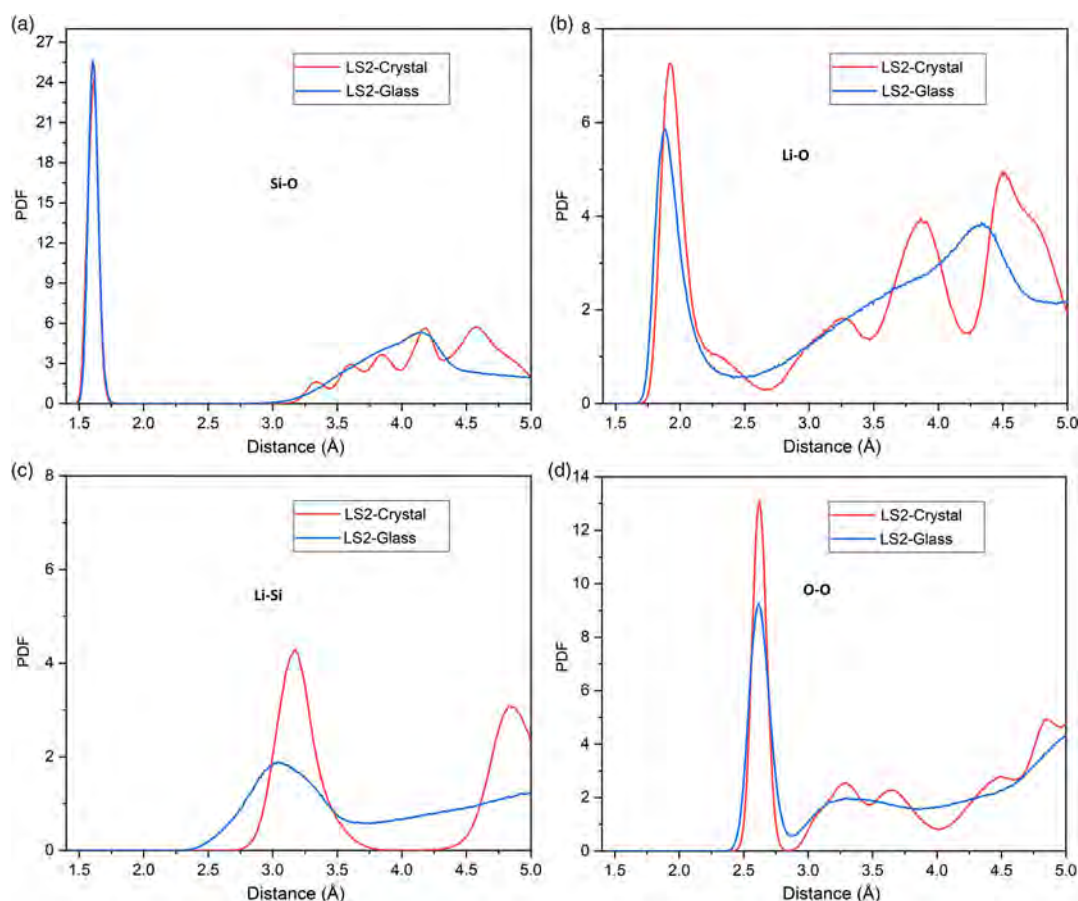


**Figure 3.** PDF of a) Si–O pair, b) Li–O pair, c) Li–Si pair, and d) O–O pair for bulk LS2-crystal and glass.

**Table 2.** Coordination number distribution of various elements in bulk LS2-crystal and LS2-glass (the cutoff of each pair is chosen based on the PDF curves in Figure 3).

	Cutoff [Å]	2	3	4	5
LS2-crystal					
Si	2.0			100%	
Li	2.7			100%	
LS2-glass					
Si	2.0			100%	
Li	2.4	7.3%	62.1%	29.4%	1.2%

A comparison of Li–Si and O–O PDFs for the two systems is shown in Figure 3c,d. In general, the LS2-glass structure has much broader distributions of Li–Si pairs, with a higher intensity and longer Li–Si bond length in the LS2-crystal than in LS2-glass. The main peak of O–O PDF of the two structures is located at 2.63 Å, with the corresponding value for LS2-glass reported from neutron diffraction as 2.64–2.66 Å.<sup>[39–41]</sup>

The BADs of O–Si–O and O–Li–O bonds in LS2-crystal and LS2-glass are shown in Figure 4. In Figure 4a, the O–Si–O BAD for both structures is quite similar (at around 109°), close to the

ideal tetrahedral angle of 109.47°, but the peak intensity is lower for LS2-glass than for LS2-crystal. These results are in good agreement with previous MD and ab initio MD simulation of variety of glasses, such as lithium disilicate glass,<sup>[35]</sup> sodium tetrasilicate glass,<sup>[42]</sup> and LiAlSi<sub>2</sub>O<sub>6</sub> glass,<sup>[43]</sup> further confirming the insensitivity of the local environment around Si species to the composition of silicate glasses. The O–Li–O BADs of the two structures show broad peaks, as shown in Figure 4b. The BAD of LS2-crystal has a range from 91.7° to 136.9° with a peak at 106.8°. For the LS2-glass structure, the BAD for O–Li–O angle shows a peak at around 106.5° with a considerably larger breadth ranging from 70.1° to 173.1°.

The  $Q_n$  species, which denote the number ( $n$ ) of bridging oxygen per [SiO<sub>4</sub>] tetrahedron, are often used to describe how the network formers connect with each other in glass at medium range. The values of  $Q_n$  for the two samples are shown in Table 3. Due to the long-range order of the atomic arrangement in crystal, the  $Q_n$  distribution of LS2-crystal shows 100%  $Q_3$  concentration. This unique feature differentiates the LS2-crystal and LS2-glass and, therefore, can be useful to identify crystallization in the interface region. For the LS2-glass, it is shown in Table 3 that there exist  $Q_1$ ,  $Q_2$ ,  $Q_3$ , and  $Q_4$  species from MD simulation in this work, with the percentages of 3.54%, 21.25%, 45.62%, and 29.58%, respectively. The four  $Q_n$  species agree reasonably with reported MD simulations,<sup>[44,45]</sup> which showed lower

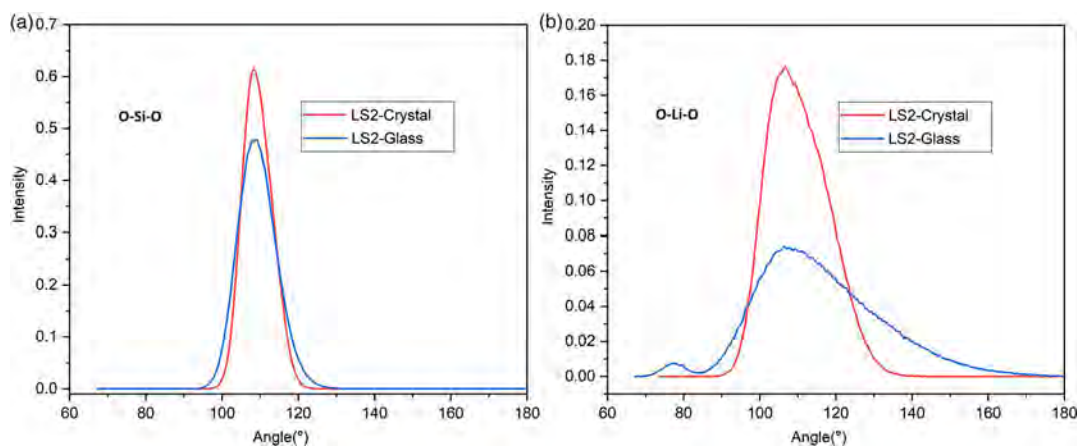


**Figure 4.** BAD of a) O–Si–O and b) O–Li–O for bulk LS2-crystal and glass.

**Table 3.**  $Q_n$  distribution (%) in bulk LS2-crystal and LS2-glass from a) present work and b) literature.

$n =$	1	2	3	4	Method
a) From this work					
LS2-crystal			100		MD
LS2-glass	3.54	21.25	45.62	29.58	MD
b) From the literature					
LS2-glass <sup>[48]</sup>		20.8	58.4	20.8	AIMD
LS2-glass <sup>[44]</sup>	4.6	21.4	42.3	31.9	MD
LS2-glass <sup>[45]</sup>	3.5	21.1	42.2	31.6	MD
LS2-glass <sup>[46]</sup>		24	55	21	NMR
LS2-glass <sup>[47]</sup>		21.9	57.3	14.6	Raman

concentration of  $Q_3$  and higher concentration of  $Q_4$ . The results of NMR,<sup>[46]</sup> Raman,<sup>[47]</sup> and ab initio MD (AIMD) simulations<sup>[48]</sup> reported only three  $Q_n$  species,  $Q_2$ ,  $Q_3$ , and  $Q_4$ .

### 3.2. Atomic Density Profiles of LS2-Crystal (110)/LS2-Glass Interface

The atomic number density normal to the interface, i.e., the  $z$ -density profile, is an effective and simple parameter to characterize the overall crystal/glass interface region. To acquire this profile, we first divided the interface system into a series of equal sections along the  $z$ -direction. This step was followed by a calculation of the number of atoms in each section by considering the  $z$  coordinate of each atom and then divided by the volume of the slice in the  $xy$  plane. Finally, the number density was plotted as a function of  $z$  position of the slab.

The structures and atomic distributions of LS2(110)/LS2-glass were clearly captured by the schematic structural configuration and  $z$ -density profiles, as shown in **Figure 5**. For convenience, the atom color of each type in Figure 5a corresponds to the color of  $z$ -density profiles in Figure 5b; the same representation is used for describing all the other interface models in this work.

In Figure 5a, deep red, blue, and black colors denote O, Si, and Li atoms in crystal, whereas lighter versions represent the same atoms in glass, respectively. The LS2(110) surface model, shown in Figure 2c, contains repetitive  $\text{Si}_2\text{O}_3$  and  $\text{Li}_4\text{Si}_2\text{O}_7$  layers. The two terminations, SiO termination on one side and  $\text{SiO}_2$  termination on the other side, belong to incomplete  $\text{Si}_2\text{O}_3$  layer within the sequence. It is shown that Si atoms from the glass are absorbed onto two LS2(110) surfaces, bonding with the O atoms from both outer layers from the crystal side forming  $[\text{SiO}_4]$  tetrahedra. In addition, an ordered local structure in glass can be observed directly near the crystal surface, yet it only comes from the Si and O species.

The distributions of Si, O, and Li atoms are then established from the density profiles in Figure 5b, where the dashed lines represent crystal side and solid lines denote to the glass part. For O and Si, the peak intensity increases dramatically near both sides of the crystal side, which indicates the ordered structure that consists of these species from LS2-glass. As the atomic profiles shift into bulk glass away from the interface, these sharp peaks with high intensity start broadening. Eventually, they broaden and disappear within the average intensity fluctuations, indicative of the amorphous structure of glass bulk. However, the peaks of  $\text{Li}^+$  ion maintain an average height from the interface onward into glass bulk, confirming the observation of  $\text{Li}^+$  ion distribution in Figure 5a.

Examining further in detail we note that for Si, the first two layers from the original interface have symmetrical  $z$ -positions on the two sides (marked as Si1/Si1' and Si2/Si2' in Figure 5b). While for O, the layer closest to the SiO-terminated side, O1, has a similar  $z$  position but a broader peak than the layer closest to the  $\text{SiO}_2$ -terminated side, O1'. This is due to the incomplete crystal outer layers on the surface becoming complete (110)  $\text{Si}_2\text{O}_3$  layers after interface formation, which is demonstrated in Figure 5c. The broad O1 layer, which consists of two adjacent O layers very close to each other, filling up the SiO crystal layer together with the Si1 layer. On the  $\text{SiO}_2$ -terminated side, full  $\text{Si}_2\text{O}_3$  layer is formed by adding O1' and Si1' layers from glass, as shown in Figure 5c. Interestingly, based on the positions and intensities of O2/O2' and Si2/Si2' peaks, the next layers with high ordering segregated in glass belong to part of the



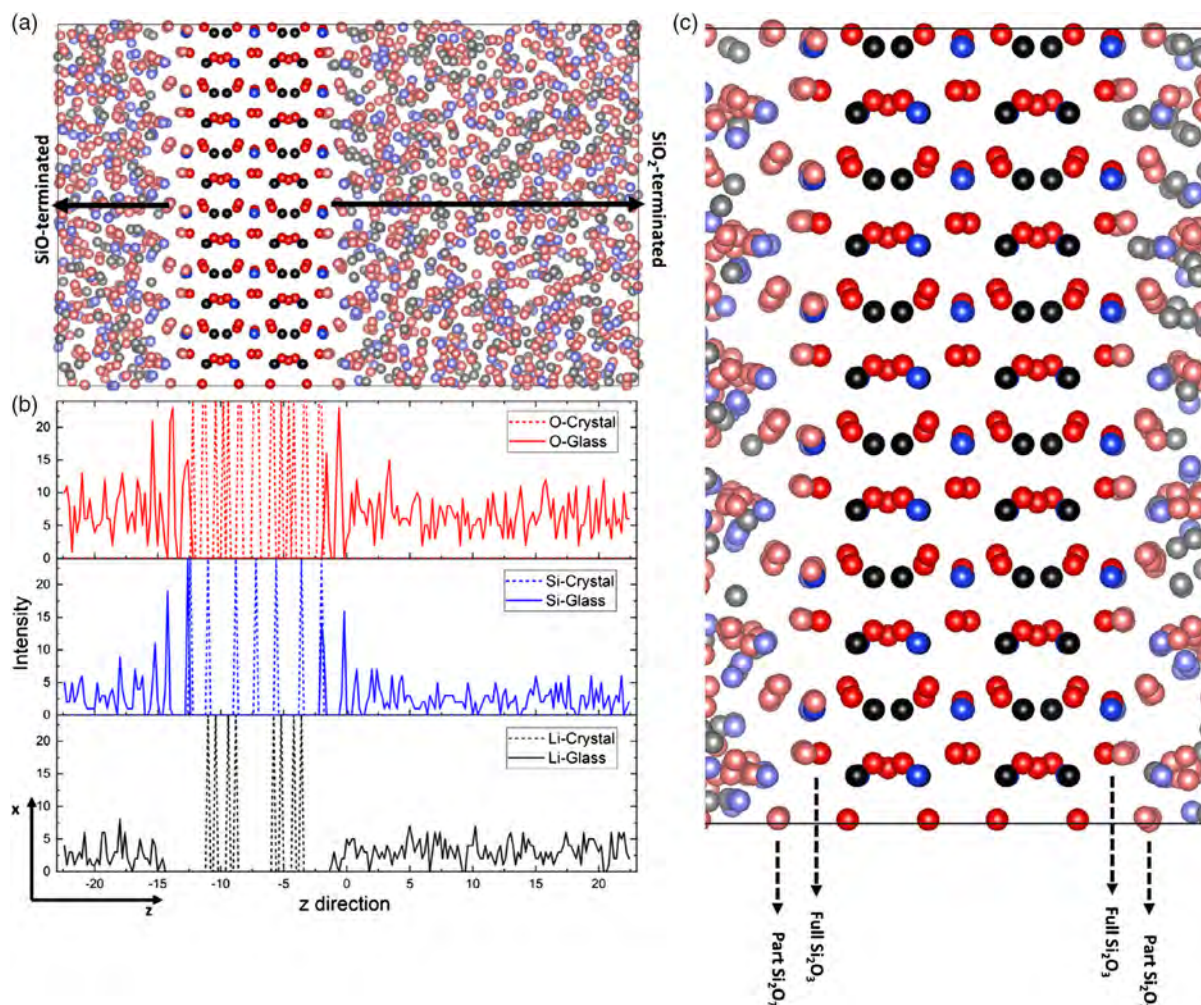


**Figure 5.** a) LS2(110)/LS2-glass interface structure at 300 K, b) z-density atomic profiles of LS2(110)/LS2-glass interface, and c) local structure of interface region.

$\text{Li}_4\text{Si}_2\text{O}_7$  layer of LS2-crystal (110), duplicating the sequence of (110) of  $\dots\text{Si}_2\text{O}_3\text{--Li}_4\text{Si}_2\text{O}_7\text{--Si}_2\text{O}_3\dots$ . This result indicates that not only ordered structures formed in glass near the crystal surface, but also a trace of crystal growth can be observed that follows the crystalline sequence. It is worth noting that although the density profile of Li shows no high sharp peaks, it still exhibits ordering and crystal-like sequence to some extent. In Figure 5b, we can see that two Li-free regions (intensity being zero in density profile) exist on both  $\text{SiO}$ -terminated and  $\text{SiO}_2$ -terminated sides, with the gaps of 3.19 and 2.0 Å, respectively. These two Li-free regions correspond to the  $\text{SiO}_3$  layer of (110), which has no Li atoms within.

### 3.3. Effect of Surface Orientation on Crystal Growth

To study the effects of surface orientation of crystal side on the crystallization of glass side, crystal surfaces with distinct layer constructions were chosen to analyze the interface. In the LS2-crystal system, (100) and (010) are orientations with unique terminations and layer arrangement. The LS2(100) surface has a

layer stacking sequence of  $\dots\text{LiSiO}_3\text{--LiSiO}_2\text{--LiSiO}_3\text{--LiSiO}_2\dots$ , with  $\text{LiSiO}_3$  termination on both sides. By comparison, LS2(010) has a layer sequence of  $\dots\text{LiSiO}_2\text{--O}_2\text{--LiSiO}_2\text{--O}_2\text{--LiSiO}_2\dots$ , with  $\text{LiSiO}_2$ -terminated sides on the top and bottom. In addition, another feature that differentiates LS2(010) from LS2(100) and other orientations listed in Figure 1 is that the layered structure is separated by the O atoms that are only connected to one Si ion (i.e., non-bridge oxygens). For LS2(100) and other orientations in LS2-crystal, unbroken  $\dots\text{Si--O--Si--O}\dots$  chains exist along surface normal direction.

The schematic structures and atomic density profiles of LS2(100)- and LS2(010)-based interfaces are shown in Figure 6. Both the LS2(100) and (010) surface models used in the construction of interfaces contain the same termination on each side, which makes it straightforward and convenient to compare the interface region of these two orientations. For LS2(100), shown in Figure 6a, well-arranged O and Si layers can be observed beyond the outer layers of crystal part. However, highly ordered  $[\text{SiO}_4]$  tetrahedra formed on the glass side of LS2(100) interfaces are not observed within the LS2(010)/



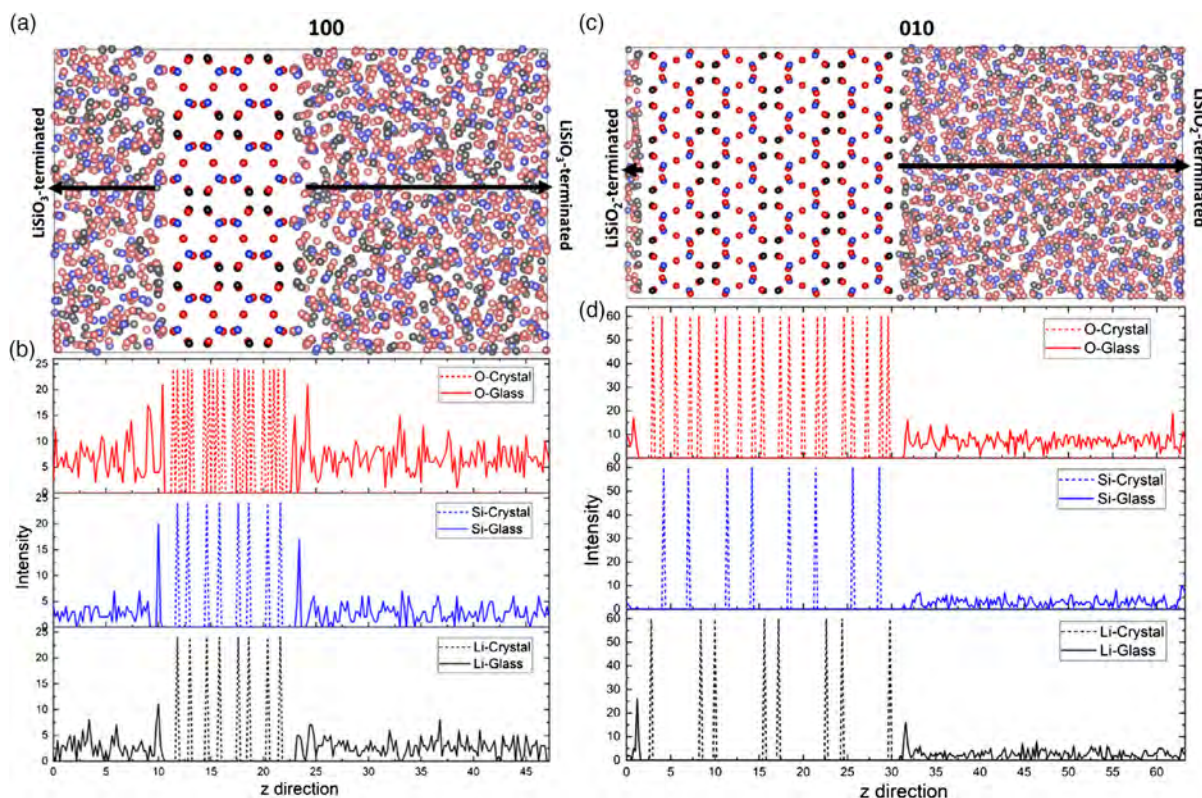


**Figure 6.** a,b) LS2(100)/LS2-glass interface structure and corresponding z-density atomic profiles. c,d) Generated LS2(010)/LS2-glass interface structure and corresponding z-density atomic profiles.

LS2-glass interface region in Figure 6b. The atomic density profiles (Figure 6b,d) show detailed atomic distributions, confirming these differences. Note that the strong peaks of O and Si from glass are organized into the LS2(100) surface, and then decay into the glass bulk. Similar to LS2(110) shown in Figure 5, the z positions of O and Si peaks on the two sides of (100) are symmetric due to the same termination of this surface model, though the intensities of the opposite peaks are different. For the (010)/glass interface, the density profiles indicate ambiguous O and Si atomic distribution in glass, suggesting that the amorphous structures containing O and Si exist in the interface region with much weaker trace of crystallization. Interestingly, relatively higher intensity peaks of Li are shown for this structure, which gives a usual interface environment compared with (110) and (100).

Due to the different atomic layer constructions, each orientation results in different atomic distributions in glass when interface forms, as described earlier. Although all the three interface structures exhibit different atomic profiles along the z-direction to some extent, the LS2(010)/glass, in particular, shows distinctly unusual behaviors compared with other two. For instance, the layered structure obviously plays a significant role in determining the atomic segregation and resulting average atomic distributions from interface toward glass bulk, especially for Si and O. Furthermore, the interface region from the LS2-glass has the tendency of following the planar sequence of corresponding crystal part, whether or not crystal growth is obvious. This

conclusion can be clearly observed in the contrasting density profiles of LS2(110)/glass and LS2(100)/glass interfaces, which contain continuous ...O–Si–O–Si... chain along the surface normal direction. Interestingly, the z-density profiles of LS2(010)/glass in Figure 6d still indicate the very initial signs of crystal growth to some degree, even though there are no obvious high sharp peaks in the interface region. Notably, besides the distinct sharp peaks, the regions near crystal surface without any atoms (density profiles with zero intensity) still can represent structural ordering in glass. On the other hand, these “atom-free” regions in LS2-glass near (010) surfaces show similar distances to those in the crystal region in the z-direction. In LS2(010), the distances between adjacent layers for O, Si, and Li are 1.51, 2.59, and 1.42 Å, respectively. These are very close to the distances between the outer layer from crystal side and the adjacent layer from glass side, 1.4 Å for O, 2.60 Å for Si, and 1.2 Å for Li, respectively.

#### 3.4. Atomic Density Profiles of Differently Terminated LS2(001)/LS2-Glass Interfaces

As the crystal part is fixed in this study, the interface area consists of the terminated layer from crystal side and few angstroms of surface region within the glass region, which is generated and considered as glass bulk due to the periodic boundary condition.<sup>[27,28]</sup> As expected, the crystal surface terminations impact atomic reorganization in glass that comes directly in their contact. In Figure 5b, the two terminations of LS2(110) result in

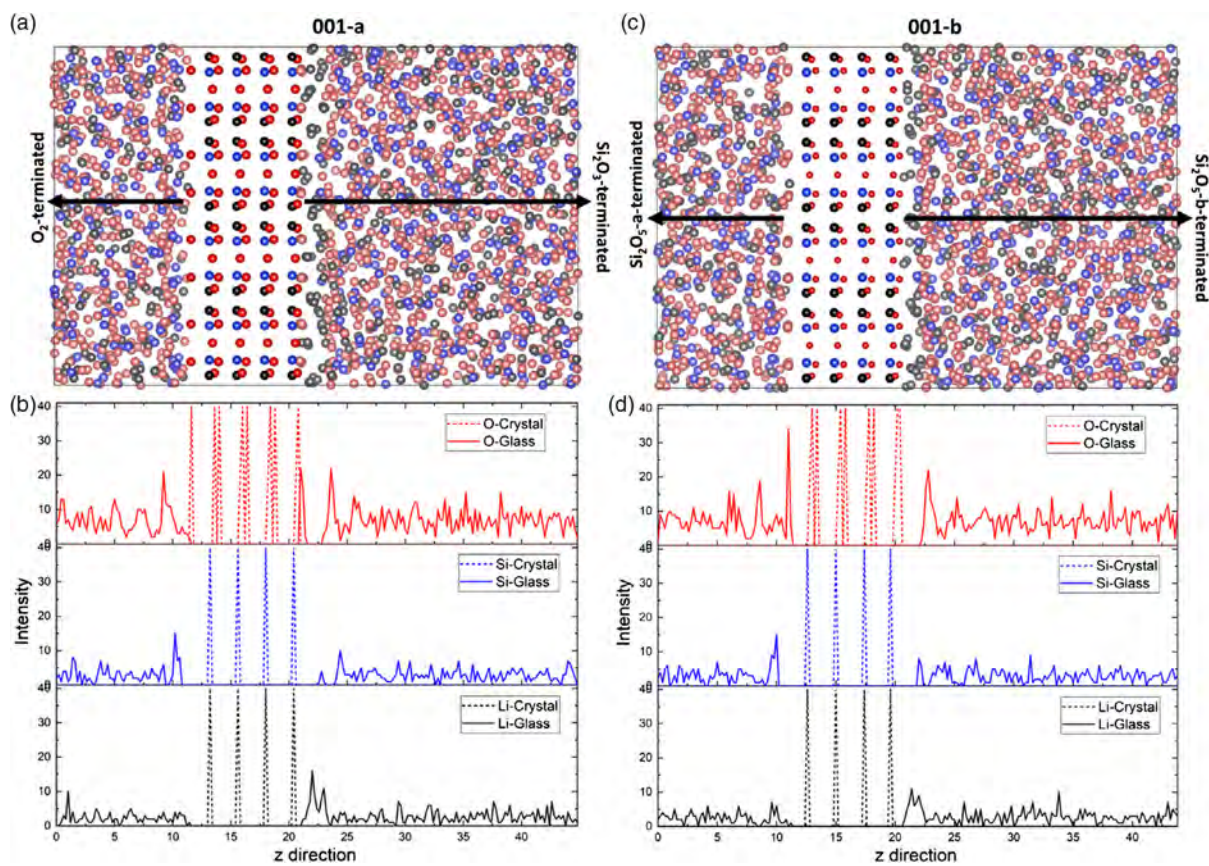


**Figure 7.** a,b) LS2(001)-a/LS2-glass interface structure and corresponding z-density atomic profiles. c,d) LS2(001)-b/LS2-glass interface structure and corresponding z-density atomic profiles. LS2(001)-a has  $O_2$  and  $Si_2O_3$  terminations on left-hand and right-hand sides, respectively, and LS2(001)-b has  $Si_2O_5$  termination on both sides.

different z-density profiles for the two interface regions. To further investigate such termination effects, the interfaces constructed of LS2(001) planes with two sets of terminations with LS2-glass were calculated. As shown in Figure 2c,d, one (001) surface contains  $O_2$  and  $Si_2O_3$  terminations, and the other (001) surface has the outer layer of  $Si_2O_5$  on both sides. Note that the two  $Si_2O_5$  terminations of the second (001) surface show different outer layers (considered as sub-layer of the  $Si_2O_5$  layer) on the two sides, with Si/Li (marked as  $Si_2O_5$ -a in Figure 7c) on one side and O (marked as  $Si_2O_5$ -b in Figure 7c) on the other side.

Figure 7 shows a comparison of the two interfaces determined by MD simulation. The (001) surface in Figure 7a, with a basic layer of  $Li_2Si_2O_5$  stacking on the surface normal direction, has an asymmetric slab model and a single O layer on the left-hand side, where each of the O ions is bonded with only one Si ion. As shown in Figure 7b, the atomic density profiles on the O-terminated side show the closest distinct peak from Si, but with only 1/3 the intensity of the crystal side. On the other hand, a well-defined, high-intensity O peak adjacent to the outer  $Si_2O_3$  layer occurs next to the short Si peak. Overall, for the glass part, the  $Si_2O_3$ -terminated side shows relatively sharper and higher O peaks than for the  $O_2$ -terminated side, indicating the formation of a higher ordering structure triggered by  $Si_2O_3$  termination. The other LS2(001)/glass interface model (Figure 7c,d) contains

the same termination but different outer layers on the crystal part. On the  $Si_2O_3$ -a-terminated side, the Si and Li constructed outer layers attract substantial amount of O atoms from glass, resulting in high sharp peaks of O and Si. However, on the other side, with O formed outer layer, the peaks of ordered O and Si atoms on the glass side have smaller widths and lower intensities.

#### 4. Discussion

Crystal growth of LS2-glass on the LS2-crystal is indicated from z-density profiles shown in Figure 5–7 where distinct peaks exist in the crystal/glass interface region. These sharp peaks, which have high intensity, are quite different from that within the glass bulk and provide an evidence of crystallization and ordering. Some ordered structures can be observed even directly in the visualized interface structures, such as the  $Si_2O_3$  layer of LS2(110)/glass layer in Figure 5c. However, establishment of the long-range ordered structure of a macroscopic crystal in glass remains a challenge for studying crystal growth. Therefore, often structural differences in the short and medium ranges between crystal and glass are used to differentiate them. For example, the different coordination numbers of Al atoms in  $MgAl_2O_4$  glass



and spinel crystal (four in glass and six in crystal) allow the ability of identifying crystal growth by analyzing Al coordination changes in different regions in glass part.<sup>[28]</sup> In the lithium silicate system, the Si atoms in both LS2-crystal and LS2-glass demonstrate very similar behaviors on PDF, BAD, and coordination number distributions. The most noticeable difference in short range comes from pairs including Li atoms. However, Li ions, as a charge compensator, did not tend to associate with crystallization of glass in LS2-crystal/glass interfaces according to the density profiles results where most Li peaks near crystal surface have similar behaviors to glass bulk. With such small impact of Li atoms involved in crystallization, the short-range behaviors mentioned earlier are ambiguous between the ordered and amorphous structures, hence not appropriate for identifying crystallization of the glass part next to the crystal at the interface.

Based on the results listed in Table 2, the distribution of bridging and non-bridging oxygens, i.e.,  $Q_n$  species of silicon tetrahedron, is another indication of the local ordering in glass, because it shows distinct behaviors in the LS2-crystal and glass in terms of Si and O species that greatly contribute to the formation of ordered structures in glass. Similar to atomic density profiles, we obtained the profiles of  $Q_n$  species, which describe their distribution and evolution as one probes them from crystal side to the glass side along the z-direction (i.e., normal to the interface). **Figure 8** shows the  $Q_n$  distribution profiles of  $[\text{SiO}_4]$  tetrahedron within the LS2(100)/LS2-glass and LS2(010)/LS2-glass interfaces, where only  $Q_n$  from glass part is displayed, and the gray shades represent crystal parts. For the LS2(100)/glass interface shown in Figure 8a,  $Q_3$  concentration is higher within the interface region near the crystal surface than that in glass bulk. However, the LS2(010)/glass model (Figure 8b) shows the same average  $Q_2$ ,  $Q_3$ , and  $Q_4$  distribution along the whole glass part. As  $Q_3$  is the only  $[\text{SiO}_4]$  species in LS2-crystal, the increased concentration of  $Q_3$  above the LS2(100)-crystal surface indicates that the Si and O atoms are more crystal-like, which agrees well with the results in Figure 6. In addition, the  $Q_4$  concentration within the interface region of LS2(100)/glass also increases and shows a much higher concentration than that in the glass bulk. This result is attributed to the finite formation of ordered structure within the medium range of  $Q_4$  species, which contains part ordered and part

amorphous structures. It is shown in Figure 6b that only one distinct peak exists on each side of the interface, representing limited crystallization in these areas. Therefore, the increased  $Q_4$  structures in LS2(100)/glass may be forming first during crystal growth and then transforming to the crystal-like  $Q_3$  structures. This indication of forming an intermediate metastable structure can have strong impact on the kinetics of devitrification and, therefore, should be explored and confirmed further. Meanwhile, the LS2(010)/glass interface shows much less ordering near the interface area from Figure 6d, and thus, no  $Q_4$  concentration change is observed in Figure 8 either.

The forming of ordered structures of LS2-glass in the interface model is affected by both orientation and termination of crystal part. The z-density profiles show that the orientation of crystal surface (or seed) determines the positions of those crystal-like high sharp peaks in the interface region for all four LS2-crystal surface models calculated in this study. These positions indicate that the ordered layers formed in glass replicate the layer sequence of corresponding crystal part in terms of atomic arrangement and the inter-planar spacing. Together, they represent the initial stage of crystal growth accordingly. This conclusion is mainly from the same or similar atom concentration and density of crystal and glass parts, resulting in a homogeneous crystal growth.

In all the LS2-crystal/LS2-glass interface models, the LS2(010) crystal shows unique layer arrangement along surface normal directions, containing layered structures with oxygen ions that separate these  $[\text{SiO}_4]_n$  layers. Each of these O ions in surface-terminated layers, as shown in Figure 1c, is bonded with only one Si ion in LS2-crystal and surrounded by Li ions. When forming interface with LS2-glass, the O ions within a Li-rich environment in the terminated layer of (010) behave as non-bridging oxygens in glass. As a consequence, relatively more Li ions segregate, and a much less ordered  $\text{SiO}_n$  structure of adjacent glass part is found compared with the other three orientations studied in this work. The consecutive Si–O–Si–O chains in LS2-crystal (110), (100), and (001) clearly benefit the crystal growth in terms of Si and O in LS2-glass. Therefore, the crystal orientation mainly affects the magnitude of crystallization but not very sensitively within the  $\text{Li}_2\text{O}$ – $\text{SiO}_2$  crystal/glass system, demonstrating crystal

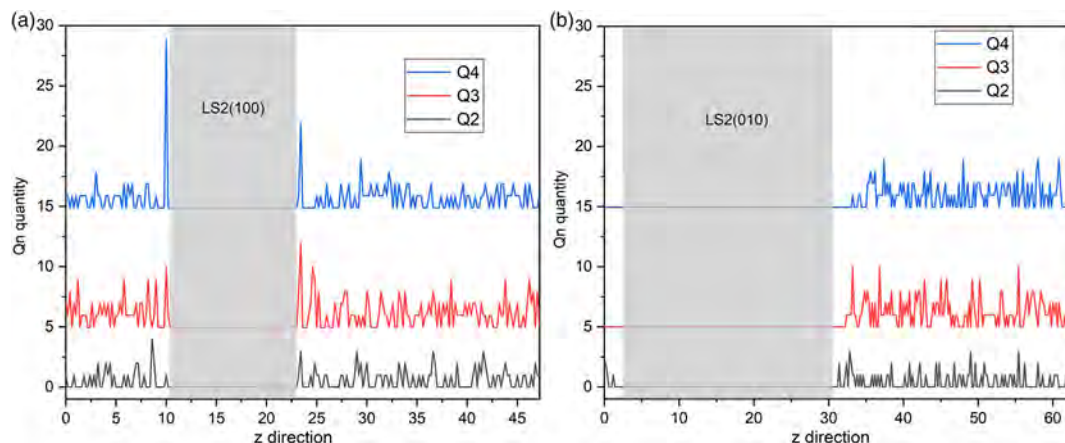


**Figure 8.**  $Q_n$  distribution of Si in LS2-glass along interface normal direction for a) LS2(100)/glass and b) LS2(010)/glass interfaces. Only  $Q_n$  in glass part is shown, and the region in gray shade represents the crystal part.



growth in varying degrees. In limited experimental studies, the  $\text{Li}_2\text{Si}_2\text{O}_5$  crystal growth occurs preferentially along the [001] direction<sup>[49,50]</sup> and shows a needle-shaped structure.<sup>[51]</sup> Although such preferable growth direction cannot be determined in this study, the present results show impact of different orientations on crystal growth at the early stages.

As high sharp peaks in z-density profile represent ordered crystalline structures of corresponding species, the magnitude of crystallization on that basis can be compared at least in the first order. Among all the four interface models, SiO-terminated LS2(110) side shown in Figure 5b results in the most distinct O and Si peaks for the glass side that shares the same width and height with the ones from the crystal part. In addition, as shown in Figure 5, on the SiO-terminated LS2(110), there are three O peaks and two Si peaks completing the  $\text{Si}_2\text{O}_3$  layer and forming the next  $\text{Si}_2\text{O}_7$  layer, which show the greatest extent of ordered structures compared with others. In addition, the coordination of Si ions in crystal surface terminations has a huge impact on the magnitude of crystallization of LS2-glass. As shown in Figure 7d, although both sides of LS2(001) are terminated with  $\text{Si}_2\text{O}_5$ , the one with under-coordinated Si ions shows remarkably high structural ordering of both Si and O species, whereas on the other side, the four-coordinated Si layer results in lower and wider Si and O peaks from glass. Consequently, the terminations of LS2-crystal surfaces that contain zero-coordinated O or under-coordinated Si would result in a relatively faster crystal growth in the adjacent LS2-glass. Note that all the crystal surface models in this work are as-cleaved and kept fixed to create limiting conditions to study the orientation and termination effects. For real and simulated materials in vacuum or ambient environment, the O layer that does not bond with any Si in terminated layer is difficult to form due to the large dipole moment along surface normal direction. The atoms of surface layers would have large reconstructions when such surface slabs are relaxed in vacuum to saturate the dangling bonds in crystal surface. In this work, the vacuum layer between crystal and glass parts gets filled after interface formation. As a result, the dangling bonds from terminated layers are saturated, allowing for a highly polar surface to exist and be stable within the interface model.

## 5. Conclusion

The interfacial structures of lithium disilicate glass with a variety of surface orientations of lithium disilicate crystals were studied by MD simulations. The analyses of short- and medium-range structures and z-density profile were used to characterize the bulk and interfacial structures. Ordering of the structure as in crystallization on the glass side near crystal surface was observed clearly. It was used to understand the initial stage of LS2-crystal growth. Besides high sharp peaks in z-density profiles of silicon and oxygen, change of  $Q_i$  distribution also provided evidence of crystallization. For the LS2-crystal/glass interface, an increase in the  $Q_3$  and  $Q_4$  concentrations was found on the glass side of the interface region, indicating the formation of LS2-crystal-like structures.

Finally, the influence of crystal orientation and surface termination on the ordering and crystallization on the glass side of interface was compared for various interfaces. It was found that

the formation of ordered structures in LS2-glass side followed the layer orientation of crystal part. As for the effect of nature of termination layer, under-coordinated Si ions within the outer crystal layer result in higher ordered structures and enhanced crystallization than the terminated layers containing four-coordinated Si and non-bridging O ions in the  $\text{Li}_2\text{O}$ – $\text{SiO}_2$  crystal/glass system.

## Supporting Information

Supporting Information is available from the Wiley Online Library or from the author.

## Acknowledgements

This work was supported by the Basic Energy Sciences Division of the Department of Energy under project DE-SC0005010. The authors would like to acknowledge David A. Drabold (Ohio University), Matthew E. McKenzie (Corning Inc.), and Edgar D. Zanotto (Federal University of Sao Carlos) for helpful discussions in setting up the computer simulation of crystallization.

## Conflict of Interest

The authors declare no conflict of interest.

## Keywords

crystal growth, glass-ceramics, interface structures, lithium disilicate, molecular dynamics

Received: July 31, 2020

Revised: November 10, 2020

Published online: December 6, 2020

- [1] M. Bliss, P. M. Aker, C. F. Windisch, *J. Non-Cryst. Solids* **2012**, 358, 751.
- [2] P. Goharian, A. Nemati, M. Shabanian, A. Afshar, *J. Non-Cryst. Solids* **2010**, 356, 208.
- [3] W. Lien, H. W. Roberts, J. A. Platt, K. S. Vandewalle, T. J. Hill, T. M. Chu, *Dent. Mater.* **2015**, 31, 928.
- [4] M. Mahmoud, D. C. Folz, C. T. A. Suchicital, D. E. Clark, *J. Am. Ceram. Soc.* **2012**, 95.
- [5] L. L. Burgner, M. C. Weinberg, P. Lucas, P. C. Soares Jr, E. D. Zanotto, *J. Non-Cryst. Solids* **1999**, 255, 264.
- [6] L. L. Burgner, M. C. Weinberg, P. Lucas, P. C. Soares Jr, E. D. Zanotto, *J. Non-Cryst. Solids* **2000**, 274, 188.
- [7] J. Deubener, R. Brückner, M. Sternitzke, *J. Non-Cryst. Solids* **1993**, 163, 1.
- [8] Y. Iqbal, W. E. Lee, D. Holland, P. F. James, *J. Mater. Sci.* **1999**, 34, 4399.
- [9] E. D. Zanotto, M. L. G. Leite, *J. Non-Cryst. Solids* **1996**, 202, 145.
- [10] R. S. Soares, R. C. Monteiro, M. M. Lima, R. J. Silva, *Ceram. Int.* **2015**, 41, 317.
- [11] C. Bischoff, H. Eckert, E. Apel, V. M. Rheinberger, W. Höland, *Phys. Chem. Chem. Phys.* **2011**, 13, 4540.
- [12] P. Soares, E. D. Zanotto, V. M. Fokin, H. Jain, *J. Non-Cryst. Solids* **2003**, 331, 217.
- [13] M. L. F. Nascimento, V. M. Fokin, E. D. Zanotto, A. S. Abyzov, *J. Chem. Phys.* **2011**, 135, 194703.

- [14] J. W. P. Schmelzer, *J. Non-Cryst. Solids* **2008**, 354, 269.
- [15] S. Karthika, T. K. Radhakrishnan, P. Kalaichelvi, *Cryst. Growth Des.* **2016**, 16, 6663.
- [16] L. Cormier, L. Galois, J. M. Delaye, D. Ghaleb, G. Calas, *C. R. Acad. Sci. Ser. IV Phys.* **2001**, 2, 249.
- [17] M. Barlet, A. Kerrache, J. M. Delaye, C. L. Rountree, *J. Non-Cryst. Solids* **2013**, 382, 32.
- [18] J. M. Delaye, *Curr. Opin. Solid State Mater. Sci.* **2001**, 5, 451.
- [19] L. H. Kieu, J. M. Delaye, L. Cormier, C. Stolz, *J. Non-Cryst. Solids* **2011**, 357, 3313.
- [20] M. E. McKenzie, S. Goyal, T. Loeffler, L. Cai, I. Dutta, D. E. Baker, J. C. Mauro, *npj Comput. Mater.* **2018**, 4, 59.
- [21] S. Blonski, S. H. Garofalini, *J. Phys. Chem.* **1996**, 100, 2201.
- [22] S. Blonski, S. H. Garofalini, *J. Am. Ceram. Soc.* **1997**, 80, 1997.
- [23] S. Zhang, S. H. Garofalini, *J. Am. Ceram. Soc.* **2005**, 88, 202.
- [24] D. A. Litton, S. H. Garofalini, *J. Mater. Res.* **1999**, 14, 1418.
- [25] Y. Jiang, S. H. Garofalini, *Scr. Mater.* **2016**, 113, 97.
- [26] M. J. D. Rushton, R. W. Grimes, S. L. Owens, *J. Non-Cryst. Solids* **2011**, 357, 3278.
- [27] W. Sun, J. Du, *Int. J. Appl. Glas. Sci.* **2019**, 10, 41.
- [28] W. Sun, J. Du, *J. Am. Ceram. Soc.* **2019**, 102, 4583.
- [29] J. Du, A. N. Cormack, *J. Am. Ceram. Soc.* **2005**, 88, 2532.
- [30] H. Bradtmüller, M. C. Villas-Boas, E. D. Zanotto, H. Eckert, *J. Non-Cryst. Solids* **2020**, 535, 119844.
- [31] J. Schneider, V. R. Mastelaro, H. Panepucci, E. D. Zanotto, *J. Non-Cryst. Solids* **2000**, 273, 8.
- [32] C. M. Schramm, B. H. W. S. de Jong, V. E. Parziale, *J. Am. Chem. Soc.* **1984**, 106, 4396.
- [33] L. Deng, J. Du, *J. Am. Ceram. Soc.* **2020**, 103, 2933.
- [34] J. D. Gale, *J. Chem. Soc., Faraday Trans.* **1997**, 93, 629.
- [35] J. Du, L. R. Corrales, *J. Chem. Phys.* **2006**, 125, 114702.
- [36] D. M. Zirl, S. H. Garofalini, *J. Am. Ceram. Soc.* **1990**, 73, 2848.
- [37] Y. Xiang, J. Du, M. M. Smedskjaer, J. C. Mauro, *J. Chem. Phys.* **2013**, 139, 44507.
- [38] G. N. Greaves, A. Fontaine, P. Lagarde, D. Raoux, S. J. Gurman, *Nature* **1981**, 293, 611.
- [39] J. Zhao, P. H. Gaskell, M. M. Cluckie, A. K. Soper, *J. Non-Cryst. Solids* **1998**, 232–234, 721.
- [40] H. Uhlig, M. J. Hoffmann, H. P. Lamparter, F. Aldinger, R. Bellissent, S. Steeb, *J. Am. Ceram. Soc.* **1996**, 79, 2833.
- [41] A. C. Hannon, B. Vessal, J. M. Parker, *J. Non-Cryst. Solids* **1992**, 150, 97.
- [42] S. Ispas, M. Benoit, P. Jund, R. Jullien, *J. Non-Cryst. Solids* **2002**, 307–310, 946.
- [43] M. Ren, J. Du, *J. Am. Ceram. Soc.* **2016**, 99, 2823.
- [44] J. Du, L. R. Corrales, *Phys. Rev. B* **2005**, 72, 92201.
- [45] J. Habasaki, K. L. Ngai, *J. Chem. Phys.* **2013**, 139, 64503.
- [46] U. Voigt, H. Lammert, H. Eckert, A. Heuer, *Phys. Rev. B* **2005**, 72, 64207.
- [47] H. Maekawa, T. Maekawa, K. Kawamura, T. Yokokawa, *J. Non-Cryst. Solids* **1991**, 127, 53.
- [48] J. Du, L. R. Corrales, *J. Chem. Phys.* **2006**, 125, 114702.
- [49] H. Pinto, L. Ito, M. Crovace, E. B. Ferreira, F. Fauth, T. Wroblewski, E. D. Zanotto, A. R. Pyzalla, *J. Non-Cryst. Solids* **2007**, 353, 2307.
- [50] C. L. Booth, G. U. Y. E. Rindone, *J. Am. Ceram. Soc.* **1964**, 47, 25.
- [51] I. Denry, J. A. Holloway, *Materials* **2010**, 3, 351.

# Au and Pt Diffusion in Electrodeposited Amorphous Sb<sub>2</sub>Te<sub>3</sub> Thin Films

Chandrasiri A. Ihalawela, Mayur Sundararajan, Kevin W. Cooper, Martin E. Kordesch, David C. Ingram, Xiao-Min Lin, and Gang Chen\*

Dedicated to Professor David A. Drabold on the occasion of his 60th birthday

Amorphous Sb<sub>2</sub>Te<sub>3</sub> thin films are synthesized using electrodeposition in different thicknesses to explore their solid electrolytic nature with respect to some noble metals. Au and Pt are used as the substrate materials and thermally diffused into the Sb<sub>2</sub>Te<sub>3</sub> films under passivated and nonpassivated conditions. Rutherford backscattering spectrometry is used to study the Au and Pt diffusion into the films as a function of depth. It is found that Au diffuses into the Sb<sub>2</sub>Te<sub>3</sub> thin films even at room temperature. In contrast, there is no observable diffusion of Pt at room temperature. At a higher temperature (i.e., 200 °C), both Au and Pt diffuse into the Sb<sub>2</sub>Te<sub>3</sub> thin films and Au diffusion is more significant than Pt. The findings suggest that amorphous Sb<sub>2</sub>Te<sub>3</sub> can be used as a good solid electrolyte to permit the diffusion of some noble metals such as Au and Pt.

understanding the ionic diffusion observed in CBRAM during the electron-conducting filament formation. In addition, for future device applications there is a considerable demand for high-aspect-ratio-structured devices such as nanowire-based PCM.<sup>[8]</sup> The most widely used method for synthesizing PCM and CBRAM materials is sputtering.<sup>[6,9]</sup> However, sputtering is incapable of creating high-aspect-ratio structures to fulfill the future needs. Among all the synthesis methods, electrochemical deposition has an excellent capability of growing high-aspect-ratio structures. Therefore, it is important to study electrodeposited materials to understand their solid electrolytic nature.

## 1. Introduction

Amorphous chalcogenides have been widely used in different device applications.<sup>[1–5]</sup> More importantly, they have played a major role in memory applications such as phase-change memory (PCM) and conductive-bridge random access memory (CBRAM).<sup>[6,7]</sup> Among the amorphous chalcogenides, Sb<sub>2</sub>Te<sub>3</sub> is a well-known prototypical PCM material. Moreover, Sb- and Te-based amorphous materials have been used as CBRAM switching materials.<sup>[6]</sup> In both memory applications, the amorphous chalcogenides are sandwiched between two electrodes with one of them being an electrochemically inert element such as Au, Pt, or W. Therefore, understanding the solid electrolytic nature of Sb<sub>2</sub>Te<sub>3</sub> with respect to the contacting electrodes (e.g., Au and Pt) is important. Moreover, the atomic diffusion in this simple binary material could provide a new insight into

In this study, we have focused on exploring the solid electrolytic nature of stoichiometric Sb<sub>2</sub>Te<sub>3</sub> thin films synthesized by an electrochemical method. Au and Pt atoms were diffused into Sb<sub>2</sub>Te<sub>3</sub> films with and without thermal annealing. Scanning electron microscopy (SEM), energy dispersive X-ray spectroscopy (EDXS), Rutherford backscattering spectroscopy (RBS) and X-ray diffraction (XRD) were used to characterize the morphology, composition, compositional depth profiling, and atomic structure, respectively. It is hoped that this study will enhance the understanding of noble metal diffusion in amorphous chalcogenide thin films and provide some implications for their device applications.


## 2. Results and Discussion

According to our previous studies of electrodeposited binary Sb–Te thin films, by carefully controlling the deposition parameters, one can obtain an amorphous Sb–Te thin film with controllable morphology, composition, and structure.<sup>[10]</sup> Figure 1a,b shows the SEM micrographs of Sb<sub>2</sub>Te<sub>3</sub> thin films after 45 s of deposition on Au and Pt, respectively. The films are more or less uniform and free of pinholes, so a density as 6.5 g cm<sup>−3</sup> was used in the Rutherford Universal Manipulation Program (RUMP) modeling. Moreover, the composition of the electrodeposited thin film was confirmed by analyzing the EDX spectra (an example of such spectra is shown in Figure 1c). For the Sb<sub>2</sub>Te<sub>3</sub> films deposited on Au and Pt, both are amorphous as confirmed by the XRD (data not shown).

To understand the Au and Pt diffusion into the Sb<sub>2</sub>Te<sub>3</sub> thin films, first, RBS spectra of the same thickness of Sb<sub>2</sub>Te<sub>3</sub>

Dr. C. A. Ihalawela, Dr. M. Sundararajan, Dr. K. W. Cooper,  
Prof. M. E. Kordesch, Prof. D. C. Ingram, Prof. G. Chen  
Department of Physics and Astronomy  
Ohio University  
Athens, OH 45701, USA  
E-mail: cheng3@ohio.edu

Dr. X.-M. Lin  
Center for Nanoscale Materials  
Argonne National Lab  
Lemont, IL 60439, USA

 The ORCID identification number(s) for the author(s) of this article can be found under <https://doi.org/10.1002/pssb.202000428>.

DOI: 10.1002/pssb.202000428



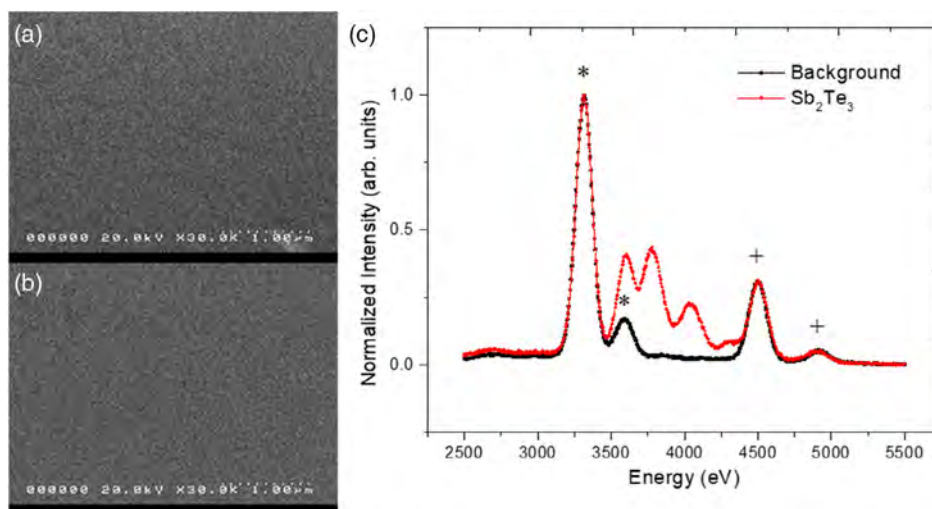


**Figure 1.** SEM micrographs of  $\text{Sb}_2\text{Te}_3$  thin films electrodeposited for 45 s on a) Au and b) Pt. c) The EDX spectra of  $\text{Sb}_2\text{Te}_3$  with contribution of the substrate K (\*) and the Ti (+) peak in the background. The micrographs confirm the pinhole free and smooth deposition.

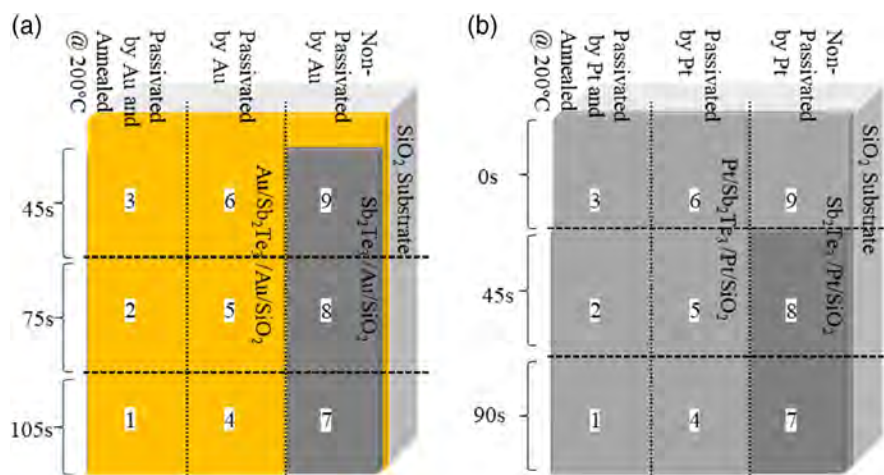


**Figure 2.** Schematics of  $\text{Sb}_2\text{Te}_3$  thin film electrodeposited on a) Au and b) Pt to represent different thicknesses and unpassivated, passivated and passivated–annealed regions for RBS study. Increase of deposition time was related to the thickness of deposited  $\text{Sb}_2\text{Te}_3$ , and the main areas of interest were 3, 6, 9 in (a) and 2, 5, 8 in (b) for 45 s.

films but different processing conditions (passivated–annealed, passivated, and nonpassivated) were studied. **Figure 2** shows the schematics of an amorphous  $\text{Sb}_2\text{Te}_3$  thin film electrodeposited on Au (Figure 2a) and Pt (Figure 2b) with three different processing conditions: nonpassivated, passivated, and passivated–annealed. Different deposition times represent different thicknesses of the  $\text{Sb}_2\text{Te}_3$  thin film. The main focus of the analysis is on the 45 s of deposition which is marked as 3, 6, and 9 for Au and 2, 5, and 8 for Pt in Figure 2a,b, respectively. As mentioned in the Experimental Section, the acquired RBS spectra under different processing conditions are shown in **Figure 3**. Moreover, the modeled results of these experimental data are given in **Table 1** in which multiple layers with various thicknesses have been defined to acquire compositional depth profiling starting from the outermost or surface layer (i.e., layer 1) to the glass substrate (i.e., level 5 for nonpassivated films, level

4 for both passivated and passivated–annealed films). For the passivated films, the layered structures can be seen in the RBS spectra for Au (Pt)/ $\text{Sb}_2\text{Te}_3$ /Au (Pt) from Figure 3b (for Au) and Figure 3e (for Pt). However, the bottom layer Au peak is not resolved from the  $\text{Sb}_2\text{Te}_3$  peak and it appears as a shoulder toward the high-energy side of that merged peak in the RBS spectra. In contrast, for the Pt, just one atomic number difference is sufficient to resolve the RBS spectra from  $\text{Sb}_2\text{Te}_3$ .

Au has been observed on the surface up to a depth of a very few angstroms (layer 1) in the nonpassivated film deposited on Au, and we believe that is due to improper masking during the Au sputtering. Nevertheless, the high Au incorporation in layer 3 relative to layer 2 (note: both layers are within the  $\text{Sb}_2\text{Te}_3$  film) in the nonpassivated film implies Au has diffused into the  $\text{Sb}_2\text{Te}_3$  film from the bottom Au layer. In contrast, no Pt was detected in the nonpassivated  $\text{Sb}_2\text{Te}_3$  film electrodeposited on the Pt

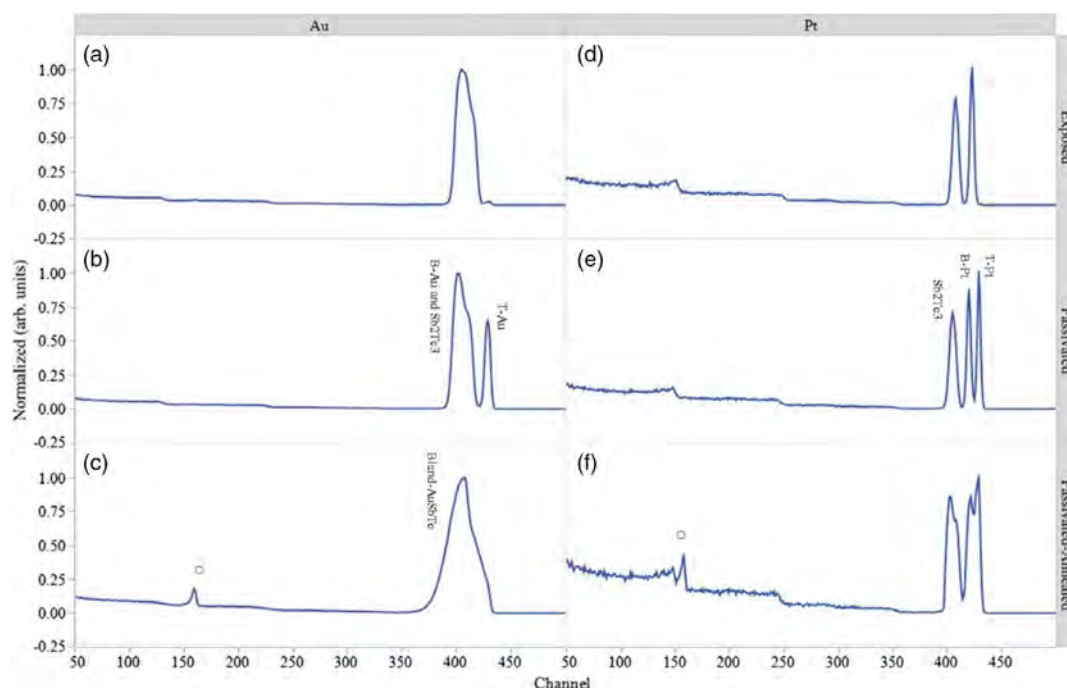


**Figure 3.** RBS spectra for the passivated–annealed, passivated, and nonpassivated regions, where  $\text{Sb}_2\text{Te}_3$  thin films were electrodeposited for 45 s on a,b,c) Au and d,e,f) Pt, respectively. “S” (surface), “T” (top), and “B” (bottom) were used to denote different levels of thin films. For the passivated systems, the Au peak from the substrate layer and the  $\text{Sb}_2\text{Te}_3$  peaks overlapped, but the three-layer structure can be clearly seen for the Pt system. Similar observations can be made for the nonpassivated systems. However, with thermal annealing, the Au system blended significantly compared to the Pt system, and was unable to retain its layered structure. Moreover, oxidation is confirmed for both Au- and Pt-passivated annealed systems.

**Table 1.** Compositional variation of nonpassivated, passivated, and passivated–annealed regions with respect to modeled multiple layers. Layer 1 is the top (surface) layer, and the larger the layer number, the closer the layers are to the glass substrate (the bottom layer). NA thickness is referring to the Si substrate.

Region	Layer	Thickness [nm]	Sb	Te	Au	O <sub>Au</sub>	Pt	O <sub>Pt</sub>	Ti	Zn	Si
Nonpassivated	1	25	0.40	0.60	0.15	0.15	0.00	–	–	–	–
	2	117	0.40	0.60	0.03	0.10	0.00	–	–	–	–
	3	155	0.40	0.60	0.60	–	0.00	–	–	–	–
	4	60	–	–	1.00	–	1.00	–	–	–	–
	5	NA	–	–	–	2.00	–	2.00	0.50	0.50	1.00
Passivated	1	25	–	–	1.00	–	1.00	–	–	–	–
	2	265	0.40	0.60	0.01	–	0.00	–	–	–	–
	3	80	–	–	1.00	–	1.00	–	–	–	–
	4	NA	–	–	–	2.00	–	2.00	0.50	0.50	1.00
Passivated–annealed	1	112	0.40	0.60	0.40	1.00	0.90	0.80	–	–	–
	2	75	0.40	0.60	0.80	0.30	0.20	0.20	–	–	–
	3	276	0.40	0.60	1.80	1.00	0.90	0.80	–	–	–
	4	NA	–	–	–	2.00	–	2.00	0.50	0.50	1.00

substrate. In other words, Pt is more stable than Au against diffusion in amorphous  $\text{Sb}_2\text{Te}_3$  at room temperature. A similar trend is observed in the Au- and Pt-passivated films. In the passivated  $\text{Sb}_2\text{Te}_3$  films, a small amount of Au was detected throughout the  $\text{Sb}_2\text{Te}_3$  film, whereas no Pt was seen within the film.

As the main purpose of the passivation was to stop the oxygen diffusion into the  $\text{Sb}_2\text{Te}_3$  films, it is important to study the

distribution of oxygen along the depth of the films under different processing conditions. To specifically probe the oxygen as a function of depth, alpha particles with oxygen resonance energy (3.035 MeV) were used. From the RUMP analysis of the experimental data, it was found that the outermost layer of the  $\text{Sb}_2\text{Te}_3$  film electrodeposited on Au has higher oxygen incorporation than the next layer in depth (nonpassivated layer 1 vs 2);

therefore, it is more likely that the oxygen incorporation initiated from the surface and diffused into the thin film. In contrast, no observable surface oxidation can be seen from RBS for the nonpassivated  $\text{Sb}_2\text{Te}_3$  film electrodeposited on Pt.

To study the effect of passivation on stopping the oxygen diffusion, the nonpassivated  $\text{Sb}_2\text{Te}_3$  films were passivated/coated with Au or Pt within 2 h of the electrodeposition. As shown in Table 1, no oxygen incorporation was found in both the Au- and Pt-passivated films, suggesting that the passivation effectively stopped the oxygen diffusion from the surface to the film.

The passivated-annealed region for Au consists of crystallized and phase-separated materials. Furthermore, the complete vanishing of the layered nature in  $\text{Au/Sb}_2\text{Te}_3/\text{Au}$  (as shown in the RBS spectrum in Figure 3c) is due to the intermixing of the materials, which confirms the high mobility of the participating atoms under thermal activation. Unlike Au, the mobility of Pt seems to be insignificant, and Pt was able to preserve its layered structure, as shown in the RBS spectrum (Figure 3f), even after the thermal annealing. Coincidentally, the trends observed for the  $\text{Sb}_2\text{Te}_3$  thin films deposited for 45 s are the same for all other different deposition times. This effective blending of atoms or promising solid electrolytic nature is due to the very large thermal vibrations in crystalline phases of the Sb–Te system which randomize the atomic distribution similar to a liquid phase, as discussed in Yamada.<sup>[11]</sup> However, with respect to Pt, the high capability of blending with Au is probably due to the negative bonding enthalpy for  $\text{AuTe}_2$  and  $\text{AuSb}_2$  compounds.<sup>[12]</sup> It is interesting to note that after thermal annealing, the Te concentration does not change along the depth of the film for both Au- and Pt-passivated films. This is probably due to the covalent nature of Te atoms, which are not as mobile as the metal species, and the fact that the electrodeposited  $\text{Sb}_2\text{Te}_3$  films are uniform in chemical composition along the depth of the film and thus there is no concentration gradient to promote the diffusion. Another interesting feature of this work is that in general, Ag and Cu have been commonly used as active electrodes in CBRAM devices<sup>[13,14]</sup>; however, our accidental discovery of the diffusive nature of some noble metals such as Au and Pt in a chalcogenide solid electrolyte (i.e., amorphous  $\text{Sb}_2\text{Te}_3$ ) could open a new area in chalcogenide-based CBRAM devices.

### 3. Conclusion

In conclusion, amorphous  $\text{Sb}_2\text{Te}_3$  thin films with different thicknesses were successfully electrodeposited to study the diffusion of noble metals (Au and Pt) under different processing conditions. The as-electrodeposited  $\text{Sb}_2\text{Te}_3$  films were amorphous. Regardless of the thickness of the  $\text{Sb}_2\text{Te}_3$  films, Au diffusion seems to be more significant than Pt. Even at room temperature, Au diffusion was clearly observed for the nonpassivated thin films. The passivation of  $\text{Sb}_2\text{Te}_3$  films with Au or Pt is effective at stopping oxygen diffusion from the surface to the film. The effect of thermal annealing at 200 °C is more significant for the Au-passivated film, with observed intermixing of the multilayer. In contrast, the passivated-annealed Pt system was able to preserve its layered structure even though diffusion of Pt also occurs at that temperature. Overall, amorphous  $\text{Sb}_2\text{Te}_3$  is a good solid electrolyte to permit the diffusion of Au and Pt.

### 4. Experimental Section

Amorphous  $\text{Sb}_2\text{Te}_3$  thin films were electrodeposited potentiostatically (Princeton Applied Research Model 273A) using a standard three-electrode cell at room temperature under  $-600$  mV and 200 rpm. The electrolyte for the electrodeposition was prepared according to similar procedures described elsewhere by using  $\text{SbCl}_3$  (Acros Organic 99.5%) and  $\text{TeO}_2$  (Acros Organic 99+%) as precursors.<sup>[15,16]</sup> To avoid any dissolvability issues,  $\text{SbCl}_3$  and  $\text{TeO}_2$  were dissolved in sodium citrate (NaCit) and concentrated  $\text{HNO}_3$ , respectively. After electrolyte preparation, the relative species concentrations for the final volume (80 mL) were  $\text{SbCl}_3:\text{TeO}_2:\text{NaCit}:\text{HNO}_3 = 7.5 \text{ mM}:7.5 \text{ mM}:0.21 \text{ M}:1 \text{ M}$  and pH was adjusted to 2.3 by adding 1 M NaOH.

Au and Pt were deposited onto #1  $\text{SiO}_2$  glass slides with a thickness of 200–300 nm by DC magnetron sputtering (Denton Vacuum 502-A) and used as the working electrodes (WEs). A standard wafer cleaning procedure was performed for the WE prior to the electrodeposition. A saturated calomel electrode and Pt mesh were used as the reference and counter electrodes, respectively. To obtain different thicknesses in the same sample, different dip levels were maintained with respect to the deposition time. For the first 45 s of electrodeposition, the Au working electrode was dipped in the electrolyte to cover an approximate area of  $15 \times 10 \text{ mm}^2$ , and then the dipping area was reduced to  $10 \times 10$  and  $5 \times 10 \text{ mm}^2$  by raising the working electrode, respectively, to deposit material for a total of 75 and 105 s. Similar steps were performed to deposit different thicknesses on Pt at deposition times of 45 and 90 s. After electrodeposition, one-third of the deposition was masked and sputtered with Au (Pt) (same as the back layer) to passivate the deposition and half of the passivated area was separated and annealed at 200 °C for 100 min. Figure 2 shows the schematics of an  $\text{Sb}_2\text{Te}_3$  thin film electrodeposited on a) Au and b) Pt to different thicknesses and exposed, passivated, and passivated-annealed regions for RBS study. Both samples have different regions to study with respect to nonpassivation, passivation, thermal treatment, and thickness of the deposited material.

The morphology and composition of depositions were studied using field emission scanning electron microscopy (FESEM) (Hitachi S4500) and EDX (Thermo Fisher Scientific NORAN System SIX X-ray Microanalysis in Hitachi S2460N), respectively. Cu K $\alpha$  XRD under transmission mode (SAXSess, tabletop small-angle X-ray scattering system) was used to study the structural changes of the deposition before and after thermal treatment. To probe the Au and Pt diffusion in  $\text{Sb}_2\text{Te}_3$  by compositional depth profiling, RBS was used. RBS experiments were performed at Edwards Accelerator Laboratory, Ohio University, using  $\alpha$  particles with energies of 3.035 and 3.070 MeV and an angle of 168° with respect to the incident beam. The RUMP analysis package was used to model the acquired RBS spectra.

### Acknowledgements

This work was supported by the National Science Foundation Directorate for Mathematical and Physical Sciences DMR-0906825 and DMR-1507670.

### Conflict of Interest

The authors declare no conflict of interest.

### Data Availability Statement

Research data are not shared.

### Keywords

antimony telluride, conductive-bridge random access memory, electrodeposition, Rutherford backscattering spectrometry, solid electrolytes



Received: July 31, 2020  
Revised: December 22, 2020  
Published online: January 29, 2021

- 
- [1] F. J. DiSalvo, *Science* **1999**, 285, 703.
  - [2] N. Romeo, A. Bosio, R. Tedeschi, A. Romeo, V. Canevari, *Sol. Energy Mater. Sol. Cells* **1999**, 58, 209.
  - [3] L. van Pieterson, M. H. R. Lankhorst, M. van Schijndel, A. E. T. Kuiper, J. H. J. Roosen, *J. Appl. Phys.* **2005**, 97, 083520.
  - [4] M. Breitwisch, in *Phase Change Materials* (Eds: S. Raoux, M. Wuttig), Springer US, New York **2009**, Ch. 17.
  - [5] J. Zhu, J. L. Zhang, P. P. Kong, S. J. Zhang, X. H. Yu, J. L. Zhu, Q. Q. Liu, X. Li, R. C. Yu, R. Ahuja, W. G. Yang, G. Y. Shen, H. K. Mao, H. M. Weng, X. Dai, Z. Fang, Y. S. Zhao, C. Q. Jin, *Sci. Rep.* **2013**, 3, 2016.
  - [6] D. Jana, S. Roy, R. Panja, M. Dutta, S. Z. Rahaman, R. Mahapatra, S. Maikap, *Nanoscale Res. Lett.* **2015**, 10, 188.
  - [7] S. Raoux, W. Wetnic, D. Ielmini, *Chem. Rev.* **2010**, 110, 240.
  - [8] Y. Bin, S. Xuhui, J. Sanghyun, D. B. Janes, M. Meyyappan, *IEEE Trans. Nanotechnol.* **2008**, 7, 496.
  - [9] D. Milliron, Q. Huang, Y. Zhu, in *Phase Change Materials* (Eds: S. Raoux, M. Wuttig), Springer US, New York **2009**, Ch. 11.
  - [10] C. A. Ihalawela, *PhD Dissertation*, Ohio University **2016**.
  - [11] N. Yamada, in *Phase Change Materials* (Eds: S. Raoux, M. Wuttig), Springer US, New York **2009**, Ch. 10.
  - [12] H.-G. Boyen, A. Cossy-Favre, P. Oelhafen, A. Siber, P. Ziemann, C. Lauinger, T. Moser, P. Häussler, F. Baumann, *Phys. Rev. B* **1995**, 51, 1791.
  - [13] S. Ginnaram, J. T. Qiu, S. Maikap, *IEEE Electron Device Lett.* **2020**, 41, 709.
  - [14] S. Ginnaram, J. T. Qiu, S. Maikap, *ACS Omega* **2020**, 5, 7032.
  - [15] G. Leimkuhler, I. Kerkamm, R. Reineke-Koch, *J. Electrochem. Soc.* **2002**, 149, C474.
  - [16] Q. Huang, A. J. Kellock, S. Raoux, *J. Electrochem. Soc.* **2008**, 155, D104.

# Effect of Ion Irradiation on Amorphous and Crystalline Ge–Se and Their Application as Phase Change Temperature Sensor

Al-Amin Ahmed Simon, Lyle Jones, Yoshifumi Sakaguchi, Henri Kunold, Isabella van Rooyen, and Maria Mitkova\*

Dedicated to Professor David A. Drabold on the occasion of his 60th birthday

Research on phase change materials is predominantly focused on their application as memory devices or for temperature control which requires low phase change temperature. The Ge–Se binary chalcogenide glass system with its wide glass-forming region is a potential candidate for high-temperature and high-radiation phase change applications. Herein, the concept of employing  $\text{Ge}_x\text{Se}_{100-x}$  glasses to monitor high temperature (450–528 °C) using the phase change effect, is reported. Materials selection, device structure, and performance of prototype sensors are analyzed. In addition, the effect of heavy ion irradiation by Xe ions with energies of 200, 600, and 1000 keV (fluence  $\approx 10^{14} \text{ cm}^{-2}$ ) on the  $\text{Ge}_x\text{Se}_{100-x}$  ( $x = 30, 33, 40$ ) thin films and phase change devices is studied. The irradiation effect on the amorphous and crystalline structure of the thin films is evaluated by Raman spectroscopy and X-ray diffraction (XRD). Although the changes in the structural units of amorphous films are negligible, in crystalline films orthorhombic-GeSe<sub>2</sub> crystals are found to be most affected by irradiation and a new phase, orthorhombic GeSe is found in the thin films after irradiation. The performance of a sensor with an active film of  $\text{Ge}_{40}\text{Se}_{60}$  is also shown as an example.

## 1. Introduction

The synergy between theoretical/simulation and experimental research has always been very beneficial for better understanding and knowledge about matter. So, collaborating with and exploring the work of David Drabold, has been a guiding light for author's (M.M.) studies. Notably, preliminary information about what to expect when Ag diffuses in chalcogenide glasses,<sup>[1–4]</sup> the mechanism of diffusion,<sup>[5,6]</sup> how the structure of these glasses is developing,<sup>[7–9]</sup> and the secrets of the phase change effect.<sup>[10,11]</sup> The phase change effect and the invention of the phase change memory devices based on chalcogenide glasses in 1968<sup>[12]</sup> established a new era in the development of the information storage and the study of recrystallization of the disordered systems.<sup>[13,14]</sup> Although the effects on which the phase change memory devices rely on are well studied, namely, crystallization of the disordered active


material by a slow increase in its temperature by external stimuli (e.g., heating by Joule effect,<sup>[15]</sup> optical irradiation,<sup>[16]</sup> or external heating sources<sup>[17]</sup>), they still pose many questions. However, this did not stop the growing research of these materials and newer applications, extending from resistive switching electronic memory<sup>[18,19]</sup> toward optical memory.<sup>[20,21]</sup> One of the most applied methods to study phase transition (amorphous to crystalline) is by measuring resistivity, since the amorphous phase of chalcogenide glass demonstrates dielectric behavior, whereas the crystalline exhibits excellent conductive characteristics. Usually, there is a well-measurable contrast of the resistivity between the phases and is reproducible. The nonisothermal switching to the crystalline phase is typically a speedy process,<sup>[22]</sup> which advances numerous applications based on it. The speed can be attributed to a very short distance, the atoms have to travel for rearrangement<sup>[23]</sup> because by this solid–solid transition, the system achieves its equilibrium. Moreover, even if the stimuli which transform the system to its crystalline condition are ceased, the material keeps its crystallinity—in this case, its high conductivity state, thus making the effect nonvolatile.<sup>[24,25]</sup> Furthermore

A.-A. Ahmed Simon, L. Jones, Dr. M. Mitkova  
Department of Electrical and Computer Engineering  
Boise State University  
Boise, ID 83725, USA  
E-mail: mariamitkova@boisestate.edu

Y. Sakaguchi  
Neutron Science and Technology Center  
Comprehensive Research Organization for Science and Society  
Tokai, Naka-gun, Ibaraki 319-1106, Japan

H. Kunold  
Micron School of Materials Science and Engineering  
Boise State University  
Boise, ID 83725, USA

Dr. I. van Rooyen  
Fuel Design and Development Department  
Idaho National Laboratory  
Idaho Falls, ID 83415, USA

 The ORCID identification number(s) for the author(s) of this article can be found under <https://doi.org/10.1002/pssb.202000429>.

DOI: 10.1002/pssb.202000429

retaining the solid state, during this phase transition process, the total number of covalent bonds does not change during crystallization. This is an additional reason for the good reliability of devices. The reverse switching goes, however, through melting the material followed by quenching.<sup>[26]</sup> Indeed, quenching sounds quite obscure to appear, having in mind that the heating results only in the film, which is located on a substrate at room temperature. However, cooling of the film occurs very fast given that its volume is orders of magnitude smaller than that of the much cooler substrate. Because of this volume difference, the heat dissipation from the film appears quite fast and the film vitrifies.

Due to the lack of order, high number of defects and availability of lone-pair electrons on chalcogenide atoms, the electrical properties of chalcogenide glasses are radiation hard. The reason behind this is that the intrinsic defects, carriers and the defects caused by irradiation<sup>[27]</sup> populate in very close proximity and they recombine rapidly. The intrinsic defects manifest themselves as “gap states” in the bandgap of the chalcogenide glasses.<sup>[28,29]</sup> Near the center of the gap, the states are highly localized so, the electron exchange or hopping probability is low. It was proposed<sup>[28,30]</sup> that in chalcogenide glasses, these defect states are at dangling bonds  $D^0$ , and the lattice (not in the crystalline but in the network sense) distortion is powerful enough to produce charged centers  $D^+$  and  $D^-$  out of  $D^0$ . Moreover, the lone-pair electrons form the upper portion of the valence band and the  $D^+$  charged centers interact with the neighboring lone-pair electrons. This interaction distorts the environment. The localized states play a vital role in making the chalcogenide glasses radiation hard and indifferent to doping up to some extent. These states behave like recombination centers and traps in the bandgap. A high number of these traps contribute significantly to capture free carriers produced by ionizing radiation. So, it is difficult to move the Fermi level ( $E_F$ ) either by doping or by irradiation. This is the so-called “Fermi level pinning” phenomenon by which the electrical properties of the material remain stable. This effect is manifested at the performance of many types of devices based on chalcogenide glasses which demonstrate stable operation under irradiation with visible light,<sup>[31]</sup> high-intensity X-rays,<sup>[32]</sup> gamma irradiation,<sup>[33]</sup> and irradiation with 50 MeV protons<sup>[34]</sup> and low-intensity  $Ar^+$ .<sup>[35]</sup>

All the aforementioned are incredibly interesting and important properties of chalcogenide glasses and the thermally induced phase change effect in them motivated our study of their function as a temperature sensor in a high-radiation environment to replace traditionally used sensors in nuclear facilities, like the “Melt Wire Sensors”. Melt wire sensors are used to measure temperature post factum as they do not supply real-time information. The suggested temperature sensor offers real-time temperature measurement, reversibility and reuse, as well as the option for fabrication of an array. By the combination of several devices built up by different compositions of chalcogenide glasses with different crystallization temperatures, the array can provide data regarding the temperature development. A similar design has been patented by IBM<sup>[36]</sup> in 2012. However, its fabrication and application are very much limited by the active material  $Ge_2Sb_2Te_5$ , which crystallizes at 160 °C. This article is focused on the investigation of the performance of glasses from the Ge–Se system. Although this system is slightly away from the major phase change memory materials’ group studied for

electronic switching,<sup>[37]</sup> where low crystallization temperature and fast switching are the key attributes, it has been chosen because of the relatively high crystallization temperature and thermal stability. These make the glasses a good candidate for temperature monitoring of the cladding of light water reactors (LWRs) and for metallic or ceramic sodium-cooled fast reactors (SFRs) within a temperature range of 450 to 528 °C. In an earlier article, we presented a detailed study of the crystallization of  $Ge_xSe_{100-x}$  ( $x = 30, 33, 40$ ) glasses<sup>[17]</sup> along with a prototype temperature sensor based on the optical effects of phase change. In this article, the focus is on the effect of ion bombardment (emulating neutron irradiation) on the material property and the performance of electrical phase change temperature sensors. The material in the devices changes its solid-state condition (the material crystallizes) after external heating and this effect is measured through the conductivity change by analyzing the current–voltage ( $I$ – $V$ ) characteristics of the devices. The data about the effect of irradiation with Xe ions over the structure of the active material (Ge–Se glasses) are described and discussed based on three different compositions from the studied system:  $Ge_{30}Se_{70}$ —which is a Se-rich member of the Ge–Se glasses,  $Ge_{33}Se_{67}$ —the stoichiometric composition, and  $Ge_{40}Se_{60}$ —a Ge-rich material. In the end, the performance of several devices, made with Ge-rich material with reversibility, is demonstrated (both as-prepared and irradiated).

Xe ion’s choice is based on the fact that xenon is chemically inert, nonradioactive, and one of the typical fission products, offering a cost-effective and safer alternative to neutron irradiation. Moreover, since the thermal neutron cross sections of naturally abundant Ge, Se, and Al isotopes used in the sensor are quite low (Ge 0.4, Se 0.61, and Al 0.231),<sup>[38]</sup> the possibility of nuclear transmutation is low and so this article is focused on ion-induced damage only. The other advantages of ion irradiation are as follows: higher damage rate ( $10^4$  times) compared to reactor irradiation reducing the experimental duration to days instead of decades; the irradiated samples are not radioactive, so postirradiation characterization cost is reduced; and ion irradiation experiments can be controlled better to some extent (e.g., temperature, damage rate, and damage level) than reactor irradiation and there is the provision to observe the damage in situ. However, the emulation of neutron irradiation using ion is a new idea and the experiments must be tailored according to the materials and higher control of parameters is needed. This article can be used as a guideline for material testing by emulating reactor irradiation with well-controlled ion irradiation.

## 2. Experimental Section

### 2.1. Glass Synthesis

The standard melt quenching technique was used to synthesize bulk chalcogenide glasses. After weighing accurately, the required amounts of pure 5 N elements were loaded into fused silica ampoules. Then, the ampoules were sealed under vacuum ( $\approx 10^{-4}$  mbar) and placed in a programmable tube furnace. To assure the melting of the components, the furnace was programmed depending upon the characteristic temperatures of each composition according to the phase diagram of the



Ge–Se system. At the last step, for good glass homogenization, the ampoules were kept at 750 °C for 144 h.<sup>[39]</sup> This temperature was on an average 20–50 °C above the melting of the synthesized compositions. The importance of the glass melt homogenization arose from the fact that at equilibrium presented in the phase diagrams, glass-forming compositions were usually bordered by congruently melting crystalline phases,<sup>[40]</sup> which can nucleate in melts when quenched and produce microscopic heterogeneities.<sup>[41,42]</sup> To ensure the slow aging of the glasses, which was a warranty for the stability of both bulk glasses and thin films, it was important to avoid the formation of microscopic heterogeneities. After 168 h, the ampoules were taken out of the furnace and rapidly cooled in a water–sand bath at room temperature.

## 2.2. Thin Films and Devices Preparation

The chalcogenide glass thin films were prepared by thermal evaporation in a Cressington 308 R coating system on thermally oxidized (SiO<sub>2</sub>) substrates. The pressure inside the chamber was kept at 10<sup>−6</sup> mbar and the evaporation rate was 0.3 Å s<sup>−1</sup>. A quartz crystal microbalance was used to estimate the thickness of the films in situ. For device fabrication, circular aluminum electrodes were also deposited by thermal evaporation with the help of a shadow mask on the top of the chalcogenide glass film. **Figure 1** shows a schematic of a device and its operation.<sup>[42]</sup>

## 2.3. Energy Dispersive Spectroscopy

Energy dispersive spectroscopy (EDS), used to confirm the exact composition of the produced films, was conducted using a FEI Teneo scanning electron microscope (SEM) with an Oxford Instruments Energy + EDS system. Each sample was measured at five different locations for the collection of an accurate average value and the standard deviation. The study showed that the composition of the thin films deviated ±1.5 at% from the composition of the bulk material.

## 2.4. Raman Spectroscopy

To identify any changes in the bonding and physical structure of the materials after irradiation, Raman analysis was performed in a Horiba LabRAM HR Evolution Raman Spectroscopic System in backscattering mode, using a parallel-polarized 632.817 nm He:Ne laser, focused to a spot of 6 μm, with a power of 17 mW. Samples were observed at room temperature and under standard atmospheric pressure.

## 2.5. X-ray Diffraction Spectroscopy

To investigate the crystalline phases of the thin films, X-ray diffractometer was used. The measurement was done on a Rigaku MiniFlex600 ( $\lambda = 1.5406$  Å) at 40 kV and 15 mA. At 10 °C min<sup>−1</sup> scanning rate, the data were collected at room temperature, in a range of  $2\theta = 10^\circ$ – $65^\circ$ .

## 2.6. Devices Characterization

The devices were characterized in a semiconductor parametric analyzer (Agilent 4155B). *I*–*V* characteristics were measured from 0 to 3 V at a resolution of 30 mV/step and the compliance current was set to 50 nA. To achieve a phase change of initially amorphous active material, the devices were kept for 15 s at each temperature, including the onset of crystallization temperature. Crystallized devices were pulsed with a pulse generating unit (PGU) at different duration for amorphization with square wave amplitude 2 V, period 1 μs, and ON time: 200 ns.

## 2.7. Ion Irradiation

Samples from each composition were bombarded with Xe<sup>+1</sup>/ Xe<sup>+2</sup>/ Xe<sup>+3</sup> ions, having an initial ion energy of 200, 600, and 1000 keV and an achieved fluence of 10<sup>14</sup> cm<sup>−2</sup> which corresponded to ≈5 displacement per atom (DPA) at each energy level. Ion bombardment was performed with 1.7 MV Tandem Particle Accelerator (in Michigan Ion Beam Lab) at an angle

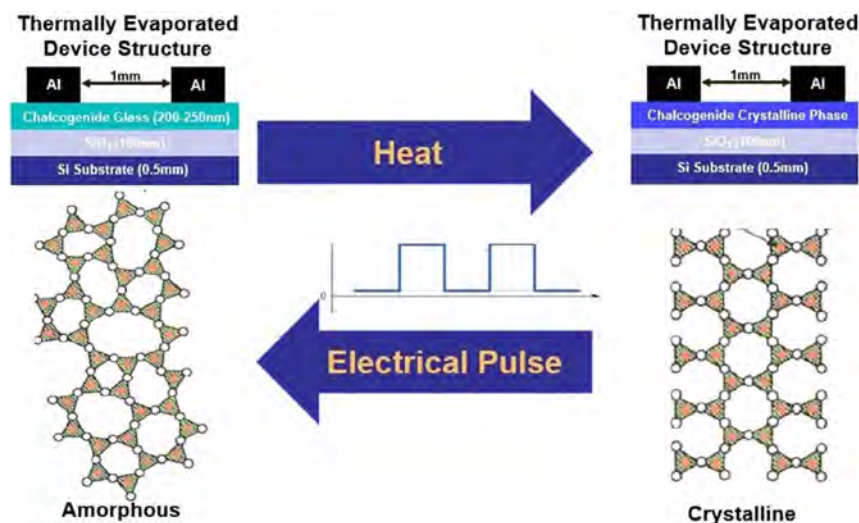


**Figure 1.** Device structure and operation.

normal to the surface of each sample using a 100 nA beam current and chamber pressure of  $10^{-8}$  Torr.

## 2.8. Displacement Per Atom Calculation

With the help of The Stopping and Range of Ions in Matter (SRIM) simulation software, the calculation of the DPA was done. SRIM is a group of programs that calculate the stopping and range of ions (up to 2 GeV amu<sup>-1</sup>) into the matter. The software used a quantum mechanical treatment of ion-atom collisions (assuming a moving atom as an “ion”, and all target atoms as “atoms”). To make the calculation efficient, statistical algorithms that allowed the ion to make jumps between calculated collisions and then averaging the collision results over the intervening gap were used. Among the programs, the Transport of Ions in Matter (TRIM) accepted complex targets made of compound materials with up to eight layers. It calculated the final 3D distribution of the ions as well as kinetic phenomena associated with the ion’s energy loss like target damage, sputtering, ionization, and phonon production.<sup>[43]</sup>

For simplicity of the simulation, TRIM had the option to utilize “Kinchin–Pease Approximation” to calculate ion-induced damage. In this article, this approximation was used where no spatial extension of the damage after the first recoil was initiated since full cascade was not calculated. So, all the damage was calculated, assuming it only occurred during the initial collision.<sup>[44]</sup> Moreover, ions were incident on the thin films and devices at a normal angle and since the fluence ( $10^{14}$  cm<sup>-2</sup>) was much lower than the atomic density ( $10^{22}$  cm<sup>-3</sup>) of Ge–Se, the sputtering was neglected. At room temperature, most of the implantation damage normally “self-anneals”, because the atoms have enough energy to allow simple target damage to regrow into its original form at room temperature. However, since there are no thermal effects in TRIM, the damage which was calculated was the one that would happen for implantation at 0 K. Although, ignoring the thermal effects changed the quantity of final damage, the basic damage types still occurred.

Ion irradiation introduced displacements of atom in a material. Both vacancies (empty lattice site which was originally occupied) and replacement collisions (atom sites with a new atom identical to the original atom) were considered as displacement. From full cascade simulation, it was seen that for all the irradiation conditions, replacement collision was one order of

magnitude lower than total vacancies produced and so it was not considered.

An example of DPA calculation is given in the following (and all results are displayed in Table 1):

Let us take a damage rate  $DR = 3.6 \text{ \#}/(\text{\AA} \cdot \text{ion})$  (for maximum damage rate from SRIM simulation for Ge<sub>40</sub>Se<sub>60</sub>, from Figure 8);

Atomic density,  $N = 3.4 \times 10^{22} \text{ cm}^{-3}$  (calculated from SRIM, considering density  $4.38 \text{ g cm}^{-3}$ , from Figure 7);

Current = 1  $\mu\text{A}$  (from experimental setup);

Charge of the ion,  $q = +1$  for  $+1$  ions, and  $e = 1.6 \times 10^{-19} \text{ C}$ ,  $Q = q \times e$ ;

Sample area,  $A = 4 \text{ cm}^2$  (from experimental setup).

Then, to induce (for example) 5 DPA of damage on 250 nm Ge<sub>40</sub>Se<sub>60</sub> on SiO<sub>2</sub> with 600 keV Xe<sup>1+</sup> ions, is going to take

$$\text{Time} = \frac{\text{DPA} \times Q \times N \times A}{(\text{Current} \times DR)} \text{ s} \quad (1)$$

$$= 3108 \text{ s} = 52 \text{ min}$$

$$\text{Fluence} = \frac{\text{Time} \times \text{Current}}{Q \times A} \text{ cm}^{-2} \quad (2)$$

$$= 4.88 \times 10^{14} \text{ cm}^{-2}$$

## 3. Results

As mentioned before, it is expected that during irradiation, microstructural deformation and defects will be recombined up to some extent. Raman spectroscopy of the amorphous thin films confirms this hypothesis. It is seen that the Ge<sub>30</sub>Se<sub>70</sub> glass Figure 2a is built predominantly by corner sharing (CS) and edge sharing (ES) tetrahedra and Se chains (CH). The presence of such structural units is proved by the high-frequency bands  $A_1$  and  $A_1^C$  at  $200 \text{ cm}^{-1}$  (CS) and  $219 \text{ cm}^{-1}$  (ES), respectively. The occurrence of Se chains is demonstrated by the vibration spectra at  $230\text{--}280 \text{ cm}^{-1}$ .<sup>[45,46]</sup> After irradiation with 200 keV, the Raman spectra demonstrate an increased areal intensity of the Se–Se chain mode and breaking of the ES building blocks, which at higher irradiation are restored and at irradiation with 1000 keV, their aerial intensity related to the areal intensity of the CS units is close to the initial one before irradiation although their absolute values are smaller, Figure 2a. The crystalline structure, Figure 2b, firmly demonstrates phase change and

**Table 1.** Calculation of DPA.

Energy [keV]	Ge at% (x)	Damage rate [ $\#/(cm \text{ ion})$ ]	Time [s]	Fluence [ $\text{cm}^{-2}$ ]	Charge, $Q$ [C]	Area, $A$ [ $\text{cm}^2$ ]	Current, $I$ [ $\mu\text{A}$ ]	Density [ $\text{atoms cm}^{-3}$ ]	DPA
200	30	$3.40 \times 10^8$	900	$4.92 \times 10^{14}$	$1.6 \times 10^{-19}$	4	0.35	$3.36 \times 10^{22}$	4.98
200	33	$3.35 \times 10^8$	900	$4.92 \times 10^{14}$	$1.6 \times 10^{-19}$	4	0.35	$3.34 \times 10^{22}$	4.94
200	40	$3.60 \times 10^8$	900	$4.92 \times 10^{14}$	$1.6 \times 10^{-19}$	4	0.35	$3.45 \times 10^{22}$	5.14
600	30	$3.25 \times 10^8$	3108	$4.88 \times 10^{14}$	$3.2 \times 10^{-19}$	4	0.201	$3.36 \times 10^{22}$	4.72
600	33	$3.30 \times 10^8$	3108	$4.88 \times 10^{14}$	$3.2 \times 10^{-19}$	4	0.201	$3.34 \times 10^{22}$	4.82
600	40	$3.40 \times 10^8$	3108	$4.88 \times 10^{14}$	$3.2 \times 10^{-19}$	4	0.201	$3.45 \times 10^{22}$	4.81
1000	30	$3.00 \times 10^8$	11 160	$5.81 \times 10^{14}$	$4.8 \times 10^{-19}$	4	0.1	$3.36 \times 10^{22}$	5.19
1000	33	$3.05 \times 10^8$	11 160	$5.81 \times 10^{14}$	$4.8 \times 10^{-19}$	4	0.1	$3.34 \times 10^{22}$	5.31
1000	40	$3.25 \times 10^8$	11 160	$5.81 \times 10^{14}$	$4.8 \times 10^{-19}$	4	0.1	$3.45 \times 10^{22}$	5.48

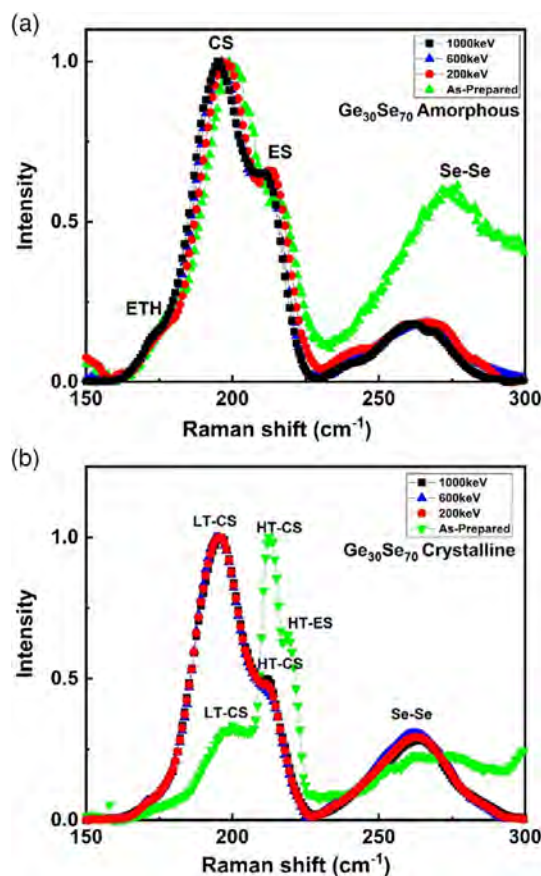


**Figure 2.** Raman spectra of  $\text{Ge}_{30}\text{Se}_{70}$  under different irradiation. a) Amorphous and b) crystalline.

crystalline structure characteristic for the low temperature (LT) polymorph form of  $\text{GeSe}_2$ .<sup>[47]</sup> However, this crystal structure loses stability after irradiation, the Raman modes undergo low energy shift, which is characteristic of the modes arising from a more disordered structure. With the increase in the irradiation energy, the formation of ES breathing mode becomes more prominent, which is an indication for crystallization of the LT polymorph form of  $\text{GeSe}$ .

In addition to CS, ES, and Se-Se peak,  $\text{Ge}_{33}\text{Se}_{67}$  thin films exhibit a distinct peak in **Figure 3a** around  $178\text{ cm}^{-1}$ , which indicates vibrations of Ge-Ge bonds representing the formation of ethane-like structure  $\text{Ge}_2(\text{Se}_{1/2})_6$  (ETH).<sup>[48]</sup> After irradiation, a reduction of both Ge-Ge and Se-Se aerial peak intensity is seen along with an increase in ES peak intensity, suggesting structural reorganization and consuming the wrong bonds for the formation of ES structures. The Raman spectra of as-prepared crystallized films shown in **Figure 3b** exhibit only well-expressed CS vibrations, characteristic for the high temperature (HT)  $\text{GeSe}_2$  polymorph form. After irradiation, structural transformation occurs by which formations of ES vibrations are well shaped on the Raman spectra, indicating crystallization of LT  $\text{GeSe}$ . This effect is accompanied by a decrease in the areal intensity of the Se-Se chain mode.

As expected, the ETH structure dominates in the Raman spectra of the  $\text{Ge}_{40}\text{Se}_{60}$  films in **Figure 4a**. Moreover, the vibrational

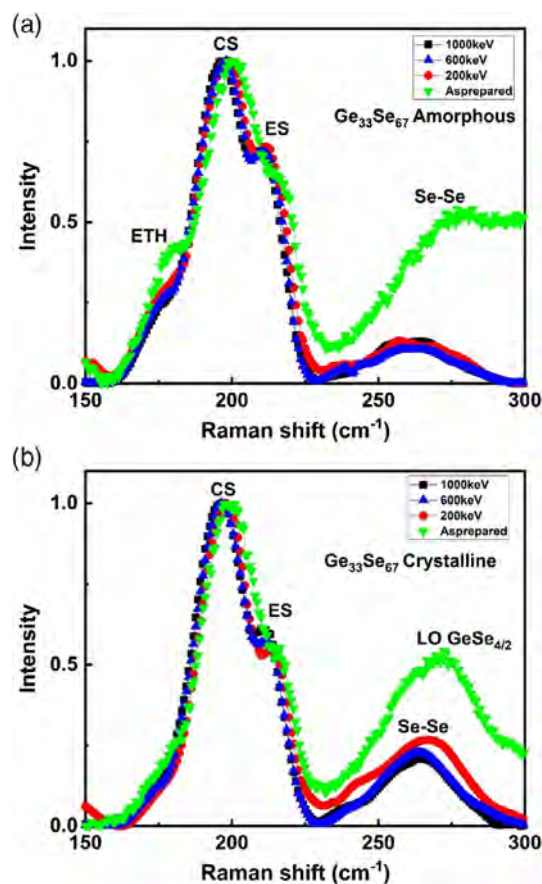


**Figure 3.** Raman spectra of  $\text{Ge}_{33}\text{Se}_{67}$  under different irradiation. a) Amorphous and b) crystalline.

band in the range of  $270\text{ to }310\text{ cm}^{-1}$  can be fitted with one Gaussian, which implies the presence of only one type of structural unit. The size of the vibrational mode and the composition suggest that it is unrealistic to consider this vibrational band is occurring from Se-Se chains which are energetically not favorable.<sup>[49]</sup> It is more logical to consider this vibration as rather related to asymmetric vibrations of tetrahedral structures containing Ge and Se. So, we suggest that these vibrations are related to asymmetric ES breathing mode. Based on this hypothesis, the Ge-rich glasses are anticipated to be quite phase separated. Up to 1000 keV energy, these films keep their basic structure. However, at irradiation with 1000 keV, the structure is totally destroyed, representing only CS and ES vibrations simultaneously with a substantial decrease in the areal intensity around  $267\text{ cm}^{-1}$ . The nonirradiated crystals suggest the formation of the LT  $\text{GeSe}_2$  in **Figure 4b**. After irradiation, there is a growth of the areal intensity at lower energy, which suggests a strong development of CS and ES structural units, leading to the formation of the LT  $\text{GeSe}$ .

The X-ray diffraction (XRD) spectra of the crystallized thin films are shown in **Figure 5a-c**. The XRD data confirm the Raman results in this that they demonstrate a presence of the LT and HT  $\text{GeSe}_2$  phase at the initial crystallization, which then is transformed into an LT  $\text{GeSe}$  phase. Hexagonal Se is present in all thin films and its crystal size is related to the availability to form wrong bonds after irradiation. In many cases,  $\text{GeSe}$  crystals



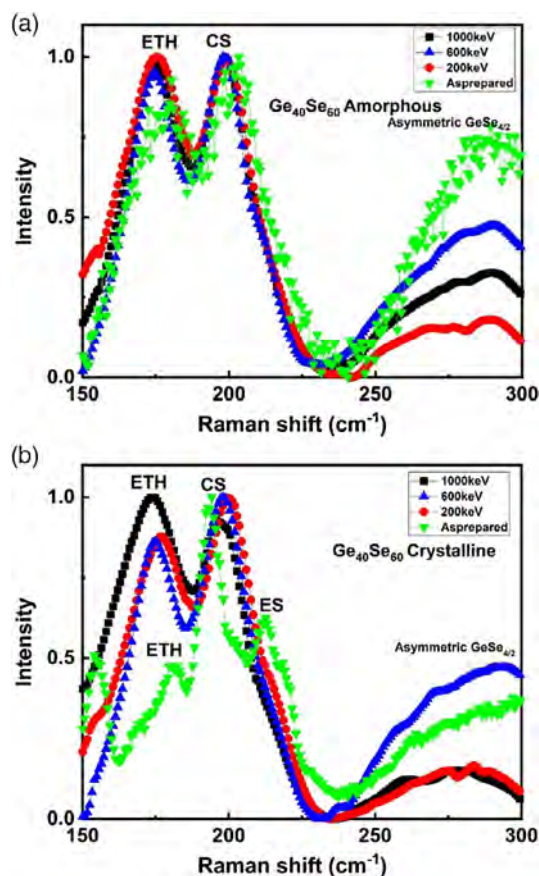


**Figure 4.** Raman spectra of  $\text{Ge}_{40}\text{Se}_{60}$  under different irradiation. a) Amorphous and b) crystalline.

are also present and although their appearance seems to be very sporadic, it needs in-depth discussion. In  $\text{Ge}_{30}\text{Se}_{70}$ , GeSe is not present in the as-prepared film. It only emerges after 200 keV irradiation and after 600 and 1000 keV, the GeSe peak is missing, Figure 5a. In  $\text{Ge}_{33}\text{Se}_{67}$ , the GeSe peak emerges after 200 keV irradiation and is missing only for 600 keV, Figure 5b. In  $\text{Ge}_{40}\text{Se}_{60}$ , all three peaks are present for each condition, Figure 5c. But for 600 keV, the GeSe peak suggests the formation of crystals with the smallest size. To further understand the effect of irradiation, the size of the crystals was calculated (Table 2).

## 4. Discussion

Traveling through solids ions interact/collide with stationary atoms and change their initial trajectory. While traveling, they also lose energy in radiative processes. Since the radiative processes like bremsstrahlung and Cherenkov radiation are very limited for ions, they can be neglected. In addition, ions can pick up electrons from various shells and become a very slow-moving ion going through cascade collisions and ultimately stop. So, there are two types of energy transfer mechanisms involved i) elastic scattering: collision of nuclei, and ii) inelastic collision: excitation and ionization of atoms. Typically, when ion energy is below  $10 \text{ keV amu}^{-1}$ , elastic scattering dominates.<sup>[50]</sup>

TRIM simulation showed the penetration range of the Xe ions in different compositions. The TRIM simulation of the Xe ions' interaction example of which is shown in Figure 6 for  $\text{Ge}_{40}\text{Se}_{60}$  demonstrates that at the chosen fluence, ions with energy 200 keV ( $1.53 \text{ keV amu}^{-1}$ ) penetrate only in the chalcogenide glass film, the ions with energy 600 keV ( $4.58 \text{ keV amu}^{-1}$ ) reach the  $\text{SiO}_2$  film and stop close to the interface  $\text{ChG/SiO}_2$ , and those with 1000 keV ( $7.65 \text{ keV amu}^{-1}$ ) energy penetrate the  $\text{SiO}_2$  substrate. It should be noted here that Figure 6 shows both the range of the ions (d) and actual depths (a–c).

This is characteristic for all studied compositions with small variations in the particular penetration depth, which depends upon the density of the chalcogenide glass (Figure 7) which is one other factor to be considered.<sup>[51]</sup>

The simulation shows that the longitudinal penetration range increases with ion energy and decreases with the density of the material. The peak damage rate calculated from TRIM shows an opposite to the penetration pattern in Figure 8. Damage goes lower with energy and is proportional to the density. We suggest that with more energy, the ions penetrate further and more interaction happens at the interface or in the substrate. Also, ions interact more with denser materials, since they come in contact with a higher number of atoms, therefore higher damage rate in  $\text{Ge}_{40}\text{Se}_{60}$ .

Another important factor here is the size of the atoms compared to the ions. The  $\text{Xe}^+$  ion ( $1.08 \text{ \AA}$ ) is smaller than Ge atoms ( $1.25 \text{ \AA}$ ) but similar to Se atoms ( $1.03 \text{ \AA}$ ).<sup>[52]</sup> The effect is clear from the simulation, Figure 9, which shows only for Ge-rich glass  $\text{Ge}_{40}\text{Se}_{60}$ , Ge target vacancy was higher than for Se. This phenomenon plays an important role in irradiated crystalline films.

Due to the amorphous nature of the glassy films, the effect of irradiation is not so prominent. But the crystalline films showed the effect of the irradiation clearly. Since Se can be displaced more than Ge, due to the ion–atom size equality, it was expected that the Se-rich composition  $\text{Ge}_{30}\text{Se}_{70}$  will be most affected by the irradiation. For this composition, two important factors interplay during the interaction with ions. On one hand, the structural stability of the Se-rich  $\text{Ge}_{30}\text{Se}_{70}$  amorphous films, Figure 2a,b. This is mainly based on their floppiness,<sup>[53]</sup> which allows an easy arrangement of the structural units during external stimuli by changing the angles under which the tetrahedra are organized without affecting the basic ratio of the structural units. On the other hand, the cation–cation distance, in this case, is smaller than in the stoichiometric composition as revealed by X-ray photoelectron spectroscopy (XPS) studies<sup>[54]</sup> and so the interaction with the Xe ions will be much stronger compared to with smaller ions, such as Kr ions, for example.<sup>[55]</sup> Figure 5a shows that a very dominant peak of orthorhombic GeSe is present after irradiation with 200 keV ions. This is an indication of the formation of Se deficient structure. However, the GeSe peak is missing at irradiation with 600 and 1000 keV. In addition to having the smallest size of GeSe crystals compared to the other two compositions, this can also mean that the GeSe crystals form near the glass-substrate interface, and since higher energy ions penetrate further, these crystals are affected. The Raman spectra at these conditions exhibit well-expressed ES structure formation. This indicates the presence of crystals with structure combining CS and ES building blocks, which is characteristic of the LT polymorph form of

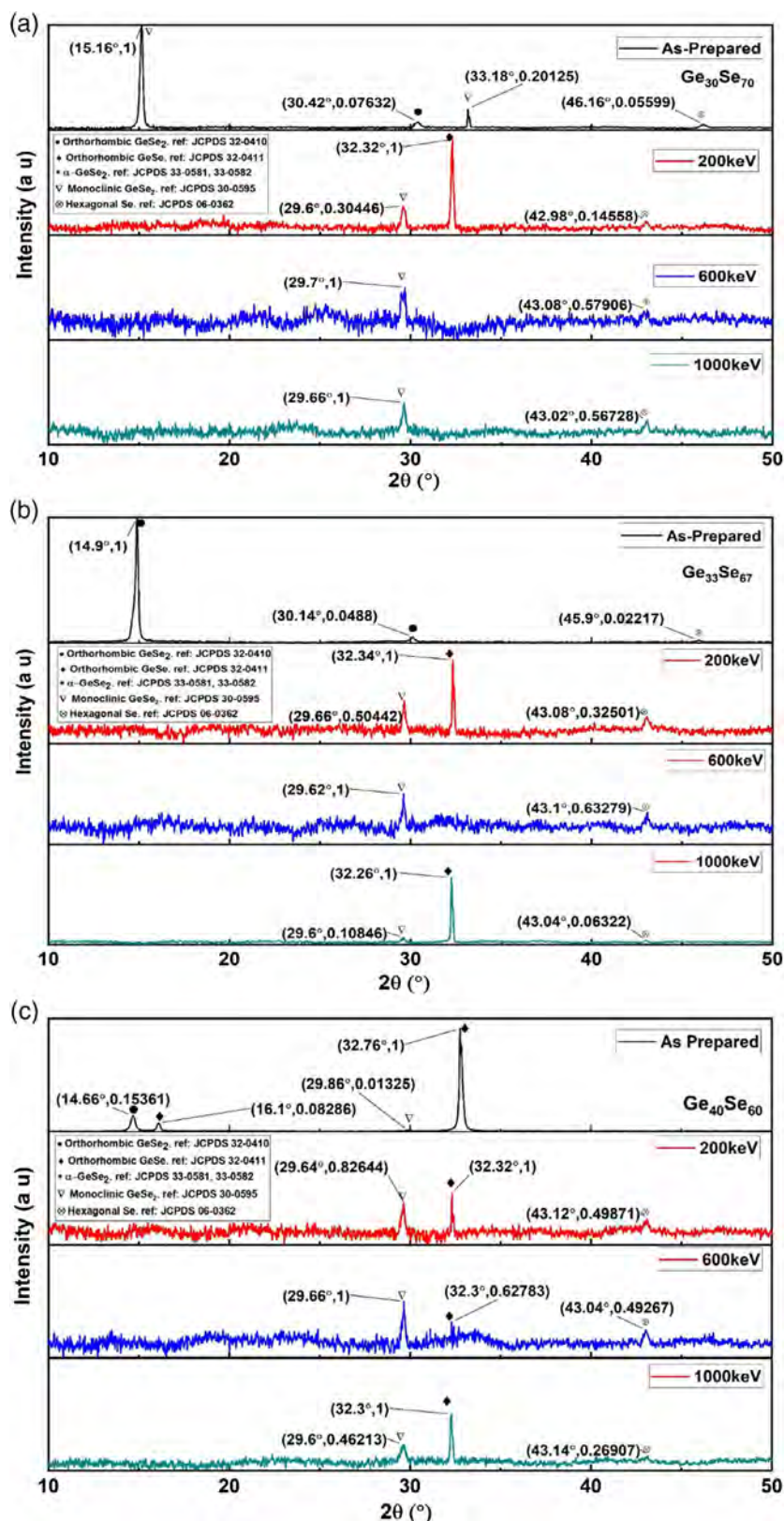


**Figure 5.** XRD of irradiated and as-prepared crystallized thin films. a)  $\text{Ge}_{30}\text{Se}_{70}$ , b)  $\text{Ge}_{33}\text{Se}_{67}$ , and c)  $\text{Ge}_{40}\text{Se}_{60}$ .

**Table 2.** Crystal thickness from XRD.

Composition	Ion energy [keV]	Crystals	Peak $[2\theta]^\circ$	Crystal grain thickness [nm]
Ge <sub>30</sub> Se <sub>70</sub>	200	Orthorhombic GeSe	32.32	41.34
Ge <sub>30</sub> Se <sub>70</sub>	200	Monoclinic GeSe <sub>2</sub>	29.6	35.44
Ge <sub>30</sub> Se <sub>70</sub>	200	Hexagonal Se	42.98	38.82
Ge <sub>30</sub> Se <sub>70</sub>	600	Monoclinic GeSe <sub>2</sub>	29.7	29.34
Ge <sub>30</sub> Se <sub>70</sub>	600	Hexagonal Se	43.08	23.72
Ge <sub>30</sub> Se <sub>70</sub>	1000	Monoclinic GeSe <sub>2</sub>	29.66	58.68
Ge <sub>30</sub> Se <sub>70</sub>	1000	Hexagonal Se	43.1	44.94
Ge <sub>33</sub> Se <sub>67</sub>	200	Orthorhombic GeSe	32.34	119.32
Ge <sub>33</sub> Se <sub>67</sub>	200	Monoclinic GeSe <sub>2</sub>	29.66	47.78
Ge <sub>33</sub> Se <sub>67</sub>	200	Hexagonal Se	43.08	21.86
Ge <sub>33</sub> Se <sub>67</sub>	600	Monoclinic GeSe <sub>2</sub>	29.62	59.25
Ge <sub>33</sub> Se <sub>67</sub>	600	Hexagonal Se	43.1	94.87
Ge <sub>33</sub> Se <sub>67</sub>	1000	Orthorhombic GeSe	32.26	60.77
Ge <sub>33</sub> Se <sub>67</sub>	1000	Monoclinic GeSe <sub>2</sub>	29.6	71.42
Ge <sub>33</sub> Se <sub>67</sub>	1000	Hexagonal Se	43.04	47.42
Ge <sub>40</sub> Se <sub>60</sub>	200	Orthorhombic GeSe	32.32	145.35
Ge <sub>40</sub> Se <sub>60</sub>	200	Monoclinic GeSe <sub>2</sub>	29.64	43.69
Ge <sub>40</sub> Se <sub>60</sub>	200	Hexagonal Se	43.12	40.66
Ge <sub>40</sub> Se <sub>60</sub>	600	Orthorhombic GeSe	32.3	250.53
Ge <sub>40</sub> Se <sub>60</sub>	600	Monoclinic GeSe <sub>2</sub>	29.66	43.24
Ge <sub>40</sub> Se <sub>60</sub>	600	Hexagonal Se	43.04	37.11
Ge <sub>40</sub> Se <sub>60</sub>	1000	Orthorhombic GeSe	32.3	51.67
Ge <sub>40</sub> Se <sub>60</sub>	1000	Monoclinic GeSe <sub>2</sub>	29.6	37.33
Ge <sub>40</sub> Se <sub>60</sub>	1000	Hexagonal Se	43.14	121.99

GeSe.<sup>[47,56]</sup> It indeed has been registered on the XRD spectra, Figure 5a with growing crystal size as a function of the irradiation energy.

Regarding the Ge<sub>33</sub>Se<sub>67</sub> composition, the interaction with the Xe ion affects mainly the Ge–Ge bonds (bond enthalpy 263.6 kJ mol<sup>−1</sup>)<sup>[57]</sup> in the ETH-like structure and facilitates the reaction of the newly formed Ge dangling bonds with Se atoms from the Se chains. The irradiation with higher energy leads to phase separation and redshift of the tetrahedral breathing modes, giving rise to the appearance of the A<sub>1</sub> breathing mode at 200 cm<sup>−1</sup>, characteristic for the LT phase of GeSe<sub>2</sub>,<sup>[56]</sup> and well expressed Se-chain mode. It is important to note that in the crystalline phase, the A<sub>1</sub><sup>C</sup> mode is appearing at 218 cm<sup>−1</sup>. Figure 3a shows the presence of ES tetrahedra and this structure is preserved during the irradiation. The predominant formation of hetero-bonding in the network explains the structural stability of this composition after irradiation, as presented in the Raman data, Figure 3b. Indeed due to the Ge/Se ratio, which in the ideal case would lead to the formation of a particular number of only CS and ES tetrahedra, the structure of both—the amorphous and crystalline phases, remains very stable during the irradiation with Xe ions after the Ge–Ge bonds collapse. This new structure occurring after irradiation brings about to formation after crystallization of LT GeSe, Figure 5b. We suggest that the formation

is due to the interaction of the Ge–Se network with the Xe ions. Xe replaces some of the Se atoms and depletes the Ge–Se matrix of selenium as discussed for Se-rich composition. A similar effect has been registered in the study by Abdel-Rahim et al.<sup>[58]</sup> with increasing Ge concentration in the films. Here, one more phenomenon needs explanation—the lack of formation of GeSe at irradiation with 600 keV. We suggest this is due to the reasons already explained about the Ge<sub>30</sub>Se<sub>70</sub> composition but in this case, there is a clear appearance of GeSe crystals at 1,000 keV irradiation. The stoichiometric composition Ge<sub>33</sub>Se<sub>67</sub> is the least dense among all the studied glasses, Figure 7. Nevertheless, its density is still higher than that of SiO<sub>2</sub> (2.27 g cm<sup>−3</sup>) and Si (2.33 g cm<sup>−3</sup>).<sup>[59,60]</sup> So, there would be massive penetration of Xe ions which reach the Si substrate where repulsion of charged species can occur. It is for this reason that the Raman spectrum at the highest irradiation energy shows biggest damage of the amorphous structure, Figure 3b and consequently forms Se-depleted GeSe crystals, Figure 5b.

The amorphous Ge-rich composition Ge<sub>40</sub>Se<sub>60</sub> displays big structural stability, although there are expectations that the interaction with the Xe ions will be the strongest due to its closest packaging and highest density.<sup>[56]</sup> However, Wang et al.<sup>[61]</sup> gave evidence that the Ge-rich structure is quite phase separated. As revealed by TRIM simulation, Figure 9, in the area of Ge–Ge bonding, the interaction with the incoming ions would be limited because of the bigger size of Ge atoms and therefore the lower density seen by the Xe ions. The networks beyond the chalcogenide film (the SiO<sub>2</sub> film and the Si substrate), which are reached by the ions with the energies of 600 keV and 1000 keV, respectively, provide channels for these ions because of their lower density. Therefore, Xe ions interact only with the higher density clusters in the chalcogenide glass matrix and escape to the lower density regions (SiO<sub>2</sub> and Si) affecting the chalcogenide network only at the highest energy used. Similarly, in the crystalline phase, unstable crystalline organization before irradiation is seen. But after irradiation, the structural organization is left unbroken even at highest irradiation energy giving rise to LT GeSe crystalline in accordance with the results reported by Wang et al.<sup>[46]</sup> Figure 9 shows that for this composition, the number of the Ge vacancies is much higher than the number of Se vacancies which is an exception compared to the other compositions. Although from the chemical point of view, we consider Ge<sub>40</sub>Se<sub>60</sub> as Ge-rich, from the atomistic point of view, there are more Se than Ge atoms in all regarded compositions. Moreover, Se is heavier than Ge and it would have been more intuitive if Ge showed more vacancies at even Ge<sub>33</sub>Se<sub>67</sub>. We propose that for  $x \leq 33$ , the damage/vacancy is “size-dependent” and for  $x \geq 33$ , the damage is “mass-dependent”. From Figure 9, it is also evident that with higher density, we get higher damage. So, the whole ion–matter interaction is a multivariate multiphysics problem that becomes much more complex when it comes to irradiating crystalline materials. In addition to all of these phenomena, surprisingly, the crystalline materials have been known to change to a different crystal phase after irradiation<sup>[62–64]</sup> and such transition is observed in our case. Experiments suggest that ion irradiation is also a stabilizing process for such a phase transition.<sup>[65]</sup> In this case, the main reason for this stability is that the ES structure requires less energy to form and their formation opens the



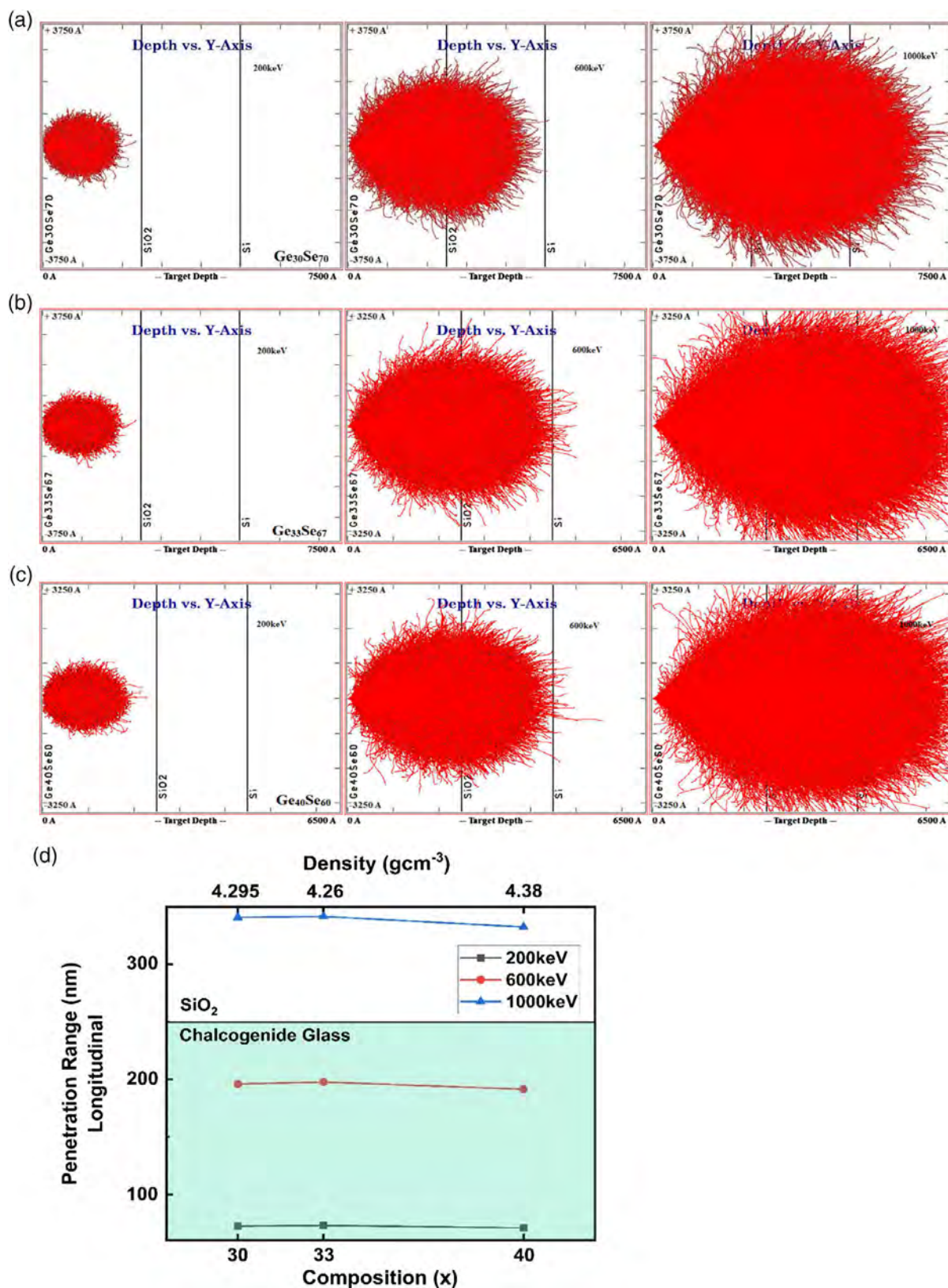


**Figure 6.** Ion penetration depth in chalcogenide glass a)  $\text{Ge}_{30}\text{Se}_{70}$ , b)  $\text{Ge}_{33}\text{Se}_{67}$ , c)  $\text{Ge}_{40}\text{Se}_{60}$  from simulation, and d) penetration range.

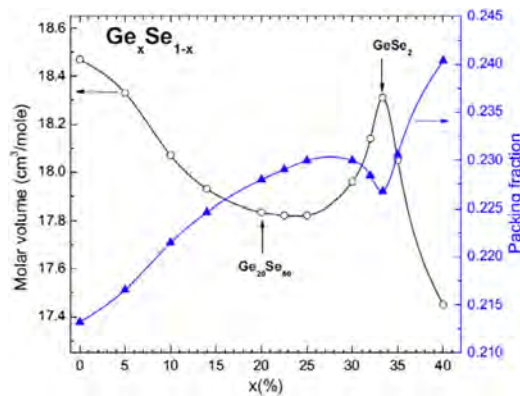


**Figure 7.** Molar volume and packing fraction of Ge-Se glasses as a function of composition (cf. ref. [51]).

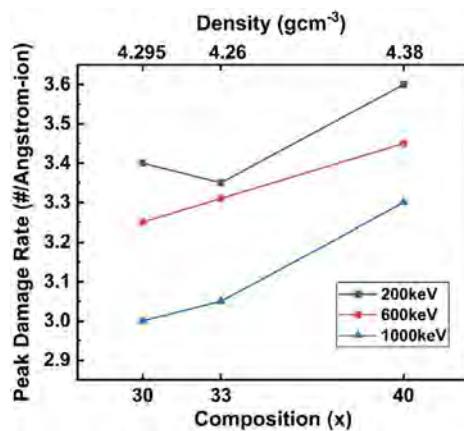


**Figure 8.** Peak damage rate versus composition.

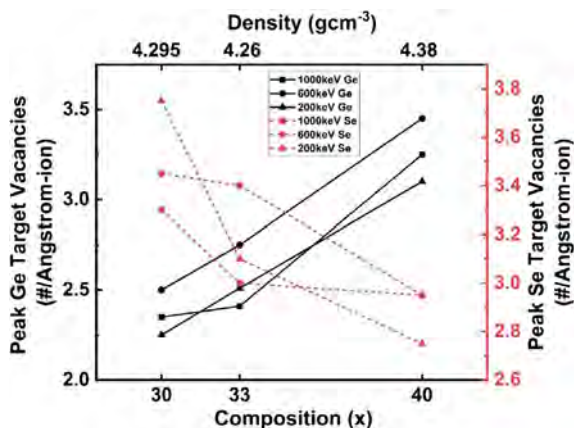


**Figure 9.** Vacancy produced in germanium and selenium atoms.

structure<sup>[66]</sup> which reduces the opportunity for crystal damage by the incoming Xe ions.

A proof of concept for the application of phase change effect for temperature monitoring under irradiation with Xe ions was given by testing a batch of prototypes of a phase change

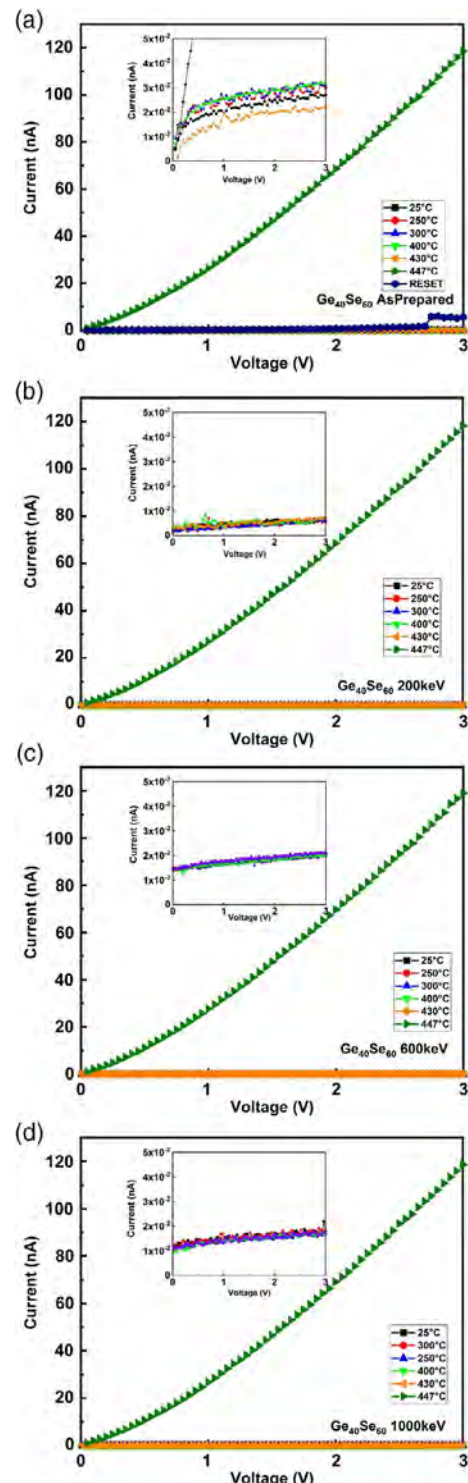


**Figure 10.** Ge<sub>40</sub>Se<sub>60</sub> device characterization. a) As-prepared; irradiated with Xe ions of b) 200 keV, c) 600 keV, and d) 1000 keV.

temperature sensor, **Figure 10**. Those are devices based on Ge<sub>40</sub>Se<sub>60</sub> composition. The *I*-*V* characteristics of devices are stable without any significant changes in the current up to the onset of crystallization. After 15 sec of heating at the onset of

crystallization temperature, the current of the devices rises significantly (ON state) compared to the one for the amorphous (OFF state) phase ( $I_{\text{on}}/I_{\text{off}} = 10^3$ ) and from the  $I$ - $V$  characteristic it is evident that the conduction mechanism has also changed, as in the ON state shows Ohmic characteristic. The as-prepared devices were reversed (RESET) by electrically pulsing them for 10 min. A closer look at the  $I$ - $V$  characteristic shows that the reversed devices' conductivity is within the frames of the initial device performance (inset of Figure 10). Further research is required to optimize and establish the parameters of reversibility.

This process should be much easier for the irradiated cases having in mind the amorphization of the crystalline phases occurring during the ion-chalcogenide films interaction. The OFF state conductivity of the irradiated devices is very stable. This is not a surprise considering the structural stability of this composition demonstrated in the Raman spectra obtained at different irradiation doses. Because of the structural inhomogeneity of this composition and the expected fluctuation of the interactions with the Xe ions, the average of the OFF state current is not a function of the irradiation energy which is within  $10^{-2}$  nA and keeping the ON/OFF current ratio stable.

## 5. Conclusion

The collected data presented here draw a complete picture of the application of Ge-Se chalcogenide glasses in a high-radiation environment as a temperature-sensing material. From TRIM simulation, ion irradiation parameters are chosen to study the effect of chalcogenide glass, glass/insulator interface, and Si substrate. This article reveals that irradiation with Xe ions, although introducing some small changes in the structure of the studied amorphous phases, they remain stable even at high-irradiation energies. More expressed structural changes occur in the crystalline phases which in the course of irradiation change their structure from LT/HT GeSe<sub>2</sub> to LT GeSe. This stabilizes it and opens up the structure reducing the damaging effects in it. From XRD data, the evidence of ion-irradiation induced crystal-crystal phase change in crystalline Ge-Se thin films is found. The emergence of Se-depleted, orthorhombic-GeSe transition has been attributed to complex interaction of Xe ion size, energy, density, and temperature. From the presented devices, it is seen that the OFF currents are within  $10^{-2}$  nA with or without irradiation and the ON/OFF current ratio is  $10^3$  which is considerably high.

## Acknowledgements

This work was financially supported by the USA Department of Energy (DOE), grant number DOE-NE 0008691 and DOE-NSUF grant, 19-2832. The authors gratefully acknowledge DOE's contribution to the advancement of their research. The authors also acknowledge the usage of the Raman spectroscopy system at Boise State Surface Science Lab.

## Conflict of Interest

The authors declare no conflict of interest.

## Keywords

Ge-Se glasses, ion-induced damage, ion irradiation, phase change, temperature sensors

Received: August 3, 2020

Revised: October 14, 2020

Published online: October 20, 2020

- [1] B. Prasai, M. E. Kordes, D. A. Drabold, G. Chen, *Phys. Status Solidi B* **2013**, 250, 1785.
- [2] K. Prasai, D. A. Drabold, *Nanoscale Res. Lett.* **2014**, 9, 594.
- [3] K. Prasai, G. Chen, D. A. Drabold, *Phys. Rev. Mater.* **2017**, 1, 015603.
- [4] D. Igram, H. E. Castillo, D. A. Drabold, *J. Non-Cryst. Solids* **2019**, 514, 1.
- [5] D. N. Tafen, D. A. Drabold, M. Mitkova, *Phys. Status Solidi B* **2005**, 242, R55.
- [6] D. N. Tafen, D. A. Drabold, M. Mitkova, *Phys. Rev. B* **2005**, 72, 054206.
- [7] F. Inam, D. N. Tafen, G. Chen, D. A. Drabold, *Phys. Status Solidi B* **2009**, 246, 1849.
- [8] G. Chen, F. Inam, D. A. Drabold, *Appl. Phys. Lett.* **2010**, 97, 131901.
- [9] B. Cai, X. Zhang, D. A. Drabold, *Phys. Rev. B* **2011**, 83, 092202.
- [10] B. Cai, B. Prasai, D. A. Drabold, Atomistic Simulations of Flash Memory Materials Based on Chalcogenide Glasses, in *Flash Memories* (Ed: I. Stievano), IntechOpen **2011**, Ch. 12.
- [11] B. Prasai, D. A. Drabold, in *Molecular Dynamics Simulations of Disordered Materials: From Network Glasses To Phase-Change Memory Alloys* (Eds: C. Massobrio, J. Du, M. Bernasconi, P. S. Salmon), Springer International Publishing, Cham **2015**, pp. 511–524.
- [12] S. R. Ovshinsky, *Phys. Rev. Lett.* **1968**, 21, 1450.
- [13] F. H. Stillinger, P. G. Debenedetti, *Annu. Rev. Condens. Matter Phys.* **2013**, 4, 263.
- [14] T. Yanagishima, J. Russo, H. Tanaka, *Nat. Commun.* **2017**, 8, 15954.
- [15] G. W. Burr, M. J. Brightsky, A. Sebastian, H.-Y. Cheng, J.-Y. Wu, S. Kim, N. E. Sosa, N. Papandreou, H.-L. Lung, H. Pozidis, E. Eleftheriou, C. H. Lam, *IEEE J. Emerg. Select. Topics Circuit. Syst.* **2016**, 6, 146.
- [16] A. R. Barik, M. Bapna, D. A. Drabold, K. V. Adarsh, *Sci. Rep.* **2014**, 4, 1.
- [17] A.-A. Ahmed Simon, B. Badamchi, H. Subbaraman, Y. Sakaguchi, M. Mitkova, *J. Mater. Sci. Mater. Electron.* **2020**, 31, 11211.
- [18] W. Wełnic, A. Pamungkas, R. Detemple, C. Steimer, S. Blügel, M. Wuttig, *Nat. Mater.* **2006**, 5, 56.
- [19] Y. Imanishi, H. Hayashi, T. Nakaoka, *J. Mater. Sci.* **2018**, 53, 12254.
- [20] M. Wuttig, N. Yamada, *Nat. Mater.* **2007**, 6, 824.
- [21] A. V. Kolobov, P. Fons, A. I. Frenkel, A. L. Ankudinov, J. Tominaga, T. Uruga, *Nat. Mater.* **2004**, 3, 703.
- [22] A. V. Kolobov, P. Fons, J. Tominaga, *Sci. Rep.* **2015**, 5, 13698.
- [23] P. Guo, A. M. Sarangan, I. Agha, *Appl. Sci.* **2019**, 9, 530.
- [24] D. Adler, M. S. Shur, M. Silver, S. R. Ovshinsky, *J. Appl. Phys.* **1980**, 51, 3289.
- [25] P. Noé, A. Verdy, F. d'Acapito, J.-B. Dory, M. Bernard, G. Navarro, J.-B. Jager, J. Gaudin, J.-Y. Raty, *Sci. Adv.* **2020**, 6, eaay2830.
- [26] J. Takeda, W. Oba, Y. Minami, T. Saiki, I. Katayama, *Appl. Phys. Lett.* **2014**, 104, 261903.
- [27] T. Kavetsky, O. Shpotyuk, V. Balitska, G. Dovbeshko, I. Blonsky, I. Kaban, W. Hoyer, M. Iovu, A. Andriesh, in *Proc. of Sixth Int. Conf. on Advanced Optical Materials and Devices (AOMD-6)*, Proc. SPIE Vol. 7142, SPIE, Bellingham, WA **2008**, p. 71420B.
- [28] R. A. Street, N. F. Mott, *Phys. Rev. Lett.* **1975**, 35, 1293.
- [29] S. R. Ovshinsky, E. J. Evans, D. L. Nelson, H. Fritzsche, *J. Ovov. Res.* **1968**, 15, 311.



- [30] T. Shimizu, *Jpn. J. Appl. Phys.* **1978**, 17, 463.
- [31] A. Mishchenko, J. Berashevich, K. Wolf, D. A. Tenne, A. Reznik, M. Mitkova, *Opt. Mater. Express* **2015**, 5, 295.
- [32] M. Mitkova, K. Wolf, G. Belev, M. Ailavajhala, D. A. Tenne, H. Barnaby, M. Kozicki, *Phys. Status Solidi B Basic Res.* **2016**, 253, 1060.
- [33] M. S. Ailavajhala, Y. Gonzalez-Velo, C. Poweleit, H. Barnaby, M. N. Kozicki, K. Holbert, D. P. Butt, M. Mitkova, *J. Appl. Phys.* **2014**, 115, 043502.
- [34] J. L. Taggart, Y. Gonzalez-Velo, D. Mahalanabis, A. Mahmud, H. J. Barnaby, M. N. Kozicki, K. E. Holbert, M. Mitkova, K. Wolf, E. Deionno, A. L. White, *IEEE Trans. Nucl. Sci.* **2014**, 61, 2985.
- [35] T. Nichol, M. R. Latif, M. S. Ailavajhala, D. A. Tenne, Y. Gonzalez-Velo, H. Barnaby, M. N. Kozicki, M. Mitkova, *IEEE Trans. Nucl. Sci.* **2014**, 61, 2855.
- [36] N. Habib, C. H. Lam, R. McMahon, US8114686B2, **2012**.
- [37] D. Lencer, M. Salinga, B. Grabowski, T. Hickel, J. Neugebauer, M. Wuttig, *Nat. Mater.* **2008**, 7, 972.
- [38] V. F. Sears, *Neutron News* **1992**, 3, 29.
- [39] S. Bhosle, K. Gunasekera, P. Boolchand, M. Micoulaut, *Int. J. Appl. Glass Sci.* **2012**, 3, 189.
- [40] S. Bhosle, K. Gunasekera, P. Chen, P. Boolchand, M. Micoulaut, C. Massobrio, *Solid State Commun.* **2011**, 151, 1851.
- [41] S. Ravindren, K. Gunasekera, Z. Tucker, A. Diebold, P. Boolchand, M. Micoulaut, *J. Chem. Phys.* **2014**, 140, 134501.
- [42] M. Mitkova, M. N. Kozicki, H. C. Kim, T. L. Alford, *J. Non-Cryst. Solids* **2006**, 352, 1986.
- [43] J. Ziegler, *SRIM & TRIM*, <http://www.srim.org/SRIM/SRIMINTRO.htm>.
- [44] J. Ziegler, J. Biersack, M. Ziegler, in *SRIM – The Stopping and Range of Ions in Matter*, 5th ed, SRIM Co. **2008**, Ch. 7.
- [45] X. Feng, W. J. Bresser, P. Boolchand, *Phys. Rev. Lett.* **1997**, 78, 4422.
- [46] Y. Wang, K. Tanaka, T. Nakaoka, K. Murase, *J. Non-Cryst. Solids* **2002**, 299–302, 963.
- [47] K. Murase, in *Insulating and Semiconducting Glasses*, World Scientific, Singapore **2000**, pp. 415–463.
- [48] K. Jackson, *Phys. Status Solidi B* **2000**, 217, 293.
- [49] R. Holomb, V. Mitsa, S. Akyuz, E. Akalin, *Philos. Mag.* **2013**, 93, 2549.
- [50] D. K. Avasthi, G. K. Mehta, in *Swift Heavy Ions For Materials Engineering And Nanostructuring*, (Eds: D. K. Avasthi, G. K. Mehta) Springer Netherlands, Dordrecht **2011**, pp. 47–66.
- [51] V. Georgieva, M. Mitkova, P. Chen, D. Tenne, K. Wolf, V. Gadjanova, *Mater. Chem. Phys.* **2012**, 137, 552.
- [52] CrystalMaker Software, <http://crystallmaker.com/>.
- [53] P. Boolchand, G. Lucovsky, J. C. Phillips, M. F. Thorpe, *Philos. Mag.* **2005**, 85, 3823.
- [54] M.-L. Theye, A. Gheorghiu, C. Senemaud, M. F. Kotkata, K. M. Kandil, *Philos. Mag. B* **1994**, 69, 209.
- [55] P. K. Dwivedi, S. K. Tripathi, A. Pradhan, V. N. Kulkarni, S. C. Agarwal, *J. Non-Crystal. Solids* **2000**, 266–269, 924.
- [56] H. Takeuchi, O. Matsuda, K. Murase, *J. Non-Crystall. Solids* **1998**, 238, 91.
- [57] J. Rumble, in *Handbook of Chemistry And Physics*, 84th ed. (Ed: D. R. Lide), CRC Press, Cleveland, OH **2003**, pp. 9–55.
- [58] M. A. Abdel-Rahim, M. M. Hafiz, A. M. Shamekh, *Phys. B: Condens. Matter* **2005**, 369, 143.
- [59] L. Filipovic, *Topography Simulation of Novel Processing Techniques*, <https://www.iue.tuwien.ac.at/phd/filipovic/node26.html>.
- [60] E.-C. Inc, *Properties of Silicon and Silicon Wafers*, <https://www.el-cat.com/silicon-properties.htm>.
- [61] Y. Wang, K. Tanaka, T. Nakaoka, K. Murase, *Physica B: Condens. Matter* **2002**, 316–317, 568.
- [62] A. Sharma, M. Varshney, H.-J. Shin, Y. Kumar, S. Gautam, K. H. Chae, *Chem. Phys. Lett.* **2014**, 592, 85.
- [63] N. C. Mishra, *Radiat. Eff. Defects Solids* **2011**, 166, 657.
- [64] D. Simeone, D. Gosset, J. L. Bechade, A. Chevarier, *J. Nucl. Mater.* **2002**, 300, 27.
- [65] B. Schuster, C. Trautmann, F. Fujara, *Sci. Rep.* **2010**, 2011, 370.
- [66] T. G. Edwards, S. Sen, *J. Phys. Chem. B* **2011**, 115, 4307.

# Space-Projected Conductivity and Spectral Properties of the Conduction Matrix

Kashi N. Subedi,\* Kiran Prasai, and David A. Drabold

Herein, the Kubo–Greenwood formula is utilized to project the electronic conductivity into real space, and a Hermitian positive semidefinite matrix  $\Gamma$  is discussed, which is called the *conduction matrix*, that reduces the computation of spatial conduction activity to a diagonalization. It is shown that for low-density amorphous carbon, connected  $sp^2$  rings and  $sp$  chains are conduction-active sites in the network. In amorphous silicon, transport involves hopping through tail states mediated by the defects near the Fermi level. It is found that for liquid silicon, thermal fluctuations induce spatial and temporal conductivity fluctuations in the material. The frequency-dependent absorption of light as a function of wavelength in an amorphous silicon suboxide (a-SiO<sub>1.3</sub>) is also studied. It is shown that the absorption is strongly frequency dependent and selects out different oxygen vacancy subnetworks depending on the frequency.  $\Gamma$  is diagonalized to obtain conduction eigenvalues and eigenvectors, and it is shown that the density of states of the eigenvalues for FCC aluminum has an extended spectral tail that distinguishes metals from insulators and semiconductors. The method is easy to implement with any electronic structure code, providing suitable estimates for single-particle electronic states and energies.

formula (KGF). This was later generalized as the “Fluctuation-Dissipation theorem” that mathematically connects dissipative processes with equilibrium fluctuations.<sup>[5]</sup> The ultimate roots of this work extend through time to Einstein and his work on Brownian motion and diffusion.<sup>[6]</sup>

In this article, we briefly review our recently proposed method to estimate the spatially projected conductivity (SPC),<sup>[7]</sup> apply it to a range of materials, and provide insights both into the materials we study and the method itself. The rest of this article is organized as follows. In Section 2, we review the KGF. In Section 3, we discuss background material on computing spatial transport information from computer models of materials. In Section 4, we describe our method, and in Section 5 we offer computational details and the models used. In Section 6, we explore five different systems: a low-density phase of amorphous carbon (a-C), amorphous and liquid silicon (l-Si), amorphous silicon (a-Si) suboxide,

and for a useful contrast, FCC aluminum. We draw conclusions in Section 7.

## 1. Introduction


Practical calculation of electron transport in materials<sup>[1]</sup> always involves assumptions and approximations. The most natural and oldest approach is to use Boltzmann’s equation,<sup>[2]</sup> which is ideal for a crystalline system with relatively weak impurity or thermal disorder. Implicit to such a picture is the assumption that  $\mathbf{k}$  is a good quantum number associated with the assumed lattice. A different way of framing the problem is due to Kubo,<sup>[3]</sup> who in 1957 computed the linear response (current) to an external electric field. The resulting expression for the electrical conductivity, further approximated within a single-particle picture of the electronic structure,<sup>[4]</sup> is called the Kubo–Greenwood

## 2. Kubo Formula

For calculations of charge transport in topologically disordered systems (amorphous or liquid), for which there is no underlying lattice, it is natural to adopt the Kubo approach. Mott and Davis<sup>[8]</sup> and Moseley and Lukes<sup>[9]</sup> offered an appealing physical derivation of the KGF that we tersely repeat here. Consider a system with an applied (external) AC electric field  $\mathbf{E}$ . The system absorbs photons from the electromagnetic field, and this drives electronic transitions near the Fermi level,  $\epsilon_F$ . Associated with this field, there is an electric current density  $\mathbf{j}$ . The Joule heat produced by the electric field per unit time is  $\Omega \mathbf{j} \cdot \mathbf{E}$ , where  $\Omega$  is the cell volume. The rate at which energy is absorbed from electronic transitions is  $\gamma = \sum_{if} \epsilon_{fi} (w_{fi} P_i - w_{if} P_f)$ . Here  $\epsilon_{fi}$  is the energy difference between initial and final states,  $w_{fi}$  is the transition probability per unit time between final state  $f$  and initial state  $i$ , and  $P_{i(f)}$  is the occupation probability of the initial (final) state. Next, one assumes that  $\gamma = \Omega \mathbf{j} \cdot \mathbf{E}$ . By using Fermi’s Golden Rule to estimate the transition probabilities, and defining the conductivity  $\sigma$  from the identification that  $\sigma E^2/2$  is the mean rate of energy loss per unit volume, one obtains the KGF for each  $k$ -point  $\mathbf{k}$ <sup>[3,4]</sup> (written here in a form most convenient for our purposes)

K. N. Subedi, Prof. D. A. Drabold  
 Department of Physics and Astronomy  
 Ohio University  
 Athens, OH 45701, USA  
 E-mail: ks173214@ohio.edu, kashi.subedi@gmail.com

Dr. K. Prasai  
 E. L. Ginzton Lab  
 Stanford University  
 Stanford, CA 94305, USA

 The ORCID identification number(s) for the author(s) of this article can be found under <https://doi.org/10.1002/pssb.202000438>.

DOI: 10.1002/pssb.202000438

$$\sigma_{\mathbf{k}}(\omega) = \sum_{i,j} g_{ij}(\mathbf{k}, \omega) \sum_{\alpha} |p_{ij}^{\alpha}|^2 \quad (1)$$

In the shorthand notation of Equation (1), we averaged over diagonal elements of the conductivity tensor ( $\alpha$  represents Cartesian directions),  $i$  and  $j$  index Kohn–Sham orbitals (or other single-particle states)  $\psi_{i,\mathbf{k}}(x)$  with associated energies  $\epsilon_{i,\mathbf{k}}$ ,  $p^{\alpha}$  is the momentum operator (for direction  $\alpha$ :  $p^{\alpha} = -i\hbar \partial / \partial x_{\alpha}$ ) and  $g_{ij}(\mathbf{k}, \omega) = 2\pi e^2 [f_i(\mathbf{k}) - f_j(\mathbf{k})] \delta(\epsilon_j(\mathbf{k}) - \epsilon_i(\mathbf{k}) - \hbar\omega) / (3m^2 \omega \Omega)$ , and  $f$  is the Fermi–Dirac distribution. The matrix elements of the momentum operator are  $p_{ij}^{\alpha} = \langle \psi_j | p^{\alpha} | \psi_i \rangle$ . This is devised for amorphous materials which are assumed to be isotropic; it is equally easy to implement this method for a particular direction to explore anisotropy of conduction. It is remarkable that this expression for the conductivity, which exactly coincides with the study by Greenwood,<sup>[4]</sup> does not require an explicit expression for the current density. By carefully deriving the current density  $\mathbf{j}$ , one discovers that this derivation, and also Greenwood's, veils significant approximations involving the DC limit, and more subtly, the spatial homogeneity of carrier density. We will not further dwell on these technical issues here, and adopt the “standard” KGF (Equation (1)). See, for example, Equation 19 in the study by Zhang and Drabold<sup>[10]</sup> and associated discussion. For a full many-body picture, see the previous studies by Zhang and Drabold.<sup>[11,12]</sup>

The Kubo formula has been heavily used in liquids,<sup>[13–16]</sup> amorphous semiconductors,<sup>[17]</sup> and mixed systems.<sup>[18,19]</sup> In its usual application, the KGF is applied to a static disordered lattice. As such, it provides no information about thermal disorder and its consequences to conduction. For applications of the KGF in disordered systems, the electron–phonon coupling is large for localized single-particle states,<sup>[20,21]</sup> especially those orbitals near the Fermi energy. In a room temperature thermal molecular dynamics simulation, energy levels may fluctuate with a thermally induced root mean squared fluctuation  $\sigma_E \gg kT$ .<sup>[22,23]</sup>

Above the Debye temperature, it is sensible to estimate the temperature-dependent conductivity by undertaking a long constant-temperature molecular dynamics (MD) simulation and averaging the KGF over the trajectory. This seems to give reasonable results for the temperature dependence of pure and hydrogenated a-Si, and explains the high-temperature coefficient of resistance and functionality of doped a-Si:H as a material for night-vision device applications.<sup>[24]</sup>

Apart from the approximations mentioned earlier, there are many technical details for properly using the KGF, including finite size effects and such details as the broadening of the  $\delta$  function in Equation (1). A recent review details many issues about the use of KGF in hot condensed matter.<sup>[25]</sup> The KGF is a valuable tool, linking as it does transport experiments to the quantum mechanics of materials, but in its usual implementation gives just one function (the AC conductivity) or one *number* (the DC conductivity). It provides no spatial information about the conduction.

### 3. Computing Spatial Information about Transport

For heterogeneous systems, a basic question is: “what parts of the network are conducting?” Some emerging computer memory technologies (resistive random access memory [RAM] and

conducting bridge RAM) involve specific conduction pathways, and our microscopic understanding of such systems might be improved by a detailed atomistic understanding of the flow of charge through the systems. Conducting bridge RAM can be made from many amorphous insulating hosts (such as GeSe<sub>3</sub> or Al<sub>2</sub>O<sub>3</sub>, heavily doped with a transition metal like Ag or Cu). These are technologically important electrochemical devices for which basic questions arise about whether transport is simply through metal filaments or a more intricate process involving transport through metal-rich regions.<sup>[26]</sup> We have provided insight into this elsewhere.<sup>[7,26–29]</sup> Another example of keen current interest is physical unclonable function (PUF) devices for computer security, made from a-Si suboxide materials, as we discuss on more detail in Section 6.4. Another example of interest is conductance fluctuation in amorphous systems.<sup>[30]</sup>

With this tool in hand, the idea might also be pushed in an engineering direction as a common inverse problem of materials science: “what is the structure that I need to have a particular conductivity?”, or “what is the structure required to have a particular absorption of light of frequency  $\omega$ , eg., for the design of waveguides?” The inverse problem is always challenging: a robust tool of the form  $\mathbf{R} \rightarrow \emptyset$  (given coordinates what is the conducting path) is required before we can handle  $\emptyset \rightarrow \mathbf{R}$  (given the conducting path we seek, what coordinates—structure—will yield it?).

Some existing schemes yield insight into the spatial character of conduction. A principal message of the KGF is that the DC conductivity arises from transitions between states at or near the Fermi level. To obtain a nonzero conductivity, it is necessary that the momentum matrix element not vanish between the relevant occupied and unoccupied states (Equation (1)). If two such states  $\psi_i$  and  $\psi_j$  do not overlap, there is no contribution to the conductivity: transitions between spatially nonoverlapping orbitals are forbidden. So, to the extent that there is a large overlap between the two states, there is likely to be a larger momentum matrix element too. This is the idea behind a primitive approximation, the “ $q_i - q_j$ ” method that we use in ref. [27]. An even simpler scheme is to compute the charge density around the Fermi level<sup>[31]</sup>—it must be that the spatial conductivity involves those parts of space where this charge density is large, but this totally ignores the momentum matrix elements which lie at the heart of the KGF—these matrix elements are a legacy of the current–current correlation function, and it is not desirable to neglect these contributions. Other ideas related to spatial decomposition of conductivity have emerged in the literature before, including a computation of current densities for a randomly disordered system,<sup>[32]</sup> using the methods of Baranger and Stone.<sup>[33]</sup> Also, within a Landauer picture, the concept of transmission eigen-channels was introduced and later implemented with non-equilibrium Green's functions.<sup>[34]</sup>

## 4. Theory

### 4.1. SPC

The KGF (Equation (1)) gives the conductivity as a weighted sum of the modulus squared momentum matrix elements. The sums on Latin indices are over single-particle, for this article, Kohn–



Sham orbitals. The spatial dependence of the states is obviously important, but only insofar as this modulates the momentum matrix elements. Thus, it is desirable to rewrite the KGF expressing the matrix element quadratures as sums on a real space grid to find a spatial decomposition. Suppressing the explicit dependence of  $\sigma$  on  $\mathbf{k}$  and  $\omega$ , we write

$$\sigma = \sum_{ij\alpha} \int d^3x \int d^3x' g_{ij} [\psi_i^*(x) p^\alpha \psi_j(x)] [\psi_i^*(x') p^\alpha \psi_j(x')]^* \quad (2)$$

Next, define complex-valued functions

$$\xi_{ij}^\alpha(x) = \psi_i^*(x) p^\alpha \psi_j(x) \quad (3)$$

on a discrete real-space grid (call the grid points  $x$ ), and suppose, for simplicity, that the grid is uniformly spaced in 3D space with spacing  $h$ . Approximating the integrals as sums on the grid, and obtaining the operation of  $p^\alpha$  from centered finite differences, we easily arrive at

$$\sigma \approx h^6 \sum_{x,x'} \sum_{ij\alpha} g_{ij} \xi_{ij}^\alpha(x) [\xi_{ij}^\alpha(x')]^* \quad (4)$$

We find it useful to introduce what we will call the *conduction matrix*  $\Gamma$  defined as

$$\Gamma(x, x') = h^6 \sum_{ij\alpha} g_{ij} \xi_{ij}^\alpha(x) [\xi_{ij}^\alpha(x')]^* \quad (5)$$

$\Gamma$  is Hermitian and positive semidefinite. Note that  $\Gamma$  has the dimension of conductivity, and we have summed out the Kohn–Sham orbitals, leaving only spatial dependence. It follows from Equation (4) that  $\sigma = \sum_{x,x'} \Gamma(x, x')$  as  $h \rightarrow 0$ . We take the SPC to be  $\zeta(x) = |\sum_{x'} \Gamma(x, x')|$ . To obtain a real value for the scalar field  $\zeta$ , the modulus operation is required: while the full double sum is, of course, real, summing only one index of  $\Gamma$  yields a function that is, in general, complex.  $\zeta(x)$  is of interest as it is positive, and by construction indicates the conduction-active parts of the system. Similar forms are possible for the SPC. If, for example, only one of the matrix elements is computed on a grid, then if  $\phi_{ij} = h^3 g_{ij} p_{ij}^\alpha$ , then for  $\tau(x) = \sum_{ij\alpha} \phi_{ij} \xi_{ij}^\alpha(x)$ ,  $|\tau|$  also serves as an estimate for SPC, identical to  $\zeta$  as  $h \rightarrow 0$ .

## 4.2. Spectral Properties of the Conduction Matrix

The eigenvalue problem for  $\Gamma$  reads:  $\Gamma|\chi_\mu\rangle = \Lambda_\mu|\chi_\mu\rangle$ , for which  $\mu = 1, n_g$ .  $n_g$  is the number of points in the spatial grid (thus, for example,  $n_g = n^3$  for  $n$  points in each Cartesian direction in 3D). Diagonalization provides a spectral representation:  $\hat{\Gamma} = \sum_\mu |\chi_\mu\rangle \Lambda_\mu \langle \chi_\mu|$ , from which

$$\sigma = \sum_\mu \Lambda_\mu [1 + \sum_{x, x', x \neq x'} \chi_\mu(x) \chi_\mu^*(x')] \quad (6)$$

Equation (6) introduces the concept of conduction eigenvalues and modes. The spectral decomposition of  $\sigma$  of Equation (6) categorizes the conductivity into a finite and, in practice, small (compared with the dimension of  $\Gamma$ ) set of conduction channels. Because of trace invariance of  $\Gamma$ ,  $\sum_\mu \Lambda_\mu = \sum_x \Delta(x)$ , for  $\Delta(x) = \Gamma(x, x)$ . The spectral form for the SPC is thus

$$\zeta_s(x) = \left| \sum_\mu \Lambda_\mu \{ |\chi_\mu(x)|^2 + \sum_{x', x' \neq x} \chi_\mu(x) \chi_\mu^*(x') \} \right| \quad (7)$$

and  $\zeta(x) = \zeta_s(x)$ . We observe that if we take a diagonal approximation  $\Delta(x)$ , by omitting the second term on the RHS in Equation (6), the eigenvalue  $\Lambda_\mu$  would exactly give the conductance through channel  $\mu$ . In such an approximation,  $\sigma \sim \sum_\mu \Lambda_\mu = \text{Tr}(\Gamma)$ , a form reminiscent of the transmission eigen-channels,<sup>[34]</sup> but note that our full expression for  $\sigma$  is *not just a trace* over  $\Gamma$  in contrast with the transmission matrix appearing in the Landauer expression for conductance.

It is of interest to determine the value of an approximate  $\zeta_s$  (e.g., computed from only a handful of the eigenvectors conjugate to the largest eigenvalues) to  $\zeta$ . We discuss the density of states (DOS) of  $\Gamma$  later. For complex mixed conducting/insulating phases, we find that the eigenvectors  $\chi$  conjugate to extremal eigenvalues produce a remarkably compact and efficient description of the conduction, often reproducing the full  $\zeta$  with only a few tens of eigenvectors, even though  $\dim(\Gamma)$  is in the tens of thousands. For a metal (e.g., FCC Al), we again find a great accumulation of eigenvalues at  $\Lambda = 0$  but with a significant spectral tail unseen in less metallic systems. Thus, the high conductivity of a metal accrues from integrating over this tail. The DOS of  $\Gamma$  is yet another way to distinguish insulators, semiconductors, and metals.

So far, we have computed the eigenvectors of  $\Gamma$  by exact diagonalization. However, it is clear that this problem is ideal for a Lanczos technique.<sup>[35]</sup> A maximum entropy reconstruction of the DOS of  $\Gamma$  is also under investigation.<sup>[36]</sup>

## 5. Computational Details

### 5.1. Models

In this article, we used Vienna Ab initio Simulation Package (VASP)<sup>[37]</sup> code to carry out DFT calculations. The generalized gradient approximation (GGA) of Perdew–Burke–Ernzerhof (PBE)<sup>[38]</sup> was used as the exchange–correlation functional. Brillouin zone sampling was restricted to the gamma point ( $\mathbf{k} = 0$ ), and periodic boundary conditions were used throughout.

A model of low-density a-C was examined with density  $1.5 \text{ g cm}^{-3}$  and consisted of 216 atoms.<sup>[39]</sup>

An a-Si model with 216 atoms ( $\rho = 2.33 \text{ g cm}^{-3}$ ) was taken from the study by Djordjević et al.<sup>[40]</sup> and was relaxed using a conjugate gradient method. While relatively small by current standards, this model is an excellent representation of the topology of a-Si, and is 100% fourfold, though some of the sites are strained. The a-Si model was then melted at 2000 K for 6 ps to create representative snapshots for l-Si.

We modeled a-Si suboxide (a-SiO<sub>1.3</sub>) in cells with 184 atoms and density  $1.68 \text{ g cm}^{-3}$ <sup>[41]</sup> that was obtained using a melt-quench scheme.<sup>[42]</sup> We began with a supercell with a random initial configuration at the experimental density and desired stoichiometry, which was then heated above melting point. The supercell was then cooled to room temperature in successive steps. The final model was obtained by performing a relaxation to minimize the forces acting on each atom to below  $\approx 0.005 \text{ eV \AA}^{-1}$ .

A cubic model of crystalline FCC Al (c-Al) with 500 atoms was constructed.

We use various values of grid spacing ( $h$ ) throughout this article. We find that the SPC is fairly insensitive to  $h$ , and has checked the results presented here by considering a few different choices for  $h$  and verifying that the predicted SPCs were consistent.

## 5.2. Methods

To carry out the calculations, we used Kohn–Sham orbitals computed with VASP.<sup>[43]</sup> The  $\xi$  (of Equation (4)) was obtained using finite central differences with  $\delta r = 0.05$  Å. To estimate the SPC ( $\zeta$ ), we adopted a discrete grid with variable dimensions depending upon the supercell used. We selected a temperature of  $T = 1000$  K for the Fermi–Dirac distribution and approximated the delta function in  $g_{ij}$  by a Gaussian with width 0.05 eV. The numerical value of the conductivity is sensitive to these choices, the SPC plots far less so.

The extent of the localization of eigenvectors was quantitatively gauged by calculating the inverse participation ratio (IPR) defined as

$$\mathcal{I}_\mu = \frac{\sum_x (\chi_\mu(x))^4}{(\sum_x (\chi_\mu(x))^2)^2} \quad (8)$$

The value of  $\mathcal{I}$  lies between 0 and 1. Higher  $\mathcal{I}_\mu$  signifies that the eigenvector  $\chi_\mu$  is more spatially localized.

## 6. Results and Discussion

### 6.1. Low-Density a-C

Carbon materials have produced two Nobel prizes in the last quarter century. a-C has applications including protective coatings, radiation protection, electronic circuits, and biomedicine.<sup>[44–46]</sup> Carbon-based electronics is a major field of research in materials science.<sup>[47–50]</sup> Carbon in different forms

such as carbon nano tubes (CNTs) is being studied for PUF applications.<sup>[51]</sup> Carbon-based electrodes are used as electrochemical sensors for biological applications.<sup>[52]</sup>

a-C at low densities ( $< 2$  g cm<sup>−3</sup>) consists primarily of  $sp^2$  sites, with some  $sp$  and  $sp^3$  sites. Bhattarai *et al.* have shown that a-C at low densities ( $\rho = 0.92$ – $1.6$  g cm<sup>−3</sup>) exhibits  $sp^2$  configurations with  $\approx 66$ – $81\%$ ,  $sp$  chains with  $\approx 14$ – $33\%$ , and  $sp^3$  configurations with  $\approx 0$ – $9\%$ .<sup>[39]</sup> The presence of  $sp^2$  and  $sp$  configurations may render the materials electrically conductive and optically absorbing. Intuitively, it is clear that the connectivity between the  $sp$ ,  $sp^2$ , and  $sp^3$  subnetworks might also play a role in conduction. For densities below 1 g cm<sup>−3</sup>, it has been shown that the material consists of warped and wrapped regions of amorphous graphene, with considerable ring disorder.<sup>[53]</sup>

In this subsection, we discuss SPC in low-density a-C ( $1.5$  g cm<sup>−3</sup>) and also provide spectral information from the conduction matrix by diagonalizing it. We discretized the supercell into  $40 \times 40 \times 40$  grid points ( $h = 0.355$  Å) and obtained the conduction matrix  $\Gamma(x, x')$  which has dimension of 64 000. The conductivity path was obtained by calculating space-projected conductivity at each grid point as discussed in earlier section (Section 4.1). The SPC is projected as an isosurface (yellow blob) in left plot of Figure 1. As a technical exercise, we also compare the results to the diagonal approximation  $\Delta(x)$ .

The isosurface in the left plot shows that SPC is due to both  $sp$  and  $sp^2$  configurations in the network. It reveals active participation of  $sp$  chains in the network that form a clear connected conducting path and follow  $sp^2$  configurations to a pentagonal ring. Pentagonal and the hexagonal ring structures that are connected with  $sp$  chains form the other active sites for conduction. These rings are highlighted in the middle plot of Figure 1 that show only those atoms contributing significantly to conduction. The arrows indicate the continuous conduction path along the C atoms displayed in the left plot.  $sp^3$  configurations do not appear as SPC sites. As a consequence, they do not contribute to charge transport, as expected. To provide a simpler picture of the conduction, we projected  $\Delta(x)$ , the diagonal approximation of  $\zeta$ , as an isosurface in the right plot of Figure 1.  $\Delta$  is primarily centered on the

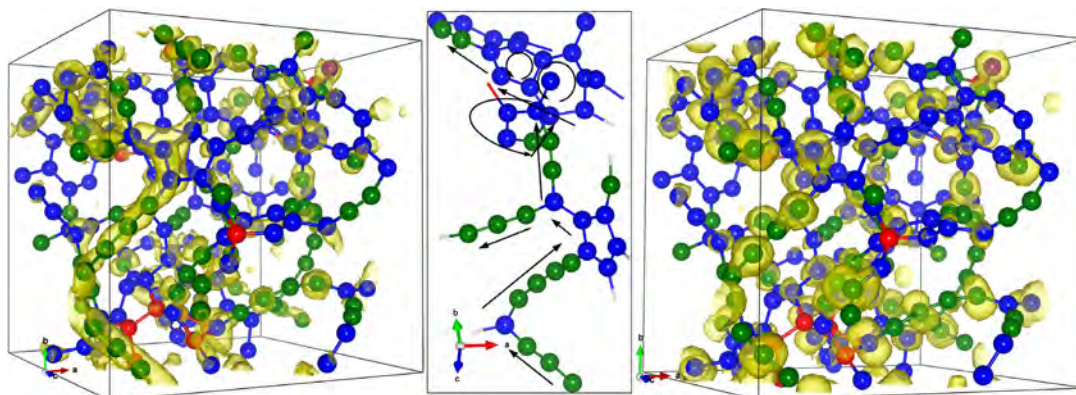


**Figure 1.** a-C: Left and right images correspond to the SPC ( $\zeta$ ) and the diagonal approximation  $\Delta(x)$  projected on grids as an isosurface plot (yellow blobs), respectively. The middle plot corresponds to the structural topology of the network in one region of the supercell that forms a continuous conduction path. The straight and the curved lines with arrowhead are guides to the eye to indicate the conduction path. The colored spheres represent C atoms with different configurations; red ( $sp^3$ ), blue ( $sp^2$ ), green ( $sp$ ), and purple (singly bonded).

atomic sites and shows discrete path. The isosurface blobs show that  $\Delta$  picks almost the same sites that are active in  $\zeta$ . So,  $\Delta$  qualitatively provides a similar picture of the conduction path as  $\zeta$  shown in left plot of Figure 1 for a-C.

Next, we discuss the spectral properties of conduction matrix,  $\Gamma(x, x')$ , for a-C by diagonalizing it as discussed earlier (Section 4.2). The DOS from the eigenvalues and the extent of the localization of the eigenvectors measured by IPR ( $\mathcal{I}$ ) were calculated and are shown in **Figure 2**.

The DOS in Figure 2 reveals an overwhelming fraction of eigenvalues very near  $\Lambda = 0$ . These states are mostly localized as represented by the values of  $\mathcal{I}$  shown by the scattered red dots. We find a few eigenvalues significantly shifted from  $\Lambda = 0$  in the spectrum; only eigenvectors corresponding to these extreme eigenvalues are important to the DC conductivity. To better estimate the number of such eigenvectors, we calculated the spectral form of SPC, ( $\zeta_s$ ), defined in Equation (7), from the

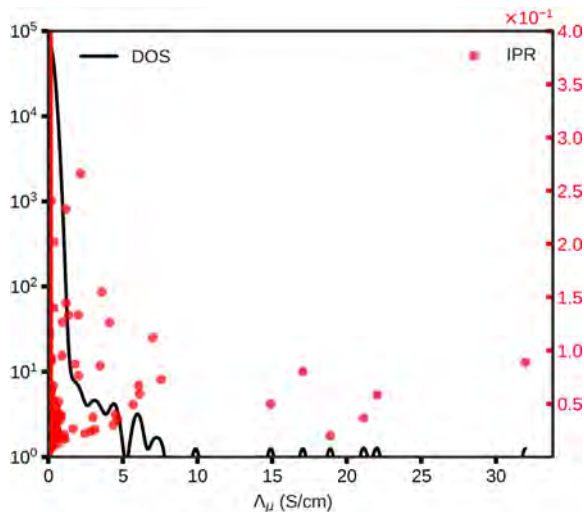


**Figure 2.** a-C: Logarithmic spectral DOS of  $\Gamma$  matrix. The left scale represents the DOS of the eigenvalues displayed in a log scale (solid black line) and the right scale corresponds to the extent of localization of eigenvectors measured as IPR ( $\mathcal{I}$ ) (red circles). Large  $\mathcal{I}$  implies a spatially localized eigenvector of  $\Gamma$ .

largest 75 and 100 eigenvectors, and these are shown in **Figure 3**. Both isosurface plots in Figure 3 show almost the same path as  $\zeta$  that is displayed in the left plot of Figure 1. This shows that 75–100 eigenvectors suffice to obtain the conduction path in a-C.

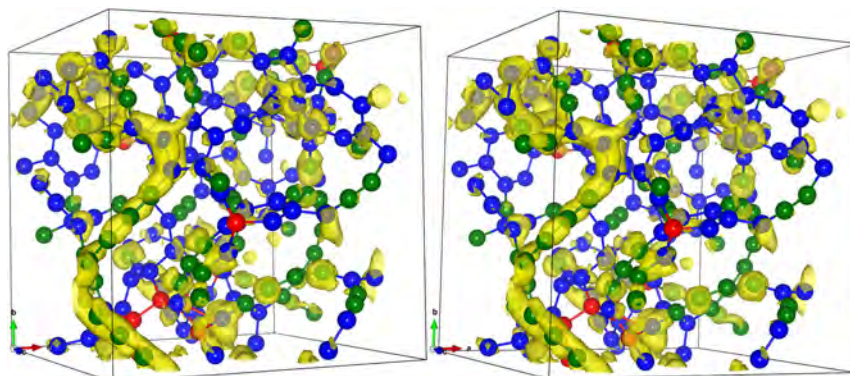
To see how two eigenvectors conjugate to the largest eigenvalues contribute to transport, see **Figure 4**. We see that from  $\Lambda_\mu |\chi_\mu|^2$ , these extremal eigenvectors either form a short channel or lie within spatially separated parts of the network. The eigenvector corresponding to the second largest eigenvalue (left plot in Figure 4) picks out mostly the  $sp$  sites. The  $sp^2$  configurations which are adjacent to the  $sp$  configurations are other active sites for this eigenvalue. The extremal eigenvector selects both  $sp^2$  and  $sp$  sites. Both eigenvectors pick more or less the same  $sp^2$  sites in the network that are the active sites for the conduction as shown by  $\zeta$  shown in left plot of Figure 1.

The physical conclusion is that  $sp$  chains play an important role in electronic transport in phases of carbon that possess them. The SPC that emerges reveals charge transport through interconnected  $sp$  chains and  $sp^2$  rings. It is expected that the relative fraction of these conducting constituents is strongly density, impurity, and sample preparation dependent.

## 6.2. a-Si

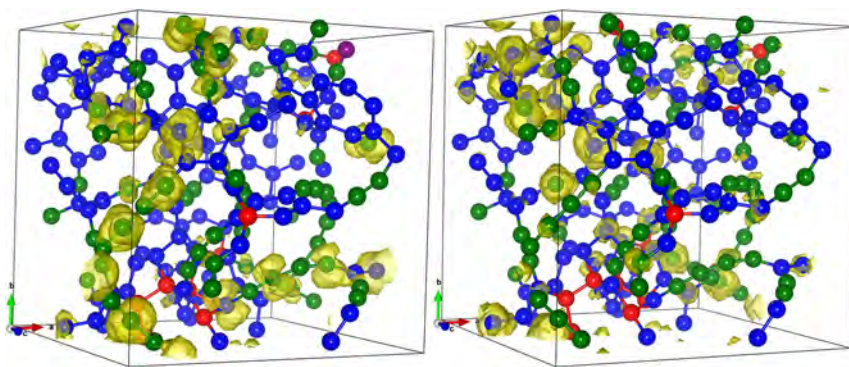
a-Si plays an important role in technological applications, such as thin-film transistors, photovoltaics, infrared imaging devices, and active-matrix displays.<sup>[54]</sup> Being an electronic material, understanding the conduction mechanisms is of obvious importance. In this subsection, we discuss the conduction-active sites in the material and also discuss the spectral properties of the conduction matrix  $\Gamma$ . The supercell was partitioned into  $42 \times 42 \times 42$  grid points ( $h = 0.39 \text{ \AA}$ ) and the  $\Gamma$  matrix was obtained. The SPC at each grid was then calculated and is shown as a heat map plot in **Figure 5**.

Earlier works on the electronic bandtails (Urbach tails) of a-Si have shown that the valence tail states are built from chains or clusters of Si atoms with bonds shorter than average and conduction tail states are due to chains of Si atoms with longer bonds.<sup>[55–58]</sup> It is therefore to be expected that these tail states (and gap states due to badly strained fourfold sites or coordination defects) will play a role in conduction.

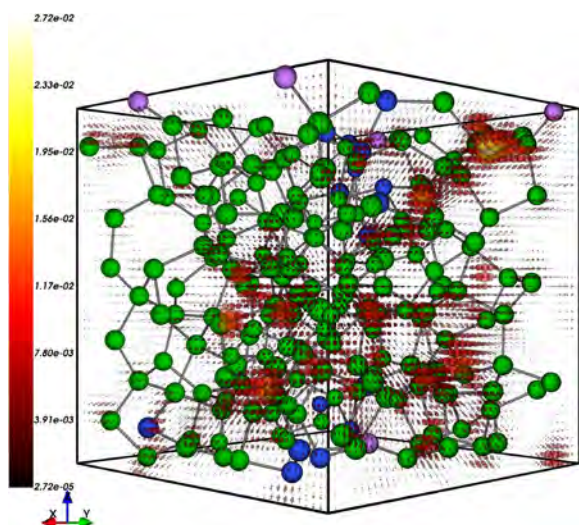


**Figure 3.** a-C: Spectral form for SPC ( $\zeta_s$ ) projected on grids as an isosurface plot (yellow blobs). Left and right plots correspond to the  $\zeta_s$  from the sum of last 75 and 100 eigenvectors, respectively. Same cutoff for the isosurface has been used in both plots and the left plot in Fig. 1. Same color code is used to describe atoms as in Fig. 1.  $\zeta_s$  from extreme 75–100 eigenvectors is equivalent to  $\zeta$  and is sufficient to essentially exactly determine the SPC in a-C.





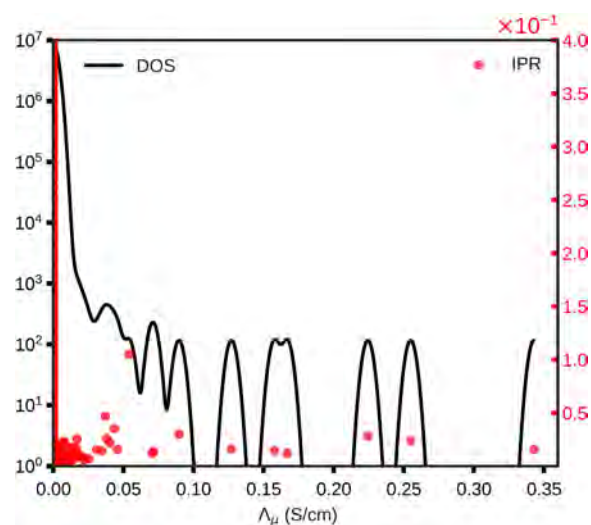
**Figure 4.** a-C: Eigenvectors projected on grids as an isosurface plot (yellow blobs). Left and right plots correspond to the second largest ( $\Lambda_\mu = 22.04 \text{ S cm}^{-1}$ ) and the largest ( $\Lambda_\mu = 31.98 \text{ S cm}^{-1}$ ) eigenvalues, respectively (refer to Figure 2). Same color code is used to describe atoms as in Figure 1.



**Figure 5.** a-Si: SPC ( $\zeta$ ) projected on grids as heat map plot (labeled by colorbars on left of the plot) scaled with maximum value in each plot. The size of the hot spheres is scaled with the magnitude of the SPC value. The colored spheres represent Si atoms with different bonding environment; the blue and heliotrope colored spheres represent fourfold coordinated Si atoms with one and two very long Si-Si bonds, respectively. The green colored spheres represent typical Si atoms with normal bond lengths. The bond cutoff distance of 2.72 Å was chosen.

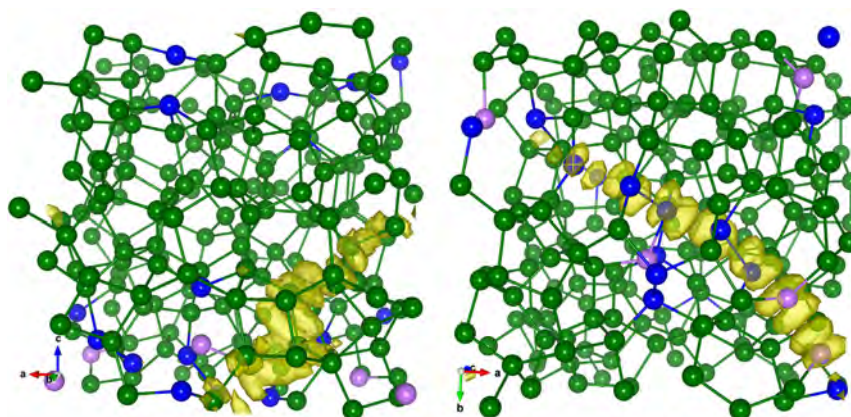
Figure 5 shows the SPC for a-Si. Analysis of the SPC shows special weight for atoms with bonds shorter than 2.32 Å and longer than 2.43 Å (the average bond length is about 2.35 Å). The heat map shows that the SPC also sits at strain defects (fourfold atoms with large variation in bond angles or bond lengths from tetrahedral symmetry). The conduction involves all the states near the Fermi level ( $\epsilon_F$ ), thus involving tail states (of long and short bond structures) and, of course, defect states near  $\epsilon_F$ . We diagonalized  $\Gamma$  to understand the spectral information of the conduction eigenvalues and the eigenvectors. The DOS of the eigenvalues and the extent of localization ( $\mathcal{I}$ ) of the eigenvectors were calculated and are shown in Figure 6.

Figure 6 shows a very large accumulation of eigenvalues near  $\Lambda = 0$ . Much about the transport can be obtained from only a few extremal eigenvalues and conjugate eigenvectors of  $\Gamma$  to



**Figure 6.** a-Si: Logarithmic spectral DOS of  $\Gamma$  matrix. The left scale corresponds to DOS of the eigenvalues displayed in a log scale (solid black line) and the right scale corresponds to the extent of localization measured as IPR ( $\mathcal{I}$ ) (red circles).

approximate the SPC of the material. We plot  $|\chi|^2$  for the largest two eigenvalues in Figure 7. We find that these eigenvectors select out specific sites in the network. The eigenvector corresponding to the second largest eigenvalue (left plot in Figure 7) picks the atomic sites with short-bonded Si atoms with maximum bond length of 2.32 Å. The eigenvector corresponding to the largest eigenvalue picks entirely different parts of the network. This eigenvector follows a path among those atoms that form adjacent strain defect sites,<sup>[59]</sup> nominally fourfold but with one or two long bonds shown in blue and heliotrope, respectively, and also involves filaments of long Si-Si bonds with minimum bond length of 2.43 Å. This calculation reinforces the predicted short-bond (long-bond) association with valence (conduction) tails, and shows an interesting conduction mixing of the defects and tail structures (long- and short-bond subnetworks). In a system with dangling (threefold) or floating (fivefold) configurations, yielding states near  $\epsilon_F$ , we would expect these sites to also participate in the resulting  $\zeta(x)$ .



**Figure 7.** a-Si: Eigenvectors projected on grids as an isosurface plot (yellow blobs). Left and right plots correspond to the second largest ( $\Lambda_\mu = 0.26 \text{ S cm}^{-1}$ ) and the largest ( $\Lambda_\mu = 0.34 \text{ S cm}^{-1}$ ) eigenvalues, respectively. For atoms, the color code is same as used in Figure 5. As the atoms picked by the eigenvectors that are adjacent to each other are separated by the periodic box, we shifted the coordinates to make these atoms include in the same side of the box to make the connectivity clear. The left panel emphasizes short bonds, right panel long bonds, and defects.

In future work, we will explore defect-rich phases of amorphous Si including dangling and floating bonds (as well as nominally fourfold structures with strain defects) and explore the role of defects in conduction. There is no doubt that such defects will play a role, as their electronic energies are well known to be in the gap, and for dangling bonds especially, near the middle of the gap. We speculate that there may be interesting SPC linkages between such defects and the filamentary structures associated with the Urbach tails,<sup>[56]</sup> perhaps reminiscent of the *sp*-ring mixing of a-C. Conductivity will certainly depend on delocalization that accrues from mixing/banding between defect state: such effects are included in our computations.

### 6.3. Conductivity Fluctuations in l-Si

l-Si is a metal in contrast to a-Si or c-Si which is tetrahedral semiconductors. Although it is metallic, the first neighbor atomic coordination number is between 5 and 6,<sup>[60]</sup> hinting at a prevalence of covalent bonds in the liquid state of Si and differentiating it from other metals in terms of structural topology.<sup>[61]</sup> In the liquid state, thermal fluctuations cause the structure to continuously change and so too the SPC in the network. To model the liquid metal, we annealed the a-Si model at 2000 K for 6 ps.

The thermal fluctuations induce fluctuations in the Fermi level ( $\epsilon_F$ ) and also the electronic gap associated with it. The fluctuation of the frontier of highest occupied molecular orbital (HOMO), lowest unoccupied molecular orbital (LUMO), and the Fermi level with simulation time is shown in **Figure 8** for a brief time interval.

From Figure 8, we see that the minute gamma-point gap opens and closes with time due to the thermal fluctuations. We chose four configurations as shown by different markers in the inset plot of Figure 8 where such feature exists. For these snapshots, we find that the coordination environment does not drastically change within the network for this short time interval. A majority of the Si atoms are fivefold and sixfold coordinated ( $\approx 56$ – $57\%$ ); fourfold and sevenfold coordinated Si atoms account

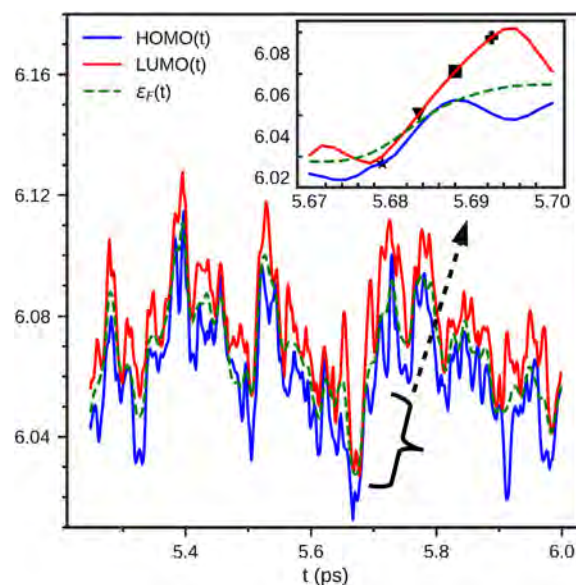


**Figure 8.** l-Si: A snapshot showing fluctuations of energy levels near the Fermi level (in eV) plotted against simulation time. The inset plot shows a specific region (shown by the curly brace) with closing and opening of the electronic gap. The markers correspond to the time step for the atomic configurations that were selected for the SPC calculations.

for  $\approx 33$ – $35\%$  of the total coordination; and eightfold coordinated Si atoms account for  $5.1$ – $9.7\%$  of the network. For each of these configurations, we obtained the SPC on a  $40 \times 40 \times 40$  grids ( $h = 0.41 \text{ \AA}$ ) and these are shown as heat map plots in **Figure 9**.

The heat map plot of SPC shows that the fluctuation in the energy levels results in slight variation in the SPC. For all models, we find that the SPC is quite extended, indicating the metallic character of the material. All coordinations seem involved in the conduction, suggesting a truly delocalized metallic form of conduction.

We also picked four temporally well-separated snapshots at simulation times 1.95, 3.15, 4.35, and 5.55 ps to capture the



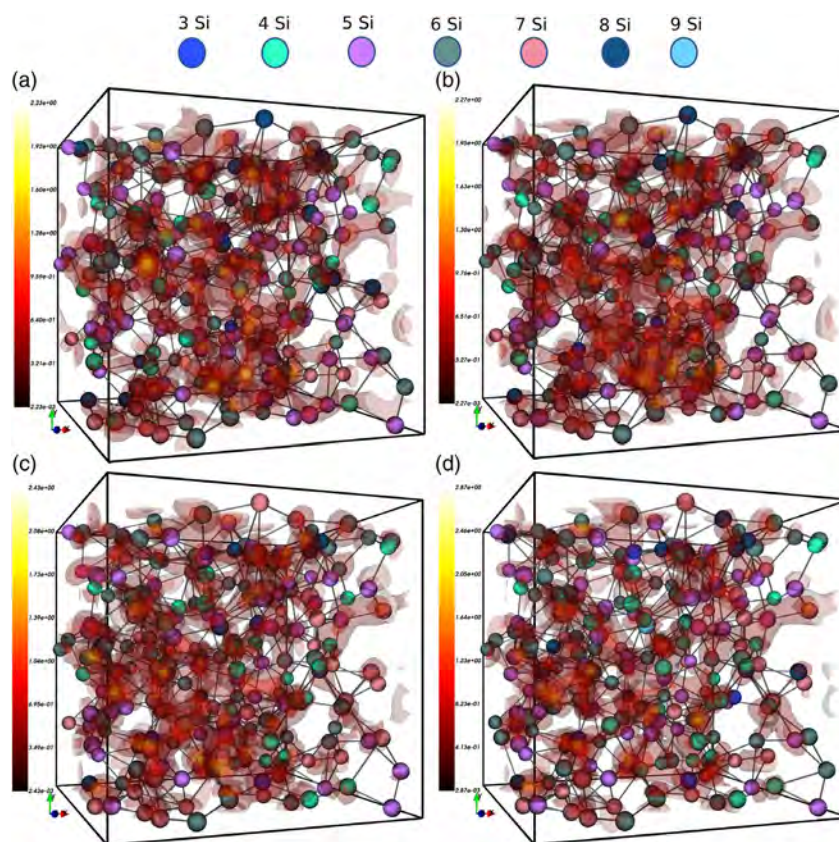


**Figure 9.** l-Si: SPC ( $\zeta$ ) projected on grids as a heat map (labeled by colorbars on left of each subplots) for atomic configurations at that are temporally close to each other shown by the marker signs in the inset plot of Figure 8. a–d) The atomic configurations shown by star, triangle, square, and the plus signs in the inset plots of Figure 8, respectively. Atom color represents Si with different instantaneous coordination as labeled and shown at the top of the figure. The cutoff distance of 3.10 Å is used to define the coordination.

variation of the conduction path on longer time scales. The SPC for each of these snapshots is shown on grids as a heat map in **Figure 10**. The dominating regions appear in different parts of the cell for these snapshots, an expected kind of “local conductance fluctuation” as the Si atoms diffuse in the liquid state and continuously change their local bonding and thus local electronic structure. The variation in the conduction path is displayed, and colored spheres in each plot of Figure 10 indicate the fluctuation in the local atomic environments. We find that, within the top 6% of SPC values in Figure 10a, one of the conduction paths is along the chain with fourfold, fivefold, sixfold, sevenfold coordinated Si atoms in the middle region of the network. Similarly, in Figure 10b, we find a continuous path along fourfold, fivefold, sixfold, sevenfold, eightfold Si atoms where four of such sixfold coordinated atoms contributing to the path. In Figure 10c, there exists a conduction path along a chain of five Si atoms that are all sixfold coordinated. We also find the conduction path along the chain of fourfold, fivefold, sixfold coordinated Si atoms where three of such fivefold coordinated Si exist in the chain. In Figure 10d, we find one of the conduction paths along six Si atoms with fivefold, sixfold, sevenfold, eightfold coordinated Si atoms forming a chain where three of them are fivefold coordinated. So, the SPC calculations from these snapshots show that the most conduction-active sites in l-Si are fivefold and sixfold

coordinated. We find Si atoms with fourfold, sevenfold, and eightfold coordinated forming the other sites of conduction. It would be of interest to properly analyze these fluctuations with suitable space-time correlation functions.

#### 6.4. a-Si Suboxide: Application for Finite $\omega$

Optical materials are critically important, and there is always a demand for novel optically functional and transparent materials. Electromagnetic waves of different frequencies may be absorbed by different parts of the inhomogeneous material. Having *a priori* information on the absorption-active sites/regions in the material could be helpful to engineers, for example, to design waveguides or other optical devices. Optical PUFs are an ongoing research topic for computer security applications.<sup>[62]</sup>

Silicon suboxides, a-SiO<sub>x</sub> ( $0 < x < 2$ ), have complex structures and two different pictures of suboxide structure are mainly discussed: random mixture<sup>[63]</sup> and random bonding.<sup>[64]</sup> The former model suggests the segregation of Si in silica separated by the interfacial boundary and the latter model suggests a continuous random network of tetrahedral units of SiSi<sub>y</sub>O<sub>4-y</sub> where  $y = 0$  to 4. The complexity of the network makes the material electronically interesting and, of course, span a-Si to amorphous silica.



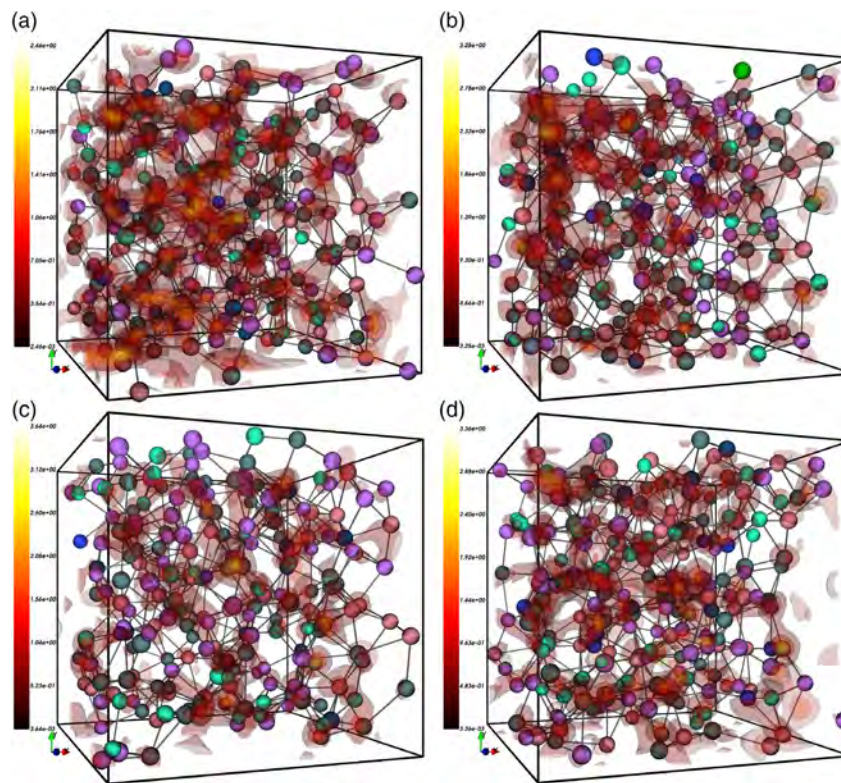


**Figure 10.** I-Si: SPC ( $\zeta$ ) projected on grids as a heat map plot (labeled by colorbars on left of each subplots) for configurations at intervals of 1.2 ps. a–d) The SPC plot at simulation time 1.95, 3.15, 4.35, and 5.55 ps, respectively. Atoms color represents Si with different coordination environment and we adopt the same convention as in Figure 9. The cutoff distance of 3.10 Å is used to define the coordination. Note the spatial fluctuation in the heat maps over these snapshots.

If one imagines starting in a-SiO<sub>2</sub>, a superb insulator, one can imagine a process of randomly depleting O atoms from the network. If  $x$  is close to 2, O-vacancies will be widely separated with little conduction. As O depletion proceeds, more and more hopping will accrue and the conduction paths will be determined by the locations and electronic structure associated with the O-vacancy subnetwork. The electrical conductivity therefore has a stochastic character depending on the existence and details of a hopping pathway involving the vacancies. For small enough systems, the stochasticity in conduction path affects the observed DC conductivity, and makes an excellent PUF, as we report elsewhere.<sup>[65]</sup>

In this article, we look very briefly at an AC version of this, and show that light absorption is very sensitive to wavelength, and in particular, show that different vacancy subnetworks contribute to the absorption. This suggests that an “optical PUF” might be possible for the silicon suboxide materials. We limit the discussion to a qualitative indication of how different parts of the network participate for two different wavelengths, and we note for completeness that to really carry out such calculations realistically better excited states should be computed with more intricate methods.

In this subsection, we discuss light absorption in a-SiO<sub>1.3</sub> at two frequencies. To enable this, we calculated the space-projected conductivity on  $40 \times 40 \times 40$  grids ( $h = 0.39$  Å) for two different wavelengths with  $\lambda = 2000$  nm and  $\lambda = 1600$  nm. The SPC for both cases are shown in Figure 11. It is of interest that the

absorbing parts of the models are *qualitatively* different, and more to the point, the computation predicts *which* parts of the matrix will absorb light of a specified wavelength. The isosurface plots in Figure 11 show that the absorption meanders along adjacent O-vacancy sites in the network because different frequencies pick out different paths  $\phi$  in the network. As such, changing the frequency and changing the path make it likely that external observables, such as absorption, will also change, making the system potentially attractive for PUF applications.

## 6.5. FCC Aluminum

So far we have discussed conduction in noncrystalline semiconductor materials. In this subsection, we consider FCC aluminum (c-Al), a metal, with a focus on the spectral properties of the conduction matrix  $\Gamma$ .  $\Gamma(x, x')$  for the 500 atoms Al cell was obtained on a  $42 \times 42 \times 42$  grids ( $h = 0.48$  Å) so that  $\dim(\Gamma) = 74\,088$ .  $\Gamma$  was exactly diagonalized to obtain eigenvalues ( $\Lambda_\mu$ ) and the eigenvectors ( $\chi_\mu$ ).

Figure 12 shows the DOS of the conduction eigenvalues and the extent of the localization of the conjugate eigenvectors ( $\mathcal{L}$ ). The DOS in Figure 12 shows that a majority of the eigenvalues lie near  $\Lambda = 0$ . This is clear from the inset that shows the evolution of the conduction eigenvalues in increasing magnitude where only the last  $\approx 24\,088$  among 74 088 eigenvalues have magnitude

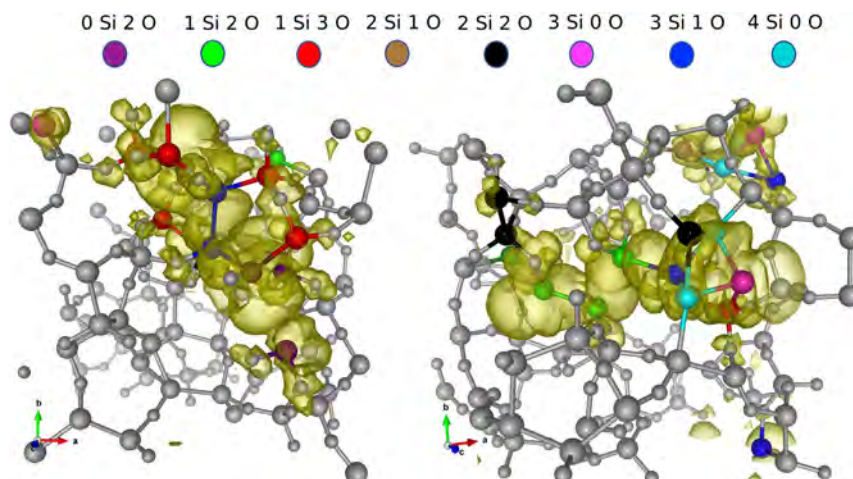


**Figure 11.** a-SiO<sub>1.3</sub>: SPC ( $\zeta$ ) projected on grids as isosurface (yellow blobs) plots. Left and right plots correspond to  $\hbar\omega = 0.62$  and  $0.76$  eV, respectively. Multicolored spheres refer to Si atoms within the conduction-active region having different coordination environment shown as legends at the top of the figure. Top 3.7% SPC values are included in both plots. The gray colored spheres represent Si and O atoms that lie outside the conduction active region for the given cutoff. The small size spheres represent O atoms.

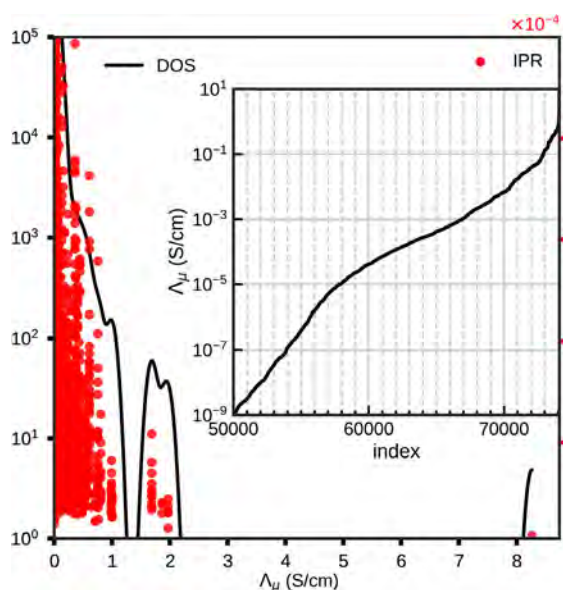


**Figure 12.** c-Al: Logarithmic spectral DOS of  $\Gamma$  matrix. The left scale corresponds to DOS of the eigenvalues displayed in a log scale (solid black line) and the right scale corresponds to the extent of localization measured as IPR ( $\mathcal{I}$ ) (red circles). The inset shows the magnitude of conduction eigenvalues in ascending order.

greater than  $10^{-9} \text{ S cm}^{-1}$ . Even in a metal, most eigenvalues of  $\Gamma$  are effectively zero.

In contrast with our previous examples, the spectrum shows the presence of an extended tail in the DOS that reveals a signature of metallic conduction in Al. This is supported by the inset plot where the eigenvalue increases in a linear fashion at different regimes. The inset also provides a tentative picture of the transition from an insulating to conducting spectral character near the high- $\Lambda$  end of the spectrum between indices

$\approx 60\,000$ – $67\,000$ . Beyond index  $\approx 67\,000$ , we observe that the density of eigenvalues increases in a more quadratic manner. The presence of the tail in the DOS requires many eigenvectors to be considered to obtain the conduction path in Al (which is, of course, fully delocalized through the cell). A small spectral gap appears near  $\Lambda_\mu = 1.3 \text{ S cm}^{-1}$  from a physical origin that we have not yet determined. The other difference we find is the localization of the conduction eigenvectors where the modes are more extended for Al compared with what was observed in a-Si and the low-density a-C model.

**Figure 13** shows the conduction eigenvalues ( $\Lambda_\mu$ ) plotted against IPR ( $\mathcal{I}$ ). We see that for small IPR, there exists a fairly clear inverse relation between eigenvalues and the IPR. We also see  $\Lambda_\mu$  near zero for low IPR. The eigenvectors corresponding to such eigenvalues can involve many sites, but always without forming any connected pattern and therefore corresponds to the nonconductive structures.

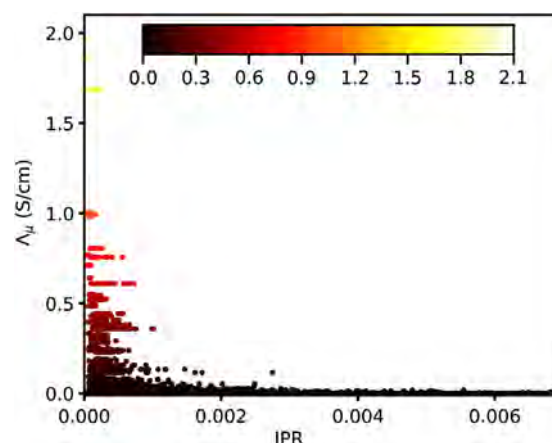


**Figure 13.** c-Al: The correlations of the eigenvalues with IPR ( $\mathcal{I}$ ) shown by the scattered plots as heatmap. The colorbar at the central top of the figure refers to the magnitude of eigenvalues.



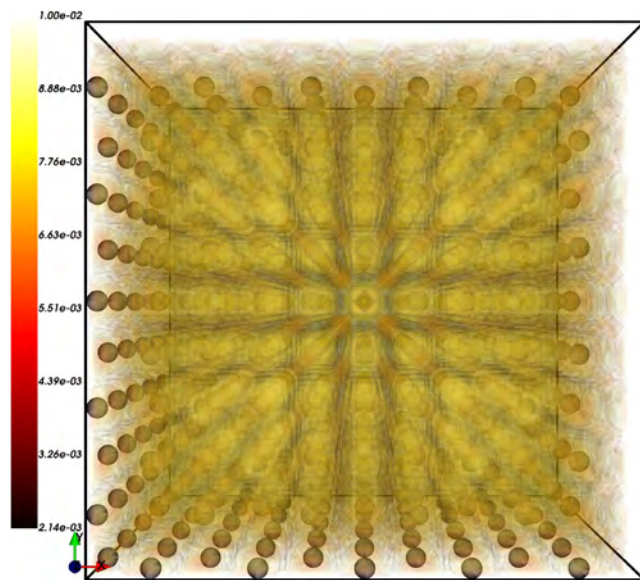


**Figure 14.** c-Al: Conductivity projected on grids weighted by the eigenvalues from all eigenvectors as a heat map plot (labeled by colorbars on the left) scaled with maximum value. The spheres represent Al atoms.

To visualize the conduction (really to see how a metallic conducting continuum emerges from this theory), we projected the conductivity from all the eigenvectors weighted by their eigenvalues and this is shown as a heat map plot in **Figure 14**. The electrons in c-Al are highly delocalized, as a result the projected values are essentially the same throughout the cell as shown in Figure 14. This is, of course, quite different from the semiconductors like a-Si and low-density a-C where only some parts of the material serve as the conduction-active sites in the network that we discussed in the earlier subsection.

The other interesting property we find in the spectrum of the DOS in c-Al (refer to Figure 12) is the presence of the degenerate eigenvalues toward the large  $\Lambda$  end of the spectrum. This is absent in the spectrum of a-Si and the low-density a-C. The degeneracy is surely a manifestation of the degeneracy present in the electronic levels, accruing in turn from the crystalline

symmetry (Only the  $k=0$  point is used to sample the Brillouin zone, perhaps reasonable for a 500 atoms cell for this application, though in general this would be a doubtful approximation for a metal with its Fermi surface.). To visualize the conduction channel formed by the family of such degenerate eigenvalues, we projected the eigenvectors onto real space grids. **Figure 15** shows the projection of eigenvectors for one of such family of the degenerate eigenvalues as a heatmap plot. The left plot shows that the eigenvectors split into four conduction channels within the supercell. The channels possess an inversion symmetry at the center of the supercell. The middle and the right heat maps correspond to the eigenvectors for other two eigenvalues in the family which direct along different directions, namely, along  $x$  and  $y$  direction.

## 7. Conclusions

We presented a method to compute a conductivity projected onto real space grids, and we analyzed the spectral properties of the conduction matrix for a representative systems. For low-density a-C, we find that the  $sp^2$  and  $sp$  configurations form active conduction sites. The conduction path is formed between the  $sp$  chains and the pentagonal or hexagonal graphene rings in the network. For a-Si, we find SPC is distributed at nearby atomic sites at different parts in the network, suggesting the possibility of hopping mechanisms for the electronic conduction. For a-Si, we find that the extreme eigenvectors pick atomic sites with different topology, involving tail states and strain defects for this fourfold WWW model. We also studied fluctuations in the energy levels in l-Si and provided the conduction path for few configurations. We showed that the fourfold, fivefold, sixfold, and sevenfold Si atoms form the conduction sites in the l-Si. We showed that diagonalization of  $\Gamma(x, x')$  provides essential information about the nature of the conduction eigenmodes in different materials and helpfully categorizes the “paths” according to eigenvalue. From the spectrum of DOS of conduction eigenvalues, we always find a very large weight near  $\Lambda = 0$ . So, for materials like a-Si and a-C, only a few eigenvectors are sufficient to define the conduction path. For c-Al, we find that despite a significant accumulation of eigenvalues near  $\Lambda = 0$ ,

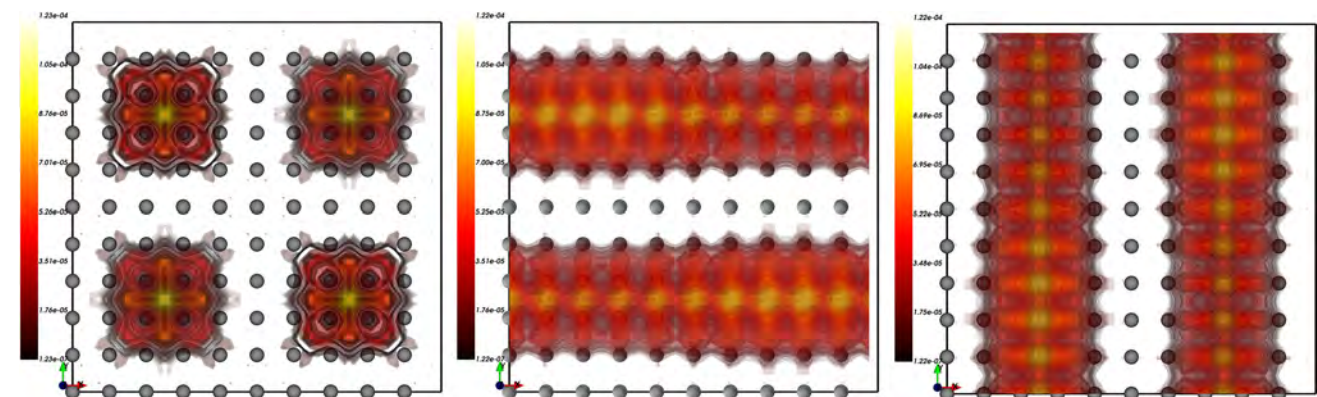


**Figure 15.** c-Al: Isosurface plots for eigenvectors corresponding to the degenerate eigenvalues ( $\Lambda_\mu = 1.0013 \text{ S cm}^{-1}$ ). The isosurface plot displayed as a heat map (labeled by the colorbars on left of each subplots) includes the values within 0.001 times the maximum value on the grids. Al atoms are represented by gray spheres in each plot.



there is a spectral tail in the DOS and the channels corresponding to these states are extended. So, for metals, many eigenvectors are necessary to describe the conduction. We also observe a degeneracy in the conduction eigenvalues in the DOS of c-Al absent in the amorphous systems. We analyzed eigenvectors for one such degenerate eigenvalue near the extreme side of the spectrum and showed that these eigenvectors form a well-defined conduction channel. We also provided an example of a silicon suboxide ( $\alpha\text{-SiO}_{1.3}$ ), where we projected the SPC for ( $\omega > 0$ ) and showed that the O-vacancy sites form the major sites of conduction in such material.

In our previous works, we studied conduction mechanisms in few resistive memory materials, namely,  $\alpha\text{-Al}_2\text{O}_3:\text{Cu}$ <sup>[7,28]</sup> and  $\alpha\text{-Ta}_2\text{O}_5:\text{Cu}$ .<sup>[29]</sup> In both cases, we find that the Cu atoms segregate and form a cluster-like structure in the highly ionic host. We obtained the SPC and showed that these clustered Cu atoms form major conduction-active sites in these materials, indicating the metallic conduction in such systems. In  $\alpha\text{-Ta}_2\text{O}_5:\text{Cu}$ , we also find that the under-coordinated Ta atoms (O-vacancies) that are neighbors to Cu atoms are other sites of conduction. In  $\alpha\text{-Al}_2\text{O}_3:\text{Cu}$ , we showed that the connectivity of the Cu atoms in the network is vital to enhance the conductivity in the material. We also showed that in such a mixed (insulating/conducting) system, only a few eigenvectors of  $\Gamma$  are required to characterize conduction in the system.

No article is complete without *caveats*. It is not easy to extract quantitative conductivities for amorphous solids. Electron-phonon couplings are not included in static lattice computations and such temperature dependence is hardly a small effect. This is probably one reason why there are more computations of electrical conductivity in liquid metals, where dynamical effects (changes in electronic structure and therefore conduction due to atomic motion) are treated with Born–Oppenheimer dynamics. Also, in principle, methods producing accurate excited states perhaps using hybrid functionals should be used, and would doubtless make a significant difference in the numerical value of the conductivity. However, we emphasize that the qualitative character of the SPC is far less sensitive to these effects than the numerical value of the conductivity, and the method offers a fairly robust picture of conduction activity in complex materials.

## Acknowledgements

The authors thank the National Science Foundation (NSF) for support under DMR award 1507670, and Extreme Science and Engineering Discovery Environment (XSEDE), supported by NSF grant number ACI-1548562 for providing computational resources under allocations DMR-190008P. The authors thank Prof. M. N. Kozicki of Arizona State University, who catalyzed and collaborated with us on this research, Mr. Greg Rosen of Ohio University, and Dr. Felix Mocuano of the University of Cambridge for helpful comments concerning conduction processes in a-C. The authors thank Dr. Bishal Bhattarai for providing the model of low-density a-C.

## Conflict of Interest

The authors declare no conflict of interest.

## Keywords

conduction eigenvectors, electronic conductivity, Kubo–Greenwood formula

Received: August 8, 2020

Revised: November 12, 2020

Published online: December 16, 2020

- [1] P. B. Allen, in *Conceptual Foundations of Materials: A Standard Model for Ground- and Excited-State Properties* (Eds.: S. G. Louie, M. L. Cohen), Elsevier, Amsterdam **2006**, Ch. 6.
- [2] J. M. Ziman, *Principles of the Theory of Solids*, 2 ed., Cambridge Press, Cambridge, **1972**.
- [3] R. Kubo, *J. Phys. Soc. Jpn.* **1957**, 12, 570.
- [4] D. A. Greenwood, *Proc. Phys. Soc.* **1958**, 71, 585.
- [5] R. Kubo, M. Toda, N. Hashitsume, N. Saito, *Statistical Physics. II: Nonequilibrium Statistical Mechanics*, Springer, Berlin **1985**.
- [6] A. Einstein, *Ann. Phys. (Leipzig)* **1905**, 322, 549.
- [7] K. Prasai, K. N. Subedi, K. Ferris, P. Biswas, D. A. Drabold, *Phys. Status Solidi RRL* **2018**, 12, 1800238.
- [8] N. F. Mott, E. A. Davis, *Electronic Processes in Non-crystalline Materials*, 2nd ed. (Eds.: N. F. Mott, E. A. Davis), Clarendon Press/Oxford University Press, Oxford/New York **1979**.
- [9] L. L. Moseley, T. Lukes, *Am. J. Phys.* **1978**, 46, 676.
- [10] M. Zhang, D. A. Drabold, *J. Phys.: Condens. Matter* **2011**, 23, 085801.
- [11] M.-L. Zhang, D. A. Drabold, *Phys. Rev. B* **2010**, 81, 085210.
- [12] M. Zhang, D. A. Drabold, *Phys. Rev. E* **2011**, 83, 012103.
- [13] G. Galli, R. M. Martin, R. Car, M. Parrinello, *Phys. Rev. B* **1990**, 42, 7470.
- [14] A. N. Sobolev, A. A. Mirzoev, *J. Phys.: Conf. Ser.* **2008**, 98, 062015.
- [15] S. K. Bose, O. Jepsen, O. K. Andersen, *Phys. Rev. B* **1993**, 48, 4265.
- [16] M. P. Desjarlais, J. D. Kress, L. A. Collins, *Phys. Rev. E* **2002**, 66, 025401.
- [17] J. Dong, D. A. Drabold, *Phys. Rev. Lett.* **1998**, 80, 1928.
- [18] C. Landauro, H. Solbrig, *Mater. Sci. Eng., A* **2000**, 294–296, 600.
- [19] B. D. Hoi, M. Yarmohammadi, *J. Magn. Magn. Mater.* **2018**, 451, 57.
- [20] D. Drabold, *J. Non-Cryst. Solids* **2000**, 266–269, 211.
- [21] R. Atta-Fynn, P. Biswas, D. A. Drabold, *Phys. Rev. B* **2004**, 69, 245204.
- [22] K. Prasai, P. Biswas, D. A. Drabold, *Semicond. Sci. Technol.* **2016**, 31, 073002.
- [23] D. A. Drabold, P. A. Fedders, *Phys. Rev. B* **1999**, 60, R721.
- [24] T. A. Abtew, M. Zhang, D. A. Drabold, *Phys. Rev. B* **2007**, 76, 045212.
- [25] L. Calderin, V. Karasiev, S. Trickey, *Comput. Phys. Commun.* **2017**, 221, 118.
- [26] K. Prasai, G. Chen, D. A. Drabold, *Phys. Rev. Materials* **2017**, 1, 015603.
- [27] K. N. Subedi, K. Prasai, D. A. Drabold, *Modelling of Glasses: Electronic conduction mechanisms in  $\text{GeSe}_3\text{:Ag}$  and  $\text{Al}_2\text{O}_3\text{:Cu}$* , World Scientific Publishing, Singapore **2020**.
- [28] K. N. Subedi, K. Prasai, M. N. Kozicki, D. A. Drabold, *Phys. Rev. Materials* **2019**, 3, 065605.
- [29] R. Thapa, B. Bhattarai, M. N. Kozicki, K. N. Subedi, D. A. Drabold, *Phys. Rev. Mater.* **2020**, 4, 064603.
- [30] C. E. Parman, N. E. Israeloff, J. Kakalios, *Phys. Rev. B* **1993**, 47, 12578.
- [31] B. Xiao, T. Gu, T. Tada, S. Watanabe, *J. Appl. Phys.* **2014**, 115, 034503.
- [32] R. B. S. Oakeshott, A. MacKinnon, *J. Phys.: Condens. Matter* **1994**, 6, 1513.
- [33] H. U. Baranger, A. D. Stone, *Phys. Rev. B* **1989**, 40, 8169.
- [34] M. Paulsson, M. Brandbyge, *Phys. Rev. B* **2007**, 76, 115117.
- [35] C. Lanczos, *Applied Analysis*, Prentice-Hall, Englewood Cliffs, NJ **1956**.
- [36] D. A. Drabold, O. F. Sankey, *Phys. Rev. Lett.* **1993**, 70, 3631.
- [37] G. Kresse, J. Hafner, *Phys. Rev. B* **1993**, 47, 558.
- [38] J. P. Perdew, K. Burke, M. Ernzerhof, *Phys. Rev. Lett.* **1996**, 77, 3865.

- [39] B. Bhattacharai, D. A. Drabold, *Carbon* **2017**, 115, 532.
- [40] B. R. Djordjević, M. F. Thorpe, F. Wooten, *Phys. Rev. B* **1995**, 52, 5685.
- [41] A. Barranco, F. Yubero, J. P. Espinós, P. Groening, A. R. González-Elipe, *J. Appl. Phys.* **2005**, 97, 113714.
- [42] D. A. Drabold, *Eur. Phys. J. B* **2009**, 68, 1.
- [43] R. M. Feenstra, M. Widom, [www.andrew.cmu.edu/user/feenstra/wavetrans](http://www.andrew.cmu.edu/user/feenstra/wavetrans), **2012**.
- [44] D. S. da Silva, A. D. S. Cortes, M. H. Oliveira, E. F. Motta, G. A. Viana, P. R. Mei, F. C. Marques, *J. Appl. Phys.* **2011**, 110, 043510.
- [45] A. Grill, *Diamond Rel. Mater.* **1999**, 8, 428.
- [46] K. Park, E. Chin, *Polym. Degrad. Stab.* **2000**, 68, 93.
- [47] P. L. McEuen, *Nature* **1998**, 393 585.
- [48] R. J. Nicholas, A. Mainwood, L. Eaves, *Philos. Trans. R. Soc., A* **2008**, 366, 189.
- [49] K. S. Novoselov, A. K. Geim, S. V. Morozov, D. Jiang, Y. Zhang, S. V. Dubonos, I. V. Grigorieva, A. A. Firsov, *Science* **2004**, 306, 666.
- [50] A. K. Geim, K. S. Novoselov, *Nat. Mater.* **2007**, 6, 183.
- [51] S. T. C. Konigsmark, L. K. Hwang, D. Chen, M. D. F. Wong, In *2014 19th Asia and South Pacific Design Automation Conf. (ASP-DAC)*, Singapore **2014**, pp. 73–78.
- [52] S. A. Wring, J. P. Hart, *Analyst* **1992**, 117, 1215.
- [53] B. Bhattacharai, P. Biswas, R. Atta-Fynn, D. Drabold, *Phys. Chem. Chem. Phys.* **2018**, 20, 19546.
- [54] R. A. Street, *Hydrogenated Amorphous Silicon*, Cambridge Solid State Science Series, Cambridge University Press, Cambridge **1991**.
- [55] P. A. Fedders, D. A. Drabold, S. Nakhmanson, *Phys. Rev. B* **1998**, 58, 15624.
- [56] Y. Pan, F. Inam, M. Zhang, D. A. Drabold, *Phys. Rev. Lett.* **2008**, 100, 206403.
- [57] T. Abtew, M. Zhang, Y. Pan, D. Drabold, *J. Non-Cryst. Solids* **2008**, 354, 2909.
- [58] F. Inam, J. P. Lewis, D. A. Drabold, *Phys. Status Solidi A* **2010**, 207, 599.
- [59] P. A. Fedders, D. A. Drabold, S. Klemm, *Phys. Rev. B* **1992**, 45, 4048.
- [60] T. H. Kim, G. W. Lee, B. Sieve, A. K. Gangopadhyay, R. W. Hyers, T. J. Rathz, J. R. Rogers, D. S. Robinson, K. F. Kelton, A. I. Goldman, *Phys. Rev. Lett.* **2005**, 95, 085501.
- [61] J. T. Okada, P. H.-L. Sit, Y. Watanabe, Y. J. Wang, B. Barbiellini, T. Ishikawa, M. Itou, Y. Sakurai, A. Bansil, R. Ishikawa, M. Hamaishi, T. Masaki, P.-F. Paradis, K. Kimura, T. Ishikawa, S. Nanao, *Phys. Rev. Lett.* **2012**, 108, 067402.
- [62] C. Mesaritis, M. Akriotou, A. Kapsalis, E. Grivas, C. Chaintoutis, T. Nikas, D. Syvridis, *Sci. Rep.* **2018**, 8, 9653.
- [63] G. W. Brady, *J. Phys. Chem.* **1959**, 63, 1119.
- [64] H. R. Philipp, *J. Non-Cryst. Solids* **1972**, 8–10, 627.
- [65] K. N. Subedi, M. N. Kozicki, D. A. Drabold, *Conduction Mechanisms in Silicon Suboxides*, unpublished.

# On the Origin and Structure of the First Sharp Diffraction Peak of Amorphous Silicon

Devilal Dahal, Hiroka Warren, and Parthapratim Biswas\*

Dedicated to Professor David A. Drabold on the occasion of his 60th birthday

The structure of the first sharp diffraction peak (FSDP) of amorphous silicon (a-Si) near  $2 \text{ \AA}^{-1}$  is addressed with particular emphasis on the position, intensity, and width of the diffraction curve. By studying a number of continuous random network (CRN) models of a-Si, it is shown that the position and intensity of the FSDP are primarily determined by radial atomic correlations in the amorphous network on the length scale of  $15 \text{ \AA}$ . A shell-by-shell analysis of the contribution from different radial shells reveals that key contributions to the FSDP originate from the second and fourth radial shells in the network, which are accompanied by a background contribution from the first shell and small residual corrections from the distant radial shells. The results from numerical calculations are complemented by a phenomenological discussion of the relationship between the peaks in the structure factor in the wavevector space and the reduced pair-correlation function in the real space. An approximate functional relation between the position of the FSDP and the average radial distance of Si atoms in the second radial shell in the network is derived, which is corroborated by numerical calculations.

The FSDP is ubiquitous in many disordered condensed-phase systems. Numerous experimental<sup>[1,2,6–8]</sup> and theoretical<sup>[3,9,10]</sup> studies have reported the (near) universal presence of the FSDP in glasses and liquids/melts. In glasses, the origin of the FSDP can be largely attributed to the presence of layered structures,<sup>[11]</sup> interstitial voids,<sup>[3–5]</sup> chemical disorder,<sup>[4]</sup> and large ring structures<sup>[8]</sup> in the networks, which constitute a real-space description of atomic correlations on the nanometer length scale. Elliott<sup>[3]</sup> has shown that the FSDP in binary glasses can be interpreted as a prepeak in the concentration–concentration structure factor, which is caused by the presence of the chemical ordering between constituent atoms in the networks. Likewise, the interstitial voids have been found to play an important role in the formation of the FSDP in


## 1. Introduction

Professor David Drabold has contributed significantly in the field of amorphous materials. It is therefore an opportune moment to contribute to his Festschrift on a topic that is very close to his heart. The first sharp diffraction peak (FSDP) is a distinct feature of many noncrystalline solids, which are characterized by the presence of a peak in the low wavevector region ( $1\text{--}2 \text{ \AA}^{-1}$ ) of the structure factor of the solids. Although the origin of the FSDP in many multinary glasses is not yet fully understood from an atomistic point of view, it has been shown that the FSDP is primarily associated with the presence of the short-range order and medium-range order, which entail voids, chemical ordering, large ring structures, local topology, and atomic correlations between constituent atoms in the amorphous environment of the solids.<sup>[1–5]</sup>

tetrahedral amorphous semiconductors,<sup>[4]</sup> for example, amorphous silicon (a-Si). On the other hand, Susman et al.<sup>[8]</sup> have reported that in binary  $AX_2$  glasses, the A–A and A–X correlations within the extended ring structures can give rise to the FSDP. Busse and Nagel<sup>[11]</sup> have suggested that the existence of the FSDP in  $g\text{-As}_2\text{Se}_3$  can be ascribed to the interlayer atomic correlations in the glassy network. Experimental studies on  $\text{GeSe}_3$  and  $\text{GeSe}_5$  glasses by Armand et al.<sup>[12]</sup> have indicated that the Ge–Ge atomic correlation on the length scale of  $6\text{--}7 \text{ \AA}$  is the primary cause of the FSDP, which is supported by molecular dynamics studies by Vashishta et al.<sup>[9]</sup>

The behavior of the FSDP in covalent glasses often shows an anomalous dependence with respect to temperature,<sup>[2,13]</sup> pressure,<sup>[13,14]</sup> and composition.<sup>[6,15]</sup> Following the well-known Debye–Waller<sup>[16]</sup> behavior, one may assume that the peaks in the structure factor should decrease with the increase of the temperature of the system. However, the first (sharp) diffraction peak of many glassy systems has been found to remain either invariant or become more intense and narrower at high temperature.<sup>[2,17]</sup> A notable exception is vitreous silica ( $v\text{-SiO}_2$ ), which does not follow the behavior stated earlier. The intensity of the FSDP of  $v\text{-SiO}_2$  has been observed to decrease with increasing temperature, due to the thermally induced motion of the atoms and the associated diffused scattering,<sup>[18]</sup> leading to the broadening of the first peak.<sup>[13]</sup> Likewise, the position and width of the FSDP have been observed to vary with the pressure or

D. Dahal, H. Warren, Prof. P. Biswas  
 Department of Physics and Astronomy  
 The University of Southern Mississippi  
 Hattiesburg, Mississippi 39406, USA  
 E-mail: partha.biswas@usm.edu

 The ORCID identification number(s) for the author(s) of this article can be found under <https://doi.org/10.1002/pssb.202000447>.

DOI: 10.1002/pssb.202000447



density of the glasses.<sup>[14,17]</sup> Neutron diffraction<sup>[19]</sup> and molecular dynamics studies of densified v-SiO<sub>2</sub><sup>[20]</sup> have indicated that the intensity and width of the FSDP can change with the density of the samples/models. These changes can be attributed to the frustration induced by the reduction of Si—O—Si bond angles and the changes in the Si—Si and O—O atomic correlations on the length scale of 4–10 Å when the system is densified. A similar conclusion can be made for GeO<sub>2</sub> glass when the glass is densified.<sup>[21]</sup> The addition of extrinsic atoms in glassy networks has been also found to affect the FSDP. Lee and Elliott<sup>[15]</sup> have noted that the inclusion of extrinsic atoms in v-SiO<sub>2</sub> can change the chemical ordering of the interstitial voids in the glassy network, which can alter the shape/width of the FSDP.

The great majority of earlier studies mostly examined the origin and behavior of the FSDP in borate, chalcogenide, oxide, and silicate glasses.<sup>[5,22–24]</sup> However, there exist only a few studies<sup>[3,4,25]</sup> that address the structure of the FSDP in tetrahedral amorphous semiconductors, such as a-Si and a-Ge. Elliott and co-workers<sup>[4,25]</sup> have addressed the problem at length, but their studies are primarily focused on the origin of the extended-range oscillations (EROs) in a-Si. The results from their studies, which are based on the (Fourier) inversion of experimental structure-factor data of Fortner and Lannin<sup>[26]</sup> in the vicinity of the FSDP and highly defective a-Si models of Holender and Morgan,<sup>[27]</sup> suggest that the EROs arise from the preferential propagation of second-neighbor correlations in the network, which in turn can significantly affect the intensity of the FSDP up to a radial length scale of 20 Å. However, no systematic analysis of the results with respect to the size of models is provided and, thus, in the absence of direct numerical evidence, it is not clear to what extent the intensity of the FSDP is truly affected by atomic correlations originating from radial distances beyond 15 Å.

The key purpose of this article is to provide a systematic study of the structure of the FSDP, with an emphasis on the position, intensity, and width of the peak, with the size of the models. In addition, the origin of the FSDP in a-Si is addressed by obtaining a quantitative estimate of the contribution of atomic pair correlations from different radial shells and their effect on the intensity and position of the FSDP. The relationship between the peaks in the structure factor and its real-space counterpart, the reduced pair-correlation function (PCF), is addressed, and an approximate functional relation between the position of the FSDP in a-Si and the radial distance of the atoms in the second radial shell of the amorphous network is obtained. Throughout this study, we shall use the term “FSDP” to refer to the first peak of the structure factor of a-Si at  $Q_0 = 1.9\text{--}2\text{ Å}^{-1}$  in discussing our results. Likewise, the term “principal peak” will be used to indicate the second peak at  $Q_1 = 3.6\text{ Å}^{-1}$ . For a-Si, this terminology has been used previously by others,<sup>[4,25]</sup> and it is consistent with the fact that the peak at  $Q_0$  is indeed the first peak of  $S(Q)$  and that it is reasonably sharp and strong with a value of the intensity  $S(Q_0)$ , which is  $\approx 67\%$  of the intensity of the principal peak. A further justification of the use of the terminology will be evident later from our discussion of the results in Section 3.1.

The rest of the study is planned as follows. Section 2 provides a brief description of the simulation method for producing atomistic models of a-Si via the modified Wooten–Winer–Weaire (WWW)<sup>[28,29]</sup> method, the calculation of the radial PCF, and the structure factor for these models. This is followed by results

and discussion in Section 3, with an emphasis on the origin and structure of the FSDP. The conclusions of this study are presented in Section 4.

## 2. Computational Section

For the purpose of generating atomistic models of a-Si, we have used the well-known WWW method. The details of the method can be found in previous studies.<sup>[28,29]</sup> Here, we have used the modified version of the method, developed by Barkema and Mousseau (BM).<sup>[29]</sup> In the modified WWW approach, one starts with a random configuration that consists of  $N$  atoms in a cubic supercell of length  $L$ . The volume of the supercell is chosen in such a way that the mass density of the model corresponds to  $\approx 2.28\text{ g cm}^{-3}$ , as observed in a-Si samples produced in laboratories.<sup>[30,31]</sup> Initially, following the BM ansatz, the nearest neighbors of each atom are so assigned that a tetravalent network is formed.<sup>[32]</sup> This is achieved by choosing a suitable nearest-neighbor cutoff distance, up to 3 Å, between Si atoms. The resulting tetravalent network is then used as the starting point of the WWW bond-switching algorithm.<sup>[28]</sup> New configurations are generated by introducing a series of WWW bond switches, which largely preserve the tetravalent coordination of the network and the energy of the system is minimized using Monte Carlo (MC) simulations. The acceptance or rejection of a proposed MC move is determined via the Metropolis algorithm<sup>[33]</sup> at a given temperature. Here, the energy difference between two configurations is calculated locally by using the Keating potential,<sup>[34]</sup> which employs an atomic-index-based nearest-neighbor list of the tetravalent network during MC simulations. In addition, the total energy of the entire system is relaxed from time to time using the Stillinger–Weber potential.<sup>[35]</sup> Finally, the configurations obtained from the modified WWW method were relaxed using the first-principles density-functional code Siesta.<sup>[36]</sup> For the models with 216 atoms to 3000 atoms, a full self-consistent-field calculation, using the generalized-gradient approximation (GGA)<sup>[37]</sup> and a set of double-zeta basis functions, was conducted. The remaining models of size from 4096 atoms to 6000 atoms were treated using the non-self-consistent Harris-functional approach<sup>[38]</sup> in the density-functional theory (DFT) with a single-zeta basis set in the local density approximation (LDA).<sup>[39]</sup> To conduct configurational averaging of simulated data, we have generated ten models for each size starting with different random configurations using independent runs.

Once the atomistic models are generated, the calculation of the structure factor proceeds by computing the reduced PCF. The latter is defined as  $G(r) = 4\pi r n_0 [g(r) - 1]$ , where  $g(r)$  and  $n_0$  are the PCF and the average number density of a model, respectively. Assuming that the distribution of the atoms in a disordered network is isotropic and homogeneous, the structure factor,  $S(Q)$ , can be written as

$$\begin{aligned} S(Q) &= 1 + \frac{1}{Q} \int_0^\infty G(r) \sin(Qr) dr \\ &\approx 1 + \frac{1}{Q} \int_0^{R_c} G(r) \sin(Qr) dr \end{aligned} \quad (1)$$

where  $R_c$  is the length of the half of the cubic simulation cell. The conventional periodic boundary conditions are used to minimize surface effects and to calculate the PCF in Equation (1).

### 3. Results and Discussion

Equation (1) suggests that the shape of the FSDP can be fully determined via the Fourier (sine) transformation of the reduced PCF  $G(r)$ , provided that  $G(r) \rightarrow 0$  as  $r \rightarrow R_c$ . As the shape of the FSDP is primarily determined by the structure factor in the vicinity of  $Q_0 \approx 2 \text{ \AA}^{-1}$ , it is apparent that one requires sufficiently large models of a-Si to satisfy the aforementioned condition, for an accurate determination of the FSDP. To this end, we first validate the structural models of a-Si, obtained from the modified WWW method. As the latter is a well-established method, we restrict ourselves to the PCF, the bond-angle distribution (BD), and the coordination number (CN) of Si atoms in the network. It has been shown elsewhere<sup>[40]</sup> that knowledge of the PCF, BD, and CN of the atoms is sufficient to establish whether a structural model can produce the correct electronic and vibrational properties of a-Si or not. The full structure factor and the normalized BD, obtained from a set of 3000-atom models of a-Si, are plotted in Figure 1, and 2, respectively. For the purpose of configurational averaging, the results were averaged over ten independent models of an identical size. The simulated values of  $S(Q)$  in Figure 1 can be seen to agree well with the corresponding experimental data reported in Laaziri et al.<sup>[31]</sup> Likewise, the full width at half-maximum (FWHM) of the BD in Figure 2,  $\approx 21.4^\circ$ , matches with the observed value of 18–24 obtained from the Raman “optic peak” measurements.<sup>[41]</sup> The FWHM of the BD for the WWW models is also found to be consistent with those obtained from high-quality molecular dynamics simulations,<sup>[42,43]</sup> and data-driven information-based approaches,<sup>[40,44]</sup> developed in recent years. A further characterization of the models is possible by examining the statistics of the CN of Si atoms, the dihedral-angle distribution, and the presence of various irreducible rings in the amorphous structures. However, as the WWW models have been extensively studied and validated in the literature, we will not linger over the

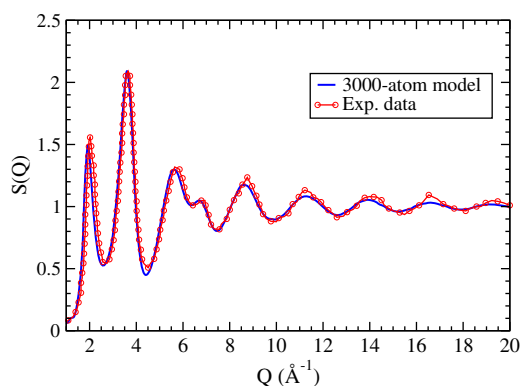


**Figure 1.** The structure factor of a-Si obtained from simulations and experiments. The simulated data are from 3000-atom WWW models of density  $2.28 \text{ g cm}^{-3}$ , whereas the experimental data correspond to those from Laaziri et al.<sup>[31]</sup> The simulated data were obtained by averaging over ten models from independent runs.

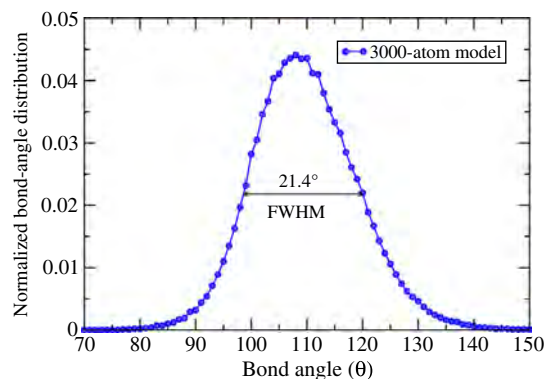


**Figure 2.** The normalized BD for a-Si, obtained for 3000-atom WWW models. The FWHM corresponds to a value of  $21.4^\circ$ . The distribution was obtained by averaging over ten independent models.

validation issue and get back to the central topic of this study by listing the coordination-number statistics of the atoms and some key structural properties of the WWW models in Table 1. The corresponding results for the DFT-relaxed models are provided in Table 2.

#### 3.1. Characterization, Origin, and the Structure of the FSDP in a-Si

Figure 3 shows the structure factor of a-Si obtained from four different models, of size from 216 to 3000 atoms, and experiments.<sup>[30]</sup> As before, the simulation data were obtained by averaging over ten independent models for each size, whereas the experimental data refer to as-implanted samples of a-Si in Xie et al.<sup>[30]</sup> An examination of Figure 3 leads to the following observations. First, it is apparent that the 216-atom model shows a marked deviation from the experimental data near the FSDP, indicating noticeable finite-size effects originated from small models of linear size of  $\approx 16 \text{ \AA}$ . By contrast, the larger models,

**Table 1.** Structural properties of a-Si models before DFT relaxation.

Size $N$	Bond angle and width		Coordination number <sup>a)</sup>			Bond length $\langle r \rangle$
	$\langle \theta \rangle$	$\Delta \theta$	$n_4$	$n_3$	$n_5$	
216	109.25	9.11	100	0	0	2.35
300	109.25	9.32	100	0	0	2.35
512	109.26	9.41	100	0	0	2.35
1000	109.27	9.16	100	0	0	2.35
2000	109.27	9.31	99.95	0	0.05	2.35
3000	109.26	9.39	99.94	0	0.06	2.35
4096	109.26	9.26	99.95	0	0.05	2.35
5000	109.27	9.31	99.97	0	0.03	2.35
6000	109.26	9.39	99.96	0	0.04	2.35

<sup>a)</sup>The number of  $i$ -fold-coordinated atoms (in percent) in the network is indicated as  $n_i$ . Bond lengths and bond angles/widths are expressed in angstrom (Å) and degree, respectively. The results were obtained by averaging over ten configurations using a nearest-neighbor cutoff value of  $2.8 \text{ \AA}$ .

**Table 2.** Structural properties of DFT-relaxed models of a-Si.

Model size <sup>a)</sup> N	Bond angle and width		Coordination number			Bond length $\langle r \rangle$
	$\langle \theta \rangle$	$\Delta \theta$	$n_4$	$n_3$	$n_5$	
216	109.11	10.14	100	0	0	2.36
300	109.15	10.22	100	0	0	2.36
512	109.13	10.45	100	0	0	2.36
1000	109.15	10.14	100	0	0	2.36
2000	109.14	10.3	99.95	0	0.05	2.36
3000	109.13	10.4	99.96	0.01	0.03	2.36
4096*	109.02	10.82	99.95	0.01	0.04	2.37
5000*	109.01	10.9	99.94	0.01	0.05	2.37
6000*	109.01	10.92	99.95	0.01	0.04	2.37

<sup>a)</sup>The total number of *i*-fold-coordinated atoms (in percent) present in the relaxed networks is indicated as  $n_i$ . Average bond lengths and bond angles/widths are expressed in angstrom (Å) and degree, respectively. Asterisks indicate the use of single-zeta basis functions and the non-self-consistent Harris-functional approximation for relaxation of large models.

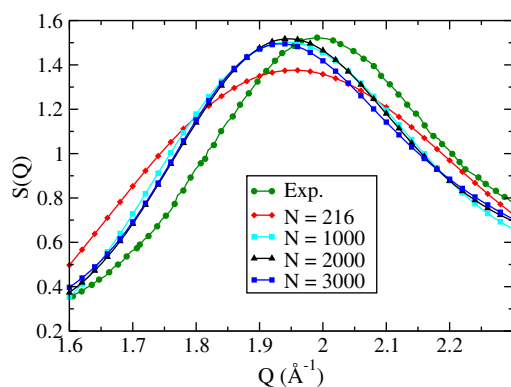


**Figure 3.** The structure factor of a-Si in the vicinity of the FSDP from simulations and experiments. Experimental data (●) correspond to as-implanted samples from Xie et al.,<sup>[30]</sup> whereas simulated data refer to 216-atom (◆), 1000-atom (■), 2000-atom (▲), and 3000-atom (■) unrelaxed WWW models.

consisting of 1000–3000 atoms, have produced the peak intensity more accurately. Second, all the models consistently underestimate the position of the experimental FSDP<sup>[30]</sup> at  $Q_0 = 1.99 \text{ Å}^{-1}$ , by an amount of  $0.045 \text{ Å}^{-1}$ . One can surmise a number of possible reasons for this discrepancy. These include the inadequacy of the classical potentials, the uncertainty of the actual density of the a-Si sample(s) used in experiments, and a possible sample-to-sample dependence of the experimental results. The last point can be appreciated by noting that the experimental values of  $Q_0$ , for as-implanted samples of a-Si, reported by Fortner and Lannin,<sup>[26]</sup> Xie et al.,<sup>[30]</sup> and Laaziri et al.<sup>[31]</sup> differ from each other by  $\approx 0.07 \text{ Å}^{-1}$  (see Figure 11). Finally, a first-principles total-energy relaxation of the models, using the density-functional code Siesta,<sup>[36]</sup> somewhat remedies this issue at the expense of the reduction of the peak intensity. This is shown in Figure 4, where we have plotted both the reduced pair-

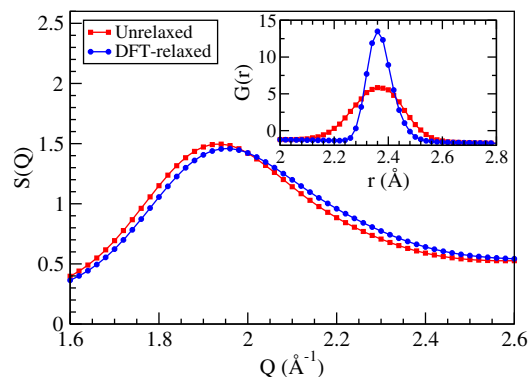


**Figure 4.** Effects of approximate first-principles relaxations on the position and intensity of the FSDP of a-Si for a 3000-atom model before (■) and after (●) relaxation. A small shift of the diffraction peak toward higher values of  $Q$  is accompanied by a slight reduction of the peak intensity in the relaxed model. The corresponding reduced PCFs near the first peak are shown in the inset.

correlation function (see inset) and the configurational-average structure factor from ten 3000-atom models before and after total-energy relaxation. The increase of the peak height of  $G(r)$  upon relaxation is not surprising in view of the fact that first-principles relaxations minimized the total energy of the system by reducing the bond-length disorder at the expense of a minor increase of the bond-angle disorder. The latter is reflected in the root-mean-square (RMS) width,  $\Delta \theta$ , of the BD before and after relaxation in Table 1 and 2, respectively. By contrast, the shape of the structure factor near the FSDP remains more or less the same after relaxation, except for a small shift of the FSDP toward higher values of  $Q$ .

Having addressed the overall shape of the structure factor and the FSDP for a number of models of varying sizes, we now examine the origin of the FSDP in terms of the real-space structure of a-Si networks. Although it is well understood that the FSDP in a-Si arises from the medium-range order in the network, which entails a length scale of a few to several angstroms, a quantitative characterization of the contribution from different radial shells is still missing in the literature. We address this aspect of the problem by examining the role of radial atomic correlations in forming the FSDP, via the Fourier transform of the reduced PCF, and provide a quantitative measure of the contributions that originate from the increasingly distant radial shells in the amorphous environment of silicon. This can be achieved by writing

$$S(Q) = 1 + F(Q) = 1 + \sum_{i=1}^n F_i(Q; R'_i, R'_{i+1}) \quad (2)$$

where

$$F_i(Q; R'_i, R'_{i+1}) = \frac{1}{Q} \int_{R'_i}^{R'_{i+1}} G(r) \sin(Qr) dr \quad (3)$$

In Equation (2),  $F_i(Q; R'_i, R'_{i+1})$  is the contribution to  $F(Q)$  from the reduced PCF,  $G(r)$ , at distances between  $R'_i$  and  $R'_{i+1}$ . The contribution from a given radial shell can be obtained by a suitable choice of  $R'_i$  and  $R'_{i+1}$ , where  $R'_{i+1} > R'_i$ , and an appropriate set  $\{R'_1, \dots, R'_n\}$  covers the entire radial



(integration) range to obtain the full  $F(Q)$ . For example, a choice of  $R'_1 = 0 \text{ \AA}$  and  $R'_2 = 2.8 \text{ \AA}$  yields  $F_1(Q; R'_1, R'_2)$ , and  $R'_2 = 2.8 \text{ \AA}$  and  $R'_3 = 4.9 \text{ \AA}$  provides  $F_2(Q; R'_2, R'_3)$ . The origin of the FSDP and the principal peak can be studied by computing various  $F_i(Q)$  in the vicinity of 2 and  $3.6 \text{ \AA}^{-1}$ , respectively. The appropriate values of  $R'_i$  for different radial shells can be obtained by inspecting the reduced PCF of a-Si. This is shown in **Figure 5** by plotting the configurational-average  $G(r)$  obtained from a set of ten 3000-atom models. We should emphasize that the radial shells correspond to the radial regions between two neighboring minima in the reduced PCF. Except for the first radial shell, the radial regions, defined by a pair of consecutive minima in  $G(r)$ , are not necessarily identical to the corresponding atomic coordination shells due to the overlap of the atomic distribution from different coordination shells.

**Figure 6** shows the contribution to  $F(Q)$  in the vicinity of  $2 \text{ \AA}^{-1}$  from the first six radial shells. The plots for different radial shells are indicated by the corresponding shell color as shown in **Figure 5**. It is evident that the chief contribution to the FSDP comes from  $F_2(Q)$ , which is followed by  $F_4(Q)$  and  $F_6(Q)$  in the descending order of magnitude.  $F_2(Q)$  and  $F_4(Q)$  play a

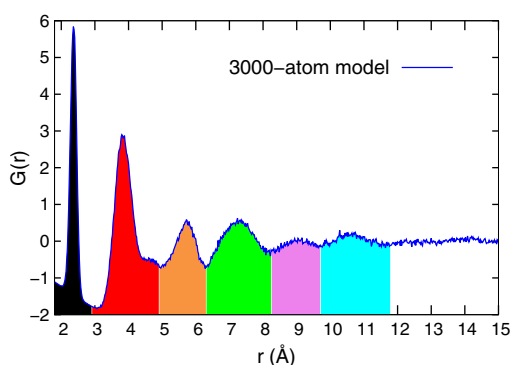


**Figure 5.** The reduced PCF,  $G(r)$ , of a-Si obtained from configurational averaging of ten 3000-atom WWW models. The presence of the first six radial shells, which extend up to a distance of  $\approx 12 \text{ \AA}$ , is highlighted in different colors.

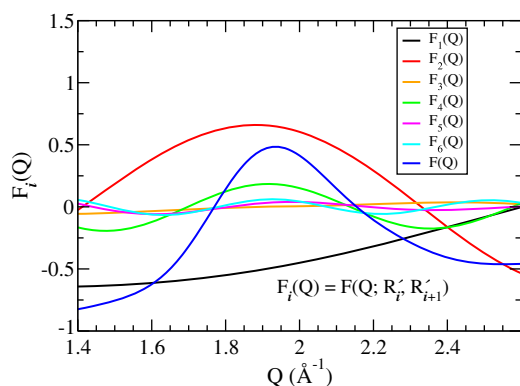


**Figure 6.** The contribution to the FSDP,  $F_i(Q)$ , near  $Q_0$ , originating from the first six radial shells and the total  $F(Q)$  (blue). The results correspond to 3000-atom WWW models, and are averaged over ten configurations. The color of the plots corresponds to the color of the radial shells in **Figure 5**.

crucial role in determining both the intensity and the position of the FSDP, whereas  $F_3(Q)$  and  $F_5(Q)$  contribute very little or not at all. By contrast,  $F_1(Q)$  monotonically changes in the vicinity of the FSDP and thus contributes to the intensity (and the shape) of the FSDP near  $Q_0$  to some degree but does not play any noticeable role in determining the position of  $Q_0$ . It is therefore apparent that the position of the FSDP in a-Si is primarily determined by the information from the second radial shell, followed by the fourth and sixth radial shells, whereas the rest of the distant radial shells provide small perturbative corrections. The enumeration of the radial shell-by-shell contribution to  $F(Q)$  is a significant result to our knowledge, which cannot be quantified from a phenomenological understanding of the Fourier transform of  $G(r)$  in Equation (1). A similar analysis reveals that the contribution to the principal peak at  $3.6 \text{ \AA}^{-1}$  mostly arises from  $F_2(Q)$ ,  $F_1(Q)$ ,  $F_4(Q)$ , and  $F_3(Q)$ , in the decreasing order of magnitude. Once again,  $F_1(Q)$  is found to provide a positive but monotonically decreasing contribution with increasing  $Q$  in the vicinity of the principal peak. Thus, the peak at  $3.6 \text{ \AA}^{-1}$  is principally determined by the first four radial shells in the reduced PCF. This observation amply justifies the use of the term “principal peak” to describe the peak at  $3.6 \text{ \AA}^{-1}$  in the structure factor of a-Si. **Figure 7** shows the results for the principal peak using the same color code as in **Figure 5**.

### 3.2. Relation Between Peaks in $S(Q)$ and $G(r)$

The results presented in the preceding section on the basis of the partitioning of  $F(Q)$  reveal that the information from the second and fourth radial shells largely determines the structure, that is, the position, intensity, and width, of the FSDP in a-Si. We now provide a physical interpretation of the numerical results and demonstrate that the emergence of the first two peaks in  $S(Q)$ , near 2 and  $3.6 \text{ \AA}^{-1}$ , respectively, can be deduced simply from knowledge of the reduced PCF and the behavior of the integral, involving the  $\text{sinc}(x)$  (i.e.,  $\sin x/x$ ) function, which defines the structure factor. Noting that the structure factor can be written as

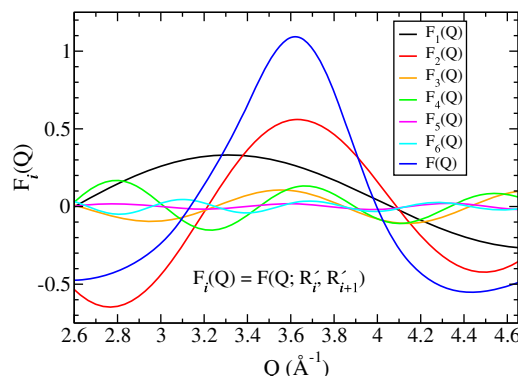


**Figure 7.** The contribution,  $F_i(Q)$ , to the principal peak at  $Q_1 = 3.6 \text{ \AA}^{-1}$  from the first six radial shells of the reduced PCF. The total  $F(Q)$  is shown in blue color for comparison. The results were obtained via configurational averaging of data from ten 3000-atom models.

$$S(Q) = 1 + F(Q) = 1 + \frac{1}{Q} \int_0^{R_c} G(r) \sin(Qr) dr$$

$$= 1 + \int_0^{R_c} r G(r) \left[ \frac{\sin(Qr)}{Qr} \right] dr \quad (4)$$

it is elementary that the peaks in  $F(Q)$  (and hence  $S(Q)$ ) should appear approximately for those values of  $Qr$  for which both  $\sin(Qr)/Qr$  and  $rG(r)$  are maximum. Here, the  $r$  values in  $Qr$  are given by the maxima of  $rG(r)$ . As the maxima of  $\sin(Qr)/Qr$  and  $\sin(Qr)$  are very close to each other<sup>[45]</sup> for  $Qr > 0$ , and the maxima of  $G(r)$  and  $rG(r)$  practically coincide, one may use the maxima of  $\sin(Qr)$  and  $G(r)$  in determining the approximate location of the first two peaks in  $S(Q)$ . This implies  $Qr$  must satisfy  $\sin(Qr) = 1$ , or  $Qr = (4m + 1)\pi/2$ , where  $m = 0, 1, 2, \dots$  etc. As the first two maxima of  $G(r)$  are given by  $r_1 \approx 2.35$  and  $r_2 \approx 3.8$  Å, respectively, and  $m = 0$  does not admit a physical solution, the first major contribution to the  $F(Q)$  comes from the second radial shell for  $r_2 = 3.8$  Å and  $m = 1$ . This gives  $Q_0 = 5\pi/(2 \times r_2) = 2.07$  Å<sup>-1</sup>. Likewise, the next contribution, for  $m = 2$ , comes from the fourth radial shell with a peak at  $r_4 \approx 7.24$  Å in  $G(r)$ . This yields  $Q_0 = 9\pi/(2 \times r_4) = 1.95$  Å<sup>-1</sup>. A similar analysis shows that the principal peak ( $Q_1$ ) gets its share from the first radial shell, for  $m = 1$ , at  $Q_1 = 5\pi/(2 \times r_1) = 3.34$  Å<sup>-1</sup>, which is followed by the second radial shell, for  $m = 2$ , at  $Q_1 = 9\pi/(2 \times r_2) = 3.72$  Å<sup>-1</sup>, the fourth radial shell, for  $m = 4$ , at  $Q_1 = 17\pi/(2 \times r_4) = 3.69$  Å<sup>-1</sup>, and the third radial shell, for  $m = 3$  and  $r_3 = 5.72$  Å, at  $Q_1 = 13\pi/(2 \times r_3) = 3.57$  Å<sup>-1</sup>. The exact position of a peak in  $S(Q)$  is determined by the sum of the contribution from the relevant radial shells, which introduces a minor deviation from the earlier individual estimate due to the approximate nature of our calculations. **Table 3** displays a summary of the results obtained from the previous reasoning. The estimated position of the peaks in  $F_i(Q)$ , for  $i = 1-6$ , is listed in the table. The first column corresponds to the maxima ( $r_i$ ) of  $G(r)$  up to a radial distance of 11 Å, whereas the second row lists the values of  $Qr = (4m + 1)\pi/2$  for  $m = 1-6$ . The remaining six rows, between columns 1 and 8, indicate the peak positions in  $F_i(Q)$  that are obtained by dividing the  $Qr$  values by the corresponding  $r_i$  value from the first column. The estimated positions of the FSDP and the principal peak for a number of combinations of ( $r_i, m$ ) are indicated in Table 3 by asterisks and daggers, respectively.

Conversely, assuming that the FSDP is located at  $Q_0 \approx 2$  Å<sup>-1</sup>, one arrives at the conclusion, by dint of our logic, that the contribution to the FSDP should come from  $r = (4m + 1)\pi/(2 \times Q_0) = \pi/4, 5\pi/4, 9\pi/4$ , and  $13\pi/4$ , etc., for  $m = 0-3$ . The first value of  $r$ , for  $m = 0$ , does not provide a physical solution but the remaining values at 3.93, 7.07, and 10.21 Å approximately correspond to the second peak, fourth peak, and sixth peak of  $G(r)$  (cf. Figure 5). A similar analysis can be done for the principal peak. The argument presented here suffices to explain why the information from the distant radial shells, for  $r \geq 15$  Å, cannot contribute significantly in the formation of the FSDP. At large radial distances, when the reduced PCF rapidly vanishes and the concomitant numerical noises in  $G(r)$  become increasingly stronger,  $\sin(Qr)/Qr$  cannot find, or sample, suitable values of  $r$  with a large  $G(r)$ , for  $Q$  values near the FSDP, to satisfy the aforementioned condition. This leads to small  $F_i(Q)$  for the distant radial shells. We have verified that the analysis presented here is consistent with the results from numerical calculations of  $F_i(Q)$ .

The results and discussion presented so far indicate that the radial information from the reduced PCF of up to a length scale of 15 Å plays a significant role in the formation of the FSDP. To further establish this point, we conducted a systematic study of the structure of the FSDP in terms of the intensity and width of the peak. The variation of the peak intensity with the size of the models was studied by plotting the value of  $S(Q_0)$  against  $R_c$  for a number of DFT-relaxed/unrelaxed models, consisting of 216 atoms to 6000 atoms. Because  $R_c$  is given by the half of the linear size of the models, **Figure 8** essentially shows the dependence of  $S(Q_0)$  on the radial pair correlations up to a distance of  $R_c$ , through the Fourier transform of  $G(r)$ . It is clear from the plots (in Figure 8) that the intensity of the FSDP for both the relaxed and unrelaxed models varies considerably until  $R_c$  increases to a value of the order of 14 Å. This roughly translates to a model of size of  $\approx 1000$  atoms. For even larger values of  $R_c$ , the peak intensity is more or less converged to 1.48 for the unrelaxed models but considerable deviations exist for the value of DFT-relaxed models from the experimental value of  $S(Q_0)$  of 1.52 in Xie et al.<sup>[30]</sup> The deviation of the peak intensity from the experimental value for small models of a-Si can be readily understood. Because  $G(r)$  carries considerable real-space information up to a radial distance of 15 Å, possibly 20 Å for very large models, small

**Table 3.** Estimated values of the peak position,  $Q$ , in  $F_i(Q)$ , obtained from  $Qr = (4m + 1)\pi/2$  for  $m = 1-6$ ,<sup>a)</sup> and the maxima of  $G(r)$  (first column) in angstrom (Å).

Maxima of $G(r)$	1	2	3	4	5	6	$\leftarrow m$
	7.854	14.137	20.42	26.704	32.987	39.27	$\leftarrow Qr$
2.35	3.34 <sup>†</sup>	6.02	8.69	11.36	14.04	16.71	Peaks in $F_1$
3.8	2.07*	3.72 <sup>†</sup>	5.37	7.03	8.68	10.33	Peaks in $F_2$
5.72	1.37	2.47	3.57 <sup>†</sup>	4.67	5.77	6.87	Peaks in $F_3$
7.24	1.08	1.95*	2.82	3.69 <sup>†</sup>	4.56	5.42	Peaks in $F_4$
9.16	0.86	1.54	2.23	2.92	3.6	4.29	Peaks in $F_5$
10.74	0.73	1.32	1.9*	2.49	3.07	3.66	Peaks in $F_6$

<sup>a)</sup>The positions of the FSDP and the principal peak (PP) in  $F_i$  are indicated by asterisks and daggers, respectively. The radial shells that contribute to the FSDP and the PP can be directly read off the first column.

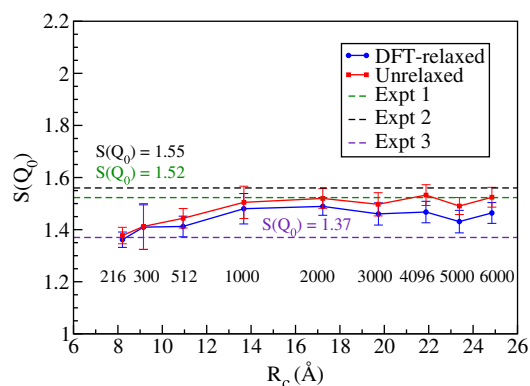


**Figure 8.** The dependence of the intensity of the FSDP,  $S(Q_0)$ , with the radial cutoff distance,  $R_c$ , for a number of models of different sizes, as indicated in the plot. The experimental values of  $S(Q_0)$  reported in the literature are shown as horizontal dashed lines: 1)  $S(Q_0) = 1.52$  from Xie et al.,<sup>[30]</sup> 2)  $S(Q_0) = 1.55$  from Laaziri et al.,<sup>[31]</sup> and 3)  $S(Q_0) = 1.37$  from Fortner and Lannin.<sup>[26]</sup>

models with  $R_c$  values less than 15 Å cannot accurately produce the peak position using Equation (1). On the other hand, the peak intensities for the DFT-relaxed models deviate noticeably ( $\approx 0.2$ – $12\%$ ) from their unrelaxed counterparts and the experimental values for as-implanted samples in Xie et al.,<sup>[30]</sup> Fortner and Lannin,<sup>[26]</sup> and Laaziri et al.<sup>[31]</sup> This apparent deviation for the bigger models is not particularly unusual and it can be attributed, at least partly, to 1) the use of approximate total-energy calculations in the relaxation of large models, via the non-self-consistent Harris-functional approach using minimal single-zeta basis functions; 2) the intrinsic difficulties associated with quantum-mechanical relaxations of large models; and 3) the sample dependence of experimental results, showing a considerable difference in the value of  $S(Q_0)$  for as-implanted samples in Figure 8, which is as high as 0.18 from one experiment to another. Thus, the results obtained in this study are well within the range of the experimental values reported in the literature.<sup>[26,30,31]</sup>

The FWHM of the FSDP for different models is plotted against  $R_c$  in Figure 9. A somewhat high value of the FWHM for the large DFT-relaxed models is a consequence of the reduction of the peak intensity. As the intensity of the peak reduces, the FWHM increases slightly due to the widening of the diffraction plot away from the peak. An inspection of Figure 8 and 9 appears to suggest that the values of FWHM and  $S(Q_0)$  are somewhat correlated with each other. In particular, a-Si models exhibiting smaller values of  $S(Q_0)$  (in Figure 8) tend to produce somewhat larger values of FWHM (in Figure 9), irrespective of the size of the models and DFT relaxation. This is apparent in Figure 10, where FWHM and  $S(Q_0)$  values for all configurations and sizes are shown in the form of a scatter plot. A simple analysis of FWHM and  $S(Q)$  data by computing the Pearson correlation coefficient,  $r_{XY}$ , confirms the suggestion that FWHM and  $S(Q_0)$  values are indeed linearly correlated with each other and have a correlation coefficient of  $r_{XY} = -0.9$ . The linear least-square fits of the data are also shown in Figure 10 by a solid (red) line. The great majority of the FWHM and  $S(Q)$  values in Figure 10 can be seen to cluster along the straight line within a rectangular region bounded by the experimental values of

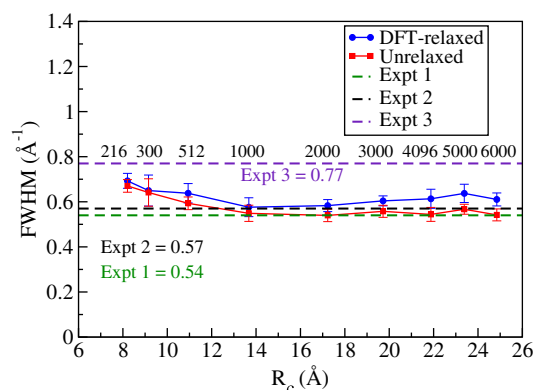


**Figure 9.** The FWHM of the FSDP at  $Q_0$  for a number of models before (■) and after (●) DFT relaxations. The horizontal dashed lines indicate the experimental values of  $0.54 \text{ Å}^{-1}$  (green),  $0.57 \text{ Å}^{-1}$  (black), and  $0.77 \text{ Å}^{-1}$  (indigo) for as-implanted samples of a-Si from Xie et al.,<sup>[30]</sup> Laaziri et al.,<sup>[31]</sup> and Fortner and Lannin,<sup>[26]</sup> respectively.

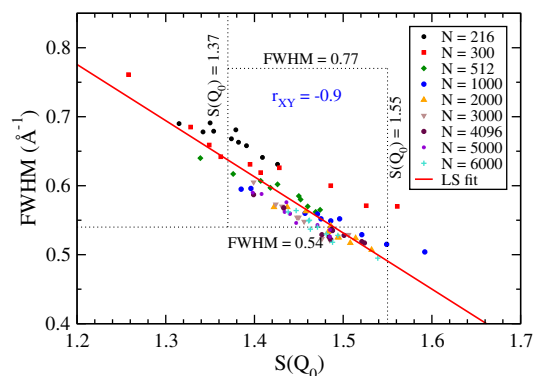


**Figure 10.** A scattered plot showing the presence a clear correlation between the FWHM and  $S(Q_0)$  of the FSDP for a number of models of varying system sizes. The solid (red) line corresponds to the linear least-squares (LS) fit of the data, whereas  $r_{XY} = -0.9$  indicates the Pearson correlation coefficient for the data sets. The horizontal and vertical dotted lines indicate the experimental values of FWHM and  $S(Q_0)$ , respectively, obtained for as-implanted samples of a-Si.

FWHM and  $S(Q_0)$ , from  $0.54$  to  $0.77 \text{ Å}^{-1}$  and  $1.37$  to  $1.55$ , respectively.

Likewise, the dependence of the position of the FSDP with  $R_c$  for the unrelaxed and DFT-relaxed models is shown in Figure 11. For the unrelaxed models,  $Q_0$  is observed to converge near  $1.95 \text{ Å}^{-1}$ , whereas the corresponding value for the DFT-relaxed models hovers around  $1.97 \text{ Å}^{-1}$ . In both the cases,  $Q_0$  is found to be within the range of the experimental values, from  $1.95$  to  $2.02 \text{ Å}^{-1}$ , as shown in Figure 11.

In summary, a systematic study of a-Si models, consisting of 216–6000 atoms, firmly establishes that the structure of the FSDP in a-Si is mostly determined by radial pair correlations up to a distance of 15 Å, as far as the size of the largest models used in this study is concerned. Further, the major contribution to the FSDP arises from the second and fourth radial shells, along with small residual contributions from the distant radial shells at a distance of up to 15 Å.



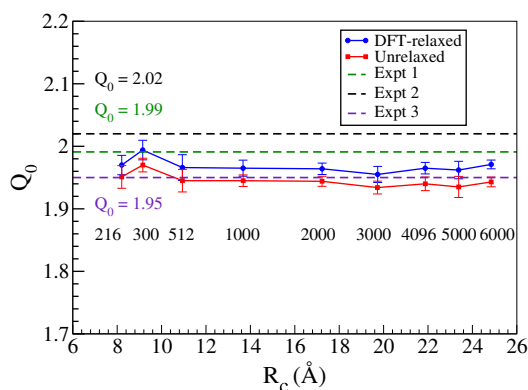


**Figure 11.** The dependence of the position of the FSDP,  $Q_0$ , with the size of the models before (■) and after (●) DFT relaxations. The horizontal lines correspond to the experimental value of  $Q_0$  for as-implanted samples of a-Si from Xie et al.<sup>[30]</sup> (green), Laaziri et al.<sup>[31]</sup> (black), and Fortner and Lannin<sup>[26]</sup> (indigo).

### 3.3. The FSDP and the Radial Shell Structures of a-Si

Earlier, in Sections 3.1 and 3.2, we have demonstrated that the position of the FSDP,  $Q_0$ , is primarily determined by  $F_2(Q)$  and, to a lesser extent,  $F_4(Q)$ . This leads to a possibility of the existence of a simple functional relationship between  $Q_0$  and a suitable length scale in the real space involving the radial atomic correlations in the network. In this section, we will show that an *approximate* relationship between  $Q_0$  and the average radial distance,  $\langle R_2 \rangle$ , of the atoms in the second (radial) shell does exist. To this end, we first provide a rationale behind the origin of this relationship, which is subsequently corroborated by results from direct numerical calculations.

The first hint that an approximate relationship may exist follows from the behavior of  $Q_0$  with the (mass) density,  $\rho$ , of the models. In **Figure 12**, we have plotted the variation of  $Q_0$  against  $\rho$  for a-Si. For this purpose, the density of a set of 3000-atom

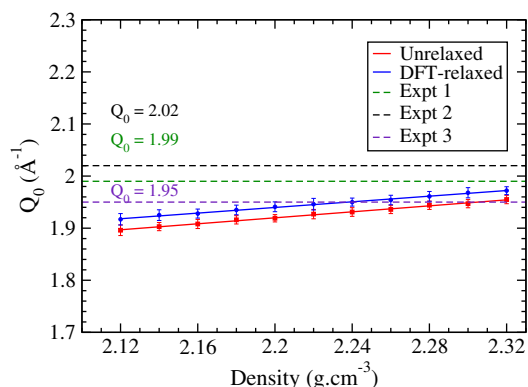


**Figure 12.** The variation of the peak position ( $Q_0$ ) for 3000-atom models of a-Si with its mass density,  $\rho$ , of the models. The value of  $Q_0$  has been observed to vary linearly with the density of the model. The experimental values of  $Q_0$  (horizontal dashed lines) correspond to as-implanted samples of density  $2.28 \text{ g.cm}^{-3}$  from Laaziri et al.<sup>[31]</sup> (black), Xie et al.<sup>[30]</sup> (green), and Fortner and Lannin<sup>[26]</sup> (indigo).

models is varied, within the range  $2.12\text{--}2.32 \text{ g cm}^{-3}$ , by scaling the length of the cubic simulation cell and the position of the atoms therein. This involves a tacit assumption that for a small variation of the density, by  $\approx \pm 5\%$ , the atomistic structure of the network would remain unchanged and that a simple scaling approach should suffice to generate low/high-density models. Given that the WWW models of a-Si do not include any extended defects and voids in the network, the scaling assumption is reasonably correct and suitable to produce models with a small variation of the density. Figure 12 displays the results from our calculations, which show a linear relationship between  $Q_0$  and the density,  $\rho$ , of the models. This linear variation of  $Q_0$  with  $\rho$  is not particularly unique to a-Si; a similar behavior has been observed experimentally by Inamura et al.<sup>[14,17]</sup> for densified silica.

The results from Figure 12 and the experimental data from Inamura et al.<sup>[14,17]</sup> suggest that  $Q_0$  can vary approximately linearly with the average density,  $\rho$ , of the models/samples. As  $\rho$  is inversely proportional to the cubic power of the simulation cell size ( $L$ ) for a given number of atoms,  $Q_0$  also varies as  $1/L^3$  when the density is varied by rescaling the volume. Thus, for homogeneous and isotropic models with no significant variation of the local density, which the WWW models satisfy in the absence of extended defects and voids, it is reasonable to assume that  $Q_0 \propto 1/r_{ij}^3$ , where  $r_{ij}(\rho)$  is the distance between any two atoms in the network, at sites  $i$  and  $j$ , of average density  $\rho$ . In view of our earlier observation that the position of the FSDP is largely determined by  $F_2(Q)$  (see Figure 6), one may posit that  $r_{ij}$  values between  $R_2'$  and  $R_3'$  in  $G(r)$  mostly affect the peak position at  $Q_0$ . These considerations lead to the suggestion that by substituting  $r_{ij}^3$  by its average value of  $\langle r_{ij}^3 \rangle = \langle R_2^3 \rangle$  for the atoms in the second radial shell,  $Q_0 \langle R_2^3 \rangle$  should remain constant, on average, upon density variations via volume rescaling. Likewise, one can invoke the same reasoning and may expect  $Q_0 \langle R_4^3 \rangle$  should be also constant, but only approximately, due to the limited role and contribution of the atoms in the fourth radial shell in determining the position of  $Q_0$ .

The efficacy of our argument can be verified by results from direct numerical calculations. A plot of  $Q_0 \langle R_2^3 \rangle$  (and  $Q_0 \langle R_4^3 \rangle$ ) versus the average density  $\rho$  in **Figure 13** (and **Figure 14**) indeed confirms our prediction. It may be noted that the observed (absolute) deviation,  $\Delta$ , of  $Q_0 \langle R_2^3 \rangle$  values in the density range  $2.15\text{--}2.3 \text{ g cm}^{-3}$  in Figure 13 is of the order of  $\pm 0.46\sigma$ , where  $\sigma$  is the (largest) standard deviation obtained by averaging results from ten independent models for each density. By contrast, the corresponding deviation for  $Q_0 \langle R_4^3 \rangle$  in Figure 14 is found to be more than two standard deviations, as indicated in the plot. The large deviation of  $Q_0 \langle R_4^3 \rangle$  values is not unexpected in view of the small contribution of  $F_4(Q)$  (to the FSDP) that originates from the fourth radial shell. Thus, the results from Figure 13 lead to the conclusion that  $Q_0$  is approximately proportional to the inverse of the average cubic power of the radial distance,  $\langle R_2^3 \rangle$ , of the atoms in the second radial shell in a-Si. It goes without saying that the use of  $\langle R_2 \rangle^3$ , instead of  $\langle R_2^3 \rangle$ , does not change the conclusion of our work, as the difference between these two values is found to be  $\approx 1.92\text{--}2.1 \text{ Å}^3$ , for mass density in the range  $2.15\text{--}2.3 \text{ g cm}^{-3}$ , which simply shifts the plot (in Figure 13) vertically downward by a constant amount.

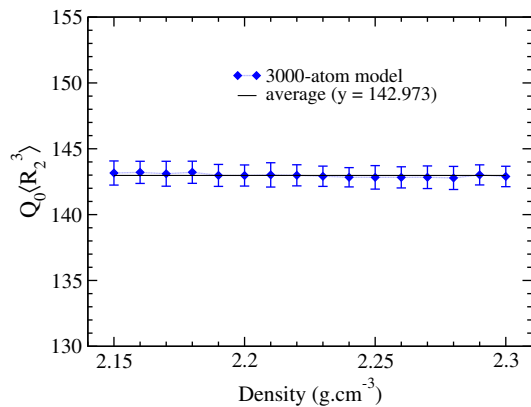


**Figure 13.** The relation between  $Q_0$  and  $\langle R_2^3 \rangle$  of the atoms in the second radial shell. A constant value of  $Q_0 \langle R_2^3 \rangle$  with respect to the density of a-Si models indicates that  $Q_0$  is approximately proportional to the inverse of  $\langle R_2^3 \rangle$ . The horizontal black line indicates the average value of  $Q_0 \langle R_2^3 \rangle$  within the density range shown in the plot.

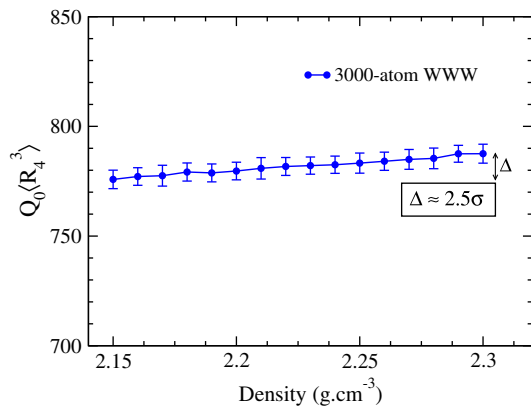


**Figure 14.** The dependence of  $Q_0$  and  $\langle R_4^3 \rangle$  for the atoms in the fourth radial shell of a-Si in the density range 2.15–2.3 g cm<sup>-3</sup>. The large deviation of  $Q_0 \langle R_4^3 \rangle$  values, indicated by  $\Delta \approx 2.5\sigma$ , from a constant value suggests that no simple relationship between  $Q_0$  and  $\langle R_4^3 \rangle$  exists.

We end this section by making a comment on the possible role of distant radial atomic correlations, or EROs, in  $G(r)$  on the FSDP, based on our preliminary results from 6000-atom models. Although the presence of EROs in ultralarge models of a-Si beyond 15 Å is an undisputed fact,<sup>[25]</sup> a direct determination of the effect of the EROs on the FSDP in a-Si is highly nontrivial due to the presence of intrinsic noises in  $G(r)$  at large radial distances. Numerical calculations using 6000-atom models of a-Si indicate that only a minute fraction of the total intensity of the FSDP results from the radial region beyond 15 Å. These calculations do not include any possible artifacts that may arise from the noises in  $G(r)$  at large distances. The observed deviation in the peak intensity, due to the truncation of the radial distance at 15 Å and at higher values, is found to be  $\approx 1$ –2%, which is less than one standard deviation ( $\sigma$ ) associated with  $S(Q_0)$ , obtained from using the maximal radial cutoff distance  $R_c (= L/2)$ , as far as the results from 6000-atom models are

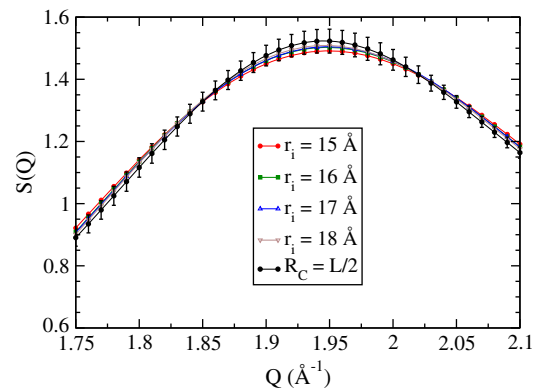


**Figure 15.** The structure factor,  $S(Q)$ , in the vicinity of the FSDP from 6000-atom a-Si models. The change in  $S(Q)$  due to varying radial cutoff distances,  $r_i$ , is found to be less than one standard deviation ( $\Delta S(Q_0) \approx 0.85\sigma$  for  $r_i = 15$  Å, and  $0.46\sigma$  for  $r_i = 18$  Å). The standard deviation,  $\sigma$ , is obtained from using the maximal radial cutoff  $L/2$ , which is given by 24.85 Å. The results correspond to the average values of  $S(Q)$  obtained from ten configurations.

concerned. **Figure 15** shows the variation of the intensity near the FSDP for five different cutoff values from 15 to 18 and 24.85 Å. It is apparent that the changes in  $S(Q)$  near  $Q_0$  are very small as the radial cutoff value increases from 15 to 18 Å. These small changes in the intensity values are readily reflected in **Figure 16**, where the fractional errors, from  $S(Q, R_c)$ , associated with the calculation of  $S(Q, r_i)$  are plotted against  $Q$  for  $r_i = 15$ –18 Å. Thus, as far as the current study and the maximum size of the models are concerned, the EROs do not appear to contribute much to the FSDP. However, an accurate study of the EROs in a-Si would require high-quality ultralarge models, consisting of several tens of thousands of atoms, and a suitable prescription to handle noises in  $G(r)$  at large distances. These and some related issues concerning the origin of the EROs in a-Si and their possible role in  $S(Q)$  will be addressed in a future studies.

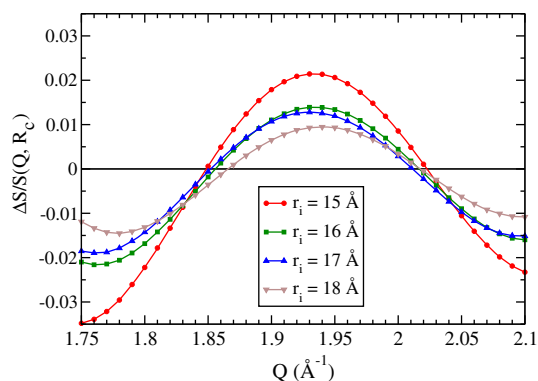


**Figure 16.** The fractional error associated with the calculation of the structure factor in the vicinity of the FSDP with a varying radial cutoff distance,  $r_i$ , from 15 to 18 Å.  $\Delta S(Q)$  is the absolute error and  $R_c (= 24.85$  Å) is the half-length of the cubic simulation cell for 6000-atom models. The error due to the truncation of the radial distance at  $r_i$  can be seen to be around 1–2%, which is well within one standard deviation of  $S(Q_0)$  (see **Figure 15**).

## 4. Conclusion

In this study, we have studied the origin and structure of the FSDP of a-Si with an emphasis on the position, intensity, and width of the diffraction peak. The study leads to the following results: 1) By partitioning the contribution of the reduced PCF to the FSDP, which originates from the Fourier transform of radial atomic correlations in the real space, a quantitative measure of the contribution to the FSDP from different radial shells is obtained. The results show that the position of the FSDP in a-Si is principally determined by atomic pair correlations in the second, fourth, and sixth radial shells, in the descending order of importance, supplemented by small residual contributions from beyond the sixth radial shell. 2) A convergence study of the position, intensity, and width of the FSDP, using a set of models of size from 216 to 6000 atoms, suggests that the minimum size of the models must be at least 1000 atoms or more for the results to be free from finite-size effects. This approximately translates into a radial length of 14 Å, which is consistent with the results obtained from the radial-shell analysis of the reduced PCF. 3) A theoretical basis for the results obtained from numerical calculations is presented by examining the relationship between the peaks in the structure factor and the reduced PCF. Contrary to the common assumption that the peaks in the structure factor and the reduced PCF are not directly related to each other, we have shown explicitly that the knowledge of the reduced PCF alone is sufficient to determine not only the approximate position of the FSDP and the principal peak but also the relevant radial regions that are primarily responsible for the emergence of these peaks in the structure factor, and vice versa. 4) The study leads to an approximate relation between the position of the FSDP and the average radial distance of the atoms in the second radial shell of a-Si networks. For homogeneous and isotropic models of a-Si with no significant variation of the local density, it has been shown that the position of the FSDP is inversely proportional to the cubic power of the average radial distance of the atoms in the second radial shell. The result is justified by providing a phenomenological explanation—based on experimental and computational studies of the variation of the FSDP with the average density of a-Si samples and models—which is subsequently confirmed by direct numerical calculations for a range of densities from 2.15 to 2.3 g cm<sup>-3</sup>.

## Acknowledgements

The work was partially supported by the US National Science Foundation (NSF) under Grant No. DMR 1833035. P.B. thanks Profs. Gerard Barkema (Utrecht, the Netherlands) and Normand Mousseau (Montreal, Canada) for providing their modified WDW code. The authors gratefully acknowledge one of the anonymous referees for the suggestion to include Table 3.

## Conflict of Interest

The authors declare no conflict of interest.

## Data Availability Statement

Research data are not shared.

## Keywords

amorphous silicon, first sharp diffraction peak, pair-correlation functions, static structure factor

Received: August 17, 2020  
Revised: December 31, 2020  
Published online: January 27, 2021

- [1] P. S. Salmon, R. A. Martin, P. E. Mason, G. J. Cuello, *Nature* **2005**, 435, 03475.
- [2] G. D'Angelo, C. Crupi, M. A. González, E. Basile, V. C. Nibali, C. Mondelli, *J. Phys. Chem. B* **2010**, 114, 12565.
- [3] S. Elliott, *J. Non-Cryst. Solids* **1995**, 182, 40.
- [4] A. Uhlherr, S. R. Elliott, *Philos. Mag. B* **1995**, 71, 611.
- [5] C. Crupi, G. Carini, G. Ruello, G. D'Angelo, *Philos. Mag.* **2016**, 96, 788.
- [6] E. Bychkov, C. J. Benmore, D. L. Price, *Phys. Rev. B* **2005**, 72, 172107.
- [7] O. Uemura, Y. Sagara, T. Satow, *Phys. Status Solidi A* **1975**, 32, K91.
- [8] S. Susman, D. Price, K. Volin, R. Dejus, D. Montague, *J. Non-Cryst. Solids* **1988**, 106, 26.
- [9] P. Vashishta, R. K. Kalia, G. A. Antonio, I. Ebbsjö, *Phys. Rev. Lett.* **1989**, 62, 1651.
- [10] D. Price, S. Susman, K. Volin, R. Dejus, *Physica B* **1989**, 156–157, 189.
- [11] L. E. Busse, S. R. Nagel, *Phys. Rev. Lett.* **1981**, 47, 1848.
- [12] P. Armand, A. Ibanez, Q. Ma, D. Raoux, E. Philippot, *J. Non-Cryst. Solids* **1994**, 167, 37.
- [13] S. Susman, K. J. Volin, D. G. Montague, D. L. Price, *Phys. Rev. B* **1991**, 43, 11076.
- [14] Y. Inamura, M. Arai, N. Kitamura, S. Bennington, A. Hannon, *Physica B* **1997**, 241–243, 903.
- [15] J. Lee, S. Elliott, *J. Non-Cryst. Solids* **1995**, 192–193, 133.
- [16] P. Debye, *Ann. Phys.* **1913**, 348, 49.
- [17] Y. Inamura, Y. Katayama, W. Utsumi, *J. Phys.: Condens. Matter* **2007**, 19, 415104.
- [18] The effect of temperature on the structure factor of polycrystalline and disordered aggregates can be rather complicated due to the presence of attendant thermal diffuse scattering, which originates from the self-scattering of an atom with respect to itself. Here, we refer to the effect of the Debye-Waller factor, which simply dampens the Bragg peaks of crystalline samples at high temperature.
- [19] S. Susman, K. J. Volin, D. L. Price, M. Grimsditch, J. P. Rino, R. K. Kalia, P. Vashishta, G. Gwanmesia, Y. Wang, R. C. Liebermann, *Phys. Rev. B* **1991**, 43, 1194.
- [20] O. Pilla, L. Angelani, A. Fontana, J. R. Gonçalves, G. Ruocco, *J. Phys.: Condens. Matter* **2003**, 15, S995.
- [21] S. Sampath, C. J. Benmore, K. M. Lantzky, J. Neuefeind, K. Leinenweber, D. L. Price, J. L. Yarger, *Phys. Rev. Lett.* **2003**, 90, 115502.
- [22] G. Lucovsky, J. C. Phillips, *Nanoscale Res. Lett.* **2010**, 5, 550.
- [23] P. H. Gaskell, D. J. Wallis, *Phys. Rev. Lett.* **1996**, 76, 66.
- [24] J. Du, L. R. Corrales, *Phys. Rev. B* **2005**, 72, 092201.
- [25] A. Uhlherr, S. R. Elliott, *J. Phys.: Condens. Matter* **1994**, 6, L99.
- [26] J. Fortner, J. S. Lannin, *Phys. Rev. B* **1989**, 39, 5527.
- [27] J. M. Holender, G. J. Morgan, *J. Phys.: Condens. Matter* **1991**, 3, 7241.
- [28] F. Wooten, K. Winer, D. Weaire, *Phys. Rev. Lett.* **1985**, 54, 1392.
- [29] G. T. Barkema, N. Mousseau, *Phys. Rev. B* **2000**, 62, 4985.
- [30] R. Xie, G. G. Long, S. J. Weigand, S. C. Moss, T. Carvalho, S. Roorda, M. Hejna, S. Torquato, P. J. Steinhardt, *Proc. Natl. Acad. Sci. USA* **2013**, 110, 13250.
- [31] K. Laaziri, S. Kycia, S. Roorda, M. Chicoine, J. L. Robertson, J. Wang, S. C. Moss, *Phys. Rev. B* **1999**, 60, 13520.



- [32] An alternative approach to generate a fourfold-coordinated disordered network is to employ the reverse Monte Carlo (RMC) approach using a suitable cost function. The resulting tetravalent network can be used as a starting configuration for the WWW bond switches between atoms.
- [33] N. Metropolis, A. W. Rosenbluth, M. N. Rosenbluth, A. H. Teller, E. Teller, *J. Chem. Phys.* **1953**, 21, 1087.
- [34] P. N. Keating, *Phys. Rev.* **1966**, 145, 637.
- [35] F. H. Stillinger, T. A. Weber, *Phys. Rev. B* **1985**, 31, 5262.
- [36] J. M. Soler, E. Artacho, J. D. Gale, A. Garcia, J. Junquera, P. Ordejón, D. Sánchez-Portal, *J. Phys.: Condens. Matter* **2002**, 14, 2745.
- [37] J. P. Perdew, K. Burke, M. Ernzerhof, *Phys. Rev. Lett.* **1996**, 77, 3865.
- [38] J. Harris, *Phys. Rev. B* **1985**, 31, 1770.
- [39] J. P. Perdew, A. Zunger, *Phys. Rev. B* **1981**, 23, 5048.
- [40] D. K. Limbu, S. R. Elliott, R. Atta-Fynn, P. Biswas, *Sci. Rep.* **2020**, 10, 7742.
- [41] D. Beeman, R. Tsu, M. F. Thorpe, *Phys. Rev. B* **1985**, 32, 874.
- [42] R. Atta-Fynn, P. Biswas, *J. Chem. Phys.* **2018**, 148, 204503.
- [43] V. L. Deringer, N. Bernstein, A. P. Bartók, M. J. Cliffe, R. N. Kerber, L. E. Marbella, C. P. Grey, S. R. Elliott, G. Csányi, *J. Phys. Chem. Lett.* **2018**, 9, 2879.
- [44] D. K. Limbu, R. Atta-Fynn, D. A. Drabold, S. R. Elliott, P. Biswas, *Phys. Rev. Materials* **2018**, 2, 115602.
- [45] The positions of the maxima of  $\sin(x)/x$  asymptotically converge to  $(4m+1) \times \pi/2$ , where  $m$  is a positive integer. The first four positions of the maxima of  $\sin(x)/x$ , for  $x \geq 0$ , are given by  $x = 0, 7.725, 14.065$ , and  $20.37$ . The corresponding values for  $\sin(x)$  are at  $x = 1.570$  ( $\pi/2$ ),  $7.853$  ( $5 \times \pi/2$ ),  $14.137$  ( $9 \times \pi/2$ ), and  $20.420$  ( $13 \times \pi/2$ ). This also explains why  $m=0$  does not provide a physical solution (as it corresponds to  $Qr=0$ ).

# Generalized Langevin Equation Theory of Thermal Conduction across Material Interfaces

Yi Zeng, Jalaan T. Avritte, and Jianjun Dong\*

Dedicated to Professor David A. Drabold on the occasion of his 60th birthday

The thermal conduction across material interfaces is studied using a generalized Langevin equation (gLE) theory. A general statistical formula of thermal interfacial conductance (TIC) is derived at the slow fluctuation limit in terms of the time auto-correlation functions of interfacial heat current (QACF)  $\langle q(t)q(0) \rangle$  and the heat capacity  $C_V$ . At the bulk limit of  $C_V \rightarrow \infty$ , this general TIC formula reduces to the previously proposed Green–Kubo type of TIC formula. Beyond the bulk limit, the TIC of a material with finite  $C_V$  can be calculated using the first and second moments of the interfacial QACF. These statistical TIC formulas provide the basis to adopt equilibrium molecular dynamics simulations to calculate the TIC of real material interfaces beyond the bulk limit, including the interfaces at the nanoscale. The TIC of two types of non-Markov model interfaces with analytic forms of QACF is predicted by the reported gLE theory, and the results of these non-Markov interfaces are compared with those of a Markov interface.

response theory,<sup>[3,4]</sup> transport coefficients of bulk materials can be directly calculated based on the time-correlation functions (tcf) of the corresponding physical quantities at thermal equilibrium.<sup>[5]</sup> For example, the thermal conductivity ( $\kappa$ ) of a material with volume ( $V$ ) can be expressed with a time ( $t$ ) integral of its ensemble averaged tcf of heat currents ( $J(t)$ ), also referred to as the time auto-correlation function of heat current (QACF), at a temperature of  $T$

$$\begin{aligned}\kappa &= \lim_{s \rightarrow 0} \frac{1}{Vk_B T^2} \int_0^\infty dt e^{-st} \langle J(t)J(0) \rangle \\ &= \frac{1}{Vk_B T^2} \int_0^\infty dt \langle J(t)J(0) \rangle\end{aligned}\quad (1)$$

## 1. Introduction


At the beginning of last century, Einstein unveiled the groundbreaking Einstein's relation in Brownian motion.<sup>[1]</sup> Built upon Einstein's hypothesis that both thermal fluctuation and thermal dissipation in Brownian motion have the same stochastic origin at the atomic level, Langevin proposed a stochastic differential equation, now known as the Langevin equation, to quantitatively describe the stochastic dynamics of a Brownian particle.<sup>[2]</sup> This Langevin equation theory, which has now been adopted to study a wide range of stochastic dynamics with some generalizations, started a new paradigm of non-equilibrium statistical theory for stochastic processes. By the end of 1960s, physicists had made a remarkable advance in the fundamental theory of non-equilibrium statistical mechanics. Within the theoretical framework of fluctuation–dissipation theorem and linear

where  $k_B$  is the Boltzmann constant and  $\langle \dots \rangle$  represents the equilibrium ensemble average. Equation (1) is commonly referred to as the Green–Kubo formula of thermal conductivity. By the end of the 20th century, computational capacity had reached the level that atomic molecular dynamics (MD) simulations can be carried out to robustly calculate QACF for real materials. Some early successful reports include the studies of SiC crystals,<sup>[6]</sup> Si crystals,<sup>[7]</sup> diamond crystals and related materials,<sup>[8]</sup> and Ge crystal, amorphous Ge, and cage-like Ge clathrates.<sup>[9]</sup> These early equilibrium MD (EMD) calculations not only numerically verified many statistical assumptions adopted in the derivation of Green–Kubo formula, but also proposed numeric algorithms to estimate and/or correct finite-size artifacts in EMD simulations. Two decades later, the EMD-based Green–Kubo approach has emerged as a mainstream computational method for atomic scale calculations of bulk  $\kappa$ , because of the rapid increase in computational power and the steady improvement in methodology development. Extensive studies have demonstrated that the EMD predicted values of bulk  $\kappa$  are in agreement with those directly extracted from the simulated steady-state temperature profiles in non-equilibrium MD (NEMD) simulations when the finite-size artifacts are properly corrected.<sup>[10]</sup> As an NEMD approach typically requires a more intensive computational load to minimize the finite-size artifacts to the same level of an EMD simulation, the majority of MD-based  $\kappa$  calculations reported in recent years are based on the Green–Kubo formula shown in Equation (1).

On the other hand, similar EMD studies of thermal conduction across material interfaces remain rather limited. Analogous to the definition of bulk  $\kappa$  by the Fourier Law of bulk thermal

Dr. Y. Zeng  
Department of Mechanical Engineering  
Auburn University  
Auburn, AL 36849-5341, USA

Dr. Y. Zeng, J. T. Avritte, Prof. J. Dong  
Department of Physics  
Auburn University  
Auburn, AL 36849-5311, USA  
E-mail: dongjia@auburn.edu

 The ORCID identification number(s) for the author(s) of this article can be found under <https://doi.org/10.1002/pssb.202000454>.

DOI: 10.1002/pssb.202000454

conduction, the thermal interfacial conductance (TIC) ( $G_k$ ) is defined as the ratio of net interfacial heat current ( $q_{\text{int}}$ ) and the temperature discontinuity ( $\Delta T$ ) between the two sides of the interface of area ( $A$ ) at a macroscopic steady state

$$q_{\text{int}} = -G_k A \Delta T \quad (2)$$

So far, an overwhelming majority of the reported MD-based calculations of TIC in the literature is based on Equation (2), using various NEMD simulations to numerically evaluate  $\Delta T$  and  $J_{\text{int}} = \frac{q_{\text{int}}}{A}$ . The scarcity of the EMD-based TIC calculations in the current literature is in part due to the lack of in-depth theoretical analyses to extend the fundamental statistical theories developed for the bulk systems in the 1950s and 1960s to the cases of thermal conduction across materials' interfaces, especially interfaces at the nanoscale.

Using a classical Langevin equation to approximate the thermal conduction across a material interface as a Markov process, Puech, Bonfait, and Castaing (PBC) derived the first statistical formula that expresses the transport coefficient TIC in terms of the tcf of fluctuating interfacial heat current at thermal equilibrium<sup>[11]</sup>

$$G_k = \frac{1}{Ak_B T^2} \int_0^\infty dt \langle q(t)q(0) \rangle \quad (3)$$

Equation (3) is commonly referred to as the Green–Kubo-type formula for TIC, because it is obviously analogous to the Green–Kubo formula for bulk  $\kappa$  (Equation (1)). The derivation in the original report of PBC was based on an over-simplification for the random component of the interfacial heat current  $q_R(t)$  being strictly a white noise, i.e.,  $\langle q_R(t)q_R(0) \rangle = 2B\delta(t)$ , and the tcf in Equation (3) was referred to  $\langle q_R(t)q_R(0) \rangle$ , not that of the total heat current  $\langle q(t)q(0) \rangle$ . As additional assumptions have to be adopted to split the total interfacial heat current  $q(t)$  into the sum of the dissipation current  $q_D(t)$  and the randomly fluctuating current  $q_R(t)$ , the original PBC formula is not practical for an MD simulation study. Although heuristic, the original PBC formula for TIC, in principle, has only limited applicability for studies of real and complex interfaces of materials.

In 2003, Barrat and Chiaruttini (BC)<sup>[12]</sup> re-derived the TIC formula to replace the QACF of the random heat currents  $q_R(t)$  with the QACF of the total interfacial heat currents  $q(t)$ , which can be calculated in MD simulations. BC demonstrated that the formula in Equation (3) is valid only at the bulk limit, i.e., the heat capacity  $C_V \rightarrow \infty$ . Although BC also provided some arguments based on the concept of “memory kernel” that the TIC formula in Equation (3) remains valid for the non-white noise/non-Markov cases, they stop short to provide enough derivation details for the non-Markov cases. BC also carried out an EMD simulation study for a solid–liquid interface using a simulation model of a finite size. Their MD results indicate that 1) the fluctuating  $q(t)$  is indeed of the non-Markov type with its QACF consisting of small yet finite oscillation components, and 2) the running integral of their QACF reaches a clearly defined plateau before decaying to zero at the  $t \rightarrow \infty$  limit. The clearly defined plateau indicates that it is promising to correct the artifacts associated with the finite  $C_V$  values in MD simulations. However, later EMD studies suggest that the finite- $C_V$  correction can be more complicated for interfaces with large  $G_k$  and/or small

$C_V$ , because the expected “plateaus” in running integral of QACF are often poorly defined. In 2013, Liang, Evans, and Koblinski (LEK) proposed a simple empirical correction model to extract the TIC for a system of finite  $C_V$  from fitting to the running integral of QACF<sup>[13]</sup>

$$G_k e^{-\alpha t_s} = \frac{1}{Ak_B T^2} \int_0^{t_s} dt \langle q(t)q(0) \rangle \quad (4)$$

where  $\alpha$  is supposed to be proportional to  $\frac{AG_k}{C_V}$ . The validity of this LEK correction model (Equation (4)) has not yet been extensively tested.

In 2012, Chalopin, Esfarjani, Henry, Volz, and Chen (CEHVC) reported a general statistical derivation of TIC formula,<sup>[14]</sup> based on the local equilibrium theory (LET)<sup>[15]</sup> to approximate the non-equilibrium ensemble. Assuming a specific form of non-equilibrium distribution function proposed for the case of bulk thermal transport,<sup>[15]</sup> CEHVC analyzed the interfacial heat transfer  $\langle q_{\text{II} \rightarrow \text{I}} \rangle$  across an interface between two macroscopic systems, I and II, with two different temperatures  $T_I$  and  $T_{\text{II}}$ , and derived a formula for TIC as

$$G_k = \frac{1}{Ak_B T^2} \langle q_{\text{II} \rightarrow \text{I}}(t) E_{\text{II}}(t) \rangle = \frac{-1}{Ak_B T^2} \langle q_{\text{II} \rightarrow \text{I}}(t) E_{\text{I}}(t) \rangle \quad (5)$$

where  $q_{\text{II} \rightarrow \text{I}}(t)$  is the instantaneous  $q$  flowing from subsystem II to subsystem I, and  $E_{\text{I}}(t) = E_{\text{I}}(t_0) + \int_{t_0}^t dt' q_{\text{II} \rightarrow \text{I}}(t')$  is the fluctuating total energy of the subsystem I. By setting  $t_0 \rightarrow \infty$ , CEHVC obtained a TIC formula that  $C_V$  is identical to the Green–Kubo-type formula proposed by PBC and BC (Equation (3)). CEHVC further demonstrated that this Green–Kubo-type formula for TIC (Equation (3)) is valid to calculate TIC of Si/Ge super-lattices, and no finite  $C_V$  correction is needed. It is interesting to note that the reported QACF of Si/Ge super-lattices is characteristically different from those reported for the solid–liquid interfaces<sup>[12]</sup> or solid–gas interfaces.<sup>[13]</sup> The LET adopted by CEHVC was originally proposed only for bulk system, and the validity of this approximation for the cases of  $\frac{G_k A}{C_V} \neq 0$  has not been analyzed.

Clearly, some key approximations adopted in the previous statistical analyses, such as the Markov approximation, or the bulk approximation, significantly limit the applications of the previously proposed Green–Kubo-type TIC formulas to study TIC of real materials, especially nano-materials. In the current study, we treat the thermal conduction across a material interface as a non-Markov process and describe its stochastic dynamics with a generalized Langevin equation (gLE).<sup>[4]</sup> Our goal is to derive a general statistical expression of the TIC in terms of interfacial QACF  $\langle q(t)q(0) \rangle$  for material interfaces of all length scales, from the nano-scale to the bulk limit. Our newly derived general TIC formula is compared with the previously proposed Green–Kubo-type TIC formula at the bulk limit. Beyond the bulk limit, we propose a simplified TIC formula for interfaces of nano-materials. The simplified TIC formula beyond the bulk limit is adopted to predict TIC of two model interfaces of the non-Markov type.



## 2. Generalized Langevin Equation

### 2.1. Non-Markov Dynamics

We consider a macroscopic system at thermal equilibrium with a surrounding heat bath of temperature  $T$  via a conducting interface of area  $A$ . The dynamic heat exchange between the system and the heat bath is modeled with a gLE.<sup>[4]</sup> Using  $E(t)$  and  $q(t)$  to denote the instantaneous energy of the system and the interfacial heat current flowing into the system respectively, we have

$$\frac{dE(t)}{dt} = q(t) = q_D(t) + q_R(t) \quad (6)$$

with the interfacial heat currents  $q(t)$  divided into two distinct components, i.e., the dissipation currents  $q_D$  that bring to system back to its equilibrium states and the noise-like random currents  $q_R$  that drive the thermal fluctuation.

As the stochastic dynamics of an interfacial heat exchange is likely non-Markov, the dissipation current  $q_D$  in a gLE has to be expressed with a memory kernel function  $\gamma(t)$  to properly account the historic effects of energy/temperature fluctuations

$$q_D(t) = - \int_{-\infty}^t dt' \gamma(t-t') (E(t') - E_{eq}) \quad (7)$$

Here,  $E_{eq}$  is the equilibrium value of the fluctuating  $E(t)$ , and the variance of this fluctuation is known to be proportional to  $C_V$ , i.e.,  $\sigma_E^2 = \langle (E(t) - E_{eq})^2 \rangle = C_V k_B T^2$ . Previous derivations of PBC<sup>[11]</sup> and BC<sup>[12]</sup> were carried out based on an over-simplified Markov model, whose memory kernel function is simply a  $\delta$ -function, i.e.,  $\gamma(t-t') = 2\gamma_0 \delta(t-t')$  and  $q_D(t) = \gamma_0 [E(t) - E_{eq}]$ .

As in the classical Langevin equation, we assume that 1)  $q_R$  randomly fluctuates around a zero mean, i.e.,  $\langle q_R(t) \rangle = 0$ , and 2) its value at any instance is independent of its history, i.e.,  $\langle q_R(t) E(t') \rangle = 0$  for  $t > t'$ . The fluctuation–dissipation theorem for a non-Markov process<sup>[3,4]</sup> also states that

$$\langle q_R(t) q_R(0) \rangle = \sigma_E^2 \gamma(t) = C_V k_B T^2 \gamma(t) \quad (8)$$

As discussed in the Section 1,  $\langle q_R(t) q_R(0) \rangle \neq \langle q(t) q(0) \rangle$ . To calculate the memory kernel function  $\gamma(t)$  of a material's interface using numeric techniques, such as EMD simulation methods, additional analyses are needed to connect  $\gamma(t)$  function with the interfacial QACF of the total interfacial heat current  $\langle q(t) q(0) \rangle$ . Nevertheless, the gLE theory for thermal conduction across a material interface, as expressed in Equation (6)–(8), is applicable to a wide range of materials interfaces, whose length scales range from the nanoscale to the bulk limit, and interfacial bonding types range from rigid valance/ionic bonds to flexible van der Waals (vdW) forces or hydrogen bonds.

### 2.2. Macroscopic TIC at Slow Fluctuation Limit

Within the gLE theory of interfacial thermal conduction, the memory kernel function  $\gamma(t)$  (Equation (7) and (8)) manifests the fundamental relation between the heat dissipation at an interface and the thermal fluctuation of an interfacial current. Here, we also refer to  $\gamma(t)$  as the dissipation kernel function and

consider it as a general and dynamic characterization of the interfacial heat transfer properties. In comparison, the TIC defined in Equation (2) represents a macroscopically averaged static transport coefficient, which should correspond to a coarse-grain average of this dynamic dissipation kernel function  $\gamma(t)$ .

To analyze the relation between the dissipation kernel function in the gLE and the fluctuating currents, we take an ensemble average at the both sides of Equation (6) and express the energy fluctuation in terms of the temperature fluctuation, i.e.,  $\langle E(t) \rangle - E_{eq} = C_V \Delta T(t)$ . We find an expression of  $\langle q(t) \rangle$  as follows

$$\begin{aligned} \langle q(t) \rangle &= \frac{d\langle E(t) \rangle}{dt} \\ &= - \int_{-\infty}^t dt' \gamma(t-t') C_V \Delta T(t') + \langle q_R(t) \rangle \\ &= - \int_{-\infty}^t dt' \gamma(t-t') C_V \Delta T(t') \end{aligned} \quad (9)$$

Next, we compare two dynamic rates in Equation (9), i.e., the decay rate of the kernel function  $\gamma(t)$  versus the fluctuation rate of temperature  $\Delta T(t)$ . At the slow fluctuation limit, we can approximate  $\Delta T(t') \approx \Delta T$  in Equation (9) and find that  $\langle q \rangle \approx -[\int_0^\infty dt' \gamma(t')] C_V \Delta T$ . By comparing this ensemble averaged current with the macroscopic net current in Equation (2), we find that the memory kernel function defined in Equation (7) relates to the transport coefficient TIC as follows

$$G_k = \frac{C_V}{A} \int_0^\infty dt \gamma(t) = \frac{1}{A k_B T^2} \int_0^\infty dt \langle q_R(t) q_R(0) \rangle \quad (10)$$

Because of the distinction between  $\langle q_R(t) q_R(0) \rangle$  and the interfacial QACF  $\langle q(t) q(0) \rangle$  (see discussion in earlier text), our TIC formula in Equation (10) is conceptually different from that derived by BC<sup>[12]</sup> or CEHVC<sup>[14]</sup> (Equation (3)). Our newly derived TIC formula (Equation (10)) is a generalization of the original formula proposed by PBC,<sup>[11]</sup> who only considered the limiting case of Markov processes.

The derivation of our TIC formula for non-Markov thermal conduction suggests that: 1) the concept of static TIC is based on the slow fluctuation assumption, i.e., the fluctuation rate of temperature at an interface is slower than the decay rate of the interface's dissipation kernel function, and 2) a general formula for TIC beyond the bulk limit and Markov limit is a time integral of the dissipation kernel function (Equation (10)) at this slow fluctuation limit. For the cases where the rate of temperature fluctuation is significantly faster than the decay rate of its dissipation kernel function, the concept of static TIC, as defined in Equation (2), likely need be revised with frequency-dependent transport coefficients to properly describe the such dynamic interfacial heat transfer processes.

### 2.3. Statistical Formulas for TIC

As discussed in earlier texts, it is impractical to numerically calculate the tcf  $\langle q_R(t) q_R(0) \rangle$ , because  $q_R$  is only a part of total interfacial current  $q(t)$ . To apply EMD simulation techniques to calculate TIC using Equation (10), we need to find expressions of  $\gamma(t)$  in terms of interfacial QACF  $\langle q(t) q(0) \rangle$  or other related

tcf that can be calculated with EMD methods. For this effort, we first define and analyze three relevant tcf that describe the fluctuation of energy and heat current, which are defined as follows

$$c_0(t) \equiv \langle \Delta E(t) \Delta E(0) \rangle = \langle (E(t) - E_{\text{eq}})(E(0) - E_{\text{eq}}) \rangle \quad (11)$$

$$c_1(t) \equiv \langle q(t) \Delta E(0) \rangle = \langle q_D(t)(E(0) - E_{\text{eq}}) \rangle \quad (12)$$

$$c_2(t) \equiv \langle q(t)q(0) \rangle = \langle q_D(t)q_D(0) \rangle + \langle q_R(t)q_R(0) \rangle + \langle q_D(t)q_R(0) \rangle \neq \langle q_R(t)q_R(0) \rangle \quad (13)$$

Here, the auto-correlation function of energy fluctuation (EACF),  $c_0(t)$ , is a continuous even function of  $t$  with  $c_0(0) = \sigma_E^2 = C_V k_B T^2$ , the current-energy tcf,  $c_1(t)$ , is an odd function that might have a discontinuity at  $t = 0$ , and the interfacial QACF,  $c_2(t)$ , is a continuous even function that might include a  $\delta$ -function at  $t = 0$ . From the practical viewpoint, we can first explicitly calculate interfacial QACF  $c_2(t)$  using EMD simulation methods, and then derive the other correlation functions, based on the following equations:  $c_1(t) = \frac{dc_0(t)}{dt}$  and  $c_2(t) = -\frac{dc_1(t)}{dt} = -\frac{d^2 c_0(t)}{dt^2}$ .

A convenient mathematical tool to solve a gLE is the Laplace transformation (LT). Accordingly, we express the LT functions of  $c_0(t)$  or  $c_1(t)$  in terms of the LT function of interfacial QACF,  $\phi(s)$

$$\phi(s) \equiv \int_0^\infty dt e^{-st} c_2(t) \quad (14)$$

$$C_1(s) \equiv \int_0^\infty dt e^{-st} c_1(t) = -\frac{\phi(s)}{s} \quad (15)$$

$$C_0(s) \equiv \int_0^\infty dt e^{-st} c_0(t) = -\frac{\phi(s) - s C_V k_B T^2}{s^2} \quad (16)$$

Furthermore, the LT function  $\phi(s)$  can also be expressed in terms of moments of the QACF function ( $\mu_n$ )

$$\phi(s) = \sum_{n=0}^{\infty} \frac{(-1)^n \mu_n}{n!} s^n \quad (17)$$

where the  $n$ th moment  $\mu_n$  is defined as

$$\mu_n \equiv \int_0^\infty dt [t^n \langle q(t)q(0) \rangle] = (-1)^n \phi^{(n)}(0) \quad (18)$$

Next, we multiply the  $\Delta E(0) = E(0) - E_{\text{eq}}$  term to both sides of Equation (9) and take an ensemble average to get

$$c_1(t) = - \int_{-\infty}^t dt' \gamma(t-t') c_0(t') = - \int_0^\infty dt' \gamma(t') c_0(t-t') \quad (19)$$

Finally, we apply LT to both sides of Equation (19) to derive an expression for the LT of the dissipation kernel function  $\Gamma(s)$  in terms of  $C_0(s)$  or  $\phi(s)$

$$\Gamma(s) \equiv \int_0^\infty dt e^{-st} \gamma(t) = -\frac{C_1(s)}{C_0(s)} = \frac{s\phi(s)}{s C_V k_B T^2 - \phi(s)} \quad (20)$$

Although finding the solution of  $\gamma(t)$  using inverse LT of  $\Gamma(s)$  can be numerically difficult, except for a few known forms of  $\Gamma(s)$  functions, we note that the calculation of TIC using Equation (10) requires only a time integration of  $\gamma(t)$  that is equivalent to the value of  $\Gamma(s=0)$ . Therefore, we can directly express TIC in terms of the integration of interfacial QACF without an explicit solution of  $\gamma(t)$

$$G_k = \frac{C_V \Gamma(0)}{A} = \frac{k_B T^2}{A} \frac{C_V^2}{C_0(s=0)} = \frac{1}{A k_B T^2} \lim_{s \rightarrow 0} \frac{\phi(s)}{1 - \phi(s)/(s C_V k_B T^2)} = \frac{1}{A k_B T^2} \lim_{s \rightarrow 0} \left[ \int_0^\infty dt e^{-st} \langle q(t)q(0) \rangle \right] \times \left[ 1 - \frac{\int_0^\infty dt e^{-st} \langle q(t)q(0) \rangle}{s C_V k_B T^2} \right]^{-1} \quad (21)$$

It is important to emphasize that Equation (21) unequivocally demonstrates that the TIC of a non-Markov interface can be uniquely derived with the EMD simulation results of interfacial QACF  $\langle q(t)q(0) \rangle$ , assuming that the slow fluctuation approximation is valid. We now refer to Equation (21) as the general TIC formula for all types of materials interfaces. Next, we will simplify this general TIC formula at two conditions, i.e., 1) the bulk limit, where  $\frac{G_k A}{C_V} \rightarrow 0$ , and 2) beyond the bulk limit, where  $\frac{G_k A}{C_V}$  is a positive constant value.

### 2.3.1. Bulk Limit

We will first discuss the TIC of an interface at the bulk limit. For the macroscopic systems considered in our derivation, the bulk limit corresponds to the case of a system having a surface-to-volume ratio  $\rightarrow 0$ . For the systems considered by CEHVC,<sup>[14]</sup> this bulk limit corresponds to two semi-infinite objects, I and II, adjoined at an interface with a finite area. By taking the  $C_V \rightarrow \infty$  limit before taking the  $s \rightarrow 0$  limit in Equation (21), we can derive an approximate TIC formula at the bulk limit that is identical to the Green-Kubo-type TIC formula in Equation (3). Using Equation (20), we can also show that the dissipation kernel function at the bulk limit is simply proportional to the interfacial QACF

$$\gamma_{\text{bulk}}(t) = \frac{1}{C_V k_B T^2} \langle q(t)q(0) \rangle \quad (22)$$

There are direct implications on the properties of zeroth- and first-order moments of the interfacial QACF at the condition of  $\frac{G_k A}{C_V} \rightarrow 0$

$$\mu_0 = \int_0^\infty dt \langle q(t)q(0) \rangle_{\text{bulk}} = G_k A k_B T^2 > 0 \quad (23)$$

and

$$\mu_1 = \int_0^\infty dt [t \langle q(t)q(0) \rangle] \rightarrow \infty \quad (24)$$

The results of Equation (23) and (24) suggest that as  $\frac{G_k A}{C_V} \rightarrow 0$ , the  $\langle q(t)q(0) \rangle$  function asymptotically approaches to  $\frac{1}{t^{1+\delta}}$  with  $0 < \delta \leq 1$  as  $t \rightarrow \infty$ .

We caution that the adoption of the approximate TIC formula at the bulk limit (Equation (3)) in an EMD-based study should be justified whether the  $\frac{G_k A}{C_V} \approx 0$  assumption is valid. From a pragmatic viewpoint, we need to calculate a running integral of QACF over a period of  $\tau$ :  $I(\tau) = \int_0^\tau dt \langle q(t)q(0) \rangle$ . The bulk limit can be justified if the  $I(\tau)$  function shows a clearly defined “plateau” for large values of  $\tau$ .

### 2.3.2. Beyond the Bulk Limit

Most materials of our consideration have small, yet finite the surface-to-volume ratios. As a result,  $\frac{G_k A}{C_V}$  in our derivation is a small positive number. This  $\frac{G_k A}{C_V}$  ratio can be considerably larger in nano-materials because of their larger surface-to-volume ratios. The Green–Kubo type of TIC formula does not apply beyond the bulk limit. Instead, we can combine Equation (17) and (21) to prove that at the condition of  $\frac{G_k A}{C_V} \neq 0$ , the first three moments of  $\langle q(t)q(0) \rangle$  function can be expressed as follows

$$\phi(0) = \mu_0 = \int_0^\infty dt \langle q(t)q(0) \rangle = 0 \quad (25)$$

$$\phi'(0) = -\mu_1 = - \int_0^\infty dt [t \langle q(t)q(0) \rangle] = C_V k_B T^2 > 0 \quad (26)$$

$$\phi''(0) = \mu_2 = \int_0^\infty dt [t^2 \langle q(t)q(0) \rangle] = - \frac{2C_V k_B T^2}{G_k A / C_V} < 0 \quad (27)$$

With Equation (25)–(27), we can further simplify the general TIC formula (Equation (21)) as

$$\begin{aligned} G_k &= \frac{1}{A k_B T^2} \frac{-2\phi'(0)^2}{\phi''(0)} = \frac{1}{A k_B T^2} \frac{-2\mu_1^2}{\mu_2} \\ &= \frac{1}{A k_B T^2} \frac{-2 \left\{ \int_0^\infty dt [t \langle q(t)q(0) \rangle] \right\}^2}{\int_0^\infty dt [t^2 \langle q(t)q(0) \rangle]}. \end{aligned} \quad (28)$$

Now, we refer Equation (28) as the TIC formula beyond the bulk limit, because the heat capacity  $C_V$  is a thermal equilibrium quantity that can be calculated independently. Consequently, Equation (25) and (26) can also be adopted as two “sum rules” of  $\langle q(t)q(0) \rangle$  to identify and/or correct numeric artifacts in EMD simulation results.

## 3. Non-Markov Interfaces

Results of MD simulation are known to contain artifacts due to finite-size of a simulation model, the finite number of ensemble averages, and/or the finite-period of simulation time. Effects of these simulation artifacts to the calculated transport coefficients

are likely more significant than those observed in the EMD calculations of bulk  $\kappa$ . The size of possible artifacts remains largely unknown. Very few empirical models have been proposed to identify and/or correct such artifacts. Here, we study two representative types of non-Markov interfaces, whose interfacial QACF is similar to the QACF reported in some early EMD studies of real material interfaces. We focus on identifying their distinct non-Markov characters and the asymptotic behaviors of  $\langle q(t)q(0) \rangle$  for large  $t$ . These results of simple model interfaces should serve as baseline models for studies of non-Markov interfaces in real materials.

### 3.1. Quasi-Markov Interfaces

The Markov model is an over-simplification for interfacial thermal conduction in real materials. However, some previous reports of EMD calculated interfacial QACF of solid–liquid<sup>[12]</sup> and solid–gas<sup>[13]</sup> interfaces seem to be close to those of Markov interfaces. Here, we first derive the interfacial QACF and other related tcf of energy and current at this Markov limit to gain insights into the properties of some quasi-Markov processes. Then, we study the TIC of a simple model interface, whose  $\langle q(t)q(0) \rangle$  is close to that of a Markov interface.

#### 3.1.1. Markov Interfaces

At the Markov limit of  $\gamma(t) = 2\gamma_0\delta(t)$ , or  $\Gamma(s) = \gamma_0$ , the slow-fluctuation assumption is valid, and Equation (9) can be simplified as

$$\langle q(t) \rangle = - \int_{-\infty}^t dt' C_V 2\gamma_0 \delta(t-t') \Delta T(t') = -C_V \gamma_0 \Delta T(t) \quad (29)$$

By equalizing this ensemble average of microscopic  $q(t)$  and the net interfacial heat current  $q_{\text{int}}$  in the macroscopic heat transfer equation of Equation (2), we infer that  $\gamma_0 = \frac{G_k A}{C_V}$ , or this kernel function of dissipation currents at the Markov limit is:  $\gamma(t) = \frac{2G_k A}{C_V} \delta(t)$ , or  $\Gamma(s) = \frac{G_k A}{C_V}$ . Using Equation (20), we can show that

$$\phi(s) = \frac{G_k A k_B T^2 s}{s + G_k A / C_V} \quad (30)$$

and

$$c_0(t) = G_k A k_B T^2 e^{-G_k A t / C_V} \quad (31)$$

$$c_1(t) = -G_k A k_B T^2 e^{-G_k A t / C_V} \quad (32)$$

$$c_2(t) = 2G_k A k_B T^2 \delta(t) - \frac{G_k^2 A^2 k_B T^2}{C_V} e^{-G_k A t / C_V} \quad (33)$$

Accordingly, the running integral of the tcf over a period of  $\tau$  is found to be

$$I(\tau) \equiv \int_0^\tau dt \langle q(t)q(0) \rangle = G_k A k_B T^2 e^{-\frac{G_k A}{C_V} \tau} \quad (34)$$

Our Equation (34) proves that the correction model proposed by LEK is exact at the Markov limit.



### 3.1.2. Quasi-Markov Interfaces

In comparison with the interfacial QACF  $\langle q(t)q(0) \rangle$  of a Markov interface (Equation (33)), we consider an interface as a quasi-Markov interface if its  $\langle q(t)q(0) \rangle$  has the following patterns: starting with a very large, yet finite value, and decaying rapidly to a very small value in a short period of time. We also assume that quasi-Markov interfaces have finite values of the  $\frac{G_k A}{C_V}$  ratio, and its TIC can be expressed with Equation (28). Here, we focus on a simple model interface of the quasi-Markov type, whose QACF is formulated as

$$\langle q(t)q(0) \rangle = \frac{2}{\sqrt{2\pi}\sigma} e^{-\frac{t^2}{2\sigma^2}} - \frac{1 + \omega^2\tau^2}{\tau} e^{-t/\tau} \cos(\omega t) \quad (35)$$

Here  $\sigma$ ,  $\tau$ ,  $\omega$  are three positive parameters of this type of quasi-Markov interfaces, whose LT functions can be derived analytically as

$$\phi(s) = e^{\frac{\sigma^2 s^2}{2}} \operatorname{erfc}\left(\frac{\sigma s}{\sqrt{2}}\right) - (1 + \omega^2\tau^2) \frac{\tau s + 1}{(\tau s + 1)^2 + \omega^2\tau^2} \quad (36)$$

with  $\operatorname{erfc}(x)$  being the complementary error function.

From Equation (36), we can derive that  $\phi'(0) = -\mu_1 = -\int_0^\infty dt [t \langle q(t)q(0) \rangle] = \tau \frac{1 - \omega^2\tau^2}{1 + \omega^2\tau^2} - \frac{2\sigma}{\sqrt{2\pi}}$ ,  $\phi''(0) = \mu_2 = \int_0^\infty dt [t^2 \langle q(t)q(0) \rangle] = -2\tau^2 \frac{1 - 3\omega^2\tau^2}{(1 + \omega^2\tau^2)^2} + \sigma^2$ , and the effective TIC

of this quasi-Markov interface can be solved analytically as

$$\begin{aligned} \widetilde{G}_k &= G_k A k_B T^2 = \frac{-2\mu_1^2}{\mu_2} \\ &= 2 \left[ \tau \frac{1 - \omega^2\tau^2}{1 + \omega^2\tau^2} - \frac{2\sigma}{\sqrt{2\pi}} \right]^2 / \left[ 2\tau^2 \frac{1 - 3\omega^2\tau^2}{(1 + \omega^2\tau^2)^2} - \sigma^2 \right] \end{aligned} \quad (37)$$

We can confirm that at the limit of  $\sigma \rightarrow 0$  and  $\omega \rightarrow 0$ , the properties of this non-Markov interface approach to those of a Markov interface, with  $\widetilde{G}_k = 1$ .

Figure 1 shows the results of an interface of this class with  $\sigma = 1$ ,  $\tau = 10$ , and  $\omega = 0.05$ . The similarity between the calculated  $\langle q(t)q(0) \rangle$  (Figure 1a) and that at the Markov limit (Equation (33)) verifies that the quasi-Markov approximation is valid for this non-Markov interface. The calculated LT function  $\phi(s)$  of this quasi-Markov interface, shown in Figure 1b, is also close to that of a Markov interface (Equation (30)). The  $\phi(s)$  function agrees well with the  $\phi(s) \approx \phi'(0)s + 1/2\phi''(0)s^2$  model at the limit of  $s \rightarrow 0$ , with  $\mu_1 = -\phi'(0) = -5.20$  and  $\mu_2 = \phi''(0) = 31.0$ . Using Equation (37), we find the effective TIC of the quasi-Markov interface shown in Figure 1 is about 1.746.

As discussed in a paragraph described earlier, a correction model was proposed by LEK<sup>[13]</sup> (Equation (4)) to fit the running integral function of  $\langle q(t)q(0) \rangle$  of EMD simulated data based on a formula derived at the Markov limit. As shown in Figure 1c,

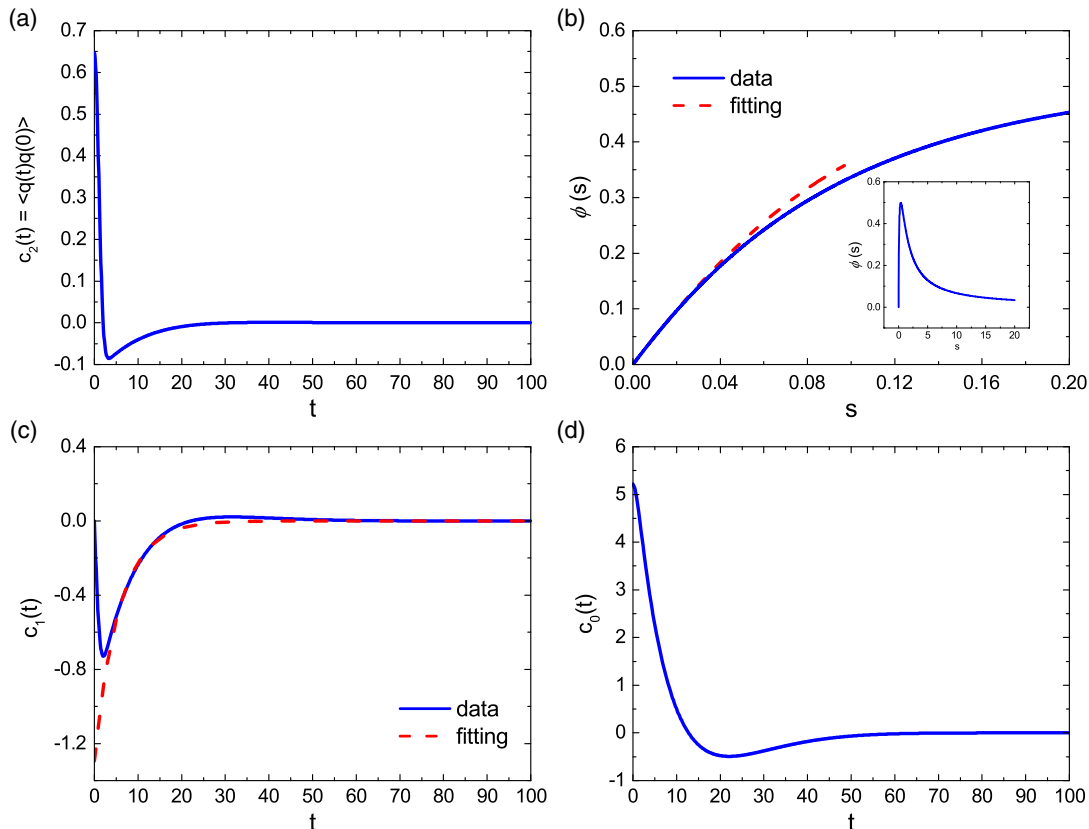


**Figure 1.** A quasi-Markov interface described by Equation (35), with  $\sigma = 1$ ,  $\tau = 10$ , and  $\omega = 0.05$ . a) The current auto-correlation function QACF:  $c_2(t) = \langle q(t)q(0) \rangle$ , b) the LT function of QACF:  $\phi(s)$ , c) the cross-correlation function between the fluctuating current and the fluctuating energy:  $c_1(t)$ , and d) the energy auto-correlation function:  $c_0(t)$ .

the LEK model (shown with the red dashed line and labeled as fitting) seems to fit well of the  $c_1(t)$  function, which is the negative of the running integral function, for intermediate values of  $t$ , while  $c_1(t)$  deviates from the LEK model at the  $t \rightarrow 0$  limit to manifest the non-Markov properties of this interface. We fit the data between  $t = 5$  and  $t = 15$  and estimated  $\tilde{G}_k = 1.3$ , which is about 20% less than the  $\tilde{G}_k$  value we derived analytically (Equation (37)). This comparison also suggests that if the interfacial QACF of some quasi-Markov-type interfaces can be better fitted with the  $\langle q(t)q(0) \rangle$  formula in Equation (35), we can have a more accurate evaluation of their TIC using the formula in Equation (37) than using the LEK correction model (Equation (4)).

### 3.2. Interfaces with an Exponential Kernel Function

Here, we study a non-Markov-type model interface, whose dissipation kernel function is simply an exponential function. Based on Equation (10), we can express the kernel function  $\gamma(t)$  and its LT function  $\Gamma(s)$  as

$$\gamma(t) = \frac{2G_k A}{C_V \tau} e^{-\frac{2t}{\tau}} \quad (38)$$

$$\Gamma(s) = \frac{2G_k A}{C_V \tau} \frac{1}{s + 2/\tau} \quad (39)$$

Again, we focus on the interfaces with finite  $\frac{G_k A}{C_V}$  ratios and adopt Equation (28) to model their TIC beyond the bulk limit.

With Equation (39), we first derive  $\phi(s)$  of the interfaces of this class as

$$\phi(s) = \frac{2G_k A k_B T^2}{\tau} \frac{s}{(s + 1/\tau)^2 + [\frac{2G_k A}{C_V \tau} - \frac{1}{\tau^2}]} \quad (40)$$

and then perform an inverse LT to  $\phi(s)$  to solve for  $\langle q(t)q(0) \rangle$ . The derived interfacial QACF  $\langle q(t)q(0) \rangle$  function has three possible forms, depending on the value of  $\frac{2G_k A \tau}{C_V}$ .

At the condition of  $\frac{2G_k A \tau}{C_V} > 1$ , we have  $\omega = \frac{1}{\tau} [\frac{2G_k A \tau}{C_V} - 1]^{1/2}$ , and the interfacial QACF can be derived as

$$\langle q(t)q(0) \rangle = 2G_k A k_B T^2 \tau^{-1} e^{-\frac{|t|}{\tau}} [\cos(\omega t) - \frac{1}{\omega \tau} \sin(\omega |t|)] \quad (41)$$

At the condition of  $\frac{2G_k A \tau}{C_V} = 1$ , the interfacial QACF can be derived as

$$\langle q(t)q(0) \rangle = 2G_k A k_B T^2 \tau^{-1} e^{-\frac{|t|}{\tau}} \left( 1 - \frac{|t|}{\tau} \right) \quad (42)$$

At the condition of  $\frac{2G_k A \tau}{C_V} < 1$ , we have  $\beta = \frac{1}{\tau} [1 - \frac{2G_k A \tau}{C_V}]^{1/2}$ , and the interfacial QACF is

$$\langle q(t)q(0) \rangle = 2G_k A k_B T^2 \tau^{-1} \left[ \frac{\tau^{-1} + \beta}{2\beta} e^{-(\tau^{-1} + \beta)|t|} - \frac{\tau^{-1} - \beta}{2\beta} e^{-(\tau^{-1} - \beta)|t|} \right] \quad (43)$$

**Figure 2** plots the normalized  $\langle q(t)q(0) \rangle$ , i.e.,  $\langle q(t)q(0) \rangle / \langle q^2 \rangle$ , as a function of  $t$  for the three conditions defined in our newly derived TIC equations (Equation (41)–(43)). The running integral

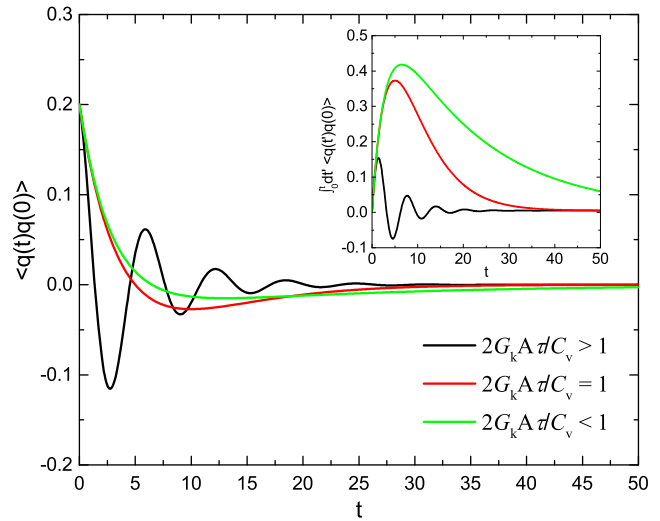


**Figure 2.** The normalized interfacial QACF function of three different  $\frac{2G_k A \tau}{C_V}$  ratios. The corresponding running integral functions of the normalized  $\langle q(t)q(0) \rangle$  are also plotted in inset.

functions of these three cases are also shown in the inset. Although the results shown here are for the ideal case that corresponds to an exact exponential dissipation kernel function, the interfacial QACF models expressed in our newly derived TIC equations can be adopted to fit EMD calculated  $\langle q(t)q(0) \rangle$  function of real material interfaces, if their dissipation functions are exponential-function-like. We note that for all three types of  $\langle q(t)q(0) \rangle$  functions, the TIC can be simply expressed in terms of two parameters, the variance of the fluctuation  $q(t)$ ,  $\langle q^2 \rangle$ , and the decay constant  $\tau$

$$G_k = \frac{\langle q^2 \rangle \tau}{2A k_B T^2} \quad (44)$$

This result suggests that for a quasi-exponential-type interfaces, we can fit the EMD calculated  $\langle q(t)q(0) \rangle$  with models expressed in Equation (41)–(43) to evaluate  $\langle q^2 \rangle$  and  $\tau$ , and estimate its TIC based on Equation (44).

## 4. Conclusion

We have extended previous work of PBC<sup>[11]</sup> and BC<sup>[12]</sup> to derive a general statistical formula for TIC beyond the Markov limit. Our general formula reduces to the previously proposed Green–Kubo-type formula at the bulk limit. Beyond the bulk limit, we have shown that the TIC of a material with finite heat capacity can be calculated based on the first- and second-order moments of the auto-correlation function of the interfacial current. We have adopted our statistical theory to study two classes of simple model interfaces: the quasi-Markov interfaces and the interfaces with exponential dissipation kernel functions, whose TIC can be derived analytically. Our analysis results provide the theoretical foundation to calculate TIC using EMD simulation methods for a wide range of material interfaces, including the interfaces at the nanoscale.

## Acknowledgements

J.D. would like to dedicate this paper to his friend and former mentor, the late Prof. Otto F. Sankey of Arizona State University, who pioneered molecular dynamics calculations of thermal conductivity of real and complex materials more than two decades ago. A major part of the theoretical study reported in this article was conducted during J.D.'s sabbatical in 2019. J.D. would like to thank Auburn University for the financial support, and his hosts for their hospitality: Prof. J. Zhao and Prof. T. Wang (Tianjin University), Dr. S. Wei and Dr. H. Lin (BCSRC), Dr. M.-Y. Chou (IAMS, Academia Sinica), Prof. F. Dong and Prof. X. Zhou (Nankai University), and Dr. Y. Ding and Dr. H.-K. Mao (HPSTAR).

## Conflict of Interest

The authors declare no conflict of interest.

## Keywords

Green–Kubo formulas, Langevin equations, molecular dynamics simulations, thermal conduction, thermal interfacial conductance, time-correlation functions

Received: August 20, 2020

Revised: October 2, 2020

Published online: October 27, 2020

- [1] A. Einstein, *Annalen der Physik* **1905**, 323, 639.
- [2] P. Langevin, *Compt. Rendus* **1908**, 146, 530.
- [3] R. Kubo, M. Toda, N. Hashitsume, *Statistical Physics II: Nonequilibrium Statistical Mechanics*, Springer-Verlag, Berlin Heidelberg **1992**.
- [4] R. Zwanzig, *Nonequilibrium Statistical Mechanics*, Oxford University Press, Oxford **2001**.
- [5] R. Zwanzig, *Annu. Rev. Phys. Chem.* **1965**, 16, 67.
- [6] J. Li, L. Porter, S. Yip, *J. Nucl. Mater.* **1998**, 255, 39.
- [7] S. G. Volz, G. Chen, *Phys. Rev. B* **2000**, 61, 2651.
- [8] J. Che, T. Çağın, W. Deng, W. A. Goddard III, *J. Chem. Phys.* **2000**, 113, 6888.
- [9] J. Dong, O. F. Sankey, C. W. Myles, *Phys. Rev. Lett.* **2001**, 86, 2361.
- [10] P. K. Schelling, S. R. Phillpot, P. Keblinski, *Phys. Rev. B* **2002**, 65, 144306.
- [11] L. Puech, G. Bonfait, B. Castaing, *J. Low Temp. Phys.* **1986**, 62, 315.
- [12] J.-L. Barrat, F. Chiaruttini, *Mol. Phys.* **2003**, 101, 1605.
- [13] Z. Liang, W. Evans, P. Keblinski, *Phys. Rev. E* **2013**, 87, 022119.
- [14] Y. Chalopin, K. Esfarjani, A. Henry, S. Volz, G. Chen, *Phys. Rev. B* **2012**, 85, 195302.
- [15] H. Mori, *J. Phys. Soc. Jpn.* **1956**, 11, 1029.



# Mean Free Path of Photoelectronic Excitations in Hydrogenated Amorphous Silicon and Silicon Germanium Alloy Semiconductors

Nikolas J. Podraza,\* David B. Saint John, Maxwell M. Junda, and Robert W. Collins

Dedicated to Professor David A. Drabold on the occasion of his 60th birthday

Hydrogenated amorphous silicon germanium alloy ( $a\text{-Si}_{1-x}\text{Ge}_x\text{H}$ ) films are prepared by plasma enhanced chemical vapor deposition (PECVD) and characterized by in situ real time spectroscopic ellipsometry (RTSE). From complex dielectric function spectra extracted, the broadening width energy ( $\Gamma$ ) of the primary absorption feature centered near 3.7 eV is quantified using the Cody–Lorentz oscillator model. Mean free path length of photoelectronic excitations is calculated from  $\Gamma$  based on reasonable estimates for speed of electron–hole photoexcitations. A model is applied with excited state lifetime assumed to be limited by scattering from network disorder and provides a relative measure of short-range order. The simple model applied is an extension of that widely used to characterize broadening of optical transitions in polycrystalline semiconductors. Decreases in mean free path of up to  $\sim 30\%$  occur with germanium. Relative increases in mean free path with increased hydrogen during PECVD  $a\text{-Si:H}$ ,  $a\text{-Si}_{0.73}\text{Ge}_{0.27}\text{H}$ , and  $a\text{-Si}_{0.60}\text{Ge}_{0.40}\text{H}$  occur from  $\sim 5\%$  to  $\sim 8\%$  and with hydrogen plasma treatment of  $a\text{-Si:H}$  by  $\sim 6\%$ . Mean free path changes are tracked with thickness to provide short range order evolution and the effect of the underlying material. Mean free path of photoexcitations in electronic quality  $a\text{-Si}_{1-x}\text{Ge}_x\text{H}$  is estimated at  $\sim 3.5 \text{ \AA}$ , on the same order as interatomic spacing.

semiconductors of interest for thin film optoelectronic technologies often exhibit substantially different optical and electronic properties compared with their bulk crystalline counterparts. Optical features above the bandgap for bulk crystalline semiconductors occur at the critical points in the joint density of states and are understood to be lifetime broadened by the electron–phonon interaction.<sup>[1]</sup> In the case of nano-, micro-, and polycrystalline materials, the corresponding features are broadened relative to the bulk crystal, and this broadening can be understood to occur homogeneously through reductions in the lifetimes of the excited states and, thus, in the mean free path lengths of the photoexcited electrons and holes.<sup>[2–7]</sup> For such materials, a model proposing that the mean free path of photoexcitations is limited predominately by the grain size due to scattering at grain boundaries or grain surfaces consistently accounts for experimental observations. For amorphous materials, the lack of long-range crystalline

## 1. Introduction

Most materials of technological relevance are neither single crystals nor epitaxial films but rather exhibit some form of polycrystalline structure with finite crystallite size or lack long-range order altogether and are considered as amorphous. In particular, nano-, micro-, and polycrystalline and amorphous


order in the amorphous network itself is similarly expected to lead to scattering of photoexcited electrons and holes. As a result, further reduction in mean free paths of these photoexcitations is expected to occur as a natural extension of the behavior observed for nano-, micro-, and polycrystalline materials.<sup>[8–10]</sup> However, all amorphous samples of a given composition do not have identical properties, indicating that variations in the short- and

Prof. N. J. Podraza, Dr. M. M. Junda, Prof. R. W. Collins  
Department of Physics and Astronomy  
The University of Toledo  
Toledo, OH 43606, USA  
E-mail: Nikolas.Podraza@utoledo.edu

Prof. N. J. Podraza, Dr. M. M. Junda, Prof. R. W. Collins  
Wright Center for Photovoltaics Innovation and Commercialization  
The University of Toledo  
Toledo, OH 43606, USA

Dr. D. B. Saint John  
Mathematical Manufacturing  
LLC  
Detroit, MI 48206, USA

Dr. M. M. Junda  
Covalent Metrology Services, Inc.  
Sunnyvale, CA 94085, USA

 The ORCID identification number(s) for the author(s) of this article can be found under <https://doi.org/10.1002/pssb.202000473>.

DOI: 10.1002/pssb.202000473

medium-range order of the amorphous network substantively impact measured macroscopic properties.

Hydrogenated amorphous silicon (a-Si:H) and related thin films have been implemented in device applications, including absorbers in thin film solar cells,<sup>[11–21]</sup> passivation layers in wafer silicon photovoltaics,<sup>[22–28]</sup> and imaging layers in uncooled infrared (IR) sensing microbolometers.<sup>[29–37]</sup> The a-Si:H network varies in terms of incorporated hydrogen content and bonding configuration,<sup>[23,26,38–41]</sup> the presence of nanoscale voids and vacancy structures,<sup>[38,39]</sup> and film stress<sup>[42]</sup> as deduced from experimental measurements. The formation of short and long filamentary structures, bond length distributions, and bond angle distributions has been identified through advanced computational modeling.<sup>[43,44]</sup> The amorphous network may be further modified by alloying a-Si:H with other group-IV elements, usually carbon or germanium. For applications as thin film solar cell absorbers, carbon and germanium are added to widen and narrow the bandgap, respectively, compared with that of a-Si:H for optimization of single and multijunction solar cells.<sup>[12,13,15,17–20]</sup> Incorporation of either carbon or germanium into a-Si:H also alters the film resistivity, temperature coefficient of resistance, and  $1/f$  noise, which impact microbolometer performance.<sup>[30–32,34–37]</sup>

For plasma-enhanced chemical vapor deposited (PECVD) a-Si:H-based materials developed for such device applications, spectra in the complex optical response in the form of the complex dielectric function ( $\epsilon = \epsilon_1 + i\epsilon_2$ ) obtained by in situ real time spectroscopic ellipsometry (RTSE) have been reported to vary as functions of deposition and processing conditions,<sup>[11,14,16,17,21,23–26,32–34,41,45–51]</sup> alloying with carbon or germanium,<sup>[45–50]</sup> post-deposition plasma or annealing treatments,<sup>[28,49]</sup> accumulated film thickness,<sup>[21,51]</sup> and underlying substrate material.<sup>[14,51]</sup> A reduction in the width of the primary absorption feature evident in  $\epsilon_2$  centered at photon energies near  $\approx 3.5$ – $3.9$  eV is often attributed to increased relative order in the material and has been directly linked to improved performance of thin film solar cells with a-Si:H-based absorber layers.<sup>[11,14,16,17]</sup> By modeling the  $\epsilon$  spectra for the a-Si:H-based films, a link has been proposed between changes in the mean free path length of photoexcited electron–hole pairs in the amorphous network and measurable macroscopic properties. This approach is based on a model of homogeneous broadening of the primary absorption feature as an extension of the previous studies of polycrystalline and nanocrystalline materials.<sup>[2–7]</sup>

Additional broadening mechanisms due to local statistical fluctuations in bond length, bond angle, and Si–H bonding are inhomogeneous in nature and introduce complications in interpretation of the optical spectra. In fact, inhomogeneous broadening mechanisms are expected to exhibit the same trends with short-range order as does the homogeneous lifetime mechanism, and, thus, would be difficult to resolve. The introduction of inhomogeneous broadening mechanisms is not necessary for interpretation of the  $\epsilon$  spectra, however, which are closely fit with a single Lorentzian line shape modified at photon energies immediately above the bandgap in the region of the mobility gap. In contrast, optical transitions near the bandgap may be dominated by inhomogeneous broadening, because the photoexcited electron–hole pairs here are no longer mobile. In spite of this, both the optical absorption spectra, ranging from the Urbach tail to the mobility gap, as well as the

photoluminescence spectra, are adequately modeled in terms of the joint densities of one-electron states at the valence and conduction band edges, without appealing to any broadening mechanisms beyond those represented by the relatively narrow ( $<0.06$  eV) valence and conduction band tails.<sup>[52–58]</sup> The potential complications introduced in these one-electron models involve not additional inhomogeneous site-dependent broadening as described, but rather the proper choice of the energy dependence of the band densities of states and the matrix element for the case of optical absorption,<sup>[59,60]</sup> and the possible presence of electron–phonon coupling that generates an additional phonon broadening mechanism and a Stokes shift for the case of photoluminescence.<sup>[52,61]</sup>

By applying physically realistic parametric models describing the spectra in  $\epsilon$  measured by RTSE in the present study, the broadening width energy of the primary absorption feature is quantified. This broadening width is assumed to be inversely proportional to the lifetime of the photoexcitation, assigned to be that of the photoexcited electron–hole pair. This assignment is based on the understanding that  $\epsilon$  spectra, in general, can only be modeled quantitatively on an ab initio basis by considering the interaction between the photoexcited electron and hole. From this broadening width energy, the mean free path of the photoexcitations can be calculated, applying reasonable estimates of the speed that characterizes the motion of photoexcited electron–hole pairs.<sup>[2,4]</sup> The mean free path is shown to decrease with increasing germanium content in hydrogenated amorphous silicon germanium (a-Si<sub>1–x</sub>Ge<sub>x</sub>:H) films as expected due to additional disorder from alloying. In series of fixed alloy composition, the mean free path increases with the amount of hydrogen dilution of the reactive silicon and germanium carrying source gases in PECVD. This increased mean free path correlates well with the observed improvement in thin film a-Si:H-based solar cell performance with similar process parameter variations. In addition, narrowing of the absorption feature width upon treatment by a hydrogen plasma also shows an increase in the mean free path length due to modification of the underlying a-Si:H material. The temperature dependence of the mean free path has been modeled, accounting for the increased broadening in the absorption feature with temperature and the empirically observed relationship between the effective mass and the bandgap applied from studies of crystalline silicon. With accumulated thickness in a-Si:H, the mean free path either increases or slightly decreases dependent upon the underlying substrate material and its interactions with the growing a-Si:H film. Combining this information, the mean free path length of the photoexcited electron–hole pairs in relatively highly ordered a-Si:H, a-Si<sub>0.73</sub>Ge<sub>0.27</sub>:H, and a-Si<sub>0.60</sub>Ge<sub>0.40</sub>:H at room temperature is estimated to be  $\approx 3.5$  Å, of the same order as the interatomic spacing, as is expected for amorphous materials.<sup>[5,8–10]</sup>

## 2. Experimental Methods and Modeling

### 2.1. Film Preparation

All a-Si<sub>1–x</sub>Ge<sub>x</sub>:H films studied here have been prepared by PECVD and characterized by in situ RTSE. RTSE provides information on the growth evolution and spectra in  $\epsilon$ . Variations in the spectra in  $\epsilon$  are tracked among experiments comparing different

compositions,<sup>[34,47]</sup> relative degrees of order,<sup>[46–48]</sup> and temperature.<sup>[47]</sup> RTSE measurements have been performed using either a single<sup>[62,63]</sup> or dual<sup>[64]</sup> rotating compensator multichannel ellipsometer having a spectral range from 1.5 to 5.0 eV with 128 spectral points or from 0.75 to 5.9 eV with 695 spectral points, respectively. PECVD conditions common to all films include radio frequency (RF;  $f = 13.56$  MHz) plasma excitation, a deposition temperature of 475 K, a fixed 1.9 cm electrode spacing, a total pressure of <0.5 Torr, and the minimum power possible for a stable plasma of 0.08<sup>[34,46–48]</sup> or 0.02 W cm<sup>−2</sup><sup>[51]</sup> depending on the deposition chamber. Variable deposition parameters include the hydrogen (H<sub>2</sub>) to reactive silane (SiH<sub>4</sub>) + germane (GeH<sub>4</sub>) gas flow ratio,  $R = [\text{H}_2]/[\text{SiH}_4] + [\text{GeH}_4]$ , and the alloying gas flow ratio,  $G = [\text{GeH}_4]/[\text{SiH}_4] + [\text{GeH}_4]$ . Unless otherwise noted, samples have been prepared on native oxide-coated crystalline silicon (c-Si) wafers.

The effects of germanium content, hydrogen dilution and plasma treatment, temperature, accumulated film thickness, and substrate on  $\epsilon$  and the derived mean free path length of photoexcited electron-hole pairs are evaluated through several film series and experiments. Two series of films have been prepared at fixed  $R = 10$  as functions of  $G$ , one deposited on the powered cathode (approximately −20 V self-bias)<sup>[47]</sup> from  $G = 0$  to 0.167 and the other on the grounded anode<sup>[34]</sup> from  $G = 0$  to 1. Three series have been deposited on the powered cathode at variable  $R$  but  $G$  fixed at 0, 0.083, and 0.167.<sup>[46–48]</sup> A  $R = 0$  a-Si:H film prepared on the anode has been exposed to a H<sub>2</sub> plasma under the same PECVD conditions but without SiH<sub>4</sub> or GeH<sub>4</sub> source gases. This film is also tracked with plasma exposure time.<sup>[49]</sup> The measurement temperature dependence of spectra in  $\epsilon$  for  $R = 10$  amorphous films prepared at  $G = 0$ , 0.083, and 0.167 has also been tracked from the deposition temperature near 475 K during cooling to near 325 K with  $\epsilon$  extrapolated to a room temperature of 300 K.<sup>[47]</sup> Additional  $R = 0.5$  a-Si:H thin film depositions have been performed under identical conditions on native oxide covered c-Si, p-type hydrogenated amorphous silicon carbon (a-Si<sub>1−x</sub>C<sub>x</sub>:H) in the p-i-n thin-film solar cell structure, and fluorine-doped tin oxide (SnO<sub>2</sub>:F)-coated soda lime glass (Pilkington NSG TEC-15) for comparison of the effect of substrate material.<sup>[51]</sup> Finally,  $R = 5$  and 10 a-Si:H films have also been prepared on TEC-15 for comparison with the  $R = 0.5$  depositions.<sup>[51]</sup>

## 2.2. Optical Property Modeling

Spectra in  $\epsilon$  for most films are obtained from the analysis of RTSE data collected during PECVD growth using a global sum-of- $\sigma$  minimization procedure to determine bulk film thickness and surface roughness thickness.<sup>[34,45–50]</sup> The optical response of the surface roughness layer is represented by a Bruggeman effective medium approximation consisting of 0.5 amorphous film + 0.5 void volume fractions.<sup>[65,66]</sup> Numerical inversion is performed on single sets of ellipsometric spectra to obtain spectra in  $\epsilon$  using the obtained bulk and surface roughness thicknesses.<sup>[67]</sup> Spectra in  $\epsilon$  for plasma-treated a-Si:H are obtained using the same measurement and analysis procedure during plasma etching. Changes in  $\epsilon$  with measurement temperature are also obtained from in situ spectroscopic ellipsometry measurements, assuming fixed final film structural parameters

as the samples cool from the deposition temperature. Typical film thicknesses are ~20–50 nm. More details regarding optical property extraction are available in the previous studies.<sup>[34,46–48]</sup> Example spectra in  $\epsilon$  obtained by numerical inversion for  $R = 10$  a-Si:H and  $R = 10$ ,  $G = 0.167$  a-Si<sub>0.60</sub>Ge<sub>0.40</sub>:H are shown in Figure 1. For the  $R = 0.5$  a-Si:H films prepared on different underlying materials and for the films prepared on TEC-15 as a function of  $R$ , a virtual interface analysis approach<sup>[51]</sup> is used to track changes in  $\epsilon$  with accumulated film thickness using a parametric database.<sup>[68]</sup>

Over a wide spectral range from below to well above the bandgap energy, a parametric model of a single modified Lorentz oscillator fits the measured  $\epsilon$  spectra remarkably well. The modification of the oscillator is designed to model the  $\epsilon$  spectra near the bandgap by suppressing the tail of the Lorentz oscillator extending into the bandgap region and incorporating a joint density of states function based on square root valence and conduction band densities of states as functions of hole and electron energies, respectively. The Tauc–Lorentz oscillator model assumes a constant momentum matrix element for the optical transitions near the bandgap,<sup>[68,69]</sup> and the Cody–Lorentz oscillator model assumes a constant dipole matrix element.<sup>[68]</sup> For a-Si:H, a-Ge:H, and a-Si<sub>1−x</sub>Ge<sub>x</sub>:H alloys, the Cody–Lorentz model has been found to be a more physically realistic representation of the optical response than the Tauc–Lorentz model.<sup>[34,47,68]</sup> For this work, the numerically inverted spectra in  $\epsilon$  are parameterized as functions of photon energy ( $E$ ) with the real and imaginary parts defined as

$$\epsilon_1(E) = \epsilon_\infty + \frac{2}{\pi} P \int_0^\infty \frac{\xi \epsilon_2(\xi)}{\xi^2 - E^2} d\xi$$

$$\epsilon_2(E) = \begin{cases} 0 & 0 < E \leq E_G \\ \frac{(E - E_G)^2}{(E - E_G)^2 + E_p^2} \cdot \frac{AE_0 E}{[(E^2 - E_0^2)^2 + \Gamma^2 E^2]} & E > E_G \end{cases} \quad (1)$$

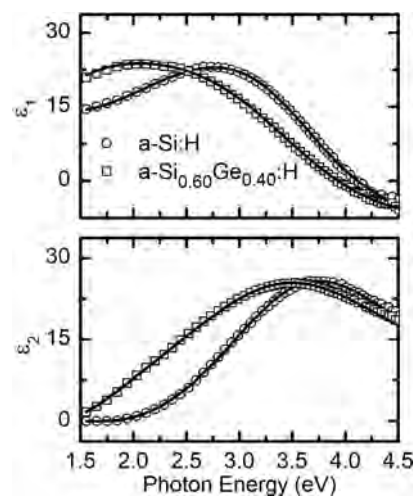


**Figure 1.** Complex dielectric function ( $\epsilon = \epsilon_1 + i\epsilon_2$ ) spectra for hydrogenated amorphous silicon (a-Si:H) and silicon germanium alloy (a-Si<sub>1−x</sub>Ge<sub>x</sub>:H,  $x = 0.40$ ) thin films obtained at a measurement temperature of 475 K from in situ RTSE measurements using numerical inversion (symbols) and parameterized by Cody–Lorentz oscillators (lines).<sup>[47]</sup>



The six energy-independent parameters in these equations include an oscillator amplitude  $A$ , broadening  $\Gamma$ , resonance energy  $E_0$ , bandgap energy  $E_G$ , transition energy from gap-like to Lorentz-like behavior  $E_p$ , and a constant additive term to  $\epsilon_1$  denoted  $\epsilon_\infty$ . The real and imaginary parts of  $\epsilon$  are related through the Kramers–Kronig integral, which can be solved analytically as reported in the study given by Ferlauto et al.<sup>[68]</sup> The Cody–Lorentz oscillator model fits to numerically inverted spectra in  $\epsilon$  are shown in Figure 1.

It should be noted that to fit the numerically inverted spectra in  $\epsilon$  and determine  $\Gamma$  in Figure 2–4, the Cody–Lorentz model of Equation (1) has at most only five free parameters, because  $\epsilon_\infty$  is fixed at 1 in the model. The bulk film and surface roughness layer thicknesses defining the structure of each thin film do not enter into the analysis of the spectra in  $\epsilon$ , as these are obtained from global sum-of- $\sigma$  minimization of RTSE data prior to fitting  $\epsilon$  to the Cody–Lorentz model. For the data sets from Podraza et al.,<sup>[47]</sup> the  $E_0$  values are initially all within the mathematical fitting error for each respective series, so this parameter is fixed at the average value for each series with all other parameters subsequently fit again. For the data set from Saint John,<sup>[34]</sup>  $E_0$  is a variable parameter. For each of these series, the variation in the fit parameter  $\Gamma$  used for the calculation of the mean free path of photoexcitations is greater than the mathematical error from the fitting procedure. The correlation between  $\Gamma$  and its most correlated other fit parameter describing  $\epsilon$  is  $\leq 0.844$  in magnitude, indicating that  $\Gamma$  is not substantially correlated with the other fit parameters.

For the data sets analyzed using virtual interface analysis to track variations in  $\epsilon$  with accumulated thickness, a parametric database linking all parameters of the Cody–Lorentz oscillator

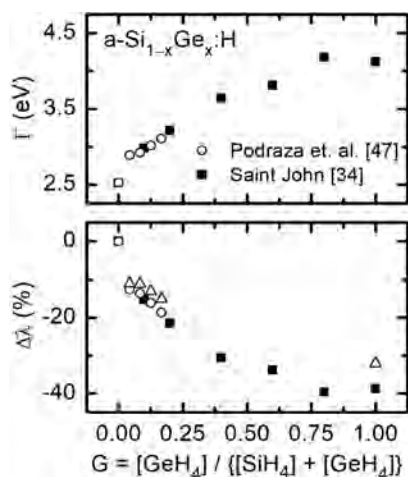


**Figure 2.** (Top) Cody–Lorentz oscillator broadening parameters measured at 475 K for  $a\text{-Si}_{1-x}\text{Ge}_x\text{:H}$  alloy films prepared at fixed hydrogen ( $\text{H}_2$ ) to total silane ( $\text{SiH}_4$ ) + germane ( $\text{GeH}_4$ ) dilution ratio  $R = 10$  as functions of  $\text{GeH}_4$  to total  $\text{SiH}_4 + \text{GeH}_4$  gas flow ratios from data reported in the study by Podraza et al.<sup>[47]</sup> (open circles) and Saint John<sup>[34]</sup> (solid squares). (Bottom) Change in the mean free path of photoexcitations relative to that of pure  $a\text{-Si:H}$ , assuming composition independent (open circles and solid squares) and dependent (open triangles) speeds of electron–hole pairs.

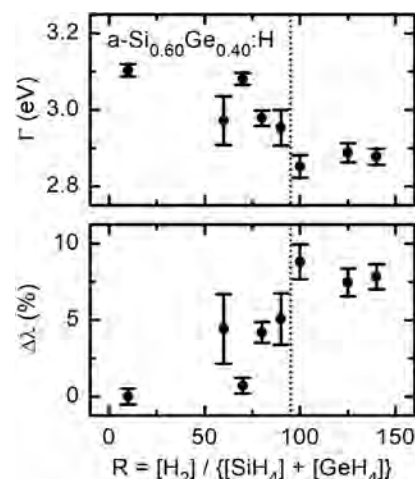


**Figure 3.** (Top) Cody–Lorentz oscillator broadening parameters measured at 475 K for  $a\text{-Si}_{0.60}\text{Ge}_{0.40}\text{:H}$  films prepared at different hydrogen dilution ratios from data reported in the study by Podraza et al.<sup>[47]</sup> (Bottom) Change in the mean free path of photoexcitations relative to that of  $R = 10$ . The vertical line demarcates  $R$  at which the material begins to nucleate nanocrystallites.

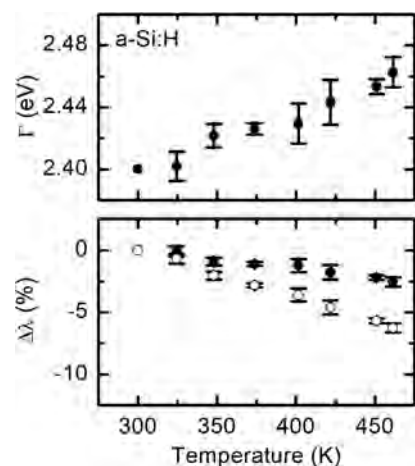


**Figure 4.** (Top) Cody–Lorentz oscillator broadening parameters for  $a\text{-Si:H}$  measured at different temperatures from 325 to 475 K and extrapolated to 300 K from data reported in the study by Podraza et al.<sup>[47]</sup> (Bottom) Change in the mean free path of photoexcitations relative to that at 300 K, assuming temperature independent (solid circles) and dependent (open circles) speeds of electron–hole pairs.

model has been applied to reduce the number of fit parameters in the analysis procedure.<sup>[68]</sup> All spectra in  $\epsilon$  reported here are parameterized with this model; however, the primary parameter of interest is the dielectric function broadening energy  $\Gamma$ . In the virtual interface analysis applied by Junda et al.,<sup>[51]</sup>  $\Gamma$  fully defines  $\epsilon$  when it is linked to all other Cody–Lorentz model parameters.<sup>[68]</sup> Thus, in this analysis,  $\Gamma$  has no correlations, as it is the only fit parameter given that the surface roughness thickness and growth rate at each time point are ascertained by global sum-of- $\sigma$  minimization of RTSE data and then fixed as reported by Junda et al.<sup>[51]</sup>

### 2.3. Calculation of Mean Free Path Length of Photoexcitations

The broadening  $\Gamma$  associated with the observed single dominant absorption feature having resonance energy  $E_0$  is linked to the mean free path length of the photoexcited electron-hole pairs, which, in turn, is controlled by scattering of the pairs photoexcited in that transition. The broadening parameter  $\Gamma$  measured for a nano-, micro-, or polycrystalline sample may be considered as the summation of the broadening found in a single crystalline material without extended defects ( $\Gamma_{\text{Crystal}}$ ) as controlled by electron-phonon interaction<sup>[1]</sup> and additional broadening arising from scattering of photoexcitations via the dominant defect scattering mechanism ( $\Gamma_{\text{Defects}}$ )<sup>[2,4]</sup>

$$\Gamma = \Gamma_{\text{Crystal}} + \Gamma_{\text{Defects}} \quad (2)$$

The scattering of photoexcitations due to defects will result in broadening associated with a particular electronic transition and is represented as

$$\Gamma_{\text{Defects}} = \frac{2\pi\nu\hbar}{\lambda} \quad (3)$$

Here,  $\nu$  is the speed of the photoexcited electron-hole pair, assuming that the electron and hole remain coupled in the final state of the transition,  $\hbar$  is Planck's constant, and  $\lambda$  is the mean free path of the pair within the material as limited by defect scattering. For nano-, micro-, and fine-grained polycrystalline materials, the dominant defect type is likely to be the grain boundary with the crystallite radius represented by  $\lambda$  and  $\Gamma > \Gamma_{\text{Crystal}}$ . The combined expression is

$$\Gamma = \Gamma_{\text{Crystal}} + \frac{2\pi\nu\hbar}{\lambda} \quad (4)$$

For the dominant transitions in a-Si:H and a-Ge:H, the Cody-Lorentz oscillator model parameter  $E_0$  ranges from  $\approx 3.5$  to  $3.9$  eV, and  $\Gamma$  ranges from  $\approx 2.5$  to  $4.0$  eV,<sup>[34,47]</sup> respectively, the latter compared with the  $E_1$  transitions in bulk crystalline Si and Ge with  $\Gamma \approx 0.1$  eV.<sup>[70,71]</sup> Thus, because  $\Gamma \gg \Gamma_{\text{Crystal}}$ , Equation (4) simplifies, and  $\lambda$  is obtained from

$$\lambda = \frac{2\pi\nu\hbar}{\Gamma} \quad (5)$$

Estimates of carrier speeds will be derived for these amorphous materials assuming one-electron states and equal speeds for the correlated electrons and holes, the latter being a characteristic of parallel band transitions in crystalline materials. For the amorphous materials, the optical transitions are most closely related to the lowest energy direct transitions in the corresponding single crystals, which are the  $E_1$  transitions. These transitions arise from the parallel nature of the valence and conduction bands along the  $\Lambda$  line of the band structure. The maximum values of  $\nu = (1/\hbar)(dE/dk)$  for both carriers in Si and Ge along this line are estimated as  $2.5 \times 10^5$  and  $2.9 \times 10^5$  m s<sup>-1</sup>, respectively.<sup>[72]</sup> An additional approach for estimating these speeds that relies only on the carrier effective masses  $m^*$  is the approximate expression

$$\nu = \frac{\pi\hbar}{2m^*a} \quad (6)$$

where  $a = 2.35$  and  $2.45$  Å, the Si-Si and Ge-Ge bond lengths, respectively. Although a general effective mass theory has been developed that is applicable to crystalline and amorphous solids and applied to shallow acceptor levels in a-Si:H,<sup>[73]</sup> the average masses instead are estimated from single crystal Si as an average of the longitudinal masses along the  $\Lambda$  direction near the zone boundary at L. Although these values have been given as  $1.63m_e$  and  $1.29m_e$  for Si and Ge, respectively, at the L point,<sup>[74]</sup> the bands flatten considerably, as the center of the  $\Lambda$  line is approached. Average values appropriate for the highest speed carriers are  $\approx 2.4m_e$  and  $\approx 1.9m_e$ , respectively. For photoexcitations consisting of electron-hole pairs, it is reasonable to expect a factor of two increase in these masses, yielding the speeds of  $1.6 \times 10^5$  m s<sup>-1</sup> for Si and  $2.0 \times 10^5$  m s<sup>-1</sup> for Ge. By way of comparison, the thermal speeds of electron-hole pairs at the L minimum can be determined, applying the conduction band effective mass parameters of the previous study<sup>[74]</sup> to deduce the conductivity effective masses, assumed to be the same for both electrons and holes. The results are  $1.9 \times 10^5$  m s<sup>-1</sup> for Si and  $2.2 \times 10^5$  m s<sup>-1</sup> for Ge. It is interesting that these thermal speeds for the electron-hole pairs lie between these two estimates given previously in this paragraph.

For evaluation of the temperature dependence of  $\lambda$  in Equation (5), the empirical temperature-dependent behavior observed in crystalline Si is applied. In crystalline Si, the temperature dependence of  $m^*$  is related to the experimentally measured temperature-dependent bandgap energies,  $E_G(T)$ ,<sup>[47]</sup> approximately as<sup>[75,76]</sup>

$$m^*(T) = m^*(300 \text{ K}) \cdot \frac{E_G(300 \text{ K})}{E_G(T)} \quad (7)$$

This relationship can be understood by attributing an increasing effective mass with increasing temperature to an enhanced electron-phonon interaction, which reduces the speed of the carrier. The same electron-phonon interaction dominates the decrease in bandgap with increasing temperature. Inserting masses for the  $E_1$  transitions of the single crystal into Equation (7), it then appears relevant to amorphous semiconductors due to the similarity in the temperature coefficients of the  $E_1$  transition energies to those of the amorphous semiconductor bandgap for both Si and Ge. For the c-Si and c-Ge  $E_1$  transitions, the temperature coefficients at 400 K are  $-4.1 \times 10^{-4}$  and  $-5.8 \times 10^{-4}$  eV K<sup>-1</sup>,<sup>[70,71]</sup> whereas the corresponding measured and extrapolated values for a-Si:H and a-Ge:H are  $-4.2 \times 10^{-4}$  and  $-5.5 \times 10^{-4}$  eV K<sup>-1</sup>, respectively.<sup>[47]</sup> The closeness of the temperature coefficients for the crystalline  $E_1$  transitions and the absorption onset energy of the dominant oscillator in the corresponding hydrogenated amorphous phase supports the above-mentioned use of  $E_1$  crystalline quantities in the estimates of the amorphous quantities.

Because of the uncertainties in the excited electron-hole pair speeds in particular, however, it is more accurate to represent the trends in the mean free path of the photoexcitations in terms of positive (increase) and negative (decrease) percentage changes in the mean free path by

$$\Delta\lambda = \left( \frac{\lambda}{\lambda_0} - 1 \right) \cdot 100\% \quad (8)$$

when comparing series of materials. In Equation (8),  $\lambda$  remains the photoexcitation mean free path for a sample relative to that of a chosen sample in the series  $\lambda_0$ . When absolute values of  $\lambda$  are desired, the speed values are each taken as an average of the two estimates given earlier, yielding  $2.1 \times 10^5 \text{ m s}^{-1}$  for a-Si:H and  $2.5 \times 10^5 \text{ m s}^{-1}$  for a-Ge:H. For compositions between the two endpoints, a linear relation between the speed and composition is used:  $v = v_{\text{Ge}} x + v_{\text{Si}} (1-x)$ .

### 3. Results and Discussion

Of the series of films evaluated here, the largest variations in broadening  $\Gamma$  are observed for a-Si<sub>1-x</sub>Ge<sub>x</sub>:H films prepared as functions of  $G$ , which is varied to control the germanium content  $x$  (Figure 2). The films are prepared at fixed  $R = 10$  and remain in the amorphous phase throughout the accumulated thickness. Even though the films in the two series of Figure 2 are prepared under different PECVD conditions,<sup>[34,47]</sup> the trends in  $\Gamma$  with  $G$  overlap. For compositions reported in the previous study,<sup>[47]</sup> X-ray photoelectron spectroscopy yielded germanium contents  $0.00 \leq x \leq 0.40$ . The broadening parameters for a-Si:H are the narrowest and overlap for the two series, indicating the longest mean free path of photoexcited electron-hole pairs among the films of each series, which are  $\lambda_0$  for each. The broadening energy increases with  $G$  to reach a maximum for the  $G = 0.8$  film with a slight reduction for a-Ge:H. This increase and subsequent decrease in  $\Gamma$  corresponds to an expected decrease in order with alloying, characteristic of a-Si:H, in general, being more ordered than a-Ge:H. Without considering compositionally dependent excited electron-hole pair speeds, a decrease in mean free path of photoexcitations of  $\approx 40\%$  is observed from a-Si:H to a-Ge:H (Figure 2b). Considering the differences in excitation speeds assigned to a-Si:H and a-Ge:H, the mean free paths of the photoexcitations in a-Si<sub>1-x</sub>Ge<sub>x</sub>:H and a-Ge:H are now reduced by up to  $\approx 30\%$  with respect to a-Si:H. A reduced mean free path is expected not only due to alloying disorder but also because hydrogen is less effectively incorporated into a-Si<sub>1-x</sub>Ge<sub>x</sub>:H and a-Ge:H relative to a-Si:H.<sup>[77]</sup> Such trends are expected to apply for films of different compositions prepared by PECVD with the same  $R$  within the amorphous growth regime. This reduction in mean free path coincides with diminished electronic quality and stability observed for thin-film solar cells fabricated with a-Si<sub>1-x</sub>Ge<sub>x</sub>:H absorbers compared with those based on a-Si:H.

If  $R$  is increased to increase the amount of hydrogen present in the plasma,  $\Gamma$  decreases while films remain in the amorphous growth regime as shown for  $G = 0.167$  a-Si<sub>0.60</sub>Ge<sub>0.40</sub>:H in Figure 3.<sup>[47]</sup> For a fixed alloy composition, it is reasonable to assume that the electron-hole pair speed is constant. Using the mean free path of photoexcitations for the  $R = 10$  sample as  $\lambda_0$ , an increase in mean free path of  $\approx 5\%$  is observed up to  $R = 90$ . At  $R > 90$ ,  $\Gamma$  and the associated mean free path stabilize somewhat. This stabilization coincides with the lowest  $R$  at which films nucleate crystallites with accumulated bulk layer thickness, as demarcated by the vertical line in Figure 3. For protocrystalline material prior to the onset of crystallite nucleation, a

greater amount of hydrogen is expected to be incorporated into the films compared with material prepared at lower  $R$  that remains in the amorphous phase throughout growth. Among a series of similar films, protocrystalline material is likely to exhibit the highest relative degree of order. Such trends are also observed for  $G = 0.083$  a-Si<sub>0.73</sub>Ge<sub>0.27</sub>:H and for a-Si:H, which show increases in the mean free path of photoexcitations of  $\approx 8\%$  from  $R = 10$  to 40 and  $\approx 6\%$  from  $R = 10$  to 15, respectively.<sup>[46]</sup> A similar reduction in  $\Gamma$  is observed for  $R = 0$  a-Si:H exposed to a hydrogen plasma for short times prior to substantial etching by that same plasma, and this reduction corresponds to a  $\approx 6\%$  increased mean free path when analyzed by this method.<sup>[49]</sup> These increases in the mean free path with increased  $R$  tend to suppress the observed reduction in mean free path due to alloying when considering protocrystalline material prepared at the highest  $R$  prior to the nucleation of crystallites. However, the mean free path of photoexcited electron-hole pairs is still longer in a-Si:H compared with the alloys. The implied reduced order in the alloys accompanies the aforementioned lower performance of solar cells incorporating alloy absorbers as well as higher Urbach energies and a greater density of defect states within the bandgap for unoptimized a-Si<sub>1-x</sub>Ge<sub>x</sub>:H.<sup>[68]</sup> It should also be noted that the increase in the mean free path of photoexcitations upon hydrogen plasma treatment corresponds to the effect that occurs upon subsurface modification of low  $R$  a-Si:H when over-deposited by higher  $R$  material.<sup>[11,16]</sup>

The results in Figures 2 and 3 discussed previously have been obtained for  $\Gamma$  at the film deposition temperature of 475 K. The temperature dependence of  $\Gamma$  for  $0.00 \leq x \leq 0.40$  has been previously reported<sup>[47]</sup> and used to extrapolate  $\Gamma$  to room temperature, nominally 300 K, which will be set as  $\lambda_0$ . As  $\Gamma$  increases with increasing temperature in a-Si:H, a reduction in the mean free path of photoexcitations is observed by 2.5%, assuming a temperature-independent speed of electron-hole pairs (Figure 4). The reduction in mean free path as indicated by  $\Gamma(T)$  is enhanced by an increase in effective mass with  $T$  according to Equation (7). Including this effect, the decrease in mean free path with increasing temperature from 300 to 475 K is  $\approx 6\%$  for a-Si:H, 8% for a-Si<sub>0.73</sub>Ge<sub>0.27</sub>:H, and 9% for a-Si<sub>0.60</sub>Ge<sub>0.40</sub>:H. These increases in magnitude arise due to the simultaneous increase in the temperature coefficient of the bandgap, indicating enhanced electron-phonon interaction, and decrease in bandgap, both with the incorporation of Ge into a-Si:H.

As mentioned earlier, increases in  $\Gamma$  have been found to correlate with increases in the Urbach energy defining the subgap absorption tail of a-Si<sub>1-x</sub>Ge<sub>x</sub>:H.<sup>[68]</sup> From Ferlauto et al.,<sup>[68]</sup> the Urbach energy ( $E_u$ ) is related to  $\Gamma$  via different expressions for a-Si<sub>1-x</sub>Ge<sub>x</sub>:H. For material optimized as a solar cell absorber, the relationship is

$$E_u(\text{meV}) = 49.0 + 4.90[\Gamma(\text{eV}) - 2.12] \quad (9)$$

and for material that is not optimized, the relationship is

$$E_u(\text{meV}) = 49.0 + 12.9[\Gamma(\text{eV}) - 2.12] \quad (10)$$

Using  $\Gamma$  for a-Si:H prepared at the maximal  $R$  prior to crystallite nucleation and extrapolating the temperature dependence of  $\Gamma$  to room temperature,  $\Gamma = 2.31 \text{ eV}$  for  $R = 15$  a-Si:H. This broadening value is close to the value reported for a-Si:H optimized as a solar cell absorber.<sup>[68]</sup> Applying Equation (9) yields  $E_u = 50 \text{ meV}$

for  $R = 15$  a-Si:H, which is also close to  $E_u$  reported for optimized a-Si:H. Assuming the same optimization criteria for  $R = 40$  a-Si<sub>0.73</sub>Ge<sub>0.27</sub>:H and  $R = 90$  a-Si<sub>0.60</sub>Ge<sub>0.40</sub>:H apply,  $E_u$  is calculated to be 52 and 53 meV, respectively, which are also similar to the results for optimized a-Si<sub>1-x</sub>Ge<sub>x</sub>:H. Assuming that the material prepared at  $R = 10$  for a-Si:H, a-Si<sub>0.73</sub>Ge<sub>0.27</sub>:H, and a-Si<sub>0.60</sub>Ge<sub>0.40</sub>:H is not fully optimized, and applying Equation (10) yields the higher  $E_u$  values of 53, 58, and 60 meV, respectively. It should be noted that the criteria for optimization of these materials are relative, so the general trends observed are likely to be more relevant than the actual values. Regardless, these calculated values of  $E_u$  increase with increasing germanium content and decrease with increasing hydrogen dilution, which are the same trends exhibited by  $\Gamma$ . The reduction in short-range order that leads to a widening of the Urbach tail and an increase in  $E_u$  are likely the same as that acting to reduce the mean free path of the photoexcited electron-hole pairs.

For a-Si:H films,  $\Gamma$ <sup>[51]</sup> and, thus, the mean free path of photoexcitations are not constant with accumulated thickness, given the reasonable assumption of thickness independent electron-hole pair speeds (Figure 5). For  $R = 0.5$  a-Si:H prepared on native oxide covered c-Si, the effect is weak with  $\Gamma$  slightly increasing as a function of accumulated thickness. In plotting  $\Delta\lambda$ ,  $\lambda$  is measured relative to the value of  $\lambda_0$  at 10 nm of accumulated thickness. This behavior implies that the thickness dependences of  $\Gamma$  and the mean free path are also weak for the previously discussed series of films, which were also prepared on native oxide covered c-Si. For  $R = 0.5$  films prepared on p-type a-Si<sub>1-x</sub>C<sub>x</sub>:H or on TEC-15,  $\Gamma$  decreases and the mean free paths increase with increasing thickness. In calculating  $\Delta\lambda$ ,  $\lambda_0$  at 10 nm accumulated thickness for the  $R = 0.5$  film on native oxide covered c-Si is again used here. Initially, the mean free paths for the

films prepared on the p-type a-Si<sub>1-x</sub>C<sub>x</sub>:H and on TEC-15 are substantially lower than for the film on c-Si but begin to converge at higher accumulated thicknesses.

This substrate-dependent behavior implies that the order in the c-Si substrate surface initially induces more order within the growing a-Si:H due to the protocrystalline nature of the film.<sup>[14]</sup> As the memory of the underlying substrate is lost with accumulated thickness, the disorder in the a-Si:H film on c-Si increases slightly. Similarly, for the films prepared on p-type a-Si<sub>1-x</sub>C<sub>x</sub>:H and TEC-15, the higher substrate disorder relative to c-Si induces more disorder in the a-Si:H film.

When comparing  $R = 0.5, 5$ , and 10 a-Si:H on TEC-15 relative to that of  $R = 0.5$  a-Si:H on c-Si, the mean free path of electron-hole pair photoexcitations decreases with increasing  $R$ . This behavior is opposite to that observed for a-Si:H and a-Si<sub>1-x</sub>Ge<sub>x</sub>:H films prepared as a function of  $R$  on native oxide covered c-Si discussed earlier. For the TEC-15 substrate, more hydrogen present in the plasma at higher  $R$  during PECVD increasingly etches the underlying SnO<sub>2</sub>:F layer, resulting in a more disordered surface, which, in turn, reduces the order and mean free path in the growing a-Si:H films. As reported by Junda et al.,<sup>[51]</sup> modification of the SnO<sub>2</sub>:F in TEC-15 occurs dynamically and simultaneously with a-Si<sub>1-x</sub>C<sub>x</sub>:H and a-Si:H deposition. At small accumulated bulk film thicknesses, oscillations in  $\Gamma$  are observed for these depositions that do not appear for the deposition on c-Si. These oscillations arise either from imperfect fits to the experimental data due to correlations among the thicknesses serving as fit parameters in the model, from a breakdown in the pseudo-substrate approximation used in virtual interface analysis to describe the rather complicated TEC-15 substrate, or from both.<sup>[51]</sup> Thus, the evolution of  $\Gamma$  due to modification of the underlying SnO<sub>2</sub>:F during growth is superimposed on the thickness correlations and/or breakdown of the pseudo-substrate approximation. These oscillations in  $\Gamma$  diminish with thickness accumulation, which minimizes the role of correlation artifacts, enhances the validity of the pseudo-substrate approximation, or both. The more gradual change in  $\Gamma$  occurs, as each film tends toward a degree of order characteristic of the growth process rather than imposed by the modified substrate. These cases illustrate that the underlying relative order of the substrate, interactions between the growing a-Si:H film and the underlying material, and the protocrystalline nature of a-Si:H all will influence the mean free path of electron-hole pair photoexcitations and the associated evolution of short-range order with increasing thickness.

Due to the approximations involved in Equation (5)–(7) and the uncertainties in the speed and effective mass of electron-hole pair photoexcitations applied here, it has been useful to calculate the relative change in the mean free path of photoexcitations instead of the absolute value. By applying  $\Gamma$  for material prepared at the maximal  $R$  prior to crystallite nucleation, extrapolating the temperature dependence of  $\Gamma$  to room temperature, and assuming room temperature photoexcitation speeds, the room temperature estimates for mean free path of photoexcitations in a-Si:H, a-Si<sub>0.73</sub>Ge<sub>0.27</sub>:H, and a-Si<sub>0.60</sub>Ge<sub>0.40</sub>:H are calculated to be 3.8, 3.4, and 3.3 Å, respectively. These distances are small, but reasonable, considering the relatively large broadenings of  $\Gamma \approx 2$  to 3 eV in the films and their amorphous nature.<sup>[5,8–10]</sup> These calculated mean free paths decrease

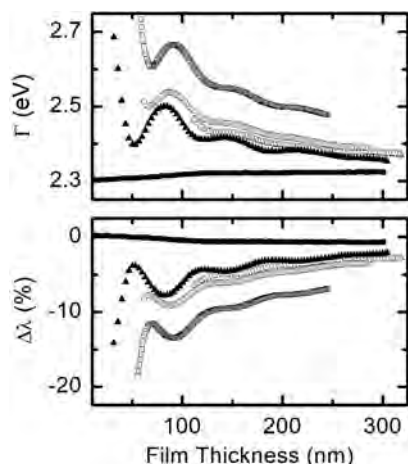


**Figure 5.** (Top) Cody–Lorentz oscillator broadening parameters for a-Si:H measured as the functions of accumulated film thickness,  $R$ , and substrate as in Junda et al.<sup>[51]</sup> Films include a-Si:H prepared at  $R = 0.5$  on native oxide covered crystalline silicon (solid squares);  $R = 0.5$  on p-type hydrogenated amorphous silicon carbon (a-Si<sub>1-x</sub>C<sub>x</sub>:H) in a p-i-n configuration solar cell (solid triangles); and  $R = 0.5, 5$ , and 10 on TEC-15 fluorinated tin oxide-coated glass (open triangles, open circles, and open squares, respectively). (Bottom) Change in the mean free path of photoexcitations relative to that of 10 nm thick  $R = 0.5$  a-Si:H on native oxide covered crystalline silicon,  $R$ , and substrate.



systematically with increasing germanium content. Error in the measured values of  $\Gamma$ , extrapolation of  $\Gamma$  to room temperature, and assumptions in the calculation, however, should be considered when comparing samples.

## 4. Conclusion

Variations in the mean free path of photoexcited electron–hole pairs in a-Si:H and a-Si<sub>1-x</sub>Ge<sub>x</sub>:H thin films have been tracked as functions of composition, hydrogen dilution during preparation and post-deposition hydrogen plasma treatment, measurement temperature, accumulated film thickness, and underlying substrate material. The addition of germanium systematically reduces the mean free path up to ~30% relative to that of a-Si:H. Increased hydrogen dilution up to the maximal  $R$  prior to crystallite nucleation generally increases the mean free path by ~5%–8% relative to  $R = 10$  material prepared for a given composition. Short exposure to hydrogen plasma similarly increases the mean free path. The temperature dependence consists of a reduction in mean free path reflected in increasing  $\Gamma$  with temperature and a larger decrease in the mean free path due to an empirically determined increase in effective mass with temperature. Higher disorder in materials underlying the growing a-Si:H films such as TEC-15 SnO<sub>2</sub>:F or a-Si<sub>1-x</sub>C<sub>x</sub>:H relative to native oxide covered c-Si leads to lower mean free path of photoexcitations in the over-deposited a-Si:H, although some order is recovered with sufficient accumulated film thickness. Combining this information allows for estimation of the room temperature mean free path as values near 3.5 Å for a-Si:H, a-Si<sub>0.73</sub>Ge<sub>0.27</sub>:H, and a-Si<sub>0.60</sub>Ge<sub>0.40</sub>:H.

## Acknowledgements

This work was supported by the Ohio Department of Development (ODOD) Ohio Research Scholars Program (Northwest Ohio Innovators in Thin Film Photovoltaics, Grant No. TECH 09-025).

## Conflict of Interest

The authors declare no conflict of interest.

## Data Availability Statement

Data sharing is not applicable to this article as no new data were created or analyzed in this study.

## Keywords

amorphous silicon, amorphous silicon germanium alloys, mean free path, photoelectronic excitations, optical properties, spectroscopic ellipsometry

Received: August 31, 2020  
Revised: May 25, 2021  
Published online: July 3, 2021

- [1] P. Lautenschlager, P. B. Allen, M. Cardona, *Phys. Rev. B* **1986**, 33, 5501.
- [2] G. F. Feng, R. Zallen, *Phys. Rev. B* **1989**, 40, 1064.
- [3] S. Bouloutakis, S. Logothetidis, S. Ves, *J. Appl. Phys.* **1992**, 72, 3648.
- [4] H. V. Nguyen, R. W. Collins, *Phys. Rev. B* **1993**, 47, 1064.
- [5] P. K. Giri, S. Tripurasundari, G. Raghavan, B. K. Panigrahi, P. Magudapathy, K. G. M. Nair, A. K. Tyagi, *J. Appl. Phys.* **2001**, 90, 659.
- [6] J. Li, N. J. Podraza, R. W. Collins, *Phys. Status Solidi A* **2008**, 205, 901.
- [7] J. Li, J. Chen, R. W. Collins, *Appl. Phys. Lett.* **2010**, 97, 181909.
- [8] R. Zallen, *The Physics of Amorphous Solids*, Wiley-VCH, Weinheim, Germany **1983**, pp. 252–296, Chapter 6.
- [9] N. F. Mott, E. A. Davis, *Electronic Processes in Non-Crystalline Materials*, Oxford University Press, Oxford, UK **2012**, pp. 7–64, Chapter 2.
- [10] K. Saaskilahti, J. Oksanen, J. Tulkki, A. J. H. McGaughey, S. Volz, *AIP Adv.* **2016**, 6, 121904.
- [11] J. Koh, Y. Lee, H. Fujiwara, C. R. Wronski, R. W. Collins, *Appl. Phys. Lett.* **1998**, 73, 1526.
- [12] S. Guha, J. Yang, A. Banerjee, *Prog. Photovolt.: Res. Appl.* **2000**, 8, 141.
- [13] X. Deng, E. A. Schiff, in *Handbook of Photovoltaic Science and Engineering* (Eds: A. Luque, S. Hegedus), John Wiley & Sons, Chichester, UK **2003**, p. 505, Chapter 12.
- [14] R. W. Collins, A. S. Ferlauto, G. M. Ferreira, C. Chen, J. Koh, R. J. Koval, Y. Lee, J. M. Pearce, C. R. Wronski, *Sol. Energy Mater. Sol. Cells* **2003**, 78, 143.
- [15] X. Liao, W. Du, X. Yang, H. Povolny, X. Xiang, X. Deng, in *31st IEEE Photovoltaic Specialists Conf.*, **2005**, p. 1444.
- [16] J. M. Pearce, N. Podraza, R. W. Collins, M. M. Al-Jassim, K. M. Jones, J. Deng, C. R. Wronski, *J. Appl. Phys.* **2007**, 101, 114301.
- [17] J. A. Stoke, N. J. Podraza, J. Li, X. Cao, X. Deng, R. W. Collins, *J. Non-Cryst. Solids* **2008**, 354, 2435.
- [18] Q. H. Fan, C. Chen, X. Liao, X. Xiang, S. Zhang, W. Ingler, N. Adiga, Z. Hu, X. Cao, W. Du, X. Deng, *Sol. Energy Mater. Sol. Cells* **2010**, 94, 1300.
- [19] B. Yan, G. Yue, L. Sivec, J. Yang, S. Guha, C.-S. Jiang, *Appl. Phys. Lett.* **2011**, 99, 113512.
- [20] S. Kim, J.-W. Chung, H. Lee, J. Park, Y. Heo, H.-M. Lee, *Sol. Energy Mater. Sol. Cells* **2013**, 119, 26.
- [21] M. M. Junda, A. Shan, P. Koirala, R. W. Collins, N. J. Podraza, *IEEE J. Photovoltaics* **2015**, 5, 307.
- [22] M. Tanaka, M. Taguchi, T. Matsuyama, T. Sawada, S. Tsuda, S. Nakano, H. Hanafusa, Y. Kuwano, *Jpn. J. Appl. Phys.* **1992**, 31, 3518.
- [23] H. Fujiwara, M. Kondo, *Appl. Phys. Lett.* **2005**, 86, 032112.
- [24] H. Fujiwara, T. Kaneko, M. Kondo, *Appl. Phys. Lett.* **2007**, 90, 013503.
- [25] H. Fujiwara, T. Kaneko, M. Kondo, *Appl. Phys. Lett.* **2007**, 91, 133508.
- [26] H. Fujiwara, M. Kondo, *J. Appl. Phys.* **2007**, 101, 054516.
- [27] T.-H. Chang, Y.-H. Chu, C.-C. Lee, J.-Y. Chang, *Appl. Phys. Lett.* **2012**, 101, 241601.
- [28] B. Macco, J. Melskens, N. J. Podraza, K. Arts, C. Pugh, O. Thomas, W. M. M. Kessels, *J. Appl. Phys.* **2017**, 122, 035302.
- [29] A. J. Syllaos, T. R. Schimert, R. W. Gooch, W. L. McCardel, B. A. Ritchey, J. H. Tregilgas, *Mater. Res. Soc. Symp. Proc.* **2000**, 609, A14-04.
- [30] M. Garcia, R. Ambrosio, A. Torres, A. Kosarev, *J. Non-Cryst. Solids* **2004**, 338–340, 744.
- [31] A. Torres, M. Moreno, A. Kosarev, A. Heredia, *J. Non-Cryst. Solids* **2008**, 354, 2556.
- [32] D. B. Saint John, H.-B. Shin, M.-Y. Lee, E. C. Dickey, N. J. Podraza, T. N. Jackson, *Proc. SPIE* **2011**, 8012, 80123U.

- [33] D. B. Saint John, H.-B. Shin, M.-Y. Lee, S. K. Ajmera, A. J. Syllaios, E. C. Dickey, T. N. Jackson, N. J. Podraza, *J. Appl. Phys.* **2011**, 110, 033714.
- [34] D. B. Saint John, *Optical and Electrical Characterization of High Resistivity Semiconductors for Constant-Bias Microbolometer Devices*, Ph.D. Thesis, The Pennsylvania State University **2012**.
- [35] H.-B. Shin, D. Saint John, M.-Y. Lee, N. J. Podraza, T. N. Jackson, *J. Appl. Phys.* **2013**, 114, 183705.
- [36] H. A. Basantani, D. B. Saint John, N. J. Podraza, T. N. Jackson, M. W. Horn, *Proc. SPIE* **2014**, 9070, 901701P.
- [37] M. Moreno, R. Jimenez, A. Torres, R. Ambrosio, *IEEE Trans. Electron Devices* **2015**, 62, 2120.
- [38] A. H. M. Smets, M. C. M. van de Sanden, *Appl. Phys. Lett.* **2003**, 82, 1547.
- [39] A. H. M. Smets, M. C. M. van de Sanden, *Phys. Rev. B* **2007**, 76, 073202.
- [40] D. B. Saint John, H. Shen, H.-B. Shin, T. N. Jackson, N. J. Podraza, in *38th IEEE Photovoltaic Specialists Conf.*, **2012**, p. 3112.
- [41] D. Adhikari, M. M. Junda, S. X. Marsillac, R. W. Collins, N. J. Podraza, *J. Appl. Phys.* **2017**, 122, 075302.
- [42] E. Johlin, N. Tabet, S. Castro-Galnares, A. Abdallah, M. I. Bertoni, T. Asafa, J. C. Grossman, S. Said, T. Buonassisi, *Phys. Rev. B* **2012**, 85, 075202.
- [43] Y. Pan, F. Inam, M. Zhang, D. A. Drabold, *Phys. Rev. Lett.* **2008**, 100, 206403.
- [44] D. Igram, B. Bhattarai, P. Biswas, D. A. Drabold, *J. Non-Cryst. Solids* **2018**, 492, 27.
- [45] H. Fujiwara, J. Koh, R. W. Collins, *Thin Solid Films* **1998**, 313–314, 474.
- [46] N. J. Podraza, C. R. Wronski, M. W. Horn, R. W. Collins, *Mater. Res. Soc. Symp. Proc.* **2006**, 910, A03-02.
- [47] N. J. Podraza, C. R. Wronski, M. W. Horn, R. W. Collins, *Mater. Res. Soc. Symp. Proc.* **2006**, 910, A10-01.
- [48] N. J. Podraza, C. R. Wronski, R. W. Collins, *J. Non-Cryst. Solids* **2006**, 352, 1263.
- [49] N. J. Podraza, J. Li, C. R. Wronski, M. W. Horn, E. C. Dickey, R. W. Collins, *Mater. Res. Soc. Symp. Proc.* **2008**, 1066, A10-01.
- [50] N. J. Podraza, D. Saint John, J. Li, C. R. Wronski, E. C. Dickey, R. W. Collins, in *Proc. of the 35th Photovoltaic Specialists Conf.*, **2010**, p. 158.
- [51] M. M. Junda, L. Karki Gautam, R. W. Collins, N. J. Podraza, *Appl. Surf. Sci.* **2018**, 436, 779.
- [52] R. A. Street, *Hydrogenated Amorphous Silicon*, Cambridge University Press, Cambridge, UK **1991**, Chapter 3, pp. 83–85, Chapter 8, pp. 294–297.
- [53] G. D. Cody, in *Semiconductors and Semimetals*, Vol. 21, Part B: *Hydrogenated Amorphous Silicon, Optical Properties* (Ed: J. I. Pankove), Academic Press, Orlando, FL **1984**, pp. 11–82, Chapter 2.
- [54] S. K. O'Leary, S. R. Johnson, P. K. Lim, *J. Appl. Phys.* **1997**, 82, 3334.
- [55] L. Jiao, I. S. Chen, R. W. Collins, C. R. Wronski, *Appl. Phys. Lett.* **1998**, 72, 1057.
- [56] D. J. Dunstan, F. Boulitrop, *J. Phys.* **1981**, 42, C4.
- [57] D. J. Dunstan, F. Boulitrop, *Phys. Rev. B* **1984**, 30, 5945.
- [58] T. M. Searle, W. A. Jackson, *Philos. Mag. B* **1989**, 60, 237.
- [59] W. B. Jackson, S. M. Kelso, C. C. Tsai, J. W. Allen, S.-J. Oh, *Phys. Rev. B* **1985**, 31, 5187.
- [60] R. M. Dawson, Y. M. Li, M. Gunes, D. Heller, S. Nag, R. W. Collins, C. R. Wronski, M. Bennett, Y. M. Li, in *Amorphous Silicon Technology – 1992* (Eds: M. J. Thompson, Y. Hamakawa, P. G. Lecomber, A. Madan, E. Schiff), Materials Research Society Symp. Proc., Vol. 258, MRS, Pittsburgh, PA **1992**, pp. 595–600.
- [61] R. A. Street, *Philos. Mag. B* **1978**, 37, 35.
- [62] J. Lee, P. I. Rovira, I. An, R. W. Collins, *Rev. Sci. Instrum.* **1998**, 69, 1800.
- [63] B. Johs, J. A. Woollam, C. M. Herzinger, J. N. Hilfiker, R. Synowicki, C. Bungay, *Crit. Rev. Opt. Sci. Technol.* **1999**, CR 72, 29.
- [64] C. Chen, I. An, G. M. Ferreira, N. J. Podraza, J. A. Zapien, R. W. Collins, *Thin Solid Films* **2004**, 455–456, 14.
- [65] D. E. Aspnes, *Thin Solid Films* **1982**, 89, 249.
- [66] H. Fujiwara, J. Koh, P. I. Rovira, R. W. Collins, *Phys. Rev. B* **2000**, 61, 832.
- [67] W. G. Oldham, *Surf. Sci.* **1969**, 16, 97.
- [68] A. S. Ferlauto, G. M. Ferreira, J. M. Pearce, C. R. Wronski, R. W. Collins, X. Deng, G. Ganguly, *J. Appl. Phys.* **2002**, 92, 2424.
- [69] G. E. Jellison, F. A. Modine, *Appl. Phys. Lett.* **1996**, 69, 2137.
- [70] L. Vina, S. Logothetidis, M. Cardona, *Phys. Rev. B* **1979**, 30, 1984.
- [71] P. Lautenschlager, M. Garriga, L. Vina, M. Cardona, *Phys. Rev. B* **1987**, 36, 4821.
- [72] J. R. Chelikowsky, M. L. Cohen, *Phys. Rev. B* **1976**, 14, 556.
- [73] S. Kivelson, C. D. Gelatt, *Phys. Rev. B* **1979**, 19, 5160.
- [74] C. V. Fischetti, *IEEE Trans. Electron Devices* **1991**, 38, 634.
- [75] R. K. Jain, R. J. Van Overstraeten, *IEEE Trans. Electron Devices* **1974**, 21, 155.
- [76] V. Gopal, *Indian J. Pure Appl. Phys.* **1982**, 20, 180.
- [77] W. Paul, D. K. Paul, B. von Roedern, J. Blake, S. Oguz, *Phys. Rev. Lett.* **1981**, 46, 1016.

# Quantitative Photoresponse of the First Photosynthetic Biomaterials: Physical Measurements and Analysis of Microalgae Systems

Edward T. Drabold\* and David J. Bayless

Dedicated to Professor David A. Drabold on the occasion of his 60th birthday

Herein, results of photoinduced pH oscillatory phenomena of microalgae in laboratory systems are presented. Microalgae are an extremely complex biomaterial in which light-induced quantum mechanical processes induce changes in the surrounding aqueous environment (medium). A phenomenological understanding of the photoresponse by a quantitative study of pH oscillations of the medium is provided. The biochemical processes of algal metabolism and photosynthesis and the impact of light on a nitrate-enriched medium are examined. pH variations in the external medium and the impact on future applications of microalgae are presented. External pH dominantly impacts conductivity in the solution of algal biophotovoltaic devices. This is the first dynamic study of the light-induced pH behavior of microalgae with direct relevance to carbon capture, biophotovoltaic electricity generation, and quantum photosynthesis.

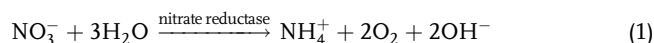
## 1. Introduction

The world faces a host of environmental challenges.<sup>[1–3]</sup> These include excess CO<sub>2</sub> in the atmosphere, vast wastewater pollution, and a need to produce energy cleanly and efficiently. Research in condensed matter science and solar energy (photovoltaics) has successfully begun to ameliorate these environmental challenges.<sup>[4]</sup> Yet, biologically, microalgae and plants have used solar energy for millions of years to power themselves and indirectly produce fossil fuels.<sup>[5]</sup> Recent studies have shown that the quantum yield of photosynthesis, which approaches 100%, could be

due to the unique solid-state quantum mechanical properties of chlorophyll and surrounding protein structures.<sup>[6]</sup>

Despite these discoveries, it remains mathematically challenging to analytically study the photoresponse of a whole biological system.<sup>[7,8]</sup> Thus, experimental techniques are required. One of the most photosensitive and readily studied variables in microalgal systems is pH. Within seconds of light exposure, the photoresponse can be detected by pH change in the external medium.<sup>[9]</sup> In this initial phase, the excited electron from the delocalized magnesium–chlorin cloud of the chlorophyll's either red or blue bandgap peak is sent by varying chemical intermediates to responsible enzymes for metabolism.<sup>[6,7]</sup>


A major part of algal metabolism is the reduction of the common anions HCO<sub>3</sub><sup>−</sup>, NO<sub>3</sub><sup>−</sup>, and PO<sub>4</sub><sup>3−</sup> for carbon, nitrogen, phosphorus, and other nutrients.<sup>[10]</sup> The reduction of these nutrients from the energy provided by the excited electron ultimately releases the oxygen in these common anions as O<sub>2</sub> or OH<sup>−</sup> into the external medium.<sup>[11,12]</sup> A simple pH electrode can then be used to study the production of OH<sup>−</sup> from the microalgae and the photoresponse. To illustrate this, the enzyme nitrate reductase undertakes the reaction shown in Equation (1)



The photoresponse and time dependence of the pH has significant implications for algal carbon capture and the conductivity of the external medium.<sup>[6,13]</sup> Mass transfer and absorption of inorganic carbon (via CO<sub>2</sub>) into water is exponentially increased by the presence of OH<sup>−</sup> in the medium.<sup>[14]</sup> As CO<sub>2</sub> is a significant source of carbon in the algae industry, understanding and optimizing this metabolism could significantly improve algae production. In addition, algae have been shown to grow slower in high-pH (<9) environments. pH has been described as the most important variable to control in the biotechnology industry.<sup>[15]</sup> pH cyclic phenomena can be detected in the oceans and large bodies of fresh or salt water, where pH generally rises during the day and falls at night in an oscillatory behavior.<sup>[16,17]</sup> pH change is dependent on a variety of variables, including concentration of algae, nutrient composition, light intensity, and

E. T. Drabold  
Honors Tutorial College  
Ohio University  
35 Park Pl, Athens, OH 45701, USA  
E-mail: ed700415@ohio.edu

Prof. D. J. Bayless  
Department of Mechanical Engineering  
Russ College of Engineering and Technology  
Ohio University  
28 W Green Dr, Athens, OH 45701, USA

 The ORCID identification number(s) for the author(s) of this article can be found under <https://doi.org/10.1002/pssb.202000475>.

DOI: 10.1002/pssb.202000475

water alkalinity. Researchers have not yet studied pH dynamics in large bodies of water.

Where biophotovoltaic devices are concerned, high conductivity of the external media is required for cation–anion transfer in the electrochemical cell.<sup>[6]</sup> Therefore, the pH and its variation impact electricity generation from the biophotovoltaics. Limited work has been done on the dynamic nature of external pH in biophotovoltaics. Yet, the experiments that have recorded pH display a changing variable—where pH starting at 7 exponentially grows to pH 10 near the experiment's end.<sup>[15]</sup> Previous experiments, at least published, have not provided continuous pH data (every minute or second for a period of days or weeks). These experiments also have not quantified the interplay between microalgae growth, charge transfer, and carbon capture. However, all these experiments describe pH affecting these key areas under varying conditions.<sup>[15,16,18]</sup> This leaves pH as a continually significant dynamic variable for the optimization and understanding of biophotovoltaic technology.

The objective of this study is to analyze the photoresponse of microalgal systems as a function of time, including when and how microalgae stop or keep absorbing light indirectly from metabolism. The novelty of this research lies in its detailed and controlled study of pH to understand algal photoresponse and metabolism. External pH is usually considered a challenge in the applied algae field.<sup>[12]</sup> This study attempts to understand why microalgae pH is a challenge from a dynamic viewpoint, how it can be resolved, and to connect the photoresponse and metabolism to carbon capture, electrical conductivity in biophotovoltaic cells, and quantum photosynthesis.

## 2. Results

As shown in **Figure 1**, the pH generally rose rapidly for the first few hours of light exposure. After the pH reached  $\approx 9$ , its

derivative steadily decreased until the lights were turned off. At this point, the pH dropped sharply as photosynthesis and metabolic function largely stopped. Over the 10 day period, the pH also generally oscillated with smaller maxima and minima. This coincided with an oscillatory increase of total inorganic carbon (TIC) in the medium (also shown in **Figure 1**). The small oscillatory behavior at the trials' beginning coincided with the acclimatization and rapid growth of the microalgae. Once the pH oscillatory minima did not reach lower than a pH of 8.5, this led to algae growth plateauing or death, even though excess nutrients remained in the media.

**Figure 2** shows photoresponse pH data using a solution of BG-11 media with the addition of a buffer ( $1 \text{ g L}^{-1} \text{ NaHCO}_3$ ). Results indicate that the photoresponse of the buffered medium was just as immediate as in BG-11. However, the buffered medium did not exhibit rapid pH changes, but rather linear and smaller “saw-tooth” oscillations. Similarly to BG-11, the pH increased and then plateaued. However, the pH began to decrease around day 8. This coincided with decreased photosynthesis and decreased growth. Unlike in BG-11, the TIC decreased in the buffered medium. To determine whether the uptake of  $\text{NO}_3^-$  was directly light-induced, similar to TIC uptake,  $\text{NO}_3^-$  concentrations were measured every hour over an 18 h period on BG-11. Data from **Figure 3** indicate that  $\text{NO}_3^-$  uptake was mostly continuous, except for a possible plateau from 3 to 6 am.

A control experiment was run with ammonia as the nitrogen source (as opposed to nitrate) to determine if nitrate metabolism was the primary cause of the pH oscillatory behavior. All other nutrient levels remained the same. As shown in **Figure 4**, the pH decreased during light periods, as opposed to the previously observed increase during similar conditions with nitrate. In addition, the microalgae grew poorly in the ammonia media. TIC did not accumulate in the medium as it had when using BG-11. This suggests oxidized nutrients, primarily  $\text{NO}_3^-$ , are mainly responsible for the oscillatory behavior.

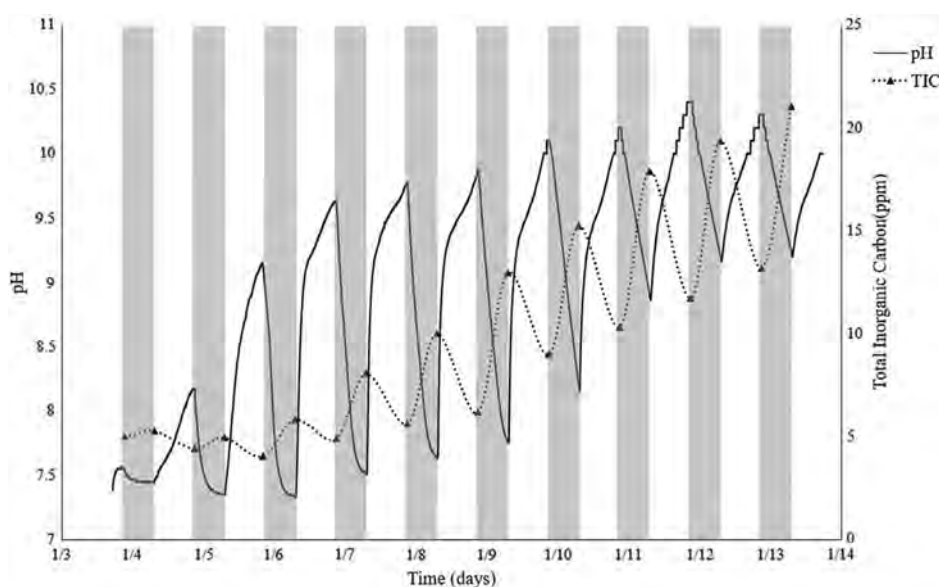


**Figure 1.** Photoduced pH behavior of BG-11 trials. Shaded areas denote lights off.



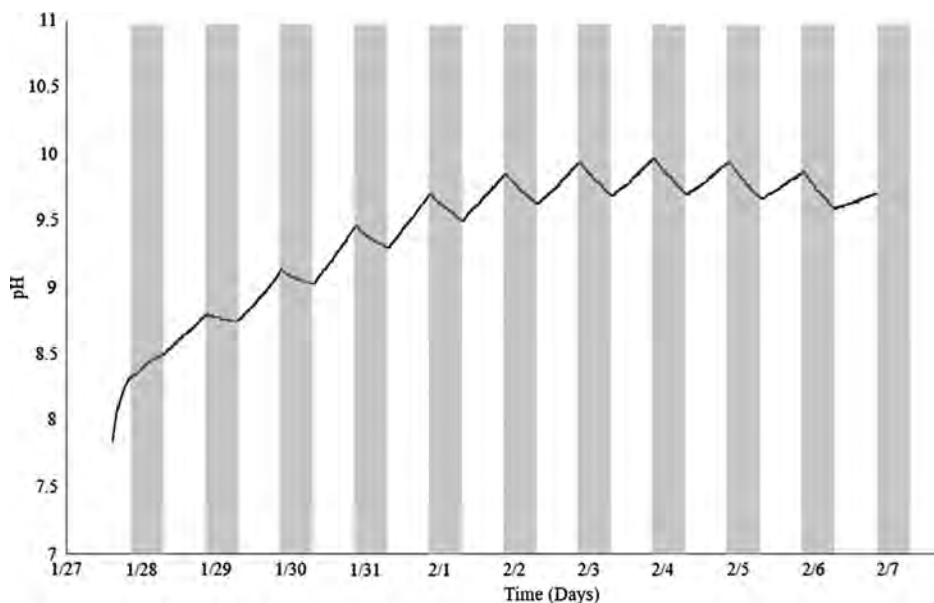


**Figure 2.** Photoinduced pH behavior of buffered ( $1 \text{ g L}^{-1} \text{ NaHCO}_3$ ) BG-11 media. Shaded areas denote lights off.

In addition to an ammonia control, an NaOH control was performed to determine whether the inorganic carbon was originating from algae or another source. NaOH was dosed into the raceways with 50 L of BG-11 media without microalgae inoculation. By the end of these control experiments, TIC reached an average of 14 ppm in the raceways. This indicated that the inorganic carbon the microalgae were utilizing was entirely from atmospheric concentrations of  $\approx 412 \text{ ppm}$  and reaction with  $\text{OH}^-$ . This was further proven by the fact that TIC did not accumulate in BG-11 medium that was not dosed with NaOH. Conversely, this indicates that a significant portion of the pH decline in the night is due to uptake of atmospheric  $\text{CO}_2$ , not

just respiration. Mainly, pH decline at night is caused by the reaction of atmospheric  $\text{CO}_2$  with  $\text{OH}^-$  and  $\text{H}_2\text{O}$  from a weak base,  $\text{HCO}_3^-$ , or an acid,  $\text{H}_2\text{CO}_3$ .

Figure 1–4 show the results of single experiments. However, primary experiments such as algal pH oscillations in BG-11 and TIC-enriched media were replicated eight times. As shown in **Table 1**, relative standard deviations and averages were recorded for all 16 experiments. The pH stayed reliably consistent throughout experimentation. Values of the pH maxima and minima were within a standard deviation of 3%. Values of the pH maxima and minima for the buffered solution remained with a standard deviation of 1%. Growth had more error than pH.

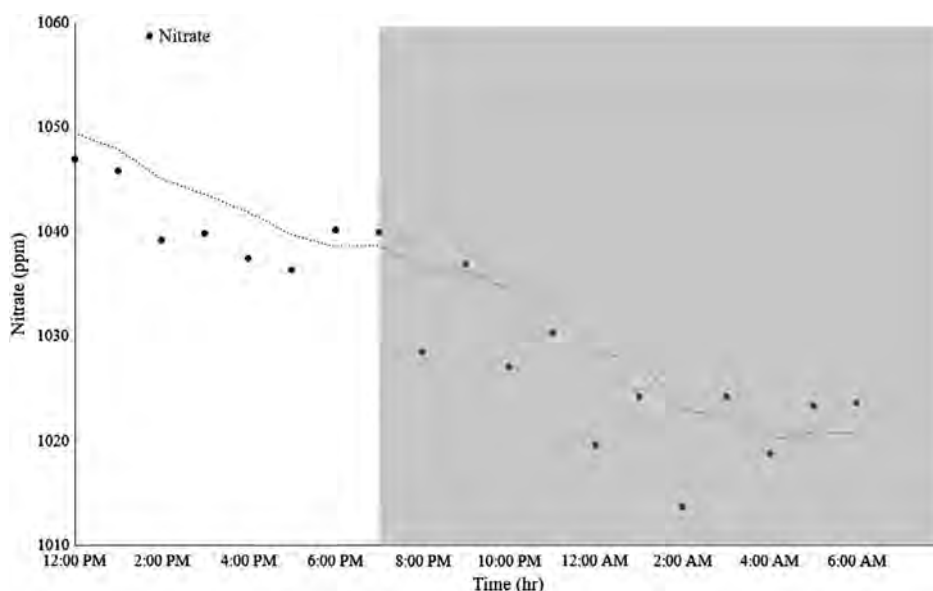


**Figure 3.** Eighteen hour study of each hour uptake of nitrate in BG-11 algae medium. Shaded areas denote lights off.

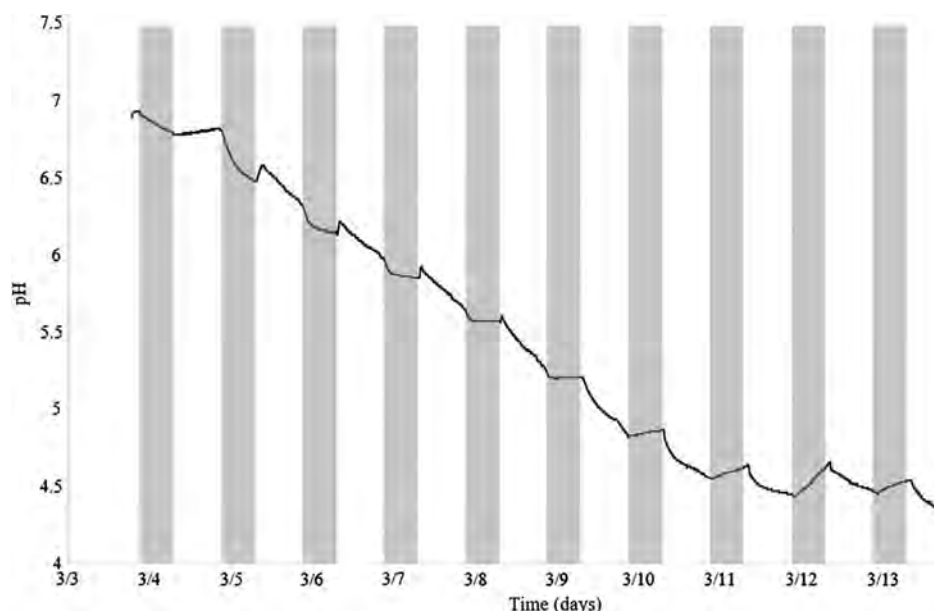


**Figure 4.** Photoinduced pH behavior with ammonia stoichiometrically placed as the nitrogen source as opposed to nitrate. Shaded areas denote lights off.

**Table 1.** A table of standard deviation (SD) of various important experimental parameters.

	pH maxima (BG-11)	pH minima (BG-11)	Max growth (BG-11)	pH maxima (buffered)	pH minima (buffered)	Max growth (buffered)	TIC increase (BG-11)	TIC increase (enriched)
Relative SD [%]	2.1	2.6	14	0.82	0.84	25	10	18
Average	–	–	140 mg L <sup>-1</sup>	–	–	78 mg L <sup>-1</sup>	10 ppm	28 ppm

It is possible this is derived from the fact that the spectrophotometric method intrinsically has an  $\approx 10\%$  error.<sup>[19]</sup>

### 3. Discussion

The objective of these experiments was to determine the potential of using the photoinduced pH behavior of microalgae as an analytical proxy for photosynthesis in controlled systems. The study also considers applications to carbon capture, conductivity, and quantum biology.

#### 3.1. Mathematical Modeling

pH oscillatory behavior is a readily identifiable marker of microalgae in systems large and small. As microalgae and cyanobacteria are the only photosynthesizers in water, an inexpensive pH probe may be used to identify whether microalgae are present. Although more research is required, if an understanding of water buffering and light–dark scheduling is achieved, a relationship could be proposed between photoinduced pH behavior and algal concentration or growth. Although such a model may be highly approximate, it could be applied to a vast array of systems—ranging from streams to lakes and oceans. This model

could even be applied to harmful algal blooms to indicate the onset of the bloom.<sup>[20]</sup> Nitrate is a major pollutant causing these blooms; therefore, similar behavior to what was displayed in the reported controlled experiments might be expected. Alternatively, the growth model could be applied to test the health of watershed streams as microalgae play an important role in many water-related ecological systems.<sup>[21]</sup> In kind, pH mathematical modeling could be applied to controlled industrial systems.

#### 3.2. Carbon Capture

For controlled systems, the understanding of pH oscillations could be useful for many areas. An area of special importance is carbon capture. The main requirement of algal photosynthesis is access to soluble carbon. One finding from analysis of photoinduced pH oscillation data is the dependence of pH on capturing of atmospheric carbon. In terms of chemical kinetics, the high pH at the days' end enhanced the uptake of CO<sub>2</sub> in the air with the basic media.<sup>[14]</sup> The provision of OH<sup>-</sup>, in the meantime, is provided by the normal metabolic function (reduction of nutrients) by the microalgae during the day.<sup>[10]</sup> This cycle, unique to microalgae, is a major process by which they attain their carbon source.

Due to capture of atmospheric  $\text{CO}_2$ , a buffer began to form in the medium as shown by the general increase of TIC in Figure 1. This buffer in both experimental cases, BG-11 and enriched, eventually caused the microalgae growth to plateau, or in some cases decrease. Other experiments have shown that a buffer forms, although without dynamic detail.<sup>[10–12]</sup> The metabolism of the microalgae is such that there is no clear regulation of  $\text{NO}_3^-$  uptake. This behavior is shown in Figure 3, where the microalgae uptake  $\text{NO}_3^-$  even at night. The buffer ultimately results in high values of pH minima and even though nutrients are in excess, microalgae growth stops. A common procedure in the algae industry is to “sparge” high-concentration  $\text{CO}_2$  air into the media to increase mass transfer and  $\text{CO}_2$  reaction with the water.<sup>[21]</sup> However, the chemical equilibria suggest this will eventually lead to a buffer, which will lead to algal decline.<sup>[12]</sup> Once formed, the buffered media must be either treated or drained and replaced—both expensive options. To prevent the economic loss of these options, the biochemical equilibria of the algal metabolism must be controlled.<sup>[11]</sup>

Some success has been achieved by mixing ratios of ammonia and nitrate to balance the pH oscillations. However, more research is required. Another possibility is not to use inorganic carbon. Instead organic carbon, such as acetate, can be directly incorporated into the algal metabolism without the need for reduction (and excretion of  $\text{OH}^-$ ).<sup>[22,23]</sup> Ultimately, this research suggests the most economical algae system that incorporates inorganic carbon would be one that incorporates balanced pH control from the metabolism which hybridizes passive carbon capture approaches from atmospheric  $\text{CO}_2$ , not pressurized  $\text{CO}_2$  sparging.

### 3.3. Biophotovoltaics

Biophotovoltaics use microalgae photosynthesis, particularly from photolysis outside the algae cell wall, to produce electricity.<sup>[6]</sup> For reference, a photograph of an open-air algae

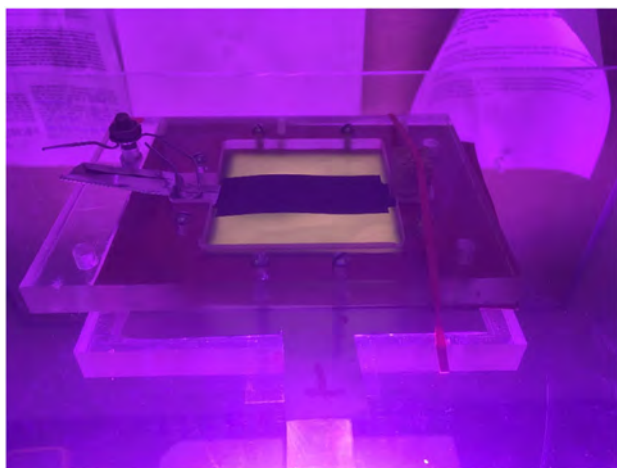


**Figure 5.** Photograph of an open-air algal biophotovoltaic device. The electrochemical cell is made complete by a platinum-dosed carbon anode (black film on top) and a transparent indium tin oxide anode connected to the algae film below the cathode. The photograph was taken by the authors, all rights reserved.

biophotovoltaic device is shown in **Figure 5**. Small electrochemical devices such as algal biophotovoltaics are sensitive to pH oscillation. Just as for carbon capture, a biochemical pH balance is required; otherwise a buffer may form and cause decline on the algae biofilm. The oscillatory behavior, if controlled, can increase conductivity in biophotovoltaics and improve electricity generation. Future biophotovoltaics could incorporate algal nutrients to balance the metabolism and provide enough surface area for  $\text{CO}_2$  mass transfer. This research did not use a biophotovoltaic device as the bioreactor system for experimentation. Rather raceways were used to acquire a general understanding of pH dynamics previously unreported. If the pH oscillatory behavior was studied in a biophotovoltaic cell, special study of biofilm suspension, the impact of irradiance levels on carbon capture and power generation as well as accumulation of  $\text{HCO}_3^-$  (buffering) could elucidate important underlying mechanisms for optimization. These areas have been studied before, but not with a focus on pH dynamics.<sup>[24,25]</sup>

### 3.4. Photosynthesis

In both experiments, BG-11 and buffered, pH change was inextricably tied to photoresponse, although, depending on the chemical kinetics, if buffered, a “saw-tooth” pH oscillation may be opposed to one that is more exponential. The complementary oscillatory behavior of TIC, mostly  $\text{HCO}_3^-$ , with the pH behavior is highly indicative of photosynthetic processes.<sup>[6]</sup> Photosynthesis is the primary process in algae that metabolizes  $\text{HCO}_3^-$ .

A major step forward in quantum biology will be connecting the atomic impacts of quantum mechanics with the macroscopic physiological “real world.”<sup>[8]</sup> The sensitivity of algal photosynthesis to external pH may provide a simple method to study the degree to which far more sensitive complex quantum mechanical processes impact the efficiency of photosynthesis. It has become clear from both experimental and theoretical research that there is a high probability that photosynthesis uses quantum mechanical processes such as coherence to improve charge transfer efficiency.<sup>[6–8]</sup> However, experiments are planned to determine whether quantum mechanical properties improve the overall growth and functioning of organisms, which could include comparing two mutants with various charge-separation efficiencies and disrupted resonances (therefore spatially separated and non-quantum mechanical).<sup>[8]</sup> Growth is correlated with photosynthetic efficiency, but as this research has shown, pH has a far more sensitive and instantaneous connection to photosynthesis and metabolism. In addition, early mutants will likely be inept to robust growth.<sup>[7,8]</sup> Therefore, growth would not be an effective output to consider in early trials. Future experiments could use pH as a rapid physiological response, in a matter of seconds, to determine quantum efficiencies of mutants and help determine whether quantum mechanics is effective in photosynthesis.

## 4. Conclusion

This study describes and explains photoinduced pH oscillatory phenomena of microalgae with remarks on applications. Microalgae photosynthesis initiates a cycle of reduction of nutrients to capture atmospheric carbon for future

photosynthesis and growth. This biochemical process can be displayed by inexpensively recording pH oscillations in the external medium. Modeling of this process could provide a basic method for algae growth in large or rural systems such as in watersheds or for harmful algae blooms. In controlled systems, the biochemical equilibria of the photosynthetic cycle of industrial algae applications may suffer from buffering and ultimately uneconomical draining of systems or inefficient CO<sub>2</sub> mass transfer. Most interesting of all may be the unique connection and rapid sensitivity external pH has to photosynthesis and metabolism in algae with application to analytical methods for better understanding quantum photosynthetic processes.

## 5. Experimental Section

**Experimental Design:** *Chlorella* sp. was extracted from a 300 L photobioreactor at the Institute for Sustainable Energy and the Environment (ISEE) at Ohio University. The photobioreactor was originally cultured with a microalgae blend of *Chlorella* sp. from Clearas Water Inc. The culture's DNA was sequenced and verified to be *Chlorella* sp. For each experiment, the microalgae were collected in 1 L flasks and allowed to settle for 24 h. Then the microalgae were cultured in 50 L BG-11 (ATCC medium: 616 Medium BG-11 for blue-green algae) in raceways. BG-11 was prepared within the raceways by the addition of 50 L deionized (DI) water followed by the dissolution of nutrients. pH was reduced to 7.1 by the addition of 0.1 M of hydrochloric acid. BG-11 was used as opposed to a freshwater media (such as Bold's Basal) to track the pH interaction of algae in a high-NO<sub>3</sub><sup>-</sup> medium. The medium was not autoclaved due to the scale of the experiment.

Micro bio RM 0.5 raceways were enhanced to control variables associated with raceway algal cultivation. "Raceway" refers to the vessel holding and circulating the algae. Raceways are open-air and have a divider in the middle to keep media flowing continuously in a circular motion. The raceway system was housed inside a temperature-controlled laboratory set to an ambient temperature of 25 °C. The raceway paddlewheels rotated at 35 RPM during experimentation to gently but continuously circulate the algae. A DI water evaporation system was designed to maintain the desired water level. The temperature of each medium was maintained at 25 °C by means of immersed electric heaters.<sup>[15]</sup> Viparspectra V450 grow lights were used as light sources stationed 26 in. above the raceway surface water. The light cycle protocol was 14 h with lights on and 10 with lights off. Blue light was used due to its enhanced long-term growth effects.<sup>[16]</sup> Raceways were divided by reflective barriers that ensured minimal light overlap. An Aqua Controller APEX system was programmed to control the evaporation system and electric heaters. The APEX recorded pH at 5 min intervals to obtain sufficient oscillatory data. pH probes were calibrated at the end of every 10 day trial and soaked in 0.4 M HCl to remove any organic residue.

Trials were performed over an ≈2 month period. Sixteen main trials were performed—eight trials under BG11 conditions and another eight trials under BG11 conditions with NaHCO<sub>3</sub> enrichment to 1 g L<sup>-1</sup> batch. Control trials were performed under four separate sets of conditions over eight trials to reinforce the main experiment. Many of the control experiments had already been observed in the literature, so the individual trial quantity was reduced to a repetition of two instead of eight. These control trials included testing: 5 day total inorganic carbon (TIC) change when DI water was artificially alkalized via NaOH dissolution, TIC change when BG11 was prepared without biologicals, NO<sub>3</sub><sup>-</sup> change over the same 10 day experimental procedure, and TIC change with ammonium (NH<sub>4</sub>Cl) as a nitrogen source.

**Analytical and Experimental Methods:** The biomass concentration was estimated by optical density using a HACH DR 6000 spectrophotometer.<sup>[19]</sup> A calibration curve for estimating biomass concentration was obtained by weighing dry microalgae grown under the same experimental parameters. The absorbance was plotted versus dry biomass concentration and a calibration curve was developed. A wavelength of 750 nm

was used as chlorophyll affects absorbance minimally at this wavelength. Biomass concentration was estimated using Equation (2).

$$\text{biomass}(\text{mg L}^{-1}) = 1482.3 \times \text{OD}_{750} \quad (2)$$

Here, biomass is the concentration of microalgae in mg L<sup>-1</sup> milligrams per liter and OD<sub>750</sub> is the absorbance of light at wavelength  $\lambda = 750$  nm.

Irradiance was measured in quantum units of photosynthetically active radiation (PAR). A Stellar Net Spectroradiometer PS-200 was used to measure the PAR and spectral graph associated with each raceway. The PAR was recorded at the center of each raceway an inch away from the center paddlewheel axial. The PAR for each raceway was ≈160 μmol photons m<sup>-2</sup> s<sup>-1</sup>. Light was not evenly spread across all surface media; however, the PAR was consistent for each raceway.

A Shimadzu TOC-VWP Total Organic Carbon Analyzer was used to estimate changes in TIC levels in the raceway medium over the 10 day cultivation period. Measurements were made before microalgae were introduced to the medium and after 10 days of cellular growth to estimate the amount of TIC utilized by the algae during their growth. Samples were centrifuged, and the upper layer solution was filtered to remove microalgae before analysis.

For control trials, Ionic Chromatography (IC) analysis was used to measure the decrease in NO<sub>3</sub><sup>-</sup> over the 10 day cultivation period. Samples were extracted from the raceways 15 min before lights turned on and 15 min before lights turned off to see metabolic function as a function of light. Samples were centrifuged at 3750 RPM and filtered. Following these steps, the samples were kept in centrifuge tubes, blown with nitrogen gas, and wrapped with parafilm. The samples were then placed in refrigeration. IC analysis was later undertaken when the trial was finished. Inductively coupled plasma (ICP) spectroscopy was used to determine whether any undesired contaminating metals may have affected inorganic uptake by an alkaline medium.

## Acknowledgements

This article is dedicated to E.T.D. to my father in honor of his 60th birthday, for both his scholarly and family achievements. Many thanks to the whole team at the Institute for Sustainable Energy and the Environment. The authors thank Prof. Martin Kordesch for his insight on electrodynamics, Dr. Wen Fan, and David Ogden. Special thanks to Ahmad Abu-Hajer for his tireless help with this project.

## Conflict of Interest

The authors declare no conflict of interest.

## Data Availability Statement

The data that support the findings of this study are available from the corresponding author upon reasonable request.

## Keywords

algae, biophotovoltaics, nitrate metabolism, pH control, quantum photosynthesis

Received: August 31, 2020

Revised: January 19, 2021

Published online: February 24, 2021

[1] M. L. Parry, C. Rosenzweig, A. Iglesias, M. Livermore, G. Fischer, *Global Environ. Change* **2004**, *14*, 53.



- [2] I. Andrić, J. Fournier, B. Lacarrière, O. Le Corre, P. Ferrão, *Energy* **2018**, 150, 926.
- [3] A. J. Garner, M. E. Mann, K. A. Emanuel, R. E. Kopp, N. Lin, R. B. Alley, B. P. Horton, R. M. DeConto, J. P. Donnelly, D. Pollard, *Proc. Natl. Acad. Sci. USA* **2017**, 114, 11861.
- [4] J. M. Luther, J. C. Johnson, *Nature* **2019**, 571, 38.
- [5] L. A. Lewis, R. M. McCourt, *Am. J. Botany* **2004**, 91, 1535.
- [6] *Biophotoelectrochemistry: From Bioelectrochemistry to Biophotovoltaics* (Ed: L. J. C. Jeuken), Springer International Publishing, Cham, Switzerland **2016**.
- [7] N. Keren, Y. Paltiel, *Trends Plant Sci.* **2018**, 23, 497.
- [8] Quantum Design of Photosynthesis for Bio-Inspired Solar-Energy Conversion | Nature, <https://www.nature.com/articles/nature22012> (accessed: January 2020).
- [9] Y. Shiraiwa, A. Goyal, N. E. Tolbert, *Plant Cell Physiol.* **1993**, 34, 649.
- [10] J. Wang, W. R. Curtis, *J. Appl. Phycol.* **2016**, 28, 43.
- [11] J. Wang, T. Rosov, P. Wensel, J. McGowen, W. R. Curtis, *Algal Res.* **2016**, 18, 288.
- [12] M. L. Scherholz, W. R. Curtis, *BMC Biotechnol.* **2013**, 13, 39.
- [13] A. Juneja, R. M. Ceballos, G. S. Murthy, *Energies* **2013**, 6, 9.
- [14] M. Sheng, C. Xie, B. Sun, Y. Luo, L. Zhang, G. Chu, H. Zou, J.-F. Chen, *Ind. Eng. Chem. Res.* **2019**, 58, 11082.
- [15] B. R. Glick, J. J. Pasternak, C. L. Patten, *Molecular Biotechnology: Principles and Applications of Recombinant DNA*, 4th ed., ASM Press, Washington, DC **2009**.
- [16] J. A. Raven, C. J. Gobler, P. J. Hansen, *Harmful Algae* **2020**, 91, 101594.
- [17] W. A. Wurts, R. M. Durborow, *Interactions of pH, Carbon Dioxide, Alkalinity and Hardness in Fish Ponds*, Report No. 464, Southern Regional Aquaculture Center, Stoneville, Miss. **1992**.
- [18] L. Gonzalez Olias, P. J. Cameron, M. Di Lorenzo, *Front. Energy Res.* **2019**, 7, 105.
- [19] M. J. Griffiths, C. Garcin, R. P. van Hille, S. T. L. Harrison, *J. Microbiol. Methods* **2011**, 85, 119.
- [20] W. W. Carmichael, G. L. Boyer, *Harmful Algae* **2016**, 54, 194.
- [21] H. Paerl, J. Dyble, J. Pinckney, L. M. Valdes, D. F. Millie, P. H. Moisander, J. T. Morris, D. Bendis, M. F. Pieler, in *Estuarine Indicators* (Ed: S. Bortone), CRC Press, Boca Raton, FL 2004, pp. 145–174.
- [22] K. McCaughy, A. Abu Hajer, E. Drabold, D. Bayless, M. T. Reza, *Sustainability* **2019**, 11, 3454.
- [23] M. Prathima Devi, S. Venkata Mohan, *Bioresource Technol.* **2012**, 112, 116.
- [24] F.-L. Ng, M. M. Jaafar, S.-M. Phang, Z. Chan, N. A. Salleh, S. Z. Azmi, K. Yunus, A. C. Fisher, V. Periasamy, *Sci. Rep.* **2014**, 4, 7562.
- [25] C.-H. Thong, S.-M. Phang, F.-L. Ng, V. Periasamy, T.-C. Ling, K. Yunus, A. C. Fisher, *Energy Sci. Eng.* **2019**, 7, 2086.

# Ab Initio Hydrogen Dynamics and the Morphology of Voids in Amorphous Silicon

Parthapratim Biswas\* and Dil Limbu

Dedicated to Professor David A. Drabold on the occasion of his 60th birthday

This article presents an ab initio study of hydrogen dynamics inside nanometer-size voids in amorphous silicon (*a*-Si) within the framework of the density-functional theory for a varying hydrogen load of 10–30 atoms per void at the low and high temperature of 400 and 700 K, respectively. Using the local density approximation (LDA) and its generalized-gradient counterpart (GGA), the dynamics of hydrogen atoms inside the voids are examined with an emphasis on the diffusion of H atoms/molecules, and the resulting nanostructural changes of the void surfaces. The results from simulations suggest that the microstructure of the hydrogen distribution on the void surfaces and the morphology of the voids are characterized by the presence of a significant number of monohydride Si–H bonds, along with a few dihydride Si–H<sub>2</sub> configurations. The study also reveals that a considerable number (about 10–45 at%) of total H atoms inside a void can appear as H<sub>2</sub> molecules for a hydrogen load of 10–30 H atoms per void. The approximate shape of the voids is addressed from a knowledge of the positions of the void-surface atoms using the convex-hull approximation and the Gaussian broadening of the pseudoatomic surfaces of Si and H atoms.

*a*-Si:H is altered by the light-induced creation of metastable defect states, known as the Staebler–Wronski effect (SWE),<sup>[4]</sup> which adversely affects the performance of *a*-Si:H-based solar cells. Nuclear magnetic resonance (NMR) studies<sup>[5]</sup> on *a*-Si:H samples have indicated that the motion of H atoms, which are produced by the light-induced breaking of Si–H bonds, plays an important part in recovering the photovoltaic stability of the affected *a*-Si:H samples upon annealing at 350–400 °C.<sup>[6]</sup> Thus, an understanding of the motion of H atoms in *a*-Si in the presence of inhomogeneities is of crucial importance to address the photovoltaic stability of *a*-Si:H upon light irradiation.


Although a number of earlier theoretical/computational studies on the microstructure of the hydrogen distribution in *a*-Si:H<sup>[7–12]</sup> have focused on the silicon–hydrogen bonding configurations in the

bulk environment of *a*-Si and their effects on structural, electronic, and optical properties of the material, there exist only a few computational studies that directly address the role of non-bonded hydrogen (NBH) and voids on the network structure of *a*-Si:H.<sup>[10,13,14]</sup> Sekimoto et al.<sup>[15]</sup> have recently shown experimentally that the presence of large amount of NBH (e.g., H<sub>2</sub> molecules inside voids) can broaden the vacancy-size distribution and enhance the size of the optical gap in *a*-Si.<sup>[16]</sup> The mass density of *a*-Si:H has been also found to be somewhat dependent on the number of NBH, and therefore on the distribution of hydrogen inside nanometer-size voids. Following our recent study on the temperature-induced nanostructural evolution of voids in *a*-Si and its effect on the intensity of small-angle X-ray scattering (SAXS),<sup>[11]</sup> the present study focuses on accurate calculations of the atomistic dynamics of hydrogen inside voids obtained from the density-functional theory (DFT). The emphasis here is on the dynamical aspects of hydrogen motion inside voids on the timescale of several picoseconds at low and high temperatures in the environment of a varying hydrogen concentration. The formation and dissociation of Si–H bonds on the surface of voids are discussed from a kinetic point of view. The movement of H atoms inside nanometer-size voids and its resulting effects on the hydrogen microstructure and the reconstruction of the void surfaces are also addressed here. The presence of voids in the amorphous matrix suggests that, for an accurate

## 1. Introduction

Hydrogen plays an important role in the electronic and optical properties of amorphous silicon (*a*-Si).<sup>[1]</sup> Although the presence of a small amount (about 6–12 at%) of hydrogen in *a*-Si is particularly beneficial for producing device-grade samples of *a*-Si:H, via passivation of coordinating defects (e.g., threefold-coordinated Si atoms or dangling bonds), the presence of too much hydrogen in *a*-Si can be detrimental to the electronic and optical properties of *a*-Si:H-based devices. Thin films of *a*-Si:H are often used for surface passivation of crystalline silicon, which is useful for the generation of high open-circuit voltages in silicon-heterojunction solar cells.<sup>[2]</sup> A relatively high hydrogen content, in void-rich environment of *a*-Si:H, is preferred for this purpose to achieve high-quality *a*-Si:H/*c*-Si interfaces,<sup>[3]</sup> indicating the benevolent role of H in *a*-Si. By contrast, the structure of

Prof. P. Biswas, D. Limbu  
 Department of Physics and Astronomy  
 The University of Southern Mississippi  
 Hattiesburg, MS 39406, USA  
 E-mail: partha.biswas@usm.edu

 The ORCID identification number(s) for the author(s) of this article can be found under <https://doi.org/10.1002/pssb.202000494>.

DOI: 10.1002/pssb.202000494

determination of the motion of H atoms within a void, one must take into account the inhomogeneities in the electronic charge distribution in the vicinity of the void surface. The standard protocol in DFT calculations advises us to address the problem by computing the self-consistent-field (SCF) solution of the Kohn–Sham (KS) equation, and the presence of voids suggests that the generalized-gradient approximation (GGA) should be used to deal with the density fluctuations near the void surface. We shall therefore address the problem using the GGA and compare the results with those from the local density approximation (LDA). The presence of weak dispersion forces, which are usually included via the van der Waals corrections, is not taken into account in this article due to the computational complexity of the problem and the somewhat limited accuracy of local basis functions used in our work.

The rest of the article is organized as follows. Section 2 provides a short description of the method for generating *a*-Si models with hydrogenated voids, using the Wooten–Winer–Weaire (WWW) method and ab initio molecular-dynamics (AIMD) simulations. The results are discussed in Section 3, with an emphasis on the dynamics of H atoms inside voids and the resulting microstructure of the hydrogen distribution on the void surface for a varying number of hydrogen atoms. A discussion on the kinetics of Si–H bond formation and dissociation and the shape of the voids is also provided in this section. This is followed by the conclusions of the study in Section 4.

## 2. Computational Method

For AIMD simulations of hydrogen dynamics inside voids in *a*-Si, we started with four independent 1000-atom models of *a*-Si, obtained from the WWW method.<sup>[17,18]</sup> A spherical void of radius 5 Å was created at the center of each model and the geometry of the resulting structure was thoroughly relaxed, using the first-principles density-functional code SIESTA.<sup>[19]</sup> A number of models with a hydrogenated void were then produced by adding 10, 20, and 30 H atoms inside the central cavity so that the mass density of the final models was about  $2.22 \text{ g cm}^{-3}$ . A single void of radius 5 Å corresponded to a number density of void of  $4.82 \times 10^{19} \text{ cm}^{-3}$  and a void-volume fraction of 2.52%, which were close to the values reported in experiments.<sup>[20,21]</sup> The H atoms were initially distributed in such a way that they were at a distance of at least 2 Å from Si atoms and 1 Å from each other. The silicon atoms within the spherical region of radius between 5 and 8 Å from the center of the voids were labeled as the void-surface atoms for the analysis of the void surface upon annealing and total-energy optimization of the systems.<sup>[22]</sup>

To study hydrogen diffusion and the microstructure of hydrogen distribution on the void surfaces, AIMD simulations were performed at 400 and 700 K to examine the temperature dependence of H dynamics and the resulting effects on the morphological structure of the void surfaces, using the density-functional code SIESTA. SIESTA employs local basis functions, based on numerical pseudoatomic orbitals,<sup>[23]</sup> and the norm-conserving Troullier–Martins pseudopotentials<sup>[24]</sup> to obtain the SCF solutions of the KS equation in the density-functional theory. Electronic and exchange correlations between electrons were taken into account via the LDA and the GGA, by using

the Perdew–Zunger<sup>[25]</sup> and the Perdew–Burke–Ernzerhof (PBE)<sup>[26]</sup> parameterizations for the LDA and the GGA, respectively. Due to the computational complexity of the problem involving a large number of atoms and the necessity for simulating a reasonably long-time dynamics for studying the diffusive behavior of H atoms, using the SCF solution of the KS equation, the AIMD simulations were conducted using the single-zeta (SZ) basis functions for Si atoms and the double-zeta-polarized (DZP) basis functions for H atoms. The high computational cost associated with the calculation of total energy and forces restricted us to use SZ basis functions for Si atoms during the course of MD simulations. The subsequent total-energy optimizations, however, were conducted using the double-zeta (DZ) basis functions for Si atoms until the total force on each atom was less than or equal to  $5 \times 10^{-3} \text{ eV Å}^{-1}$ . During AIMD simulations, the temperature of the system was controlled by using the Nosé thermostat,<sup>[27]</sup> and a time step of 0.8 fs was used to ensure that the movement of light H atoms can be described accurately at a high temperature of 700 K. The evolution of the system was monitored and recorded for a total time of 20 ps. The simulation procedure was repeated for each of the four independent models, indicated by M1 to M4, with a central void for a hydrogen load of 10, 20, and 30 H atoms per void. In each case, we have used a different random distribution of H atoms within the void to gather as much as statistics as possible. The final results were obtained by averaging over the four independent configurations.

## 3. Results and Discussion

### 3.1. Hydrogen Dynamics Inside Voids in *a*-Si

In this section, we discuss results from the density-functional calculations for studying the dynamics of H atoms/molecules inside voids in *a*-Si. To this end, we mostly focus on those H atoms/molecules which are within the cavity during the entire course of simulations at a low and high temperature of 400 and 700 K, respectively. **Figure 1** shows the time evolution of the average number of H atoms (molecules included) within a void-surface region of radius 8 Å at 400 and 700 K. The results correspond to two different values of the hydrogen load, 10 and 30 H atoms per void, and are obtained by averaging over four independent voids/models using the LDA and GGA. At 400 K, the great majority of H atoms stayed within the void, with the exception of one or two H atoms that left the void-surface region of radius 8 Å. The LDA and GGA dynamics exhibit a more or less similar behavior at a given temperature, although the GGA tends to knock out one or two more H atoms outside the cavity for high H loads at 700 K. Despite limited statistics, it would not be inappropriate to conclude that, on average, the LDA and GGA do not differentiate much as far as the (average) number of H atoms leaving the voids at 400 K is concerned.

To study the effect of the hydrogen load on the mean-square displacement (MSD) of H atoms at low and high temperature, of 400 and 700 K, respectively, we have examined the variation of the MSD with time for 10, 20, and 30 H atoms per void using the GGA. Once again, the results were obtained by averaging over four independent voids and are shown in **Figure 2**. The results (in Figure 2) lead to the following observations. First,

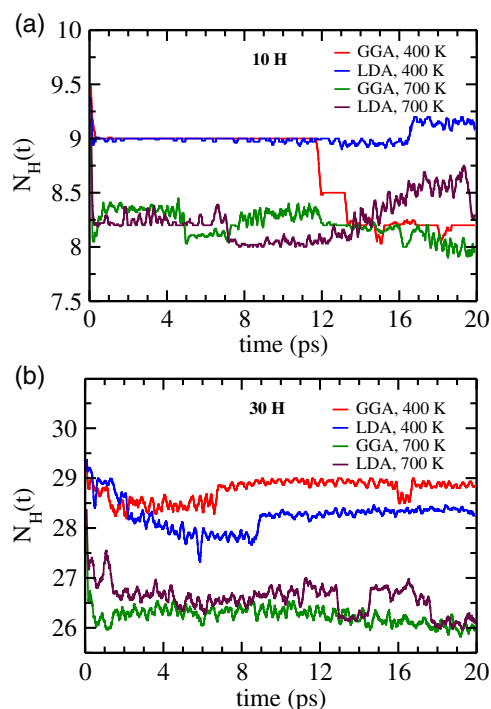


**Figure 1.** The time evolution of the average number of H atoms (including  $\text{H}_2$  molecules) within a void at 400 and 700 K. The results correspond to a hydrogen load of: a) 10 H atoms per void; b) 30 H atoms per void. The average is taken over four voids for each temperature from independent simulations.

the MSD of H atoms decreases with an increasing presence of H atoms within the voids. This is particularly so as the hydrogen load increases from 10 to 30 H atoms per void. This reduction in the MSD is due to the decrease in the average distance between any two H atoms within the cavity for an increasing presence of hydrogen within the same volume. Second, the sharp rise of the MSD for a hydrogen load of 10 H atoms per void near 12 ps at 400 K can be attributed to a hydrogen atom leaving the void. For a hydrogen load of 10 H atoms per void, H atoms can move a bit more freely than those with a load of 20 or 30 H atoms per void. This makes it possible for few H atoms to diffuse rapidly in the vicinity of the void surface, and eventually to escape the void region—and the simulation cell in one or two cases—depending upon the temperature of the system. In contrast, the presence of too many H atoms for a high value of H load can impede the diffusion process and thus reduces the MSD at a given temperature. Third, the motion of H atoms is affected by the temperature of the system as well. This is evident in Figure 2b, where the MSD for a load of 20 H atoms per void was observed to increase at 700 K during 15–16 ps and it continued to remain so until the end of the simulation at 20 ps. This observation contrasts with the case of 30 H atoms per void at the same temperature, where none of the H atoms was found to leave the void but remained within a root-mean-square (RMS) distance of 5 Å from the center of the void. Finally, one may note that the available statistics do not permit us to comment on the dynamical behavior of few H atoms that diffuse out of the cavity

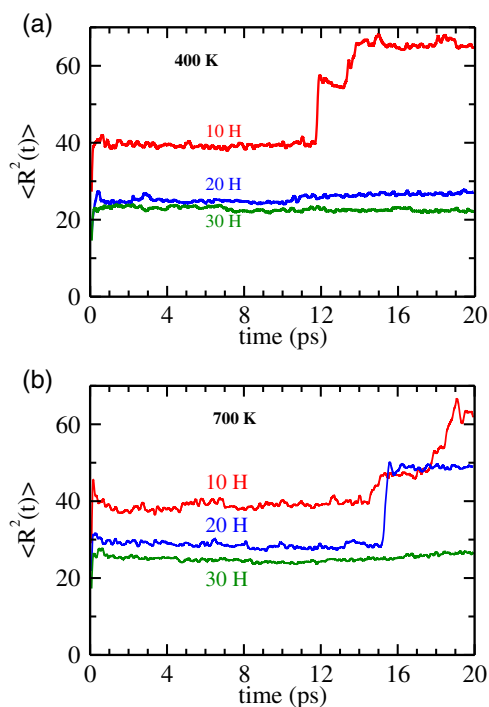


**Figure 2.** The variation of the MSD of H atoms, averaged over all hydrogen in four models, with time for three different hydrogen loads as indicated: a) 400 K; b) 700 K. The results were obtained from the SCF calculations with the GGA, and averaged over four independent voids for each H load and temperature.

at an earlier time (e.g., the H atom in Figure 2a for a hydrogen load of ten atoms per void), based on the results from four configurations. The movement of H atoms is driven by a combination of factors, such as the concentration of H atoms in a void, temperature, and the disorder in the atomic distribution on the void surface. Since we are not particularly interested in the dynamical behavior of few H atoms that escape the void-surface region of 8 Å, we will not discuss this further.

Having discussed the variation of the MSD with respect to the hydrogen load, we now address to what extent the exchange-correlation (XC) approximation may affect the motion of H atoms inside the voids as far as the MSD is concerned. Figure 3 shows the evolution of the MSD with time for a hydrogen load of 30 H atoms per void at 400 and 700 K. Since we are interested in the dynamics of H atoms inside the void, and the resulting hydrogen microstructure of the void surface, the MSD was computed using only those H atoms that were *inside* the void region of radius 8 Å for the entire duration of simulation. The plots in Figure 3 suggest that the LDA slightly overestimates the MSD (of H atoms) compared to the value obtained from its generalized-gradient counterpart. The RMS values of the displacement of H atoms inside the void in the LDA and the GGA at 400 K have been found to be about 4.5 and 4.15 Å, respectively. A more or less similar observation applies to the high-temperature dynamics at 700 K, as shown in Figure 3b. It thus appears that the MSD of the H atoms within the void is not particularly strongly affected by the XC approximation at 400 and 700 K.



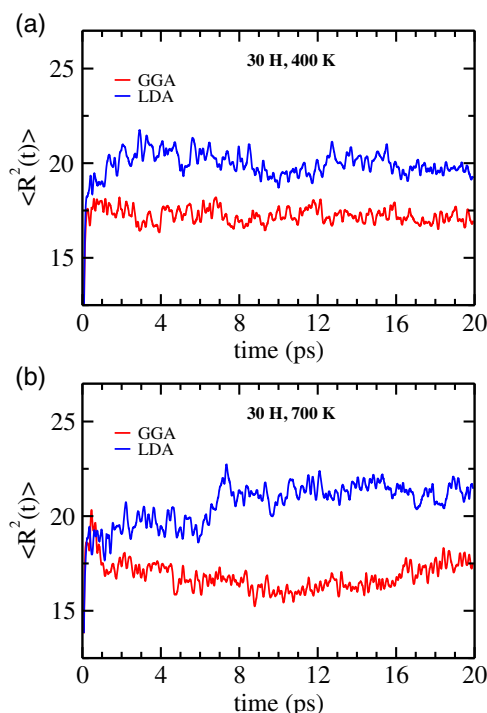


**Figure 3.** The time evolution of the MSD of H atoms *within* voids for a hydrogen load of 30 H atoms per void in the LDA (blue) and the GGA (red). The results for 400 and 700 K are shown in (a) and (b), respectively.

This is due to the fact that the majority of H atoms within a void reside as bonded hydrogen (BH) (to Si atoms) on the void surface, mostly in the form of Si–H configurations, and few Si–H<sub>2</sub> configurations, along with a few H<sub>2</sub> molecules within the cavity. Since the calculation of the MSD excludes a few mobile H atoms that have already left the void region, the remaining bonded H atoms show a more or less converged value of the MSD during the course of simulation. Thus, in a sense, a more or less converged value of the MSD (in Figure 3) is reflective of the distribution of bonded H atoms on the walls of the void. We shall see later that a slightly larger value of the MSD of H atoms that we observe here for the LDA case (see Figure 3) results from a minor expansion of the void surface in the LDA calculations. Following Sekimoto et al.,<sup>[15]</sup> one may conclude that the expansion originates from the stress on the void surface due to the presence of a significant number of Si–H bonds in the LDA calculations. Finally, it may be mentioned that the dihydride Si–H<sub>2</sub> configurations are found on the void surface at a distance, which is closer to the center of the void than their monohydride (Si–H) counterpart. **Figure 4** shows the average distances of the Si–H<sub>2</sub> and Si–H bonding configurations, which are located on the walls of the voids, from the center of the voids for the GGA at 400 K. This observation is consistent with the results reported by Kageyama et al.<sup>[28]</sup> from dielectric measurements.

We now briefly discuss the diffusion of a few highly mobile H atoms. Earlier in this section, we have seen that the MSD of H atoms can increase occasionally very rapidly for a hydrogen load of 10 H atoms per void. This behavior of the MSD has been

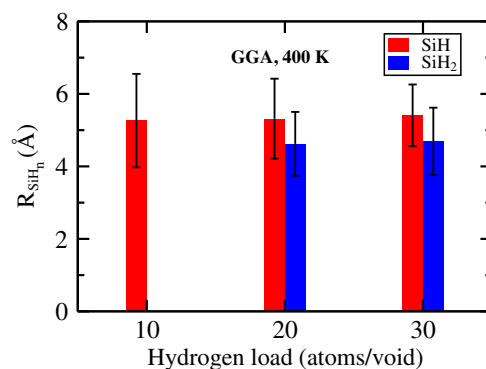


**Figure 4.** The average (radial) distance of SiH and SiH<sub>2</sub> bonding configurations from the center of the voids. The dihydride SiH<sub>2</sub> bonds have been found to form on the walls of the voids at a distance which is closer to the center of the void than their SiH counterpart.

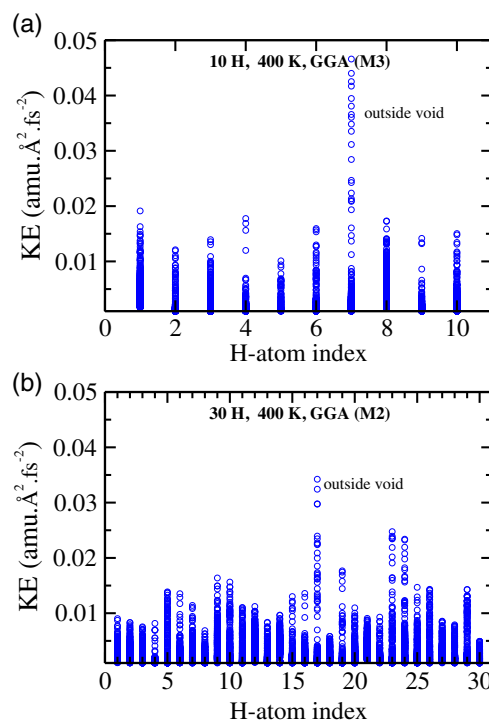


**Figure 5.** The instantaneous KE of H atoms in two voids (in models M2 and M3) at 400 K, obtained from the GGA. The results for the void with a hydrogen load of a) 10 H atoms per void, and b) 30 H atoms per void. The atoms with the largest KE, H7 (upper panel) and H17 (lower panel), are found to diffuse out of the void region. The range and the frequency of KE values are indicated by the numbers and shading (of blue circles) along the Y axis, respectively.

attributed to the movement of few H atoms out of the void region, defined by a sphere of radius 8 Å. It has been observed that such a steep rise of the MSD (see Figure 2a at 12 ps) originates from the high mobility of few H atoms inside the hydrogenated voids. **Figure 5** shows the plot of the instantaneous kinetic energy (KE) of H atoms at 400 K, obtained from using the GGA for a period 20 ps. The distribution of the KE values

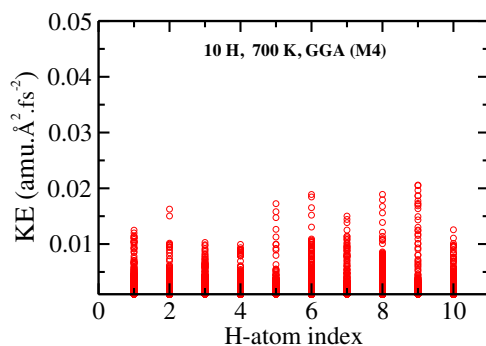


**Figure 6.** The distribution of KE along the Y axis for H atoms inside a void (in model M4) at 700 K. The range and the frequency of KE values are indicated by the numbers and shading (of red circles) along the Y axis, respectively.

along the Y axis for a given H atom indicates the range and the frequency of the KE of the atom during the course of AIMD simulations. An analysis of the real-space trajectory of the H atoms in the vicinity of the void region in models M2 and M3, and the results from Figure 5 revealed that a few highly mobile H atoms, such as H7 in Figure 5a and H17 in Figure 5b, left the void region sometime during the course of simulations. This observation was found to be true for other voids as well, where H atoms were observed to leave the void region due to their high KEs. Conversely, we have noted that all the H atoms in model M4 remained inside the void throughout the course of simulation even at the high temperature of 700 K. The results obtained from such a void is shown in **Figure 6**, where the KE values of the H atoms are found to be considerably lower than those shown in Figure 5.

### 3.2. Kinetics of Si–H Bond Formation and Dissociation on Void Surfaces of *a*-Si

We now address a question of considerable importance concerning the kinetics of Si–H bond formation and dissociation on the surface of voids in *a*-Si. Although a complete understanding of these events requires the knowledge of bond formation and dissociation energies, the problem can be addressed approximately by considering the KE of H atoms in AIMD simulations.

Earlier, in Figure 3, we have seen that the MSD of H atoms inside the voids fluctuates within the range of 17–22 Å<sup>2</sup>, depending upon the XC approximation. These values are indicative of the fact that the great majority of H atoms stay bonded to Si atoms on the void surface as the time evolution of the system continues. However, it has been observed that a few H atoms in Si–H bonds can break free of the surface and move through the cavity to form new Si–H bonds at nearby active Si sites. This behavior is particularly pronounced at 700 K for a hydrogen load of 30 H atoms per void, where the presence of few H atoms with high KE makes it possible to dissociate an existing Si–H bond and form a new Si–H bond in the vicinity of the void surface. This is shown in **Figure 7**, which shows the snapshots of two silicon–hydrogen bonding configurations obtained from the GGA at 3 and 18 ps. Figure 7a shows a set of four Si–H bonds,

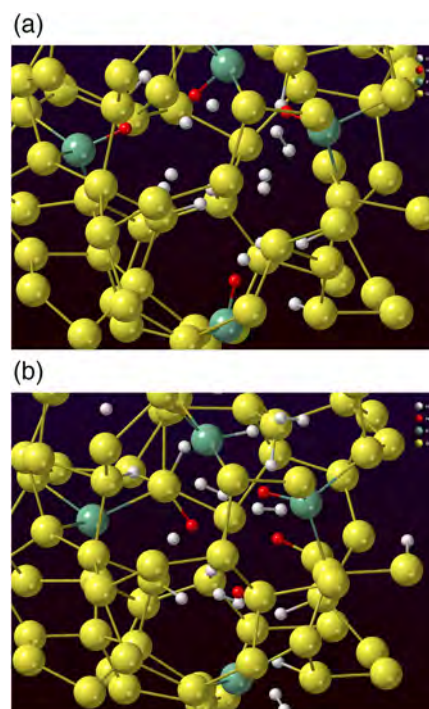


**Figure 7.** The kinetics of Si–H bond formation and dissociation at 700 K for a hydrogen load of 30 H atoms per void obtained from the GGA in model M4. a) The Si–H bonds that dissociated during MD simulations are shown as green–red pairs at 3 ps. b) The H atoms (red) resulted from the dissociation of SiH bonds diffused through the void-surface region to form new Si–H bonds, which are indicated as yellow–red pairs at 18 ps. The presence of a green–red pair suggests that the Si–H broke and formed again, but with another (dissociated) H atom.

involving H12, H16, H24, and H30, indicated as green–red pairs, at 3 ps, which are found to dissociate later during simulation. The breaking of Si–H bonds is reflected in Figure 7b, which shows that the H atoms (red) resulted from the dissociation of four Si–H bonds moved through the void and formed new Si–H bonds. The latter are shown as yellow–red pairs, with the exception of one where a dissociated H atom (red) is found to be bonded with an active Si site (green). The breaking of Si–H bonds at 700 K can be understood from a kinetic point of view. **Figure 8** shows the time evolution of the KE of two H atoms, H2 and H30, bonded to silicon atoms, Si40 and Si48, respectively, as monohydride Si–H bonds. As the simulation proceeds, the KE values fluctuate around the average translational KE value of  $3 k_B T/2$  at temperature  $T$ , where  $k_B$  is the Boltzmann constant. However, the large KE of H30 atom at around 5.5 ps, which is about three times larger than the average KE at 700 K, leads to a rupture of the Si–H bond and subsequent formation of a new Si–H bond with a silicon atom in the vicinity of the void. By contrast, H2 forms a stable Si–H bond due its low KE during time evolution. We have verified that the remaining three H atoms—H12, H16, and H24—exhibit a similar behavior as H30 as far as the KE values are concerned.

The dissociation of Si–H bonds due to the high KE of H atoms can be observed by tracking the silicon–hydrogen bond length of a dissociated pair (Si48, H30) with time. **Figure 9** shows the

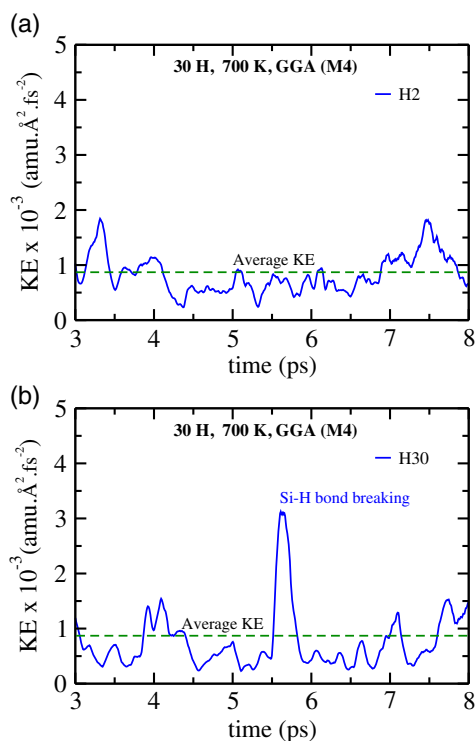


**Figure 8.** The evolution of the KE of two H atoms, H2 and H30, in monohydride Si—H bonds at 700 K. a) The KE of H2 atom is found to stay below the average KE at 700 K. b) The Si—H bond involving the high-energy H30 atom dissociates near 5.5 ps and forms a new Si—H bond. The average KE of the H atoms is indicated as a dashed horizontal line (green). The KE values correspond to a central moving average over 100 fs.

evolution of Si—H bond lengths associated with the pairs (Si40, H2) and (Si48, H30). The pair (Si48, H30) breaks at 5.3 ps, which is followed by the formation of a new pair (Si65, H30) at 5.6 ps, but the low-energy pair (Si40, H2) continues to stay bonded during its evolution. The variations of the bond length of the (dissociated) pair before and after dissociation are shown in Figure 9b in blue and green colors, respectively. The transient isolated state of H30, between 5.3 and 5.6 ps, is shown as red squares, where the “bond length” corresponds to the distance between H30 and the nearest Si atom in the void region. It goes without saying that the dissociation and subsequent formation of Si—H bonds on the void surface do not affect the MSD values of the H atoms as long as the H atoms stay within the cavity through the formation of new bonding configurations.

### 3.3. Morphology of Hydrogenated Voids in $\alpha$ -Si

The discussion in the preceding subsections so far is mostly confined to the dynamics of H atoms inside the voids and to what extent the motion of H atoms is affected by the XC approximation and the hydrogen load inside the voids, as far as the MSD of H atoms is concerned. We now examine the microstructure of hydrogen distributions on void surfaces and the morphological character of the voids, which result from the movement of hydrogen and silicon atoms in the vicinity of the voids for a varying

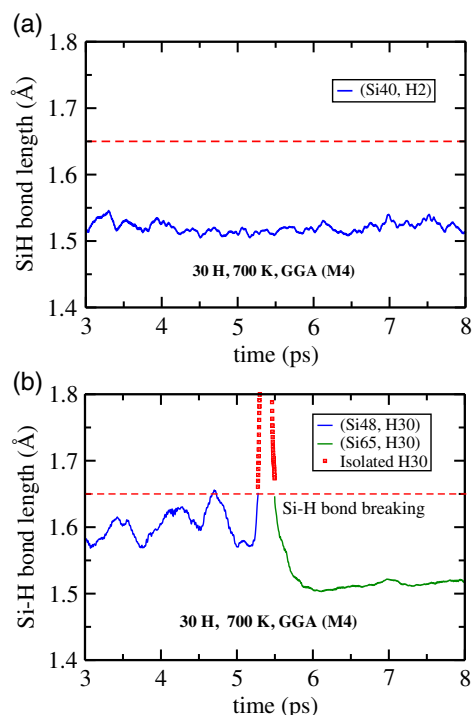


**Figure 9.** a) The variation of the bond length of a stable monohydride pair (Si40, H2) with time. b) The dissociation of a monohydride Si—H bond during MD simulations. The Si—H bond associated with the pair (Si48, H30) breaks at 5.3 ps, which is followed by the formation of a new pair (Si65, H30) at 5.6 ps. The isolated state of H30 atom is indicated by red squares, where the “bond length” refers to the distance between H30 and the nearest Si atom. The cutoff value of the Si—H bond length, 1.65 Å, is indicated by a dashed horizontal line (red).

hydrogen load. In particular, we discuss the formation of various BHs and NBHs, as well as the restructuring of the void surfaces during annealing, with an increasing concentration of H atoms within voids, and the dependence of hydrogen microstructure on the LDA and GGA. The BH and NBH play an important role in characterizing the structural and optical properties of  $\alpha$ -Si: H.<sup>[9,15,16]</sup> These properties can be studied experimentally using an array of experiments, such as positron-annihilation lifetime (PAL) spectroscopy,<sup>[15]</sup> Rutherford backscattering spectrometry (RBS),<sup>[16]</sup> hydrogen-effusion measurements,<sup>[29,30]</sup> and Fourier-transform infrared spectroscopy-attenuated total reflections (FTIR-ATR).<sup>[31]</sup>

Table 1 shows the statistics of various silicon–hydrogen bonding configurations and NBHs, e.g., H<sub>2</sub> molecules and one or two isolated H atoms, near the void, defined by a spherical region of radius 8 Å. The presence of isolated H atoms in the network is an artifact (of simulations), which arises from our choice of the cut-off value of 1.65 Å for Si—H bonds. It has been observed that the isolated H atoms at 700 K, listed in Table 1, are at a distance of 1.66 Å from the nearest Si atom (for the GGA) and at distances of 1.67 and 1.7 Å from the neighboring Si atoms (for the LDA). Thus, these H atoms are not truly isolated and can be viewed as somewhat stretched Si—H bonds at 700 K. The results from Table 1 and an analysis of the void surfaces for the hydrogen load of 10, 20, and 30 H atoms per void show that the surface of the

**Table 1.** Statistics of bonded and NBHs inside voids for varying hydrogen loads. The tabulated values indicate the amount of H atoms (in percent of total H) that resides as isolated hydrogen ( $H_{iso}$ ),  $H_2$  molecules, and SiH/SiH<sub>2</sub> bonds. Hydrogen atoms outside the void region are listed as  $Ex_H$ . Asterisks denote the actual number of isolated H atoms.

H load	XC	$H_{iso}$	$H_2$	SiH	SiH <sub>2</sub>	$Ex_H$
400 K						
10	GGA	0	15.0	67.50	0	17.50
	LDA	0	10.0	82.50	0	7.50
20	GGA	0	32.50	47.50	10.0	10.0
	LDA	0	25.0	62.75	5.0	7.50
30	GGA	0	45.0	40.0	11.67	3.33
	LDA	0	28.33	47.50	18.33	5.83
700 K						
10	GGA	0	25.0	55.0	0	20.0
	LDA	0	0	77.50	5.0	17.50
20	GGA	0	27.50	45.0	12.50	15.0
	LDA	0	17.50	66.25	2.50	13.75
30	GGA	0.83 (1*)	35.56	41.11	8.89	13.33
	LDA	1.65 (2*)	16.67	56.67	11.67	13.33

voids is mostly decorated with monohydride Si—H bonds. A few dihydride Si—H<sub>2</sub> bonds are also spotted for a hydrogen load of 20 and 30 H atoms per void. A noted amount of hydrogen can be seen to appear inside the voids as  $H_2$  molecules, especially for hydrogen loads of 20 and 30 H atoms per void. It is also evident from Table 1 that, in comparison with the GGA, the LDA overestimates the number of SiH bonds but underestimates the count of  $H_2$  molecules. The presence of few SiH<sub>2</sub> bonding configurations makes it difficult to comment on the dependence of SiH<sub>2</sub> configurations with respect to the XC approximation from the available data. **Figure 10** shows a 3D rendering of Si—H and Si—H<sub>2</sub> bonds in the vicinity of a void surface, along with a few  $H_2$  molecules for a hydrogen load of 30 H atoms per void at 400 and 700 K.

Experimental studies using infrared measurements by Chabal and Patel<sup>[32]</sup> suggest that the number density of  $H_2$  molecules in nanometer-size voids is of the order of  $10^{21} \text{ cm}^{-3}$ . This observation is found to be consistent with the values listed in Table 1, which can be roughly translated into  $3\text{--}13 \times 10^{21} \text{ cm}^{-3}$  for the GGA and  $2\text{--}8 \times 10^{21} \text{ cm}^{-3}$  for the LDA at 400 K, assuming a spherical void of radius 5–8 Å and a hydrogen load of 30 H atoms per void. None of the AIMD runs in this article showed any isolated H atoms within the voids, except one at 700 K, which is statistically insignificant. As discussed earlier, a few highly mobile H atoms are found to diffuse out of the void region due to high KE values of these atoms. The number of such atoms is listed as  $Ex_H$  in Table 1. The results from Table 1 are summarized in **Figure 11**, where the number of Si—H, Si—H<sub>2</sub>, and  $H_2$  molecules for a hydrogen load of 20 H atoms per void at 400 and 700 K is shown.

Since the restructuring of the void surface is largely characterized by monohydride Si—H bonds on the walls of the voids, it is instructive to examine the formation of these bonds during the

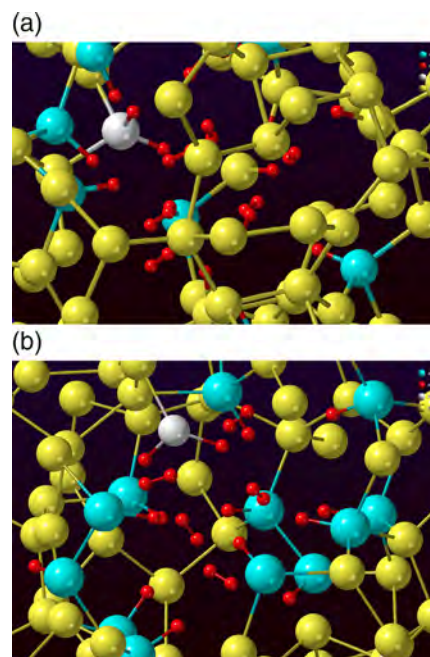


**Figure 10.** Hydrogen-bonding configurations, including  $H_2$  molecules, in a void-surface region of radius 8 Å for a hydrogen load of 30 H atoms per voids at a) 400 K and b) 700 K from the GGA in model M4. Silicon atoms associated with monohydride (SiH) and dihydride (SiH<sub>2</sub>) configurations are shown in cyan and white colors, respectively, whereas bonded H atoms and molecules are shown in red color.

course of simulation. **Figure 12a** shows the time evolution of the hydrogen content of SiH bonds (in percent of total H) for a hydrogen load of 20 H atoms per voids in the GGA and the LDA at 400 K. The formation of Si—H bonds begins very rapidly within the first few picoseconds and then it gradually converges by 18 ps. The LDA seems to overestimate the number of SiH bonds by about 32%, compared with the same from the GGA (see, for example, Table 1). This noted difference between the LDA and the GGA results indicates the need for choosing an accurate XC functional and a long simulation time for studying the microstructure of SiH and SiH<sub>2</sub> on the walls of the voids. Likewise, the formation of H—H pairs, or  $H_2$  molecules, during annealing is shown in **Figure 12b**, by plotting the evolution of the RMS distance between two pairs of H atoms at 400 K in the GGA for a hydrogen load of 20 H atoms per void. The first  $H_2$  molecule, consists of (H1, H12), was formed within the first 4 ps, whereas the second one, (H5, H13), was formed near 14 ps. The RMS distances between the pair of H atoms and the corresponding standard deviation are obtained by averaging over a moving time window of width 200 fs.

We conclude this section by making a few comments on the linear size and the shape of the voids obtained from annealing and total-energy relaxations in the presence of H atoms. Although the linear size of a void can be estimated from the radius of gyration of a set of atoms, which define the void surface, the reconstruction of a 3D shape of a void from a finite set of atomic positions is a nontrivial problem. A somewhat crude but simple and useful approach is to approximate the void shape



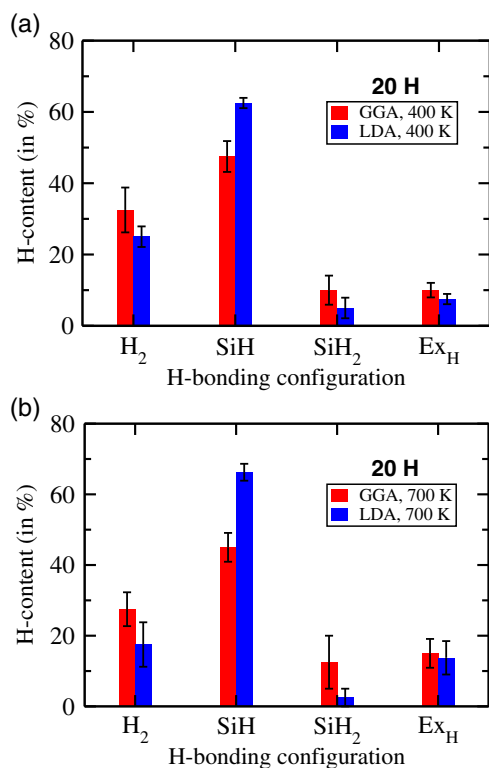


**Figure 11.** Histograms showing the various bonded and NBHs in the vicinity of voids in *a*-Si for a hydrogen load of 20 H atoms per void at a) 400 K and b) 700 K. The results are obtained from the SCF GGA and LDA calculations and averaged over all voids.

by constructing the minimal convex polyhedron, or a convex hull, formed by the set of void-surface atoms. The approach assumes that any restructuring of the void surface—caused by the movement of the void-surface atoms—would be reflected in the shape of the convex hull, which is associated with the void region. However, it has been observed<sup>[33]</sup> that the actual 3D shape of voids can be rather complex and nonconvex in nature, and it may not be represented accurately by a convex polyhedron. An approximate nonconvex surface can be constructed via convolution of the position of the void-surface atoms using the 3D Gaussian basis functions and choosing a suitable value of the isosurface parameter for the atomic pseudosurface of Si and H atoms. The Xcrysden<sup>[34]</sup> package can generate such pseudosurfaces. A more general discussion on the reconstruction of such nonconvex void shapes can be found in the studies by Biswas et al. and Biswas and Elliott.<sup>[11,33]</sup>

**Figure 13** shows the approximate shape of a void with a hydrogen load of 30 H atoms per void (in model M3) obtained from annealing at 400 K, followed by a total-energy optimization. The convex polyhedra shown in Figure 13a,b correspond to the set of void-surface atoms obtained from the GGA and the LDA, respectively. The respective nonconvex shapes of the void, obtained via the convolution of the same set of void-surface atoms using the Gaussian functions centered at the atomic sites, are shown in Figure 13c,d. Although the polyhedra in Figure 13a,b appear different, the difference is not particularly noteworthy

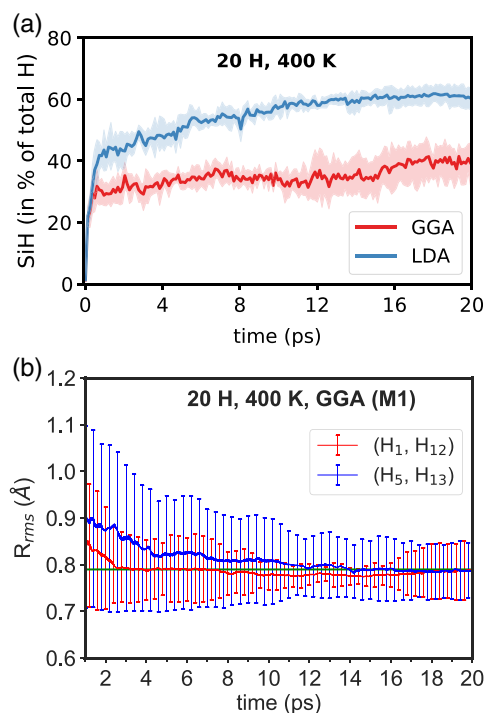


**Figure 12.** a) The evolution of monohydride Si-H bonds at 400 K in the GGA and the LDA for a hydrogen load of 20 H atoms per void. The Y axis indicates the amount of hydrogen atoms (in percent of total H atoms) that resides in Si-H bonds. b) The formation of H<sub>2</sub> molecules within a void at 400 K in the GGA for a hydrogen load of 20 H atoms per void. The RMS distance and its standard deviation between two pairs of H atoms, averaged over a rolling window of width 200 fs, are shown against time.

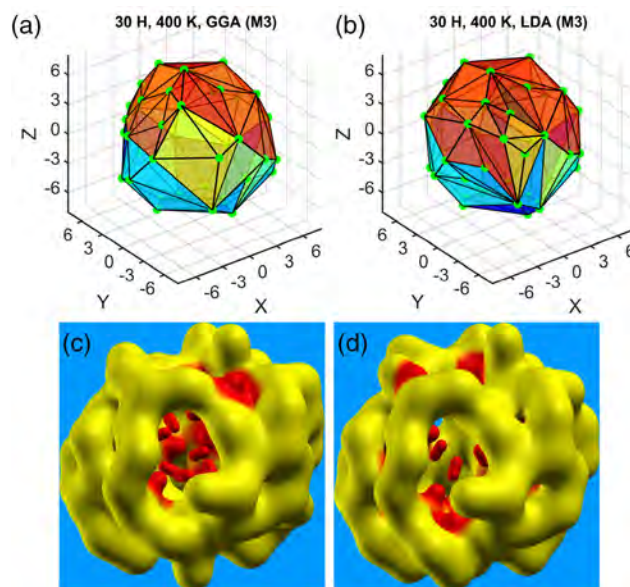


**Figure 13.** The reconstruction of a 3D shape of a void (in M3) from two sets of void-surface atoms at 400 K for a hydrogen load of 30 H atoms per void. The convex polyhedra obtained from the void-surface atoms in a) the GGA and b) the LDA, using the convex-hull approximation. The corresponding nonconvex surfaces using the same set of void-surface atoms are shown in (c) and (d), respectively. Silicon-hydrogen and H<sub>2</sub> molecules are shown in yellow-red and red-red colors, respectively.

**Table 2.** Linear [ $\text{\AA}$ ] and volumetric [ $\text{\AA}^3$ ] measures of the voids, reconstructed from the convex-hull approximation.  $R_G$ ,  $R_H$ , and  $V_H$  indicate the radius of gyration, the convex-hull radius, and the volume of the hull, respectively.  $S$  and  $N_H$  represent the sphericity and the number of atoms on the convex hull, respectively.

H load	XC	$R_G$	$R_H$	$V_H$	$S$	$N_H$
400 K						
10	GGA	6.392	7.162	1275.04	0.884	41
	LDA	6.517	7.205	1305.45	0.888	41
20	GGA	6.416	7.204	1295.95	0.883	41
	LDA	6.566	7.218	1316.80	0.890	42
30	GGA	6.489	7.231	1318.42	0.885	42
	LDA	6.541	7.263	1332.45	0.887	42
700 K						
10	GGA	6.192	7.102	1242.36	0.883	40
	LDA	6.347	7.175	1287.78	0.887	41
20	GGA	6.365	7.242	1299.63	0.880	39
	LDA	6.461	7.274	1323.15	0.879	39
30	GGA	6.430	7.202	1319.43	0.892	42
	LDA	6.475	7.238	1317.39	0.882	41

as far as the hull radius, the convex-hull volume, and the sphericity of the polyhedra are concerned. These values are listed in Table 2. The sphericity,  $S$ , of an object is defined as the ratio of the surface area of a sphere,  $A_s$ , to that of the object,  $A$ , both having an identical volume  $V$ . This definition leads to<sup>[35]</sup>

$$S = \frac{A_s}{A} = \frac{\pi^{\frac{1}{3}}(6V)^{\frac{2}{3}}}{A} \quad (1)$$

Here, we have used the volume and the corresponding surface area of the convex hull of a void surface to estimate  $V$  and  $A$ , respectively. A review of  $S$  and other values in Table 2 suggests that the LDA marginally overestimates the volume of the void, which is evident from the gyration and hull radii, and the hull volume of the voids for all hydrogen loads and temperatures. This observation is also consistent with the somewhat smaller values of the MSD of H atoms (within voids) that we have observed for the GGA calculations in Figure 3a,b.

## 4. Conclusion

In this article, we have studied the ab initio dynamics of hydrogen atoms inside voids in  $\alpha$ -Si with an emphasis on hydrogen diffusion and the resulting structure of the void surfaces with respect to a varying concentration of hydrogen at 400 and 700 K. A comparison of the results obtained from the LDA and the GGA reveals that the former considerably overestimates the number of monohydride Si–H bonds but underestimates the presence of  $H_2$  molecules inside the cavities, irrespective of the annealing temperature and the concentration of hydrogen. The surfaces of the voids are found to be primarily passivated with monohydride Si–H bonds and a few dihydride  $SiH_2$  bonds at high concentration of hydrogen. Neither the LDA nor the

GGA shows any presence of  $SiH_3$  configurations even for a high concentration/load of 30 H atoms per void. The densities of the bonded and NBHs observed in this work are found to be consistent with those from the infrared and RBS measurements. The study reveals that the kinetics of Si–H bond formation and dissociation during AIMD simulations can be approximately described and understood by considering the (translational) KE of H atoms inside the voids. Hydrogen atoms with a KE value significantly higher than the average KE of the system at a given temperature are found to dissociate from Si–H bonds on the surface of the voids. The resulting isolated H atoms then diffuse through the void region to form new bonds with nearby active Si atoms within a fraction of a picosecond in our simulations. Finally, a somewhat higher value of the MSD of the H atoms within voids in the LDA can be attributed to the reconstruction of the void surface through the formation of Si–H bonds. This has been found to be reflected in linear size of the voids obtained from a convex-hull approximation.

## Acknowledgements

The work was partially supported by the USA National Science Foundation (NSF) under Grant No. DMR 1833035. The authors acknowledge the use of computing resources at the University of Southern Mississippi, supported by the NSF under the Major Research Instrumentation (MRI) program via Grant No. ACI 1626217.

## Conflict of Interest

The authors declare no conflict of interest.

## Keywords

amorphous silicon, hydrogen dynamics, voids

Received: September 13, 2020

Revised: November 17, 2020

Published online: January 7, 2021

- [1] R. A. Street, *Adv. Mater.* **2009**, 21, 2007.
- [2] S. DeWolf, A. Descoeudres, Z. Holman, C. Ballif, *Green* **2012**, 2, 7.
- [3] J. Ge, Z. Ling, J. Wong, T. Mueller, A. Aberle, *Energy Proc.* **2012**, 15, 107.
- [4] D. L. Staebler, C. R. Wronski, *Appl. Phys. Lett.* **1977**, 31, 292.
- [5] T. Su, P. C. Taylor, G. Ganguly, D. E. Carlson, *Phys. Rev. Lett.* **2002**, 89, 015502.
- [6] D. C. Bobela, H. M. Branz, P. Stradins, *Appl. Phys. Lett.* **2011**, 98, 201908.
- [7] P. Biswas, R. Atta-Fynn, D. A. Drabold, *Phys. Rev. B* **2007**, 76, 125210.
- [8] S. Chakraborty, D. A. Drabold, *Phys. Rev. B* **2009**, 79, 115214.
- [9] P. Biswas, R. Timilsina, *J. Phys.: Condens. Matter* **2011**, 23, 065801.
- [10] P. Biswas, D. Paudel, R. Atta-Fynn, D. A. Drabold, S. R. Elliott, *Phys. Rev. Appl.* **2017**, 7, 024013.
- [11] P. Biswas, D. Paudel, R. Atta-Fynn, S. R. Elliott, *Nanoscale* **2020**, 12, 1464.
- [12] D. K. Limbu, S. R. Elliott, R. Atta-Fynn, P. Biswas, *Sci. Rep.* **2020**, 10, 7742.
- [13] P. Biswas, D. A. Drabold, R. Atta-Fynn, *J. Appl. Phys.* **2014**, 116, 244305.

- [14] E. Guerrero, D. A. Strubbe, *Phys. Rev. Mater.* **2020**, 4, 025601.
- [15] T. Sekimoto, M. Matsumoto, A. Sagara, M. Hishida, A. Terakawa, *J. Non-Cryst. Solids* **2016**, 447, 207.
- [16] T. Sekimoto, M. Matsumoto, A. Terakawa, *Jpn. J. Appl. Phys.* **2018**, 57, 08RB07.
- [17] F. Wooten, K. Winer, D. Weaire, *Phys. Rev. Lett.* **1985**, 54, 1392.
- [18] G. T. Barkema, N. Mousseau, *Phys. Rev. B* **2000**, 62, 4985.
- [19] J. M. Soler, E. Artacho, J. D. Gale, A. García, J. Junquera, P. Ordejón, D. Sánchez-Portal, *J. Phys.: Condens. Matter* **2002**, 14, 2745.
- [20] A. H. Mahan, Y. Xu, D. L. Williamson, W. Beyer, J. D. Perkins, M. Vanecek, L. M. Gedvilas, B. P. Nelson, *J. Appl. Phys.* **2001**, 90, 5038.
- [21] D. L. Young, P. Stradins, Y. Xu, L. M. Gedvilas, E. Iwaniczko, Y. Yan, H. M. Branz, Q. D. L. Wang, D. L. Williamson, *Appl. Phys. Lett.* **2007**, 90, 081923.
- [22] The effective width of the void surface is chosen to be about 3 Å. This is based on the results from the test calculations at 700 K, which show that the majority of silicon atoms near the void surface can move up to a distance of 2.5–3.0 Å. This distance is roughly equal to the first nearest-neighbor distance between Si atoms in the amorphous environment. For structural analysis of voids, we thus use a void-surface region of 8 Å.
- [23] J. Junquera, O. Paz, D. Sánchez-Portal, E. Artacho, *Phys. Rev. B* **2001**, 64, 235111.
- [24] N. Troullier, J. Martins, *Phys. Rev. B* **1991**, 43, 1993.
- [25] J. P. Perdew, A. Zunger, *Phys. Rev. B* **1981**, 23, 5048.
- [26] J. P. Perdew, K. Burke, M. Ernzerhof, *Phys. Rev. Lett.* **1996**, 77, 3865.
- [27] S. Nosé, *J. Chem. Phys.* **1984**, 81, 511.
- [28] S. Kageyama, M. Akagawa, H. Fujiwara, *Phys. Rev. B* **2011**, 83, 195205.
- [29] W. Beyer, *Sol. Energy Mater. Sol. Cells* **2003**, 78, 235.
- [30] W. Beyer, H. Wagner, *J. Appl. Phys.* **1982**, 53, 8745.
- [31] T. Sekimoto, M. Matsumoto, M. Hishida, A. Terakawa, *Jpn. J. Appl. Phys.* **2014**, 53, 095501.
- [32] Y. J. Chabal, C. K. N. Patel, *Phys. Rev. Lett.* **1984**, 53, 210.
- [33] P. Biswas, S. R. Elliott, *J. Phys.: Condens. Matter* **2015**, 27, 435201.
- [34] A. Kokalj, *J. Mol. Graph. Model.* **1999**, 17, 176.
- [35] H. Wadell, *J. Geol.* **1935**, 43, 250.

# Annealing-Induced Changes in the Atomic Structure of Amorphous Silica, Germania, and Tantalum Using Accelerated Molecular Dynamics

Kiran Prasai,\* Riccardo Bassiri, Hai-Ping Cheng, and Martin M. Fejer

Dedicated to Professor David A. Drabold on the occasion of his 60th birthday


The effects of annealing on the atomic structures of  $\text{SiO}_2$ ,  $\text{GeO}_2$ , and  $\text{Ta}_2\text{O}_5$  are investigated using accelerated molecular dynamics (MD) simulations. Using population annealing with Boltzmann resampling to expedite the MD simulations, it is shown that annealed models demonstrate subtle but statistically significant changes in the structure. Consistent with experiments, the simulations show that effects of annealing on the atomic structures of these amorphous oxides are more pronounced in the medium-range order than in the short-range order.

## 1. Introduction

Thin films of amorphous oxides are used in a variety of optical, electronic, and photovoltaic applications. Optical films of the highest quality are often produced by energetic processes like ion-beam sputtering (IBS) or magnetron sputtering, and the as-grown films are generally submitted to postdeposition annealing to further improve their optical and mechanical performance.<sup>[1–5]</sup> It has been observed that postdeposition annealing of amorphous oxide thin films often reduces the optical absorption at sub-bandgap energies until the onset of crystallization. Similarly, postdeposition annealing changes the mechanical loss (also known as internal friction) of thin films in a way that depends on the structure of the material.<sup>[6–9]</sup> Optical absorption and mechanical loss are performance-limiting properties for thin films used in a variety of applications. Understanding the effect of annealing on the atomic structure of these films could provide design, deposition, and postprocessing strategies to optimize the performance of future thin-film devices.

Dr. K. Prasai, Dr. R. Bassiri, Prof. M. M. Fejer  
 E. L. Ginzton Laboratory  
 Stanford University  
 Stanford, CA 94305, USA  
 E-mail: prasai@stanford.edu

Prof. H.-P. Cheng  
 Department of Physics and Quantum Theory Project  
 University of Florida  
 Gainesville, FL 32611, USA

 The ORCID identification number(s) for the author(s) of this article can be found under <https://doi.org/10.1002/pssb.202000519>.

DOI: 10.1002/pssb.202000519

There has been interest in understanding the relaxation behavior of amorphous oxides like  $\text{SiO}_2$ ,  $\text{GeO}_2$ , and  $\text{Ta}_2\text{O}_5$  with respect to their use in dielectric thin-film mirrors in gravitational-wave detectors LIGO and Virgo.<sup>[10]</sup> Thermal noise of the dielectric coatings used in LIGO and Virgo interferometers forms an important barrier against increasing the detector sensitivity.<sup>[8,11]</sup> Coatings made of alternating layers of  $\text{SiO}_2$  and  $\text{TiO}_2$ -doped  $\text{Ta}_2\text{O}_5$  are currently being used in these detectors.

To improve their sensitivity, it is critical to find coatings that produce lower thermal noise.<sup>[12,13]</sup> The thermal noise spectral density due to the coatings is proportional to their mechanical losses. While the mechanical loss at the temperatures of interest is largely dependent on the coating material, coating deposition processes and postdeposition annealing can also influence its value. Measured values of room-temperature mechanical loss of amorphous oxides like  $\text{SiO}_2$ ,  $\text{Ta}_2\text{O}_5$ ,  $\text{TiO}_2$ -doped  $\text{Ta}_2\text{O}_5$ , and  $\text{ZrO}_2$ -doped  $\text{Ta}_2\text{O}_5$  are seen to decrease as a function of annealing temperature until the process of crystallization starts.<sup>[6,8,9,14,15]</sup> These amorphous oxides are promising materials and are actively being explored for use in LIGO and Virgo. To understand and optimize the mechanical loss, and hence the thermal noise of the coatings, it is important to understand the annealing-induced changes in the structure of these coatings.

Structural changes in amorphous thin films caused by annealing can be probed by a number of experiments. For example, X-ray or electron pair distribution function (PDF) measurements can show changes in the short- and medium-range order.<sup>[9,16–18]</sup> Similarly, Raman spectra measurements before and after annealing can show changes in densities of modes originating from particular structural motifs, e.g., certain types of ring structures or bond-angle (BA) distributions.<sup>[14]</sup> Nuclear magnetic resonance (NMR) measurements before and after annealing can show if there are changes in the atomic environment around probed atoms.<sup>[19]</sup> Similarly, X-ray diffraction measurements can be used to probe the onset of crystallization after annealing runs, whereas optical absorption experiments can indicate if the densities of certain types of structural defects have changed.<sup>[20,21]</sup>

Atomic modeling has been widely used to study the structure and relaxation behavior of amorphous materials and explain or predict their functional properties. Recently, we combined



atomic modeling of amorphous oxides with grazing-incidence PDF (GIPDF) measurements to characterize annealing-induced changes in submicrometer-thick amorphous thin films.<sup>[9]</sup> The approach in the latter work is seeking experimental guidance to incorporate the annealing-induced effects into structural models. It is therefore clear that carefully designed atomic modeling calculations, when combined with appropriate experiments, can provide valuable insights into the relaxation processes induced by annealing. However, it is not always practical to obtain experimental probes into the coating structure before and after annealing, especially when many materials are being considered for multifunction optimization problems. Therefore, it is desirable to investigate annealing-induced effects in the structure using unaided atomic modeling approaches.

Conventional atomic modeling approaches like Monte Carlo (MC) or molecular dynamics (MD) fall short in capturing the annealing-induced effects because these approaches are only able to simulate timescales from a few to several hundred nanoseconds depending on the nature of the force field.<sup>[22,23]</sup> Such timescales are vastly smaller than the tens of hours of laboratory annealing times for coatings used in gravitational-wave detectors and may be too short to capture the relevant relaxation processes. As a result, MC or MD simulations cannot fully explore the potential energy landscape (PEL) and get trapped in local minima that are far from the effective global minimum (Existence of the global minimum for amorphous materials is debated. We use the term ‘effective global minimum’ to indicate a structure solution with the lowest energy that is still amorphous and that could be accessed if long time is allowed for relaxation). In terms of atomic structure, this often translates to a high concentration of geometrical defects in the short range and/or diminished order in the medium range. It is therefore important to explore ways to expedite the conventional MD or MC modeling approaches or search for their alternatives to realistically study annealing.

Many advanced sampling methods have been developed to partially mitigate the “timescale problem” discussed earlier. Parallel tempering,<sup>[24]</sup> population annealing,<sup>[25]</sup> and activation-relaxation technique (ART)<sup>[26]</sup> are some of the leading examples of this effort; for a review of accelerated sampling methods, see other studies.<sup>[27,28]</sup> For MD-based methods, parallel tempering has been shown to provide superior acceleration of dynamics.<sup>[24,29]</sup> Recently, an MD-based population annealing approach, called “population annealing MD” or “PAMD,” has been shown to yield similar acceleration as parallel tempering while featuring an added benefit of being scalable to arbitrarily large computer clusters.<sup>[30]</sup>

In this work, we use PAMD with classical two-body force fields to study annealing-induced effects in the atomic structures of amorphous SiO<sub>2</sub>, GeO<sub>2</sub>, and Ta<sub>2</sub>O<sub>5</sub>. While an acceleration of MD to realistic timescales is still far away, PAMD seems to provide the best acceleration of MD, considering its scalability to arbitrary resources. This work is an attempt to explore if PAMD can, when applied with simple force fields in a typical computational resource available in academic institutions, capture structure relaxations seen in laboratory annealing. PAMD would provide a relatively inexpensive way to study annealing effects on thin films, especially when one or more of the experimental deposition/annealing/measurement processes becomes infeasible. We note that more advanced force fields are needed

to capture atomic structure and annealing effects more accurately—but accelerating the timescales of simulation with advanced force fields is prohibitively difficult in terms of the time and resource needed. In this regard, recently developed machine learning-based potentials, which have shown a good combination of accuracy and speed, can hold some promise.<sup>[31]</sup>

## 2. Experimental Section

In the following sections, we present details of our computational approach.

### 2.1. Main Approach

In this work, we develop atomic models of SiO<sub>2</sub>, GeO<sub>2</sub>, and Ta<sub>2</sub>O<sub>5</sub> using the conventional melt-quench MD in classical two-body force fields. We refer to these atomic models as “melt-quenched” models. We then use the accelerated sampling method PAMD, with melt-quenched models as starting configurations, to find the lower-energy solutions of the underlying PEL. We refer to the final atomic models from PAMD as “annealed” models. We then probe the melt-quenched and annealed models by computing X-ray PDFs, X-ray structure factors, coordinations, BA distributions, ring-size distributions, evolution of ordered clusters, and density of phonon modes.

### 2.2. Interatomic Potentials

We use classical two-body interatomic potentials with the “BKS” functional form.<sup>[32]</sup> For SiO<sub>2</sub>, we use the parametrization developed by Sundararaman et al.<sup>[33]</sup> For GeO<sub>2</sub>, we use the parametrization developed by Oeffner and Elliott.<sup>[34]</sup> For Ta<sub>2</sub>O<sub>5</sub>, we use the parametrization developed by Trinastic et al.<sup>[35]</sup>

### 2.3. Generating Melt-Quenched Models

We generate 1000 melt-quenched atomic models for each system: SiO<sub>2</sub>, GeO<sub>2</sub>, and Ta<sub>2</sub>O<sub>5</sub>. Each of those 1000 atomic models was generated by following the conventional melt-quench protocol of MD simulation. This protocol generally has three parts. 1) Selection of starting configuration: We begin by taking a semirandomized collection of atoms in a cubic supercell of a size that corresponds to the known densities of the respective systems. We take 2400 atoms for SiO<sub>2</sub> and GeO<sub>2</sub> and 3500 atoms for Ta<sub>2</sub>O<sub>5</sub>; periodic boundary conditions were applied in all directions for all systems. The initial collection of atoms is semirandomized (as opposed to fully randomized) in the sense that a threshold interatomic distance of at least 1.9 Å is enforced even when randomly choosing the positions of atoms within the supercell. We take the densities of 2.20, 3.69, and 7.50 gm cm<sup>-3</sup> for SiO<sub>2</sub>, GeO<sub>2</sub>, and Ta<sub>2</sub>O<sub>5</sub>, respectively, for determining the size of the supercell at the starting point. 2) Melting the system: We take the system to a high temperature, following some initial equilibrations at lower temperature. The latter is required for the stability of MD simulations at a higher temperature, given that the starting configurations are semirandomized. The systems are equilibrated at a high temperature (3000 K for SiO<sub>2</sub>, 3000 K for

GeO<sub>2</sub>, and 6000 K for Ta<sub>2</sub>O<sub>5</sub>). 3) Quenching the melt: The systems are then cooled to 300 K from the high-temperature melt and subsequently equilibrated at 300 K. NPT ensemble is simulated for 2) and 3) except for the low-temperature equilibrations at the start of 2). The total timespan of the simulation for 2) and 3) combined is 1.17 ns for each atomic model; a time step of 1 fs was used throughout the simulation. These configurations at the end of the run at 300 K were taken as the melt-quenched models for the structure analysis done in this article. For the calculations of phonon densities of states, these models are further relaxed to their local minima using the FIRE algorithm.<sup>[36]</sup>

## 2.4. Generating Annealed Models

We use PAMD as a way to expedite MD simulations so that a larger part of the PEL can be explored and structure relaxation analogous to those induced by laboratory annealing can be mimicked in computer-generated models. For details on the PAMD method itself, see the study by Christiansen et al.<sup>[30]</sup> This work is an implementation of basic PAMD on amorphous oxides with a focus on characterizing effects of the said basic PAMD on atomic structure.

PAMD involves taking an ensemble of  $N$  independent copies of the system through  $M$  successive constant temperature MD simulations. A population resampling based on Boltzmann probability is conducted between two adjacent MD runs. In this work, we take the 1000 ( $=N$ ) independent melt-quenched MD models described earlier as the starting points of the first (of  $M$ ) MD runs. During these runs, NVT dynamics is conducted for  $m$  time-steps. Each successive MD run is conducted at a lower temperature than the preceding MD run and a resampling of the population is done based on the relative Boltzmann weight of each sample. Between two adjacent NVT runs at temperatures  $T_i$  and  $T_{i-1}$ , where  $T_i < T_{i-1}$ , relative Boltzmann weight of a sample  $j$  with energy  $E_j$  is calculated as

$$\tau_j = \frac{e^{\frac{E_j}{k_B}(T_i^{-1} - T_{i-1}^{-1})}}{Q} \quad (1)$$

where  $Q = \sum_{j=1}^N e^{\frac{E_j}{k_B}(T_i^{-1} - T_{i-1}^{-1})} / N$  is a normalization factor. For all results reported in this article, we used  $m = 50000$ . For SiO<sub>2</sub> and GeO<sub>2</sub>, the temperatures of the first batch of MD simulations ( $T_1$ ) are taken be 3900 and 2100 K, respectively, which are roughly twice their melting temperatures. We choose the value of  $M = 10$  for SiO<sub>2</sub> and GeO<sub>2</sub> with  $T_{10} = 300$  K. For Ta<sub>2</sub>O<sub>5</sub>, we take more closely spaced temperatures for adjacent MD runs by choosing  $M = 23$ ,  $T_1 = 2500$  K, and  $T_{23} = 300$  K.

Energy distributions for the melt-quenched and annealed models at 300 K are shown in Figure 1. The distributions are presented in units of full width half maxima (FWHM) of energy distribution of melt-quenched models of respective systems. The plots show that energy distributions for annealed models are narrower and their peaks lie at lower energies than the peaks of corresponding melt-quenched models by  $\approx 2.5$  FWHM for SiO<sub>2</sub>,  $\approx 1.5$  FWHM for GeO<sub>2</sub>, and  $\approx 5$  FWHM for Ta<sub>2</sub>O<sub>5</sub>. We also conducted additional PAMD simulations for Ta<sub>2</sub>O<sub>5</sub> with  $m = 10000$  for testing purposes, and the resulting energy distribution is shown in Figure 1 in magenta triangles. For the latter case, a distribution with a peak at energy  $\approx 2$  FWHM lower than

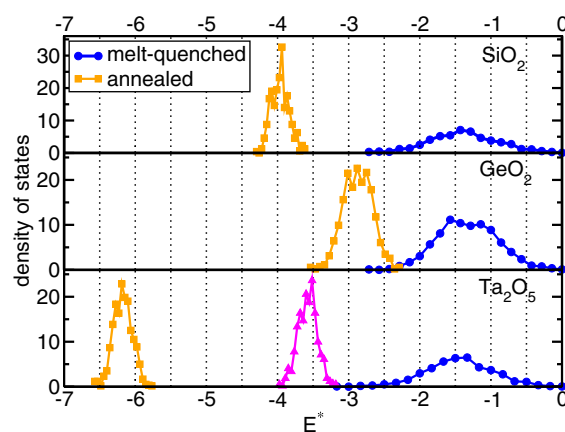


**Figure 1.** Energy distributions of melt-quenched and annealed models at 300 K. To enable comparison, the energy axis is shown in units of FWHM of the distribution of energies of melt-quenched ensembles of respective systems. i.e.,  $E^* = (E - E_0)/\lambda$ , where  $E$  is energy computed using the force fields and  $E_0$  and  $\lambda$  are maxima and FWHM of melt-quenched energy distributions of corresponding systems. The magenta triangles in Ta<sub>2</sub>O<sub>5</sub> plot are from PAMD simulations with  $m = 10000$ , whereas the orange squares are from  $m = 50000$ .

that of the melt-quenched ensemble is obtained. It is clear that a more systematic study of the parameter space is required to achieve optimum performance of PAMD with respect to the resources at hand. As such, we make no attempts to improve upon or optimize the method itself beyond making some consistency tests necessary for a basic implementation. In the remainder of this article, we report on the structural changes observed between the melt-quenched and annealed models.

## 2.5. Fidelity of the Atomic Models

Realistic atomic models are necessary to capture the relaxation processes in real-world materials. Although BKS potentials are inexpensive in terms of resource usage and thus are convenient for large-scale simulations like the ones being presented in this article, they are limited in their scope for capturing various aspects in the structure and properties of the systems they describe. The particular parametrizations of BKS potentials used in this study have been shown to be able to model the basic structural features of corresponding systems reasonably well, see other studies.<sup>[33–35,37,38]</sup> In Figure 2, we compare the PDFs obtained using the BKS potentials used in this work with PDFs from ab initio MD (AIMD) simulation. It is seen that PDFs from BKS-based models and AIMD models align reasonably well. We have also checked the partial PDFs and find that the BKS-based models show reasonable agreement with AIMD models, except for some disagreement in the first peaks of Si–Si/Ge–Ge/Ta–Ta pair correlations. This result obviously does not imply a wider validity of BKS-based models; nevertheless, it is an important indication that the models used in this article correctly represent the basic structural order in these systems.

The LAMMPS simulation package<sup>[39]</sup> was used to conduct the MD simulations in this work. All the results reported in

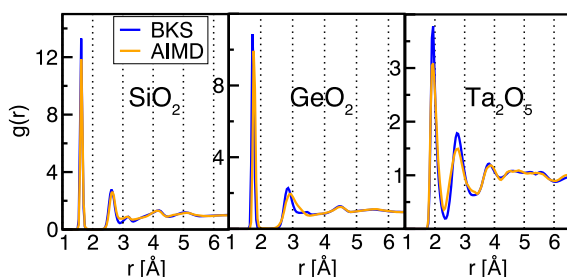


**Figure 2.** PDFs of  $\text{SiO}_2$ ,  $\text{GeO}_2$ , and  $\text{Ta}_2\text{O}_5$ . The blue curves (labeled BKS) represent the PDFs from melt-quenched models presented in this article. The orange curves (labeled AIMD) represent the PDFs from melt-quenched models from AIMD simulations. The AIMD models of  $\text{SiO}_2$  and  $\text{GeO}_2$  contain 360 atoms, whereas those of  $\text{Ta}_2\text{O}_5$  contain 350 atoms. To obtain the AIMD models, PBE functionals<sup>[71,72]</sup> and plane-wave basis sets of up to 400 eV were used in the simulation framework provided with the Vienna ab initio software package (VASP).<sup>[73,74]</sup> A total of 105 ps of melt-quench MD was simulated.

this articles are averages of 1000 models, unless otherwise indicated.

### 3. Results and Discussion

We computed the X-ray PDFs from melt-quenched and annealed models. **Figure 3** shows the plots of X-ray PDFs for  $\text{SiO}_2$ ,  $\text{GeO}_2$ , and  $\text{Ta}_2\text{O}_5$ . There are three main points to be noted in Figure 3. First, in all three systems, we find that changes in the short-range order (SRO) are nominal with most of the changes occurring in medium range order (MRO). This observation is consistent with GIPDF measurements of as-deposited and annealed films of several oxides, including  $\text{GeO}_2$  and  $\text{Ta}_2\text{O}_5$ , where only small changes are seen in the short range and most of the changes are in the medium range.<sup>[9,16,40]</sup> Second, even though the changes in MRO are small, these are statistically significant as these are averages of 1000 independent models. In particular, changes in intensities and positions of peaks at  $r > 5 \text{ Å}$  in Figure 3c are generally consistent with those reported in the study by Shyam et al.<sup>[16]</sup> Third, we note that many features of X-ray PDFs are not captured well. For example, in the measured X-ray PDF of  $\text{Ta}_2\text{O}_5$ , the second peak features a hump at  $\approx 3.4 \text{ Å}$ , which is known to correspond to Ta–Ta correlations from edge-shared polyhedra (ESP).<sup>[9,16]</sup> The computed PDFs shown in Figure 3c show a much diminished peak both for the melt-

quenched and for the annealed models. Furthermore, the ratios of intensities of the first and second peak of  $\text{GeO}_2$  are over estimated in Figure 3b compared with those in the measured X-ray PDFs.<sup>[40]</sup> Our comparison of partial PDFs of BKS-based models with those of AIMD models has shown that BKS models underestimate the order in Ge–Ge, Si–Si, or Ta–Ta correlations in these systems. As for PAMD, we can reasonably expect that an improved potential would mitigate these shortcomings.

We also compute the coordination and polyhedral connection statistics and the results of these calculations are shown in **Table 1**. We find that the concentrations of fourfold Si/Ge and twofold O in  $\text{SiO}_2$  and  $\text{GeO}_2$  increase due to annealing and all other coordinations decrease. For  $\text{Ta}_2\text{O}_5$ , the concentrations of sixfold Ta and twofold O increase in annealed models, and other coordinations decrease. Although the changes in coordination appear small, these changes are significant, considering that, for example, over- and undercoordinated Si atoms are eliminated from  $\text{SiO}_2$  due to annealing, and concentrations of one-coordinated and three-coordinated O atoms are reduced to almost half. Such types of sparse bad actors are known to be the source of optical losses, and postdeposition annealing is known to reduce these losses.<sup>[41–44]</sup> Damart and Rodney have shown that two-level systems (TLSs) of  $\text{SiO}_2$  with a high-energy barrier, which give rise to the mechanical loss near room temperature, involve highly localized displacements around ill-coordinated atoms.<sup>[45]</sup> Lane et al. observed similar trends on Si and O coordinations by microsecond-long MD simulation.<sup>[46]</sup> Kim and Stebbins observed a slight decrease in Ta and O coordinations in  $^{17}\text{O}$  NMR measurements of unannealed and annealed thin films of IBS  $\text{Ta}_2\text{O}_5$ .<sup>[19]</sup> The latter observation is also consistent with our results presented in Table 1. Table 1 also shows that the polyhedral connections in  $\text{SiO}_2$  and  $\text{GeO}_2$  are overwhelmingly corner-shared, and annealing reduces the concentration of ESP with a corresponding increase in corner-shared polyhedra (CSP). For  $\text{Ta}_2\text{O}_5$ , ESP form a relatively larger fraction ( $\approx 15\%$ ) of polyhedral connections. In fact, ESP polyhedra in  $\text{Ta}_2\text{O}_5$  register a distinct peak in Ta–Ta partial correlation and the total X-ray PDF measurements capture this distinct peak as a hump at  $r = 3.4 \text{ Å}$  before the second major peak at  $r = 3.8 \text{ Å}$  (see ref. [16]). However, as that peak is much less apparent in the computed X-ray PDF shown in Figure 3, it can be expected that the fraction of ESP is underestimated in our models of  $\text{Ta}_2\text{O}_5$ . This results in an underestimation of threefold O atoms—our models show the fraction of threefold-coordinated atoms to be at  $\approx 35\%$ ,

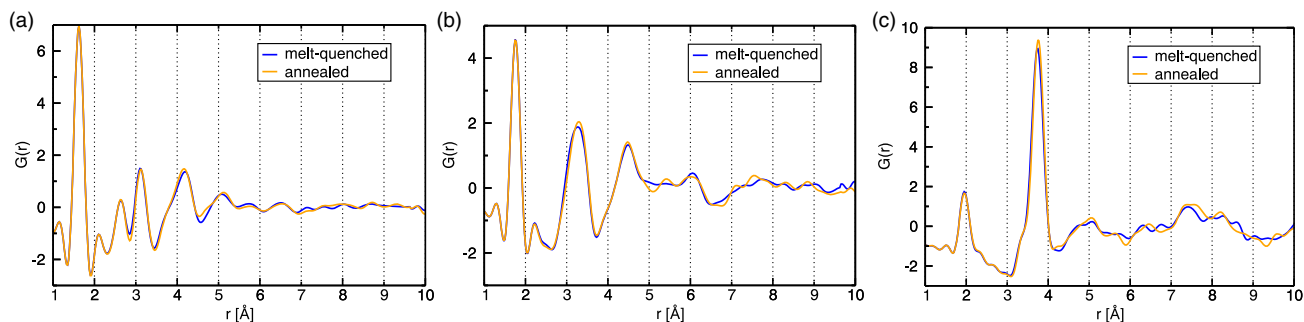


**Figure 3.** X-ray PDFs computed from melt-quenched and annealed models of a)  $\text{SiO}_2$ , b)  $\text{GeO}_2$ , and c)  $\text{Ta}_2\text{O}_5$ .

**Table 1.** Coordination distributions and polyhedral connections present in the melt-quenched and annealed models of  $\text{SiO}_2$ ,  $\text{GeO}_2$ , and  $\text{Ta}_2\text{O}_5$ .  $n_\alpha$  represents average coordination around  $\alpha$  atoms. The first minimum of the PDF is used as a cutoff to define the coordination sphere. CSP, ESP, and FSP represent corner-, edge-, and face-shared polyhedra, respectively. Values less than 0.01% are not shown.

System = $\text{SiO}_2$	$n_{\text{Si}} = 3$	$n_{\text{Si}} = 4$	$n_{\text{Si}} = 5$	$n_{\text{O}} = 1$	$n_{\text{O}} = 2$	$n_{\text{O}} = 3$	CSP	ESP
Melt quenched	0.02%	99.78%	0.20%	0.79%	98.33%	0.88%	99.57%	0.43%
Annealed	0.00%	100.00%	0.00%	0.44%	99.12%	0.44%	99.75%	0.25%
System = $\text{GeO}_2$	$n_{\text{Ge}} = 4$	$n_{\text{Ge}} = 5$	$n_{\text{Ge}} = 6$	$n_{\text{O}} = 1$	$n_{\text{O}} = 2$	$n_{\text{O}} = 3$	CSP	ESP
Melt quenched	99.43%	0.55%	0.01%	3.61%	92.50%	3.89%	98.42%	1.58%
Annealed	99.78%	0.21%	0.00%	3.04%	93.81%	3.15%	99.26%	0.74%
System = $\text{Ta}_2\text{O}_5$	$n_{\text{Ta}} = 4$	$n_{\text{Ta}} = 5$	$n_{\text{Ta}} = 6$	$n_{\text{Ta}} = 7$	$n_{\text{Ta}} = 8$	$n_{\text{O}} = 2$	$n_{\text{O}} = 3$	$n_{\text{O}} = 4$
Melt quenched	0.22%	18.02%	76.19%	5.48%	0.09%	65.23%	34.67%	0.10%
Annealed	0.11%	18.14%	76.71%	5.04%	0.00%	65.40%	34.52%	0.07%
							System = $\text{Ta}_2\text{O}_5$	
							CSP	ESP
							FSP	
							Melt quenched	84.56%
							Annealed	85.09%

whereas  $^{17}\text{O}$  NMR measurements show the fraction of three-fold-coordinated atoms to be at  $\approx 43\%$ .<sup>[47]</sup> The fraction of ESP in  $\text{Ta}_2\text{O}_5$  decreases from 14.57% to 14.19%, which is a relatively smaller change compared with our recent study of annealing-induced changes in  $\text{ZrO}_2$ -doped  $\text{Ta}_2\text{O}_5$ , where the fraction of Ta–Ta ESP decreases from 19.93% to 14.38%.<sup>[9]</sup> The relatively small decrease in the concentration of ESP seen in this work may be caused by the inability of the interatomic potential to accurately capture Ta–Ta correlation. We also observe a decrease in the concentration of face-shared polyhedra (FSP) from 0.87% to 0.72%.

Annealing has a greater effect in the MRO of amorphous thin films—it has been seen in GIPDF measurements of oxide thin films<sup>[9,16,40]</sup> as well as in our computed PDFs shown in Figure 3. The effect of heat treatment on MRO of  $\text{Ta}_2\text{O}_5$  has also been observed by transmission electron microscopy (TEM) measurements of the normalized variance (a measure of MRO).<sup>[43,48]</sup> Earlier works have shown that the intensity of the first peak in the structure factor,  $S(q)$ , of amorphous networks is an indication of MRO in the networks.<sup>[49–52]</sup> We compute the X-ray  $S(q)$  from melt-quenched and annealed models. From the computed X-ray  $S(q)$ , shown in Figure 4, it is observed that the intensity of the

first peak (highlighted in insets) is higher for annealed models than for melt-quenched models for all three systems. This indicates that the annealed models have a higher degree of MRO, which would also be consistent with observations from earlier probes of annealing-induced effects on various systems.<sup>[9,16,40]</sup> Hence, to better understand the annealing-induced changes in atomic structure, it is important to focus on structural features in the MRO beyond the first coordination sphere.

The MRO in  $\text{SiO}_2$  and  $\text{GeO}_2$  is often expressed in the form of ring structures and a related quantity—BA. Raman measurements have been used to probe the structure of thin films and understand annealing-induced changes.<sup>[14,53,54]</sup> Various modeling attempts have been made to understand the Raman spectra of  $\text{SiO}_2$ ,  $\text{GeO}_2$  and  $\text{Ta}_2\text{O}_5$  in terms of their atomic structure.<sup>[38,55–59]</sup> these works have shown that the features in Raman spectra are particularly sensitive to the distribution of ring sizes and BAs. In this work, we compute the distribution of ring sizes and BAs from the melt-quenched and annealed models. We computed ring distributions in  $\text{SiO}_2$  and  $\text{GeO}_2$ —results are shown in Figure 5. In both systems, we find that the concentrations of two-membered rings (2-MRs) decrease to nearly half upon annealing. 2-MRs correspond to the ESPs; hence, the latter observation is

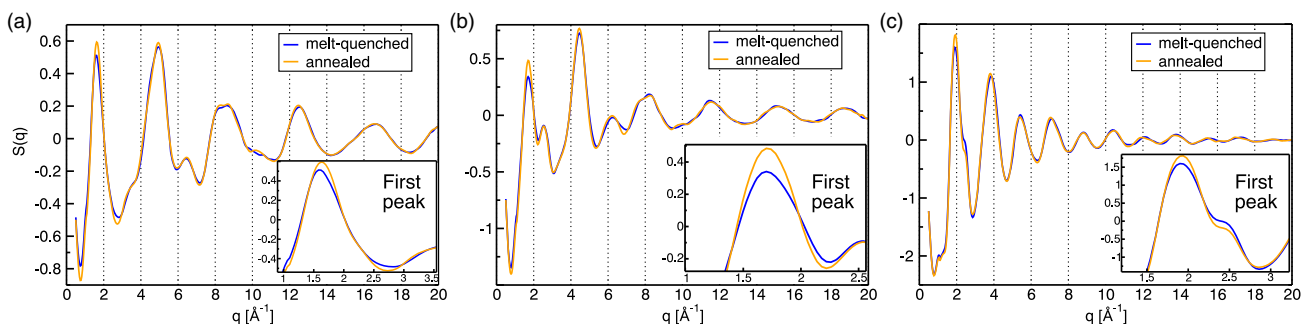


**Figure 4.** X-ray structure factor ( $S(q)$ ) computed from melt-quenched and annealed models of a)  $\text{SiO}_2$ , b)  $\text{GeO}_2$ , and c)  $\text{Ta}_2\text{O}_5$ .



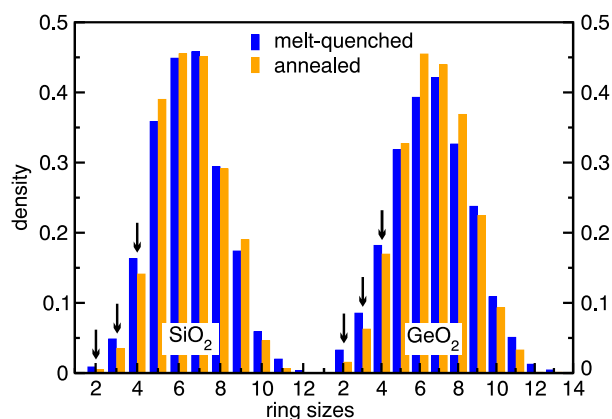


**Figure 5.** Ring-size distribution computed from the melt-quenched and annealed models of  $\text{SiO}_2$  and  $\text{GeO}_2$ . The arrows are placed to highlight that annealing significantly reduces the concentration of small rings (2-MRs, 3-MRs, and 4-MRs). Density of small rings has been shown to be related with mechanical loss—see text. We referred to definitions of primitive rings presented in ref. [75] to compute ring statistics.

internally consistent with decrease in ESP for  $\text{SiO}_2$  and  $\text{GeO}_2$  in Table 1. 2-MRs are highly strained structures and are rare in  $\text{SiO}_2$  and  $\text{GeO}_2$ , although there is some indication that 2-MRs could be present in  $\text{SiO}_2$  surfaces.<sup>[60–62]</sup> Their presence in our models could be the result of extremely large quench rates used for our models. The observed reduction in the density of 2-MRs in annealed models to about half of the melt-quenched models indicates that PAMD is efficient in mitigating the short timescale issues of MD simulations. We also observe that small-membered rings (particularly, 3-MRs and 4-MRs) are broken to form large-membered rings (5-MRs and 6-MRs) as a result of annealing. Pasquarello and Car have shown the 3-MRs and 4-MRs in  $\text{SiO}_2$  give rise to two defect lines  $D_1$  and  $D_2$  in Raman spectra at energies 495 and 606  $\text{cm}^{-1}$ .<sup>[55]</sup> Hence, following the ring distribution in Figure 5, it can be expected that annealing would reduce the defect lines  $D_1$  and  $D_2$ . In fact, Granata et al. have shown that annealing of IBS  $\text{SiO}_2$  films reduces the normalized  $D_2$  area in the Raman spectra, although  $D_1$  was seen to increase with annealing for which the authors

provide a heuristic explanation.<sup>[14]</sup> Lunin and Tokmakov have argued that highly stressed rings in  $\text{SiO}_2$ , like 3-MRs and 4-MRs, are associated with mechanical loss.<sup>[63]</sup> Granata et al. have shown a correlation of mechanical loss with the density of 3-MRs in  $\text{SiO}_2$ .<sup>[14]</sup> Figure 6 shows BA distribution in  $\text{SiO}_2$  and  $\text{GeO}_2$ . In both systems, annealing reduces the BA density in the range from 80° to 100° consistent with annihilation of ESP. We also see a slight shift in Si–O–Si and Ge–O–Ge angle distributions to larger angles, which would be consistent with the creation of low-strain large-membered rings and annihilation of high-strain small-membered rings.

We compute the vibrational density of states (VDOS) by diagonalizing dynamical matrices; the results are shown in Figure 7. Even though the BKS force fields used in this work are shown to produce reasonably good estimates of VDOS compared with measured Raman spectra or ab initio calculations (see ref. [33] for  $\text{SiO}_2$ , ref. [34] for  $\text{GeO}_2$ , and refs. [38,54] for  $\text{Ta}_2\text{O}_5$ ), we note here that simple force fields like BKS are limited in their ability to realistically model VDOS. The purpose of the calculations shown in Figure 7 is to compare the annealing-induced modifications in VDOS and draw inferences on structure. We find that there are only subtle changes in densities of states (DOS) between melt-quenched and annealed models. For statistical significance, the presented VDOS are averages of 25 models that are randomly drawn from corresponding ensemble of 1000 models. For all three systems in Figure 7, we find a slight increase in the high-energy peak for annealed models, the modes in the latter peaks are ascribed to stretching modes of twofold-coordinated O atoms. So, this observation is consistent with coordination statistics shown in Table 1. For  $\text{SiO}_2$ , small changes are seen in the positions of  $D_1$  and  $D_2$  peaks in a direction consistent with measurements by Granata et al.<sup>[14]</sup> Slightly more pronounced changes in VDOS are seen for  $\text{GeO}_2$ —these changes may be caused by a reduction in the concentration of three-coordinated O atoms,<sup>[64]</sup> particularly in the 550–750  $\text{cm}^{-1}$  region. The VDOS in the midenergy range is seen to be associated with stretching modes of three-coordinated O atoms.<sup>[54,64]</sup> For  $\text{Ta}_2\text{O}_5$ , we see subtle changes in spectra that appear to be consistent with simulated Raman spectra from the study by Joseph et al.<sup>[54]</sup> It is interesting to see that in  $\text{Ta}_2\text{O}_5$ , a small increase in VDOS in the energy range 150  $\text{cm}^{-1}$  is observed. The states in this range are typically

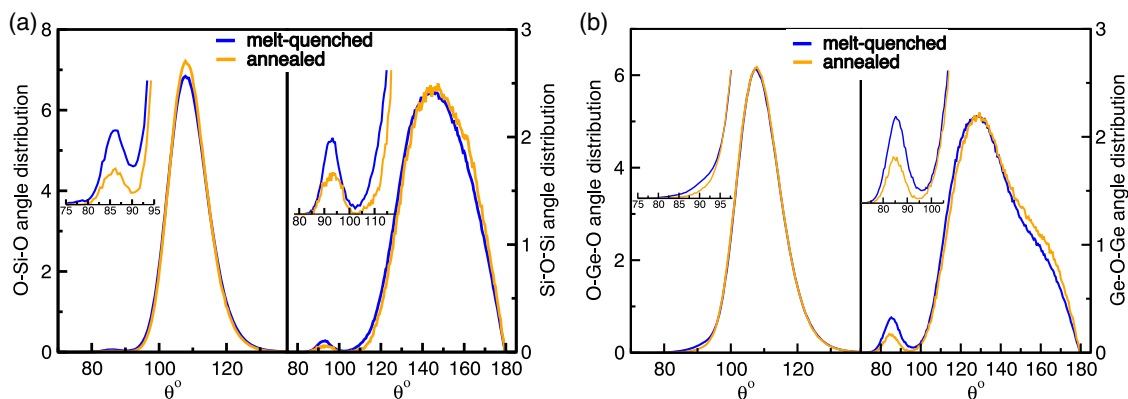


**Figure 6.** Bond-angle distribution computed from melt-quenched and annealed models of a)  $\text{SiO}_2$  and b)  $\text{GeO}_2$ . The inset in each plot shows a section of the main plot, where a significant change in bond density is observed between melt-quenched and annealed models.

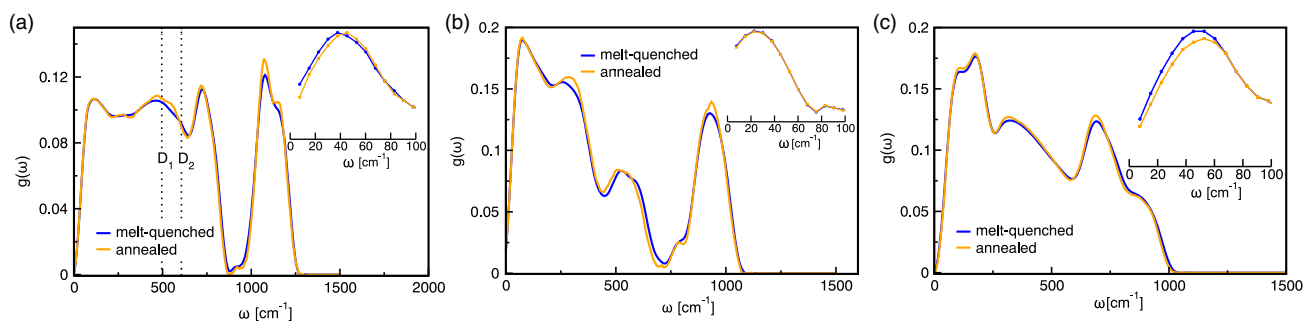


**Figure 7.** VDOS ( $g(\omega)$ ) of a)  $\text{SiO}_2$ , b)  $\text{GeO}_2$ , and c)  $\text{Ta}_2\text{O}_5$ . All  $g(\omega)$  curves shown in this plot are averages computed from 25 models which are randomly selected from the corresponding ensemble of 1000 models. In (a), the positions of  $D_1$  and  $D_2$  lines in the Raman spectra<sup>[55]</sup> of  $\text{SiO}_2$  are indicated by dotted lines. The insets in each plot show the low-energy peaks of  $g(\omega)/\omega^2$  for the corresponding systems. (For comparison of VDOS computed in this work with DFT-based VDOS, see ref. [33] for  $\text{SiO}_2$ , ref. [34] for  $\text{GeO}_2$ , and ref. [38] for  $\text{Ta}_2\text{O}_5$ ).

associated with the interpolyhedra bond-bending types of vibrations, and it is conceivable that those modes would change as a result of increased concentration of CSP. These changes in VDOS of  $\text{Ta}_2\text{O}_5$  can also be understood in light of the changes in BA distribution shown in **Figure 8**. We see that the Ta–O–Ta bond angles shift toward a higher value consistent with a slight increase in the concentration of CSP. Furthermore, the first and second peaks in Ta–O–Ta originate from ESP and CSP, respectively. The peak associated with CSP is seen to shift to a lower value and it could be associated with changes in the first peak of VDOS of  $\text{Ta}_2\text{O}_5$  below  $150\text{ cm}^{-1}$ . The insets in Figure 7 show the low-energy peaks of  $g(\omega)/\omega^2$  (where  $g(\omega)$  represents VDOS at energy  $\omega$ ). These peaks show a slight reduction in intensity (more prominent in  $\text{Ta}_2\text{O}_5$ ) and a shift of peak position to higher energy (more prominent on  $\text{SiO}_2$ ). These observations, although small, are consistent with similar calculations by Singh, Ediger, and de Pablo.<sup>[65]</sup> It is to be noted that our calculations at low energy may be affected by the small sizes of our models as our (cubic) models are only from  $\approx 32$  to  $\approx 36\text{ Å}$  in dimension.

We probe the spatial order in the melt-quenched and annealed networks using the bond-order parameters of Steinhardt et al.<sup>[66]</sup> As the polyhedral units themselves are least affected by annealing (as evidenced by the lack of change in the first peaks of the

PDFs, see Figure 3), we design our calculation to probe the interpolyhedral order. As such, we compute  $q_6$ , a widely used measure of local order for disordered systems, for each Si, Ge, or Ta atoms in  $\text{SiO}_2$ ,  $\text{GeO}_2$ , and  $\text{Ta}_2\text{O}_5$ , respectively. We take the first minima of Si–Si, Ge–Ge, and Ta–Ta partial PDFs to define cutoffs in the  $q_6$  calculation. Hence, a “bond” defined in this case is only geometrical, not chemical. The distribution of  $q_6$  for each system is shown in insets of **Figure 9**. We see subtle changes in the distributions of  $q_6$  for melt-quenched and annealed models. However, a much more pronounced change is revealed when one probes the spatial correlation of  $q_6$ . To probe this property, we compute the cluster sizes of atoms with high values of  $q_6$ , i.e.,  $q_6 \geq q_6^{\text{cut}}$ , where  $q_6^{\text{cut}}$  is chosen to be past the peak of the corresponding distribution. The inferences do not depend on the exact value of  $q_6^{\text{cut}}$ . We find that the population of large clusters grow as a result of annealing. It is a significant observation in two ways. First, even when there are minimal changes in SRO and modest changes in polyhedral connections, the evolution of ordered clusters—a medium-range phenomenon—is much more pronounced. Second, the increase in densities of large ordered-clusters upon annealing is in contrast with the observation made for the stable glasses obtained through elevated-temperature vapor-deposition simulation.<sup>[65]</sup> In the latter simulations, the density of large-ordered clusters is seen to be lower in stable glasses than in ordinary glasses. While we do not intend to make an implicit suggestion that stable glasses and annealed glasses were expected to have similar structures, it is nevertheless interesting to see the opposite trends. Perhaps this is worth further investigation, especially in the context of the manner in which TLS densities and loss spectra are modified in stable glasses versus annealed glasses.

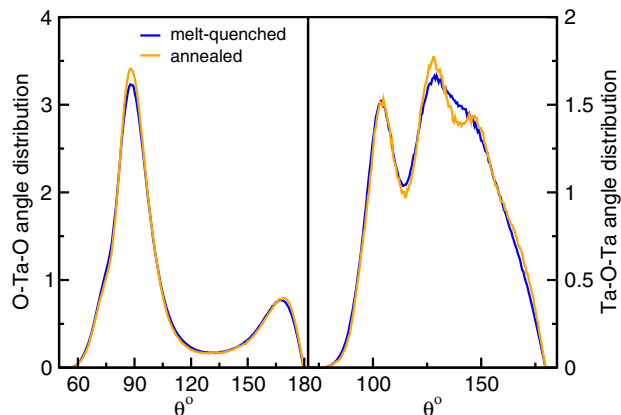


**Figure 8.** BA distribution in  $\text{Ta}_2\text{O}_5$  computed from melt-quenched and annealed models.

## 4. Conclusions and Future Work

In conclusion, we have conducted modeling of melt-quenched and annealed  $\text{SiO}_2$ ,  $\text{GeO}_2$ , and  $\text{Ta}_2\text{O}_5$  using MD simulations in two-body BKS force fields. We used the recently developed method of “population annealing” MD to expedite the sampling of the PEL as a way to mimic relaxation processes induced by annealing. We then studied the structural changes between melt-quenched and annealed models as an approximate way

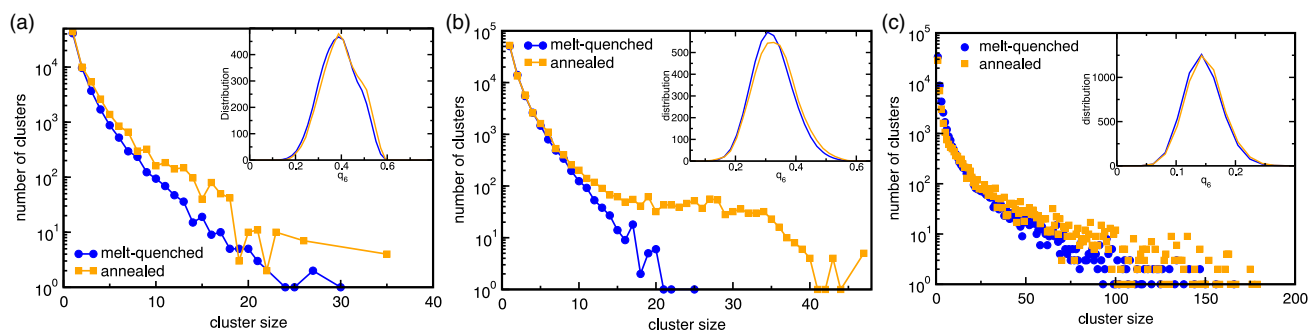


**Figure 9.** Annealing-induced evolution of ordered clusters in a)  $\text{SiO}_2$ , b)  $\text{GeO}_2$ , and c)  $\text{Ta}_2\text{O}_5$ . The main plots show the number of ordered clusters of given sizes. Atoms satisfying the condition  $q_6 \geq q_6^{\text{cut}}$  are included in same cluster if they are less than  $r_{\text{cut}}$  distance apart. We take  $q_6^{\text{cut}}$  to be 0.50, 0.40, and 0.18, respectively. Only Si/Ge/Ta subnetworks are considered for this analysis—see text for details. The values of  $r_{\text{cut}}$  are taken to be equal to the first minima of corresponding partial PDFs. The insets show the distribution of  $q_6$  of respective systems.

to study the effects of laboratory annealing of these materials. Wherever possible, we compared our results with other experimental or theoretical probes and found that our modeling of structure and annealing effects are in reasonable agreement with the literature. We computed X-ray PDFs from our models and showed that the annealing-induced effects are more pronounced in the medium range. We investigated short-range features like coordinations, polyhedral connections, and BA distributions, as well as medium-range features like distributions of ring sizes and ordered clusters. We found that subtle but significant differences are manifested in all of these probes. We computed the vibrational states using a harmonic approximation and analyzed the densities of states with respect to changes in ring structure and BA.

These findings are useful to understand the effect of annealing on mechanical loss of amorphous oxides, such as those used in low-thermal-noise optical coatings for gravitational-wave detection. The mechanical loss is often described as transitions between TLSs, which are determined by the atomic structure of the coating. For  $\text{SiO}_2$ ,  $\text{GeO}_2$ , and  $\text{Ta}_2\text{O}_5$ , room-temperature mechanical loss has been observed to decrease upon annealing, whereas mechanical loss at low temperatures often increases.<sup>[6,8,9,67]</sup> It is therefore useful to connect annealing-induced changes in atomic structure to changes in TLS densities (hence, in mechanical loss). For example, structures like under- and overcoordinated atoms, anomalous BAs, ESP and FSP, small-membered rings, etc. could be associated with TLSs in these oxides.<sup>[9,38]</sup> Furthermore, earlier works have suggested that medium-range structures are correlated with mechanical loss.<sup>[48,59,68]</sup> Modeled TLSs in  $\text{SiO}_2$  and  $\text{Ta}_2\text{O}_5$  are also shown to involve several tens of atoms extended over nanometer(s).<sup>[69,70]</sup> This indicates that the change in medium-range order observed in this work could be important to understand the TLSs and relaxation processes in these oxides.

Several future investigations would be possible. First, while we investigated the structural relaxations captured by basic PAMD, we have made no attempts to optimize the PAMD method itself. A range of improvements in PAMD, including finding optimum population sizes, temperature schedules, temperature-dependent decoupling times, etc., can produce more efficient sampling of PEL per resource unit. Second, more accurate interatomic

potentials can significantly improve these calculations. While the latter statement is true in general, we have seen that the BKS potentials used in this work are not able to model Si–Si or Ge–Ge or Ta–Ta correlations as well as VDOS very well. A three-body potential may also address some of these shortcomings.

## Acknowledgements

The authors acknowledge the support of the LSC Center for Coatings Research, jointly funded by the National Science Foundation (NSF) and the Gordon and Betty Moore Foundation (GBMF). In particular, the authors are grateful for support through NSF awards PHY-1707866, PHY-1708175, and GBMF grant no. 6793. Partial support from grant ONR no. N00014-17-1-2536 is acknowledged. The authors would like to thank the Sherlock Cluster at Stanford University for providing computational resources and support that contributed to these research results. This work also used the Extreme Science and Engineering Discovery Environment (XSEDE),<sup>[76]</sup> which was supported by National Science Foundation grant number ACI-1548562.

## Conflict of Interest

The authors declare no conflict of interest.

## Data Availability Statement

Research data are not shared.

## Keywords

annealing, germania, molecular dynamics, silica, tantalum

Received: September 30, 2020  
Revised: April 12, 2021  
Published online: May 24, 2021

[1] A. Amato, S. Terreni, V. Dolique, D. Forest, G. Gemme, M. Granata, L. Mereni, C. Michel, L. Pinard, B. Sassolas, J. Teillon, G. Cagnoli, M. Canepa, *J. Phys.: Mater.* **2019**, 2, 035004.

- [2] R. Birney, J. Steinlechner, Z. Tornasi, S. MacFoy, D. Vine, A. S. Bell, D. Gibson, J. Hough, S. Rowan, P. Sortais, S. Sproules, S. Tait, I. W. Martin, S. Reid, *Phys. Rev. Lett.* **2018**, 121, 191101.
- [3] T. Böntgen, T. Alig, I. Balasa, L. Jensen, D. Ristau, *Proc. SPIE* **2019**, 11180, 1118045.
- [4] D. Ristau, T. Gross, *Proc. SPIE* **2005**, 5963, 596313.
- [5] L. Pinard, C. Michel, B. Sassolas, J. Teillon, G. Cagnoli, M. Sigwarth, T. Kentischer, W. Schmidt, B. Reichman, *Proc. SPIE* **2018**, 10706, 107061R.
- [6] I. W. Martin, R. Bassiri, R. Nawrodt, M. M. Fejer, A. Grefarsson, E. Gustafson, G. Harry, J. Hough, I. MacLaren, S. Penn, S. Reid, R. Route, S. Rowan, C. Schwarz, P. Seidel, J. Scott, A. L. Woodcraft, *Classical Quantum Gravity* **2010**, 27, 225020.
- [7] G. Vajente, R. Birney, A. Ananyeva, S. Angelova, R. Asselin, B. Baloukas, R. Bassiri, G. Billingsley, M. M. Fejer, D. Gibson, L. J. Godbout, E. Gustafson, A. Heptonstall, J. Hough, S. MacFoy, A. Markosyan, I. W. Martin, L. Martinu, P. G. Murray, S. Penn, S. Roorda, S. Rowan, F. Schiettekatte, R. Shink, C. Torrie, D. Vine, S. Reid, R. X. Adhikari, *Classical Quantum Gravity* **2018**, 35, 075001.
- [8] G. M. Harry, M. R. Abernathy, A. E. Becerra-Toledo, H. Armandula, E. Black, K. Dooley, M. Eichenfield, C. Nwagwu, A. Villar, D. R. M. Crooks, G. Cagnoli, J. Hough, C. R. How, I. MacLaren, P. Murray, S. Reid, S. Rowan, P. H. Sneddon, M. M. Fejer, R. Route, S. D. Penn, P. Ganau, J.-M. Mackowski, C. Michel, L. Pinard, A. Remillieux, *Classical Quantum Gravity* **2006**, 24, 405.
- [9] K. Prasai, J. Jiang, A. Mishkin, B. Shyam, S. Angelova, R. Birney, D. A. Drabold, M. Fazio, E. K. Gustafson, G. Harry, S. Hoback, J. Hough, C. Lévesque, I. MacLaren, A. Markosyan, I. W. Martin, C. S. Menoni, P. G. Murray, S. Penn, S. Reid, R. Robie, S. Rowan, F. Schiettekatte, R. Shink, A. Turner, G. Vajente, H.-P. Cheng, M. M. Fejer, A. Mehta, R. Bassiri, *Phys. Rev. Lett.* **2019**, 123, 045501.
- [10] B. P. Abbott, R. Abbott, T. D. Abbott, M. R. Abernathy, F. Acernese, K. Ackley, C. Adams, T. Adams, P. Addesso, R. X. Adhikari, V. B. Adya, C. Affeldt, M. Agathos, K. Agatsuma, N. Aggarwal, O. D. Aguiar, I. Aiello, A. Ain, P. Ajith, B. Allen, A. Allocca, P. A. Altin, S. B. Anderson, W. G. Anderson, K. Arai, M. A. Arain, M. C. Araya, C. C. Arceneaux, J. S. Areeda, N. Arnaud, et al., *Phys. Rev. Lett.* **2016**, 116, 061102.
- [11] J. Steinlechner, *Philos. Trans. R. Soc. A: Math. Phys. Eng. Sci.* **2018**, 376, 20170282.
- [12] S. Hild, *Classical Quantum Gravity* **2012**, 29, 124006.
- [13] J. Miller, L. Barsotti, S. Vitale, P. Fritschel, M. Evans, D. Sigg, *Phys. Rev. D* **2015**, 91, 062005.
- [14] M. Granata, E. Coillet, V. Martinez, V. Dolique, A. Amato, M. Canepa, J. Margueritat, C. Martinet, A. Mermet, C. Michel, L. Pinard, B. Sassolas, G. Cagnoli, *Phys. Rev. Mater.* **2018**, 2, 053607.
- [15] M. Granata, A. Amato, G. Cagnoli, M. Coulon, J. Degallaix, D. Forest, L. Mereni, C. Michel, L. Pinard, B. Sassolas, J. Teillon, *Appl. Opt.* **2020**, 59, A229.
- [16] B. Shyam, K. H. Stone, R. Bassiri, M. M. Fejer, M. F. Toney, A. Mehta, *Sci. Rep.* **2016**, 6, 32170.
- [17] R. Bassiri, K. B. Borisenko, D. J. H. Cockayne, J. Hough, I. MacLaren, S. Rowan, *Appl. Phys. Lett.* **2011**, 98, 031904.
- [18] R. Bassiri, K. Evans, K. B. Borisenko, M. M. Fejer, J. Hough, I. MacLaren, I. W. Martin, R. K. Route, S. Rowan, *Acta Mater.* **2013**, 61, 1070.
- [19] N. Kim, J. F. Stebbins, *J. Non-Cryst. Solids* **2013**, 378, 158.
- [20] M. A. Fazio, G. Vajente, A. Ananyeva, A. Markosyan, R. Bassiri, M. M. Fejer, C. S. Menoni, *Opt. Mater. Express* **2020**, 10, 1687.
- [21] M. Fazio, L. Yang, A. Markosyan, R. Bassiri, M. M. Fejer, C. S. Menoni, *Appl. Opt.* **2020**, 59, A106.
- [22] D. A. Drabold, *Eur. Phys. J. B* **2009**, 68, 1.
- [23] D. A. Drabold, *Insulating and Semiconducting Glasses*, World Scientific, Singapore **2000**, pp. 607–651.
- [24] D. J. Earl, M. W. Deem, *Phys. Chem. Chem. Phys.* **2005**, 7, 3910.
- [25] J. Machta, *Phys. Rev. E* **2010**, 82, 026704.
- [26] N. Mousseau, G. T. Barkema, *Phys. Rev. E* **1998**, 57, 2419.
- [27] D. Perez, B. P. Uberuaga, Y. Shim, J. G. Amar, A. F. Voter, *Annu. Rep. Comput. Chem.* **2009**, 5, 79.
- [28] W. Wang, J. Machta, H. G. Katzgraber, *Phys. Rev. E* **2015**, 92, 013303.
- [29] U. H. Hansmann, *Chem. Phys. Lett.* **1997**, 281, 140.
- [30] H. Christiansen, M. Weigel, W. Janke, *Phys. Rev. Lett.* **2019**, 122, 060602.
- [31] N. Bernstein, B. Bhattarai, Gábor. Csányi, D. A. Drabold, S. R. Elliott, V. L. Deringer, *Angew. Chem., Int. Ed.* **2019**, 131, 7131.
- [32] B. W. H. Van Beest, G. J. Kramer, R. A. Van Santen, *Phys. Rev. Lett.* **1990**, 64, 1955.
- [33] S. Sundararaman, L. Huang, S. Ispas, W. Kob, *J. Chem. Phys.* **2018**, 148, 194504.
- [34] R. D. Oeffner, S. R. Elliott, *Phys. Rev. B* **1998**, 58, 14791.
- [35] J. P. Trinastic, R. Hamdan, Y. Wu, L. Zhang, H.-P. Cheng, *J. Chem. Phys.* **2013**, 139, 154506.
- [36] E. Bitzek, P. Koskinen, F. Gähler, M. Moseler, P. Gumbsch, *Phys. Rev. Lett.* **2006**, 97, 170201.
- [37] M. Micoulaut, Y. Guissani, B. Guillot, *Phys. Rev. E* **2006**, 73, 031504.
- [38] T. Damart, E. Coillet, A. Tanguy, D. Rodney, *J. Appl. Phys.* **2016**, 119, 175106.
- [39] S. Plimpton, *J. Comput. Phys.* **1995**, 117, 1.
- [40] K. Prasai, LIGO Scientific Collaboration, unpublished documents **2020**.
- [41] L. Skuja, *J. Non-Cryst. Solids* **1998**, 239, 16.
- [42] S. Munekuni, T. Yamanaka, Y. Shimogaichi, R. Tohmon, Y. Ohki, K. Nagasawa, Y. Hama, *J. Appl. Phys.* **1990**, 68, 1212.
- [43] R. Bassiri, C. Clark, I. W. Martin, A. Markosyan, P. G. Murray, J. Tessmer, S. Rowan, M. M. Fejer, *Proc. SPIE* **2015**, 9632, 963204.
- [44] L. Yang, E. Randel, G. Vajente, A. Ananyeva, E. Gustafson, A. Markosyan, R. Bassiri, M. Fejer, C. Menoni, *Appl. Opt.* **2020**, 59, A150.
- [45] T. Damart, D. Rodney, *Phys. Rev. B* **2018**, 97, 014201.
- [46] J. M. D. Lane, *Phys. Rev. E* **2015**, 92, 012320.
- [47] N. Kim, J. F. Stebbins, *Chem. Mater.* **2011**, 23, 3460.
- [48] M. J. Hart, R. Bassiri, K. B. Borisenko, M. Véron, E. F. Rauch, I. W. Martin, S. Rowan, M. M. Fejer, I. MacLaren, *J. Non-Cryst. Solids* **2016**, 438, 10.
- [49] S. R. Elliott, *Nature* **1991**, 354, 445.
- [50] P. S. Salmon, *Proc. R. Soc. Lond. Ser. A: Math. Phys. Sci.* **1994**, 445, 351.
- [51] P. H. Gaskell, D. J. Wallis, *Phys. Rev. Lett.* **1996**, 76, 66.
- [52] H. Masai, S. Kohara, Y. Onodera, A. Koreeda, K. Saito, E. H. Sekiya, N. Kitamura, *J. Ceram. Soc. Jpn.* **2020**, 128, 1038.
- [53] F. L. Galeener, A. J. Leadbetter, M. W. Stringfellow, *Phys. Rev. B* **1983**, 27, 1052.
- [54] C. Joseph, P. Bourson, M. D. Fontana, *J. Raman Spectrosc.* **2012**, 43, 1146.
- [55] A. Pasquarello, R. Car, *Phys. Rev. Lett.* **1998**, 80, 5145.
- [56] P. Umari, X. Gonze, A. Pasquarello, *Phys. Rev. Lett.* **2003**, 90, 027401.
- [57] L. Giacomazzi, P. Umari, A. Pasquarello, *Phys. Rev. Lett.* **2005**, 95, 075505.
- [58] J. Peralta, G. Gutiérrez, J. Rogan, *J. Phys.: Condens. Matter* **2008**, 20, 145215.
- [59] L. Yang, G. Vajente, M. Fazio, A. Ananyeva, G. Billingsley, A. Markosyan, R. Bassiri, K. Prasai, M. M. Fejer, C. S. Menoni, arXiv:2102.08526, **2021**.
- [60] B. C. Bunker, D. M. Haaland, T. A. Michalske, W. L. Smith, *Surf. Sci.* **1989**, 222, 95.
- [61] M.-H. Du, A. Kolchin, H.-P. Cheng, *J. Chem. Phys.* **2004**, 120, 1044.
- [62] A. Rimola, P. Ugliengo, *J. Chem. Phys.* **2008**, 128, 204702.
- [63] B. S. Lunin, K. V. Tokmakov, *J. Am. Ceram. Soc.* **2019**, 102, 3329.
- [64] E. Scalise, M. Houssa, G. Pourtois, V. V. Afanas'ev, A. Stesmans, *Appl. Phys. Lett.* **2011**, 98, 202110.



- [65] S. Singh, M. D. Ediger, J. J. de Pablo, *Nat. Mater.* **2013**, 12, 139.
- [66] P. J. Steinhardt, D. R. Nelson, M. Ronchetti, *Phys. Rev. B* **1983**, 28, 784.
- [67] K. A. Topp, D. G. Cahill, *Z. Phys. B: Condens. Matter* **1996**, 101, 235.
- [68] A. Amato, S. Terreni, M. Granata, C. Michel, B. Sassolas, L. Pinard, M. Canepa, G. Cagnoli, *Sci. Rep.* **2020**, 10, 1670.
- [69] C. R. Billman, J. P. Trinastic, D. J. Davis, R. Hamdan, H.-P. Cheng, *Phys. Rev. B* **2017**, 95, 014109.
- [70] J. P. Trinastic, R. Hamdan, C. Billman, H.-P. Cheng, *Phys. Rev. B* **2016**, 93, 014105.
- [71] P. E. Blöchl, *Phys. Rev. B* **1994**, 50, 17953.
- [72] J. P. Perdew, K. Burke, M. Ernzerhof, *Phys. Rev. Lett.* **1996**, 77, 3865.
- [73] G. Kresse, J. Hafner, *Phys. Rev. B* **1993**, 47, 558.
- [74] G. Kresse, J. Furthmüller, *Phys. Rev. B* **1996**, 54, 11169.
- [75] S. Le Roux, P. Jund, *Comput. Mater. Sci.* **2010**, 49, 70.
- [76] J. Towns, T. Cockerill, M. Dahan, I. Foster, K. Gaither, A. Grimshaw, V. Hazlewood, S. Lathrop, D. Lifka, G. D. Peterson, R. Roskies, J. R. Scott, N. Wilkins-Diehr, *Comput. Sci. Eng.* **2014**, 16, 62.

# Constrained Extrapolation Problem and Order-Dependent Mappings

Corbinian Wellenhofer,\* Daniel R. Phillips,\* and Achim Schwenk\*

Dedicated to Professor David A. Drabold on the occasion of his 60th birthday

The problem of extrapolating the perturbation series for the dilute Fermi gas in three dimensions to the unitary limit of infinite scattering length and into the BEC region is considered, using the available strong-coupling information to constrain the extrapolation problem. In this constrained extrapolation problem (CEP), the goal is to find classes of approximants that give well-converged results already for low perturbative truncation orders. First, it is shown that the standard Padé and Borel methods are too restrictive to give satisfactory results for this CEP. A generalization of Borel extrapolation is given by the so-called maximum-entropy (MaxEnt) extrapolation method. However, it is shown that MaxEnt requires extensive elaborations to be applicable to the dilute Fermi gas and is, thus, not practical for the CEP in this case. Instead, order-dependent-mapping extrapolation (ODME) as a simple, practical, and general method for the CEP is proposed. It is found that the ODME approximants for the ground-state energy of the dilute Fermi gas are robust with respect to changes of the mapping choice and agree with results from quantum Monte Carlo simulations within uncertainties.

*"It's the job that's never started as takes longest to finish." Sam Gamgee  
Lord of the Rings, J. R. R. Tolkien  
In recognition of Prof. Drabold's love of Middle Earth, throughout the paper, we provide inspirational quotes from a classic text.*

## 1. Introduction

Consider an observable  $F$  of a system characterized by a coupling  $x$ , and let  $F$  be defined relative to the noninteracting system. (The ground-state energy  $E/E_0$  is a canonical example.) Quantitative analytic knowledge about  $F(x)$  is, in most cases, restricted to its weak-coupling perturbation series up to a given order  $N$ , that is

$$F(x) \stackrel{x \rightarrow 0}{\simeq} 1 + \sum_{k=1}^N c_k x^k + O(x^{N+1}) \quad (1)$$

While it provides precise information about the behavior of  $F(x)$  as  $x \rightarrow 0$ , the perturbation series generally fails to yield viable approximations away from weak coupling.

Indeed, the perturbation series is generally a divergent asymptotic series, with factorially growing coefficients at large orders, e.g.,  $c_k \stackrel{k \rightarrow \infty}{\sim} k!$ .<sup>[1,2]</sup> The principle of superasymptotics<sup>[3]</sup> states that for a given  $x$ , the accuracy of the perturbation series increases with increasing  $N$  only for  $N < N_{\text{opt}}$ , where the optimal truncation order  $N_{\text{opt}}$  is given by the largest  $N$  for which  $|c_N x^N| < |c_{N-1} x^{N-1}|$ .

Resummation methods such as Padé<sup>[4,5]</sup> and Borel resummation<sup>[2]</sup> can produce estimates for  $F(x)$  beyond superasymptotics. In the case of simple idealized systems where detailed knowledge of the analytic structure of  $F(x)$  is available, Borel methods can yield approximants that converge to the exact  $F(x)$  for  $N \rightarrow \infty$ .<sup>[6–8]</sup> However, for realistic systems, standard resummation methods generally fail to give access to the regime of strong coupling, in particular, if only a few of the perturbation coefficients are available.


Experimental or computational methods provide access to the behavior of  $F(x)$  at strong coupling, yielding information on the

Dr. C. Wellenhofer, Prof. A. Schwenk  
Department of Physics  
Technische Universität Darmstadt  
64289 Darmstadt, Germany  
E-mail: wellenhofer@theorie.iikp.physik.tu-darmstadt.de;  
schwenk@physik.tu-darmstadt.de

Dr. C. Wellenhofer, Prof. A. Schwenk  
ExtreMe Matter Institute EMMI  
GSI Helmholtzzentrum für Schwerionenforschung GmbH  
6429 Darmstadt, Germany

Prof. D. R. Phillips  
Department of Physics and Astronomy and Institute of Nuclear and Particle Physics  
Ohio University  
Athens, OH 45701, USA  
E-mail: phillid1@ohio.edu

Prof. A. Schwenk  
Max-Planck-Institut für Kernphysik  
Saupfercheckweg 1, 69117 Heidelberg, Germany

 The ORCID identification number(s) for the author(s) of this article can be found under <https://doi.org/10.1002/pssb.202000554>.

DOI: 10.1002/pssb.202000554

limit  $F(x \rightarrow -\infty) = \xi$  as well as the leading coefficients  $d_k$  in the strong-coupling expansion (SCE)

$$F(x) \stackrel{x \rightarrow -\infty}{\sim} \xi + \sum_{k=1}^M \frac{d_k}{x^k} + O(x^{-M-1}) \quad (2)$$

Weak-to-strong-coupling extrapolants can then be defined as classes of functions  $F_N(x)$  that reproduce the perturbation series to order  $N$  and incorporate additional strong-coupling information—where the latter, in general, will come with numerical uncertainties. *This defines the constrained extrapolation problem (CEP).* Formally, the goal of the CEP is to find approximants  $F_N(x)$  that converge rapidly and smoothly to the correct  $F(x)$  as  $N \rightarrow \infty$ . In practice,  $F_N(x)$  should be well converged already at low orders, because typical knowledge of the perturbation series is restricted to a low truncation order  $N \lesssim 4 - 6$  (see, e.g., refs. [9–12]).

In this article, we consider the CEP for an unpolarized gas of spin-1/2 fermions interacting via short-range interactions, which are characterized by the s-wave scattering length  $a_s$  at low energies. The zero-temperature properties of the system are then determined by the single variable  $x = k_F a_s$ , where  $k_F$  is the Fermi momentum of the system. In this way, the dilute Fermi gas constitutes a prime example of low-energy universality, with relevance to a variety of systems, in particular, ultracold atoms<sup>[13–15]</sup> and neutron matter.<sup>[16–19]</sup> The weak-coupling expansion of the ground-state energy  $F = E/E_0$  was recently calculated to fourth order:<sup>[10,20]</sup>

$$c_k = \left( \frac{10}{9\pi}, \frac{44 - 8 \ln 2}{21\pi^2}, 0.0303089(0), -0.0708(1), \dots \right) \quad (3)$$

where the “(0)” after the seventh digit of the third-order coefficient means that its numerical error is smaller than  $5 \times 10^{-8}$ . (We note that in our previous paper,<sup>[21]</sup> there is a typo in the seventh digit of  $c_3$ ; i.e., Equation (3) of ref. [21] should say  $c_3 = 0.0303089(0)$  not  $c_3 = 0.0303088(0)$ ). Notably, for spins higher than 1/2, both logarithmic terms  $\sim x^n \ln|x|$  and multi-fermion couplings are present in the perturbation series.<sup>[10]</sup> The extrapolation problem is then much more intricate in that case, in particular, because more and more multi-fermion parameters appear at higher orders (the complete perturbation series has an infinite number of them). Therefore, in this article, we consider only the spin-1/2 case with the single parameter  $a_s$ . The perturbation series is then analytic in  $x = k_F a_s$ .

The strong-coupling regime of the dilute Fermi gas has been the focus of many experimental and theoretical studies in the past two decades.<sup>[13–15]</sup> Here, the salient feature at zero temperature is the BCS–BEC crossover from large negative to large positive  $a_s$ , where the point with infinite scattering length (i.e.,  $1/a_s = 0$ ) is referred to as the unitary limit. By dimensional analysis, the energy of the unitary Fermi gas is given by  $E(k_F) = \xi E_0(k_F)$ , where  $\xi$  is called the Bertsch parameter.

Regarding the CEP, what is relevant is not the functional form of the  $k_F$  dependence at  $1/a_s = 0$ , but only that  $\xi$  is the leading term in the SCE (Equation (2)). The Bertsch parameter has been determined experimentally with ultracold atoms as  $\xi = 0.376(4)$ <sup>[22]</sup> and from quantum Monte Carlo (QMC)

simulations as  $\xi = 0.372(5)$ .<sup>[23]</sup> Furthermore, QMC provides estimates for the leading two strong-coupling coefficients  $d_1$  and  $d_2$ ,  $d_1 \approx -0.9$  and  $d_2 \approx -0.8$ , with  $d_1$  known more precisely<sup>[24]</sup> (see also Navon et al.<sup>[25]</sup>). Such a situation is typical of many physics problems, because, often, only limited data are available in the nonperturbative region.

This article is organized as follows. First, in Section 2, we apply (two-point) Padé approximants to the CEP for the dilute Fermi gas. We find that Padé does not yield satisfactory results for the CEP; in particular, several of them give flawed approximants with poles in the BCS region. In Section 3, we then examine Borel methods. We find that these methods also have severe deficiencies regarding our goal of producing well-converged classes of constrained extrapolants. Next, in Section 4, we study maximum-entropy (MaxEnt) extrapolation,<sup>[26,27]</sup> which is a modification of Borel extrapolation that allows the definition of a larger class of approximant functions. It has been demonstrated that in certain cases, MaxEnt can outperform both Borel and Padé methods,<sup>[26,27]</sup> and we examine one such case, the harmonic oscillator with an octic term. However, we show that, to be applicable to the dilute Fermi gas, MaxEnt requires extensive elaborations that render it impractical in that case.

After these unsuccessful explorations, in Section 5, we then introduce order-dependent-mapping extrapolation (ODME) as a straightforward and very flexible method for the CEP. The ODME method, which was developed in our previous study,<sup>[21]</sup> improves on the order-dependent-mapping (ODM) approach invented by Seznec and Zinn-Justin<sup>[28]</sup> (see also Yukalov<sup>[29]</sup>) and builds in information on the leading strong-coupling coefficients— $d_1$  and  $d_2$  in this case. We review the connection of the original ODM to optimized perturbation theory (PT) and discuss the principles used in previous work to select the parameter  $\alpha$  of the mapping. We then explain why, in the CEP, strong-coupling information provides a physics-guided way to choose  $\alpha$  and show that the ODME leads to well-converged approximants for the ground-state energy of the dilute Fermi gas. The ODME solution to the CEP for the dilute Fermi gas compares well with QMC results throughout the BCS regime and beyond. Finally, Section 6 offers a summary and avenues for future work.

Some of these results already appeared in our previous study,<sup>[21]</sup> but, here, we provide additional discussions of them, as well as detailed comparisons to the Borel and MaxEnt methods.

## 2. Padé Approximants

*“It’s a dangerous business, Frodo, extrapolation. You step out of the perturbative regime, and if you don’t keep your analytic structure, there’s no knowing where you might be swept off to.”*

Padé extrapolation works by fixing the coefficients of a rational function  $\text{Padé}[n, m](x)$ , such that its Maclaurin series matches the perturbation series to order  $N = n + m$ . Here,  $n$  is the degree of the polynomial in the numerator,  $m$  is the denominator degree, and the Padé approximant is normalized to  $\text{Padé}[n, m](0) = 1$  in our case. Two-point Padé is the

generalization of this approach to the CEP: the Padé coefficients are matched to both the perturbation series and the SCE up to specified orders  $N$  and  $M$ . According to the definition of the CEP in our previous study,<sup>[21]</sup>  $M$  remains fixed for each  $N$ .  $N$  and  $M$  are related to the degrees of the polynomials in the Padé according to  $N + M = n + m - 2$ . As the Bertsch parameter is finite and nonzero, we are restricted to “diagonal Padé” with  $n = m$ , that is

$$\text{Padé}[n, m = n](x) = \frac{1 + \sum_{k=1}^n a_k x^k}{1 + \sum_{k=1}^n b_k x^k} \quad (4)$$

For diagonal Padé  $N + M = 2n - 2$  is even, so a further impediment is that they are applicable to the CEP only for even or odd truncation orders, respectively (depending on  $M$ ). Moreover, a general problem with Padé approximants is that they can have spurious poles in the region of interest. A simple example is given in the book by Bender and Orszag:<sup>[5]</sup> the Padé $[N, 1]$  approximant for the function  $y(x) = (x + 10)/(1 - x^2) \approx \sum_{n=0}^N a_n x^n$  is given by

$$\text{Padé}[N, 1](x) = \sum_{n=0}^{N-2} a_n x^n + \frac{a_{N-1} x^{N-1}}{1 - a_N x / a_{N-1}} \quad (5)$$

This has a simple pole at  $x = 1/10$  if  $N$  is even, and this feature is absent in the exact  $y(x)$ .

In **Figure 1**, we show the results for the ground-state energy  $F(x)$  of the dilute Fermi gas obtained from diagonal Padé approximants matched to  $\xi$ ,  $d_1$  and  $d_2$ , and  $N = 2, 4$  perturbation coefficients. In addition, we also show results obtained from the truncated perturbation series and the truncated SCE, as well as results from QMC computations.<sup>[18]</sup> One sees that the perturbation series provides well-converged results for  $|x| \lesssim 0.5$ <sup>[10]</sup> and diverges strongly for  $|x| \gtrsim 1$ . The behavior of the SCE is similar; i.e., it is well converged for  $|1/x| \lesssim 0.5$  only. Regarding the  $N = 2, 4$  two-point Padé, “2pt – Padé $[2, 2]$ ” and “2pt – Padé $[3, 3]$ ,” at weak coupling, they both improve upon

the perturbative approximants: for  $|x| \lesssim 1$  they are close to each other and near the QMC results, with the higher-order Padé more accurate. The low-order ( $N = 2$ ) Padé actually provides reasonably good results throughout the BCS region; i.e., it is not too far off the QMC data for  $1/x < 0$ . Eventually though, there is a spurious pole at  $1/x = 0.27$ , so in the BEC region, it fails to provide viable results already for small positive  $1/x$ . The  $N = 4$  Padé, on the other hand, has a pole at negative real coupling (at  $x \approx -1.49$ ), and as shown in Figure 1, this leads to a significantly impaired extrapolation. We note that the  $n = 3$  two-point Padé constructed to match  $\xi$ ,  $d_1$ ,  $d_2$ , and three perturbation coefficients has also a pole at negative real coupling, at  $x \approx -0.17$ . Because of these defects in the analytic structure, we conclude that the two-point Padé approximants are not suitable for the CEP of the dilute Fermi gas.

### 3. Borel Extrapolation Methods

*“Long years ago, in the last years of the nineteenth century, Mathematicians forged resummation methods of great power.”*

#### 3.1. General Discussion

Compared with Padé approximants, Borel extrapolation represents a more sophisticated framework that allows the construction of approximants that explicitly consider the large-order behavior of the perturbation series. The starting point of the Borel methods is the Borel(-Leroy) transformed perturbation series

$$\mathcal{B}(t) \stackrel{t \rightarrow 0}{\approx} 1 + \sum_{k=1}^{\infty} \frac{c_k}{\Gamma(k + 1 + \beta_0)} t^k \quad (6)$$

where the standard Borel transform corresponds to  $\beta_0 = 0$ . In contrast to the perturbation series, the Borel transformed series

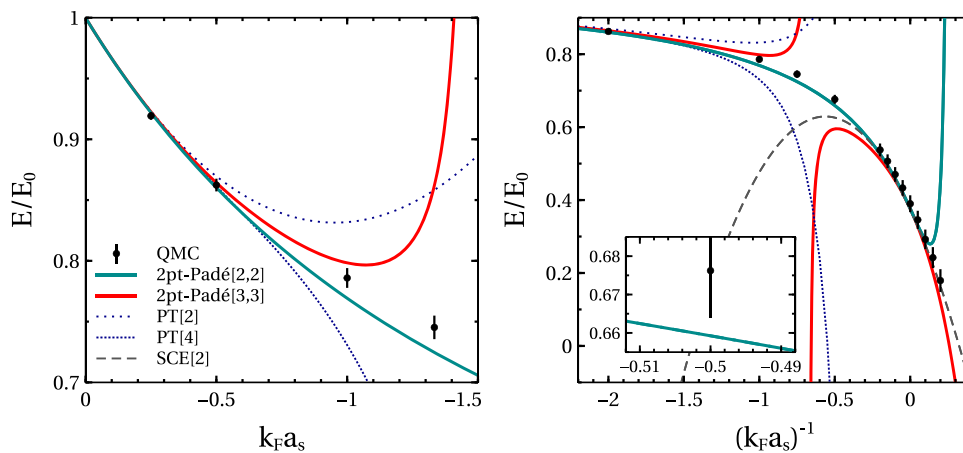


**Figure 1.** Two-point Padé approximants for the ground-state energy  $F(x)$  of the dilute Fermi gas; see text for details. The left plot shows the weak-to-intermediate coupling BCS regime of  $F(x)$  as a function of  $x = k_F a_s$ , whereas the right plot shows  $F(x)$  as a function of  $1/x = (k_F a_s)^{-1}$  throughout the BCS–BEC crossover. In each plot, we also show the truncated PT series PT $[N]$  for  $N = 2, 4$ , and in the right plot, also the SCE truncated at the second order ( $M = 2$ ). In both cases, we also show results from QMC computations.<sup>[18]</sup> (The errors of the QMC data are estimated as specified in ref. [21]). The inset in the right plot magnifies the behavior at the intermediate coupling  $x = -2$ .



has a finite convergence radius. That is, the large-order behavior

$$c_k \stackrel{k \rightarrow \infty}{\sim} a^k \Gamma(k + 1 + \beta) \quad (7)$$

together with the choice of  $\beta_0$ , determines the nature of the leading singularity of  $\mathcal{B}(t)$  at  $t = 1/a$ ; see refs. [8,9,11].

Borel resummation corresponds to constructing  $F(x)$  in terms of the inverse Borel transform  $\mathcal{B}(x)$  of the analytic continuation  $\mathcal{B}(t)$  of the Borel transformed perturbation series

$$\mathcal{B}(x) = \int_0^\infty dt e^{-t} t^{\beta_0} \mathcal{B}(tx) \quad (8)$$

In the so-called “Borel nonsummable case” where  $\mathcal{B}(tx)$  has poles on the positive real axis, one can shift the integration path infinitesimally off the real axis. In this case, the approximant for  $F(x)$  may be taken as the real part of  $\mathcal{B}(x)$ , a prescription that often gives the correct result.<sup>[2,6,28,30]</sup> The detailed study of the analytic properties of the Borel transform and the Borel nonsummable case are the subject of resurgence theory.<sup>[31,32]</sup>

In the realistic case where the perturbation series is known only to a certain order  $N$ , the goal is to construct approximants  $B_N(x)$  for  $F(x)$  via the inverse Borel transform of approximants  $\mathcal{B}_N(t)$  for  $\mathcal{B}(t)$ . There are three basic methods for that (As discussed, in each of these three methods, we incorporate the unitary limit  $F(-\infty) = \xi$ . We note that in the weak-to-intermediate coupling region (i.e., for  $|x| \lesssim 1$ ), the “unconstrained” Borel methods give results that are similar to the ones obtained from the “constrained” Borel methods.): 1) Padé–Borel: matching of Padé approximants to the Borel transform of the truncated perturbation series; 2) conformal-Borel (CB): truncated re-expansion of the Borel transform series in terms of a conformal mapping  $w(t)$  that is chosen based on the analytic properties of  $\mathcal{B}(t)$ ; and 3) Padé–conformal-Borel (PCB): matching of Padé approximants to the conformally re-expanded Borel series. In the CB and PCB cases, this corresponds to the methods we denoted as CCB and PCCB in our previous study,<sup>[21]</sup> where the additional “C” stands for “constrained.”

For each of these, to incorporate the correct unitary limit  $B_N(-\infty) = \xi$ , we introduce a rescaled version of  $F(x)$  that approaches 0 as  $x \rightarrow -\infty$

$$f(x) = \frac{F(x) - \xi}{1 - \xi} \quad (9)$$

The implementation of further strong-coupling constraints is less straightforward and not considered here. A study of this problem can be found in ref. [33], where it was found that two-point Padé–Borel approximants do not improve upon two-point Padé.

In Padé–Borel, incorporating the unitary limit  $f(-\infty) = 0$  requires that off-diagonal Padé $[n, m]$  approximants with  $m > n$  are used. Padé–Borel, in contrast to the conformal methods CB and PCB, makes no use of analytic properties of  $f(x)$ . In CB and PCB, the principal analytic information determining the choice of the conformal mapping  $w(t)$  is the large-order behavior of the perturbation series, specifically the coefficient  $a$  in Equation (7). That is, given knowledge of  $a$ , one chooses the mapping

$$w(t) = \frac{\sqrt{1 - at} - 1}{\sqrt{1 - at} + 1} \quad (10)$$

that maps the cut Borel  $t$ -plane to the interior of the unit disc.<sup>[2,11]</sup> The conformal re-expansion of the Borel series is then constructed as

$$\mathcal{B}_N(t) = (1 - w(t))^\eta \sum_{k=0}^N s_k [w(t)]^k \quad (11)$$

where the prefactor ensures the correct unitary limit  $B_N(-\infty) = 0$ . The exponent  $\eta$  of the prefactor in Equation (11) is chosen, such that the known analytic structure at infinity is best reproduced. As the SCE (Equation (2)) has no fractional powers of  $1/x$ , we set  $\eta = 1$ . The coefficients  $s_k$  are given by

$$s_k = \frac{1}{(1 - \xi)k!} \sum_{n, m=0}^k c_n \gamma_{n, m}(0) \quad (12)$$

with

$$\gamma_{n, m}(t) = \left. \frac{\partial^m [t(w)]^n}{\partial w^m} \right|_{w=w(t)} \quad (13)$$

The conformal transformation (10) yields a function that has a square-root branch point at  $t = 1/a$ . A refinement of CB resummation (compared with the standard choice  $\beta_0 = 0$ ) corresponds to setting  $\beta_0 = \beta + 3/2$ ; since then, the exact Borel transform has the same feature.<sup>[9]</sup>

### 3.2. Application to Dilute Fermi Gas

The large-order behavior of the perturbation series of the dilute Fermi gas is not known at present. The basic idea is that the (leading) large-order behavior should be determined by (dominant) nonperturbative properties of the system—that would be pairing effects in this case of the dilute Fermi gas. Based on their results for the dilute Fermi gas in 1D,<sup>[30,34]</sup> Marino and Reis recently conjectured that  $a = -1/\pi$  and  $\beta = 0$  for the 3D Fermi gas.<sup>[30]</sup> This conjecture is also motivated by their finding that the subset of ladder diagrams gives  $a = -1/(2\pi)$ , whereas the subset of particle–particle ladders yields  $a = -1/(4\pi)$ .<sup>[30]</sup>

The results from different Borel approximants for the ground-state energy  $F(x)$  of the dilute Fermi gas are shown in **Figure 2**. Regarding the two choices for the parameter  $\beta_0$  in the Borel transform (Equation (6)) considered earlier, for Padé–Borel, we use the standard choice  $\beta_0 = 0$ , whereas for CB and PCB, we use the refined choice  $\beta_0 = \beta + 3/2 = 3/2$ . In each case, this yields results that are closer to the central QMC points. (Note that the refined choice is motivated only for CB and PCB but not for Padé–Borel.) Furthermore, in contrast to the case of Padé approximants, no simple analytic continuation into the BEC region is available for Borel approximants.

Regarding Padé–Borel $[n, m]$  approximants matched to the rescaled function  $f(x)$ , in the upper row of Figure 2, we show the results obtained for  $[n, m] \in \{[0, 1], [0, 2], [1, 2], [1, 3]\}$ ,

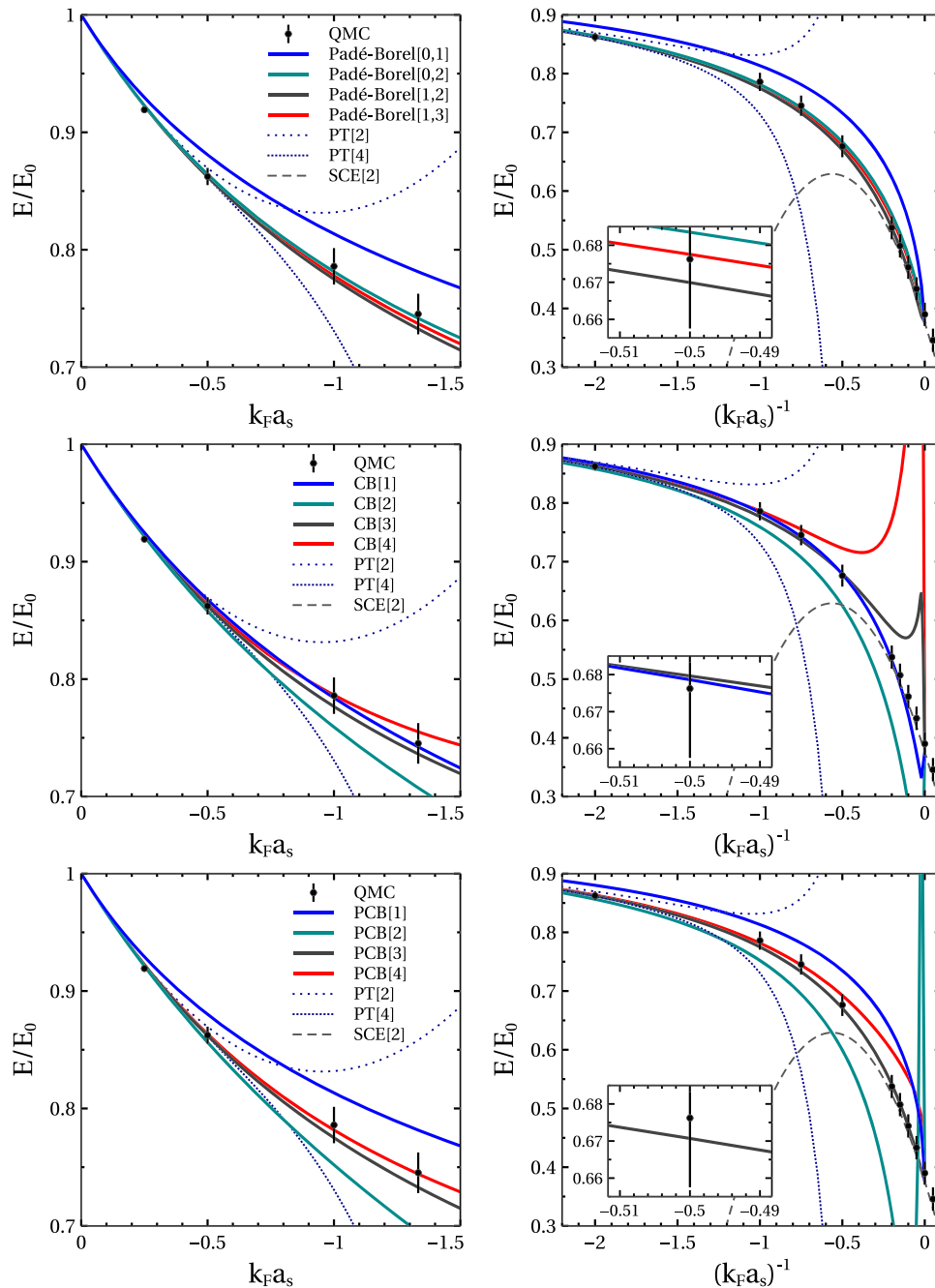


**Figure 2.** Different Borel approximants for the ground-state energy  $F(x)$  of the dilute Fermi gas; see text for details. As in Figure 1, the two plots in each row show different parts of the BCS regime. In the strong-coupling plot (right-hand side), we cut out most of the BEC regions, because Borel approximants cannot easily be continued beyond the unitary limit. The first row shows various Padé–Borel approximants with  $\beta_0 = 0$ , whereas the subsequent two rows display results obtained from the CB and PCB methods with  $\beta_0 = 3/2$ . As in Figure 1, we also show PT, the SCE, and the QMC results.

corresponding to input from the first  $N \in \{1, 2, 3, 4\}$  perturbative coefficients. One sees that at weak-to-intermediate coupling, the results from the  $N = 2, 3, 4$  Padé–Borel are within the QMC errors. The  $N = 3, 4$  results are within the QMC errors throughout the entire BCS regime. For  $|x| \lesssim 1.5$ , the  $N = 2$  results are closest to the central QMC points, whereas for larger  $|x|$ , the  $N = 4$  ones perform better.

The results from the  $CB[N]$  and  $PCB[N]$  approximants, shown in the middle and lower row of Figure 2, are notably different. (In the PCB case, we use the standard  $[n, n]$  and  $[n, n + 1]$  Padé for even and odd  $N$ , respectively.) At low  $|x| \lesssim 1.5$ , the CB results that come closest to the central QMC points are those obtained for  $N = 1$ , followed by  $N = 3$  and  $N = 4$ . In the strong-coupling regime, all CB approximants deviate substantially from the QMC

data at some point. As the correct unitary limit is enforced, this behavior is accompanied by local extrema. In the PCB case, for  $|x| \lesssim 1.5$ , the results improve with increasing  $N$ , with the  $N = 3, 4$  ones consistent with the QMC data. However, at larger  $|x|$ , only the  $N = 3$  PCB stays within the QMC error bars.

Altogether, we find that among the Borel methods, only Padé–Borel approximants give good results in the BCS region. However, no simple analytic continuation into the BEC region and no straightforward way to incorporate strong-coupling information beyond the unitary limit are available for them. Furthermore, we note that although Padé–Borel approximants perform reasonably well for the dilute Fermi gas, in other cases, such as the 0D model and the 1D Fermi gas considered in our previous study,<sup>[21]</sup> they do not give accurate results at strong coupling (see Figure A1 and A2 of ref. [21]). (To be precise, in ref. [21] we used the standard  $[n, n+1]$  (for odd  $N$ ) and  $[n, n]$  (for even  $N$ ) Padé for Padé–Borel, whereas, here, we use  $[n, n+1]$  (for odd  $N$ ) and  $[n, n+2]$  Padé. For the 0D and 1D cases considered in ref. [21], the  $[n, n+2]$  Padé–Borel approximants improve upon the  $[n, n]$  ones only near the strong-coupling limit.) Therefore, we conclude that the Borel methods are only of limited suitability for this CEP.

## 4. MaxEnt Extrapolation

*“Fermi gas drowns out all but the  
brightest extrapolations.”*

### 4.1. Setup

MaxEnt extrapolation<sup>[26,27,35]</sup> may be seen as a generalization of Borel extrapolation. That is, instead of Equation (8), we consider approximants  $f_N(x)$  for  $f(x)$  of Equation (9) of the more general form

$$f_N(x) = \int_D dt \rho(t) K(tx) \quad (14)$$

where the density  $\rho(z)$  is semipositive in the domain  $D$ , i.e.,  $\rho(z) \geq 0$  for  $z \in D$ . As we consider the rescaled function  $f(x)$  given by Equation (9), the kernel  $K(x)$  should satisfy  $K(-\infty) = 0$ . Given a choice of the kernel  $K(x)$  and the domain  $D$ , the approximant  $f_N(x)$  is then required to reproduce the first  $N$  terms of the perturbation series of  $F(x)$ . This means that one needs to solve the (finite) moment problem

$$\forall n \in \{0, \dots, N\}: \int_D dt \rho(t) t^n = \mu_n \quad (15)$$

where the moments are given by  $\mu_n = c_n/K_n$ , with  $K_n$  the Maclaurin coefficients of  $K(x)$ . Without loss of generality, we may choose a function  $K(x)$  that has  $K_0 = 1$ , so as  $F(x)$  (or  $f(x)$ ) have  $c_0 = 1$ , we may assume  $\mu_0 = 1$ .

The moment problem (Equation (15)) is solvable only in certain cases, as discussed in the following. However, even if it is solvable, the moment conditions do not determine the density  $\rho(t)$  uniquely. The MaxEnt idea is to pick the most likely solution for  $\rho(t)$ . This means that as an additional condition on  $\rho(t)$ , we require that the entropy functional  $S[\rho]$  given by

$$S[\rho] = - \int_D dt \rho(t) \ln(\rho(t)) \quad (16)$$

is maximized.<sup>[36,37]</sup> Via the method of Lagrange multipliers, the moment problem and  $\delta S/\delta \rho = 0$  can be combined into the condition

$$\frac{\delta S_N[\rho]}{\delta \rho} = 0 \quad (17)$$

with

$$S_N[\rho] = S[\rho] + \sum_{n=0}^N \lambda_n \left( \int_D dt \rho(t) t^n - \mu_n \right) \quad (18)$$

The (formal) solution of Equation (17) is readily found as

$$\rho_N(t) = \exp \left( - \sum_{n=0}^N \lambda_n t^n \right) \quad (19)$$

where the Lagrange multipliers  $\lambda_n$  are determined by the solution of the moment problem with  $\rho_N(t)$  substituted for  $\rho(t)$ , that is

$$\forall n \in \{0, \dots, N\}: \int_D dt \exp \left( - \sum_{m=0}^N \lambda_m t^m \right) t^n = \mu_n \quad (20)$$

The problem of solving these  $N+1$  nonlinear equations can be formulated as a minimization problem.<sup>[38]</sup> That is, we define the “effective potential”  $\Gamma(\lambda_1, \dots, \lambda_N)$  as

$$\Gamma = \ln Z + \sum_{n=1}^N \mu_n \lambda_n \quad (21)$$

where

$$Z = \int_D dt e^{-\sum_{n=1}^N \lambda_n t^n} \quad (22)$$

From Equation (20) together with  $\mu_0 = 1$ , it follows that  $Z = e^{\lambda_0}$ ; i.e.,  $\lambda_0$  is determined by  $\{\lambda_1, \dots, \lambda_N\}$ . Stationary points of  $\Gamma$  obey the moment conditions, and  $\Gamma$  can be shown to be convex everywhere.<sup>[38]</sup> Thus, given that  $\Gamma$  has a local minimum, this unique minimum yields the set  $\{\lambda_1, \dots, \lambda_N\}$  that solves the MaxEnt moment problem, Equation (20).

### 4.2. Moment Conditions

Here, we discuss the necessary and sufficient conditions for the existence of a (unique) solution to the MaxEnt moment problem. We consider a compact domain  $D = [a, b]$ , so Equation (15) is the finite (i.e.,  $N$  is finite) Hausdorff moment problem.<sup>[39]</sup> We refer to Equation (20) as the (finite) Hausdorff MaxEnt moment problem. The case where  $D = [a, \infty]$  is known as the Stieltjes moment problem and  $D = [-\infty, \infty]$  corresponds to the Hamburger moment problem. Notably, the Stieltjes moment conditions<sup>[40,41]</sup> deviate from the  $b \rightarrow \infty$  limit of the Hausdorff conditions discussed as follows. However, since in the Stieltjes case it is  $\rho(t) \rightarrow 0$  for  $t \rightarrow \infty$ , for practical applications we can assume a compact domain.

The Hausdorff moment problem can be rescaled to the canonical form

$$\forall n \in \{0, \dots, N\}: \int_0^1 d\zeta p(\zeta) \zeta^n = \omega_n \quad (23)$$

Here, the scaled moments  $\omega_n$  are obtained iteratively from the  $N+1$  linear equations

$$\forall n \in \{0, \dots, N\}: \sum_{k=0}^n \binom{n}{k} (b-a)^k \omega_k a^{n-k} = \mu_n \quad (24)$$

The original density  $\rho(t)$  is obtained from the scaled density  $p(\zeta)$  using the affine transformation that relates  $t$  and  $\zeta$

$$\rho(t) = \frac{1}{b-a} p\left(\frac{t-a}{b-a}\right) \quad (25)$$

As shown in the book by Akhiezer<sup>[39]</sup> (p. 74), the necessary and sufficient condition for the existence of a unique solution to the finite Hausdorff moment problem is that the eigenvalues of the matrices

$$\begin{aligned} Q &= (\omega_{i+j+1})_{i=0, \dots, m, j=0, \dots, m}, \\ R &= (\omega_{i+j} - \omega_{i+j+1})_{i=0, \dots, m, j=0, \dots, m} \end{aligned} \quad (26)$$

for odd  $N = 2m + 1$  and

$$\begin{aligned} Q &= (\omega_{i+j})_{i=0, \dots, m, j=0, \dots, m}, \\ R &= (\omega_{i+j+1} - \omega_{i+j+2})_{i=0, \dots, m-1, j=0, \dots, m-1} \end{aligned} \quad (27)$$

for even  $N = 2m$  are nonnegative. For  $N \in \{1, 2, 3\}$ , this (together with  $0 \leq \omega_{n+1} \leq \omega_n \leq 1$ ) yields the following conditions on the scaled moments  $\omega_n$

$$N = 1: 0 \leq \omega_1 \leq 1 \quad (28)$$

$$N = 2: 0 \leq \omega_1^2 \leq \omega_2 \leq \omega_1 \leq 1 \quad (29)$$

$$N = 3: 0 \leq \frac{\omega_2^2}{\omega_1} \leq \omega_3 \leq \omega_2 \leq \omega_1 \leq 1 \wedge \omega_1^2 - \omega_1(\omega_2 + \omega_3) - \omega_2(1 - \omega_2) + \omega_3 \leq 0 \quad (30)$$

Mead and Papanicolaou<sup>[38]</sup> proved that the existence conditions for the infinite Hausdorff moment problem (i.e., complete monotonicity of the sequence  $\{\omega_n\}$ ,  $n \in \{1, \dots, \infty\}$ ) guarantee the existence of a unique solution of the associated infinite Hausdorff MaxEnt moment problem. Their proof can be trivially adapted to prove that the existence conditions for the finite Hausdorff moment problem are also sufficient for the existence of a unique solution of the finite Hausdorff MaxEnt problem.

### 4.3. Application to Octic Oscillator

Before we investigate the requirements on the kernel  $K(x)$  and the domain  $D = [a, b]$  imposed by the Hausdorff moment conditions for the dilute Fermi gas, following refs. [26,27], we first study a different system where these conditions are easily

satisfied: the harmonic oscillator with an octic term, which we refer to as the octic oscillator.

The octic oscillator is defined by the Hamiltonian

$$H = p^2/2 + x^2/2 + gx^8 \quad (31)$$

where  $[x, p] = i$ . Following Bender et al.,<sup>[26]</sup> we write the ground-state energy as  $E(g) = 1/2 + 105gf(g)/16$ , where  $f(g) \rightarrow 0$  and  $E(g) \rightarrow \infty$  for  $g \rightarrow \infty$ . The weak-coupling perturbation series of  $f(g)$  reads

$$f(g) \stackrel{g \rightarrow 0}{\sim} 1 + \sum_{k=1}^N c_k g^k + O(x^{N+1}) \quad (32)$$

The leading perturbation coefficients are given by

$$c_k = \left( -\frac{643}{2}, \frac{3824275}{8}, -\frac{242134255883}{128}, \frac{8050560668350165}{512}, -\frac{973733659602733224723}{4096}, \dots \right) \quad (33)$$

and their large-order behavior is of the form<sup>[26]</sup>

$$c_k \stackrel{k \rightarrow \infty}{\sim} k^{-1/2} q^k (3k)! \quad (34)$$

It can be shown that  $f(g)$  is a generalized Stieltjes function.<sup>[26]</sup> That is,  $f(g)$  can be written as

$$f(g) = \int_0^\infty dt \frac{\rho(t)}{1+tg} \quad (35)$$

so the perturbation coefficients can be represented as

$$c_k = \int_0^\infty dt \rho(t) t^{k-1} \quad (36)$$

Because of the rapid growth of the perturbation coefficients with  $k$ , the density  $\rho(t)$  is not uniquely determined.<sup>[26]</sup> However, Equation (36) implies that the (Stieltjes) MaxEnt moment problem with kernel  $K_0(g) = 1/(1+g)$  does have a unique solution (for each  $N$ ). Thus, we consider MaxEnt approximants  $f_N(g)$  for  $f(g)$  of the form

$$f_N(g) = \int_0^\infty dt e^{-\sum_{n=0}^N \lambda_n t^n} K_0(tg) \quad (37)$$

where the kernel

$$K_0(g) = \frac{1}{1+g} \quad (38)$$

associated with Equation (35). This corresponds to the original kernel choice by Bender et al. in their pioneering study of the MaxEnt extrapolation technique.<sup>[26]</sup> An improved kernel that incorporates the leading strong-coupling behavior<sup>[42]</sup>

$$f(g) \stackrel{g \rightarrow \infty}{\sim} g^{-4/5} \quad (39)$$

was considered by Drabold and Jones,<sup>[27]</sup> that is



**Table 1.** Results from MaxEnt and Padé approximants for the inverse of the octic oscillator function  $f(g)$  are compared with the exact  $1/f(g)$  for different perturbation orders  $N$  and  $g \in \{0.001, 0.01, 0.1, 0.5, 1, 10\}$ . The exact results are taken from refs. [26,42,62].

Method	$N$	$g = 1/1000$	$g = 1/100$	$g = 1/10$	$g = 1/2$	$g = 1$	$g = 10$
Exact	–	1.21	2.04	5.46	13.37	20.46	94.98
MaxEnt $[K_{Dj}]$	1	1.25	2.49	8.47	24.20	39.18	209.9
MaxEnt $[K_{Dj}]$	2	1.24	2.41	8.02	22.43	36.75	195.9
MaxEnt $[K_{Dj}]$	3	1.22	2.25	7.14	19.83	31.83	167.6
MaxEnt $[K_0]$	1	1.26	2.68	10.66	35.43	61.65	428.6
MaxEnt $[K_0]$	2	1.25	2.57	9.94	32.68	56.68	391.1
MaxEnt $[K_0]$	3	1.22	2.37	8.61	27.58	47.44	321.8
Padé	1	1.32	4.22	33.16	161.9	322.5	3216
Padé	3	1.24	3.37	24.49	118.4	235.7	2348
Padé	5	1.23	3.08	21.49	103.3	205.5	2046
Padé	7	1.23	2.94	19.92	95.4	189.8	1888
Padé	9	1.22	2.85	18.95	90.5	179.9	1789

$$K_{Dj}(g) = \frac{1}{(1+g)^{4/5}} \quad (40)$$

In **Table 1**, we compared the low-order MaxEnt results obtained from these two kernel choices to exact results. Also shown are the results from Padé $[n, n+1]$  approximants. Note that although  $E(g)$  is a Stieltjes function, as  $c_k$  grows more rapidly than  $(2k)!$ , the Padé approximants are not guaranteed to converge to the correct answer.<sup>[26]</sup> One sees that the improved kernel of Drabold and Jones  $K_{Dj}(g)$  gives better results than the kernel of Bender et al.,  $K_0(g)$ . For both kernels, MaxEnt performs significantly better than Padé approximants.

#### 4.4. Impracticity for Dilute Fermi Gas

We now consider the application of the MaxEnt extrapolation technique for the CEP of the dilute Fermi gas, i.e., for the rescaled function  $f(x)$  given by Equation (9). In terms of the unscaled moments, the  $N \in \{1, 2\}$  Hausdorff conditions (Equation (28) and (29)) read

$$N = 1: a \leq \mu_1 \leq b \quad (41)$$

$$N = 2: a^2 \leq \mu_1^2 \leq \mu_2 \leq \mu_1(b+a) - ba \leq b^2 \quad (42)$$

For the simplest kernel choice analogous to Equation (38),  $K(x) = 1/(1-x)$ , the condition  $\mu_1^2 \leq \mu_2$  yields  $c_1^2 \leq c_2(1-\xi)$ , which is not satisfied for  $c_1 \approx 0.3537$ ,  $c_2 \approx 0.1855$ , and  $\xi \approx 0.376$ . Thus, there exists no domain  $D$ , such that MaxEnt with the kernel  $K(x) = 1/(1-x)$  is applicable for the dilute Fermi gas for  $N \geq 2$ .

A kernel for which the  $N = 2$  MaxEnt moment problem can be made solvable is given by

$$K(x) = \frac{1}{1-\alpha x} + \frac{1}{1-\beta x^2} \quad (43)$$

For this kernel, there exists a range for  $\alpha$  and  $\beta$  as well as  $a$  and  $b$  for which Equation (42) is satisfied. However, the  $N \geq 3$  conditions are still violated. To amend this, one may, for  $N = 3$ , add (e.g.,) a term  $\Delta K_3(x) = 1/(1-\gamma x^3)$  to  $K(x)$ , for  $N = 4$ , then (e.g.,) an additional term  $\Delta K_4(x) = 1/(1+\delta x^4)$ , and so on.

Then, there are two possibilities to construct a sequence of MaxEnt approximants  $f_{N'=1, \dots, N}(x)$  for a given truncation order  $N$ , i.e., 1) one chooses  $K(x)$ , such that the order  $N$  conditions are satisfied; and 2) one uses a “kernel scheme” where for each subsequent  $N'$ , a different (i.e., extended) kernel is used.

These two methods are, however, not very useful for the dilute-Fermi-gas CEP. In both, the kernel parameter space increases dimensionally with  $N$  or  $N'$ . A given sequence of MaxEnt approximants corresponds to a particular trajectory in this parameter space. The dimensional increase in the parameter space with  $N$  or  $N'$  then makes it very difficult to identify approximant sequences with good convergence properties. We, therefore, conclude that MaxEnt is not suitable for the dilute-Fermi-gas CEP.

## 5. Order-Dependent Mapping Extrapolation

*“One extrapolation to rule them all.”*

In this section, we discuss the ODME method developed in our previous study.<sup>[21]</sup> We start by introducing a 0D model problem in Section 5.1. Therefore, we show how the (bare) perturbation series for the 0D model can be improved using an order-dependent expansion point. Subsequently, we show that this improvement can be reformulated as an order-dependent re-expansion of the bare perturbation series, corresponding to the “method of order-dependent mappings (ODMs)” introduced by Seznec and Zinn-Justin.<sup>[28]</sup> In Section 5.2, we then state the general formulation of ODM and prove that, for the 0D model, it converges to the exact solution. Next, in Section 5.2, we introduce ODME and show that it provides a significant improvement over ODM. Finally, in Section 5.4, we discuss the application of ODME to the dilute-Fermi-gas CEP.

### 5.1. From Optimized PT to ODM

#### 5.1.1. Bare Perturbation Series

As in our previous study,<sup>[21]</sup> we consider the partition function of the 0D  $\varphi^4$  theory (see also Zinn-Justin<sup>[2]</sup>)

$$Z(g) = \frac{1}{\sqrt{\pi}} \int_{-\infty}^{\infty} d\varphi e^{-\varphi^2 - g\varphi^4} \quad (44)$$

This is, of course, just an integral, whose value depends on the coupling  $g$ . We refer to it as the “0D model.” Its perturbative approximants are given by

$$Z_N^{\text{PT}(0)}(g) = \frac{1}{\sqrt{\pi}} \int_{-\infty}^{\infty} d\varphi e^{-\varphi^2} \underbrace{\sum_{k=0}^N \frac{(-g\varphi^4)^k}{k!}}_{\equiv Z_N^{\text{PT}(0)}(\varphi, g)} \quad (45)$$

$$= \sum_{k=0}^N g^k \underbrace{\int_{-\infty}^{\infty} d\varphi e^{-\varphi^2} \frac{(-\varphi^4)^k}{\sqrt{\pi} k!}}_{\equiv c_k}$$

with

$$c_k = (-1)^k \frac{(4k)!}{2^{4k} (2k)! k!} \xrightarrow{k \rightarrow \infty} \frac{1}{\sqrt{2\pi}} (-4)^k (k-1)! \quad (46)$$

As shown in the first block of **Table 2**, the low-order perturbative approximants are very precise for  $g \lesssim 0.01$ , but for  $g \gtrsim 0.1$ , they diverge strongly from the exact result.

The divergent behavior of the perturbative approximants can be understood by comparing their integral representation with that of the exact partition function. The exact integrand  $e^{-\varphi^2 - g\varphi^4}$  decays smoothly with  $\varphi$ . The perturbative integrands  $z_n^{\text{PT}(0)}(\varphi, g)$ , on the other hand, have large tails with local extrema that grow with  $g$  and  $N$ ; see Pernice and Oleaga.<sup>[43]</sup>

### 5.1.2. Optimized Perturbation Series

There is a straightforward way to fix this deficiency of the perturbative integrands: one constructs an “optimized perturbation

series” where the unperturbed partition function has as integrand  $e^{-(1+g\lambda)\varphi^2}$ . This gives

$$Z_N^{\text{PT}(\lambda)}(g) = \frac{1}{\sqrt{\pi}} \int_{-\infty}^{\infty} d\varphi e^{-(1+g\lambda)\varphi^2} \underbrace{\sum_{k=0}^N \frac{(-g\varphi^4 + g\lambda\varphi^2)^k}{k!}}_{\equiv Z_N^{\text{PT}(\lambda)}(\varphi, g)} \quad (47)$$

By having the parameter  $\lambda$  depend suitably on the truncation order  $N$ , the tails of the perturbative integrands can be removed, leading to an expansion whose convergence is improved over that of the bare perturbation series. We note that this method, which we denote by “optimized perturbation series,” is often referred to as the “linear delta expansion” in the literature.<sup>[44–53]</sup> Also, note that the optimized perturbation series is similar to PT with an order-dependent reference Hamiltonian.<sup>[54]</sup>

One can choose  $\lambda(N)$ , such that the optimized perturbation series converges for all values of  $g$ . As shown by Guida et al.,<sup>[55]</sup> this requires that  $\lambda(N) \stackrel{N \rightarrow \infty}{\sim} N^{\gamma/2}$ , with  $1 < \gamma < 2$ . (For  $\gamma = 1$ , the convergence condition is  $\lambda(N) \stackrel{N \rightarrow \infty}{\sim} N^{\gamma/2}/C'$ , with  $C' < C_{\text{crit}}$ , where  $C_{\text{crit}} \approx 1.1167$ .) In the second block of **Table 2**, we show results for the choice  $\lambda(N) = \sqrt{N}$ . One sees that the optimized perturbation series indeed shows convergent behavior even for large values of  $g$ . Furthermore, it is more accurate than the bare perturbation series also at small  $g$  where both give good results.

### 5.1.3. Method of ODMs

The construction of the optimized perturbation series in this way may face technical difficulties in more complicated problems. To address this, following Seznec and Zinn-Justin,<sup>[28]</sup> we now reformulate the optimized perturbation series for the OD model, such that the bare perturbation series is used directly as input; i.e., no new path integrals have to be evaluated. We first define two new parameters  $\alpha$  and  $w$  as follows

$$\alpha = \frac{1}{\lambda + g\lambda^2}, \quad w = \frac{\sqrt{\alpha^2 - 4\alpha g} - \alpha}{\sqrt{\alpha^2 - 4\alpha g} + \alpha} \quad (48)$$

Substituting these new parameters into the optimized series, we find

$$Z_N^{\text{PT}(\lambda)}(g) = \sqrt{1-w} \sum_{k=0}^N w^k \underbrace{\int_{-\infty}^{\infty} d\varphi \frac{1}{\sqrt{\pi}} e^{-\varphi^2} (\alpha\varphi^4 - \varphi^2)^k}_{\equiv h_k(\alpha)} \quad (49)$$

$$\equiv Z_N^{\text{ODM}(\alpha)}(g)$$

which corresponds to the “method of ODMs”. As discussed further in Section 5.2, ODM corresponds to a truncated re-expansion (modulo a suitable prefactor) of the bare perturbation series.

While for the OD model, ODM and the optimized perturbation series appear to be equivalent, there is a difference: in the ODM, it is  $\alpha$  and not  $\lambda$  that is fixed at each truncation order  $N$ . (Note that the relation between  $\alpha$  and  $\lambda$  depends on  $g$ ; see Equation (48).) This difference between ODM and the optimized series is shown in **Table 2**, where in the third block, we show the results obtained

**Table 2.** Logarithmic errors  $\ln[Z_N(g) - Z(g)]/\ln[10]$  of different approximants  $Z_N(g)$  for the partition function of the OD model (Equation (44)) for orders  $N = 1, 2, 3, 4, 5$  and  $g \in \{0.01, 0.1, 1.0, 10\}$ . See text for details.

Method	$g$	$N = 1$	$N = 2$	$N = 3$	$N = 4$	$N = 5$
PT( $\lambda = 0$ )	0.01	−3.52	−4.62	−5.54	−6.35	−7.06
PT( $\lambda = 0$ )	0.1	−1.71	−1.88	−1.86	−1.72	−1.47
PT( $\lambda = 0$ )	1	−0.28	+0.44	+1.39	+2.49	+3.70
PT( $\lambda = 0$ )	10	+0.85	+2.51	+4.43	+6.51	+8.72
PT( $\lambda = \sqrt{N}$ )	0.01	−3.93	−5.12	−6.12	−7.01	−7.79
PT( $\lambda = \sqrt{N}$ )	0.1	−2.3	−2.81	−3.07	−3.22	−3.29
PT( $\lambda = \sqrt{N}$ )	1	−1.64	−2.25	−2.64	−3.20	−3.53
PT( $\lambda = \sqrt{N}$ )	10	−0.82	−0.94	−1.04	−1.14	−1.22
ODM( $\alpha = 1/N$ )	0.01	−3.80	−5.19	−6.42	−7.53	−8.57
ODM( $\alpha = 1/N$ )	0.1	−2.13	−2.80	−3.34	−3.83	−4.27
ODM( $\alpha = 1/N$ )	1	−1.21	−1.61	−1.89	−2.16	−2.39
ODM( $\alpha = 1/N$ )	10	−1.02	−1.34	−1.55	−1.75	−1.92
ODM(FAC)	0.01	−3.94	−5.31	−6.40	−7.32	−8.89
ODM(FAC)	0.1	−2.32	−2.99	−3.45	−3.81	−4.85
ODM(FAC)	1	−1.50	−1.95	−2.25	−2.49	−3.23
ODM(FAC)	10	−1.36	−1.75	−2.01	−2.22	−2.85
ODME	0.01	−4.14	−5.36	−6.98	−8.04	−9.37
ODME	0.1	−2.64	−3.19	−4.23	−4.73	−5.53
ODME	1	−2.20	−2.58	−3.32	−3.68	−4.26
ODME	10	−2.54	−2.88	−3.51	−3.83	−4.33

from ODM with  $\alpha(N) = 1/N$ . This corresponds to  $\lambda(N) = \sqrt{N}$  only in the limit  $N \rightarrow \infty$  but not at finite  $N$ . One sees that while the overall trend of the results is similar, for  $N = 3-5$ , the ODM method is slightly more precise than the optimized perturbation series both at small and large values  $g$ . However, at intermediate couplings near  $g = 1$ , the optimized perturbation series performs better.

## 5.2. ODM with FAC

For a function  $F(x)$  with weak-coupling expansion and SCE of the form of Equation (1) and (2), respectively, the ODM approximants for the rescaled function  $F(x)$  of Equation (9) are given by (with  $x$  now instead of  $g$ )

$$f_N(x) = \xi + (1 - \xi)[1 - w(x; \alpha)] \sum_{k=0}^N h_k(\alpha) [w(x; \alpha)]^k \quad (50)$$

Here,  $w(-\infty, \alpha) = 1$ , so the factor  $(1 - w)$  ensures the correct strong-coupling limit of  $F(x)$ :  $F(\infty) = \xi$ . The mapping  $w(x; \alpha)$  is chosen such that the (truncated) SCE of  $F_N(x)$  matches Equation (2). The coefficients  $h_k(\alpha)$  are chosen such that the weak-coupling expansion of  $F_N(x)$  matches Equation (1) to order  $N$ . This implies that  $h_k(\alpha)$  can be obtained by multiplying the perturbation series of the rescaled function  $f(x)$  given by Equation (57) by  $1/(1 - w)$ , substituting  $x = x(w)$ , and then expanding in powers of  $w$ . From this, we find

$$h_k = \frac{1}{(1 - \xi)k!} \sum_{n,m=0}^k c_n \gamma_{n,m}(0) \quad (51)$$

with

$$\gamma_{n,m}(x) = \frac{\partial^m [x(w)]^n}{\partial w^m} \Big|_{w=w(x)} \quad (52)$$

The SCE of the ODM model is not of the form of Equation (2) but involves fractional powers of  $g$

$$Z(g) = g^{1/4} \sum_{k=1}^{\infty} \frac{(-1)^{k-1} \Gamma(k/2 - 1/4)}{2\sqrt{\pi} (k-1)!} g^{-k/2} \quad (53)$$

To consider this feature, we use a prefactor  $\sqrt{1 - w}$  instead of  $(1 - w)$  and choose the mapping from Equation (48). The ODM approximants are then those given by Equation (49). The inverse mapping is given by

$$g(w) = \alpha \frac{w}{(1 - w)^2} \quad (54)$$

In general, the inverse mapping will not be available in a closed form. In that case, the coefficients  $\gamma_{n,m}$  can be calculated iteratively, as detailed in the Supplementary Material of our previous study.<sup>[21]</sup>

Two commonly used prescriptions for choosing  $\alpha(N)$  (or  $\lambda(N)$ , in optimized PT) are: 1) the criterion of “fastest apparent convergence (FAC)”<sup>[28,56]</sup> that fixes  $\alpha(N)$  such that the order  $N$  coefficient in the re-expanded series vanishes; and 2) the “principle of minimal sensitivity (PMS)”<sup>[29,57]</sup> meaning  $\alpha(N)$  should

be chosen such that the ODM approximant is least sensitive to variations of  $\alpha$  about its chosen value.

Both FAC and PMS may lead to complex values of  $\alpha(N)$ , in which case the resulting approximant is, for each  $N$ , defined as the real part of underlying ODM form. (There is also a PMS version of optimized PT (known as “variational PT”) where the real values of  $\lambda(N)$  are enforced; see refs. [9,58,59]).

In the original ODM by Seznec and Zinn-Justin<sup>[28]</sup> the parameter  $\alpha(N)$  is chosen by the FAC criterion, i.e., by  $h_N = 0$ . Adapting from refs. [28,48], we now show that Equation (49) indeed converges to the correct result for  $N \rightarrow \infty$  under the FAC choice. (A more elaborate convergence proof was provided by Guida et al.<sup>[55]</sup>) From Equation (47), the FAC criterion can be written as

$$\int_{-\infty}^{\infty} du e^{-N\phi(u)} = 0 \quad (55)$$

with  $u = g^2/\lambda$  and  $\phi(u) = \beta u + \ln(u^2 - u)$ , where  $\beta = (g\lambda^2 + \lambda)/N$ . Assuming the scaling  $\lambda(N) \stackrel{N \rightarrow \infty}{\sim} \sqrt{N}$  and  $\alpha(N) \stackrel{N \rightarrow \infty}{\sim} 1/N$ , respectively, we can evaluate Equation (55) by steepest descent. There are two saddle points, that is

$$u_{1,2} = \frac{1}{2} + \frac{1}{\beta} \left( 1 \pm \sqrt{1 + \beta^2/4} \right) \quad (56)$$

and  $h_N = 0$  implies that  $\phi(u_1) = \phi(u_2)$ , which leads to  $\beta = b_0 \approx 1.325487$ . From this, we obtain

$$\lambda(N) \xrightarrow{N \rightarrow \infty} \sqrt{\frac{b_0 N}{g}}, \quad \alpha(N) \xrightarrow{N \rightarrow \infty} \frac{1}{b_0 N} \quad (57)$$

From Equation (47), the remainder  $R_N(g) = Z(g) - Z_N(g)$  can be written as<sup>[47]</sup>

$$R_N(g) = \frac{\sqrt{\lambda}}{2\sqrt{\pi}} \int_{-\infty}^{\infty} \frac{du}{\sqrt{u}} \oint_C \frac{dz}{2\pi i} \frac{1}{z^{N+1}(z-1)} e^{-NS(z,u)} \quad (58)$$

where  $S(z, u) = \beta u + \beta_0 z u(u-1) + \ln(z)$ , with  $u$  and  $\beta$  as before, and  $\beta_0 = g\lambda^2/N$ . The contour  $C$  encloses the poles at  $z = 0$  and  $z = 1$ . A steepest descent evaluation leads to

$$R_N(g) \stackrel{N \rightarrow \infty}{\sim} \frac{\sqrt{\lambda}}{2\pi\sqrt{2N}} \int_{-\infty}^{\infty} \frac{du}{\sqrt{u}} \frac{1}{z_0^{N+1}} e^{-NS(z_0, u)} \quad (59)$$

with saddle point

$$z_0 = \frac{1}{\beta_0 u(1-u)} \xrightarrow{N \rightarrow \infty} \frac{1}{b_0 u(1-u)} \quad (60)$$

Finally, performing the  $u$  integral by steepest descent, one finds (see Duncan and Jones<sup>[48]</sup> for details)

$$R_N(g) \stackrel{N \rightarrow \infty}{\sim} N^{-3/4} e^{-\nu N} \quad (61)$$

with  $\nu \approx 0.662743$ , corresponding to exponential (geometric) convergence.

The results for ODM with the FAC choice of  $\alpha(N)$  are given in the fourth block of Table 2. As the FAC criterion  $h_N = 0$  yields several possibilities for  $\alpha(N)$ , we need an additional criterion:

we choose the FAC solution with smallest  $h_{N-1}$ . One sees that while the convergence pattern is qualitatively similar, FAC does yield a quantitative decrease in the errors at each order (and at each coupling) compared with what is seen with a generic  $\alpha = 1/N$  choice (the third block of Table 1). We note that we have examined ODM also with other  $\alpha(N)$  criteria, such as different versions of PMS, but we found that they give either worse or similar results as FAC with smallest  $h_{N-1}$ .

### 5.3. From ODM to ODME

Evidently, the choice of the criterion to fix the mapping parameter  $\alpha(N)$  plays an important part in the application of ODM. We have seen that, for the 0D model, the FAC criterion improves upon the simple scaling choice  $\alpha(N) = 1/N$ . However, the FAC (or PMS) choice appears somewhat heuristic, and it seems plausible  $\alpha(N)$  which give better results should exist.

A second issue is that in the CEP we want to include strong-coupling information beyond the unitary limit. One possible method for this was proposed (for optimized PT) by Kleinert.<sup>[60]</sup> However, that method still leaves the first issue, the choice of  $\alpha(N)$ .

The “ODME” approach introduced in our previous study<sup>[21]</sup> tackles these two issues at once. That is, in the ODME one fixes  $\alpha(N)$  by ensuring that the SCE of  $F_N(x)$  has a first-order coefficient equal to the first correction to the strong-coupling limit, i.e.,  $d_1$  of Equation (2). This again yields several possibilities for  $\alpha(N)$ ; we select the one that minimizes the difference between  $d_2$  and the corresponding coefficient of  $F_N(x)$ .

The ODME results for the 0D model are shown in the fifth block of Table 2. One sees that the ODME choice for  $\alpha(N)$  leads to much more precise approximants than FAC. In particular, ODME is more precise also at very small values of  $g$  where including additional strong-coupling information is not expected to give improved results. Furthermore, in our previous study<sup>[21]</sup> we showed that at low truncation orders ODME also outperforms the SCE (which has infinite radius of convergence), even at large  $g$ . For example, for  $g = 10$  and  $N \leq 4$  ODME is more accurate than the SCE truncated at the same order, and even at  $g = 100$  they reach similar precision for  $N = 4$ . Furthermore, at  $g = 1$  the SCE reaches a higher precision than ODME not until  $N \geq 14$ . Not surprisingly, in the weak-coupling regime ( $g \lesssim 1$ ), the SCE produces accurate results only for very large truncation order.

The ODME approach of our previous study<sup>[21]</sup> also makes constructive use of the mapping ambiguity of ODM: among the available mappings, in ODME one selects those that give the best converged results at low orders. As a measure for convergence, we consider the sum of the deviations of consecutive-order approximants

$$\Delta_w = \sum_{x_i} \sum_{N=2}^M \sigma_N |F_N(x_i) - F_{N-1}(x_i)| \quad (62)$$

Here,  $\{x_i\}$  are selected points in the coupling regime of interest, and  $M$  is the truncation order up to which the perturbation series is known. The weights  $\sigma_N$  may be chosen in accord with the principle that the deviation should be smaller at higher orders; e.g., one may set  $\sigma_N = N$ . In the ODME, one chooses the mappings  $w(x)$  for which the quantity  $\Delta_w$  is smallest. We

will make use of this criterion of low-order convergence when we apply ODME to the dilute-Fermi-gas CEP.

### 5.4. Application to Dilute Fermi Gas

We now discuss the application of ODME for the 3D Fermi gas. We consider mappings of the form

$$w(x) = -w_0 \frac{x}{D(x; \alpha)} \quad (63)$$

with  $w_0 = \lim_{x \rightarrow -\infty} D(x; \alpha)/x$ . A general form for  $D(x; \alpha)$  consistent with the SCE of the 1D and 3D Fermi gas is, for example

$$D(x; \alpha) = \kappa_1 \alpha - \kappa_2 x + (\kappa_3 \alpha^\mu + (-x)^\nu)^{1/\nu} \quad (64)$$

In principle, large sums of such terms could be used. However, we found that to have well-converged results at low orders, excessively complicated forms of  $D(x; \alpha)$  are disfavored.

In our previous study,<sup>[21]</sup> we examined several choices for  $D(x; \alpha)$ . We found a number of mappings that give quite similar results in the BCS regime. Among them, the two mappings for which the ODME approximants are best converged have

$$D(x; \alpha) = \alpha + \sqrt{\alpha + x^2} \quad (65)$$

and

$$D(x; \alpha) = \alpha + \sqrt{\alpha^2 + x^2} \quad (66)$$

Of the mappings we surveyed the quantity  $\Delta_w$  of Equation (62) is smallest for these two (we chose  $x_i$  evenly distributed in the BCS regime).

The results for the dilute Fermi gas CEP from these two mappings are shown in Figure 3. The bands correspond to the uncertainties in the values  $d_1 = -0.90(5)$  and  $d_2 = -0.8(1)$ . We used the central value of the experimental result for the Bertsch parameter,  $\xi = 0.376$ . For both mappings, the ODME results are below the central (variational) QMC points, and the ODME bands overlap with the QMC error bars for  $N \geq 2$ . While the first-order ( $N = 1$ ) ODME results are closer to the QMC points for the second mapping (Equation (66)), the ODME bands are smaller for the first mapping, corresponding to a slightly smaller  $\Delta_w$  (averaged over the  $d_1$  and  $d_2$  inputs).

The ODME approximants can be easily continued into the BEC region, and as shown in Figure 3, they still give reasonably well-converged results for BEC values of  $x$  that are not too far from the unitary limit. For both mappings, the dependence on the strong-coupling input in the BEC region is larger for  $N = 4$ . This may, however, be improved also by including BEC values into  $\Delta_w$  and by selecting sequences of ODME approximants according to their convergence for each  $(\xi, d_1, d_2)$  input value.

With approximant sequences that have good convergence properties in hand, we can use sequence extrapolation techniques such as the Shanks transformation to obtain estimates for  $N \rightarrow \infty$  results. For example, for  $x = -2$  and the central values of  $d_1$  and  $d_2$  quoted earlier, the second mapping (Equation (66)) gives the ODME values  $F_N(-2) \approx (0.644, 0.660, 0.663, 0.665)$  for  $N = (1, 2, 3, 4)$ , which approaches the QMC value  $F_{\text{QMC}}(-2) = 0.676(12)$ . The Shanks extrapolated



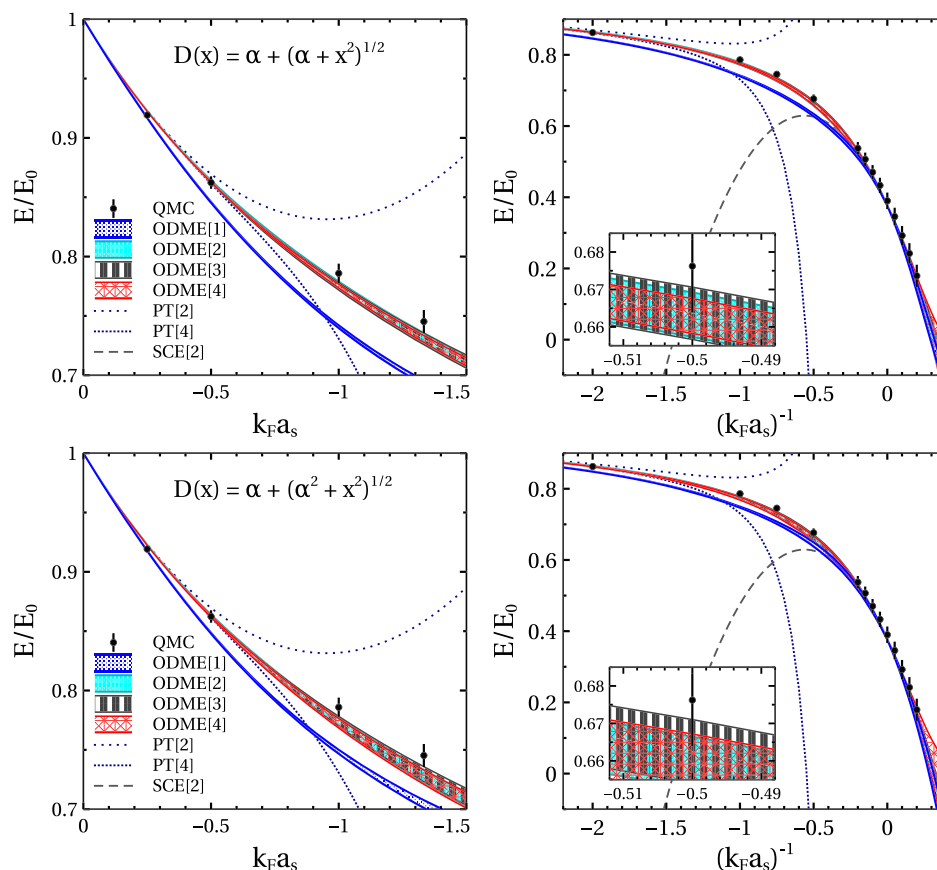


**Figure 3.** ODME results for the dilute Fermi gas for two different mappings. See text for details.

result is  $F_{\infty}(-2) \approx 0.670$ , which is well within the QMC error bar. For the first mapping (Equation (66)), we get instead  $F_N(-2) \approx (0.631, 0.664, 0.663, 0.663)$  for  $N = (1, 2, 3, 4)$ . The Shanks transformation gives  $F_{\infty}(-2) \approx 0.663$ , which is just below the QMC error bar. The larger values of  $d_1$  generally give results that are closer to the QMC data; e.g., for  $d_1 = 0.95$ , one gets  $F_N(-2) \approx (0.634, 0.669, 0.670, 0.668)$  and  $F_{\infty}(-2) \approx 0.670$ . Also, note that the QMC point at unitarity is  $F_{\text{QMC}}(-\infty) = 0.390(18)$ ; i.e., the experimental Bertsch parameter  $\xi = 0.376(4)$  lies at the lower end of the QMC error bar at unitarity. This, perhaps, provides a hint that the exact result at  $x = -2$  is actually closer to the ODME results than to the central QMC value used here.

## 6. Conclusion and Outlook

*"Don't adventures ever have an end? I suppose not. Someone else always has to carry on the story."*  
Bilbo Baggins

The problem of extrapolating a perturbation series beyond the weak-coupling regime is ubiquitous in theoretical physics. The CEP is to find sequences of perturbation-series extrapolants that consider limited strong-coupling information and are well converged at low orders. The strong-coupling information can come

either from experimental or from numerical simulations. In this article, we investigated several different approaches to the CEP. As our target problem, we focused on the constrained extrapolation of the perturbation series for the ground-state energy of the dilute Fermi gas throughout the entire BCS regime and into the BEC regime.

First, we examined two standard extrapolation methods, Padé and Borel resummation. We found that the results from these methods for our target problem are deficient in significant ways. While Padé is a straightforward approach and can implement any number of SCE constraints, it is unreliable, because unphysical poles can appear in the extrapolation region. The more sophisticated Borel method does not produce spurious poles and reliably improves the convergence of perturbative results in the weak-coupling region. However, we found that for many Borel extrapolants, the convergence breaks down at intermediate-to-strong coupling (see also the previous work by Wellenhofer, Drischler, and Schwenk<sup>[20]</sup>), even if they are constrained by strong-coupling information. Moreover, because they are based on an integral transform, Borel extrapolants cannot be easily continued into the BEC regime.

We then turned to the more flexible MaxEnt extrapolation technique, which can provide better results than standard resummation methods in certain cases. However, its application to the dilute Fermi gas is inhibited by the fact that the moment conditions, which must be satisfied for it to be applicable, require quite

intricate choices for the MaxEnt kernel. This renders the kernel highly ambiguous.

Finally, we introduced the ODME method developed in our previous study,<sup>[21]</sup> building on previous work by Seznec and Zinn-Justin.<sup>[28]</sup> Instead of matching the low-order weak-coupling coefficients to an integral form (Borel and MaxEnt) or a fixed functional form (Padé), this method uses a re-expansion of the perturbation series in terms of a mapping  $w_\alpha(x)$ . Strong-coupling constraints up to second order are implemented by adjusting the (truncation-order-dependent) mapping parameter  $\alpha(N)$ . Extrapolation into the BEC region is as straightforward as in the Padé case. We found that the ODME outperforms similar methods for a 0D model, and we showed that it provides good results for the dilute-Fermi-gas CEP. In particular, simple mappings already produce good results, and reasonable variations of the mapping choice do not significantly affect the obtained results. Overall, compared with the standard Padé and Borel methods as well as the MaxEnt technique, ODME is more generally applicable and does not induce artifacts such as spurious poles. Moreover, our results suggest that, already at low truncation orders, ODME often leads to well-converged results all the way from weak to strong coupling.

The ODME method is very flexible and can be applied to a variety of extrapolation problems. In particular, this method can also be applied in cases where the available weak- and strong-coupling data do not provide sufficient constraints, but additional information at an intermediate coupling is available. That is, by mapping the intermediate coupling point to infinity via a conformal transformation, ODME can be used to construct weak-to-intermediate coupling approximants, which can then, in a second application of the ODME method, be analytically continued to the strong-coupling regime. An interesting target for future applications of ODME along these lines is the construction of an equation of state of strongly interacting matter in neutron stars that combines constraints from low-density nuclear physics calculations, observational constraints at higher density, and ultrahigh-density perturbative quantum chromodynamics (see, e.g., ref. [61]).

## Acknowledgements

The authors thank R. J. Furnstahl, S. Gandolfi, and A. Gezerlis for useful discussions. D.R.P. is grateful for the warm hospitality of the IKP Theoriezentrum Darmstadt. He is also grateful for 20 years of friendship and stimulating discussions about science, Roman coinage, the Lord of the Rings, and disparate other topics with Dist. Prof. D. A. Drabold. This research was supported by the Deutsche Forschungsgemeinschaft (DFG, German Research Foundation)—Project-ID 279384907—SFB 1245, the US Department of Energy (contract DE-FG02-93ER40756), and by the ExtreMe Matter Institute.

## Conflict of Interest

The authors declare no conflict of interest.

## Data Availability Statement

The data that support the findings of this study are available from the corresponding author upon reasonable request.

## Keywords

dilute Fermi gas, resummation of perturbation series, maximum-entropy method, strongly correlated systems

Received: November 2, 2020

Revised: March 6, 2021

Published online: April 15, 2021

- [1] C. M. Bender, T. T. Wu, *Phys. Rev. Lett.* **1971**, 27, 461.
- [2] J. Zinn-Justin, *Phys. Rep.* **1981**, 70, 109.
- [3] J. P. Boyd, *Acta Applicandae Mathematicae* **1999**, 56, 1.
- [4] G. A. Baker, P. Graves-Morris, *Padé Approximants*, Cambridge University Press, Cambridge **1996**.
- [5] C. M. Bender, S. A. Orszag, *Advanced Mathematical Methods for Scientists and Engineers I: Asymptotic Methods and Perturbation Theory*, Springer, Berlin **1999**.
- [6] A. Cherman, P. Koroteev, M. ünsal, *J. Math. Phys.* **2015**, 56, 053505.
- [7] R. Rossi, T. Ohgoe, K. Van Houcke, F. Werner, *Phys. Rev. Lett.* **2018**, 121, 130405.
- [8] O. Costin, G. V. Dunne, *J. Phys. A* **2019**, 52, 445205.
- [9] H. Kleinert, V. Schulte-Frohlinde, *Critical Properties of f4-Theories*, World Scientific, River Edge **2001**.
- [10] C. Wellenhofer, C. Drischler, A. Schwenk, *Phys. Lett. B* **2020**, 802, 135247.
- [11] I. Caprini, *Phys. Rev. D* **2019**, 100, 056019.
- [12] Y. Hou, J. E. Drut, *Phys. Rev. Lett.* **2020**, 125, 050403.
- [13] I. Bloch, J. Dalibard, W. Zwerger, *Rev. Mod. Phys.* **2008**, 80, 885.
- [14] S. Giorgini, L. P. Pitaevskii, S. Stringari, *Rev. Mod. Phys.* **2008**, 80, 1215.
- [15] C. Chin, R. Grimm, P. Julienne, E. Tiesinga, *Rev. Mod. Phys.* **2010**, 82, 1225.
- [16] A. Schwenk, C. J. Pethick, *Phys. Rev. Lett.* **2005**, 95, 160401.
- [17] N. Kaiser, *Nucl. Phys. A* **2011**, 860, 41.
- [18] S. Gandolfi, A. Gezerlis, J. Carlson, *Annu. Rev. Nucl. Part. Sci.* **2015**, 65, 303.
- [19] I. Tews, J. M. Lattimer, A. Ohnishi, E. E. Kolomeitsev, *Astrophys. J.* **2017**, 848, 105.
- [20] C. Wellenhofer, C. Drischler, A. Schwenk, arXiv:2102.05966 [cond-mat.quant-gas], **2021**.
- [21] C. Wellenhofer, D. R. Phillips, A. Schwenk, *Phys. Rev. Res.* **2020**, 2, 043372.
- [22] M. J. H. Ku, A. T. Sommer, L. W. Cheuk, M. W. Zwierlein, *Science* **2012**, 335, 563.
- [23] J. Carlson, S. Gandolfi, K. E. Schmidt, S. Zhang, *Phys. Rev. A* **2011**, 84, 061602.
- [24] S. Gandolfi, K. E. Schmidt, J. Carlson, *Phys. Rev. A* **2011**, 83, 041601.
- [25] N. Navon, S. Nascimbene, F. Chevy, C. Salomon, *Science* **2010**, 328, 729.
- [26] C. M. Bender, L. R. Mead, N. Papanicolaou, *J. Math. Phys.* **1987**, 28, 1016.
- [27] D. A. Drabold, G. L. Jones, *J. Phys. A* **1991**, 24, 4705.
- [28] R. Seznec, J. Zinn-Justin, *J. Math. Phys.* **1979**, 20, 1398.
- [29] V. I. Yukalov, *Phys. Part. Nucl.* **2019**, 50, 141.
- [30] M. Marino, T. Reis, *J. Stat. Mech.* **2019**, 2019, 123102.
- [31] D. Dorigoni, *Ann. Phys.* **2019**, 409, 167914.
- [32] I. Aniceto, G. Basar, R. Schiappa, *Phys. Rep.* **2019**, 809, 1.
- [33] M. Honda, D. P. Jatkar, *Nucl. Phys. B* **2015**, 900, 533.
- [34] M. Marino, T. Reis, *J. Stat. Phys.* **2019**, 177, 1148.
- [35] D. Drabold, G. Jones, in *Maximum Entropy and Bayesian Methods: Laramie, Wyoming, 1990* (Eds: W. T. Grandy, L. H. Schick), Springer Netherlands, Dordrecht **1991**, pp. 79–92.

- [36] E. T. Jaynes, *Phys. Rev.* **1957**, 106, 620.
- [37] E. T. Jaynes, *Phys. Rev.* **1957**, 108, 171.
- [38] L. R. Mead, N. Papanicolaou, *J. Math. Phys.* **1984**, 25, 2404.
- [39] N. I. Akhiezer, *The classical moment problem*, Oliver & Boyd, Edinburgh **1965**.
- [40] D. Dowson, A. Wragg, *IEEE Trans. Inf. Theory* **1973**, 19, 689.
- [41] A. Tagliani, *J. Math. Phys.* **1993**, 34, 326.
- [42] F. T. Hioe, D. MacMillen, E. W. Montroll, *J. Math. Phys.* **1976**, 17, 1320.
- [43] S. A. Pernice, G. Oleaga, *Phys. Rev. D* **1998**, 57, 1144.
- [44] A. Duncan, M. Moshe, *Phys. Lett. B* **1988**, 215, 352.
- [45] S. K. Gandhi, H. F. Jones, M. B. Pinto, *Nucl. Phys. B* **1991**, 359, 429.
- [46] S. K. Gandhi, M. B. Pinto, *Phys. Rev. D* **1992**, 46, 2570.
- [47] I. R. C. Buckley, A. Duncan, H. F. Jones, *Phys. Rev. D* **1993**, 47, 2554.
- [48] A. Duncan, H. F. Jones, *Phys. Rev. D* **1993**, 47, 2560.
- [49] C. M. Bender, A. Duncan, H. F. Jones, *Phys. Rev. D* **1994**, 49, 4219.
- [50] C. Arvanitis, H. F. Jones, C. S. Parker, *Phys. Rev. D* **1995**, 52, 3704.
- [51] R. Guida, K. Konishi, H. Suzuki, *Ann. Phys.* **1995**, 241, 152.
- [52] J.-L. Kneur, M. B. Pinto, R. O. Ramos, *Phys. Rev. Lett.* **2002**, 89, 210403.
- [53] E. Braaten, E. Radescu, *Phys. Rev. Lett.* **2002**, 89, 271602.
- [54] C. Wellenhofer, *Phys. Rev. C* **2019**, 99, 065811.
- [55] R. Guida, K. Konishi, H. Suzuki, *Ann. Phys.* **1996**, 249, 109.
- [56] S. Tsutsui, T. M. Doi, *Ann. Phys.* **2019**, 409, 167924.
- [57] P. M. Stevenson, *Phys. Rev. D* **1981**, 23, 2916.
- [58] W. Janke, H. Kleinert, *Phys. Rev. Lett.* **1995**, 75, 2787.
- [59] B. Hamprecht, H. Kleinert, *Phys. Rev. D* **2003**, 68, 065001.
- [60] H. Kleinert, *Phys. Lett. A* **1995**, 207, 133.
- [61] S. Huth, C. Wellenhofer, A. Schwenk, *Phys. Rev. C* **2021**, 103, 025803.
- [62] G. M. Gayathri, B. A. Kagali, T. Shivalingaswamy, *Int. J. Sci. Res.* **2016**, 5, 361.

# Realizations of Isostatic Material Frameworks

Mahdi Sadjadi, Varda F. Haghighi, Mingyu Kang, Meera Sitharam, Robert Connelly, Steven J. Gortler, Louis Theran, Miranda Holmes-Cerfon, and Michael F. Thorpe\*

Dedicated to Professor David A. Drabold on the occasion of his 60th birthday

This article studies the set of equivalent realizations of isostatic frameworks and algorithms for finding all such realizations. It is shown that an isostatic framework has an even number of equivalent realizations that preserve edge lengths and connectivity. The complete set of equivalent realizations for a toy framework with pinned boundary in two dimensions is enumerated and the impact of boundary length on the emergence of these realizations is studied. To ameliorate the computational complexity of finding a solution to a large multivariate quadratic system corresponding to the constraints, alternative methods—based on constraint reduction and distance-based covering map or Cayley parameterization of the search space—are presented. The application of these methods is studied on atomic clusters, a model of 2D glasses and jamming.

It is, therefore, not surprising that much research has been dedicated to tuning materials properties by modifying the connectivity and geometry of networks. Within the context of solid-state physics, most studies have been focused on the topological design of networks in which bonds are arranged such that the network response is optimized for a given mechanical force/load.<sup>[5,6]</sup>

However, relatively less attention has been given to the geometrical realization of a network, i.e., the assignment of coordinates to its sites in a given spatial dimension. In the study of geometric constraint systems,<sup>[7]</sup> given a graph  $G$  with edge-length constraints, the realizations  $p$  that satisfy those constraints are called equivalent

frameworks  $(G, p)$ . A given graph with constrained edge lengths can have many realizations. For example, consider two triangles that share a common edge (four vertices and five edges). Here, there are two realizations—one fully extended with no edges that cross and the other folded about the common edge shared by the two triangles. This gives a total of two realizations which is an example of the more general case of an isostatic network having an even number of realizations that is shown and extensively used in this article.

The problem of finding network realizations has been applied to several physical problems. The most well-known example is the so-called “NMR problem” where pairwise distances between atoms are found using nuclear magnetic resonance (NMR) spectroscopy<sup>[8]</sup> and the 3D protein conformation is inferred from the

## 1. Introduction

A wide range of materials properties can be understood by modeling them as mass-spring networks, or graphs with constrained edge lengths, where sites, or vertices, are interacting via harmonic springs or edge-length constraints. Examples include auxetic phases of matter<sup>[1]</sup> and mechanical metamaterials.<sup>[2,3]</sup> This network representation contains topological and geometrical information. The topology of a network determines how sites are connected, while its geometry determines the position of sites and in turn other geometrical properties such as bond lengths and angles. Both geometrical and topological properties of networks are crucial to control its response to mechanical deformations, which determines the rigidity of that structure.<sup>[4]</sup>

Dr. M. Sadjadi, Dr. V. F. Haghighi,<sup>[†]</sup> Prof. M. F. Thorpe  
 Department of Physics  
 Arizona State University  
 Tempe, AZ 85287-1604, USA  
 E-mail: mft@asu.edu


Dr. M. Kang, Prof. M. Sitharam  
 CISE Department  
 University of Florida  
 Gainesville, FL 32611-6120, USA

Prof. R. Connelly  
 Department of Mathematics  
 Cornell University  
 Ithaca, NY 14853, USA

Prof. S. J. Gortler  
 School of Engineering and Applied Sciences  
 Harvard University  
 MA, USA

Dr. L. Theran  
 School of Mathematics and Statistics  
 University of St Andrews  
 St Andrews KY16 9SS, Scotland

Prof. M. Holmes-Cerfon  
 Courant Institute of Mathematical Sciences  
 New York University  
 New York, NY, USA

 The ORCID identification number(s) for the author(s) of this article can be found under <https://doi.org/10.1002/pssb.202000555>.

<sup>[†]</sup>Present address: James Franck Institute, University of Chicago, Chicago, IL 60637, USA

DOI: 10.1002/pssb.202000555



data.<sup>[9]</sup> Other examples include survey and satellite imaging,<sup>[10]</sup> localization of sensor networks,<sup>[11]</sup> and conformation control for allostery.<sup>[12,13]</sup> As the bond lengths are assigned to specific bonds, the problem is sometimes referred to as assigned distance problem known to be NP-hard,<sup>[14]</sup> while the problem of finding realizations given only a list of bond lengths—that are not assigned to specific bonds—is called the unassigned distance problem.<sup>[15]</sup>

The network representation of a material is useful for both crystalline and noncrystalline materials. The main difference is that crystalline structures have only a single minimal energy conformation, while disordered systems have a rough energy landscape with many local minima. Therefore, noncrystalline materials can attain various conformations if such transitions are energetically accessible. In a large class, the transition corresponds to a structural change in which atoms attain new positions, while the connectivity (the atoms they interact with) and the bond lengths remain unaltered, i.e., the conformations are in fact equivalent frameworks. For example, the anomalous properties of glasses such as silica at low temperature are attributed to the two-level states (TLSs) in which the glass can tunnel between two conformations.<sup>[16–18]</sup> These conformational changes are believed to be localized, consistent with the thermal energy available at about 1 K where the anomalous specific heat is observed. However, after half a century of intensive research on TLSs, the geometrical realizations, or equivalent frameworks, of these localized modes are still elusive. The synthesis and imaging of silica bilayers<sup>[19,20]</sup> in recent years has reinvigorated open problems in physics of glasses by unveiling a structure which follows the continuous random model<sup>[21,22]</sup> and makes the actual coordinates of atoms available, albeit in two dimensions (2D). This newly available data on 2D glasses makes the interface between theory and experiment a lot easier; not least because visualization is so much easier in two dimensions.

The remainder of this article is organized as follows. We first review the fundamental concepts in rigidity and present the theorem that states an isostatic network has an even number of realizations. Then we describe several methods to find realizations of an isostatic graph using a toy model, using constraint reduction and Cayley parameterization. Lastly, we apply these methods to a series of larger networks, generated computationally or experimentally, to find their realizations and discuss the physics of transition between such states.

## 2. Mathematical Background

We aim to find all realizations of a network or graph with vertices connected by edges with given edge lengths. A realization is the assignment of coordinates to vertices such that all edges satisfy their given lengths. A graph together with a realization is called a framework. Frameworks that satisfy the same set of edge lengths are called equivalent. A realization is a solution to the set of edge length equations. Let  $(x_i, y_i)$  be the coordinates of vertex  $i$  in two dimensions (2D). If vertices  $i$  and  $j$  are connected through an edge with the length  $s$ , we can write

$$(x_i - x_j)^2 + (y_i - y_j)^2 = s^2 \quad (1)$$

Every edge in the graph has a corresponding edge length equation. This is a geometric constraint problem that has been studied extensively from multiple perspectives, from distance geometry, to algebraic geometry and automated geometry to structural or combinatorial rigidity, and arises in a wide variety of applications. We refer a reader to a recent handbook for background, perspectives, and recent work.<sup>[7]</sup> An isostatic network has the minimum number of independent constraints or equations to make the graph rigid, i.e., to ensure locally unique solutions generically exist. It is this marginal state that separates overconstrained (more constraints than necessary for minimal rigidity) from underconstrained (fewer constraints than necessary for rigidity). As mentioned earlier, in general, checking whether a real solution exists to such a system of equations is known to be NP-hard. This means that the source of the complexity is not merely the number of solutions, which could be exponentially many in the size of the system. In fact, even if there were just a single solution, finding it may take exponential time. Regardless of this complexity, it is possible to prove that a generic isostatic framework has an even number of realizations.

This theorem is powerful as it suggests that glasses such as silica have to have more than one realization with the same topology (same set of edges and edge lengths). Now, note that the theorem guarantees the existence of such solutions, but the question of their accessibility depends on the energy considerations. If the rigid bars between vertices are replaced by springs, then there is an energy barrier between the various realizations, whose magnitude is relevant in physical process such as tunneling. In the next section, we justify this theorem using a toy model and will show how various realizations of an isostatic framework can be found. To be more precise:<sup>[23]</sup>

**Theorem 1:** A finite generic isostatic framework is not globally rigid, but has an even number of equivalent generic frameworks. Each generic framework of the underlying graph is locally rigid. (Equivalent generic networks have the same network topology and bar lengths, and are infinitesimally rigid.)

**Proof 1:** This is essentially Theorem 5.9 from the study by Hendrickson.<sup>[23]</sup> The evenness property is not explicitly stated there, but is clear in the proof. Evenness is explicitly stated in the proof of Theorem 1.14 from the study by Gortler et al.<sup>[24]</sup>

However, this theorem does not provide a way to access the solutions. Each realization has exactly the same number of vertices and the same connectivity table and bond lengths; however, the embedding of the graph is different. These configurations are not related by rigid motions such as translation and/or rotation. An approach can be designed using the nature of an isostatic framework which is on the verge of instability. The number of zero eigenvalues of the dynamical matrix of an isostatic framework is exactly equal to the number of trivial motions (or dimension of the null space). Any other motion has a finite cost in energy, if vertices are connected by springs, rather than bars, which, of course, suppresses any continuous deformations in an isostatic system. But if a single constraint of an isostatic framework is removed, there is one fewer equation of the form Equation (1), so now the null space gains one extra dimension moving along which has zero energy cost. In fact, it can be proven that the traversal along this nontrivial eigenvector is continuous and leads to an even number of

realizations with the same length on the removed bar. We state the aforementioned observations as a theorem.

**Theorem 2:** If a single edge is removed from a finite generic isostatic framework, the resulting mechanism has a configuration space that is a closed, continuous curve, on which there are an even number of configurations in which the removed edge returns to its original length.

**Proof 2:** See Theorems 5.8 and 5.9 in the study by Hendrickson.<sup>[23]</sup>

### 3. Trihex: A Toy Model

Glasses such as silica ( $\text{SiO}_2$ ) and germania ( $\text{GeO}_2$ ) are considered as a network of corner-sharing tetrahedra. Recently, silica bilayers have been synthesized<sup>[19,20]</sup> which are effectively a 2D network of corner-sharing triangle.<sup>[25]</sup> These triangles are formed with oxygens at their corners. The network has rings of many sizes, but the mean ring size is six.<sup>[26]</sup> Therefore, we propose a hexagon as a toy model: Trihex (Figure 1).

The Trihex has  $V = 9$  vertices and  $E = 12$  edges. To render Trihex isostatic, anchored boundary condition are used and the blue vertices are pinned (immobilized).<sup>[27]</sup> The pinned vertices are placed generically (not on an equilateral triangle) and all edges initially have almost, but not exactly, the same length. The other three vertices on the surface are removed because they do not change the rigidity of the network as each triangle is rigid. As the set  $V$  has six unpinned vertices, this gives a set of  $2N = 2 \times 6 = 12$  nonlinear equations for Trihex to solve using three pinned vertices whose coordinates are fixed. It is important to note that simple ruler and compass-based algorithms, that classify and find equivalent frameworks when the underlying graphs are so-called tree-decomposable or quadratically solvable,<sup>[28–31]</sup> do not directly apply to Trihex.

### 4. The Single-Cut Algorithm

Theorem 2 can be directly written as a step-by-step single-cut algorithm<sup>[32]</sup>:

Start from an isostatic network, i.e., a rigid network with no redundant edge. The number of trivial motions depends on the imposed boundary conditions. In a system with periodic

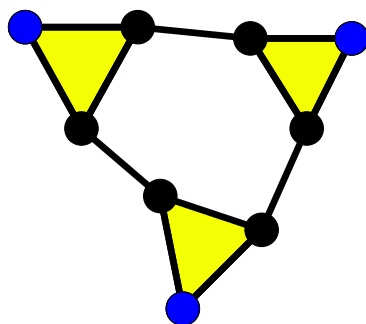


**Figure 1.** The toy model, Trihex, formed by six corner-sharing triangles proposed to find properties of realizations of an isostatic network. The other three nonpinned triangles are removed because each triangle is rigid.

boundary conditions, only rigid translations are allowed. For anchored boundary condition, no trivial motion exists, and there are exactly  $2N$  equations of the form Equation (1).

Remove an edge from the isostatic network, resulting in a system of  $2N-1$  equations and form its dynamical matrix. Find the eigenvectors corresponding to zero eigenvalues (the null space). Remove trivial motion eigenvectors to find the 1 internal degree of freedom (dof).

Eigenvector-following: Once the nontrivial direction is identified, move all sites along that direction with a small step size. The smaller the step size, the smaller is the error in traversing the closed curve in configuration space, i.e., the path that the system takes in high dimensional space. Note that this motion does not change the edge length of any other edge. Also use the dot product of the previous and current directions to make sure we only move forward in the configuration space.

Compute the dynamical matrix at the new point and repeat the aforementioned process to traverse in the configuration space. Meanwhile monitor the distance between the two vertices that had their connecting edge removed. If we continuously move through this 1D path, we eventually come back to the starting point. Once we are back to the initial point, the sum of distances from the center of mass (as a convenient metric) is plotted against the length of the cut edge, for each point along the path. This gives us a closed curve projected in 2D plane in which drawing a vertical line will identify the original framework and its equivalent frameworks in the configuration space.

A Python implementation of this algorithm can be found in the RigidPy package.<sup>[33]</sup> The single-cut algorithm is illustrated in the two parts of Figure 2.

#### 4.1. Using the Single-Cut Algorithm to Find Equivalent Sphere Packings

We tested the ability of the single-cut algorithm to find equivalent configurations of frameworks using a large database of known framework embeddings which were obtained from rigid unit sphere packings of  $N = 12, 13$  spheres.<sup>[32]</sup> For  $N = 12$ , the database in the study by Holmes-Cerfon<sup>[32]</sup> contains 11980 distinct unit sphere packings, of which there are 23 pairs with the same adjacency matrix and therefore the same underlying framework graph. We applied the single-cut algorithm to each of the 46 frameworks with multiple embeddings, breaking each single bond in turn. For all frameworks the algorithm found the other embedding, usually via several different single broken bonds. For  $N = 13$ , the database contains 98529 unit sphere packings of which there are 474 pairs with the same adjacency matrix. We tested all the frameworks with multiple embeddings, and found four pairs of frameworks that could not reach their other embedding by the single-cut algorithm. Interestingly, an additional two pairs (four frameworks) each led to new frameworks that the algorithm in the study by Holmes-Cerfon<sup>[32]</sup> failed to find. A pair of frameworks that cannot be converted to each other via the single-cut algorithm is shown in Figure 3. These atomic clusters are 3D and indeed Theorems 1 and 2 and the single-cut algorithm apply in any dimension. The remaining examples in this article are in two dimensions.

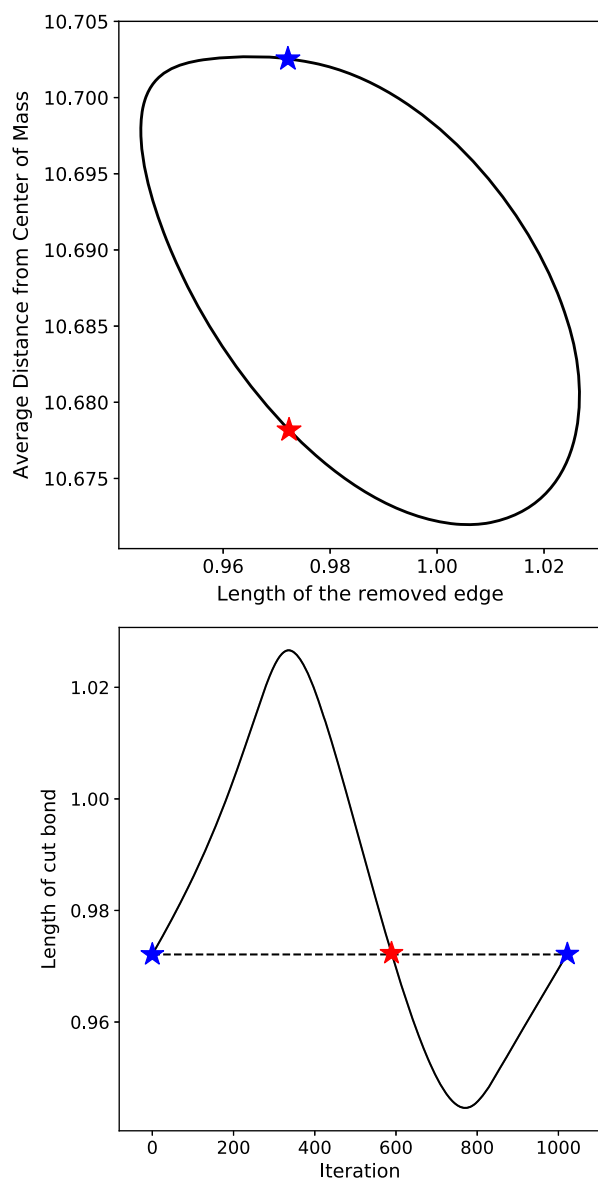


**Figure 2.** (Top) A closed curve—whose points represent equivalent frameworks or configurations of a 1-dof framework—projected on the 2D plane. The vertical axis represents the average distance of all vertices from the center of mass. The horizontal axis shows the distance between two ends of the removed edge. The blue and the red asterisks denote the original and alternative realizations, i.e., equivalent frameworks. Note that more than 2 (but an even number) of such equivalent frameworks can be found on a single closed curve (see section on CayMos). A vertical line, drawn at the location of the original bond length, has two intersections with the closed curve representing equivalent frameworks. (Bottom) The distance of two ends of the removed edge versus iteration step by moving along the path. The dashed horizontal line represents the original length. The asterisks correspond to the ones on the left.

#### 4.2. Double Cut

To find other realizations in this system, we designed more complex schemes for removing edges. For example, the single-bond cut can be modified to cutting two bonds, while another bond is

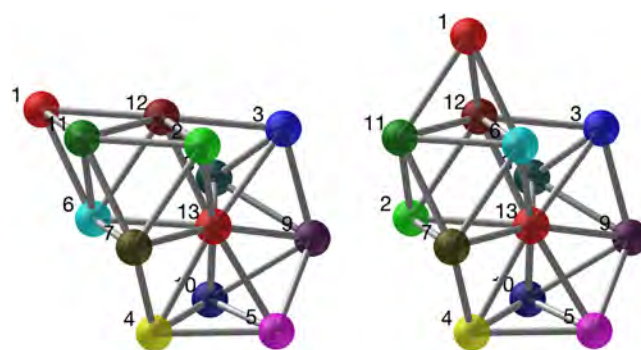


**Figure 3.** A pair of frameworks with the same underlying graph, but distinct spatial embeddings, that cannot be converted to each other via the single-cut algorithm. The embeddings differ in the locations of vertices 2 (green), 6 (cyan), and 1 (red). By breaking a single bond and flexing, there is no way to interchange the positions of vertices 2 and 6; more flexibility is required to interconvert the embeddings.

added. We tried different ways in connecting different sites, but our analysis shows that these more complex schemes do not find any new realizations. We do not find new solutions in these more complex schemes, but even more complex schemes can be imagined that perhaps might do so.

#### 4.3. An Alternative to Address Incompleteness of Single Cut

It is helpful to look at the configurations of the Trihex where the anchored vertices are close to being a unit-length equilateral triangle and edge lengths are larger than  $1/3$ , and smaller than about  $1/2$ . Otherwise, either the configuration or framework does not exist, or it has several self-intersections which do not seem physically realistic. As we will see, this allows for a great variation in the shapes of equivalent frameworks.

First, we consider the nongeneric case when the anchored triangle is exactly equilateral, which leads to some flexible frameworks, although generic frameworks of the same graph are in fact isostatic. Subsequently, we will consider generic perturbations of an anchored triangle. In **Figure 4**, sample equivalent frameworks are displayed in the form of the numbers on a clock, where each hour represents a particular configuration and there is a natural flex of frameworks from each hour to the next, forward or backward. The central hexagon in each of the flexible configurations has the property that opposite sides are parallel. All the dark edges have unit length. The two equivalent configurations in the center are rigid isostatic, and also infinitesimally rigid configurations that have threefold rotational symmetry, which we call threefold left and threefold right. They are not part of the flexible cycle of configurations on the outside clock, but they also represent realizations of the outside graph with the same edge lengths and a connection is shown for each of these to the particular odd hour configuration that share two of the three triangle configurations that are the same. The change or flex is seen by starting from the 12-o'clock configuration, and using that the opposite sides of the hexagon are parallel it maintains that property as it flexes. This is proved below. If you look at the path of three edges from one vertex to the next, it is an example of a 4-bar

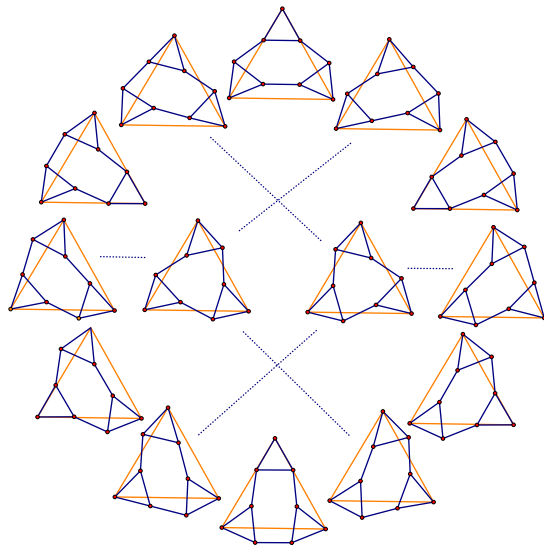


**Figure 4.** The closed path of the flexing Trihex for the case when the pinned vertices form an equilateral triangle shown in red. The positions of the sample configuration are represented by an hour on a clock. The central two threefold symmetric configurations are rigid and not part of the flex.

mechanism, and in the clock flex, each of the three 4-bar mechanisms flexes their full cycle, and when the edges of the pinned triangle are greater than the length of the inner edge length, the 4-bar mechanisms consist of one connected component.

To prove that the clock mechanism works, see **Figure 5**. We use the 1-o'clock position as a sample. The more general position is very similar. We see that the vector sum  $A + B + C = D$  represents the vectors of the 4-bar mechanism, where  $D$  is the corresponding side of the regular pinned triangle. Let  $R$  be the rotation to the right by  $120^\circ$ . Then  $RC + RA + RB = R(C + A + B) = RD$  is the other side of the pinned triangle. Applying this to other side, we can see how things close up.

We next show how this applies when the pinned triangle is perturbed to a nonequilateral, generic triangle, while the other unit bar lengths are fixed. The two threefold configurations are infinitesimally rigid, and the whole framework is isostatic with 9 vertices and  $15 = 2 \times 9 - 3$  bars. So, it has only the 0 equilibrium (self) stress. On the contrary, for perturbations of configurations of the clock mechanism it is not so simple. Indeed, there is an equilibrium stress that varies as the configuration

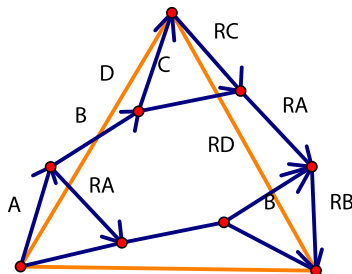


**Figure 5.** This labels the directed edges of mechanism for the proof that the clock mechanism is a mechanism.

flexes, and in a sense, the stress “blocks” some of the infinitesimal and actual motions.

For a perturbation of the pinned triangle, we may assume that one of the edges of the corresponding equilateral triangle is the same length, and each of the other two edge lengths either increases or decreases some small amount. If the stress on those lengths has the same sign as the displacement of the edge lengths, that motion is restricted. But in any case, we can start with one of the configurations along the path of the clock mechanism, and then look for another realization with the same perturbed edge lengths of the pinned triangle. **Figure 6** is an example of that process. Then fixing the new green nonequilateral base triangle, we can then find two other realizations with unit bar lengths on the dark colored bars which are perturbations of the left and right threefold.

When the upper left configuration is flexed 6 h, we can approximate that as well to get an exact Trihex with the same triangle base as in the upper right. Thus, we get four configurations with the same base altogether.

The aforementioned discussion indicates that there are various other equivalent frameworks than those obtainable by removing an edge and flexing the resulting framework. As there is a finite mechanism nearby, or a critical configuration nearby, with generic equilateral triangle of boundary vertices, that can be used as a kind of guide path, walking around the clock to find distant realizations with the same bar lengths. The idea is to approximate the given framework with one with the nearest time on the clock. For example, the framework in Figure 1 is roughly at 7-O'clock, when the clock in Figure 4 is rotated  $180^\circ$  to match

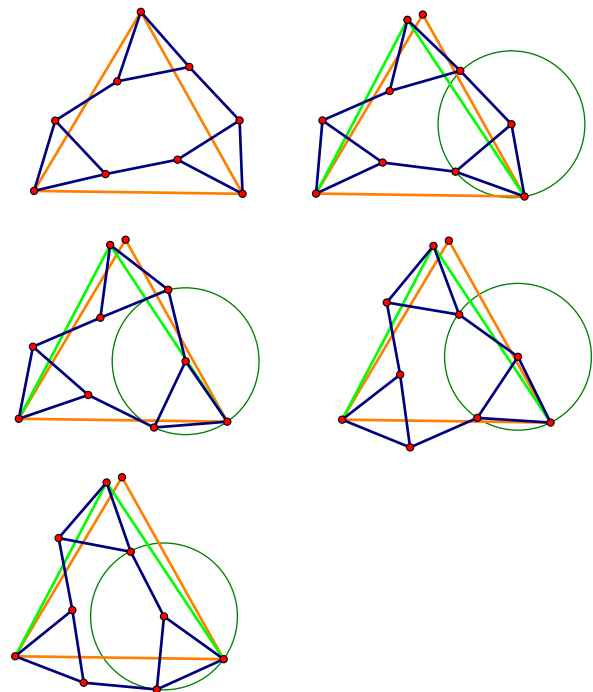


**Figure 6.** Starting with the framework in the top left, which is near the 1-o'clock flexible configuration, we perturb the starting trihexagon to get the framework on the upper right. We then find three others as shown. The thin circle is to indicate that the last bar length is of unit length because the other bar lengths are of unit length by construction.



the position of the base triangle. In fact, that is not all. It is possible to jump to either the left or right fold rather than to walk around the clock and use that as the approximation.

In the next section, we present a formal method that fleshes out these ideas.

#### 4.4. Indexing and Finding Equivalent Frameworks Using Cayley Parameters

The methods mentioned earlier use two ideas. The first is finding equivalent frameworks by removing one or more edges, and exploring the configuration space of the resulting mechanism with one or more degrees of freedom, to find other configurations that satisfy the original edge lengths of the removed edges, i.e., equivalent frameworks. The second is to classify or index the configurations based on their “clock” position around critical configurations.

These ideas are exploited in a formal method that has been used in a variety of scenarios from computer-aided engineering design to molecular modeling. Cayley parameterization (a type of covering map or projection in the terminology of algebraic topology) was introduced in the study by Sitharam and Gao,<sup>[34]</sup> as a way of describing and computing configuration spaces of flexible frameworks. The key idea is to use lengths of selected nonedges as parameters or coordinates, to represent and traverse the configuration space that could be disconnected in the usual Cartesian coordinates (a branched covering space in the terminology of algebraic topology). With sufficiently many judiciously chosen Cayley parameters or nonedges whose addition makes the framework minimally rigid or isostatic, we can efficiently compute the finitely many possible Cartesian configurations (inverse of the covering map) corresponding to each Cayley-parameterized configuration (an element of the base space of the covering projection). A bijection between Cayley configurations and frameworks is achieved by adding enough Cayley parameters, i.e., enough nonedges, so that the graph is globally rigid, i.e., has a unique realization generically, given edge lengths.

Here, we describe two algorithms based on Cayley parameterization for finding all equivalent frameworks of a given framework, or graph with fixed edge lengths.

The first is based on the results of previous studies,<sup>[35–38]</sup> which provided an analysis of a common class of 1-dof mechanisms that are obtained by removing an edge from the well-studied class of tree-decomposable graphs, which include the so-called Henneberg-I graphs.<sup>[39]</sup>

This class of graphs provides a natural classification or indexing of equivalent frameworks based on relative orientations, chiralities, or flips of certain triples of vertices. A flip vector of 1's and –1's distinguishes equivalent isostatic frameworks. Two equivalent isostatic frameworks whose flip vectors differ in a single coordinate are on “opposite sides” of a critical configuration of a 1-dof framework where the triple of vertices is collinear. The isostatic framework minus a “base” edge yield the 1-dof framework, and the Cayley configuration space of this 1-dof framework is parameterized by the length of the removed base edge, i.e., base nonedge. This Cayley configuration space has a well-defined structure of intervals bounded by critical points.

Each interval could correspond to multiple connected component curves that are generically smooth and are homeomorphic to a circle. Certain pairs of flip vectors are guaranteed to belong to different components, while others could belong to the same component. Moreover, once the unique flip vector is given, the isostatic framework with the specified length of the base non-edge or Cayley parameter can be found easily using a simple ruler and compass construction. The algorithm has been implemented as an open-source software CayMos.

Trihex becomes a 1-dof tree-decomposable graph after removing one edge  $e$ , with a Cayley configuration space parameterized by the length of a different base nonedge  $f$ , whose addition makes the graph tree-decomposable. As the different connected component curves of the configuration space are traced out for the different lengths of  $f$ , multiple equivalent frameworks, indexed by multiple flip vectors, that attain the required length for  $e$  are found. A webpage<sup>[40]</sup> illustrates CayMos analysis of the Trihex for various ratios between the pinned boundary edge length and the bond length. The two-component curves of a Trihex with bond length half the pinned boundary edge length are shown in **Figure 7**. Each component curve could have multiple equivalent frameworks with different flip vectors, i.e., frameworks that attain the required distance of the dropped edge.

The dropped edge  $e$  is  $(v4, v6)$ . Each component curve is a projection of a smooth simple curve (each point represents a unique configuration) living in 3D, parameterized by three Cayley parameters, dashed nonedges whose addition makes the graph globally rigid, i.e., generically has a unique realization given edge lengths. The driving Cayley parameter or base nonedge is one of

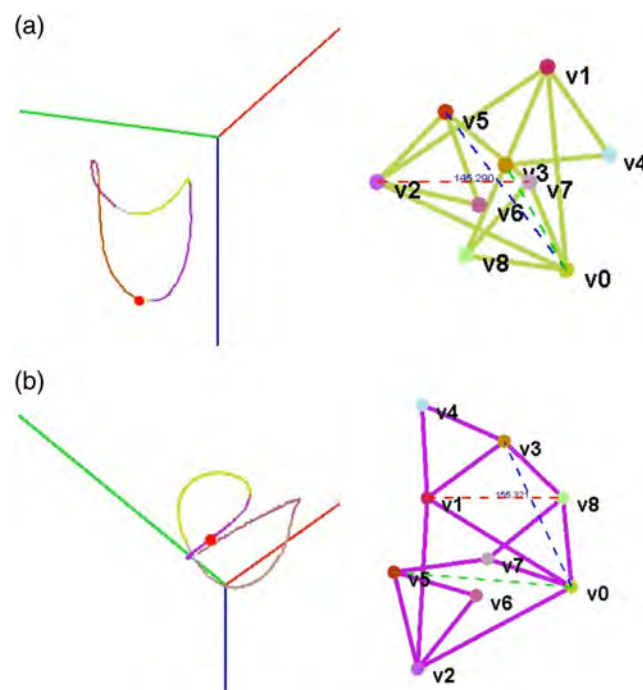


**Figure 7.** Trihex minus one edge 1-dof tree-decomposable graph's Cayley configuration space curves for bond length half of boundary edge length, solved by CayMos. The dropped edge  $(v4, v6)$  attains its required length at multiple points on each curve, giving multiple equivalent frameworks. See text for description.

the three dashed. Each colored portion of the curve represents a different flip vector. Each component curve has multiple equivalent frameworks with different flip vectors, i.e., frameworks that attain the required distance of the dropped edge.

**Figure 8** shows equivalent frameworks for Trihex found by CayMos, for two different ratios between the edge length of the pinned (nearly) equilateral boundary triangle and the (equal) length of the remaining edges (**Table 1, 2**).

The next method extends and combines two well-known algorithms. The first is the so-called decomposition–recombination (DR)-planning algorithm<sup>[41–44]</sup> that recursively decomposes minimally rigid, or isostatic graphs with edge-length constraints so that only small constraint systems need to be solved simultaneously, and recombines their solutions<sup>[45–47]</sup> to get all equivalent frameworks. The method of recombination provides an indexing of frameworks around critical configurations.<sup>[48]</sup> The second is the use of convex Cayley parameterizations.<sup>[34]</sup> The existence of a convex Cayley configuration space is a robust property of graphs underlying frameworks. For frameworks in two dimensions, the graphs are so-called partial 2-trees. Informally, complete 2-trees are constructed by pasting triangles together on edges, and partial 2-trees are subgraphs of complete 2-trees. Such characterizations exist even for frameworks whose bar lengths are in non-Euclidean, polyhedral norms, and are strongly linked to the concept of flattenability<sup>[49,50]</sup> of graphs, characterized by forbidden minor subgraphs, for example, partial 2-trees are exactly those graphs that forbid the complete subgraphs on four vertices, or  $K_4$ . Convex Cayley parameterization has been used for analyzing sphere-based assembly configuration spaces in previous studies,<sup>[51–53]</sup> further applied to predicting crucial interactions in virus assembly in previous studies.<sup>[54,55]</sup>

The idea is to drop sufficiently many edges from a glassy framework (arbitrarily large versions of the Trihex), shown in red in **Figure 9**, so that the remaining graph has a convex Cayley configuration space (is a partial 2-tree) parameterized by nonedge lengths shown in green. In this case, the boundary vertices are not pinned; instead, boundary edges are judiciously added to make the graph minimally rigid or isostatic while ensuring the convex Cayley property. This can be achieved for a class of planar graphs encompassing corner-sharing triangular or glassy graphs. **Figure 9** and **10** have light colored lines showing the chosen boundary edges. Importantly, the resulting 2-tree has a simple DR plan, called a flex DR plan because it requires

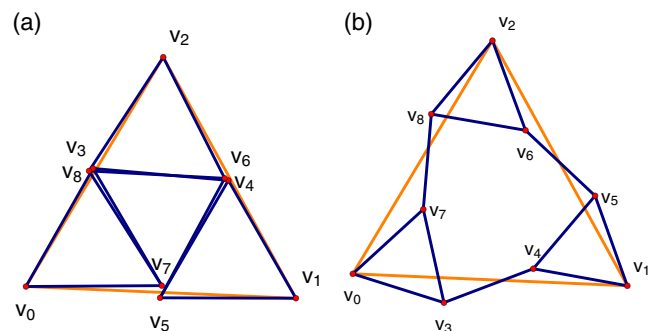


**Figure 8.** Trihex frameworks for two different boundary-to-edge length ratios, solved by CayMos.

**Table 1.** 22 solutions found for Trihex 8a.

Flip	Base edge	Solutions
–	$(\nu_2, \nu_5)$	
4	$(\nu_2, \nu_5)$	
7	$(\nu_2, \nu_5)$	
8	$(\nu_2, \nu_5)$	
3,4	$(\nu_2, \nu_5)$	
7, 8	$(\nu_0, \nu_4)$	
3, 4, 7	$(\nu_0, \nu_4)$	

**Table 1.** Continued.

Flip	Base edge	Solutions
3, 4, 8	$(\nu_0, \nu_4)$	

**Table 2.** Four solutions found for Trihex 8b.

Flip	Base edge	Solutions
–	$(\nu_0, \nu_4)$	
3	$(\nu_0, \nu_4)$	

dropping and adding edges. Furthermore, the flex DR plan permits sequential solving of univariate quadratic equations corresponding to the dropped edges one by one, i.e., flex 1, except for a single, final high degree univariate polynomial. This further permits the indexing of equivalent realizations around critical configurations. These key ideas are based on graph theory (to find the flex 1 DR plan) and numerical solution of a system of quadratic equations by solving a sequence of univariate quadratic equations (with a Cayley parameter as variable) followed by a single univariate equation of large degree (in a final Cayley parameter). The resulting algorithm to find the solution corresponding to a given index runs in polynomial time in the size of the glassy system and the required accuracy and is fleshed out in upcoming articles.<sup>[56,57]</sup>

#### 4.5. Changing Ratio of Edge Lengths to Distance between Pinned Boundary Vertices

It is trivial that if edge lengths are chosen so short, the triangles cannot span the distance between the pinned vertices. Therefore at that limit, the set of Equation (1) has no solution. If we take the vertices with coordinates, shown in Figure 1, as an initial structure (where the distance between the pinned vertices is  $l_0 \approx 1.0$ ; recall that the pins are not located on an equilateral triangle and therefore

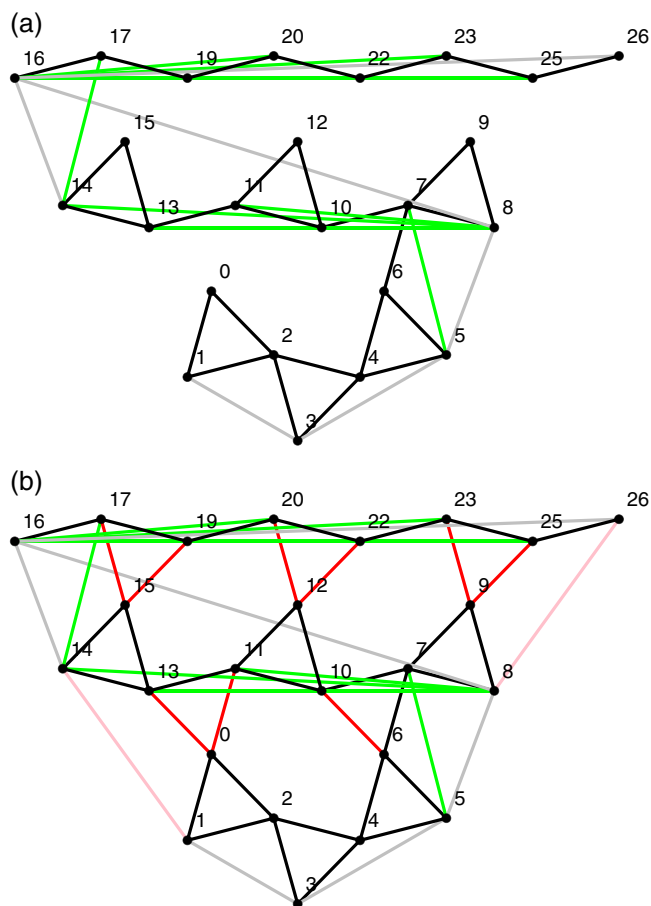


**Figure 9.** We construct the flex 1 DR plan of a hexagonal lattice manually by applying two actions to the graph: 1) add boundary edges (gray) so that the graph is infinitesimally rigid; 2) drop some of the edges and add some Cayley parameters (green) so that the new graph becomes a two-tree. During recombination, we add back those dropped edges (red, or pink if boundaries), i.e., we solve for the green Cayley parameter lengths that achieve the given red (and black) edge lengths. An important property of a DR plan of flex 1 is that we are able to solve for one red edge at a time. Empirically, we usually apply three actions by starting from a small subgraph and expand it by adding one Cayley parameter and drop one original edge. When reach the boundary we add a boundary edge if we cannot construct a two-tree by adding only one Cayley parameter.

$l_0$  is in fact the average distance between the pins), we are interested in counting the total number of realizations for a given edge length. As the Trihex is a small enough example, the complexity advantage of the methods of the previous sections, e.g., CayMos, is not as crucial. So, the realizations are found by directly solving Equation (1) for uniform edge lengths ranging from 0.34 to 2. The exact solutions are obtained through the function “NSolve” in Mathematica. The pinned boundary conditions is convenient because no trivial translation or rotation is present.<sup>[27]</sup> **Figure 11** shows the number of real solutions for a given  $s$ . The red line shows the total number of distinct complex solutions for the Trihex, which is fixed and equal to 112 computed using Magma.<sup>[58]</sup> This number is independent of the chosen edge length and is the upper bound on the number of realizations.

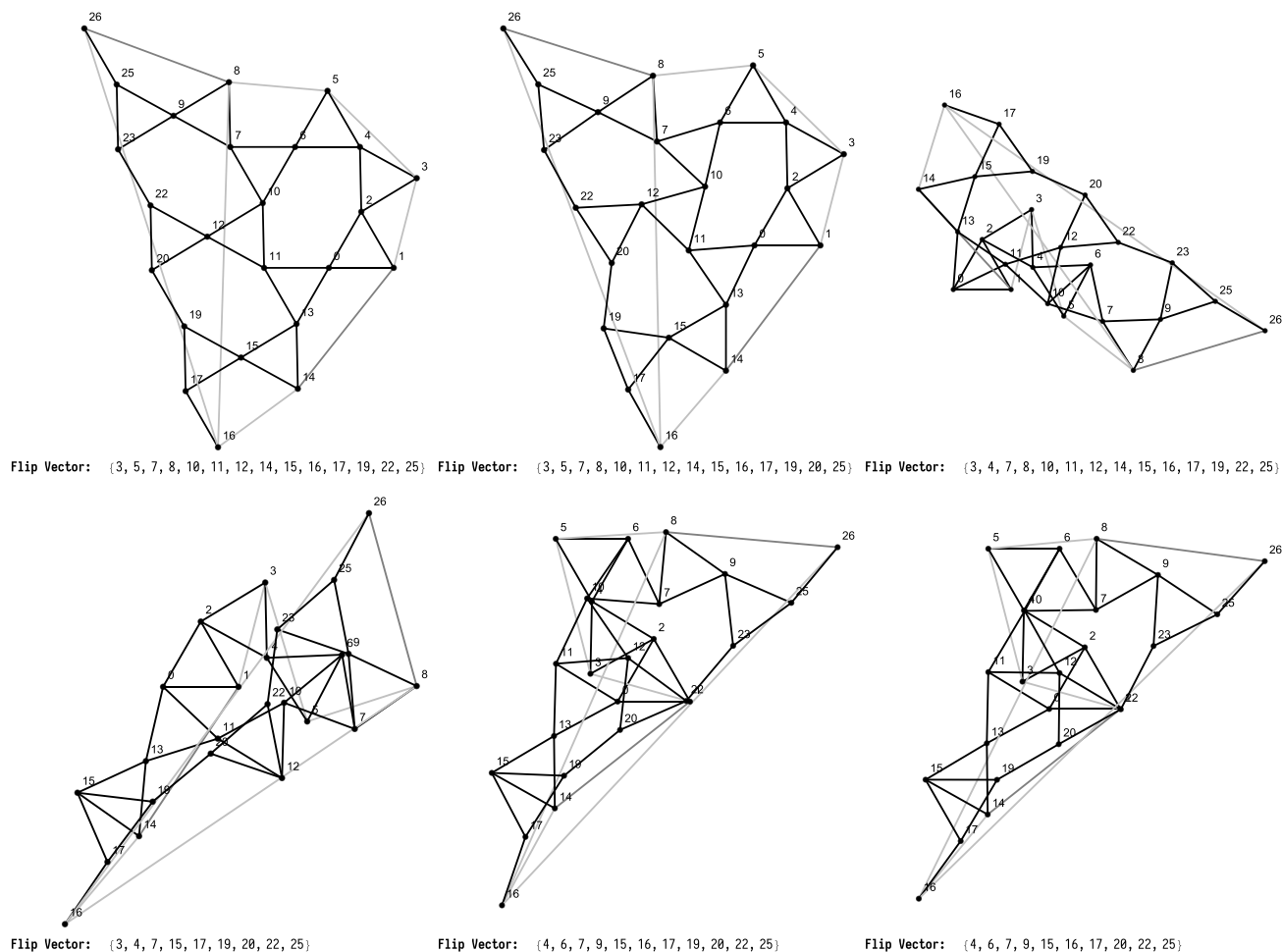


**Figure 10.** The six realizations with different flip vectors we found by the DR plan solver given Figure 9 as the input. The flip vectors are shown below each realization. The overall error of the dropped edges is  $0.07\% \pm 0.21\%$ .

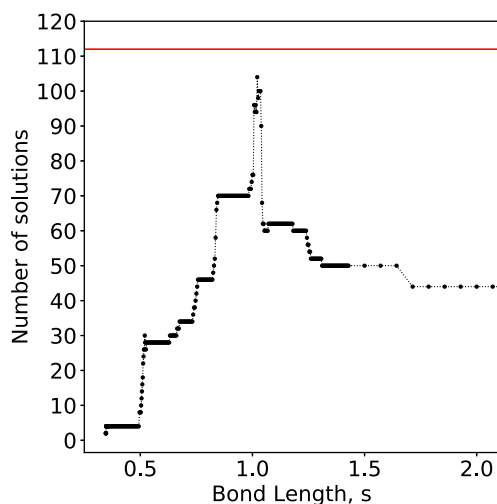


**Figure 11.** Number of realizations of Trihex shown in Figure 1 by varying edge length in the units that the distance between pins  $l_0 = 1$ . The horizontal red line shows the total number of complex solutions which is equal to 112. The number of solutions increases rapidly when the edge lengths are half and equal to the pins distance.

By changing the edge length, some but not all of complex solutions become real.

The first real solutions appear to be a single point at edge length  $\approx 0.346$  (see Figure 11). This is an interesting point as it seems there exists only one solution and the theorem is violated but in fact there are two solutions at this limit although infinitesimally close. This is the signature of a fully stretched network which has the maximum possible volume or the lowest density. From this point of view, the problem is also related to the flexibility window in glasses where naturally occurring glasses are found near their low-density limit.<sup>[59,60]</sup> As we increase the edge length  $s$ , the two infinitesimally close solutions diverge and quickly two new solutions join the previous solutions. The number of realizations in Figure 11 generally increases up to a maximum number. In fact, two sharp increases happen at  $\approx 0.5$  and  $\approx 1.0$  because the pins are roughly  $l_0 \approx 1.0$  unit apart. Therefore, when  $l_0$  is roughly an integer multiple of the edge length of the triangles, the triangles can tightly fit together and new solutions appear. **Figure 12** shows some realizations (out of 76 possible realizations) for the edge length 1.0.

After reaching a maximum of 104 realizations, the number of solutions rapidly drops. Our numerical experiments show that



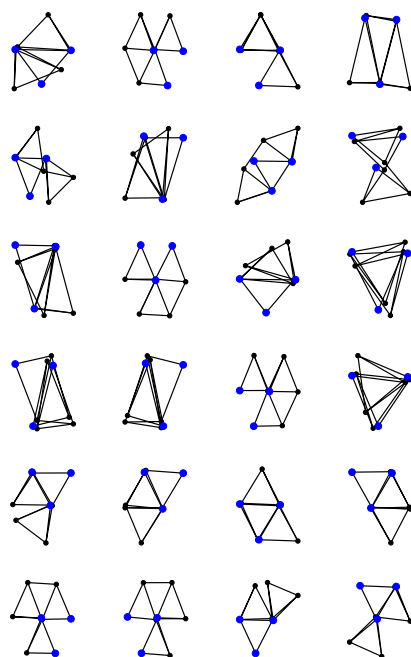


**Figure 12.** Some of the realizations with the edge length equal to  $s = 1.0$ .

a subset of solutions survives even at very large edge lengths (high density) and the number of realizations reaches a plateau of 44 solutions. **Figure 13** lists these 44 states when the edge length is set to 100, but Fig. 11 shows the number of realizations up to  $s = 2$ . Many solutions in this regime are related by an approximate mirror symmetry, as we expect the three blue pins to be coincident and the equilateral triangles are roughly arranged around a central point.

Although it is pedagogic to inspect the individual solutions visually, we need to distinguish various realizations with the same edge lengths. This also helps to track (follow continuously) how solutions at a given edge length from the previous solutions with smaller edge lengths. We choose the mean distance of vertices from the centroid of the pinned vertices as the metric.

If we plot this metric versus the edge length ratio for each realization, the result is the trajectories in **Figure 14**, showing how some solutions persist for a long range but others disappear. These trajectories represent solutions to a different set of equations than the  $2N - 1$  equations of the form Equation (1) whose solutions form the closed curves of the 1-dof mechanisms given by the single-cut or CayMos algorithms. This system has  $2N$  equations of the form Equation (1) for the bonds, but has an extra variable  $s$ , representing the bond length (boundary edge length is fixed due to pinned vertices). Red and green lines, respectively, show the linear and quadratic fit to the persistent paths, which shows an intermediate growth rate. Previously, we discussed that there is a sharp increase in the number of realizations at  $s$  around 0.5 and 1.0. Figure 14 shows that along those values, there is a tremendous amount of activity and a large set of solutions are only present in a small region of edge lengths.

The complexity of paths in Figure 14 makes it certainly constructive to look at specific regions of edge length in more detail.

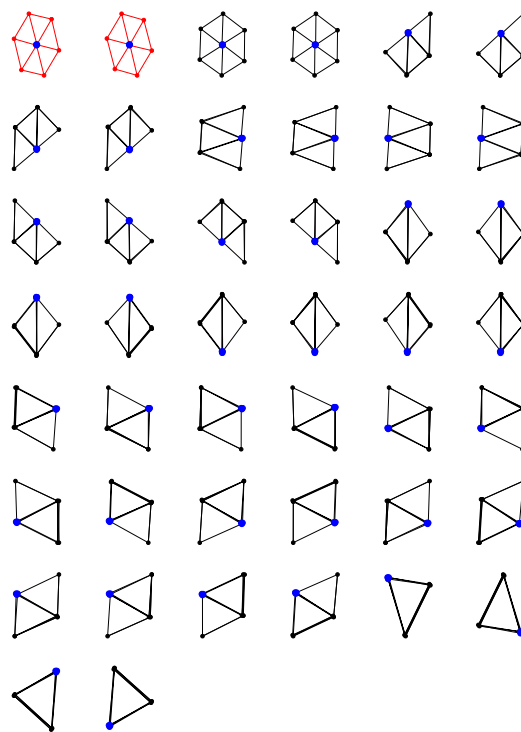


**Figure 13.** The 44 solutions in the large edge length limit where the edge length  $s$  is set to 100. Similar solutions are related by mirror symmetry but not rotation. The first two realizations are colored to emphasize that although the graphs look alike, different vertices have occupied the same coordinates and therefore they count as two distinct realizations.

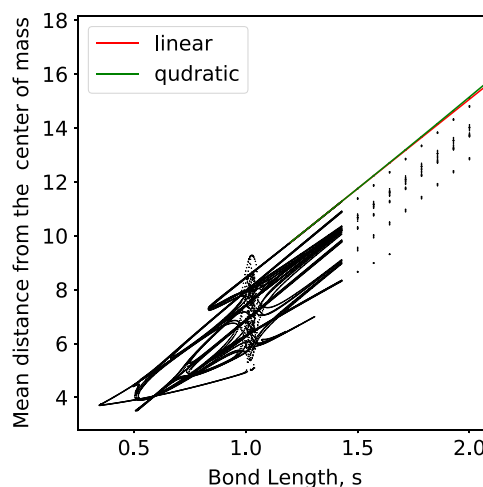


**Figure 14.** The mean distance of vertices from the centroid of the pinned vertices vs. the edge lengths. The mean distance scales quadratically (green) not linearly (red). The two curves are fitted to the topmost points with edge lengths  $s$  between 1.1 and 1.4 but are extrapolated to the outside of this window.

Our observations show that new solutions always come in as a pair. Based on the results, we have observed three mechanisms for appearance/disappearance of solutions: simple closed trajectories, open trajectories, and retrogrades. Examples of

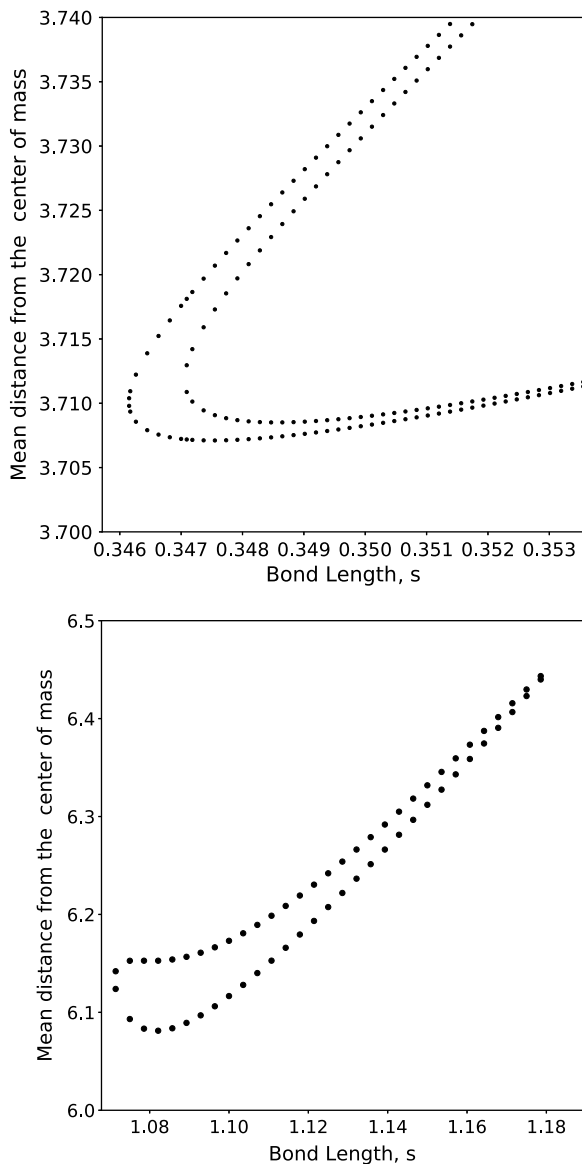


**Figure 15.** Open trajectories (top) and simple closed trajectories (bottom) are two ways in which realizations appear and disappear. The upper panel depicts the initial solutions at the low-density limit. Note that first two solutions emerge and then they diverge while at a secondary point; a new trajectory of solutions appears. In the lower, a pair of solution gradually converges and finally forms a close loop.

simple closed and open trajectories are given in **Figure 15**. Open trajectories are the persistent trajectories that continue to exist even at very large edge lengths. A retrograde is a trajectory that bends backward which is a disappearance mechanism; an example is given in the right panel of **Figure 16**. This leads to more complex circuits replacing the simple loop in upper part of **Figure 2**. For the retrograde there can be four intercepts and it is clear that any closed loop will have an even number of intercepts, consistent with Theorem 1. However, we have found no evidence of bifurcations<sup>[61,62]</sup> (**Figure 16**, left panel).

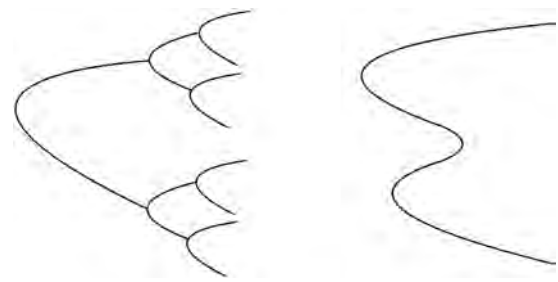


**Figure 16.** The left panel is a bifurcation which we have never observed. The right panel is a “retrograde” which is an alternative way of losing solutions, which we do observe for the Trihex.

#### 4.6. Energy Barriers

The discussion in the previous section showed that different realizations of an isostatic network can be found by solving edge length equations. Realizations of a framework are thought to be related to tunneling states in glasses. **Figure 17** shows four realizations of Trihex at  $s \approx 0.348$ . Their corresponding points are marked by red stars in the left plot. The amount of energy in transition from one state to another is a way of classifying sets of states. Note that the landscape has no minimum except the listed four solutions. We perform a linear interpolation between two given states. Let  $s_1$  and  $s_2$  be two solutions in the configuration space. We write

$$s(\lambda) = s_1 + \left( \lambda + \frac{1}{2} \right) \cdot (s_2 - s_1) \quad (2)$$

Assuming bonds are harmonic springs with spring constant equal to unity, the energy can be found as a function of  $\lambda$ , where  $\lambda = -\frac{1}{2}, \frac{1}{2}$  correspond to the two states. We can think of two paths on this plot as two trajectories of frameworks. The equivalent frameworks 1 and 4 belong to the first trajectories, while 2 and 3 lie on the second trajectory which exists only when  $s \geq 0.347$ . The pair of frameworks that belong to the same trajectory indeed has very similar configurations. In fact, the largest difference between the pairs is the reflection of the top connecting edge along horizontal axis. For the pairs that do not belong to the same trajectory, the motion involves the significant rotation of the bottom triangle. If we would assume that the edges are harmonic springs and not fixed-lengths bars, the energy path connecting the pairs of realizations on different branches has a much higher energy barrier compared with that of the pairs on the same branch. Note that the whole energy landscape of Trihex at this edge length has only four minima. The nice feature of the landscape of Trihex is that the global minimum energy is exactly zero (**Figure 18**).

This energy perspective makes an important bridge between Trihex examples and glasses. If this picture from studying Trihex remains intact in glasses, we expect to see that solutions play different roles depending on which branch they belong. **Figure 17** is particularly important because the experimental density of glasses is close to the low-density edge. So, we expect the discussion in this section would somewhat generalize to the 2D glasses. But as discussed, solving edge length equations is

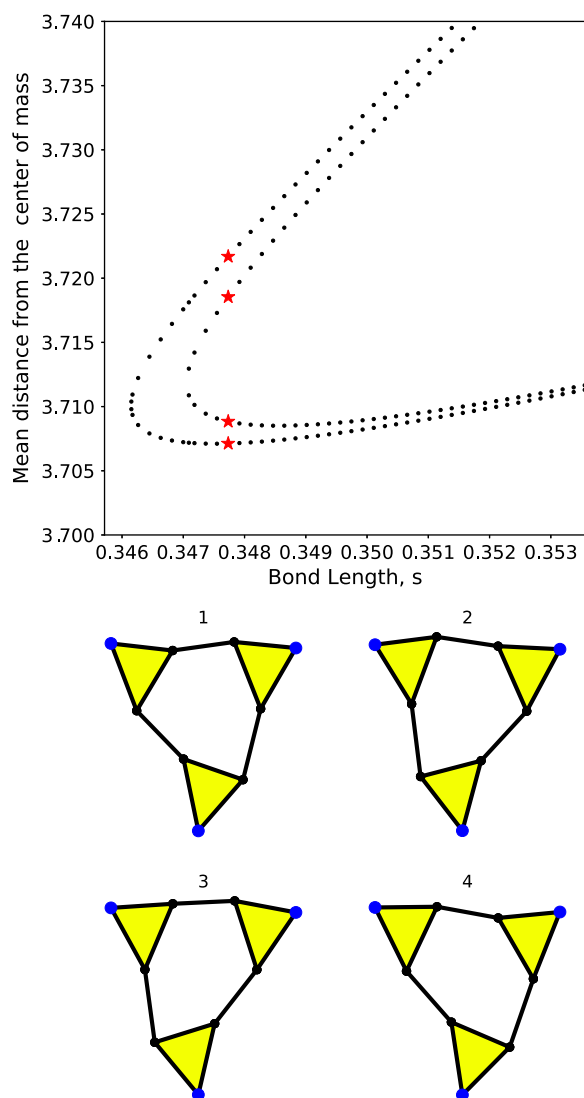


**Figure 17.** The four solutions with the edge length equal to  $\approx 0.3477$  marked with red asterisks. The solutions are numbered from the smallest mean distance from the centroid (y-axis) to the largest. The solutions on the same trajectory show a small displacement but a more significant motion is involved among the solutions from the different trajectories.

computationally expensive for a large system. On the contrary, two-level systems in glasses are rare. To have the slightest hope of finding a tunneling state, we need to study systems that are considerably larger than Trihex. This makes it inevitable to design an alternative approach to find realizations of a framework starting from already available information.

#### 4.7. 2D Glasses and Jammed Networks

Trihex serves as an illuminating toy model to present the main ideas about the existence of multiple realizations for an isostatic network and techniques to find such realizations. However, these methods are categorically applicable to the networks inspired by or modeled directly from materials such as network glasses or

jammed granular packing. Such materials are either at or very close to the isostatic states and their behavior is significantly influenced by their rigidity.<sup>[59,60,63]</sup> But our main concern here is to establish a link between the multiplicity of material realizations and their physical properties, specifically the existence of the tunneling modes in such materials.

In the case of glasses, we are focused on those glasses that can be modeled as a network of corner-sharing tetrahedra in 3D or triangles in 2D. An example of the former is  $\text{SiO}_2$  or  $\text{GeO}_2$  and of the latter is a silica bilayer which, although, is 3D dimensional, but it can be seen as two mirroring layers of 1 atom thick of oxygens connected through bridging atoms to complete the chemical bonds.<sup>[25]</sup>

In 2D glasses, every atom/vertex is fourfold coordinated (four shared constraints), but as each vertex has two degrees of freedom (translational degrees of freedom), 2D glasses are locally isostatic.<sup>[27]</sup> However, boundary conditions determine the global rigidity of the framework. For networks extracted from the experimental data, atoms on the surface are not fully connected and anchored/pinned boundary conditions are necessary and sufficient to render the system isostatic.<sup>[27]</sup> For material networks made using computer simulations, the boundary conditions are periodic which means such 2D systems contain two redundant bonds which must be removed to render the network isostatic.

These computer-generated networks are prepared using Wooten–Winer–Weaire (WWW) algorithm with the periodic boundary conditions while ensuring that the ring distribution and the area of polygons are in agreement with the experimental data.<sup>[64,65]</sup> As a consequence, the edge lengths are no longer exactly equal and 2D glasses satisfy a stronger definition of being generic. Similar to Trihex, the structure is in mechanical equilibrium; all edges are assumed to be harmonic springs initially at their rest lengths and the dynamical matrix is positive semidefinite.

In the case of granular networks, grains are often modeled as an athermal packing of circles/spheres interacting via a Hookian or Hertzian potential. To model such packings, we use the standard protocols that are common in jamming community. We start with a random distribution of bidisperse (0.5:1, 0.5:1.4) circles (to prevent crystallization), and we rescale all the radii uniformly to set any desired packing density  $\phi$ . The energy of the system, given by Equation (3), (where  $\rho_{ij}$  is the distance between nodes  $i$  and  $j$  and  $\sigma_{ij}$  is the sum of their radii) is then minimized by a standard FIRE algorithm<sup>[66]</sup> using the pyCudaPacking package, developed by Corwin et al.<sup>[67,68]</sup>

$$E = \sum_{ij} \left(1 - \frac{\rho_{ij}}{\sigma_{ij}}\right)^2 \Theta\left(1 - \frac{\rho_{ij}}{\sigma_{ij}}\right) \quad (3)$$

where  $\Theta$  is the Heaviside step function to ensure that only overlapping circles are included in energy.

If the packing density is high enough ( $\phi > 0.84$ ), the system will have several states of self-stress or redundant contacts. By decreasing the packing density quasi-statically, the system reaches a critically jammed state with zero pressure and one state of self-stress. This system can then be mapped to a network by replacing the center of mass of each circle with a node and replacing any nonzero overlap between neighboring particles with a bond between their corresponding nodes. Such a network has

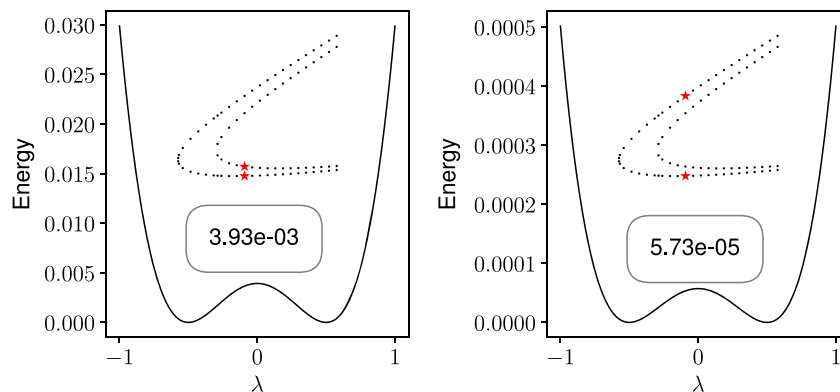


**Figure 18.** The energy landscape of transition states between various realizations of Trihex, found by linear interpolation (Equation (2)) between the realizations shown in Figure 17. The inset box shows the height of the energy barrier in the units that spring constant is set to unity. The inset figure shows the two solutions indicated by red asterisks. The energy barrier between the realizations on the same branch is significantly smaller than that of the realizations on different branches.

one bond in excess of isostaticity. By removing any one bond randomly, one can make an isostatic network.

Once a system is at the isostatic point, in principle, the same techniques used to find realizations of a Trihex are also applicable to material networks. However, such networks differ from Trihex in two significant ways. First, material networks contain many possible atomic arrangements which lead to various couplings among atoms in the set of edge length equations (Equation (1)). While Trihex is essentially a ring of triangles forming a hexagon, in experimental samples ring size varies from 4 to 8<sup>[65]</sup> which are distributed nonrandomly on a plane.<sup>[26]</sup>

Second, 2D glasses are generally much larger than Trihex and it might not be computationally feasible to apply the techniques directly. In fact, solving the set of edge length equations (Equation (1)) exactly is practically impossible for systems as large as 2D glasses with  $N \geq \mathcal{O}(10^2)$  which, in turn, means for larger systems the complete set of solutions and their evolving on branches are inaccessible.

The alternative method, the single-cut algorithm, is guaranteed to provide new realization(s) but is not an exhaustive method and some of the existing solutions will be unreachable. In this method, we need to compute the null space (the eigenvectors corresponding to zero eigenvalue) of a matrix of size  $(dN)^2$ , where  $d$  is the spatial dimensions and  $N$  is the number of vertices. Even if finding the null space can be done efficiently by avoiding diagonalizing the entire matrix, there is some error associated with moving  $N$  atoms along nontrivial zero-mode. It is possible that the path would not be closed (the system would not return to its original conformation) due to accumulation of errors. Therefore, either the step size should be chosen sufficiently small to ensure the path is smooth or frequent energy minimizations are necessary along the path; both of which are expensive.

Therefore, we slightly modify the single-cut algorithm to find the alternative realizations of large isostatic networks. As the existence of the second realization is guaranteed, we take fairly large steps along the nontrivial zero-eigenvalue eigenvector alternative. In addition, it is not necessary to complete the curve in configuration space exactly to calculate the thermal properties. Therefore, once the curve intersects the vertical line denoting the

original length of the cut edge, we have found a second realization and the path traversal can be stopped early. However, because of the larger steps along the curve, the position of vertices and subsequently the edge lengths have large errors which means the conformation has not returned exactly to its original set of edge lengths. But as the conformation is close enough to the energy basin, we only refine the last conformation by an extensive energy minimization to ensure that edge lengths are equal to their original values (Figure 19).

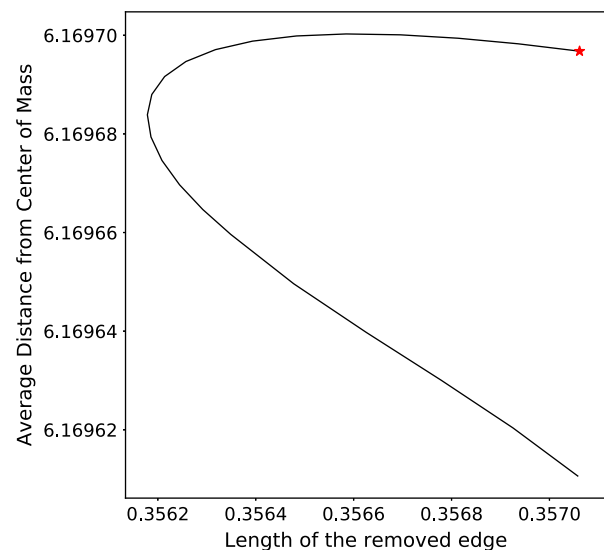


**Figure 19.** The curve found by applying the modified single-cut algorithm to a 2D glass, in which the path traversal is stopped upon finding a solution. Fairly large steps are taken along the eigenvector with zero eigenvalue as is evident from the curve roughness. The vertical axis represents the total distance of all vertices from the center of mass, while the horizontal axis shows the distance between two ends of the removed edge. The red asterisk at the bottom denotes the original network and the top asterisk shows the alternative solution found by the path traversal. The arrow is drawn to emphasize the fact that the real solution (indicated by the blue asterisk) with no error in the edge lengths does not exactly lie on the drawn curve in configuration space and further energy minimization is required to find the correct coordinates.



If the curve is complex enough, it contains more than two realizations. Based on the modified scheme, if the curve traversal is stopped after finding the first solution, we might miss a whole set of solutions. To address this concern, we note that glasses are found at the extreme of density (edge of the flexibility window).<sup>[59]</sup> At this limit, only two solutions are expected, similar to Trihex example where at the maximal density point only two solutions existed. We tested the validity of this argument by applying the original single-cut algorithm on two 2D networks ( $N = 48$  and  $300$ ) by removing all edges iteratively. It was observed that all closed curves give two and only two distinct solutions independent of which bond is removed.

After applying the modified single-cut algorithm, two realizations of a 2D glass are available; they have the same exact topology and bond lengths, but the vertices are displaced between the two states. The amount of this displacement determines whether the conformations are in fact the tunneling states. Anomalous specific heat is observed at temperatures about 1 K, where the available energy is not sufficient for the displacement of a large group of atoms over a long distance. Therefore, it is expected that atomic displacements in a tunneling state are relatively localized. To characterize to what extent the displacements between two conformations are localized, we use the participation ratio (PR). If an atom  $i$  is displaced by the vector  $\mathbf{u}_i$  between two conformations, PR is defined as

$$PR = \frac{(\sum_{i=1}^N |\mathbf{u}_i|^2)^2}{N \sum_{i=1}^N |\mathbf{u}_i|^4} \quad (4)$$

For a perfectly delocalized mode,  $|\mathbf{u}_i| \sim 1/\sqrt{N}$  and  $PR \sim 1$ . For a completely localized mode,  $|\mathbf{u}_i| \sim \delta_{ij}$ ,  $PR \sim N^{-1}$ . Hence, a small value of PR is the signature of a localized mode. In the case of tunneling modes, it is expected that by increasing the system size  $N$ , the fraction of atoms participating in the mode decreases.

In addition to the locality of the displacement, it is essential to measure the significance of the atomic displacements in the limit of large systems. For a conformation to be considered a tunneling state, the atomic displacements should be significantly larger than zero-point motion. Assuming a harmonic oscillator, the zero-point amplitude  $x_0$  is of order of

$$x_0 \sim \sqrt{\frac{\hbar}{m\omega}} = \sqrt{\frac{10^{-34}}{10^{-26} \times 10^{14}}} = 10^{-11} \text{ m} = 0.1 \text{ \AA} \quad (5)$$

for an oxygen atom. For an O—O bond length of  $2.6 \text{ \AA}$ ,  $x_0 \approx 10^{-2}$  is the unit of the bond length. If the typical motion of the atoms measured by their mean displacement  $N^{-1} \sum |\mathbf{u}_i|$  is less than  $x_0$ , such motions are not relevant to the tunneling states but, nevertheless, they are mathematically correct and give rise to other realizations.

To quantify the atomic displacements and participation ratio in large systems, we prepare four networks of corner-sharing triangles under periodic boundary conditions with varying size  $N = 48, 300, 1254, 5016$  and randomly remove two edges to satisfy the isostaticity condition. By applying the modified single-edge-cut algorithm, the corresponding second realizations are found. This allows us to study the behavior of the PR and the mean displacement of vertices as a function of the number of particles.

**Table 3.** The magnitude of displacements in the unit of the edge length found in simulations for different system sizes,  $N$ .

$N$	$\sum  \mathbf{u}_i $	$\sum  \mathbf{u}_i /N$	$\sqrt{\sum  \mathbf{u}_i ^2/N}$	PR
48	0.09	$1.89 \times 10^{-3}$	$2.12 \times 10^{-3}$	0.44
300	1.47	$4.89 \times 10^{-3}$	$5.80 \times 10^{-3}$	0.41
1254	2.03	$1.62 \times 10^{-3}$	$1.84 \times 10^{-3}$	0.47
5016	2.94	$0.59 \times 10^{-3}$	$0.67 \times 10^{-3}$	0.46

Table 3 shows the results for the mean displacement of atoms and their PR. The total displacement  $\sum |\mathbf{u}_i|$  increases slightly by system size, but the average displacement of a typical particle  $\sum |\mathbf{u}_i|/N$  generally decreases. But regardless of  $N$ , the mean displacement is smaller than that of the zero-point motion  $x_0$  and hence this motion cannot be representative of a tunneling state. In addition, all networks exhibit modes in which about  $\approx 45\%$  of all vertices are displaced in the system. Such an extended mode cannot be a tunneling state because in the limit of Avogadro number of atoms, a massive number of atoms should be involved in such states which are not energetically favorable. Unfortunately, it seems that the single-cut algorithm is not able to find realizations that are sufficiently distant from the initial realizations (evidenced by vanishingly small  $|\mathbf{u}_i|$  values) and sufficiently localized (evidenced by the constant PR/ $N$  value).

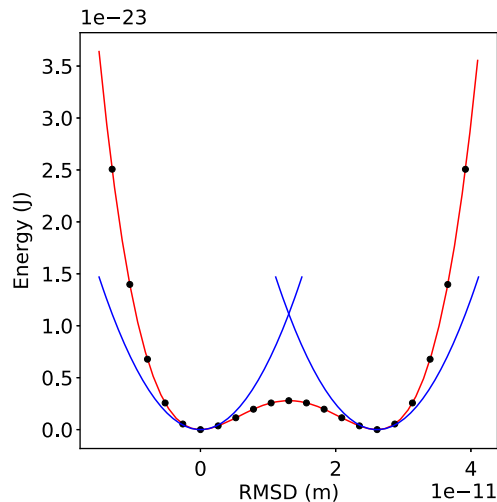
Although from the localization and displacement considerations, it is evident that the found realizations cannot account for the tunneling states; nevertheless, it would be insightful to study their thermal properties. For each system size, we can form a double-well potential where each realization sits at one of the energy minima. For every  $N$ , the energy pathway is found by the linear interpolation (Equation (2)) between the two realizations with zero energy. The height of the energy barrier  $V_b$  can be estimated from the interpolated curve, while the well separation  $d$  is calculated as the root-mean-square deviation (RMSD) of atomic positions.

Figure 20 shows an example of a double-well potential derived from the system with  $N = 300$  atoms. The black points are found using Equation (2), while the red line is a fourth-order polynomial fit to these points.<sup>[69]</sup> The two blue lines are the harmonic approximations around two equilibrium realizations. The probability of the tunneling scales as  $e^{-\lambda}$ , where  $\lambda$  is the tunneling parameter, is defined by the following equation (derived from the ratio of kinetic and potential energies)

$$\lambda = d \sqrt{\frac{2mV_b}{\hbar^2}} \quad (6)$$

where  $m$  is the mass of an oxygen atom (see Appendix B in the study by Sadjadi<sup>[69]</sup> for the derivation and a detailed discussion on the significance of the tunneling parameter).

Table 4 shows the characteristics of the double-well potential for four systems in SI units. The barrier height ( $V_b$ ) of all systems is a very small value which means the double-well is essentially flat in the middle. The well separation  $d$  is also very small and at most about 5% of O—O bond length and  $\lambda$  shows a somewhat monotonic decrease with the system size (to find the exact dependence of the values on  $N$  more samples should be used).



**Figure 20.** The double-well potential found by linear interpolation between the two realizations for  $N = 300$ . The black circles are found by linear interpolation; the red line is a fourth-order polynomial fit to the data. The blue curves show the harmonic approximations for two minima.

$T_{\max}$ , in Table 4, denotes the temperature at which the specific heat of a two-level system is maximum. To find this temperature, we solved the Schrödinger's equation numerically using the embedding method (Ref. [70] and Appendix C in the study by Sadjadi<sup>[69]</sup>) for the double-well potential in Figure 20 and found its specific heat using energy levels. In general,  $T_{\max}$  happens to be at about  $\approx 10$  K which is much higher than the range of temperatures at which the tunneling states are assumed to be active.

We also repeated the same calculations in 3D glasses, but very similar results were obtained. However, as it was discussed earlier in this section, packing of granular materials is another network matter which can be studied using this framework. In addition, because these networks are essentially different from networks glasses in terms of ring distribution, preparation method, and so on, they might shed light on the nature of multiple realizations and possibly tunneling states from a different perspective.

**Figure 21** shows an example of a computer-generated jammed packing with 247 vertices in which two realizations (original conformation and alternative realization found by the modified single-cut algorithm) are superimposed. As it is shown, in some regions the displacements are more pronounced. However, compared with network glasses, the mean displacement is about one order of magnitude smaller.

**Table 4.** Characteristics of double-well potentials in SI units for four different system sizes,  $N$ .

$N$	$V_b$ [J]	$T_b$ [K]	$d$ [Å]	$\lambda$	$T_{\max}$ [K]
48	$9.45 \times 10^{-27}$	$6.84 \times 10^{-4}$	0.04	0.0012	16
300	$2.79 \times 10^{-24}$	$2 \times 10^{-1}$	0.30	0.10	12
1254	$1.44 \times 10^{-25}$	$1.04 \times 10^{-2}$	0.17	0.02	5
5016	$3.84 \times 10^{-27}$	$2.78 \times 10^{-4}$	0.12	0.0025	23

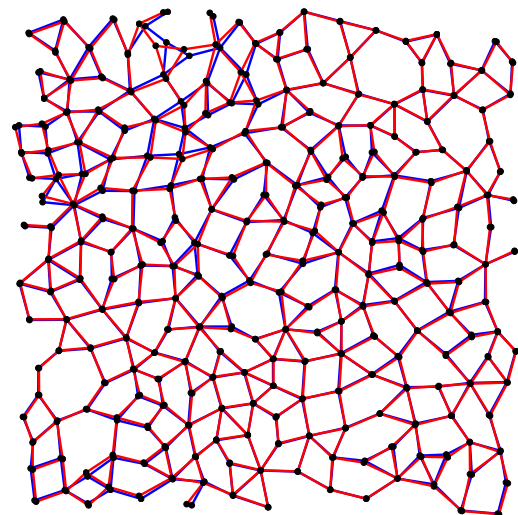


**Figure 21.** A jammed circle packing. In this representation, circles are replaced by their center. The original network is drawn with blue lines, while the equivalent configuration found by modified single-cut algorithm is shown in red.

The jammed packings are generated by minimizing the overlap among circles in contact. In the original network, all overlaps are smaller than a prespecified threshold. To find the alternative realization, however, the interaction between soft disks is replaced by harmonic springs. Therefore, both realizations have zero energy if interactions are harmonic springs since all edge lengths are equal but since adjacent vertices can also move, disks that were previously nonoverlapping can intersect leading to additional energy or the system can undergo an unjamming process. Hence, an important question is whether the alternative realization is at energy minima if the interactions are based on the overlapping soft disks. In our tests, we observed that second realizations of jammed systems have generally large overlaps between disks, but we have observed some examples in which even alternative realizations are jammed and at the energy minimum or very close to it.

To draw a comparison between Trihex and 2D glasses, it seems that the single-cut algorithm can only find solutions that belong to the same connected component while realizations on other connected components are energetically inaccessible because they contain motions of larger units such as a rigid triangle (or tetrahedron). Although we think such branches exist in glasses, it is not computationally feasible to find all the connected components for such large systems similar to Trihex.

It is worth noting that the aforementioned discussion can be directly applied to bulk glasses. We repeated the modified single-edge-cut algorithm for various silica structures in three dimensions. The only modification required in 3D is that three edges need to be removed to reach the isostatic point. Our results for bulk (3D) glasses were very similar to the 2D case.

#### 4.8. Questions

There are a number of important open questions that we list here that require this work to be examined in a larger context. The

questions are general and go beyond the models considered in this article.

The maximum number of distinct solutions for the Trihex is 112. Note that Mathematica often gives the same solution multiple times. Where does this number come from? CayMos theory gives an upper bound of 128. Using numerology it is  $2^7 - 2^4$ . Note that the problem cannot be reduced to a single polynomial where the number of real solutions is always less than or equal to the degree of the polynomial.

Why is nothing more complex than an open or closed retrograde trajectory found in all the examples here?

Why are the trajectories all “smooth” with no singularities? This can, however, be proved in the generic case for the closed curves obtained in single-cut and CayMos algorithms, which are configuration spaces of 1-dof mechanisms.

How general is this scheme?

Why are there no bifurcations in the solutions?

## 5. Discussion and Conclusion

The main purpose of this collaboration is the present Theorems 1 and 2 and the single-cut algorithm in a straightforward way so that it is accessible for future work. These are powerful statements about isostatic systems that we have just begun to explore here. It is hoped that the reader can see the potential and will pursue these methods further. We have taken the first steps with atomic clusters in three dimensions, and with tunneling modes in glasses and jammed systems in two dimensions. We emphasize again that these approaches work in any dimension. The emphasis here on two dimensions is for simplicity and for ease of visualization. Theorem 1 is counter-intuitive at first sight, but becomes very natural when the circuit associated with a single cut (see Figure 2) is understood. We have shown that modestly large systems behave in the same way as smaller systems, but the limit of large systems (tending to infinite size) is very different. This is important for solid-state problems where systems have a size of the order of Avogadro's number ( $\approx 10^{24}$ ) and this has important implications for the origin of tunneling states in glasses. Indeed, “more is different”.<sup>[71]</sup>

## Acknowledgements

M.F.T. would like to congratulate David Drabold upon reaching the temporal landmark of three score years and for all the interesting discussions at home and in more exotic locations that we have enjoyed over the years. His general approach to science and in particular his work on glassy networks have influenced the work in this article. The authors would like to thank financial support through NSF grant no. DMS 1564468 (Connelly, Gortler, Holmes-Cerfon, Sitharam, Thorpe). The authors would particularly like to thank Eric Corwin and Kenneth Stephenson for stimulating discussions.

## Conflict of Interest

The authors declare no conflict of interest.

## Data Availability Statement

Research data are not shared.

## Keywords

glasses, isostatic, jamming, networks, tunneling

Received: November 3, 2020

Revised: February 8, 2021

Published online: March 8, 2021

- [1] V. F. Hagh, M. F. Thorpe, *Phys. Rev. B* **2018**, 98, 100101.
- [2] K. Bertoldi, V. Vitelli, J. Christensen, M. van Hecke, *Nat. Rev. Mater.* **2017**, 2, 17066.
- [3] G. Baardink, A. Souslov, J. Paulose, V. Vitelli, *Proc. Natl. Acad. Sci. USA* **2017**, 115, 489.
- [4] M. F. Thorpe, *J. Non-Cryst. Solids* **1983**, 57, 355.
- [5] C. P. Goodrich, A. J. Liu, S. R. Nagel, *Phys. Rev. Lett.* **2015**, 114, 225501.
- [6] V. F. Hagh, E. I. Corwin, K. Stephenson, M. F. Thorpe, *Soft Matter* **2019**, 15, 3076.
- [7] M. Sitharam, A. St. John, J. Sidham, *Handbook of Geometric Constraint Systems Principles*, Chapman & Hall, CRC Press, Boca Raton, FL **2018**.
- [8] K. Wuthrich, *Science* **1989**, 243, 45.
- [9] B. Hendrickson, *SIAM J. Optimiz.* **1995**, 5, 835.
- [10] K. Killian, P. Meissl, in *Beiträge zur Theorie der geodätischen Netze im Raum*, Deutsche Geodät. Kommission Bayer. Akad. Wiss., Ser. A **1969**, no. 61, pp. 65–72.
- [11] D. Moore, J. Leonard, D. Rus, S. Teller, in *Proc. of the 2nd Int. Conf. on Embedded Networked Sensor Systems*, ACM, New York, NY **2004**, pp. 50–61.
- [12] J. W. Rocks, N. Pashine, I. Bischofberger, C. P. Goodrich, A. J. Liu, S. R. Nagel, *Proc. Natl. Acad. Sci. USA* **2017**, 114, 2520.
- [13] J. Z. Kim, Z. Lu, S. H. Strogatz, D. S. Bassett, arXiv:1804.00173, **2018**.
- [14] L. Liberti, C. Lavor, N. Maculan, A. Mucherino, *SIAM Rev.* **2014**, 56, 3.
- [15] P. M. Duxbury, L. Granlund, S. R. Gujarathi, P. Juhas, S. J. L. Billinge, *Discrete Appl. Math.* **2016**, 204, 117.
- [16] W. A. Phillips, *J. Low Temp. Phys.* **1972**, 7, 351.
- [17] P. W. Anderson, B. I. Halperin, C. M. Varma, *Philos. Mag.* **1972**, 25, 1.
- [18] W. A. Phillips, *Rep. Prog. Phys.* **1987**, 50, 1657.
- [19] P. Y. Huang, S. Kurasch, A. Srivastava, V. Skakalova, J. Kotakoski, A. V. Krasheninnikov, R. Hovden, Q. Mao, J. C. Meyer, J. Smet, D. A. Muller, U. Kaiser, *Nano Lett.* **2012**, 12, 1081.
- [20] L. Lichtenstein, C. Büchner, B. Yang, S. Shaikhutdinov, M. Heyde, M. Sierka, R. Włodarczyk, J. Sauer, H.-J. Freund, *Angew. Chem., Int. Ed.* **2012**, 51, 404.
- [21] W. Rosenhain, *Trans. Opt. Soc.* **1927**, 11, 77.
- [22] W. H. Zachariasen, *J. Am. Chem. Soc.* **1932**, 54, 3841.
- [23] B. Hendrickson, *J. Comput.* **1992**, 21, 65.
- [24] S. J. Gortler, A. D. Healy, D. P. Thurston, *Am. J. Math.* **2010**, 132, 897.
- [25] M. Sadjadi, B. Bhattarai, D. A. Drabold, M. F. Thorpe, M. Wilson, *Phys. Rev. B* **2017**, 96, 201405.
- [26] M. Sadjadi, M. F. Thorpe, *Phys. Rev. E* **2016**, 94.
- [27] L. Theran, A. Nixon, E. Ross, M. Sadjadi, B. Servatius, M. F. Thorpe, *Phys. Rev. E* **2015**, 92, 053306.
- [28] I. Fudos, C. M. Hoffmann, *ACM Trans. Graph.* **1997**, 16, 179.
- [29] J. C. Owen, in *Proc. First ACM Symp. on Solid Modeling Foundations and CAD/CAM Applications*, SMA '91 ACM, New York, NY, **1991**, pp. 397–407.

- [30] J. C. Owen, S. C. Power, *Trans. Am. Math. Soc.* **2007**, 359, 2269.
- [31] R. Joan-Arinyo, A. Soto-Riera, S. Vila-Marta, J. Vilaplana-Pastó, *Comput.-Aid. Des.* **2004**, 36, 123.
- [32] M. C. Holmes-Cerfon, *SIAM Rev.* **2016**, 58, 229.
- [33] V. F. Hagh, M. Sadjadi, *RigidPy package*, **2020**, <https://github.com/VardaHagh/Rigidpy>.
- [34] M. Sitharam, H. Gao, *Discrete Comput. Geometry* **2010**, 43, 594.
- [35] M. Sitharam, M. Wang, *Comput.-Aid. Des.* **2014**, 46, 205.
- [36] M. Sitharam, M. Wang, H. Gao, arXiv:1112.6008, **2011**.
- [37] M. Sitharam, M. Wang, H. Gao, arXiv:1112.6009, **2011**.
- [38] M. Wang, M. Sitharam, *ACM Trans. Math. Softw.* **2015**, 41, 27.
- [39] H. Gao, M. Sitharam, in *Proc. 2009 ACM Symp. on Applied Computing*, SAC '09, ACM, New York, NY **2009**, pp. 1122–1126.
- [40] J. Youngquist, M. Sitharam, CoSTs or Corner Sharing Triangles and Trihex using the CayMos Approach, <https://cise.ufl.edu/~jyoungqu/trihex.html> (accessed: October 2020).
- [41] T. Baker, M. Sitharam, M. Wang, J. Willoughby, arXiv:1507.01158, **2015**.
- [42] M. Sitharam, in *Geometric and Algorithmic Aspects of Computer-Aided Design and Manufacturing* (Eds: R. Janardan, M. Smid, D. Dutta), DIMACS Series in Discrete Mathematics and Theoretical Computer Science, Vol. 67, American Mathematical Society, Providence, RI **2015**, pp. 117–164.
- [43] J. Oung, M. Sitharam, B. Moro, A. Arbree, in *Proc. Sixth ACM Symposium on Solid Modeling and Applications, SMA '01*, Association for Computing Machinery, New York, NY **2001**, pp. 307–308.
- [44] M. Sitharam, J.-J. Oung, Y. Zhou, A. Arbree, *Comput. Aid. Des.* **2006**, 38, 22.
- [45] M. Sitharam, *Int. J. Comput. Geom. Appl.* **2006**, 16, 591.
- [46] M. Sitharam, J. Peters, Y. Zhou, *J. Symbol. Comput.* **2010**, 45, 481.
- [47] M. Sitharam, Y. Zhou, J. Peters, *Int. J. Comput. Geom. Appl.* **2010**, 20, 631.
- [48] M. Sitharam, A. Arbree, Y. Zhou, N. Kohareswaran, *ACM Trans. Graph.* **2006**, 25, 194.
- [49] M. Belk, R. Connelly, *Discrete Comput. Geom.* **2007**, 37, 125.
- [50] M. Sitharam, J. Willoughby, in *Automated Deduction in Geometry*, Springer International Publishing, Cham **2015**, pp. 129–148.
- [51] R. Prabhu, M. Sitharam, A. Ozkan, R. Wu, *J. Chem. Inform. Model.* **2020**, <https://doi.org/10.1021/acs.jcim.0c00763>.
- [52] A. Ozkan, R. Prabhu, T. Baker, J. Pence, J. Peters, M. Sitharam, *ACM Trans. Math. Softw.* **2018**, 44, 48.
- [53] A. Ozkan, M. Sitharam, J. C. Flores-Canales, R. Prabhu, M. Kurnikova, arXiv:1408.2481, **2014**.
- [54] R. Wu, A. Ozkan, A. Bennett, M. Agbandje-Mckenna, M. Sitharam, in *BCB'12: Proc. of the ACM Conf. on Bioinformatics, Computational Biology and Biomedicine*, Orlando, FL **2012**, pp. 690–695.
- [55] R. Wu, R. Prabhu, A. Ozkan, M. Sitharam, arXiv:2001.00316 [q-bio.BM], **2020**.
- [56] M. Kang, M. Sitharam, *Fast Flip Realization: Indexing and Efficient Solution for Planar Distance Constraint*, **2020**, unpublished.
- [57] M. Kang, M. Sitharam, *Flex dr-plans: Optimal Recursive Decomposition of Planar Distance Constraint Graphs*, **2020**, unpublished.
- [58] W. Bosma, J. Cannon, C. Playoust, *J. Symbolic Comput.* **1997**, 24, 235; *Computational algebra and number theory* (London, 1993).
- [59] A. Sartbaeva, S. A. Wells, M. M. J. Treacy, M. F. Thorpe, *Nat. Mater.* **2006**, 5, 962.
- [60] V. Kapko, C. Dawson, M. M. J. Treacy, M. F. Thorpe, *Phys. Chem. Chem. Phys.* **2010**, 12, 8531.
- [61] V. I. Arnol'd, *Catastrophe Theory*, Springer Science & Business Media, New York **2003**.
- [62] M. J. Feigenbaum, *J. Stat. Phys.* **1978**, 19, 25.
- [63] W. G. Ellenbroek, V. F. Hagh, A. Kumar, M. F. Thorpe, M. van Hecke, *Phys. Rev. Lett.* **2015**, 114, 135501.
- [64] F. Wooten, K. Winer, D. Weaire, *Phys. Rev. Lett.* **1985**, 54, 1392.
- [65] A. Kumar, D. Sherrington, M. Wilson, M. F. Thorpe, *J. Phys.: Condens. Matter* **2014**, 26, 395401.
- [66] E. Bitzek, P. Koskinen, F. Gähler, M. Moseler, P. Gumbsch, *Phys. Rev. Lett.* **2006**, 97, 170201.
- [67] P. K. Morse, E. I. Corwin, *Phys. Rev. Lett.* **2014**, 112, 115701.
- [68] P. Charbonneau, E. I. Corwin, G. Parisi, F. Zamponi, *Phys. Rev. Lett.* **2012**, 109, 205501.
- [69] M. Sadjadi, *Ph.D. Dissertation*, Arizona State University, **2018**.
- [70] V. Jelic, F. Marsiglio, *Eur. J. Phys.* **2012**, 33, 1651.
- [71] P. W. Anderson, *Science* **1972**, 177, 393.



# Enhanced Disconnectivity Graphs of the $\pm 1$ and $\pm 1, \pm 2$ Spin Glasses

Katja Biswas

Dedicated to Professor David A. Drabold on the occasion of his 60th birthday

The energy landscapes of the  $\pm 1$  and  $\pm 1, \pm 2$  small-spin glasses are studied in the form of enhanced disconnectivity graphs. This new way of displaying disconnectivity graphs incorporates the merging of minima energy states of equal energy which are connected via zero-energy spin flips. These states form connected structures on the energy landscape, which we distinguish into four basic types. The types are indicated in the disconnectivity graph by different colors and their respective sizes via a bar chart at the corresponding energy levels. This allows for an easy intuitive access to highly degenerate energy landscapes without losing the main features. Further, these connected minima structures are analyzed in terms of their occurrences, sizes, and distributions for the two models of spin glasses. This gives a deep insight into the energy structure of these systems. Further, the use of the classification of minima reduces the description of  $\pm 1$  spin models by 93%, and that of  $\pm 1, \pm 2$  models by 71% without losing the core information about these systems.

energy barriers. Although much work and insight with disconnectivity graphs have been obtained for biopolymers and nanoclusters,<sup>[1–4]</sup> their utilization in spin glasses is still behind. Describing features of energy landscapes such as energy barriers and internal structures is a recurring focus of investigation.<sup>[5–10]</sup> However, there are only very few works in which disconnectivity graphs have been obtained and utilized.<sup>[11–14]</sup> The primary reason for this is that spin glasses with discrete interactions exhibit complex energy landscapes with highly degenerate minima, making a drawing of disconnectivity graphs less amenable to an intuitive understanding.

In our work, we enhance the description of disconnectivity graphs by distinguishing between different types of connected minima on the energy landscape. This allows for a reduced description without losing


## 1. Introduction

Disconnectivity graphs are depictions of energy landscapes<sup>[1]</sup> that primarily give an easy and intuitive access to the energy structure of the system in configuration space. They project the high-dimensional potential energy landscape onto two dimensions, via the depiction of the minima of the systems and the lowest highest energy barrier connecting them. Any two minima of a system are connected by multiple pathways, for each of which the energy of the system undergoes at least one increase. With the lowest–highest energy barrier, we summarize that from all the possible pathways only the one is chosen that requires the least increase in energy to transition between the two minima. The highest increase along this pathway is taken as the representative energy barrier displayed in the disconnectivity graphs. This is in lieu of the possibility that the transition from one state to another can occur over intermediate minima with different

the key information about the energy structure of these systems. Some of the minima on the energy landscape are connected by zero-energy spins, i.e., spins that when flipped do not increase the energy of the system. We distinguish between four types of minima, which we either call regular minima or type-1, type-2, and type-3 dales, highlighting the fact that these are minima energy structures of equal energy on the energy landscape. The dales consist of multiple configurations of the system connected via zero-energy spin flips, and can be thought of as individual but degenerate states. The distinction between the types of dales is based on the accessibility of the minima to each other. The types of minima are distinguished in the disconnectivity graphs using different colors and their respective sizes are indicated by a bar chart for the corresponding energy levels. This greatly enhances the visibility of the graphs, drastically reduces the number of minima that need to be drawn in the disconnectivity graphs, and reduces the computational storage requirements.

Note that, although much work has been done to utilize zero-energy spins for the exploration of ground states, these efforts have been either restricted to describe only local structures within the individual minima<sup>[15]</sup> or while grouping entire minima do not distinguish between the different types that these groupings can occur.<sup>[16–19]</sup> The classification of entire structures, i.e., of connected points of the configuration space representing connected minima structures of equal

Dr. K. Biswas  
 Department of Physics and Astronomy  
 Texas A&M University  
 College Station, TX 77843-4242, USA  
 E-mail: katja\_schaefer@me.com

 The ORCID identification number(s) for the author(s) of this article can be found under <https://doi.org/10.1002/pssb.202000610>.

DOI: 10.1002/pssb.202000610

energy, is new in our work. Note further that it is precisely this classification of entire minima that allows for a conclusive intuitive drawing of disconnectivity graphs and gives further information into the structure of the energy landscape and the arrangement and size of its subcomponents relative to each other. This in turn may enable an intuitive approach to understanding the effectiveness of optimization routines, as for example for use in benchmarking optimization procedures.<sup>[20–27]</sup>

This article is structured in the following way. In Section 2 the classification scheme is briefly described; the application to  $\pm 1$  and  $\pm 1, \pm 2$  models of spin glasses is described in Section 3, which is divided into describing the model and method (Section 3.1) and the computationally obtained results (Section 3.2).

## 2. Classification of States

A minimum is a configuration of the spins in which no single spin flip will lower the energy of the system. However, there can still be spins for which the local energy is zero and which can be flipped without an increase in energy (i.e., zero-energy spins). A flipping of the zero-energy spin constitutes a new minimum. These connected minima form structures of equal energy on the energy landscape, which we distinguish based on the accessibility of the minima within the structures. We merge these structures into single representations. This allows visualizing highly degenerate energy landscapes of spin glasses in a reduced way without losing the core information. Though originating from local structures, our classification aims to merge minima states of the system to reduce the description and enhance the intuitive access to potential energy landscapes of highly degenerate spin-glass systems.

For this purpose, we distinguish between four types of minima. These are regular minima, type-1 dales, type-2 dales, and type-3 dales. Regular minima are minima for which any spin flip would increase the energy of the system. They are shown in the disconnectivity graphs by black vertical lines. Type-1 dales are minima in which there exists at least one spin that can be flipped without increasing the energy of the system. If there is more than one zero-energy spin, then the additional condition for the type-1 dale is that these spins can be flipped at any combination without an increase in the energy of the system. Type-2 dales are minima with at least two zero-energy spins and the restriction that only certain combinations of flipping the zero-energy spins preserve the energy of the system. In complex spin-glass structures, a necessary condition for this to occur is that at least two of the zero-energy spins are neighboring to each other. By neighboring, we mean spins that have a direct interaction in energy. Finally, type-3 dales are minima on the energy landscape that are connected via zero-energy pathways that cannot be arbitrarily traversed; for example, before joining the outermost minima a series of zero-energy spin flips has to be finished. A detailed description and examples of local structures for the types of dales can be found in Biswas and Katzgraber.<sup>[28]</sup> In the disconnectivity graphs, type-1 dales are shown by blue vertical lines, type-2

dales by green vertical lines, and type-3 dales by red horizontal lines. We chose this depiction of type-3 dales to highlight that they consist of type-1 or type-2 dales which are joined by dependent pathways.

## 3. Results

### 3.1. Method

We studied the  $\pm 1$  and  $\pm 1, \pm 2$  type spin glasses on a square lattice with nearest-neighbor interaction and periodic boundary conditions consisting of 36 spins. The Hamiltonian for these systems is

$$H = -\frac{1}{2} \sum_{i,j} L_{ij} s_i s_j \quad (1)$$

where  $L_{ij}$  denotes the interaction energy between the individual spins  $s_i$ , which can take values either up or down, i.e.,  $s_i \in \{-1, +1\}$ . The values for  $L_{ij}$  are drawn randomly, with equal probability, from the discrete distributions  $\{-1, +1\}$  (for the  $\pm 1$  model) and  $\{-2, -1, +1, +2\}$  (for  $\pm 1, \pm 2$ ). To account for the huge variety of individual systems that can be built under such conditions, we generated 100 systems of each type. The resulting analysis of the disconnectivity graphs are taken from the average of these systems.

The minima of the systems have been obtained using complete enumeration of the configuration space, and for the barriers, the procedure of Garstecki et al.<sup>[11]</sup> was followed. Note that the number of configurations that need to be checked via complete enumeration scales as  $2^N$ , with  $N$  being the number of spins.

### 3.2. Computational Results

Figure 1 shows examples of the disconnectivity graphs for our sample systems. The minima (vertical bars) are joined via their lowest energy barrier depicted by the crossing points in the disconnectivity graphs. The horizontal bars on the right side of the disconnectivity graphs show, at their respective energy levels, the average number of individual minima of the different types.

As shown in Figure 1 (left), this particular example of the  $\pm 1$  spin glass has only dales, but no regular minima. That is, there are no isolated individual minima of the system. Further, the minima occupy three energy levels with the ground state at  $H = -56$  and the excited states at  $H = -52$  and  $H = -48$ . The ground and the first excited state are type-1 dales, whereas the second excited state has type-1, type-2, and type-3 dales. The minimum energy needed to cross from the ground to the first excited state is  $H = -48$ . However, to cross to the second excited state or between minima of the second excited state, an energy of  $H = -44$  is necessary. The same minimum energy is necessary to flip between the two ground-state dales. Note that the symmetry between the dales is due to the symmetry in energy arising from the flipping of all spins. Due to the high-dimensional nature of the energy landscape, this is predominantly seen in the arrangements and connections of the ground states, but can only be hinted at higher energy states due to the limitations

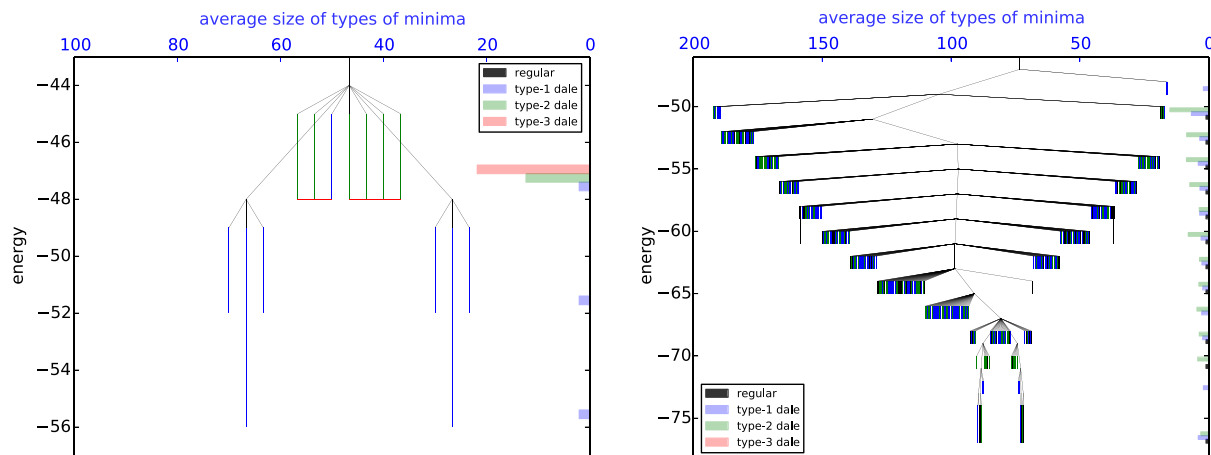


**Figure 1.** Example of the disconnectivity graphs of the 36-spin  $\pm 1$  model (left) and  $\pm 1, \pm 2$  model (right). The black vertical lines indicate regular minima. The blue vertical lines indicate type-1 dales, and type-2 dales are indicated by green vertical lines. The horizontal lines (red) joining two or more minima dales are type-3 dales. The vertical bars on the right side indicate the average number of minima that constitute the individual dales at their respective energy levels.

of projections from higher-dimensional to lower-dimensional space.

An example for the disconnectivity graph of the  $\pm 1, \pm 2$  spin model is shown in Figure 1 (right). As can be seen, this model system has 14 different energy states, in which the ground state consists of regular minima, type-1 dales, and type-2 dales. In this particular example, no type-3 dales were observed.

**Figure 2** shows the distribution of the minima for both of the models. The energy values are given with respect to the ground state. The vertical bars indicate the standard deviation. With respect to the ground state, the  $\pm 1$  model shows only up to three energy states. For this model, particularly for the ground state, the standard deviation is very high, reflective of the observation that in our sample systems we observed that some systems had just one energy state, some had two, and some three energy states. For the  $\pm 1$  model, the ground state had the highest occurrence.

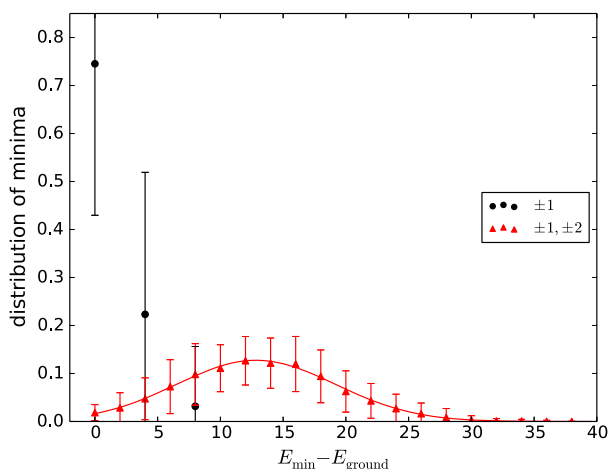


**Figure 2.** Distribution of minima relative to the ground state for the 36-spin  $\pm 1$  and  $\pm 1, \pm 2$  models.

**Figure 3** shows the distribution of the types of minima for the  $\pm 1$  (left) and  $\pm 1, \pm 2$  (right) models. These are drawn at their respective energies and not relative to the ground state energy (which can be different for different systems). This explains the difference in the number of depicted energies in this figure compared to Figure 2. As shown in Figure 3, type-2 dales were dominating for the  $\pm 1$  model and type-1 dales for the  $\pm 1, \pm 2$  model. The results indicate that at the local level the  $\pm 1$  model has more connected zero-energy spins than the  $\pm 1, \pm 2$  model. Connected zero-energy spins are a precondition for type-2 dales to occur. The dominant occurrence of type-1 dales in the  $\pm 1, \pm 2$  model indicates that most of the minima have isolated zero-energy spins, which occurs less in the  $\pm 1$  model. Regular minima are a rare occurrence for the  $\pm 1$  model, which indicates that there are only very few minima with no zero-energy spins. Note that the Gaussian fits are only guides to the eye and do not reflect a direct physical meaning as these systems can only exhibit discrete energies. In both the systems medium energies had the highest occurrence for all the types of minima, with on average a low occurrence at low- or high-energy states.

**Figure 4** shows the average size of the types of minima at their respective energies. With size, we understand the number of individual minima that make up the types. For example, because regular minima their size is always one. Type-1 dales always have at least size two, which is reflective of the occurrence of at least one zero-energy spin. For the  $\pm 1$  model, a size of two was only observed at low energies, whereas higher energies had a larger size. For the  $\pm 1, \pm 2$  model only very low energies and very high energies had the size two of type-1 dales, and greater for all other energies. This corresponds to having at least two or more isolated zero-energy spins in the individual minima. Further, we observed that type-2 dales have on average a larger size than type-1 dales and regular minima and type-3 dales have the largest size.

Interesting in the analysis is also the distribution of ground states. Note that our sample consisted of 100 systems for each of the  $\pm 1$  and  $\pm 1, \pm 2$  models. This accounts for the observation

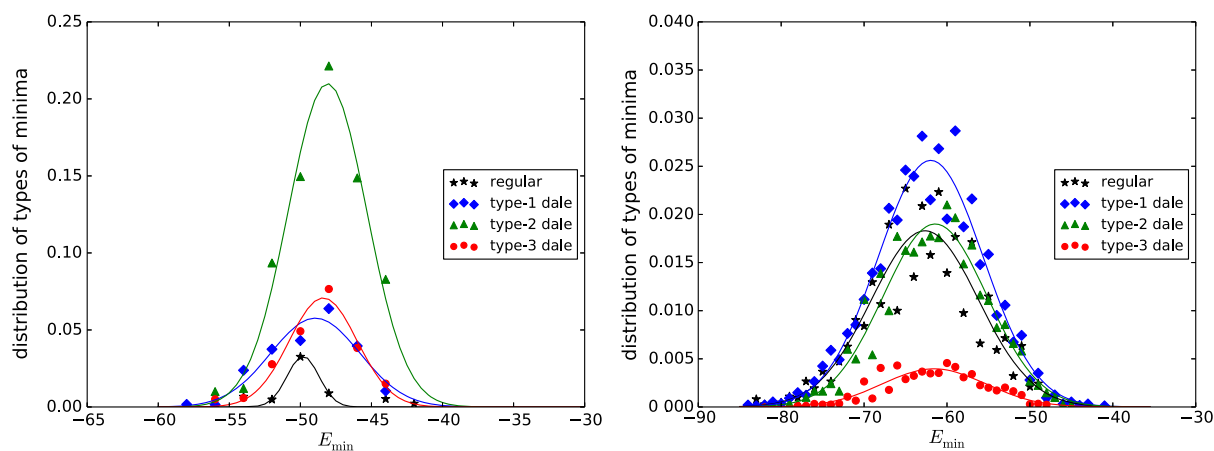


**Figure 3.** Distribution of types of minima at their respective energy levels for the 36-spin  $\pm 1$  (left) and  $\pm 1, \pm 2$  (right) models. The black stars denote regular minima, the blue diamonds type-1 dales, the green triangles type-2 dales, and the red dots type-3 dales. The fit lines are for guidance of the eye only.

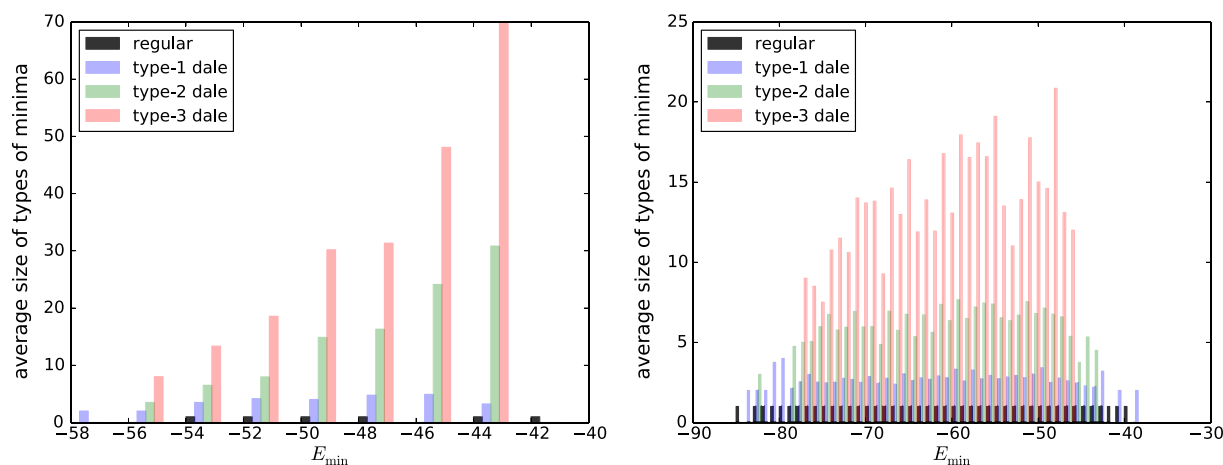


**Figure 4.** Average size of the types of minima for the 36-spin  $\pm 1$  (left) and  $\pm 1, \pm 2$  (right) models. The black bars denote regular minima, the blue bars type-1 dales, the green bars type-2 dales, and the red bars type-3 dales.

that the energies of the ground state are distributed over a range of  $H = -58$  to  $H = -44$  for the  $\pm 1$  model, and range from  $H = -85$  to  $H = -61$  for the  $\pm 1, \pm 2$  model. **Figure 5** and **6** show the distribution of the types of minima and the size of types of minima at their respective ground-state energies. As shown in **Figure 5** the  $\pm 1, \pm 2$  model exhibits lower ground-state energies than the  $\pm 1$  model. This is due to the higher value of the bonds. Further, as already seen in **Figure 2–4** the  $\pm 1$  model only exhibits energies that are even integers, whereas in the  $\pm 1, \pm 2$  model the observed energy range also includes odd integers. This is because the local contributions of energies pertaining to a single spin can only add up to even integers for the  $\pm 1$  model, but allow for uneven integers in the  $\pm 1, \pm 2$  model (As the total energy of the system can be calculated as the sum over local contributions to the energies, it is sufficient to look at the possible combinations locally. As an example of the occurrence of uneven integer energies in the  $\pm 1, \pm 2$  model, consider a spin that has the four neighbor bonds  $\{+2, +1, +1, +1\}$ . If its neighboring spins

are all pointing in the same direction, its energy will be an uneven integer, whereas for the  $\pm 1$  model there does not exist a single configuration of bonds and spin arrangements that would allow for energies of uneven integers). Overall, in the  $\pm 1$  model the ground state was made up by 8.95% regular minima, 22.73% type-1 dales, and 68.32% type-2 dales. Of the total number of ground states,  $\approx 60.33\%$  were connected by directional paths and formed type-3 dales (Note that, as type-3 dales consist of type-1 and type-2 dales joined via directional paths, they are taken separately into account in the calculation of the percentages.). This is different from the  $\pm 1, \pm 2$  model, where 36.29% of the minima were regular minima, 40.79% type-1 dales, 22.92% type-2 dales, and only 7.24% of the total ground state minima formed type-3 dales. Further, as shown in **Figure 5** (left) and **6** (left) only at four energies regular minima were observed, namely, at  $H = -54, -52, -50$ , and  $-44$ , with an occurrence of only 0.06% at  $H = -44$ . Type-2 dales had the highest occurrence. This is different from the  $\pm 1, \pm 2$  model, where



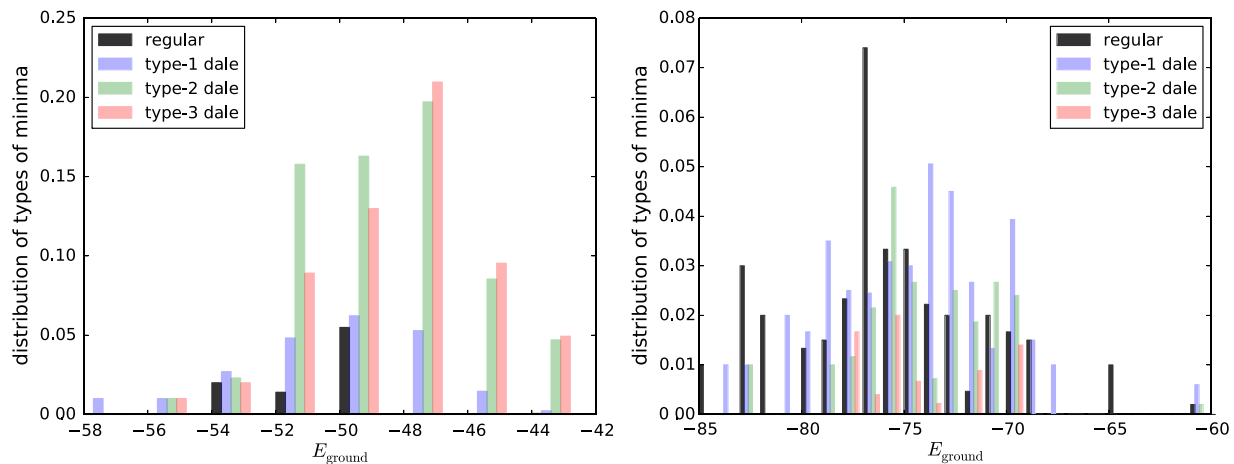


**Figure 5.** Distribution of types of minima at their ground state energy for the 36-spin  $\pm 1$  (left) and  $\pm 1, \pm 2$  (right) models. The black bars denote regular minima, the blue bars type-1 dales, the green bars type-2 dales, and the red bars type-3 dales.

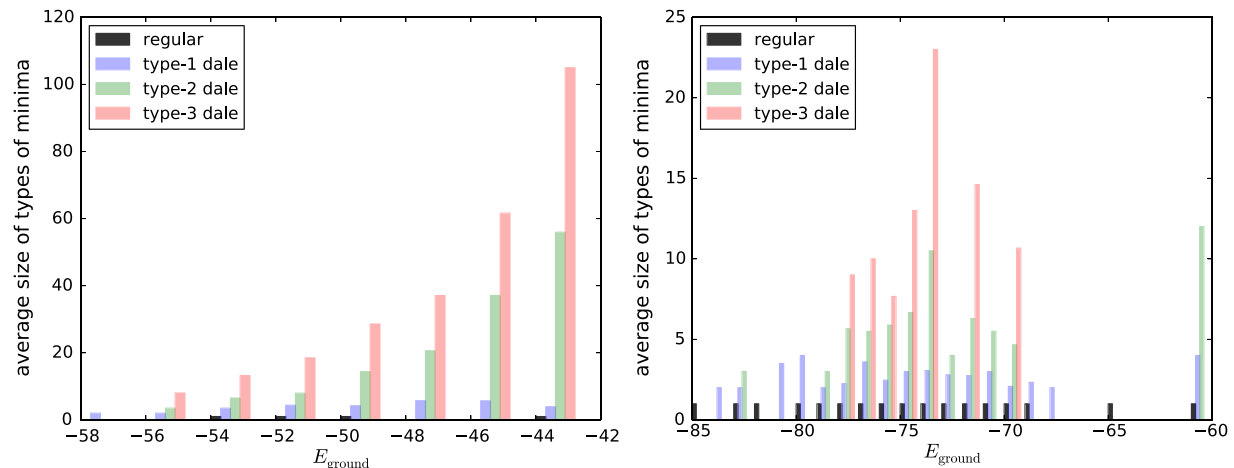


**Figure 6.** Average size of the types of minima at the ground state for the 36-spin  $\pm 1$  (left) and  $\pm 1, \pm 2$  (right) models. The black bars denote regular minima, the blue bars type-1 dales, the green bars type-2 dales, and the red bars type-3 dales.

type-1 dales occurred most in the ground state followed by regular minima and type-2 dales, and only at medium ground-state energies type-3 dales were observed; see Figure 5 (right). Notable for the  $\pm 1$  model is also that the size of the ground-state dales increases with increasing energy, indicating that at very low energies the minima are more sharply defined, i.e., have smaller dale structures.

**Table 1** shows for the  $\pm 1$  and  $\pm 1, \pm 2$  models the average number of minima  $\mathcal{N}$  and their percentage occurrence  $\% \mathcal{N}$  in the reduced disconnectivity graph. The average number of actual minima (i.e., counting every minimum individually) and their corresponding percentage occurrence for the systems are given by  $\mathcal{N}^*$  and  $\% \mathcal{N}^*$ , and their respective sizes by  $S$ . Note that the occurrences of the type-3 dales do not contribute to the percentages because these consist of type-1 and type-2 dales that are joined together. Their respective occurrences and sizes for the two models are just given for comparison. As can be seen from

the table, in the reduced description, type-2 dales had the highest occurrence for the  $\pm 1$  model and type-1 dales for  $\pm 1, \pm 2$ . However, taken together with their respective sizes, the actual number of minima forming into type-2 dales was highest for both the models. That is, it was found that on average the actual number of type-2 dales is 189.76 for the  $\pm 1$  model, and 584.48 for the  $\pm 1, \pm 2$  model, whereas in the reduced description on average only 10.11 type-2 dales occurred for the  $\pm 1$  model, and 86.59 for the  $\pm 1, \pm 2$  model. This leads to a percentage reduction  $\% \mathcal{R}$  of 94.67% for the  $\pm 1$  model and 85.19% for the  $\pm 1, \pm 2$  model. Note that regular minima do not reduce in our description because they already consist of isolated minima. The total number of minima in our description, which is on average 14.08 for the  $\pm 1$  model and 293.25 for the  $\pm 1, \pm 2$  model, is representative of an actual number of individual minima of 202.12 and 1009.46, respectively. Thus, in total, we gain with our classification a reduction of 93.03% for the  $\pm 1$  model, and 70.95%

**Table 1.** Number of the minima types  $\mathcal{N}$  in the reduced description, percentage of the minima  $\%\mathcal{N}$  in the reduced description, average size of minima types  $S$ , actual number of minima types  $\mathcal{N}^*$ , percentage of the actual number of minima  $\%\mathcal{N}^*$ .  $\%\mathcal{R}$  represents the percentage by which the number of minima is reduced with our classification, i.e.,  $\%\mathcal{R} = 1 - \mathcal{N}/\mathcal{N}^*$ . The values are averages obtained from our samples of 100 systems for the two studied  $\pm 1$  and  $\pm 1, \pm 2$  models of spin glasses.

	Regular	Type-1 dale	Type-2 dale	Type-3 dale
$\pm 1$	–	–	–	–
$\mathcal{N}$	0.85	3.12	10.11	4.71
$\%\mathcal{N}$	6.04	22.16	71.80	
$S$	1	3.69	18.77	33.25
$\mathcal{N}^*$	0.85	11.51	189.76	156.61
$\%\mathcal{N}^*$	0.42	5.69	93.88	–
$\%\mathcal{R}$	0	72.89	94.67	–
$\pm 1, \pm 2$	–	–	–	–
$\mathcal{N}$	87.36	119.30	86.59	18.48
$\%\mathcal{N}$	29.79	40.68	29.53	
$S$	1	2.83	6.75	11.4
$\mathcal{N}^*$	87.36	337.62	584.48	210.67
$\%\mathcal{N}^*$	8.65	33.45	57.90	–
$\%\mathcal{R}$	0	64.66	85.19	–

for the  $\pm 1, \pm 2$  model. This is a significant advantage, and was also already observed on tile-planted spin glasses.<sup>[28]</sup>

## 4. Conclusion

We used enhanced disconnectivity graphs to study models of spin glasses consisting of 36 spins with  $\pm 1$  and  $\pm 1, \pm 2$  interactions. In the disconnectivity graphs, we used our classification of different types of minima, namely, regular minima, type-1 dales, type-2 dales, and type-3 dales. The classification is based on the accessibility of the minima to each other and represents the various ways in which minima can be connected via zero-energy spin flips. This greatly enhanced the intuitive understanding of the disconnectivity graphs, drastically reduced the necessary depiction of minima energy lines, and allowed for a further in-depth investigation into their energy structure.

The results obtained with our enhanced disconnectivity graphs showed that for the  $\pm 1$  model type-2 dales dominated, whereas for the  $\pm 1, \pm 2$  model type-1 dales occurred the most. Further, all of the types of minima had the highest occurrence at medium energy levels, indicating the range and difficulties that need to be overcome with optimization procedures. Note, our analysis showed that on average for the  $\pm 1$  model type-2 dales were formed by  $\approx 18.8$  individual minima, and for  $\pm 1, \pm 2$  by  $\approx 6.8$  individual minima, whereas the sizes for type-1 dales were 3.7 and 2.8, respectively. Thus, our enhanced description also reduced the number of minima that have to be displayed and stored by 93% for the  $\pm 1$  model and 71% for the  $\pm 1, \pm 2$  model. Information on these dales is given by a bar chart

in the disconnectivity graphs, which show their respective sizes at the corresponding energy levels.

Note that this classification is new and, as such, the effects the system size has on the occurrence and size of the dales is not yet known. As the number of spin configurations scales as  $2^N$ , larger system sizes require checking  $2^{49}$ ,  $2^{64}$ ,  $2^{81}$ , ... configurations for minima and their corresponding barriers. This is only possible in a larger systematic and computationally intensive study, but might give further insights into fundamental concepts and relationships concerning the energy structure of spin glasses.

Our classification can be used to understand the effectiveness of optimization procedures, which is important for benchmarking problems. In addition, a similar classification of minima might also be applied to materials systems and could lead to new insights into their complex energy structure.

## Acknowledgements

The author would like to thank Prof. H. Katzgraber for discussions. This research is based upon work supported in part by the Office of the Director of National Intelligence (ODNI), Intelligence Advanced Research Projects Activity (IARPA), via MIT Lincoln Laboratory Air Force Contract No. FA8721-05-C-0002. The views and conclusions contained herein are those of the author and should not be interpreted as necessarily representing the official policies or endorsements, either expressed or implied, of ODNI, IARPA, or the US Government. The US Government is authorized to reproduce and distribute reprints for governmental purpose notwithstanding any copyright annotation thereon. The author thanks the Texas A&M University for providing high-performance computing resources.

## Conflict of Interest

The author declares no conflict of interest.

## Data Availability Statement

The data that support the findings of this study are available from the author upon reasonable request.

## Keywords

disconnectivity graphs, energy landscapes, spin glasses

Received: December 14, 2020

Revised: March 8, 2021

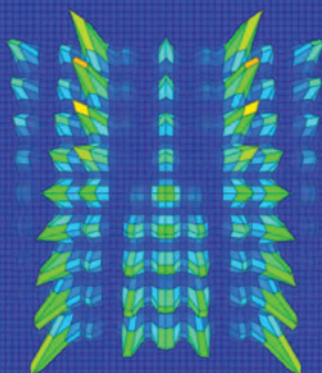
Published online: April 15, 2021

- [1] D. Wales, *Energy Landscapes: Applications to Clusters, Biomolecules and Glasses*, Cambridge University Press, Cambridge **2004**.
- [2] O. M. Becker, M. Karplus, *J. Chem. Phys.* **1997**, 106, 1495.
- [3] C. L. Brooks, J. N. Onuchic, D. J. Wales, *Science* **2001**, 293, 612.
- [4] D. J. Wales, *Phys. Biol.* **2005**, 2, S86.
- [5] Z. Burda, A. Krzywicki, O. C. Martin, Z. Tabor, *Phys. Rev. E* **2006**, 73, 036110.
- [6] Z. Burda, A. Krzywicki, O. C. Martin, *Phys. Rev. E* **2007**, 76, 051107.
- [7] J. Krawczyk, S. Kobe, *Physica A* **2002**, 315, 302.
- [8] J. Dall, P. Sibani, *Eur. Phys. J. B* **2003**, 36, 233.
- [9] J. F. Fontanari, P. F. Stadler, *J. Phys. A* **2002**, 35, 1509.
- [10] W. Hordijk, J. F. Fontanari, P. F. Stadler, *J. Phys. A* **2003**, 36, 3671.

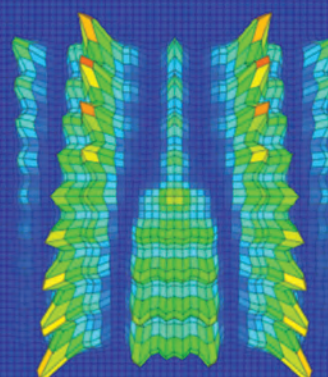
- [11] P. Garstecki, T. X. Hoang, M. Cieplak, *Phys. Rev. E* **1999**, 60, 3219.
- [12] H. Seyed-allaei, H. Seyed-allaei, M. R. Ejtehadi, *Phys. Rev. E* **2008**, 77, 031105.
- [13] Q. Zhou, W. H. Wong, *Phys. Rev. E* **2009**, 79, 051117.
- [14] Q. Zhou, *Phys. Rev. Lett.* **2011**, 106, 180602.
- [15] J. W. Landry, S. N. Coppersmith, *Phys. Rev. B* **2002**, 65, 134404.
- [16] A. K. Hartmann, *J. Phys. A: Math. Gen.* **2000**, 33, 657.
- [17] A. K. Hartmann, *Phys. Rev. E* **2000**, 63, 016106.
- [18] A. K. Hartmann, F. Ricci-Tersenghi, *Phys. Rev. B* **2002**, 66, 224419.
- [19] A. Mann, A. K. Hartmann, *Phys. Rev. E* **2010**, 82, 056702.
- [20] I. Hen, J. Job, T. Albash, T. F. Rønnow, M. Troyer, D. A. Lidar, *Phys. Rev. A* **2015**, 92, 042325.
- [21] F. Hamze, D. C. Jacob, A. J. Ochoa, D. Perera, W. Wang, H. G. Katzgraber, *Phys. Rev. E* **2018**, 97, 043303.
- [22] D. Perera, F. Hamze, J. Raymond, M. Weigel, H. G. Katzgraber, *Phys. Rev. E* **2020**, 101, 023316.
- [23] V. Martin-Mayor, I. Hen, *Sci. Rep.* **2015**, 5, 15324.
- [24] H. G. Katzgraber, F. Hamze, R. S. Andrist, *Phys. Rev. X* **2014**, 4, 021008.
- [25] M. Weigel, H. G. Katzgraber, J. Machta, F. Hamze, R. S. Andrist, *Phys. Rev. X* **2015**, 5, 019901.
- [26] W. Wang, S. Mandrà, H. G. Katzgraber, *Phys. Rev. E* **2017**, 96, 023312.
- [27] J. Marshall, V. Martin-Mayor, I. Hen, *Phys. Rev. A* **2016**, 94, 012320.
- [28] K. Biswas, H. G. Katzgraber, arXiv:2004.12431 [cond-mat.dis-nn], **2020**.



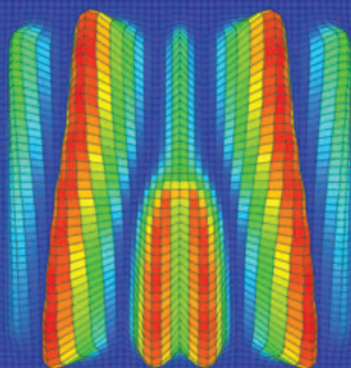
$W = 1$



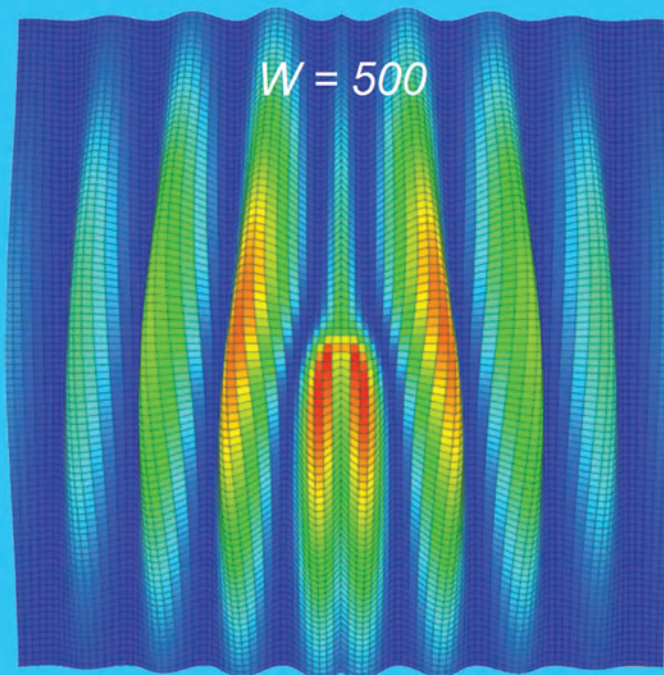
$W = 2$



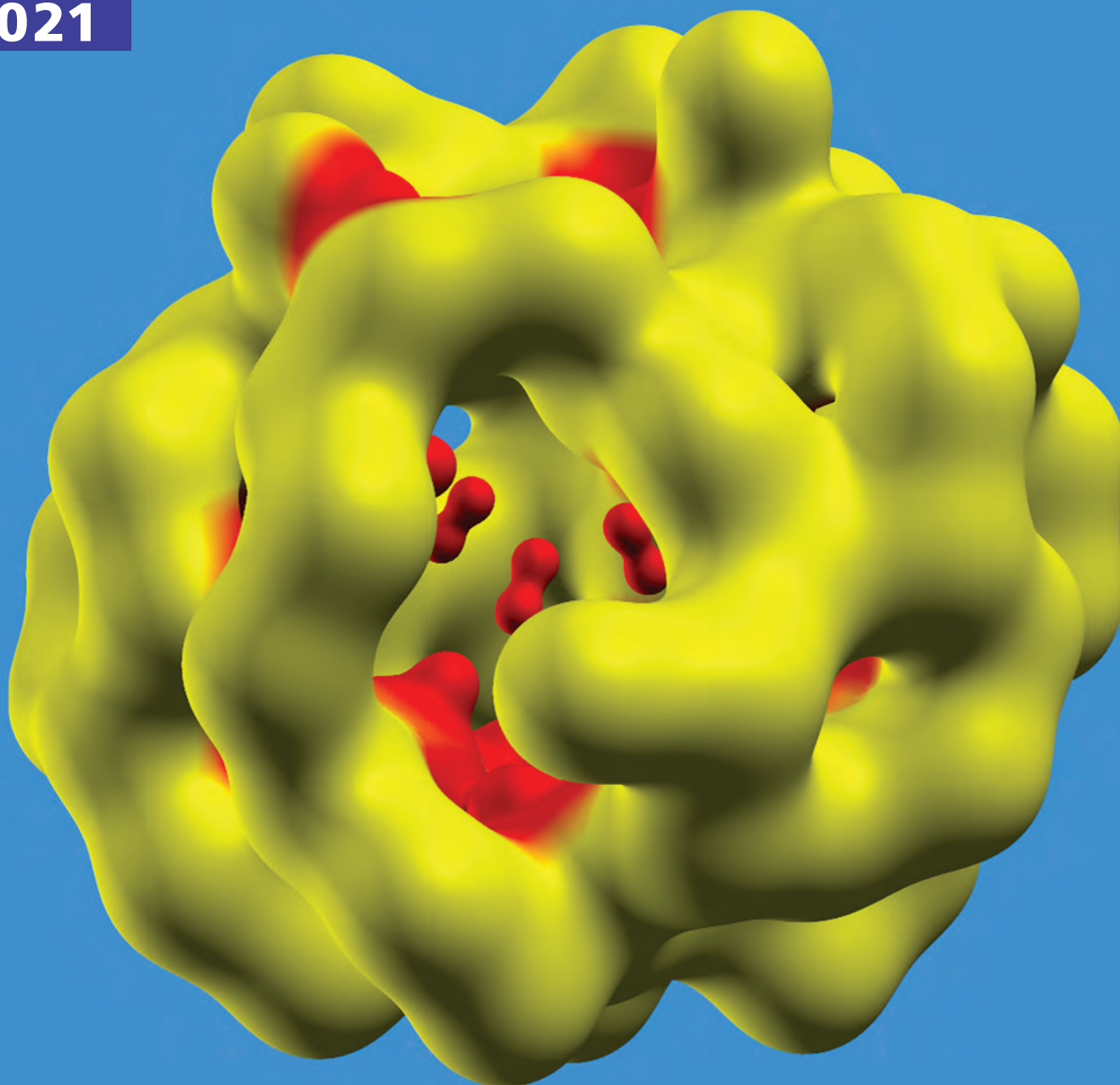
$W = 6$



$W = 500$







Ab Initio Hydrogen Dynamics and the Morphology of Voids  
in Amorphous Silicon

Parthapratim Biswas and Dil Limbu

WILEY-VCH